FUNCTIONALIZED NANOCARRIERS FOR THERANOSTICS

EDITED BY: Stefano Leporatti, Andrea Ragusa and Rawil Fakhrullin
PUBLISHED IN: Frontiers in Bioengineering and Biotechnology

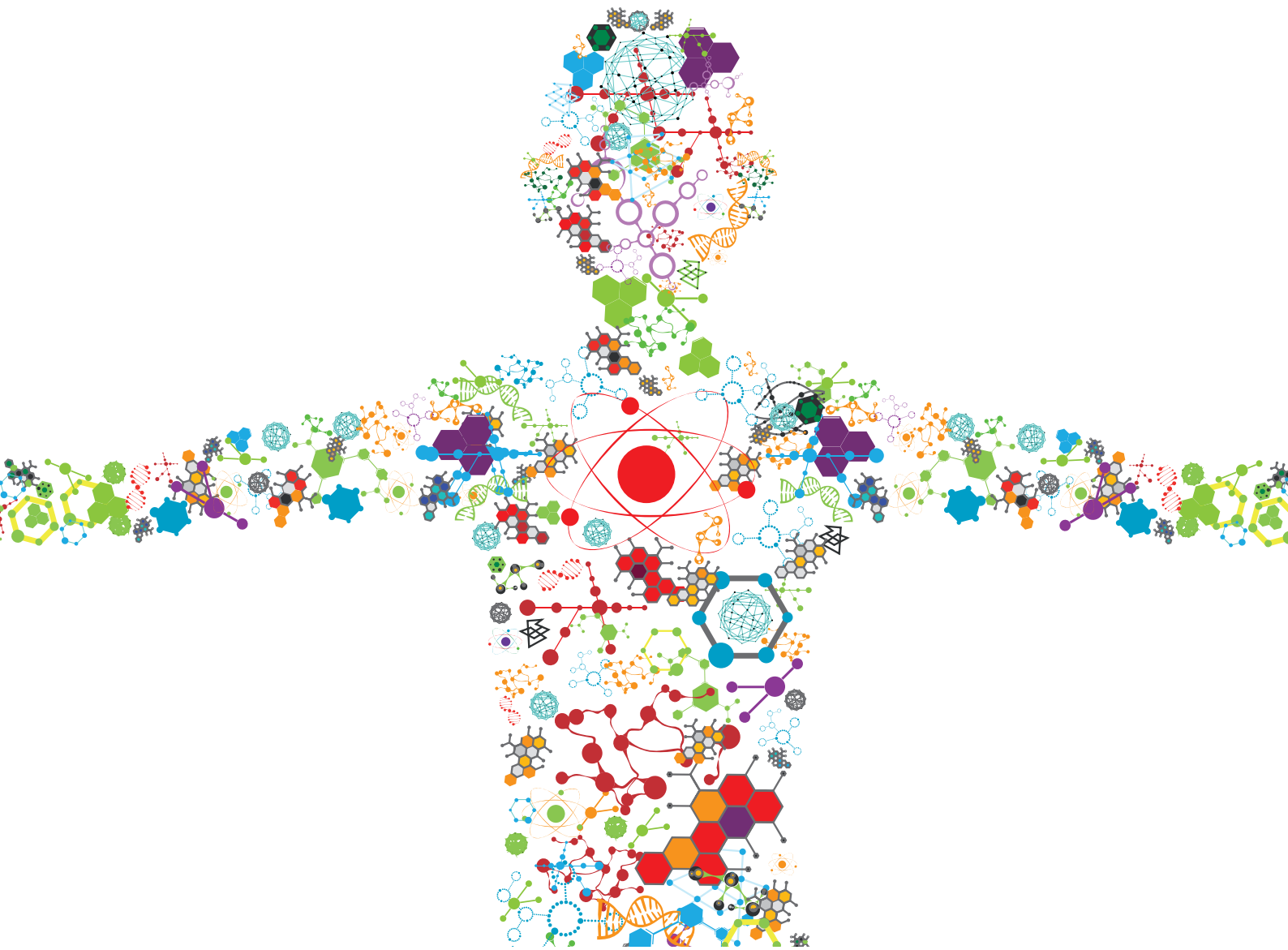

frontiers Research Topics

frontiers

ISSN 1664-8714
ISBN 978-2-88966-318-7
DOI 10.3389/978-2-88966-318-7

About Frontiers

Frontiers is more than just an open-access publisher of scholarly articles: it is a pioneering approach to the world of academia, radically improving the way scholarly research is managed. The grand vision of Frontiers is a world where all people have an equal opportunity to seek, share and generate knowledge. Frontiers provides immediate and permanent online open access to all its publications, but this alone is not enough to realize our grand goals.

Frontiers Journal Series

The Frontiers Journal Series is a multi-tier and interdisciplinary set of open-access, online journals, promising a paradigm shift from the current review, selection and dissemination processes in academic publishing. All Frontiers journals are driven by researchers for researchers; therefore, they constitute a service to the scholarly community. At the same time, the Frontiers Journal Series operates on a revolutionary invention, the tiered publishing system, initially addressing specific communities of scholars, and gradually climbing up to broader public understanding, thus serving the interests of the lay society, too.

Dedication to Quality

Each Frontiers article is a landmark of the highest quality, thanks to genuinely collaborative interactions between authors and review editors, who include some of the world's best academicians. Research must be certified by peers before entering a stream of knowledge that may eventually reach the public - and shape society; therefore, Frontiers only applies the most rigorous and unbiased reviews.
Frontiers revolutionizes research publishing by freely delivering the most outstanding research, evaluated with no bias from both the academic and social point of view. By applying the most advanced information technologies, Frontiers is catapulting scholarly publishing into a new generation.

What are Frontiers Research Topics?

Frontiers Research Topics are very popular trademarks of the Frontiers Journals Series: they are collections of at least ten articles, all centered on a particular subject. With their unique mix of varied contributions from Original Research to Review Articles, Frontiers Research Topics unify the most influential researchers, the latest key findings and historical advances in a hot research area! Find out more on how to host your own Frontiers Research Topic or contribute to one as an author by contacting the Frontiers Editorial Office: researchtopics@frontiersin.org

FUNCTIONALIZED NANOCARRIERS FOR THERANOSTICS

Topic Editors:
Stefano Leporatti, Italian National Research Council, Italy
Andrea Ragusa, University of Salento, Italy
Rawil Fakhrullin, Kazan Federal University, Russia

Citation: Leporatti, S., Ragusa, A., Fakhrullin, R., eds. (2021). Functionalized Nanocarriers for Theranostics. Lausanne: Frontiers Media SA.
doi: 10.3389/978-2-88966-318-7

Table of Contents

frontiers in Bioengineering and Biotechnology

EDITORIAL
published: 10 November 2020
doi: 10.3389/fbioe.2020.616574

Editorial: Functionalized Nanocarriers for Theranostics

Stefano Leporatti[1]*, *Andrea Ragusa*[1,2] and *Rawil Fakhrullin*[3]

[1] Consiglio Nazionale delle Ricerche CNR-Nanotec, Istituto di Nanotecnologia, c\o Campus Ecotekne, Lecce, Italy, [2] Department of Biological and Environmental Sciences and Technologies, University of Salento, Lecce, Italy, [3] Institute of Fundamental Medicine and Biology, Kazan Federal University, Kazan, Russia

Keywords: nanocarriers, theranostics, nanomedicine, nanosystems, nanoplatforms

Editorial on the Research Topic

Functionalized Nanocarriers for Theranostics

Nanotechnology has led to the development of a variety of nanocarriers with applications in diagnosis and therapy, giving rise to novel theranostic nano-tools. They combine diagnostic and therapeutic moieties into a single nano-device, potentially allowing an early detection of the pathology together with targeted treatment.

Our Research Topic has gathered several contributions describing novel functionalized nano-transporters, such as targeted nanoparticles (NPs), nanovesicles (NVs), liposomes (LPs), and nano-clays, for combined diagnosis and therapy. Eleven articles have been collected with a well-balanced ratio: five are comprehensive reviews and the other six are original research articles.

Among a plethora of different nanomaterials available to fabricate drug delivery systems (DDSs) for cancer therapy and diagnosis, poly(D,L-lactic-*co*-glycolic acid) (PLGA) has been extensively used due to its biocompatibility and biodegradability. In a comprehensive review article, Shen et al. report the employment of PLGA-based DDSs for remotely triggered cancer therapy, including photo-triggered, ultrasound-triggered, magnetic field-triggered, and radiofrequency-triggered cancer therapy, involving photodynamic therapy (PDT), photothermal therapy (PTT), and photo-triggered chemotherapeutics release. The state-of-the-art in theranostic approaches involving mesoporous silica nanoparticles (MSNs) for treating hepatocellular carcinoma (HCC) has been reviewed by Tao et al. In this work, they outline the recent advances in MSNs-based systems for HCC therapy and diagnosis and they also discuss the precision delivery strategies of MSNs in liver cancer.

The signature service and insoluble network formation of the peptide self-assemblies as hydrogels have drawn a plethora of research activity among scientists all over the globe in the past decades. In this respect, Gupta et al. review the last 5-year efforts on novel approaches for the design and development of single molecule amino acids, ultra-short peptide self-assemblies (di- and tri-peptides only) and their derivatives as drug/gene carriers and tissue-engineering systems. Peptides and small molecule-based nanostructures can be convenient alternatives for therapeutic delivery due to their good biocompatibility and their easy design, synthesis, and functionalization. These properties render their self-assembled nanostructures smart tools suitable for biomedical applications (Gupta et al.).

Parodi et al. overview the recent development of smart nanotheranostic systems responsive to pathological stimuli, including oxidative stress, altered pH, enzymatic expression, and reactive biological molecules. Therapeutic and diagnostic properties can be included in the same molecule embedded in the nanocarrier structure that can be activated at the injury site, or they can independently derive from different chemicals loaded into and/or conjugated onto the surface of the NPs.

OPEN ACCESS

Edited and reviewed by:
Gianni Ciofani,
Italian Institute of Technology (IIT), Italy

Correspondence:
Stefano Leporatti
stefano.leporatti@nanotec.cnr.it

Specialty section:
This article was submitted to Nanobiotechnology, a section of the journal Frontiers in Bioengineering and Biotechnology

Received: *12 October 2020*
Accepted: *16 October 2020*
Published: *10 November 2020*

Citation:
Leporatti S, Ragusa A and Fakhrullin R (2020) Editorial: Functionalized Nanocarriers for Theranostics. Front. Bioeng. Biotechnol. 8:616574. doi: 10.3389/fbioe.2020.616574

Currently, the onset of neurodegenerative diseases (NDs) is strongly widespread due to the increasing age of the world population and the lack of efficient therapies. In a state-of-the-art review article, Cascione et al. overview the lipid-based drug delivery improvements in *in vivo* applications against NDs. Lipid carriers have a good ability to deliver both hydrophobic and hydrophilic molecules through the Blood-Brain Barrier (BBB), demonstrating an enhanced efficacy of the drug following liposomal encapsulation.

The six original research articles contributions describe novel tailored nano-carriers for drug delivery applied to cancer and neurodegenerative diseases treatment. Two of them are dealing with the use of functionalized halloysite nanotubes (HNTs) as efficient drugs/active molecules nano-transporters (Guryanov et al.; Saleh et al.). Guryanov et al. report on prodigiosin-loaded halloysite-based nanoformulation (p-HNTs) and its effects on cell viability. By comparing the effects of p-HNTs on malignant (Caco-2, HCT116) and non-malignant (MSC, HSF) cells, the authors demonstrate selective cytotoxic and genotoxic activity. Moreover, in another very interesting and prospective article, Saleh et al. proposed the use of HNT nanocarriers to penetrate the BBB and effectively deliver the payload over an extended time period. On the other hand, the Sukhorukov's group tried to address the delivery of neuropeptides on-demand, potentially suitable for the migratory or axonal guidance of human nerve cells, by using polylactic acid (PLA)-based microchamber arrays (MCAs) (Sindeeva et al.). Optical targeting of microchambers for drug release triggered functional cell response locally.

The last three contributed articles are reporting the use of different type of NPs for delivering and releasing drug against different type of tumors. In this respect, Zacheo et al. developed lipid NVs of size varying from 100 up to 300 nm and successfully loaded them with fluorophores molecules (DOP-F-DS and a fluorescent protein), inorganic nanoparticles (quantum dots and magnetic NPs), and anti-cancer drugs (SN-38 and doxorubicin).

The synthesis and the functionalization of gold NPs with cancer-specific biomolecules may represent a winner strategy for a selective and targeted tumor-phototherapy. With this in mind, Bloise et al. described a simple approach for the synthesis of extra-small gold NPs for breast cancer therapy. Extra-small gold nanospheres stabilized with a thiol-functionalized polyamidoamine (AGMA1) and trastuzumab were synthesized and tested *in vitro* as nanovectors for breast cancer targeted drug delivery. They proposed to assemble small Au NPs into larger structures through controllable interparticle interactions by using AGMA1, with the final aim to enhance the absorption of NIR light (Bloise et al.).

To improve chemo-drug therapeutic efficiency and overcome issues such as inadequate response rates, high toxicity, severe side effects due to non-specific targeting of anti-cancer drugs, and the development of multidrug resistance during prolonged treatment, a multifunctional NP was developed to effectively target and treat melanoma by Yaman et al.. PLGA NPs were coated with a cellular membrane derived from the T-cell hybridoma, 19LF6 endowed with a melanoma-specific anti-gp100/HLA-A2 T-cell receptor (TCR) and loaded with trametinib, an FDA-approved melanoma chemotherapeutic drug.

AUTHOR CONTRIBUTIONS

SL wrote the editorial, which was revised, proofed, and accepted by all the authors.

ACKNOWLEDGMENTS

SL and AR are grateful to the Tecnopolo per la medicina di precisione (TecnoMed Puglia)—Regione Puglia: DGR no. 2117 del 21/11/2018, CUP: B84I18000540002 and Tecnopolo di Nanotecnologia e Fotonica per la medicina di precisione (TECNOMED)—FISR/MIUR-CNR: delibera CIPE no. 3449 del 7-08-2017, CUP: B83B17000010001. RF was funded by the Russian Foundation for Basic Research grant #18-29-11031 mk.

Conflict of Interest: The authors declare that the research was conducted in the absence of any commercial or financial relationships that could be construed as a potential conflict of interest.

frontiers in Bioengineering and Biotechnology

ORIGINAL RESEARCH
published: 04 March 2020
doi: 10.3389/fbioe.2020.00132

Extra-Small Gold Nanospheres Decorated With a Thiol Functionalized Biodegradable and Biocompatible Linear Polyamidoamine as Nanovectors of Anticancer Molecules

Nora Bloise[1,2], Alessio Massironi[3], Cristina Della Pina[4], Jenny Alongi[5], Stella Siciliani[6], Amedea Manfredi[5], Marco Biggiogera[6], Michele Rossi[4], Paolo Ferruti[5], Elisabetta Ranucci[5]* and Livia Visai[1,2]**

[1] Department of Molecular Medicine (DMM), Biochemistry Unit, Center for Health Technologies (CHT), UdR INSTM University of Pavia, Pavia, Italy, [2] Department of Occupational Medicine, Toxicology and Environmental Risks, Istituti Clinici Scientifici Maugeri S.p.A, IRCCS, Pavia, Italy, [3] Department of Chemistry and Industrial Chemistry, University of Pisa, UdR INSTM PISA, Pisa, Italy, [4] Dipartimento di Chimica, Università degli Studi di Milano e CNR-ISTM, Milan, Italy, [5] Dipartimento di Chimica, Università degli Studi di Milano, Milan, Italy, [6] Department of Biology and Biotechnology, University of Pavia, Pavia, Italy

OPEN ACCESS

Edited by:
Stefano Leporatti,
Italian National Research Council, Italy

Reviewed by:
Martin J. D. Clift,
Swansea University, United Kingdom
Sílvia Castro Coelho,
University of Porto, Portugal

***Correspondence:**
Cristina Della Pina
cristina.dellapina@unimi.it
Elisabetta Ranucci
elisabetta.ranucci@unimi.it
Livia Visai
livia.visai@unipv.it

Specialty section:
This article was submitted to Nanobiotechnology, a section of the journal Frontiers in Bioengineering and Biotechnology

Received: 29 November 2019
Accepted: 10 February 2020
Published: 04 March 2020

Citation:
Bloise N, Massironi A, Della Pina C, Alongi J, Siciliani S, Manfredi A, Biggiogera M, Rossi M, Ferruti P, Ranucci E and Visai L (2020) Extra-Small Gold Nanospheres Decorated With a Thiol Functionalized Biodegradable and Biocompatible Linear Polyamidoamine as Nanovectors of Anticancer Molecules. Front. Bioeng. Biotechnol. 8:132. doi: 10.3389/fbioe.2020.00132

Gold nanoparticles are elective candidate for cancer therapy. Current efforts are devoted to developing innovative methods for their synthesis. Besides, understanding their interaction with cells have become increasingly important for their clinical application. This work aims to describe a simple approach for the synthesis of extra-small gold nanoparticles for breast cancer therapy. In brief, a biocompatible and biodegradable polyamidoamine (named AGMA1-SH), bearing 20%, on a molar basis, thiol-functionalized repeat units, is employed to stabilize and coat extra-small gold nanospheres of different sizes (2.5, 3.5, and 5 nm in gold core), and to generate a nanoplatform for the link with Trastuzumab monoclonal antibody for HER2-positive breast cancer targeting. Dynamic light scattering, transmission electron microscopy, ultraviolet visible spectroscopy, X-ray powder diffraction, circular dichroism, protein quantification assays are used for the characterization. The targeting properties of the nanosystems are explored to achieve enhanced and selective uptake of AGMA1-SH-gold nanoparticles by *in vitro* studies against HER-2 overexpressing cells, SKBR-3 and compared to HER-2 low expressing cells, MCF-7, and normal fibroblast cell line, NIH-3T3. *In vitro* physicochemical characterization demonstrates that gold nanoparticles modified with AGMA1-SH are more stable in aqueous solution than the unmodified ones. Additionally, the greater gold nanoparticles size (5-nm) is associated with a higher stability and conjugation efficiency with Trastuzumab, which retains its folding and anticancer activity after the conjugation. In particular, the larger Trastuzumab functionalized nanoparticles displays the highest efficacy (via the pro-apoptotic protein increase, anti-apoptotic components decrease, survival-proliferation pathways downregulation) and internalization (via the activation of the classical clathrin-mediated

endocytosis) in HER-2 overexpressing SKBR-3 cells, without eliciting significant effects on the other cell lines. The use of biocompatible AGMA1-SH for producing covalently stabilized gold nanoparticles to achieve selective targeting, cytotoxicity and uptake is completely novel, offering an important advancement for developing new anticancer conjugated-gold nanoparticles.

Keywords: cancer cell targeting, polyamidoamines, Trastuzumab, gold nanoparticles, breast cancer nanomedicine

INTRODUCTION

Breast cancer is the most frequent and invasive cancer type in women (Rojas and Stuckey, 2016). There is an increasing demand for novel, efficient and specific diagnostic and medical tools to face the adverse side-effects of the traditional ones. Some invasive forms of breast cancer (i.e. locally advanced breast cancer) presented a twofold higher incidence than the others, suggesting an urgent improvement of Trastuzumab (Herceptin^{TM}) delivery toward erbB2 tyrosine kinase receptor (HER-2) found overexpressed in ∼25%–30% of breast cancers (Sawaki et al., 2006). Engineered delivery systems based on gold nanoparticles (AuNPs) are particularly promising to address this problem. AuNP formulations are employed for a wide range of medical applications, including contrast and photothermal agents for computed tomography (CT) and tumor photothermal ablation, respectively (Mieszawska et al., 2013). Their chemical and physical properties, that span the broader visible to near-infrared, ensure them features such as low toxicity, high stability, easy synthesis and conjugation with cancer-specific biomolecules (Lee et al., 2014; Carnovale et al., 2016). It is generally agreed that physicochemical differences in nanoparticles such as particle size, shape, surface charge and surface coating could vary the way particles are recognized, processed and excreted by the body (Carnovale et al., 2016). Notably, the molecular rules governing these properties are poorly understood, and the different set-up conditions used in the different laboratories (such as cell types, dosage schedule, measurement methods) make it difficult to drawing valid and conclusive information. Experimental and theoretical studies stated that the optimal size for AuNPs cellular uptake ranges from 25 to 50 nm, since it stimulates efficiently membrane wrapping and receptor-ligand interaction to drive the NPs into the cell (Gao et al., 2005; Jiang et al., 2008; Dreaden et al., 2012; Panariti et al., 2012; Saw et al., 2018). Surface charge can also have an effect on the cellular uptake (Zhang et al., 2015). Interacting with negative cell membranes, the electropositive nanoparticles exhibited a higher cellular uptake efficiency compared to electronegative ones. Conjugation of AuNPs with targeting molecules effectively improves the tumor target delivery (Paciotti et al., 2004). Several studies reported that Trastuzumab could be successfully immobilized on gold nanoparticles to improve their interactions with SKBR3 breast cancer cells, overcome Trastuzumab resistance and detect breast cancer (Hainfeld et al., 2006; Bickford et al., 2008; Chattopadhyay et al., 2010; Carpin et al., 2011; Lee et al., 2014). *In vitro* experiments indicated that, while human skin cells proliferated in the presence of Trastuzumab-conjugated gold nanoparticles, most of the breast cancer cells died (Rathinaraj et al., 2015). Despite the broad interest surrounding gold-based nanosystems, reproducibility, toxicity and excretion concerns limit their clinical translations (Choi et al., 2007; Lewinski et al., 2008; Tam et al., 2010). Indeed, currently no gold nanoparticles have yet been approved by the FDA agency. Different biodegradable polymers were tested for assembling and coating gold nanoparticles clusters (Tam et al., 2010), while minimizing immunogenicity reactions. Cheheltani et al. (2016) proposed a small, excretable AuNP-based platform, encapsulated into biodegradable poly di(carboxylatophenoxy)phosphazene (PCPP) nanospheres. A study by Tam et al. (2010) reported polymer/inorganic nanoclusters combining the imaging contrast and therapeutic capabilities with the biodegradability of a polymer stabilizer. Linear polyamidoamines (PAAs) have recently emerged as promising tools for drug delivery as they offer key advantages due to their ease of formulation and biodegradability (Ferruti et al., 2005; Jacchetti et al., 2008; Ferruti, 2013; Mauro et al., 2013). PAAs were previously investigated as anticancer drug carriers (Lavignac et al., 2009). In particular, the PAA nicknamed AGMA1 can be used as a potential non-viral, non-toxic and efficient vector for the intracellular delivery of siRNA and DNA (Cavalli et al., 2010; Cavalli et al., 2017). Interestingly, AGMA1, containing tert-amine, carboxyl and guanidine groups, whose repeat unit is reminiscent of the arg-gly-asp (RGD) peptide motif (Franchini et al., 2006), a well-known fibronectin sequence mediating cell attachment, can act as an excellent cell adhesion and proliferation substrate (Gualandi et al., 2016). For *in vivo* applications, gold-based nanosystems should be larger than 6 nm in diameter to ensure long blood circulation, hence accumulation in diseased tissues but slowly breaking down into sub-6 nm components for rapidly excretion via the kidneys (Arruebo et al., 2007; Choi et al., 2007). The goal of the present study was to develop more efficient gold nanoparticles for therapeutic use. To this purpose, a biocompatible and biodegradable polyamidoamine bearing 20%, on a molar basis, randomly distributed SH pendants (AGMA1-SH, indicated also as "P") was employed to stabilize AuNPs of different sizes, that is 2.5, 3.5, and 5 nm in Au core (Au@P), decorated with Trastuzumab (Au@PT), whose hydrodynamic diameter was suitable for a cellular uptake (**Figure 1**). AGMA1, besides being a biocompatible and biodegradable polymer, was found to be easily internalized in cells and, therefore,

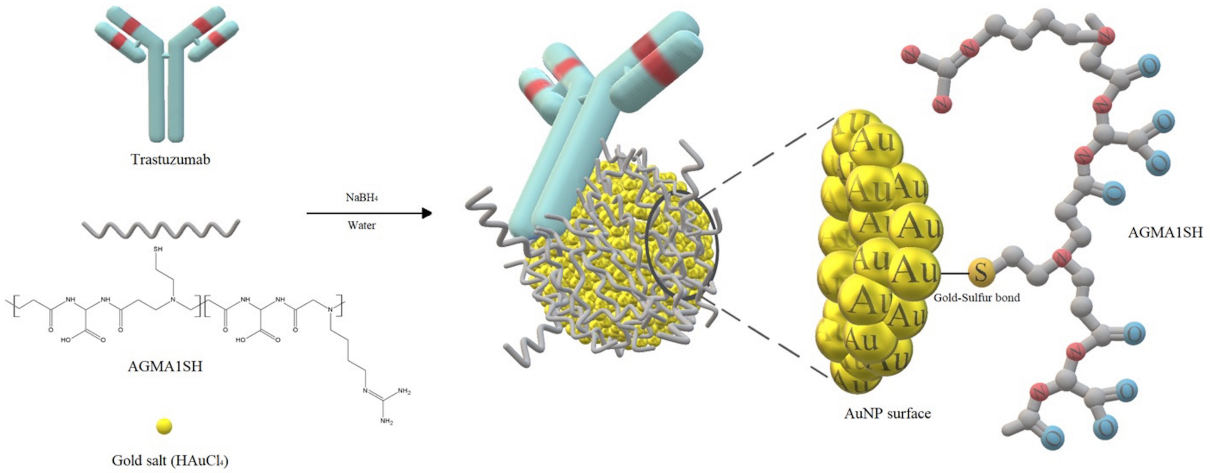

FIGURE 1 | Schematic representation of AuNPs coated with AGMA1-SH and Trastuzumab.

it can be expected to facilitate the AuNPs cellular uptake (Franchini et al., 2006; Cavalli et al., 2010), whereas thiol groups are supposed to stabilize the AGMA1-gold bond by the renowned S-Au soft-soft interaction. Once tested *in vivo*, it is reasonable to speculate that, because of the AGMA1 biodegradability, the small Au core component (ranging from 2.5 to 5 nm) may be the only one to be extruded by the urinary system. In this work, the impact size of Au@P nanoparticles on the interactions with both breast cancer cells, and healthy cells was systemically studied. The cytotoxicity and cellular uptake of all nanoparticles were studied by MTT and ICP-MS tests. Western blot analysis and cellular uptake studies by means of specific endocytosis inhibitors were further carried out to explore the interaction with and mechanism of internalization of Au@PT by SKBR-3 target cells.

MATERIALS AND METHODS

Reagents

4-Aminobutylguanidine sulfate (97%), lithium hydroxide monohydrate (99%), cystamine hydrochloride (96%), 2-mercaptoethanol (99%) and calcium chloride (97%) were purchased from Sigma-Aldrich and used as provided. 2,2-Bis(acrylamido)acetic acid (96%) was synthesized as previously described (Ferruti et al., 1999). $HAuCl_4$ solution (composition: 17 wt.% Au; concentration: 30 wt.% in dilute HCl) was purchased from Sigma-Aldrich and diluted with water to achieve a final Au concentration of 10 mg/mL. $NaBH_4$ (>96% pure), purchased from Sigma-Aldrich, was employed as the reducing agent for Au^{3+} to colloidal gold dispersion (10 mg/mL). Activated carbon Vulcan XC72R (specific area = 254 m^2 g^{-1}, pore volume = 0.19 mL g^{-1}) from CABOT was used as a supporting material for colloidal samples for XRPD analysis. MilliQ water obtained by an Academic A-10 Millipore apparatus was employed as a solvent for all aqueous solutions. Trastuzumab (Herceptin®, Roche) was kindly provided by the Chemotherapic section of Policlinico San Matteo (Pavia). For Western blot analyses, primary mouse monoclonal anti β-actin was purchased from Santa Cruz Biotechnology, mouse monoclonal anti-ERK1/2 and rabbit polyclonal anti-phospho ERK1/2 (Thr 202/204) from Abcam, rabbit monoclonal anti-AKT and rabbit polyclonal anti-phospho -AKT (Ser 473) from Cell Signaling Technologies (Danvers, MA, United States) and rabbit monoclonal anti-BAX and anti-BCL-XL from Thermo Fisher Scientific. Horseradish peroxidase (HRP)-conjugated secondary antibodies anti-mouse and anti-rabbit (Dako) anti-human (Tebu-bio) were used, and detection was performed by enhanced chemiluminescent substrate (ECL) solutions (Pierce Thermo Fisher Scientific, Rockford, IL, United States).

Instruments

^1H and ^{13}C NMR spectra were run on a Brüker Advance 400 spectrometer operating at 400.132 (^1H) and 100.623 (^{13}C) MHz. Size exclusion chromatography (SEC) traces were obtained with a Knauer Pump 1000 equipped with a Knauer Autosampler 3800, TSKgel G4000 PW and G3000 PW TosoHaas columns connected in series, Light Scattering (LS) Viscotek 270 Dual Detector, UV detector Waters model 486, operating at 230 nm, and a refractive index detector Waters model 2410. The mobile phase was a 0.1 M Tris buffer pH 8.00 (0.05 M with 0.2 M sodium chloride (Bignotti et al., 1994). The operational conditions were: sample concentration 20 mg/mL; flow rate 1 μL/min; injection volume 20 μL; column dimensions 300 × 7.5 mm^2, temperature 25°C. The instrument constants were determined using PEO 19 kDa as a narrow polymer standard. All samples were filtered through a 0.2 μm syringe Whatman filter before measurements.

Synthesis of AGMA1-SH

2,2-Bis(acrylamido)acetic acid (4.128 g, 20.0 mmol) and lithium hydroxide monohydrate (1.53 g, 36.0 mmol) were dissolved in water (18 mL) and 4-aminobutylguanidine (agmatine) sulfate (3.765 g, 16.0 mmol) was added under vigorous stirring. The reaction mixture was heated up to 40°C until dissolution and

kept under nitrogen atmosphere at room temperature with gentle stirring for 1 day (d). After this time, the reaction mixture was cooled down to room temperature and cystamine dihydrochloride (0.469 g, 2.0 mmol) and lithium hydroxide monohydrate (0.170 g, 4 mmol) were added. The resultant mixture was kept at room temperature for 10 days until a soft transparent hydrogel was obtained. Then water (40 mL) and excess mercaptoethanol (8.0 mL) were added until a clear solution was obtained. This was diluted with water (100 mL), acidified to pH 4.5 with 37% hydrochloric acid and then ultrafiltered through a membrane with nominal molecular weight cut-off 3000. The final product was retrieved by freeze-drying the retained fraction. Yield 68%, $\bar{M}n = 8400$, PDI = 1.25.

^{1}H NMR (D_2O): δ (ppm) = 1.52–1.60 (br, $NCH_2CH_2C\underline{H}_2$); 1.71–1.77 (br, $NCH_2C\underline{H}_2$); 2.64–2.76 (br, $NHCOC\underline{H}_2$); 2.92–2.94 (m, $C\underline{H}_2S$); 3.08–3.20 (m, $NCOCH_2C\underline{H}_2N$); 3.34–3.47 (br, $NC\underline{H}_2CH_2CH_2$ and $NC\underline{H}_2CH_2S$); 5.51–5.56 (s, $C\underline{H}COOH$).

^{13}C NMR (D_2O): d (ppm) = 18.5 ($\underline{C}H_2S$); 22.3 ($NCH_2CH_2\underline{C}H_2$); 25.0 ($NCH_2\underline{C}H_2$); 29.0 ($NHCO\underline{C}H_2$); 40.4 ($CH_2\underline{C}H_2NH$); 49.1 ($N\underline{C}H_2CH_2CONH$); 52.5 ($N\underline{C}H_2CH_2CH_2CH_2NH$); 54.8 ($N\underline{C}H_2CH_2S$); 56.0 ($\underline{C}HCOOH$); 155.1 ($H_2N\underline{C}=NH$); 171.3 ($NH\underline{C}O$); 173.5 ($\underline{C}OOH$).

Synthesis of Gold Nanoparticles Decorated With AGMA1-SH and Trastuzumab

Three differently sized colloidal samples of AGMA1-SH-coated gold nanoparticles decorated with Trastuzumab (Herceptin®), were prepared by varying gold solution concentration from 20 ppm to 400 ppm. The samples were labeled as 2.5Au@PT, 3.5Au@PT, and 5Au@PT, where the number indicates the average diameter of gold *core* (2.5, 3.5, and 5.0 nm, respectively), P means the polymer (AGMA1-SH) and T the antibody drug (Trastuzumab). Accordingly, the following parameters were optimized to produce stable colloidal nanosystems over time: gold solution concentration (20 ppm for 2.5Au@PT, 200 ppm for 3.5Au@PT, and 400 ppm for 5Au@PT), AGMA1-SH:Au:Trastuzumab ratio (1wt.:1wt.:1wt.) and $NaBH_4$:Au ratio (1wt.:1wt.). More in detail, proper aliquots of AGMA1-SH aqueous solution (10 mg/mL) were added under stirring to defined volumes of $HAuCl_4$ aqueous solution (10 mg/mL Au) and MilliQ® water at room temperature. Established amounts of freshly prepared $NaBH_4$ aqueous solution (10 mg/mL) were rapidly added under vigorous stirring to reduce Au^{3+} to Au^0 and, hence, produce light-tea to reddish colored colloidal dispersions. Finally, proper volumes of Trastuzumab aqueous solution (20 mg/mL) were poured drop wise. Only in the case of the 5Au@PT sample, sodium borohydride was added prior to the polymer in order to allow gold nanoparticles to grow up to 5.0 nm. **Supplementary Table S1** reports the established aliquots for each component. At the end of reaction, to remove the excess of synthesis reagents or/and to eliminate unbound antibody, each AuNPs solution was purified by dialysis for 24 h in a Float-A-Lyzer Spectra/Por G2 (MWCO of 100 kDa for Au@PT) under stirring at 4°C.

Synthesis of Gold Nanoparticles Decorated With AGMA1-SH or Trastuzumab

Three differently sized AuNP@AGMA1-SH colloidal samples without the drug (Trastuzumab) and three differently sized AuNP@Trastuzumab colloidal samples without the polymer (AGMA1-SH) were synthesized adopting the aforementioned procedure. The following parameters were optimized in order to produce stable colloidal nanosystems: gold solution concentration (20 – 400 ppm), AGMA1-SH:Au or Trastuzumab:Au ratios (1wt.:1wt.) and $NaBH_4$:Au ratio (1wt.:1wt.). The samples were labeled as 2.5Au@P, 3.5Au@P, 5Au@P and 2.5Au@T, 3.5Au@T, 5Au@T respectively. **Supplementary Table S1** reports the established aliquots for each component. At the end of reaction, to remove the excess of synthesis reagents each AuNPs solution was purified by dialysis for 24 hours (h) in a Float-A-Lyzer Spectra/Por G2 (MWCO 10 kDa for Au@P and 100 kDa for Au@T, respectively) under stirring at 4°C. As evinced by microscopic analyses (TEM), AuNPs were synthesized in uniform spherical sizes. Hence, by using the simple geometrical model of spherical particles (Eq. 1–6), the theoretical Trastuzumab molecule to gold nanoparticle ratio (T/AuNP) could be determined for the three differently sized nanosystems. Accordingly, T/AuNP = 0.65 for '2.5Au' samples, 1.79 for '3.5Au' samples and 5.21 for '5Au' samples. In addition, extrapolating the fraction of gold atoms lying at the surface (*gold dispersion* from **Supplementary Figure S1**) led to the theoretical Trastuzumab molecule to gold surface atom ratio (T/surface Au) for the three differently sized samples:

T/surface Au = 0.0025 for '2.5Au' samples, 0.0039 for '3.5Au' samples and 0.0054 for '5Au' samples.

$$volume\ AuNP = \frac{4}{3}\pi r^3 \quad (r \text{ is Au nanoparticle radius } = 1.25, 1.75, \text{ and } 2.5 \text{ nm respectively}) \quad (1)$$

$$mass\ AuNP = volume\ AuNP \times \rho \quad (\rho \text{is Au density} = 19.3\ g/cm^3) \quad (2)$$

$$number\ AuNP = \frac{mass\ Au\ in\ the\ sample}{mass\ AuNP} \quad (3)$$

$$moles\ AuNP = mass\ AuNP / atomic\ weight\ Au \quad (4)$$

$$atoms\ AuNP = moles\ AuNP \times Avogadro's\ number \quad (5)$$

$$surface\ atoms\ AuNP = gold\ dispersion\ (\%) \times atoms\ AuNP \quad (\textit{Gold dispersion} \text{ is 55\% for '2.5Au', 35\% for '3.5Au' and 25\% for '5Au'}) \quad (6)$$

Physicochemical Characterization

Dynamic light scattering (DLS) and Z-potential analyses were carried out on 1 mg/mL nanoparticle aqueous suspensions prepared using MilliQ water, with a Malvern Zetasizer NanoZS

instrument equipped with a laser fitted at 532 nm and fixed 173° scattering angle. Before analyses, samples were filtered through a 0.2 μm syringe Whatman filter. The solution pH was adjusted to the selected value, using 0.1 M HCl or 0.1 M NaOH aqueous solutions. Measurements were performed in triplicate, and the reported values averaged over of 10 runs. Regarding DLS measurements on AGMA1-SH-coated gold nanoparticles decorated with Trastuzumab (Au@PT), AGMA1-SH-coated gold nanoparticles (Au@P) and Trastuzumab-coated gold nanoparticles (Au@Trastuzumab), 20 mg/L aqueous suspensions were analyzed. X-ray powder diffraction (XRPD) analyses were performed employing a Rigaku D III-MAX horizontal-scan powder diffractometer with Cu Kα radiation (λ = 1.5418 Å) to determine the average size of gold crystallites using the *Scherrer* equation (Patterson, 1939). The *Bragg* angle was rotated in the 34°– 43° 2θ interval and the mean diameter d of gold *core* was determined considering the peak at $2\theta = 38.5°$, typical of metallic gold. All the colloidal samples were immobilized on XC72R carbon to obtain the theoretical amount of 1% Au. UV-vis spectra were collected in the 200–800 nm region using a HP 8453 diode array instrument on colloidal samples (20 ppm Au) for determining the plasmon resonance band (PRB) of gold nanoparticles detected near 500–530 nm in the 2–10-nm-diameter range.

Transmission Electron Microscopy

TEM analysis was performed by using a JEOL JEM 3010 operating at a 300-kV acceleration voltage. Briefly, 10 μL of each type of gold nanoparticle suspension in water (20 μg/mL) deposed on Parlodion™ membranes.

Efficiency of Trastuzumab Conjugation

The efficiency of Trastuzumab conjugation to nanoparticles was assessed by indirect (Bicinchoninic Acid, BCA), and direct (dot-blot) approaches as previously described (Liu et al., 2010; Zhou et al., 2015; Di Francesco et al., 2018; Codullo et al., 2019). In short, both Au@PT and Au@T nanoparticles suspensions (20 μg/mL) were centrifuged at 3000 × g for 15 min, then the supernatants were collected for determine the unbound Trastuzumab concentration by BCA assay (Pierce Biotechnology Inc., Rockford, IL, United States), while the pellets were re-suspended in 1 mL of MilliQ water for dot blot assay.

BCA Assay

The unbound content in the resulting solution was determined by BCA assay according to the specifications of the manufacturer. The unbound amounts were calculated from properly drawn Trastuzumab calibration curve. Trastuzumab amount conjugated to nanoparticles was thus obtained via reduction of the amount in the supernatant from the initial amount. The percentage of conjugation efficiency (CE) was calculated as follows (Martínez-Jothar et al., 2019):

$$\%\ CE = \frac{(total\ amount\ of\ T\ added\text{-}unbound\ T)}{total\ amount\ of\ T\ added} * 100$$

Dot Blot Assay

Different amounts of Trastuzumab-functionalized Au@P differently sized were spotted on nitrocellulose membrane Amersham Hybond ECL, GE Healthcare Life Sciences, Pittsburgh, PA, United States) and air-dried. 2.5Au@P, 3.5Au@P, 5Au@P as negative controls. In parallel, Au@T samples dot blot was also performed. The non-specific sites were blocked by soaking the membrane in 5% BSA in TBS containing 0.05% Tween 20 for 1 h at room temperature (RT). The membrane was then incubated using goat anti-human-HRP-conjugated antibody (1:1000) for 1 h at RT and after extensive washing developed with enhanced chemiluminescence reagents (LI-COR) and ImageQuant LAS4000 Imaging System (Ge Healthcare). The spots were then analyzed with ImageQuant TL software (Ge Healthcare) and the results were normalized to calibration curve containing known amounts of Trastuzumab.

Circular Dichroism

The secondary structure of the Trastuzumab free (20 μg/mL) and Trastuzumab-conjugated gold nanoparticles (20 μg/mL) were evaluated with circular dichroism (CD). CD spectra were measured using Jasco J710 spectropolarimeter (Jasco Corp., Tokyo, Japan) at 25°C and in a 1 cm path-length quartz cell under the following conditions: 300–190 nm spectral range, 2 nm of bandwidth, 200 nm min-1 of scan speed and 3 accumulation. Data was processed using 10-point smoothing in Origin 6.0 (OriginLab Corporation, Northampton, MA, United States).

In vitro Trastuzumab Release From Gold Nanoparticles Decorated With AGMA1-SH

2.5Au@PT, 3.5Au@PT, and 5Au@PT (20 μg) were suspended in 1 mL of MilliQ water, in a low-protein binding centrifuge tube, and kept at room temperature. At select time points (1 – 15 days), each type of nanoparticles suspension was centrifuged, the supernatant was collected and replaced with the same volume of fresh release medium (Colzani et al., 2018). The concentration of antibody in the supernatants was determined using the BCA Kit as described above. Standard curve of Trastuzumab was used to determine antibody concentrations in each sample. The results are expressed as the percentage of cumulative fraction of Trastuzumab released at each time point compared to the conjugated amount. The *in vitro* release of 2.5Au@T, 3.5Au@T, and 5Au@T was not analyzed due to the higher aggregation recorded immediately within the first days after their synthesis.

Cell Types and Culture Conditions

HER2 positive breast adenocarcinoma cells (SKBR-3), ERα positive breast adenocarcinoma cells (MCF-7) used as cancer negative control, murine fibroblasts cells (NIH-3T3) used as negative control. All cell lines were obtained from the American Type Culture Collection (HTB85, ATCC, Manassas, VA, United States). After thawing, SKBR-3 cell line was cultured in McCoy's 5A Medium Modified (Sigma-Aldrich), 10% of Fetal Bovine Serum (FBS, EuroClone), 1% of L-Glutamine

(Lonza), 2% sodium pyruvate (Lonza), 0.4% antibiotics (Lonza) and 0.1% fungizone. MCF-7 cell line was cultured in Minimum Essential Medium Eagle (Sigma-Aldrich), 10% of Fetal Bovine Serum (EuroClone), 1% sodium pyruvate (Lonza), 1% Non-Essential Aminoacids (EuroClone), 1% Bovine Insulin (Sigma-Aldrich), 1% L-Glutamine (Lonza) and 0.4% antibiotics (Lonza). NIH-3T3 cell line was cultured in Dulbecco's Modified Eagle Medium High Glucose 4.5 mg/mL (Sigma-Aldrich), 10% of Bovine Calf Serum (BCS, EuroClone) and 1% of L-Glutamine (Lonza). All cell lines were incubated at 37°C in 5% CO_2, routinely trypsinized (Trypsin EDTA solution 1X, Lonza) after confluence, counted and seeded into wells.

Stability of AuNPs Upon Incubation With Cell Culture Media by Dynamic Light Scattering

Prior to all biological investigations, each suspension of AGMA1-SH-coated gold nanoparticles decorated with Trastuzumab (2 μg/mL) was centrifuged and resuspended in the cell culture media appropriate for the corresponding cell line, containing 10% of serum, and incubated at physiological temperature (37°C), without shaking, to mimic cell culture conditions (Halamoda-Kenzaoui et al., 2015; Marişca and Leopold, 2019). Size change was tracked by serial DLS size measurements at 0 (directly after dispersion in the complex media) and after 4 h of incubation.

Cell Viability

Cells were seeded at 1×10^4 viable cells/well on 96-well plates and incubated for 24 h (to allow cells to attach to the well). After the culture medium removal, cells were incubated with media containing increasing concentration of each types of gold nanoparticles. At fixed incubation times, the quantitative 3-[4,5-dimethylthiazol-2-yl]-2,5 diphenyl tetrazolium bromide (MTT, Sigma Aldrich, St. Louis, MO, United States) assay was performed to assess the dehydrogenase activity, as an indicator of the metabolic state of cells, as previously described (Merli et al., 2018). The cell viability was expressed as percentage related to the control (untreated) set equal to 100%. At day 3 of incubation, a qualitative viability assay [fluorescein diacetate (FDA) assay] was performed on SKBR-3 untreated (ctrl), treated with T free (2 μg/mL), 2.5Au@PT (2 μg/mL) and 5Au@PT (2 μg/mL), as previously described (Bloise et al., 2013).

Scanning Electron Microscopy (SEM)

For morphological evaluation all types of cells were seeded on plastic cell culture coverslip disks (Thermanox Plastic, Nalge Nunc International, Rochester, NY, United States), then incubated or not with nanoparticles suspensions (2 μg/mL) and treated as previously described (Bloise et al., 2013). Before observation, samples were sputter coated with gold and observed using a Field Emission Scanning Electron Microscope (FESEM Supra 25, Zeiss).

Uptake Studies by Inductively Coupled Plasma Mass Spectrometry (ICP-MS)

All types of cell lines were plated (500000/well) on a 6-well plate and treated for 1 and 3 days with 2 μg/mL of each types of nanoparticles (2 mL volume added in each well). After treatments, cells were washed three times with PBS to eliminate the NPs which were not internalized in cells, trypsinized, counted and centrifuged in order to obtain the cellular pellet. The cellular pellet was treated with 1X RIPA buffer (diluting the 10X RIPA in sterile distilled water, EDM Millipore Corporation, Chemicon) in ice for 30 min, transferred in sterile Eppendorf and centrifuged at 13000 rpm for 15 min at 4°C. The pellet was separated from the supernatant and treated with 750 μL of freshly prepared aqua regia. The samples were diluted to 3 mL with bidistilled water and analyzed for the Au content with ICP-MS (ELAN DRC, Perkin Elmer). The nanoparticles uptake efficiency per cell was calculated as previously described (Gunduz et al., 2017): *Uptake efficiency (%) = (Number of NPs taken up by cells/Number of NPs incubated with cells) * 100%*. To obtain number of AuNP in each sample, total ppm determined by ICP-MS was divided to the mass of one AuNP. Total AuNPs number was divided to cells number as follow: number of AuNPs/n° of cells = (total mass of AuNPs by ICP-MS/mass of one AuNP)/n° of cells (where the *mass of one AuNP = ρ 4/3 $\rho^3\pi$ with ρ = density of gold; r = radius of one AuNP).*

Confocal Laser Scanning Microscopy (CLSM)

SKBR-3, cells were seeded on cover glasses with a density of 50.000 cells in a 24 well culture plate. After 24 h incubation, cells were treated with Trastuzumab free (2 μg/mL), 2.5Au@PT, 5Au@PT nanoparticles (2 μg/mL) and without any control for 24 h. Untreated cells were used as control. At the end of the culture time, the cells were washed with PBS, fixed with 4% (w/v) paraformaldehyde solution for 15 min, permeabilized with 0.1% Triton X-100, and blocked with Bovine Serum Albumin (BSA 3% in 1X PBS) for 1 hour at room temperature. Finally, cells were incubated with Alexa-Fluor-488–conjugated secondary antibodies anti-human (diluted 1:1000) for 45 min at room temperature (Invitrogen; excitation/emission maxima ∼ 495/519 nm). At the end of the incubation, the cells were washed in PBS, counterstained with a solution of Hoechst 33342 (2 μg/mL in 1X PBS; excitation/emission maxima ∼361/497 nm) to target the cellular nuclei, and then washed. Finally, samples were observed with a confocal fluorescence microscope (Leica TCS SPII Microsystems, Wetzlar, Germany). The AuNPs were visualized in reflection bands after the excitation at 545 nm.

Ultrastructural Analysis

For the ultrastructural analysis, cells underwent a Silver enhancement made with Silver Enhancer Kit (Sigma-Aldrich) in order to increase the signal of colloidal gold particles. Subsequently, cells were fixed with 2.5% glutaraldehyde in PBS and a post-fixation with 1% osmium tetroxide in dH_2O was performed to fix lipids. The samples were gradually dehydrated in

acetone and embedded in epoxy resin. Thin sections of 70–80 nm were obtained with Reichert OM3 ultramicrotome and placed on formvar-carbon-coated nickel grids (300 Mesh). Finally, the grids were stained with uranyl and lead, using an unstained grid as control. All the samples were observed on a Zeiss EM900 electron microscope operating at 80 kV.

Endocytosis Pathway Determination

Cells were seeded in 6-well culture plates at a density of 500000 cells/well, after 24 h incubated with different endocytosis inhibitors [2.5 mM amiloride (Sigma-Aldrich), 2.5 μg/mL chlorpromazine (Sigma-Aldrich) and 100 μM indomethacin (Sigma-Aldrich)] and then maintained for 1 h at 37°C with 5% of CO_2-air. The concentrations and treatment times of each chemical inhibitors were optimized in a preliminary experiment to select the maximum non-toxic doses and treatment times. After 1 h incubation, the inhibitors were removed, and the cells exposed to 2 μg/mL AuNPs in complete medium for 24 h incubation. Then ICP-MS protocol was followed as described in the previous section.

Western Blot Analysis

Cells were scraped from all the samples, including T, and lysed with ice-cold lysis buffer (1X RIPA buffer containing 1 mM and 1X protease inhibitor (Protease Inhibitor Tablets, SIGMA) for 30 min on ice. The lysates were then used for western blot analysis according literature protocol (Cristofaro et al., 2018). Primary antibodies anti-phosphorylated AKT and anti-AKT (diluted 1:500), anti-ERK and anti-phosphorylated ERK (diluted 1:1000), anti-BAX and anti-BCL-XL (diluted 1:500), anti-β-actin (diluted 1:500) and appropriate secondary antibodies HRP-conjugated were used. Detection was performed as described in the dot-blot section. Bands densitometry analysis was carried out with Image J software.

Statistical Analysis

All statistical calculations were carried out using GraphPad Prism 5.0 (GraphPad Inc., San Diego, CA, United States). Statistical analysis was performed using Student's unpaired *t*-test and through one-way variance analysis (ANOVA), followed by Bonferroni *post hoc*, for multiple comparisons (significance level of $p \leq 0.05$).

RESULTS AND DISCUSSION

Synthesis of AGMA1-SH

AGMA1-SH bearing 20% randomly distributed thiol-functionalized repeat units was synthesized following a two-step procedure previously reported for obtaining thiol-functionalized ISA23 (a cytobiocompatible, stealth-like PAA deriving from the polyaddition of 2,2-bisacrylamidoacetic acid with 2-methylpiperazine) (Donghi et al., 2009). According to this procedure (**Figure 2**), at 20% on a molar basis, cysteamine-deriving units were introduced in AGMA1 by substituting in the preparation recipe 10% cystamine for 20% agmatine. Cystamine, being a tetrafunctional monomer in Michael-type polyaddition acted as a crosslinker, and a soft hydrogel was obtained. Cystamine disulfide groups were subsequently reductively cleaved with excess 2-mercaptoethanol. The major portion of AGMA1-SH repeat units still bore 4-aminobutylguanidine pendants, as AGMA1, therefore it maintained its favorable cell-adhesive properties, but also contained cysteamine moieties capable of ensuring strong interactions with gold.

Synthesis of Gold Nanoparticles Decorated With AGMA1-SH and/or Trastuzumab

Three differently sized AGMA1-SH-coated AuNPs decorated with Trastuzumab were synthesized according to a previously established green and robust route (Comotti et al., 2004). The aim was to assess how variously sized nanosystems could affect the biological activity, in particular endocytosis and apoptosis. In order to evaluate the role of each component inside the nanosystem, three differently sized AGMA1-SH-coated AuNPs and Trastuzumab-coated AuNPs were also prepared for comparison. Tuning gold nanoparticles diameter was expected to change anti-cancer ability of the nanosystem as a consequence of different surface to volume ratios which might affect the gold interaction with the polymer and drug, as well as their surroundings. On this regard, Bond and Thompson published a plot able to determine gold dispersion per nanoparticle (percentage of surface gold atoms with respect to gold atoms per nanoparticle) as a function of nanoparticle diameter (Bond and Thompson, 1999). Surface area and gold atoms number versus diameter can be determined as well (**Supplementary Figure S1**). Accordingly, the smaller the particles, the higher the fraction of atoms on the surface thus more gold sites are available for interaction. In particular, the three tailored AuNPs sizes (2.5, 3.5, and 5 nm) would lead to marked different gold dispersions of around 55, 35, and 25%, respectively. All the nanosystems were stable over time due to the mentioned Au-S soft-soft interaction, since sulfur is present either in AGMA1-SH or Trastuzumab (Della Pina et al., 2009). Briefly, the AuNP *core* (produced by chloroauric acid reduction, see below) was coated with the biocompatible polymer AGMA1-SH in order to prevent the nanosystem either from aggregation or ingestion by phagocytes ('*stealth effect*'). The subsequent conjugation to an anticancer molecule (the antibody drug Trastuzumab) would enable gold nanovectors to recognize and inhibit only tumor cells. $HAuCl_4$ aqueous solution served as a gold source, whose concentration was tuned to achieve the desired size of AuNPs and, hence, of the whole nanosystem. Proper amounts of AGMA1-SH were then added and Au^{3+} was instantly reduced to Au^0 by $NaBH_4$ addition without the presence of any conventional stabilizer (namely PVA, PVP or sodium citrate, often cytotoxic) due to the intrinsic protecting effect of the polymer. Shortly after, the polymer-coated AuNPs were decorated with the drug. Only in the case of 5Au@PT, 5Au@P, and 5Au@T samples, sodium borohydride was added prior to the polymer or antibody drug addition in order to allow gold nanoparticles to grow up to 5.0 nm. Both the polymer and the drug, in fact, were found

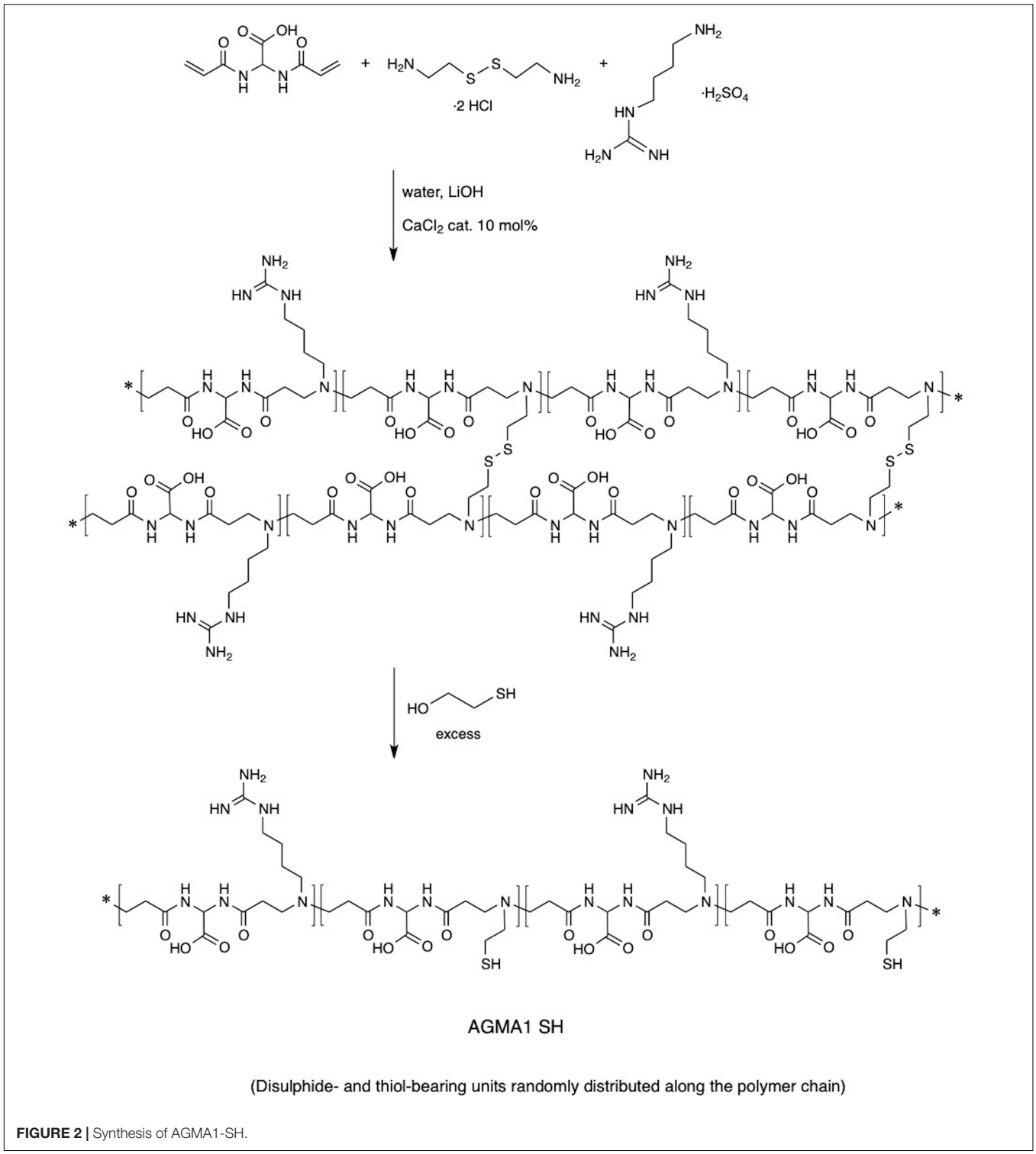

FIGURE 2 | Synthesis of AGMA1-SH.

to hinder gold nanoparticles growth when present before the reducing agent addition, probably due to their inhibiting effect against aggregation (**Figure 1**). More importantly, the innovative protocol introduces some advantages with respect to other synthetic routes commonly adopted (Rossi et al., 2016). First, the use of thiol-functionalized biocompatible PAAs allows to avoid conventional stabilizers, often cytotoxic, *via* Au-S bonds, which ensure long-term stability of the nanosystem without cytotoxicity. Second, the use of an instant reducing reagent ($NaBH_4$), whose excess can be easily removed by dialysis, leads to homogeneously sized nanoparticles, simple to be tuned by $HAuCl_4$ concentration.

Physicochemical Characterization of Gold Nanoparticles Decorated With AGMA1-SH and/or Trastuzumab

Direct TEM observation of Au@PT complexes showed that all colloidal solutions contained monodispersed and spherical-shaped nanoparticles matching their designs (**Figure 3A**). As reported in the experimental section, the gold nanoparticle average diameter was determined by XRPD analyses using *Scherrer* equation. All colloidal samples were absorbed on XC72R carbon (1%Au/C) and the peak at $2\theta = 38.5°$, typical of metallic gold, was considered. A long experimental work allowed to reach the expected theoretical values for most of the samples, especially when the polymer and the drug were both present (**Figure 3B**). Size evaluation of the whole colloidal nanosystem (gold – polymer – drug) required DLS technique. DLS measures the time-dependent fluctuations in the intensity of scattered light from a suspension of particles undergoing random *Brownian* motion. Analysis of these intensity fluctuations allows the determination of diffusion coefficients, which in turn yield the particle size through the Stokes-Einstein equation. **Table 1** reports the hydrodynamic diameter average and Z-potential for all samples. Particles size and Z-potential are very important parameter to evaluate the stability of colloidal system (Sun et al., 2016). Absolute values of Z-potential above ± 30 mV are typically considered as an indicator of suspension stability against aggregation due to charge stabilization (i.e. the electrostatic repulsive forces are high enough to counteract aggregation) (Lowry et al., 2016). Meaningfully, Z-potential value can provide an explanation about the absorption mechanisms of drugs and biological ligands on nanoparticles surface. Likewise, it can be a key factor in determining the interaction with the cells. As listed in **Table 1**, all the AuNP spheres (with or without AGMA1-SH) showed a positive Z-potential value. However, some significant differences were observed. In absence of AGMA1-SH, the Z-potential values of Au@T nanoparticles decreased dramatically toward Z-values closed to neutrality when particle size increased, especially for the 5Au@T nanoparticles, which indicated a very low stability of the nanosystems. The reason can be attributed to the absence of the stabilizing effect of AGMA1-SH, that if present on the surface may impedes nanoparticle aggregation by steric hindrance to prevent surface interactions between AuNPs (Gao et al., 2012). After the addition of AGMA1-SH, the Z-potential value of the differently sized Au@P intensely increased. The most relevant increase was observed for 5Au@P (from 0.2 to 33.8 mW), confirming the impact of AGMA1-SH to prevent nanoparticles aggregation and deposition. After the Trastuzumab conjugation, a slight and not significant decrease on Z-values was assessed in 2.5 and 3.5Au@PT suspensions than 2.5 and 5Au@P counterparts (24.2 to 18.4 mV for 2.5Au@PT and 23.0 to 21 mW for 3.5Au@PT, respectively). With value higher than 30.0 mW, 5Au@P and 5Au@PT represent the most stable nanoparticles, underling a possible effect due to the size of the nanospheres. Numerous strategies explored the attachment of a targeting ligand (i.e. sugars and peptides) through S-Au bonds (Bertrand et al., 2014; Doulain et al., 2015). Although some drawbacks, particular promising are those exploiting these bonds for the functionalization with molecules for biosensing, anticancer drug delivery (i.e. antibodies), and bioimaging (Ghosh et al., 2008; Gautier and Cisnetti, 2012). Recently, Matos et al. (2018) used an engineered Trastuzumab presenting an additional free cysteine per light chain, obtaining a stable and homogeneous gold thiol-linked Thiomab conjugate with unmodified anticancer activities. Sulfur is a component of Trastuzumab itself ($C_{6470}H_{10012}N_{1726}O_{2013}S_{42}$, hence 42 Sulfur atoms per molecule). Hence, it is reasonable to speculate that its free thiol groups may contribute on the stability enhancement of AGMA1-SH-coated gold nanoparticles interacting directly with the gold surface. The UV-vis spectra displayed a plasmon resonance band (PRB) in the strict range 498–504 nm for the smallest samples (2.5Au@PT, 2.5Au@P, and 2.5Au@T), 508–515 nm for the intermediate-sized samples (3.5Au@PT, 3.5Au@P, and 3.5Au@T) and 517–525 nm for the largest ones (5Au@PT, 5Au@P, and 5Au@T) (**Figure 3C** and **Supplementary Figure S2**). The location of PRB peak strongly depends on the size of the metal nanoparticles, as well as on the surrounding medium and its dielectric constant. In particular, the larger the nanoparticles, the higher the wavelength. Hence, the detected PRB values are coherent with the expected theoretical trend (**Figure 3C**).

In addition to the physicochemical characteristics of all nanoparticle's formulations tested, the efficiency of the conjugation reaction was also determined (**Table 2** and

TABLE 1 | Size distribution of hydrodynamic diameters (d_h) and Z-potential as determined by DLS.

Sample	Number size distribution [nm]	Z potential [mV]
AGMA1SH	1.3 (97.6%) ± 0.2; 3.2 (2.4%) ± 0.7	
Trastuzumab	9.3 (100%) ± 2	
2.5Au@PT	6.0 (100%) ± 1	18.4 (85.1%) ± 2.7; 3.2 (12.9%) ± 1.7
3.5Au@PT	9.5 (100%) ± 3	21.0 (86.2%) ± 7.2; 3.8 (13.8%) ± 1.3
5Au@PT	27.0 (100%) ± 6	32.6 (100%) ± 9.4
2.5Au@P	5.4 (100%) ± 1	24.2 (69.6%) ± 2.6; 6.7 (27.3%) ± 3.3
3.5Au@P	14.8 (100%) ± 5	23.0 (73.3%) ± 3.0; −2.8 (26.7%) ± 1.6
5Au@P	22.1 (100%) ± 7	33.8 (100%) ± 7.6
2.5Au@T	19.9 (100%) ± 6	7.4 (100%) ± 3.5
3.5Au@T	63.1 (100%) ± 21	13.6 (100%) ± 7.5
5Au@T	77.0 (100%) ± 29	0.2 (100%) ± 0.1

TABLE 2 | Conjugation efficiency of AGMA1-SH-AuNPs.

Samples	Conjugation efficiency%[a]	μg of Trastuzumab per 20 μg of nanoparticles[b]
2.5Au@PT	50.2 ± 3.9	10 ± 0.8
3.5Au@PT	60.0 ± 6.3	11.9 ± 1.3
5Au@PT	69.4 ± 7.8	13.9 ± 1.6

[a] *Conjugation efficiency% = (1 − ([Trastuzumab in the supernatant]/[Trastuzumab added in the conjugation reaction])) × 100.* [b] *μg of Trastuzumab per 20 μg nanoparticles = Trastuzumab added in the conjugation reaction − Trastuzumab in the supernatant.*

Supplementary Table S2). Trastuzumab was conjugated to the Au@P with an efficiency of ∼50–70%. In general, the percentage of conjugation efficiency augmented by increasing the gold nanoparticles sizes. It was approximately of 50.2 ± 3.9% for 2.5Au@PT, 60.0 ± 6.3% for 3.5Au@PT and 69.4 ± 7.8% for 5Au@PT, respectively, denoting that the size of gold nanoparticles intensely impacts the binding with the targeting molecules. The relative amount of T (μg) per nanoparticles (μg) are also reported (**Table 2**). Beyond to visualize Trastuzumab on the nanoparticles as spots on the nitrocellulose membrane, dot blot assay confirmed the indirect values obtained by BCA analysis (**Supplementary Table S3** and **Supplementary Figure S3**). Size-related effect was also recorded in the Trastuzumab-functionalized nanoparticles without AGMA1-SH. It is worth noting that, in all these nanoparticles, the amount of Trastuzumab per nanoparticles was lower than AGMA1-SH-coated gold nanoparticles (**Supplementary Table S2**). Gao et al. (2012) documented that a thiol-ending polyethylene glycol (PEG-SH), significantly improved to colloidal stability of gold nanoparticles in aqueous solution, facilitating their conjugation with epidermal growth factor receptor antibodies. Hence, presumably the AGMA1-SH presence, stabilizing the gold nanoparticles, may be crucial for the establishment of a successful interaction with the antibody (Gao et al., 2012). In nanobiotechnology applications, curvature of nanoparticles has a significant effect on protein structure and activities, although little is exactly known about molecular level mechanism. Likewise, hydration layer above the nanoparticles surface, the ionic strength of buffer solution and stabilizing polymers concentration can be critical factors for protein interaction with nanoparticles (Iijima and Kamiya, 2009; Kushida et al., 2014; Yu and Zhou, 2016; Lin et al., 2017). Kushida et al. (2014) showed that the interaction of the coagulation proteins with silica nanoparticles decreases with the decreasing NP size

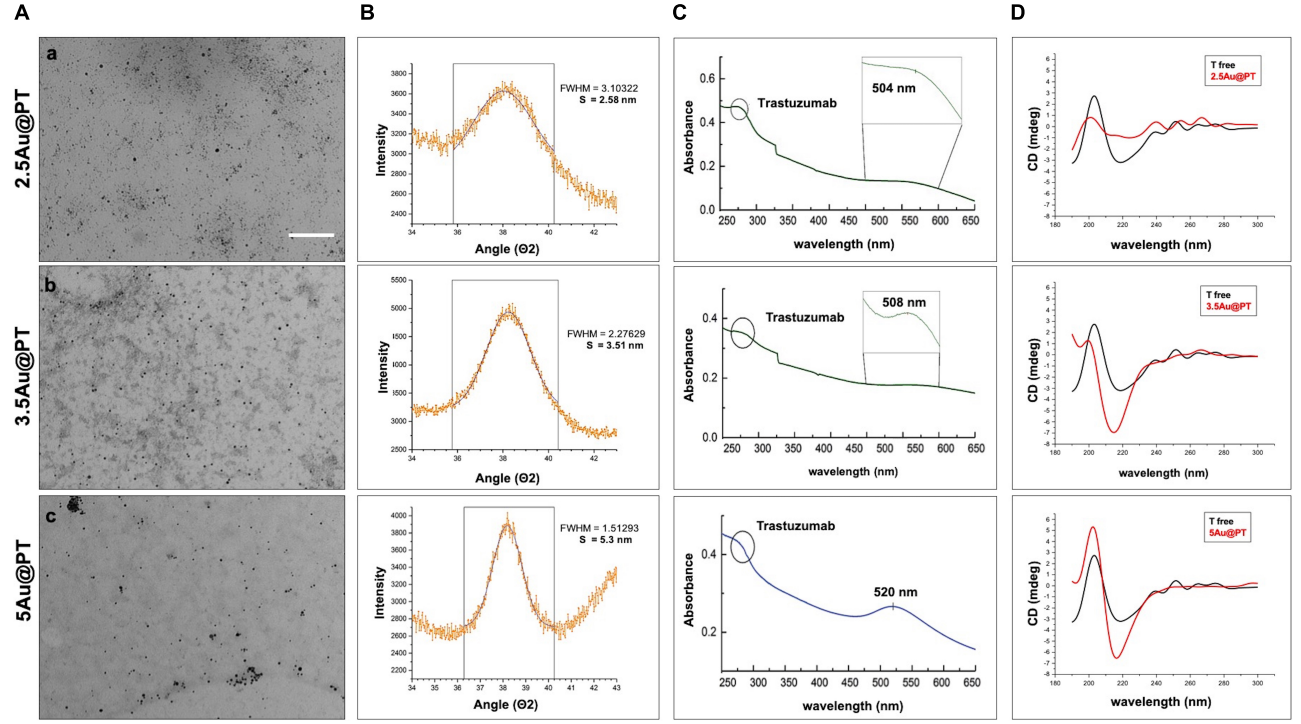

FIGURE 3 | Characterization of Trastuzumab-conjugated gold nanoparticles with different sizes. **(A)** TEM images of 2.5 **(a)**, 3.5 **(b)**, and 5 **(c)** nm core diameter Au@PT nanoparticles (Scale bar = 200 nm), **(B)** XRPD, **(C)** UV-vis absorbance spectra (circle at 280 nm indicates the Trastuzumab peak), and **(D)** circular dichroism measurements of each Trastuzumab-conjugated gold nanoparticles families as function of core size.

TABLE 3 | Hydrodynamic diameter (nm) of Trastuzumab-AGMA1-SH-gold nanoparticles dispersed in complete cell culture media at two different time points.

	2.5Au@PT		3.5Au@PT		5Au@PT	
Media	**0 (h)**	**4 (h)**	**0 (h)**	**4 (h)**	**0 (h)**	**4 (h)**
McCoy's + 10% FBS	7.3 ± 1	17.5 ± 2	10.9 ± 1	18.7 ± 1	20.1 ± 1	27.0 ± 1
MEM eagles + 10% FBS	9.1 ± 1	16.5 ± 2	8.3 ± 3	16.6 ± 1	23.3 ± 1	32.3 ± 1
DMEM + 10% BCS	9.7 ± 2	21.5 ± 2	13.0 ± 1	30.9 ± 4	21.9 ± 1	23.7 ± 3

Mean value and standard deviation of three measurements per condition are reported.

(higher curvature). Vertegel et al. (2004) observed a greater loss of lysozyme conformation adsorbed onto larger silica nanoparticles under otherwise similar conditions. About the gold nanoparticles, the effects of curvature on ligand interaction remains a complicate issue (Villarreal et al., 2017). Villarreal et al. (2017) CD spectroscopy method is commonly used to determine protein structure and its interaction with other molecules. CD spectroscopy confirmed the Trastuzumab conjugation to the gold nanoparticles (**Figure 3D** and **Supplementary Figure S4**), but also suggested a correlation between Trastuzumab-conjugated secondary structure maintenance and the particle hydrodynamic radius (R). Consistently with literature findings (Jiang et al., 2005, 2008; Worrall et al., 2006; Saptarshi et al., 2013), the correct folding increased with R growing from 2.5Au@PT to 5Au@PT (**Figure 3D**). Only the largest nanoparticles (5Au@PT) displayed CD spectra superimposable to the unconjugated antibody, indicating that the nanoparticles are a highly efficient and selective tool for HER-2 receptor. Previous studies hypothesized that the higher surface curvature of smaller nanoparticles may restrict the relative orientation between antibodies, resulting in a certain degree of conformational rigidity, that while blocking the correct protein folding, it impaired their docking receptor surface (Jiang et al., 2008). By contrast, for conjugates built on larger sizes, the antibody, once absorbed on nanoparticles surface, extended itself into the surrounding medium in a conformation allegedly better suited to interact with its receptors (Ghitescu and Bendayan, 1990; Jiang et al., 2008; Saptarshi et al., 2013). Concerning the *in vitro* release of Trastuzumab, each type of Au@PT presented a low released amount in MilliQ water up to 15 days of investigation ($5.3 \pm 0.7\%$, $4.4 \pm 0.5\%$, and $3.5 \pm 0.6\%$ for 2.5, 3.5, and 5Au@PT, respectively) (**Supplementary Figure S5**). Interestingly, analyses up to 12 months showed that 5Au@PT complex was the most stable of storage at refrigerated conditions, without any aggregate's formation and with an approximately release of $20 \pm 0.3\%$. By contrast, both 2.5 and 3.5Au@PT displayed a tendency to precipitate after few months from their synthesis. Challenging and crucial aspect of nanoparticles characterization is the measurement of their stability under condition resembling *in vitro* or *in vivo* environment. Numerous studies revealed that the proteins, salts, and antibiotics present in the different culture media can interact with AuNPs, determining radical changes in their size by forming aggregates and reducing their stability (Moore et al., 2015). Notably, all these components can confer the particles with a new biological identity and then dramatically alter their interaction with the cells (Gebauer et al., 2012). Therefore, it has been becoming increasingly evident that the nanoparticles toxicity and activity assessed *in vitro* entails the mixing nanoparticles of interest with the biological media for enhancing the comprehension of their interaction with the biological systems. Hence, to mimic the cell bioenvironment prior to cells treatment, freshly synthesized batches of Au@PT nanoparticles were re-suspended in the cell culture media (containing 10% of serum) proper for each cell lines used for biological investigation. Hydrodynamic changes were assessed by DLS analysis at 37°C after 4 h of incubation. As shown in **Table 3** after serum incubation, the hydrodynamic diameter of the three types of Au@PTs (in particular for the smaller ones) increased suggesting the serum proteins adsorption on nanoparticle surface, that forming a "corona." Although with discrepancies in the results, numerous studies on different types of nanoparticles and on various cell lines highlighted the significance of protein corona (Hajipour et al., 2015). They profoundly influence the aggregation of nanoparticles and their cellular uptake (Dominguez-Medina et al., 2016). Also, it has been demonstrated that the protein corona composition affects the internalization of gold nanoparticle coated with different polymers (Walkey et al., 2014). Recently, it was found that the "*stealth effect*" of poly(ethylene glycol) may be explained by the presence of specific proteins in their protein corona (Schöttler et al., 2016). As summarized by Moore et al. (2015) the type of basal medium can dictate the size and stability of nanoparticles. Results from Strojan et al. (2017) demonstrated that the medium in which silica nanoparticles were dispersed, had significantly affected nanoparticles protein corona composition, suggesting an important implication on nanoparticles potential biological effects. Ji et al. (2010) have found that titanium dioxide (TiO_2) nanoparticles increased their hydrodynamic in the presence of cell culture media without serum. By contrast, the addition of bovine serum protein stabilized nanoparticles, as there was only a little change in size following the addition of proteins (Spadavecchia et al., 2016). Moreover, as previously reviewed, different surface modifications (i.e. by using biocompatible polymers coating) can be used for lessening the protein corona formation then improving the stability of nanoparticles in liquid media (Iijima and Kamiya, 2009). Based on and in agreement with literature findings (Colombo et al., 2016), we inferred that the small increase observed on 5Au@PT nanoparticle size, in all complete media tested, might due to the higher surface functionalization with T, which decreased the extent of serum protein adsorption. By contrast, the lower amount of antibody per nanoparticle on 2.5Au@PT and 3.5Au@PT may favor protein absorption then resulting in an increase of hydrodynamic diameter. Overall, protein adsorption may be hindered by the functionalization of gold nanoparticles with AGMA1-SH and Trastuzumab, but it cannot be totally inhibited, and a certain amount of serum proteins do adsorb on the NP surfaces, irrespective to the presence of polymers coating, justifying then the small increase of the hydrodynamic size.

It is worth emphasizing that the NPs characterization in standard conditions for the *in vitro* biological experiments, i.e. in serum-containing cell culture medium, is still a questioned issue. Indeed, additional determining factors can regulate the nanoparticles amount reaching the cell monolayer and the type of interaction with cells. Cell types and its protein component, including the protein secreted by cells, contribute to affect the deposition of the nanoparticles in the cell-well (Halamoda-Kenzaoui et al., 2015). Recently, it was observed that nanoparticle administration method *in vitro* cell culture could alter particle-cell interaction (i.e. cellular adsorption and uptake) (Moore et al., 2019). All the factors make hard to envisage the exact behavior of the nanoparticles once in contact with the cells and should to be taken in account during the biological experiments. Whilst bearing in mind that accurate experiments are required, overall

characterization proved the efficacy of the use of AGMA1-SH to produce stable gold nanoparticles. Consequently, their anticancer activities were subsequent evaluated by *in vitro* cell models as follows described.

In vitro Cytotoxicity and Uptake: Evaluation in Breast Cancer and No-Neoplastic Cell Lines

In vitro and *in vivo* successful achievements employing delivery synthetic nanoplatforms need targeting molecules to recognize tumor cells specifically, without affecting the surrounding healthy cells.

Aiming to assess the activities of Au@P functionalized with Trastuzumab, SKBR-3, human breast cancer cell line was selected as target cell model. This cell line overexpresses HER2, itself the target of Trastuzumab, and has been used extensively as an *in vitro* model for evaluating the anticancer targeting of nanoparticles as tool to enhance the selectivity and specificity of therapies against cancer cells (Kim et al., 2011; Martínez-Jothar et al., 2019; Niza et al., 2019). Moreover, to confirm the selective effect of Au@PT toward the HER2-receptor, others two cell lines were included for comparative analysis: MCF-7, a human breast cancer expressing low HER-2 as control, and the murine fibroblasts cell line, NIH-3T3, as health cell model. Both are commonly used in experimental studies for assessing the selectivity of anticancer treatments and the nanomaterials toxicity (Xu et al., 2005; Holliday and Speirs, 2011; Shirshahi et al., 2013; Merli et al., 2018; Cruz and Kayser, 2019). All *in vitro* experiments were conducted treating all cell types (1×10^4 viable cells/well) with increasing concentrations (from 0 to 2 μg/mL) of each Au@PT size and free-Trastuzumab. The concentration range was fixed by determining the "no toxic" dose by incubating the same number of cells with increasing concentrations of the unfunctionalized Au@P counterparts (**Supplementary Figure S6**). A low cytotoxicity was observed up to 2 μg/mL, then the concentration range upper limit was set at this value. As reported in **Table 2**, 2 μg/mL of 2.5Au@PT, 3.5Au@PT, and 5Au@PT contain approximately 1–1.4 μg of Trastuzumab, which was the concentration within the effective doses against breast cancer cells (Suarez et al., 2013). 2.5Au@PT, 3.5Au@PT, and 5Au@PT cytotoxicity was tested by measuring cell viability using MTT after incubation with Au@PT. 2.5Au@PT and 5Au@PT were particularly effective in impairing the SKBR-3 viability, whereas they had low or no toxicity on MCF-7 and NIH-3T3 respectively (**Figure 4A**). Interestingly, cells exposed to Au@PT underwent viability decrease after 3 days of incubation (around 50 and 20% with 5Au@PT and 2.5Au@PT respectively). It could be argued that the difference in cells response is due to the changes observed in the secondary structure of the antibody, which was able to affect the binding capacity of Trastuzumab-AuNPs with HER-2 receptors. 3.5Au@PT was comparable to that of 2.5Au@PT treated cells, nearby 25% at 2 μg/mL (data not shown). Targeting molecule may reduce their targeting capacity and activities as protein corona adsorption (Mirshafiee et al., 2013). Also surface rigidity, ligand density affects nanoparticles effect on cell (Gong et al., 2015). Consequentially, it is conceivable that lower activity detected after the treatment with 2.5Au@PT, the ones showing the highest increase of hydrodynamic size following the incubation with the complete cell media, may be related to protein corona absorption. However, other explanations cannot be excluded. Pan et al. (2007) have demonstrated that the cytotoxicity of modified gold nanoparticles is dependent on the size and not on a particular ligand attached to them. In addition, some researchers showed that because metallic, these nanoparticles have an effect on cell membrane integrity, and their size and charge both affect significantly cell viability (Woźniak et al., 2017). Similarly, cellular uptake of gold nanoparticles was influenced by many factors including size, charge, coating, shape, incubation time and cell types (Dreaden et al., 2012; Panariti et al., 2012; Yue et al., 2017). Chithrani et al. (2006) observed that size and shape strongly influenced cellular uptake of citric acid ligand-modified Au nanospheres, and others reported a clear interrelationship between nanoparticles surface functionality an uptake (Jiang et al., 2015). Meanwhile, the adhesion of nanoparticles onto cell membrane can be reduced because of protein corona formation around nanoparticles surfaces, which in turn inhibit their cellular uptake. As reported by Cheng et al. (2015) protein from serum, modulating biomolecular corona profile, changed the AuNPs internalization in a size- and cell type-dependent manner. Aiming to explore the size contribution in Au@PT uptaking, the succeeding experiments were performed using nanoparticles differing for about fourfold in hydrodynamic radius, 2.5Au@PT and 5Au@PT. Others have previously underlined that an equilibrium between multivalent crosslinking of membrane receptors and membrane wrapping involved in receptor-mediated endocytosis exists (Jiang et al., 2008; Yue et al., 2017). Jiang et al. (2008) showed that extremely small (2 nm) or large Trastuzumab-conjugated nanoparticles (>50 nm) would both produce an inefficient uptake. Aoyama et al. (2003) and Osaki et al. (2004) investigated size effects and receptor activation, concluding that receptor-mediated endocytosis is firmly size-dependent with an optimal size equal to ≈25 nm. Others reported a theoretical model based on size and receptor-mediated endocytosis that gives an optimal radius ≈27–30 nm for spherical particles (Gao et al., 2005). Besides, Wang et al. (2010) using a 3D image process identified the AuNPs distribution, revealing that the optimal size is 45 nm for cells uptake. The results here described seem to show a broader agreement with previous experimental observations. Indeed, as compared to 2.5Au@PT ($d_h \sim 6$ nm), a significant enhancement in the uptake of 5Au@PT ($d_h \sim 22$ nm) was detected in HER-2 overexpressing human breast cancer SKBR-3 cells (**Figure 4B**). Nonetheless, the internalization of both 2.5Au@PT and 5Au@PT was highly dependent on time (**Figure 4B**). Large nanoparticles aggregates are not suitable for cellular interaction and uptakes. Using SEM-BSE mode, it was easily appreciated smaller 5Au@PT cluster coating homogenously SKBR-3 cells surface, whereas a closely 2.5Au@PT were packed into bigger aggregates (**Supplementary Figure S7**), suggesting the difficult capture of the latter by cells. In addition, uptaking studies using unconjugated-Au@P confirmed the role played by the size, with the most efficient

uptake occurring with the largest nanoparticles (5Au@P; $d_h \sim$ 22 nm) (**Supplementary Figure S8**).

The accumulation of Au@P and Au@PT inside the cells could be regulated also by the exocytosis process. It was found that Au NPs were exocytosed in a linear manner in size, with smaller AuNPs exhibiting a faster exocytosis rate and percent (after 8 h of incubation, 4 nm-AuNPs were exocytosed while > 90% of 74 nm remains into the cells) (Chithrani and Chan, 2007). Equally, the thermodynamic process could be the driving force for wrapping. In general, smaller particles must be clustered together to create enough driving for uptake, showing an uptake amount smaller than 50 nm AuNPs (Gong et al., 2015). Recently, Cruz E and Kayser V have found that Trastuzumab-attachment increased nanoparticles cellular uptake in HER2 amplified cell lines selectively (Cruz and Kayser, 2019). Although higher uptake is required in delivery applications, internalization must be specific to the targeted tumor cells. In agreement, the observation that Au@PT internalization was higher in HER2 overexpressing cell line (SKBR-3) than in both MCF-7 and NIH-3T3, it was a further evidence that cellular uptake increased through the HER2 receptor crosslinking Trastuzumab-activated (**Figure 4B**). Likely, the low percentage of uptakes detected in MCF-7 and NIH-3T3 was due to passive internalization (**Figure 4B**) (Zhao and Stenzel, 2018). Later, in line with previous studies(van der Meel et al., 2012; Martínez-Jothar et al., 2019), SKBR-3 cell line showed a significantly increased uptake for Trastuzumab-conjugated AuNPs as compared to non-targeted nanoparticles (50% vs. 10%, respectively after 3 days of incubation); these data further proved that the uptake of antibody-targeted nanocarriers is truly mediated by specific ligand-receptor interactions.

HER Targeting: Evaluation of Morphology, Viability and Intracellular Changes After Au@PT Treatment

The correct binding of a ligand molecule with cell surface receptors intimately controls the cell function and fate. Many works showed that the physical parameters of nanoparticles (i.e. size) strongly affect ligand binding and the subsequent activation of its membrane receptors (Chithrani et al., 2006; Brzóska et al., 2018). In line with quantitative results, FDA assays showed the highest number of death cells (red signal) in cultures exposed with 5Au@PT suspension (**Figure 5A**). SEM images clearly highlighted this important difference, displaying more spherical cells in shape with noticeable abnormal morphology in 5Au@PT-treated samples in comparison with control, free Trastuzumab or 2.5Au@PT (**Figure 5A**). The binding of

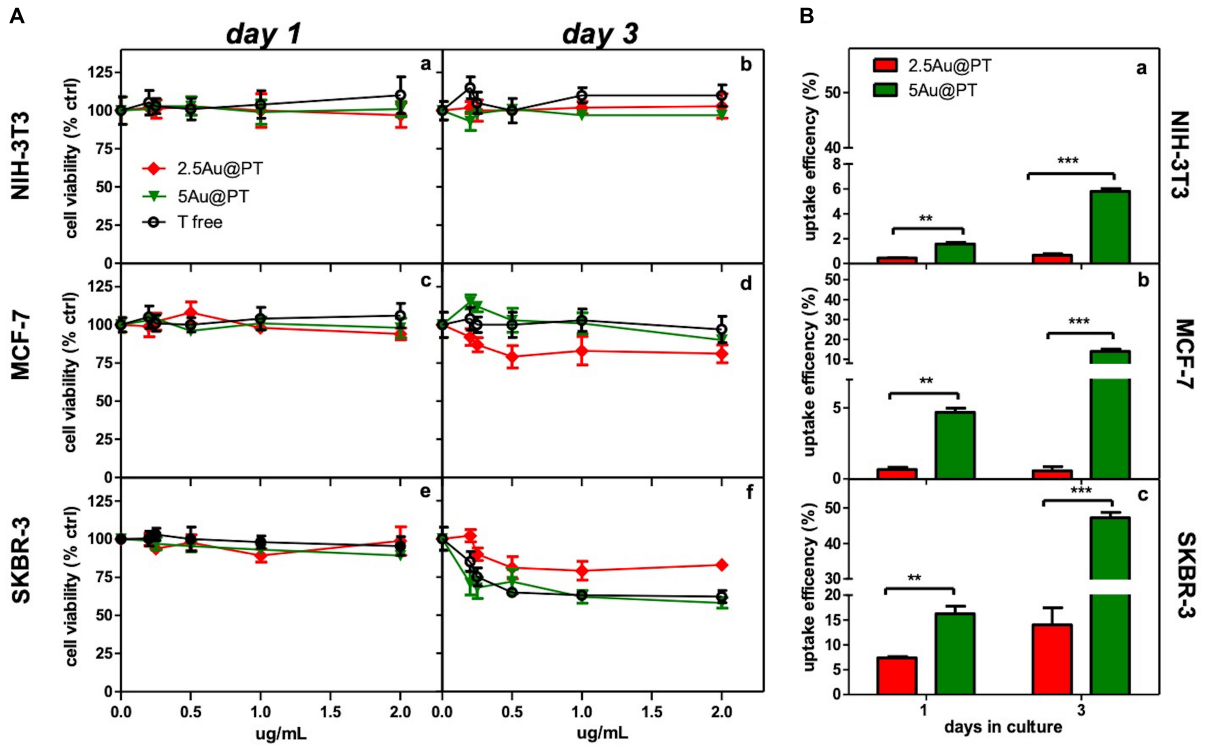

FIGURE 4 | Cytotoxicity and internalization of Trastuzumab-conjugated gold nanoparticles differently sized. **(A)** Dose- and time-dependence cell viability of different cell lines cultured with free Trastuzumab, 2.5Au@PT and 5@AuPT. SKBR-3 **(e,f)** and MCF-7 cells **(c,d)** were incubated with 2.5Au@PT or 5Au@PT suspensions with concentration in the range of 0–2 μg/mL. Similarly, the experiment was performed in NIH-3T3 fibroblasts cell line **(a,b)** as negative control. After 1 and 3 days of incubation, cell viability was expressed as percentage of viability determined in the absence of nanoparticles (set at 100%). **(B)** Uptake efficiency of 2.5Au@PT and 5Au@PT (2 μg/mL) after 1 and 3 days of incubation were determined by ICP-MS in all the indicated cell lines (**a**, NIH-3T3; **b**, MCF-7; **c**, SKBR-3) and calculated as described in *Experimental Section* (mean values ± standard deviations; $^{**}p < 0.01$ and $^{***}p < 0.001$).

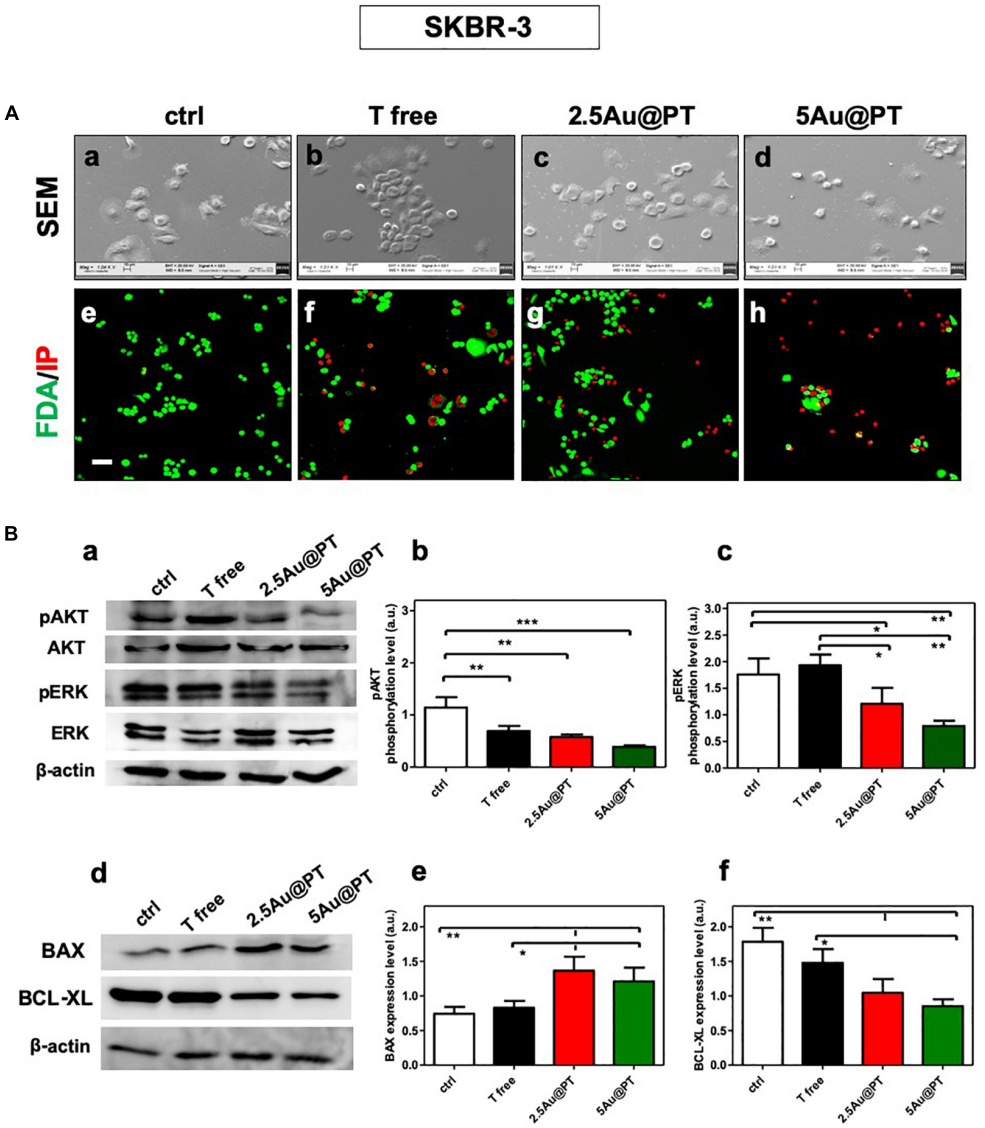

FIGURE 5 | (A) Cell morphology assessed by scanning electron microscopy in ctrl **(a)**, with Trastuzumab **(b)**, 2.5Au@PT **(c)** and 5Au@PT **(d)**, respectively, after 3 days of incubation. Scale bars = 100 μm and mag: 1000×. After 3 days of culture, all experimental groups [ctr **(e)**, T free **(f)**, 2.5Au@PT **(g)**, and 5Au@PT **(h)**] were treated with fluorescein diacetate (green cells alive) and propidium iodide (red cells dead) 20× magnification, the scale bar represents 50 μm. **(B)** Western blotting analysis of survival **(a,b)**, proliferative **(a,c)**, pro **(d,e)**, and anti-apoptotic **(d,f)** proteins extracted from SKBR-3 after 24 h incubation with the indicated treatments. The activation level of AKT or ERK is presented as a ratio between the phosphorylated and total AKT or ERK protein after normalization to β-actin housekeeping protein signal. Bar graphs show BAX and BCL-XL expression level obtained normalizing β-actin housekeeping protein signal. Statistical significance values are indicated as $^{***}p < 0.001$, $^{**}p < 0.01$, and $^{*}p < 0.05$.

the ligand to its surface receptors allows the formation of multivalent HER-crosslinking surface ErbB2 receptors, affecting intracellular signaling, consequently inhibiting downstream pathways involved in cell survival, proliferation, and metastasis (Klapper et al., 2000).

The strategy of combining the properties of AuNPs with anti-cancer molecules could be the future of cancer nanomedicine (Sun et al., 2018). Chattopadhyay et al. (2010) showed that Trastuzumab-PEG-AuNPs (30 nm) in combination with 300 kVp X-rays enhanced DNA double strand breaks (DSBs) in SKBR-3 cells. Mechanistic studies performed by Vemuri et al. (2019) revealed that the functionalization of naturally derived phytochemicals, such as Quercetin and Paclitaxel, to AuNPs were significantly effective in inhibiting cell proliferation, apoptosis, angiogenesis, colony formation and spheroid formation. AuNPs principally trigger apoptosis through intrinsic pathways, including mitochondria- and ER-related pathways. Green synthesized of AuNPs (10 – 42 nm) can induce the apoptosis activating the caspase-3 and 9 in human cervical cancer cells (Baharara et al., 2016) and the citrate-coated AuNPs (8 nm)

promoted apoptosis eliciting BAX translocation and cytochrome c release in human liver (HL7702) cells (Gao et al., 2011). In agreement with literature findings (Sun et al., 2018; Vemuri et al., 2019), Au@PT cytotoxic effects elicited significant changes in survival and proliferation (AKT/PI3K and ERK pathways, respectively) as well as apoptotic process (pro-apoptotic BAX, anti-apoptotic BCL-xL, respectively) (**Figure 5B**). AKT and ERK activation levels were significantly reduced in the treatment with 2.5Au@PT and 5Au@PT than with control (**Figures 5Ba–c**), with a slight decrease after the incubation with 5Au@PT. Additionally, both 2.5Au@PT and 5Au@PT treatments led to a substantial increase in the expression of BAX with concomitant decrease in expression of BCL-xL in comparison with free Trastuzumab and control (**Figures 5Bd–f**). As mentioned, the most marked changes were observed after 5Au@PT incubation, still proving the size-effect dependence. Overall, the results showed that Trastuzumab-AGMA1-SH-gold AuNPs conjugates retain great antimitotic and anti-apoptotic effectiveness after the conjugation to Au@PT, which could improve the cancer therapeutic effects of Trastuzumab itself.

HER-2 Targeting: Evaluation of Internalization by Confocal Laser and Transmission Electron Microscopies

As a drug delivery platform, an efficient cell uptake is important to ensure sufficient therapeutic outcomes (Carnovale et al., 2016). Some studies suggest that Trastuzumab can induce a rapid internalization of HER-2 (Rubin and Yarden, 2001; Chattopadhyay et al., 2010; Han et al., 2014), a mechanism that could facilitate 5Au@PT uptaking by SKBR-3 cells. Co-localization of HER-2 and gold nanoparticles were then studied (**Figure 6**). In cells treated with free Trastuzumab, the antibody staining (in green) was predominant in cell membrane because of its interaction with HER-2 receptors (**Figures 6Ab,c**). On the other hand, cancer cells incubated with 5Au@PT exhibited a reduced Trastuzumab staining at the cell membrane (**Figures 6Ad,e**) but increased inside the cells and co-localized with 5Au@PTs as revealed by the scattering signals of gold (in red) (**Figures 6Ad,e**).

These data, besides proving the powerful and selective ability of Trastuzumab to promote the transport of 5Au@PT into HER-2 overexpressing cells, also suggest that receptors undergo endocytosis process when bound to Au@PT of a specific size range.

Transmission electron microscopy provides an excellent tool for in-depth biological sample analysis at the cellular and organ level. In the present work, it confirmed SKBR-3 cellular internalization of 5Au@PTs (**Figure 6B**). In (c) at higher magnification, the distribution of the NPs in close proximity of the vesicle's membrane seems to evidence the binding between the drug and its receptor: a cluster of 5Au@PT was approaching the cell membrane (d) and was trapped inside vesicles of ranging sizes (e). The electron dense material appears to have a low resolution due to the silver enhancement procedure. However, a series of control experiments in absence of silver, osmium, uranyl and lead ruled out the possibility of artifacts as shown in **Supplementary Figure S9**. Generally, AuNPs were localized within early endosomes and lysosomes (Boyoglu et al., 2013; Xie et al., 2017). Therefore, it is presumable the vesicles structures visualized by TEM were the result of the

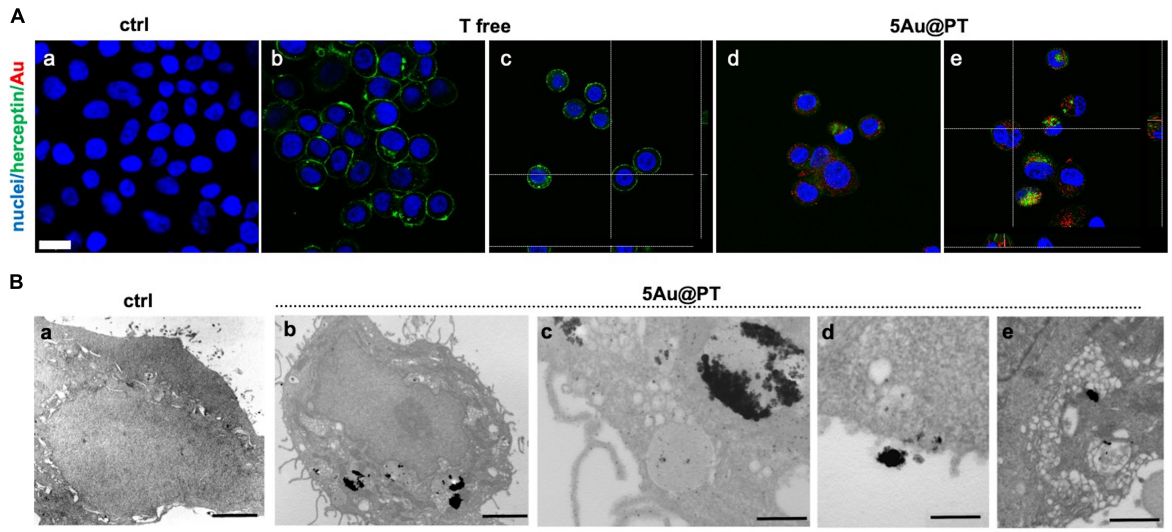

FIGURE 6 | Internalization of 5Au@PT in breast cancer target cells, SKBR-3. **(A)** CLSM images of cancer cells incubated for 3 days in absence of 5Au@PT and Trastuzumab **(a)**, with free Trastuzumab **(b,c)**, and 5Au@PT **(d,e)**. Both Au@PTs were visualized in reflection bands after the excitation at 545 nm and stained in red false color. Trastuzumab was visualized by anti-human secondary antibody-488 Alexa Fluor. Nuclei were stained with Hoechst 33342 (blue). Scale bar: 20 μm. **(B)** TEM samples stained with uranyl and lead for cell morphology: **(a)** ctrl cells; **(b)** cells treated with 5Au@PT; uptake of large clusters inside vesicles is clearly visible after silver enhancement; **(c)** detail of a cell vesicle containing 5Au@PT; **(d,e)** high magnification of 5Au@PT putative uptake nearby the cell membrane; scale bars: 2 μm, 2 μm, 500 nm, 500 nm, and 500 nm respectively.

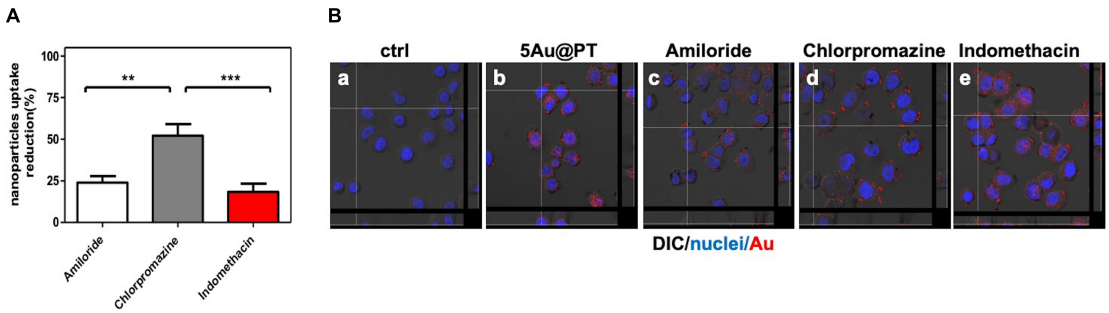

FIGURE 7 | Cellular uptake mechanism of 5Au@PT quantified with ICP-MS **(A)** and observed by CLSM **(B)**. In both experiments, uptakes of 5Au@PT were analyzed in presence of specific endocytosis inhibitors as described in *Experimental Section* (2.5 mM Amiloride; 2.5 μg/mL Chlorpromazine; 100 μM Indomethacin). **(A)** ICP-MS data are expressed as nanoparticles reduction (%). Statistical significance values are indicated as $^{***}p < 0.001$, $^{**}p < 0.01$. **(B)** CLSM-DIC (differential interference contrast) mode of cells untreated **(a)**, exposed to 5Au@PT **(b)**, and incubated with different endocytosis inhibitors (**c**, 2.5 mM amiloride; **d**, 2.5 mg/mL chlorpromazine; **e**, 100 mM indomethacin) for 1 h before the incubation with 5Au@PT for 24 h. Orthogonal view of images stacks is shown. Scattering of Au in red (false color) nuclei in blue. The focus of cells was adjusted using the differential inference contrast as a reference.

endosome/lysosome trafficking induced by Trastuzumab binding to its membrane receptor. Some of these structures may be also autophagosome. Previously, it was observed gold nanoparticles induces autophagosome accumulation in accordance with size-dependent nanoparticle uptake and lysosome impairment (Ma et al., 2011). A high-resolution technique may help to clarify the full pathway of Au@PT intake and leading to a precise subcellular localization.

HER-2 Targeting: Molecular Mechanisms Underlying the 5Au@PT Capture

In conclusion, to underscore the sensitive endocytic route responsible for 5Au@PT internalization by target cells, three different endocytosis pathways inhibitors were employed (**Figure 7**): amiloride for micropinocytosis inhibition, chloropromazine for clathrin-mediated endocytosis (receptor dependent mechanism) and indomethacin for caveolae-mediated endocytosis inhibition. The uptake of 5Au@PT was dramatically affected by chloropromazine treatment (around 50% of reduction), whereas the other two inhibitors did not substantially modify the delivery into the cells (**Figure 7A**). Cross-section analysis confirmed the aforementioned results, revealing a strong scattering distribution along the cellular surfaces due to inhibition treatment (**Figure 7B**). Receptor-mediated clathrin carries out the uptake of specific macromolecules (ligands) or ligand-coated NPs following their binding to receptors on the surface of cell membrane, promoting the invagination of the plasma membrane to form area with a higher receptor concentration (Zhao and Stenzel, 2018).This type of mechanism has been widely used strategy for the drug delivery by nanocarriers (i.e. nanogel, liposomes). Saporin-loaded nanobody-targeted polymeric nanoparticles induced HER2 clustering, and promoting its internalization causes an efficient NPs receptor-mediated endocytosis with subsequent intracellular delivery of its cytotoxic cargo (saporin) (Martínez-Jothar et al., 2019). As regard AuNPs, Trastuzumab-functionalized AuNPs mostly underwent endocytosis in breast cancer cells largely through a receptor-facilitated mechanism (Chattopadhyay et al., 2010; Han et al., 2014; Rathinaraj et al., 2015; Sun et al., 2018). Han et al. (2014) found that quantum dots-HER bound specifically to SKBR-3 membrane, inducing their internalization via a receptor-mediated mechanism. In accordance with the aforementioned findings, the present results showed that the most probable mechanism for 5Au@PT nanoparticle endocytosis in breast cancer cells (SKBR-3) was receptor-dependent, suggesting that the AuNPs-mediated delivery of monoclonal antibody toward its specific cell membrane receptor was achieved efficiently.

In summary, the conjugation of the 5Au@Ps with Trastuzumab allowed their specific binding to HER-2-overexpressing cells, and through a receptor-mediated internalization process, may trigger their deposition into the cytoplasm, where gold nanoparticles, in combination with free Trastuzumab released into the cells, likely contribute to breast cancer cell death.

CONCLUSION

The synthesis and the functionalization of gold-nanoparticles with cancer-specific biomolecules may represent a winner strategy for a selective and targeted tumor-phototherapy. Currently, a considerable number of efforts have been taken in order to obtain gold-nanoparticles by green and safe method. In this work, extra-small gold nanospheres stabilized with thiol-functionalized AGMA1 and Trastuzumab were for the first time synthesized and tested *in vitro* as nanovectors for breast cancer targeted drug delivery. The synthetic method followed an innovative protocol introducing significant advantages with respect to other routes presently adopted. *In primis*, tailoring thiol-functionalized biocompatible PAAs avoided the use of conventional stabilizers, often cytotoxic, *via* Au-S soft-soft interactions, which ensured long-term stability of the hybrid nanomaterial without any cytotoxicity. Importantly, sulfur is even a component of Trastuzumab itself. This represented an intrinsic, powerful tool for further stabilizing

the composite nanosystem. Moreover, the employment of an instant reducing reagent ($NaBH_4$) guaranteed homogeneously sized and tailored 'on demand' gold nanoparticles by properly tuning $HAuCl_4$ concentration. The cytotoxicity and cellular uptake behaviors have been investigated in no-neoplastic cells (NIH-3T3) and in two breast cancer cell lines (MCF-7 and SKBR-3) by MTT assay and inductively coupled plasma mass spectrometry (ICP-MS) respectively. It was found that 5Au@PT with the highest hydrodynamic diameter and positive charge showed much higher cell internalization ability and cytotoxicity than the smaller ones (2.5Au@PT and 3.5Au@PT). Moreover, the experimental results against Trastuzumab target cells (SKBR-3) demonstrated that the cytotoxicity of 5Au@PT was closely related to pro-apoptotic protein increase, anti-apoptotic components decrease, survival-proliferation pathways downregulation and uptaking by cells via the activation of the classical receptor-mediated endocytosis. This work thus suggests an utmost importance of size control at the AuNPs when designing molecular-cancer delivery systems. Indeed, nonetheless the present method results suitable for AuNPs synthesis, the stability and conjugation with anticancer molecules depends on particles size, which affects also the its interaction with cancer cells. AuNPs unfortunately are not the optimal candidates for photothermal therapy (PTT) due to their limited absorption in the near infrared (NIR) region. In accordance with other studies, to overcome the size dilemma is possible to assemble small AuNPs into larger structures through controllable interparticle interaction by using biodegradable AGMA1-SH, with the final aim to enhance the absorption of NIR light. Overall, this project should offer important data for particle design improvement and for speeding up AuNPs application in breast cancer therapy with enhanced and personalized therapeutic outcomes.

DATA AVAILABILITY STATEMENT

The raw data supporting the conclusions of this article will be made available by the authors to any qualified researcher on reasonable request.

AUTHOR CONTRIBUTIONS

LV, ER, and CD conceived the study, were responsible for the correctness of analyses, and contributed to writing and editing of the manuscript. All authors contributed to critical experiments and insights, participated to this manuscript writing, and approved the final manuscript.

FUNDING

Fondazione Umberto Veronesi Fellowship - Grant 2017 and Grant 2018, Piano di Sostegno alla Ricerca – Linea 2 Azione A 2018 Università degli Studi di Milano, project PSR2018_DIP_005_DELLA_PINA_CRISTINA, Pavia University's Crowdfunding on breast tumor studies (2015, https://universitiamo.eu/en/campaigns/tumore-seno-diagnosi-cura-nanoparticelle-doro) and a grant of the Italian Ministry of Education, University and Research (MIUR) to the Department of Molecular Medicine of the University of Pavia under the initiative "Dipartimenti di Eccellenza (2018–2022)."

ACKNOWLEDGMENTS

We are grateful to A. Rocchi A for her contribution in the biological part, P. Vaghi (Centro Grandi Strumenti, https://cgs.unipv.it/, University of Pavia, Italy) for the technical assistance in the CLSM studies, to Lucia Cucca (University of Pavia) for ICP analysis, to Giovanna Bruni (University of Pavia) for SEM studies support, and to M. Bordoni (University of Pavia) for revision of the English text.

SUPPLEMENTARY MATERIAL

The Supplementary Material for this article can be found online at: https://www.frontiersin.org/articles/10.3389/fbioe.2020.00132/full#supplementary-material

REFERENCES

Aoyama, Y., Kanamori, T., Nakai, T., Sasaki, T., Horiuchi, S., Sando, S., et al. (2003). Artificial viruses and their application to gene delivery. size-controlled gene coating with glycocluster nanoparticles. *J. Am. Chem. Soc.*, 125, 3455–3457. doi: 10.1021/JA029608T

Arruebo, M., Fernández-Pacheco, R., Ibarra, M. R., and Santamaría, J. (2007). Magnetic nanoparticles for drug delivery. *Nano Today* 2, 22–32. doi: 10.1016/S1748-0132(07)70084-70081

Baharara, J., Ramezani, T., Divsalar, A., Mousavi, M., and Seyedarabi, A. (2016). Induction of apoptosis by green synthesized gold nanoparticles through activation of caspase-3 and 9 in human cervical cancer cells. *Avicenna J. Med. Biotechnol.* 8, 75–83.

Bertrand, B., de Almeida, A., van der Burgt, E. P. M., Picquet, M., Citta, A., Folda, A., et al. (2014). New Gold(I) organometallic compounds with biological activity in cancer cells. *Eur. J. Inorg. Chem.* 2014, 4532–4536. doi: 10.1002/ejic.201402248

Bickford, L., Sun, J., Fu, K., Lewinski, N., Nammalvar, V., Chang, J., et al. (2008). Enhanced multi-spectral imaging of live breast cancer cells using immunotargeted gold nanoshells and two-photon excitation microscopy. *Nanotechnology* 19:315102. doi: 10.1088/0957-4484/19/31/315102

Bignotti, F., Sozzani, P., Ranucci, E., and Ferruti, P. (1994). NMR studies, molecular characterization, and degradation behavior of Poly(amido amine)s. 1. Poly(amido amine) deriving from the Polyaddition of 2-Methylpiperazine to 1,4-Bis(acryloyl)piperazine. *Macromolecules* 27, 7171–7178. doi: 10.1021/ma00102a027

Bloise, N., Ceccarelli, G., Minzioni, P., Vercellino, M., Benedetti, L., De Angelis, M. G. C., et al. (2013). Investigation of low-level laser therapy potentiality on proliferation and differentiation of human osteoblast-like cells in the absence/presence of osteogenic factors. *J. Biomed. Opt.* 18:128006. doi: 10.1117/1.JBO.18.12.128006

Bond, G. C., and Thompson, D. T. (1999). Catalysis by gold. *Catal. Rev.* 41, 319–388. doi: 10.1081/CR-100101171

Boyoglu, C., He, Q., Willing, G., Boyoglu-Barnum, S., Dennis, V. A., Pillai, S., et al. (2013). Microscopic studies of various sizes of gold nanoparticles and their cellular localizations. *ISRN Nanotechnol.* 2013, 1–13. doi: 10.1155/2013/123838

Brzóska, K., Grądzka, I., and Kruszewski, M. (2018). Impact of silver, gold, and iron oxide nanoparticles on cellular response to tumor necrosis

factor. *Toxicol. Appl. Pharmacol.* 356, 140–150. doi: 10.1016/j.taap.2018.08.005

Carnovale, C., Bryant, G., Shukla, R., and Bansal, V. (2016). Size, shape and surface chemistry of nano-gold dictate its cellular interactions, uptake and toxicity. *Prog. Mater. Sci.* 83, 152–190. doi: 10.1016/J.PMATSCI.2016.04.003

Carpin, L. B., Bickford, L. R., Agollah, G., Yu, T.-K., Schiff, R., Li, Y., et al. (2011). Immunoconjugated gold nanoshell-mediated photothermal ablation of trastuzumab-resistant breast cancer cells. *Breast Cancer Res. Treat.* 125, 27–34. doi: 10.1007/s10549-010-0811-815

Cavalli, R., Bisazza, A., Sessa, R., Primo, L., Fenili, F., Manfredi, A., et al. (2010). Amphoteric agmatine containing polyamidoamines as carriers for plasmid DNA *in vitro* and *in vivo* delivery. *Biomacromolecules* 11, 2667–2674. doi: 10.1021/bm100685t

Cavalli, R., Primo, L., Sessa, R., Chiaverina, G., di Blasio, L., Alongi, J., et al. (2017). The AGMA1 polyamidoamine mediates the efficient delivery of siRNA. *J. Drug Target.* 25, 891–898. doi: 10.1080/1061186X.2017.1363215

Chattopadhyay, N., Cai, Z., Pignol, J.-P., Keller, B., Lechtman, E., Bendayan, R., et al. (2010). Design and characterization of HER-2-targeted gold nanoparticles for enhanced X-radiation treatment of locally advanced breast cancer. *Mol. Pharm.* 7, 2194–2206. doi: 10.1021/mp100207t

Cheheltani, R., Ezzibdeh, R. M., Chhour, P., Pulaparthi, K., Kim, J., Jurcova, M., et al. (2016). Tunable, biodegradable gold nanoparticles as contrast agents for computed tomography and photoacoustic imaging. *Biomaterials* 102, 87–97. doi: 10.1016/j.biomaterials.2016.06.015

Cheng, X., Tian, X., Wu, A., Li, J., Tian, J., Chong, Y., et al. (2015). Protein corona influences cellular uptake of gold nanoparticles by phagocytic and nonphagocytic cells in a size-dependent manner. *ACS Appl. Mater. Interfaces* 7, 20568–20575. doi: 10.1021/acsami.5b04290

Chithrani, B. D., and Chan, W. C. W. (2007). Elucidating the mechanism of cellular uptake and removal of protein-coated gold nanoparticles of different sizes and shapes. *Nano Lett.* 7, 1542–1550. doi: 10.1021/nl070363y

Chithrani, B. D., Ghazani, A. A., and Chan, W. C. W. (2006). Determining the size and shape dependence of gold nanoparticle uptake into mammalian cells. *Nano Lett.* 6, 662–668. doi: 10.1021/nl052396o

Choi, H. S., Liu, W., Misra, P., Tanaka, E., Zimmer, J. P., Itty Ipe, B., et al. (2007). Renal clearance of quantum dots. *Nat. Biotechnol.* 25, 1165–1170. doi: 10.1038/nbt1340

Codullo, V., Cova, E., Pandolfi, L., Breda, S., Morosini, M., Frangipane, V., et al. (2019). Imatinib-loaded gold nanoparticles inhibit proliferation of fibroblasts and macrophages from systemic sclerosis patients and ameliorate experimental bleomycin-induced lung fibrosis. *J. Control. Release* 310, 198–208. doi: 10.1016/j.jconrel.2019.08.015

Colombo, M., Fiandra, L., Alessio, G., Mazzucchelli, S., Nebuloni, M., De Palma, C., et al. (2016). Tumour homing and therapeutic effect of colloidal nanoparticles depend on the number of attached antibodies. *Nat. Commun.* 7:13818. doi: 10.1038/ncomms13818

Colzani, B., Pandolfi, L., Hoti, A., Iovene, P. A., Natalello, A., Avvakumova, S., et al. (2018). Investigation of antitumor activities of trastuzumab delivered by PLGA nanoparticles. *Int. J. Nanomedicine* 13, 957–973. doi: 10.2147/IJN.S152742

Comotti, M., Della Pina, C., Matarrese, R., and Rossi, M. (2004). The catalytic activity of ?Naked? Gold particles. *Angew. Chemie Int. Ed.* 43, 5812–5815. doi: 10.1002/anie.200460446

Cristofaro, F., Gigli, M., Bloise, N., Chen, H., Bruni, G., Munari, A., et al. (2018). Influence of the nanofiber chemistry and orientation of biodegradable poly(butylene succinate)-based scaffolds on osteoblast differentiation for bone tissue regeneration. *Nanoscale* 10, 8689–8703. doi: 10.1039/c8nr00677f

Cruz, E., and Kayser, V. (2019). Synthesis and enhanced cellular uptake *in vitro* of anti-HER2 multifunctional gold nanoparticles. *Cancers* 11:870. doi: 10.3390/cancers11060870

Della Pina, C., Falletta, E., Rossi, M., and Sacco, A. (2009). Selective deactivation of gold catalyst. *J. Catal.* 263, 92–97. doi: 10.1016/J.JCAT.2009.01.014

Di Francesco, S., Savio, M., Bloise, N., Borroni, G., Stivala, L. A., and Borroni, R. G. (2018). Red grape (*Vitis vinifera* L.) flavonoids down-regulate collagen type III expression after UV-A in primary human dermal blood endothelial cells. *Exp. Dermatol.* 27, 973–980. doi: 10.1111/exd.13682

Dominguez-Medina, S., Kisley, L., Tauzin, L. J., Hoggard, A., Shuang, B., Indrasekara, A. S., et al. (2016). Adsorption and unfolding of a single protein triggers nanoparticle aggregation. *ACS Nano* 10, 2103–2112. doi: 10.1021/acsnano.5b06439

Donghi, D., Maggioni, D., D'Alfonso, G., Amigoni, F., Ranucci, E., Ferruti, P., et al. (2009). Tricarbonyl-Rhenium complexes of a Thiol-Functionalized amphoteric Poly(amidoamine). *Biomacromolecules* 10, 3273–3282. doi: 10.1021/bm9008638

Doulain, P.-E., Decréau, R., Racoeur, C., Goncalves, V., Dubrez, L., Bettaieb, A., et al. (2015). Towards the elaboration of new gold-based optical theranostics. *Dalton Trans.* 44, 4874–4883. doi: 10.1039/c4dt02977a

Dreaden, E. C., Austin, L. A., Mackey, M. A., and El-Sayed, M. A. (2012). Size matters: gold nanoparticles in targeted cancer drug delivery. *Ther. Deliv.* 3, 457–478. doi: 10.4155/tde.12.21

Ferruti, P. (2013). Poly(amidoamine)s: past, present, and perspectives. *J. Polym. Sci. Part A Polym. Chem.* 51, 2319–2353. doi: 10.1002/pola.26632

Ferruti, P., Bianchi, S., Ranucci, E., Chiellini, F., and Piras, A. M. (2005). Novel agmatine-containing poly(amidoamine) hydrogels as scaffolds for tissue engineering. *Biomacromolecules* 6, 2229–2235. doi: 10.1021/bm050210+

Ferruti, P., Ranucci, E., Trotta, F., Gianasi, E., Evagorou, E. G., Wasil, M., et al. (1999). Synthesis, characterisation and antitumour activity of platinum(II) complexes of novel functionalised poly(amido amine)s. *Macromol. Chem. Phys.* 200, 1644–1654. doi: 10.1002/(SICI)1521-3935(19990701)200:7<1644::AID-MACP1644<3.0.CO;2-P

Franchini, J., Ranucci, E., Ferruti, P., Rossi, M., and Cavalli, R. (2006). Synthesis, physicochemical properties, and preliminary biological characterizations of a novel amphoteric agmatine-based poly(amidoamine) with RGD-like repeating units. *Biomacromolecules* 7, 1215–1222. doi: 10.1021/bm060054m

Gao, H., Shi, W., and Freund, L. B. (2005). From the cover: mechanics of receptor-mediated endocytosis. *Proc. Natl. Acad. Sci. U.S.A.* 102, 9469–9474. doi: 10.1073/pnas.0503879102

Gao, J., Huang, X., Liu, H., Zan, F., and Ren, J. (2012). Colloidal stability of gold nanoparticles modified with thiol compounds: bioconjugation and application in cancer cell imaging. *Langmuir* 28, 4464–4471. doi: 10.1021/la204289k

Gao, W., Xu, K., Ji, L., and Tang, B. (2011). Effect of gold nanoparticles on glutathione depletion-induced hydrogen peroxide generation and apoptosis in HL7702 cells. *Toxicol. Lett.* 205, 86–95. doi: 10.1016/j.toxlet.2011.05.1018

Gautier, A., and Cisnetti, F. (2012). Advances in metal-carbene complexes as potent anti-cancer agents. *Metallomics* 4, 23–32. doi: 10.1039/c1mt00123j

Gebauer, J. S., Malissek, M., Simon, S., Knauer, S. K., Maskos, M., Stauber, R. H., et al. (2012). Impact of the nanoparticle-protein corona on colloidal stability and protein structure. *Langmuir* 28, 9673–9679. doi: 10.1021/la301104a

Ghitescu, L., and Bendayan, M. (1990). Immunolabeling efficiency of protein A-gold complexes. *J. Histochem. Cytochem.* 38, 1523–1530. doi: 10.1177/38.11.2212613

Ghosh, P., Han, G., De, M., Kim, C. K., and Rotello, V. M. (2008). Gold nanoparticles in delivery applications. *Adv. Drug Deliv. Rev.* 60, 1307–1315. doi: 10.1016/j.addr.2008.03.016

Gong, N., Chen, S., Jin, S., Zhang, J., Wang, P. C., and Liang, X.-J. (2015). Effects of the physicochemical properties of gold nanostructures on cellular internalization. *Regen. Biomater.* 2, 273–280. doi: 10.1093/rb/rbv024

Gualandi, C., Bloise, N., Mauro, N., Ferruti, P., Manfredi, A., Sampaolesi, M., et al. (2016). Poly-l-lactic acid Nanofiber–polyamidoamine hydrogel composites: preparation, properties, and preliminary evaluation as scaffolds for human pluripotent stem cell culturing. *Macromol. Biosci.* 16, 1533–1544. doi: 10.1002/mabi.201600061

Gunduz, N., Ceylan, H., Guler, M. O., and Tekinay, A. B. (2017). Intracellular accumulation of gold nanoparticles leads to inhibition of macropinocytosis to reduce the endoplasmic reticulum stress. *Sci. Rep.* 7:40493. doi: 10.1038/srep40493

Hainfeld, J. F., Slatkin, D. N., Focella, T. M., and Smilowitz, H. M. (2006). Gold nanoparticles: a new X-ray contrast agent. *Br. J. Radiol.* 79, 248–253. doi: 10.1259/bjr/13169882

Hajipour, M. J., Raheb, J., Akhavan, O., Arjmand, S., Mashinchian, O., Rahman, M., et al. (2015). Personalized disease-specific protein corona influences the therapeutic impact of graphene oxide. *Nanoscale* 7, 8978–8994. doi: 10.1039/c5nr00520e

Halamoda-Kenzaoui, B., Ceridono, M., Colpo, P., Valsesia, A., Urbán, P., Ojea-Jiménez, I., et al. (2015). Dispersion behaviour of silica nanoparticles in

biological media and its influence on cellular Uptake. *PLoS One* 10:e0141593. doi: 10.1371/journal.pone.0141593

Han, S.-J., Rathinaraj, P., Park, S.-Y., Kim, Y. K., Lee, J. H., Kang, I.-K., et al. (2014). Specific intracellular uptake of herceptin-conjugated CdSe/ZnS Quantum dots into breast cancer cells. *Biomed Res. Int.* 2014, 1–9. doi: 10.1155/2014/954307

Holliday, D. L., and Speirs, V. (2011). Choosing the right cell line for breast cancer research. *Breast Cancer Res.* 13:215. doi: 10.1186/bcr2889

Iijima, M., and Kamiya, H. (2009). Surface modification for improving the stability of nanoparticles in liquid media. *KONA Powder Part. J.* 27, 119–129. doi: 10.14356/kona.2009012

Jacchetti, E., Emilitri, E., Rodighiero, S., Indrieri, M., Gianfelice, A., Lenardi, C., et al. (2008). Biomimetic poly(amidoamine) hydrogels as synthetic materials for cell culture. *J. Nanobiotechnol.* 6:14. doi: 10.1186/1477-3155-6-14

Ji, Z., Jin, X., George, S., Xia, T., Meng, H., Wang, X., et al. (2010). Dispersion and stability optimization of TiO2 nanoparticles in cell culture media. *Environ. Sci. Technol.* 44, 7309–7314. doi: 10.1021/es100417s

Jiang, W., Kim, B. Y. S., Rutka, J. T., and Chan, W. C. W. (2008). Nanoparticle-mediated cellular response is size-dependent. *Nat. Nanotechnol.* 3, 145–150. doi: 10.1038/nnano.2008.30

Jiang, X., Jiang, J., Jin, Y., Wang, E., and Dong, S. (2005). Effect of colloidal gold size on the conformational changes of adsorbed cytochrome *c*: probing by circular Dichroism, UV-Visible, and infrared spectroscopy. *Biomacromolecules* 6, 46–53. doi: 10.1021/bm049744l

Jiang, Y., Huo, S., Mizuhara, T., Das, R., Lee, Y. W., Hou, S., et al. (2015). The interplay of size and surface functionality on the cellular uptake of Sub-10 nm gold nanoparticles. *ACS Nano* 9, 9986–9993. doi: 10.1021/acsnano.5b03521

Kim, P.-H., Sohn, J.-H., Choi, J.-W., Jung, Y., Kim, S. W., Haam, S., et al. (2011). Active targeting and safety profile of PEG-modified adenovirus conjugated with herceptin. *Biomaterials* 32, 2314–2326. doi: 10.1016/j.biomaterials.2010.10.031

Klapper, L. N., Waterman, H., Sela, M., and Yarden, Y. (2000). Tumor-inhibitory antibodies to HER-2/ErbB-2 may act by recruiting c-Cbl and enhancing ubiquitination of HER-2. *Cancer Res.* 60, 3384–3388.

Kushida, T., Saha, K., Subramani, C., Nandwana, V., and Rotello, V. M. (2014). Effect of nano-scale curvature on the intrinsic blood coagulation system. *Nanoscale* 6, 14484–14487. doi: 10.1039/c4nr04128c

Lavignac, N., Nicholls, J. L., Ferruti, P., and Duncan, R. (2009). Poly(amidoamine) conjugates containing doxorubicin bound via an acid-sensitive linker. *Macromol. Biosci.* 9, 480–487. doi: 10.1002/mabi.200800163

Lee, J., Chatterjee, D. K., Lee, M. H., and Krishnan, S. (2014). Gold nanoparticles in breast cancer treatment: promise and potential pitfalls. *Cancer Lett.* 347, 46–53. doi: 10.1016/j.canlet.2014.02.006

Lewinski, N., Colvin, V., and Drezek, R. (2008). Cytotoxicity of nanoparticles. *Small* 4, 26–49. doi: 10.1002/smll.200700595

Lin, J., Zhang, H., Morovati, V., and Dargazany, R. (2017). PEGylation on mixed monolayer gold nanoparticles: effect of grafting density, chain length, and surface curvature. *J. Colloid Interface Sci.* 504, 325–333. doi: 10.1016/j.jcis.2017.05.046

Liu, Y., Li, K., Liu, B., and Feng, S. S. (2010). A strategy for precision engineering of nanoparticles of biodegradable copolymers for quantitative control of targeted drug delivery. *Biomaterials* 31, 9145–9155. doi: 10.1016/j.biomaterials.2010.08.053

Lowry, G. V., Hill, R. J., Harper, S., Rawle, A. F., Hendren, C. O., Klaessig, F., et al. (2016). Guidance to improve the scientific value of zeta-potential measurements in nanoEHS. *Environ. Sci. Nano* 3, 953–965. doi: 10.1039/c6en00136j

Ma, X., Wu, Y., Jin, S., Tian, Y., Zhang, X., Zhao, Y., et al. (2011). Gold nanoparticles induce autophagosome accumulation through size-dependent nanoparticle uptake and lysosome impairment. *ACS Nano* 5, 8629–8639. doi: 10.1021/nn202155y

Marişca, O. T., and Leopold, N. (2019). Anisotropic gold nanoparticle-cell interactions mediated by collagen. *Materials* 12:1131. doi: 10.3390/ma12071131

Martínez-Jothar, L., Beztsinna, N., Van Nostrum, C. F., Hennink, W. E., and Oliveira, S. (2019). Selective Cytotoxicity to HER2 Positive Breast Cancer Cells by Saporin-Loaded Nanobody-Targeted Polymeric Nanoparticles in Combination with Photochemical Internalization. *Mol. Pharm.* 16, 1633–1647. doi: 10.1021/acs.molpharmaceut.8b01318

Matos, M. J., Labão-Almeida, C., Sayers, C., Dada, O., Tacke, M., and Bernardes, G. J. L. (2018). Synthesis and biological evaluation of homogeneous Thiol-Linked NHC*-Au-Albumin and -Trastuzumab bioconjugates. *Chem. A Eur. J.* 24, 12250–12253. doi: 10.1002/chem.201800872

Mauro, N., Manfredi, A., Ranucci, E., Procacci, P., Laus, M., Antonioli, D., et al. (2013). Degradable Poly(amidoamine) hydrogels as scaffolds for *in vitro* culturing of peripheral nervous system cells. *Macromol. Biosci.* 13, 332–347. doi: 10.1002/mabi.201200354

Merli, D., Profumo, A., Bloise, N., Risi, G., Momentè, S., Cucca, L., et al. (2018). Indium/Gallium Maltolate effects on human breast carcinoma cells: *in vitro* investigation on cytotoxicity and Synergism with Mitoxantrone. *ACS Omega* 3, 4631–4640. doi: 10.1021/acsomega.7b02026

Mieszawska, A. J., Mulder, W. J. M., Fayad, Z. A., and Cormode, D. P. (2013). Multifunctional gold nanoparticles for diagnosis and therapy of disease. *Mol. Pharm.* 10, 831–847. doi: 10.1021/mp3005885

Mirshafiee, V., Mahmoudi, M., Lou, K., Cheng, J., and Kraft, M. L. (2013). Protein corona significantly reduces active targeting yield. *Chem. Commun.* 49, 2557–2559. doi: 10.1039/c3cc37307j

Moore, T. L., Rodriguez-Lorenzo, L., Hirsch, V., Balog, S., Urban, D., Jud, C., et al. (2015). Nanoparticle colloidal stability in cell culture media and impact on cellular interactions. *Chem. Soc. Rev.* 44, 6287–6305. doi: 10.1039/c4cs00487f

Moore, T. L., Urban, D. A., Rodriguez-Lorenzo, L., Milosevic, A., Crippa, F., Spuch-Calvar, M., et al. (2019). Nanoparticle administration method in cell culture alters particle-cell interaction. *Sci. Rep.* 9:900. doi: 10.1038/s41598-018-36954-36954

Niza, E., Noblejas-López, M. D. M., Bravo, I., Nieto-Jiménez, C., Castro-Osma, J. A., Canales-Vázquez, J., et al. (2019). Trastuzumab-targeted biodegradable nanoparticles for enhanced delivery of Dasatinib in HER2+ metastasic breast cancer. *Nanomater* 9:1793. doi: 10.3390/nano9121793

Osaki, F., Kanamori, T., Sando, S., Sera, T., and Aoyama, Y. (2004). A quantum dot conjugated sugar ball and its cellular uptake. On the size effects of endocytosis in the subviral region. *J. Am. Chem. Soc.* 126, 6520–6521. doi: 10.1021/ja048792a

Paciotti, G. F., Myer, L., Weinreich, D., Goia, D., Pavel, N., McLaughlin, R. E., et al. (2004). Colloidal gold: a novel nanoparticle vector for tumor directed drug delivery. *Drug Deliv.* 11, 169–183. doi: 10.1080/10717540490433895

Pan, Y., Neuss, S., Leifert, A., Fischler, M., Wen, F., Simon, U., et al. (2007). Size-dependent cytotoxicity of gold nanoparticles. *Small* 3, 1941–1949. doi: 10.1002/smll.200700378

Panariti, A., Miserocchi, G., and Rivolta, I. (2012). The effect of nanoparticle uptake on cellular behavior: disrupting or enabling functions? *Nanotechnol. Sci. Appl.* 5, 87–100. doi: 10.2147/NSA.S25515

Patterson, A. L. (1939). The Scherrer formula for X-Ray particle size determination. *Phys. Rev.* 56, 978–982. doi: 10.1103/PhysRev.56.978

Rathinaraj, P., Al-Jumaily, A. M., and Huh, D. S. (2015). Internalization: acute apoptosis of breast cancer cells using herceptin-immobilized gold nanoparticles. *Breast Cancer* 7, 51–58. doi: 10.2147/BCTT.S69834

Rojas, K., and Stuckey, A. (2016). Breast cancer epidemiology and risk factors. *Clin. Obstet. Gynecol.* 59, 651–672. doi: 10.1097/GRF.0000000000000239

Rossi, M., Pina, C. D., and Falletta, E. (2016). Gold nanomaterials: from preparation to pharmaceutical design and application. *Curr. Pharm. Des.* 22, 1485–1493. doi: 10.2174/1381612822666151210123225

Rubin, I., and Yarden, Y. (2001). The basic biology of HER2. *Ann. Oncol. Off. J. Eur. Soc. Med. Oncol.* 12(Suppl. 1), S3–S8.

Saptarshi, S. R., Duschl, A., and Lopata, A. L. (2013). Interaction of nanoparticles with proteins: relation to bio-reactivity of the nanoparticle. *J. Nanobiotechnol.* 11:26. doi: 10.1186/1477-3155-11-26

Saw, W. S., Ujihara, M., Chong, W. Y., Voon, S. H., Imae, T., Kiew, L. V., et al. (2018). Size-dependent effect of cystine/citric acid-capped confeito-like gold nanoparticles on cellular uptake and photothermal cancer therapy. *Colloids Surf. B. Biointerfaces* 161, 365–374. doi: 10.1016/j.colsurfb.2017.10.064

Sawaki, M., Ito, Y., Akiyama, F., Tokudome, N., Horii, R., Mizunuma, N., et al. (2006). High prevalence of HER-2/neu and p53 overexpression in inflammatory breast cancer. *Breast Cancer* 13, 172–178. doi: 10.2325/jbcs.13.172

Schöttler, S., Becker, G., Winzen, S., Steinbach, T., Mohr, K., Landfester, K., et al. (2016). Protein adsorption is required for stealth effect of poly(ethylene glycol)- and poly(phosphoester)-coated nanocarriers. *Nat. Nanotechnol.* 11, 372–377. doi: 10.1038/nnano.2015.330

Shirshahi, V., Shamsipour, F., Zarnani, A. H., Verdi, J., and Saber, R. (2013). Active targeting of HER2-positive breast cancer cells by Herceptin-functionalized organically modified silica nanoparticles. *Cancer Nanotechnol.* 4, 27–37. doi: 10.1007/s12645-013-0035-36

Spadavecchia, J., Movia, D., Moore, C., Maguire, C. M., Moustaoui, H., Casale, S., et al. (2016). Targeted polyethylene glycol gold nanoparticles for the treatment

of pancreatic cancer: from synthesis to proof-of-concept *in vitro* studies. *Int. J. Nanomed.* 11, 791–822. doi: 10.2147/IJN.S97476

Strojan, K., Leonardi, A., Bregar, V. B., Križaj, I., Svete, J., and Pavlin, M. (2017). Dispersion of nanoparticles in different media importantly determines the composition of their protein corona. *PLoS One* 12:e0169552. doi: 10.1371/journal.pone.0169552

Suarez, E. R., Paredes-Gamero, E. J., Del Giglio, A., Tersariol, I. L., dos, S., Nader, H. B., et al. (2013). Heparan sulfate mediates trastuzumab effect in breast cancer cells. *BMC Cancer* 13:444. doi: 10.1186/1471-2407-13-444

Sun, D., Kang, S., Liu, C., Lu, Q., Cui, L., and Hu, B. (2016). Effect of zeta potential and particle size on the stability of SiO2 nanospheres as carrier for ultrasound imaging contrast agents. *Int. J. Electrochem. Sci.* 11, 8520–8529. doi: 10.20964/2016.10.30

Sun, H., Jia, J., Jiang, C., and Zhai, S. (2018). Gold nanoparticle-induced cell death and potential applications in nanomedicine. *Int. J. Mol. Sci.* 19:754. doi: 10.3390/ijms19030754

Tam, J. M., Tam, J. O., Murthy, A., Ingram, D. R., Ma, L. L., Travis, K., et al. (2010). Controlled assembly of biodegradable plasmonic nanoclusters for near-infrared imaging and therapeutic applications. *ACS Nano* 4, 2178–2184. doi: 10.1021/nn9015746

van der Meel, R., Oliveira, S., Altintas, I., Haselberg, R., van der Veeken, J., Roovers, R. C., et al. (2012). Tumor-targeted Nanobullets: Anti-EGFR nanobody-liposomes loaded with anti-IGF-1R kinase inhibitor for cancer treatment. *J. Control Release* 159, 281–289. doi: 10.1016/j.jconrel.2011.12.027

Vemuri, S. K., Banala, R. R., Mukherjee, S., Uppula, P., Subbaiah, G. P. V., Gurava Reddy, A. V., et al. (2019). Novel biosynthesized gold nanoparticles as anti-cancer agents against breast cancer: synthesis, biological evaluation, molecular modelling studies. *Mater. Sci. Eng. C* 99, 417–429. doi: 10.1016/j.msec.2019.01.123

Vertegel, A. A., Siegel, R. W., and Dordick, J. S. (2004). Silica nanoparticle size influences the structure and enzymatic activity of adsorbed lysozyme. *Langmuir* 20, 6800–6807. doi: 10.1021/la0497200

Villarreal, E., Li, G. G., Zhang, Q., Fu, X., and Wang, H. (2017). Nanoscale surface curvature effects on Ligand-Nanoparticle interactions: a plasmon-enhanced spectroscopic study of Thiolated Ligand adsorption, desorption, and exchange on gold nanoparticles. *Nano Lett.* 17, 4443–4452. doi: 10.1021/acs.nanolett.7b01593

Walkey, C. D., Olsen, J. B., Song, F., Liu, R., Guo, H., Olsen, D. W. H., et al. (2014). Protein corona fingerprinting predicts the cellular interaction of gold and silver nanoparticles. *ACS Nano* 8, 2439–2455. doi: 10.1021/nn406018q

Wang, S. H., Lee, C. W., Chiou, A., and Wei, P. K. (2010). Size-dependent endocytosis of gold nanoparticles studied by three-dimensional mapping of plasmonic scattering images. *J. Nanobiotechnology* 8:33. doi: 10.1186/1477-3155-8-33

Worrall, J. W. E., Verma, A., Yan, H., and Rotello, V. M. (2006). "Cleaning" of nanoparticle inhibitors via proteolysis of adsorbed proteins. *Chem. Commun.* 22, 2338–2340. doi: 10.1039/B517421J

Woźniak, A., Malankowska, A., Nowaczyk, G., Grześkowiak, B. F., Tuśnio, K., Słomski, R., et al. (2017). Size and shape-dependent cytotoxicity profile of gold nanoparticles for biomedical applications. *J. Mater. Sci. Mater. Med.* 28:92. doi: 10.1007/s10856-017-5902-y

Xie, X., Liao, J., Shao, X., Li, Q., and Lin, Y. (2017). The effect of shape on cellular uptake of gold nanoparticles in the forms of stars rods, and triangles. *Sci. Rep.* 7:3827. doi: 10.1038/s41598-017-04229-z

Xu, H., Yu, Y., Marciniak, D., Rishi, A. K., Sarkar, F. H., Kucuk, O., et al. (2005). Epidermal growth factor receptor (EGFR)-related protein inhibits multiple members of the EGFR family in colon and breast cancer cells. *Mol. Cancer Ther.* 4, 435–442. doi: 10.1158/1535-7163.MCT-04-0280

Yu, G., and Zhou, J. (2016). Understanding the curvature effect of silica nanoparticles on lysozyme adsorption orientation and conformation: a mesoscopic coarse-grained simulation study. *Phys. Chem. Chem. Phys.* 18, 23500–23507. doi: 10.1039/c6cp01478j

Yue, J., Feliciano, T. J., Li, W., Lee, A., and Odom, T. W. (2017). Gold nanoparticle size and shape effects on cellular uptake and intracellular distribution of siRNA nanoconstructs. *Bioconjug. Chem.* 28, 1791–1800. doi: 10.1021/acs.bioconjchem.7b00252

Zhang, J., Liu, F., Li, T., He, X., and Wang, Z. (2015). Surface charge effect on the cellular interaction and cytotoxicity of NaYF 4: Yb 3+. Er 3+ @SiO 2 nanoparticles. *RSC Adv.* 5, 7773–7780. doi: 10.1039/C4RA11374H

Zhao, J., and Stenzel, M. H. (2018). Entry of nanoparticles into cells: the importance of nanoparticle properties. *Polym. Chem.* 9, 259–272. doi: 10.1039/c7py01603d

Zhou, Z., Badkas, A., Stevenson, M., Lee, J. Y., and Leung, Y. K. (2015). Herceptin conjugated PLGA-PHis-PEG pH sensitive nanoparticles for targeted and controlled drug delivery. *Int. J. Pharm.* 487, 81–90. doi: 10.1016/j.ijpharm.2015.03.081

Conflict of Interest: The authors declare that the research was conducted in the absence of any commercial or financial relationships that could be construed as a potential conflict of interest.

frontiers in Bioengineering and Biotechnology

REVIEW
published: 10 March 2020
doi: 10.3389/fbioe.2020.00184

Emerging and Innovative Theranostic Approaches for Mesoporous Silica Nanoparticles in Hepatocellular Carcinoma: Current Status and Advances

Yaoye Tao[1,2,3,4], *Jianguo Wang*[1,2,3,4] *and Xiao Xu*[1,2,3,4]*

[1] Division of Hepatobiliary and Pancreatic Surgery, Department of Surgery First Affiliated Hospital, School of Medicine, Zhejiang University, Hangzhou, China, [2] National Health Commission (NHC) Key Laboratory of Combined Multi-Organ Transplantation, Hangzhou, China, [3] Key Laboratory of the Diagnosis and Treatment of Organ Transplantation, Chinese Academy of Medical Sciences (CAMS), Hangzhou, China, [4] Key Laboratory of Organ Transplantation, Hangzhou, China

Hepatocellular carcinoma (HCC) is one of the most prevalent and lethal solid cancers globally. To improve diagnosis sensitivities and treatment efficacies, the development of new theranostic nanoplatforms for efficient HCC management is urgently needed. In the past decade, mesoporous silica nanoparticles (MSNs) with tailored structure, large surface area, high agents loading volume, abundant chemistry functionality, acceptable biocompatibility have received more and more attention in HCC theranostic. This review outlines the recent advances in MSNs-based systems for HCC therapy and diagnosis. The multifunctional hybrid nanostructures that have both of therapy and diagnosis abilities are highlighted. And the precision delivery strategies of MSNs in HCC are also discussed. Final, we conclude with our personal perspectives on the future development and challenges of MSNs.

Keywords: mesoporous silica nanoparticles, hepatocellular carcinoma, theranostic, precision delivery, biomedical applications

OPEN ACCESS

Edited by:
Rawil Fakhrullin,
Kazan Federal University, Russia

Reviewed by:
Nanasaheb D. Thorat,
University of Limerick, Ireland
Monica Terracciano,
University of Naples Federico II, Italy

***Correspondence:**
Xiao Xu
zjxu@zju.edu.cn

Specialty section:
This article was submitted to Nanobiotechnology, a section of the journal Frontiers in Bioengineering and Biotechnology

Received: *15 October 2019*
Accepted: *25 February 2020*
Published: *10 March 2020*

Citation:
Tao Y, Wang J and Xu X (2020) Emerging and Innovative Theranostic Approaches for Mesoporous Silica Nanoparticles in Hepatocellular Carcinoma: Current Status and Advances. Front. Bioeng. Biotechnol. 8:184. doi: 10.3389/fbioe.2020.00184

INTRODUCTION

Liver cancer is currently the fourth primary cause from cancer-related deaths and its incidence and mortality is still increasing, with an estimated 841,080 new cases and 781,631 deaths from this disease in 2018 (Llovet et al., 2016; Bray et al., 2018; World Health Organization [WHO], 2018). Among all primary liver cancers, hepatocellular carcinoma (HCC) represents approximately 90% of all cases. Surgical resection and liver transplantation are considered the curative therapies for long-term control of HCC, however, the majority of HCC patients are diagnosed at advanced stages beyond the standard of surgical treatment (GBD, 2013; Roberto et al., 2016; Yegin et al., 2016). A few molecular targeting drugs such as sorafenib (SO) approved for advanced HCC, which show merely a marginal survival benefit contrasting with conventional drugs. Unfortunately, its efficacy and adverse effects for HCC patients remained unsatisfactory (Bruix et al., 2015; Gao J. et al., 2015). Therefore, new treatment and diagnose modalities for the management of HCC are urgently warranted.

With the development of nanotechnology, nanomaterials modified as multifunctional nanoplatforms for cancer therapeutics, diagnostics, or both (known as "theranostics") attracted increasing attention (Wang J. et al., 2016; Xu et al., 2018; Kesse et al., 2019). Since the first report using silica nanoparticles (Cornell Dot) accepted by the United States Food and Drug Administration (FDA) for a stage-I human clinical trial in 2011 (Benezra et al., 2011), the recent decade has witnessed a steadily increase in research on biomedical application of mesoporous silica nanoparticles (MSNs) in the liver cancer (**Figure 1**). In general, MSNs show the following unique structural and biomedical properties:

(a) Adjustable pore size. The tunable pore diameters of MSNs from 2 to 30 nm allow a variety of agents encapsulated in nanoparticles (Kobler and Bein, 2008; Keasberry et al., 2017). Moreover, hierarchically MSNs which simultaneously consist of large pores and small pores throughout the whole particle are more effective for the diffusion of two different guest molecules in one unit (Jin et al., 2014).
(b) Tunable particle size and shape. The particle size of MSNs can be controlled from 10 to 1000 nm, and the particle morphology can be controlled from rod-, sphere-, to wormlike structures (**Figure 2**; Huh et al., 2003; He et al., 2009). MSNs with different size and shape have unique characteristic (Lu et al., 2009; Meng et al., 2011b), which is convenient for researchers choosing the most suitable particle to achieve their aims.
(c) Ordered mesoporosity and large surface area. The ordered mesoporous structure with disjoint between individual porous channels enable better control of agents loading and release kinetics (Hu et al., 2011). And due to extensive porous structure, MSNs usually have a large surface area enhancing nanoparticles dissolution.
(d) High agents loading volume. Highly porous interior structure ensure a high agent payload of MSNs, usually above 200 mg, maximally about 600 mg agent per 1 g silica (He et al., 2010a). In addition, MSNs synthesized with a hollow core called hollow-type MSNs are capable of encapsulating a super-high dose of agent, typically more than 1000 mg agent per 1 g silica, which is obviously higher than those by other nanoparticles (Zhu et al., 2005a,b).
(e) Facile functional surfaces. MSNs, generally speaking, have two functional surfaces, namely exterior particle surface and cylindrical pore channel surface. However, for hollow-type MSNs, there is an extra interior particle surface. These surfaces can be easily functionalized by virtue of the silane coupling chemistry (He et al., 2010b; Cheng W. et al., 2017). Furthermore, both of exterior and interior particle surfaces which could appropriately connect and coat with other materials become the key of creating high-performing hybrid materials (Castillo and Vallet-Regi, 2019).
(f) Excellent biocompatibility. Silica is considered as "Generally Recognized As Safe" (GRAS) by the FDA (ID Code: 14808-6). He et al. discover that MSNs exhibit a three-stage degradation behavior in simulated body fluid, and almost completely degrade in 15 days (He et al., 2010a). Recently several *in vivo* biosafety evaluations of MSNs have been reported (Liu T. et al., 2011; Fu et al., 2013; Choi et al., 2015), indicating MSNs have low *in vivo* toxicity and can be excreted from the body through feces and urine.

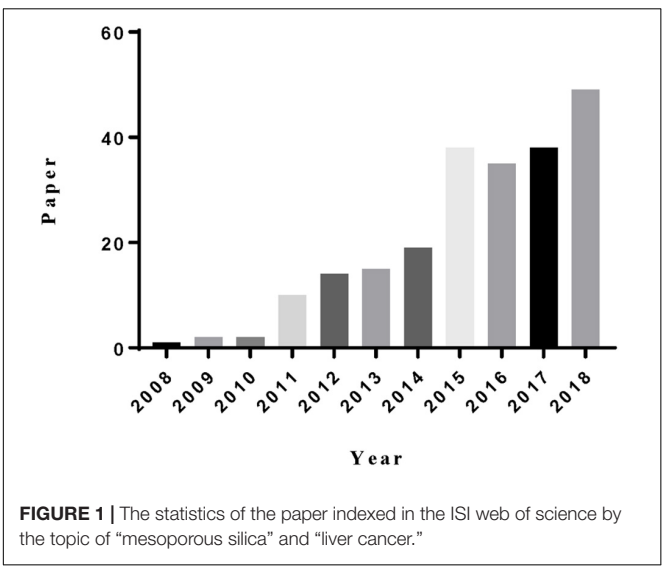

FIGURE 1 | The statistics of the paper indexed in the ISI web of science by the topic of "mesoporous silica" and "liver cancer."

These distinctive features endow MSNs with unique advantages to encapsulate a variety of therapeutic and bioimaging agents and implement the desired functions. To give an overview of recent progress of MSNs in theranostic for HCC, this review is arranged as follow. Firstly, it outlines precision delivery strategies of the agents in MSNs to HCC sites and cells. Next, the current state of the research of using MSNs in the field of HCC theranostics are highlighted. Finally, we vision the future advancements for MSNs.

PRECISION DELIVERY STRATEGIES OF MSNS IN HCC

Nanoparticles, designed to deliver agents preferentially to the HCC tissues and cells, provide the precondition for overcoming the shortcomings of conventional treatment and diagnose approaches (Bae et al., 2011). The targeting ability to tumor not only enhances the effects of agents, but also controls dose-limiting side effects in other tissue. A well-designed nanosystem always includes multiple delivery strategies to reach a high accumulation in tumor. In this part, we discuss the delivery strategies developed in MSN-based HCC theranostics (**Figure 3**).

Passive Targeting

It is well recognized that liver tumors display remarkable extensive angiogenesis with defective vascular structure, accompanying with impaired lymphatic drainage system (Zhu et al., 2011). Therefore, the vascular networks of HCC have an increased permeability to circulating nanoparticles, while the lymphatic system has a reduced disposal rate to internalized nanoparticles, which allow MSNs to accumulate in HCC tumor

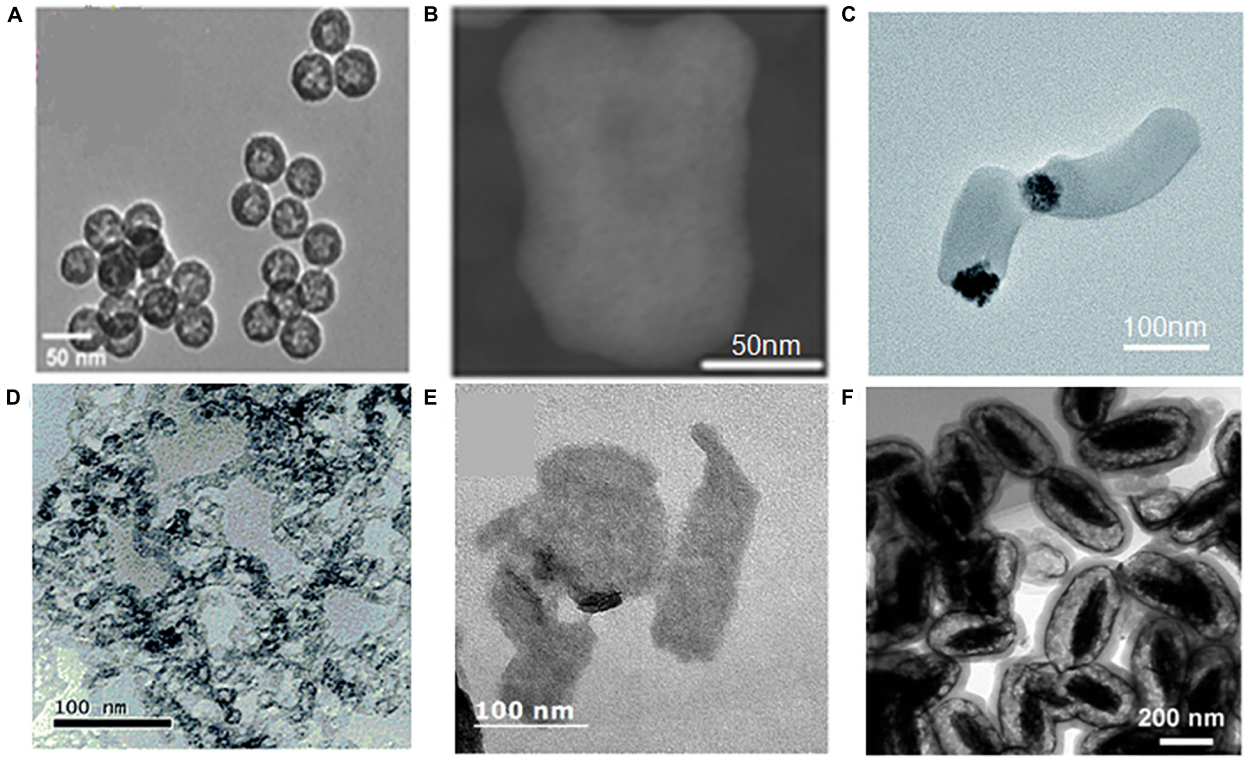

FIGURE 2 | TEM of samples **(A)** (MSNs-1), **(B)** (MSNs-2), **(C)** (MSNs-3), **(D)** (MSNs-4), **(E)** (MSNs-5), **(F)** (MSNs-6) with different size and shape. **(A)** Reproduced with permission from Li et al. (2018b). **(B)** Reproduced with permission from Li et al. (2018c). (C) Reproduced with permission from Xing et al. (2018). **(D)** Reproduced with permission from Liu et al. (2017). **(E)** Reproduced with permission from Lee et al. (2016). **(F)** Reproduced with permission from Lv et al. (2015).

interstitial space (Maeda et al., 2000). This so-called enhanced permeation and retention (EPR) effect has been considered as basics for achieving passive targeting in the nanosystems (Maeda et al., 2013).

Particle size, shape, and surface chemistry of MSNs could greatly influence the EPR effect of the nanoparticles (Lee et al., 2009; Maeda et al., 2013; Li et al., 2016). For instance, Meng et al. demonstrated 50 nm MSNs coated with PEI-PEG copolymer yield a intratumoral accumulation of about 12% of the total dose, which is significantly higher compared to 1% of 100 nm phosphonate-coated MSNs and 3% of 50 nm PEGylated MSNs. The additional cationic polymer coated on the MSNs ameliorated the potential downside of PEG surface. In conclusion, size tuning and decoration of the MSNs with PEI-PEG copolymer lead to an dramatic enhancement of EPR effect and sufficient accumulation in tumor (Meng et al., 2011a). Besides, a research from Harvard Medical School showed that combined radiation and cyclophosphamide could enhance tumor-associated vascular leaking, leading to a sixfold increase of nanoparticles accumulation in tumor (Miller et al., 2017).

Active Targeting

EPR-mediated passive targeting always lacks specificity for different tumor tissues and tumor development stages (Natfji et al., 2017). To improve the targeting efficiency, active targeting strategies have gained much attention recently.

Owing to the overgrowth and abnormality of HCC, many receptors are usually upregulated on the surface of HCC cells, compared to other normal cells. Through the recognition of these receptors by targeting ligands on MSNs, more smart targeting strategies have been achieved. The targeting ligands now used for MSN-based HCC theranostics include lactobionic acid (Zhang et al., 2012), folic acid (Chen et al., 2019), arginine-glycine-aspartate (RGD) (Chen et al., 2012), transferring (Hao et al., 2017), hyaluronic acid (Lee et al., 2018), low-density lipoprotein (LDL) (Ao et al., 2018), and others (**Table 1**).

In another way, magnetic mesoporous silica nanoparticles (M-MSNs) with superior magnetic properties maintaining the excellent advantages of MSNs could achieve magnetic-mediated targeting functions under external magnetic fields (EMFs) (Shao D. et al., 2016; Wang Y. et al., 2016; Tang et al., 2017). The targeting capacity guided by EMFs including two aspects: on the one hand, M-MSNs would mainly accumulation around the tumor site under the EMFs, which could apply a magnetic force on nanoparticles to enhance the EPR effect and overcome the drag experienced in the blood flow (Thorat et al., 2019a); on another hand, EMFs effect could enhance endocytosis of the tumor cells. Interestingly, under the EMFs about 15% higher fluorescence intensity of nanoparticles was detected in HepG2 cells than that of the non-magnetic field untreated HepG2 cells, while this phenomenon is absence in HL-7702

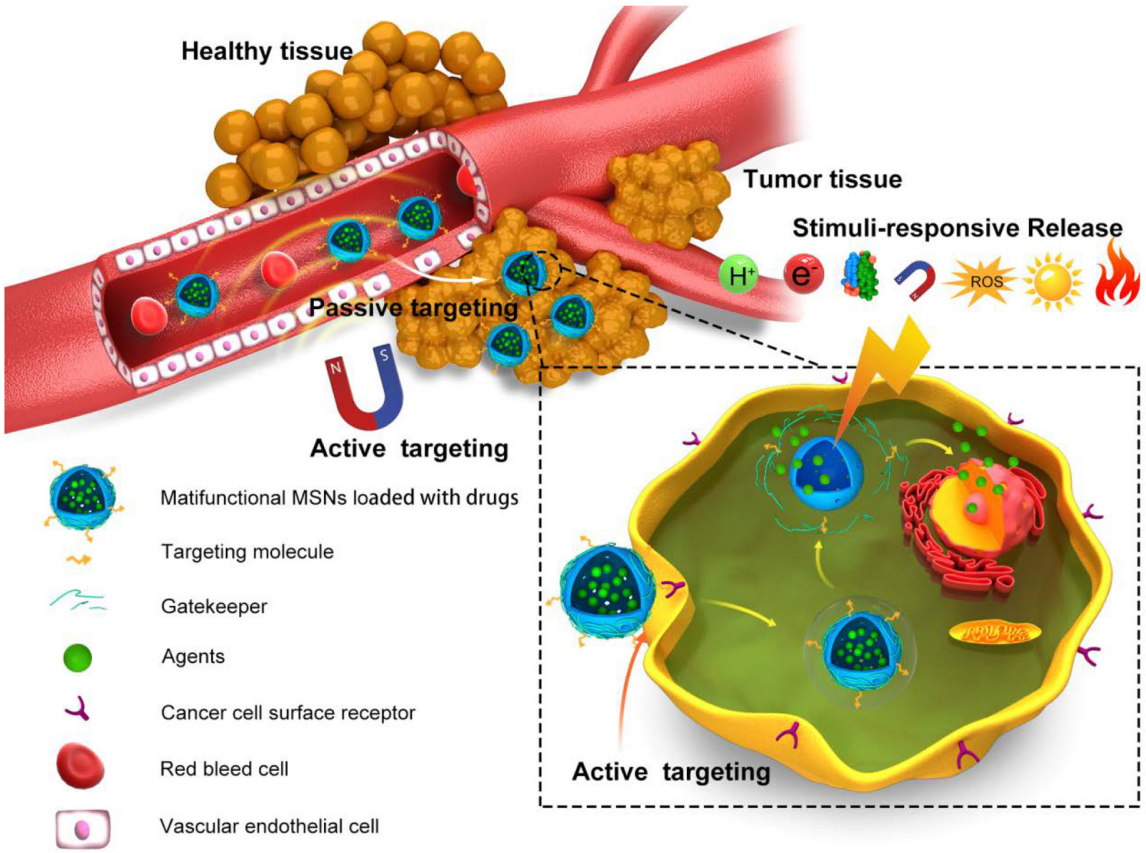

FIGURE 3 | Schema of the delivery strategies of MSNs in HCC. *In vivo* process of precision delivery, when MSNs arrive the vasculature of tumor, passive targeting would first work based on EPR effects. Next, active targeting by conjugation of targeting ligand/receptor and EMF effects would promote MSNs into tumor tissues and cells. Final, stimuli-responsive release in tumor tissues and cells would realize by virtue of pH, redox, light, and so on.

cells, which means the effect of EMFs is selective for HCC cells (Xing et al., 2018).

Stimuli-Responsive Release

Nano delivery systems are ideal with "zero premature release" before arriving the disease foci. The stimuli-responsive release can realize this point in response to internal stimuli in tumor microenvironment or external stimuli (Thorat et al., 2019b).

Internal Stimuli

Among internal stimuli, PH-responsive release plays the most promising role in HCC, since a more acidic extracellular (pH $\approx$ 6.8) environment is usually formed around solid tumor tissues than normal tissues and blood (pH $\approx$ 7.4) due to increased acid production resulting from high glycolysis (Lu et al., 2018). It has been found that electrostatic interactions between the positively charged agents [such as doxorubicin (DOX)] and negatively charged MSNs were greatly reduced by protonation in a low pH condition, which results in a pH-responsive release of DOX (Chen et al., 2018). Similarly, some gatekeepers over the pore entrance to reduce premature release of agents could be protonated under acidic pH, rapidly collapsing, thus the agents would be released from the nanoparticles (Chen et al., 2019). Besides, some chemical bonds connecting the gatekeepers and MSNs, which would be broken down by pH stimulation, are also be used in pH-responsive release (Liu et al., 2016). Differentiated from the common single pH-responsive systems, a novel cascade pH stimuli triggering nanosystem had been developed (**Figure 4A**). At first, benzoic-imine bonds would be dissociated in the tumor microenvironment pH signal (6.8) to release PEG and improve cellular uptake. Then, boronic acid-catechol ester bonds would be hydrolyzed in the endosome/lysosome pH signal (4.5–6.5) to release more drug in tumor cells, which leads to significant tumor growth inhibition. In tumor-bearing mice, the increased life span of mice treated with this nanoparticles was raised 42.4% than no pH-responsive nanoparticles (Liu et al., 2016).

In addition, HCC cells always undergo oxidative stress, which means the overproduction of various reactive oxygen species (ROS) in tumor cells. In the meantime, HCC cells also have an elevated glutathione (GSH) level to protect themselves under ROS cytotoxicity (Cheng S.B. et al., 2017; Jiang et al., 2017). Consequently, GSH-responsive become one of most popular redox-responsive precision delivery strategies because of the higher GSH level in intracellular matrix of HCC cells than that in extracellular matrix or intracellular matrix of normal

TABLE 1 | Summary of targeting ligands and receptors on MSN-based HCC theranostics.

Ligand	Receptor	Cell type	Animal model	References
Lactobionic acid	Asialoglycoprotein receptor (ASGPR)	HepG2,Huh7, SMMC-7721	HepG2 mice model, H22 mice model	Zhang et al., 2012; Dai et al., 2014; Wang et al., 2017d; Zhao et al., 2017; Pei et al., 2018; Zheng et al., 2018
Folic acid	Folate receptor	HepG2,SMMC-7721	SMMC-7721 mice model, HepG2 mice model, H22 mice model	Chen et al., 2010, 2019; Gao B. et al., 2015; Lv et al., 2015; Wang Y. et al., 2016; Wang et al., 2017a,b; Xu et al., 2017
RGD	Integrin	SMMC-7721, HepG2, Huh7	SMMC-7721 mice model, H22 mice model	Chen et al., 2012; Liao et al., 2014; Yu et al., 2015; Zeng et al., 2016; Fei et al., 2017; Li et al., 2018b
Transferrin	Transferrin receptor	Huh7	N/A	Chen X. et al., 2017; Hao et al., 2017
Hyaluronicacid	CD44	HepG2	N/A	Lee et al., 2018
LDL	LDL receptor	HepG2	HepG2 mice model	Ao et al., 2018
Galactose/lactose	ASGPR	HepG2, SMMC-7721	N/A	An et al., 2015; Quan et al., 2015
SP94	Unknown receptor(s)	Hep3B	N/A	Ashley et al., 2011; Epler et al., 2012
AS1411 aptamer	Nucleolin	HepG2	HepG2 mice model	Zhang et al., 2014
Epithelial cell adhesion molecule (EpCAM)aptamer	EpCAM	HepG2	HepG2 mice model	Babaei et al., 2017
TLS11a aptamer	Unknown receptor(s)	HepG2	N/A	Hu et al., 2017
Glycyrrhetinic acid (GA)	GA receptor	HepG2	N/A	Lv et al., 2017
Cetuximab	Epidermal growth factor receptor (EGFR)	HepG2	HepG2 mice model	Wang J.K. et al., 2017
Tumor necrosis factor-related apoptosis-inducing ligand (TRAIL)	Death receptors 4/5	HepG2	HepG2 mice model	Liu et al., 2017
Anti-CD155/anti-CD112 monoclonalantibodies	CD155/CD112	SMMC-7721, HHCC	SMMC-7721 mice model	Tao et al., 2016
Avidin	Carcinoembryonic antigen (CEA)	Huh7, LM-9	N/A	Chen et al., 2014
Phenylboronic acid	Sialic acid	HepG2	H22 mice model	Tang et al., 2017
Concanavalin A	Glycoprotein receptors	Huh7, ML-1	N/A	Chen et al., 2018
HepG2 cell membranes	Unknown receptor(s)	HepG2	HepG2 mice model	Yue et al., 2018b

cells (Chen X. et al., 2017). The disulfide bond which could be cleaved by GSH is widely used to connect the gatekeepers and MSNs (Chen X. et al., 2017; Tang et al., 2017; Wang J.K. et al., 2017). In one study, the surfaces of MSNs were functionalized by cytochrome c (CytC) via disulfide bonds, which would be rapidly cleaved in HCC cells to release the loaded drug. Around 78.9% of agents was released from MSNs with stimulus of reductive signals after incubation for 3 h, whereas only 5.11% of agents was released for the group without reductive signals (Zhang et al., 2014). Moreover, Yue et al. presented mesoporous organosilica nanoparticles (MONs) containing disulfide bridges inside, synthesized on the framework of MSNs (**Figure 4B**). In cancer cells with the high concentration of GSH, MONs would be broken into small pieces leading to greater targeting drug release. The fluorescence intensity of DOX in the MONs treated cells was approximately 20% higher than MSNs treated cells (Yue et al., 2018a). In a similar way, the ROS-responsive MSNs are also developed for HCC theranostics (Pei et al., 2018).

In other reports, it has been well established that there is over expression of some enzymes in HCC, such as protease (Menard et al., 2019), glycosidase (Hakeem et al., 2016), and esterase (Xia et al., 2017). Once the enzyme is found at higher level in the tumor site, the MSNs can be programmed to targeting release of agents via enzymatic conversion of the carrier. Some microRNAs such as miR-122 are abundant in liver cancer. Therefore, one type of microRNAs-responsive MSNs in Huh7 cells by hybridization between antagomir-122 and endogenous miR-122 obtained a unequivocal success (Yu et al., 2015).

External Stimuli

Compared with the above microenvironment-responsive systems, external stimuli-responsive systems can be easily manipulated to precisely achieve spatiotemporal control and on-demand agents release (Lin et al., 2018). The main drawback of intrinsic stimuli is that internal environment of body is complicated and unmanageable, especially for the highly heterogeneous tumor tissues, which maybe results in an uncontrolled release (Thorat et al., 2019a).

Among the various light stimuli, near-infrared (NIR) has the great advantages of minimal absorption and deep penetration into tissue (Wu et al., 2015; Sun et al., 2017). The NIR-I (700–950 nm) and NIR-II (1000–1350 nm) are the most widespread regions for light-responsive systems. The MSNs hybridized with photoabsorbing materials exploit the fine photothermal effect limited within tumor tissues through converting light energy to thermal energy, which is a particularly promising phenomenon

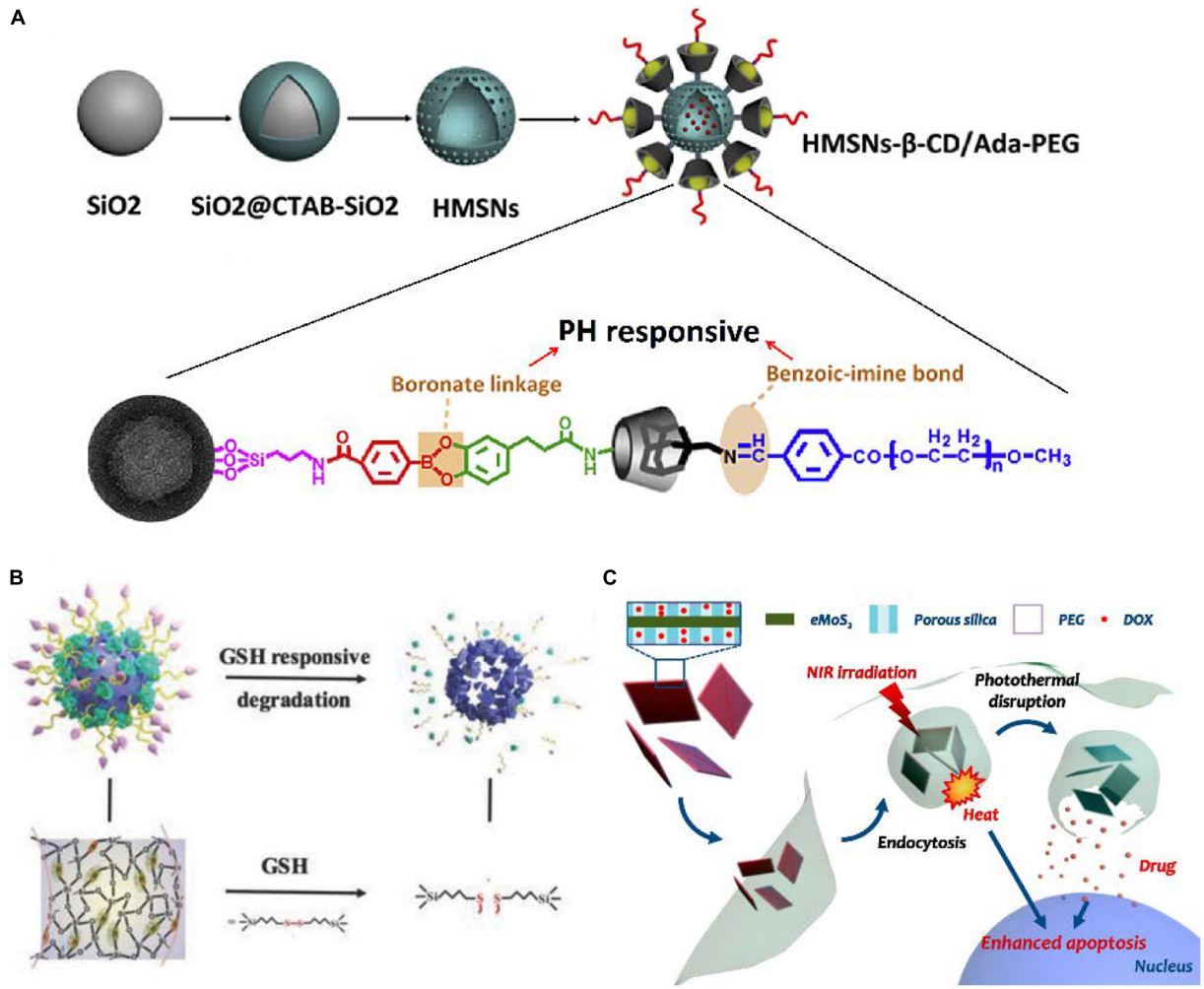

FIGURE 4 | Different stimuli-responsive MSNs. **(A)** Fabrication illustration of dual-pH-responsive MSNs. **(B)** Schematic illustration of MONs. **(C)** Schematic illustration of NIR-responsive MSNs. **(A)** Reproduced with permission from Liu et al. (2016). **(B)** Reproduced with permission from Li et al. (2018b). **(C)** Reproduced with permission from Lee et al. (2016).

for use in light-responsive agents release (**Figure 4C**; Lee et al., 2016). NIR-thermal agents precision delivery can be reasonably attributed to the following reasons: first, the Brownian motion of agents would be accelerated by the photothermal effect; second, the photothermal effect could increase tumor cells membrane permeability; third, the photothermal effect may destabilize the membrane of endosome and thus facilitate escape of the agent from the endosome (Lee et al., 2016; Shao T. et al., 2016; Chen et al., 2018).

Besides aforementioned applications, M-MSNs are not only for magnetic-mediated targeting, but also for stimtli-responsive release. Alternating magnetic field (AMF) can heat M-MSNs by the magnetothermal effect, and then, the thermal fluctuations within M-MSNs trigger agents release (He and Shi, 2014; Wang et al., 2018). The mechanisms of the magnetothermal effect by these nanoparticles are related to brownian motion, neel relaxation, and hysterysisloss. And the release profile of agents can be regulated by changing the field strength and frequency of AMF. By the way, magnetic fluid hyperthermia will cause damage on tissues surrounding the nanoparticles to kill cancer cells. But for safety of healthy tissues, combination of field amplitude of about 10 kA m^{-1} and a frequency of about 400 kHz was suggested for stimulation (Thorat et al., 2019a).

In the future, with advance of nanotechnology, more various stimuli-responsive will be realized in MSNs for precision delivery.

MSNS IN HCC DETECTION AND DIAGNOSIS

MSNs-Assisted Bioimaging

Ultrasound (US) is still the most common technique to screen the HCC since it is safe, economical and accessible (Verslype et al., 2012). However one study reported that the sensitivity of US for the small lesion (<2 cm), which is important for early detection and diagnosis of HCC, is only 27.3% (Kim et al., 2017).

To improve diagnostic accuracy and sensitivity for early stage tumor, photoacoustic (PA) imaging integrating optical and ultrasound advantages have been developed which has the highest resolution in deep tissue compared with any conventional imaging tools (Liu Y. et al., 2019). So in the integrated system, PA imaging easily combined with ultrasound imaging can strongly enhance the clinical diagnosis (Kim et al., 2016). To this end, Lee et al. synthesized a MSNs-based liver targeting PA contrast agent, hyaluronate–silica nanoparticle (HA–SiNP) conjugate. Because of strong photoacoustic signal of SiNP in NIR windows, the PA amplitude in liver after HA–SiNP conjugates injection was remarkably enhanced 95.9% compared to normal liver beyond other PA contrast agents, which provides more detail anatomical and functional information for HCC diagnosis (Lee et al., 2018).

Before treatment, dynamic contrast-enhanced magnetic resonance imaging (MRI) is considered as the best approach to define the tumor staging and assist in choosing a suitable treatment strategy. Non-specific contrast agents, Gd complexes, have been the most widely applied agents for liver MRI (Bellin et al., 2003). Nevertheless, for HCC diagnosis, liver-specific MRI contrast agents, which mainly target the liver tissue, maybe an alternative choice. Aim to make up the limitations of non-specific contrast agent, Kim et al. investigated the liver-specific MRI contrast agent, Mn^{2+}-doped SiO_2 nanoparticles (Mn-SiO_2), enhancing the visibility of HCC lesion. The nanoparticles engulfed in Kupffer cells would release the Mn^{2+} ions, thus T1-weighted MRI shows hyperintense in healthy liver tissues with abundant Kupffer cells over lesions, which are always lack of Kupffer cells (Kim et al., 2013).

Furthermore, it has been reported that intraoperative fluorescent imaging for imaging-guided surgery by virtue of MSNs could dramatically improve surgical intervention of tumor (Zeng et al., 2016). This RGD-conjugated MSN highly loaded with ICG dye could precisely delineate the margins of HCC intraoperatively by NIR. Depend on the subjective experience, only the conspicuous tumors (5.09 ± 2.31 mm) could be visually discriminated by surgeons intraoperatively. This lesion is also confirmed by fluorescent imaging. The microtumor lesions (0.4 ± 0.21 mm), which could not be recognized with the nake eye, are accurately detected by fluorescent imaging. Currently in operations, surgeons mainly rely on conventional preoperative imaging methods and subjective experience. However, in most cases, tumor microfoci can't be discovered which is regarded as one of the etiology for tumor recurrence. But in the intraoperative fluorescent imaging by MSNs, tumor microfoci in liver could easily be distinguished and resected resulting in better surgical outcomes. It is helpful to reduce the high postoperative recurrence rate of HCC.

MSNs-Assisted Liquid Biopsy

Liquid biopsy refers to non-invasive tests analyzing the bodily fluids and is a promising option to detect early stage HCC (Zhou et al., 2016; Ye et al., 2019). The source from tumor for liquid biopsy covers circulating tumor cells (CTCs), nucleic acids, proteins and circulating exosomes (Lee et al., 2018). Currently, several new MSNs have been reported for detection of tumor cells and their associated molecules. Hu et al. developed functionalized MSNs for specifically detecting HCC cells with assist of a biotin-labeled aptamer. The binding rate with hepG2 cells could reach approximately 90%, while the binding rate with L02 cells was close to 2%, which means the nanoparticles established a sensitive detection system for HCC cells (Hu et al., 2017). In another research, MSNs are utilized to detect the apoptotic tumor cells for evaluation of treatment response. This detection system contains two steps: (1) the HCC cells among various cells would be immobilized on the nanotubes; (2) the apoptotic HCC cells would be quantitated through the specific interaction between antiphosphatidyl serine antibody and phosphatidylserine. This cytosensor has a high sensitivity, which even could respond as low as 800 cells mL^{-1} (Wu et al., 2012). Besides, MSNs are also used to enrich phosphopeptides from serum of HCC patients. And then the phosphopeptides could be extract from MSNs for further analysis (Hu et al., 2009).

MSNS IN HCC TREATMENT

Drug Therapy

Systemic chemotherapy usually is the only option for patients in advanced cancer, however, no satisfactory results have been obtained in HCC (Bruix et al., 2015; Gao J. et al., 2015). Thus, numerous studies focusing on MSNs to improve the drug effect have been reported. Awing to the unique structure of MSNs, they are suitable for delivery of both hydrophobic/hydrophilic anticancer drugs. Moreover, drugs release in MSNs always experience a decrease in release rate, resulting in sustained release pharmacokinetics (Kumar et al., 2015; He et al., 2017). DOX, which is easily tracked through fluorescence effects, is widely used as a model drug for assessing drug loading and delivery capacity in MSNs (Rudzka et al., 2013; Xie et al., 2014; Yang et al., 2015). Although DOX in MSNs had showed a good antitumor effects, other drugs that is more sensitive for HCC should be explored. It's worth noting that many hydrophobic drugs loaded in MSNs overcome their poor water solubility, including paclitaxel (Li et al., 2010; He et al., 2017; Xu et al., 2017), curcumin (Lv et al., 2017; Xing et al., 2018), berberine (Yue et al., 2018b), and so on. Co-delivery multiple drugs have been recognized as a more efficient treatment than a single drug. Thus a MSNs-based nanoparticle had been developed for co-delivery of SO and ursolic acid (UA). Compared with the SO or UA respectively treated group, the expression of EGFR and VEGFR2 in SO + UA treated group decreased about 60%, which tremendously increase apoptosis of tumor cells and inhibit proliferation, adhesion, migration and angiogenesis. The further *in vivo* increased therapeutic efficacy of nanoparticles demonstrate the synergistic effect of SO and UA (Zhao et al., 2017). UA, which possesses significant antitumor activity, is limited in clinical application with its poor water solubility. By virtue of MSNs, UA can be delivered to tumor tissues, exhibiting a synergetic antitumor effect with SO. It suggested a promising approach for exploiting the potential of the drugs.

Protein Therapy

Proteins have been explored as potential therapeutic candidates in cancer therapy since they have a low amount of side effects and the immunity to multidrug resistance mechanism (Epler et al., 2012; Deodhar et al., 2017). However, due to their facile degradation and fragile structure *in vivo*, effective delivery of proteins is a great challenge in spite of the vehicles (Escoto, 2013; Deodhar et al., 2017). Thus, MSNs have been used as promising vehicles to deliver proteins in HCC therapy (Zhang et al., 2014; Liu et al., 2017). The porous and stable nature of MSNs allows proteins encapsulated inside nanoparticles and provides a stable shelter to protect proteins. Lipid bilayer-modified MSNs had been designed to deliver ricin toxin A-chain (RTA) in which a few of RTA prematurely release and the activity of the remanent proteins was retained. RTA-loaded MSNs induce apoptosis in Hep3B at picomolar concentrations of RTA, which is 3500-fold less than the IC50 values of free RTA. These excellent functions enable protein-based therapies to reach their full potential (Epler et al., 2012). Covalent modification of protein on the MSNs surface was another approach for protein delivery. The proteins in this MSNs release via cleavage of the covalent bond in the pH/redox stimulation. Moreover, the proteins immobilized on the surface can be used as gatekeepers mentioned previously since the hydrodynamic diameters of the proteins are sufficient to cover the pores of MSNs. Relatively, in this way, the protective effects for proteins may be weaker (Pei et al., 2018).

Gene Therapy

Gene therapy has been regarded as a new opportunity to satisfy the needs in treatment of cancer (Das et al., 2015). With the advancement in RNA biology, gene therapies not only introduce the exogenous genes by DNA but also change the gene expression at the mRNA level through by virtue of short interfering RNAs (siRNAs), miRNAs and antisense oligonucleotides (ASOs) (Shim et al., 2018). Recently, Clustered regularly interspaced short palindromic repeats/CRISPR-associated nuclease 9 (CRISPR-Cas9) also opens a new avenue in gene therapy to correct the mutations of cancer (Karimian et al., 2019). However, the development of an efficient and safe vector for therapeutic genetic materials is still a major issue. MSNs are promising carriers for gene delivery for their versatile payload of various genetic materials without chemical modification. For forming a stable complex with electronegative nuclei acid, MSNs are often modified to possess net positive charges by methods including amination-modification (Xiao et al., 2010; Yu et al., 2015; Zheng et al., 2018) and cationic polymer functionalization (Xue et al., 2017; Wang et al., 2018). In these terms, the modified surface can not only increase the adsorption capacity of negatively charged nuclei acid molecules, but can also facilitate MSNs to escape from endosome/lyposomes by "proton sponge effect" (Tang et al., 2012; Wang et al., 2018).

To overcome multidrug resistance in HCC, Xue et al. prepared lipid-coated MSNs containing DOX and miR-375 which can inhibit P-glycoprotein (P-gp) expression via inhibition of astrocyte elevated gene-1 (AEG-1) expression in HCC. P-gp, which is overexpressed in multidrug resistance cells in HCC, could impede the effectiveness of chemotherapy. So augment the level of miR-375 in HCC cells would serve as a credible way to overcome multidrug resistance. Further evaluation of antitumor effect in the DOX-resistant HepG2 cells xenograft tumor mouse model showed the tumor volume in DOX and miR-375 nanoparticles treated group is only about half of that in DOX nanoparticles treated group in 1 month, suggesting an alternative option to overcome multidrug resistance in HCC by these nanoparticles (Xue et al., 2017).

Phototherapy/Sonodynamic Therapy (SDT)

Recently, phototherapy has emerged as a promising strategy for HCC. Photothermaltherapy (PTT) and photodynamic therapy (PDT) are two main types of phototherapy. PTT destroies the tumor cells by light-induced photothermal effects, while PDT damages the tumor cells by light-induced cytotoxic singlet oxygen ($^1O_2$), one kind of the most representative ROS (Liu H. et al., 2011; Zhao et al., 2012). NIR is widely used in PTT and PDT because of its superiority compared to other lights. In recent reports, MSNs prepared with photothermal agents including MoS_2, C, Au, CuS and indocyanine green (ICG) showed a strong photothermal effect (Wu et al., 2015; Lee et al., 2016; Wang Z. et al., 2016; Wang et al., 2017a; Chen et al., 2018). Usually normal cells possess a higher heat tolerance over cancer cells at elevated temperatures around 43°C, so the heat generated (43°C) would trigger the death of tumor cells only (El-Boubbou, 2018). Gao B. et al. (2015), reported MSNs with gold core acted as a radiation sensitizer, thereby inducing the more effective radiotherapy by iodine 125 seed. Furthermore, Wang et al. (2019) rethink that radiosensitization strategy is not sufficient because of the hypoxic microenvironment in HCC, so they fabricated Janus-structured gold triangle-mesoporous silica nanoparticles to ameliorates hypoxia through PTT generated by gold triangle. This research indicated synergistic radio-photothermal therapy is a reasonable combination scheme. And there are some photosensitizers, such as Zinc(II)-phthalocyanine, Chlorin e6, Photosan-II loaded in MSNs for PDT in HCC (Liu et al., 2014; Lv et al., 2015; Lin et al., 2018). The success of PDT depends on the potential of photosensitizers to transfer energy from light to tumor dissolved oxygen (O_2) to generate $^1O_2$. Pre-existing hypoxia in HCC and O_2 consumption during PDT can remarkably lower down the PDT efficacy (Thorat et al., 2019a). To address this problem, *in situ* synthesized Pt nanoparticles as a catalyst to convert H_2O_2 into O_2 on MSNs was constructed. And 4.2-fold O_2 and 1.6-fold $^1O_2$ generation ability compared to normal MSNs greatly improved the PDT efficacy in HCC and exhibited threefold tumor suppression ability in HCC mice model (Lan et al., 2019).

However, when tumor locates in the deeper tissue, which is common for HCC, the lights arriving to the tumor are so weak that hardly produce an enough cytotoxic effects. Therefore, MSNs-based SDT has been developed account for the advantage of deeper tissue-penetrating of ultrasound (Li et al., 2018b). In spite of the ROS cytotoxic effects on the tumor cells, moreover, SDT can enhance the chemotherapeutic sensitivity of tumor cells by activating the cellular internalization and the

mitochondrial apoptotic pathway, and inhibiting ATP-binding cassette transporter (Xu et al., 2013; Qian et al., 2016). For example, Li et al. (2018b) chose MONs as nanocarriers for the delivery of both sonosensitizer (protoporphyrin, PpIX) and DOX. The tumor-inhibiting rates in mice increased about 21.6% with the US irradiation (Li et al., 2018b). So the combination of SDT and chemotherapy is a hopeful strategy for HCC treatment.

DUAL EFFECTS OF THERAPY AND DIAGNOSIS IN MSNS

As described, MSNs-based therapy and diagnosis for HCC have been investigated a lot separately. More importantly, MSNs-based theranostic nanostructures are capable of detecting the tumor not only before or after, but also during the treatment anytime. Recently, Chen H. et al. (2017) offered a proposal extending the concept of nanotheranostics from nanomedicine owning both diagnostic and therapeutic functions, to the approaches that use diagnosis to aid nanoparticle therapy procedures. With such approaches, medical treatments can be tuned promptly on the basis of the detection results, which means more specific therapies for individual patient (**Figure 5**; Xie et al., 2010).

The easiest way to achieve theranostics is co-delivery of therapeutic and imaging agents. Ashley et al. modified MSN with supported lipid bilayers resulting in nanostructures ("protocells"), which could be loaded with mixtures of therapeutic (drugs, proteins, genes) and diagnostic (quantum dots) agents (Ashley et al., 2011). Quantum dots as a fluorescent dyes could trace the biodistribution of content in nanostructures because mixtures of therapeutic agents and quantum dots will be released from nanostructures simultaneously. Within a certain period of time, quantum dots remaining in nanostructures could show the location of nanoparticles targeting to tumor for diagnosis. Therefore, in this way, the fluorescent dyes mainly tracked the therapeutic agents in tumor rather than diagnosis for HCC. The meaning of this monitoring is to investigate tumor accumulation and release of agents, which is an important factor for nanoparticle therapy procedures. On the contrary, if diagnostic agents stay in nanoparticles throughout, the diagnosis and therapy for tumor could be implemented at the same time (Fan et al., 2019).

In another way, because many nanomaterials are already imaging agents, hybrid nanostructures fabricated with these nanomaterials and MSNs could make diagnosis and therapy together. Among all hybrid nanostructures, the physically responsive (light/magnetic/ultrasonic) nanostructures widely explored as innovative "theranostics" in cancer have been described in excellent reviews (Thorat et al., 2019a,b). The greatest strength for these nanostructures is that their properties to physically stimulus accord with the diagnosis mode (MRI/US) in clinic. Li et al. successfully coat a mesoporous-silica layer onto the surface of Ti_3C_2 (Ti_3C_2@mMSNs). Ti_3C_2 has a high photothermal-conversion efficiency and enables Ti_3C_2@mMSNs to possess the potential contrast-enhanced PA-imaging and heat production property. So these nanostructures can monitor the photothermal hyperthermia treatment process in real-time (Li et al., 2018c). In another study, Liu et al. prepared the capping MSNs-coated iron oxide nanoparticles with programmable DNA hairpin gates to form M-MSNs, which could decrease T_2-weighted tumor signal in MRI for HCC diagnosis. Interestingly, BHQ1 (fluorescence quencher) and 6-carboxyfluorescein (FAM) were linked to the tail extension of the DNA hairpin structure. When DNA hairpin gates change the conformation after addition of HCC- specific miRNA-21, the fluorescence of FAM will significantly "ON" to monitor the release of DOX in nanostructures (Liu J. et al., 2019). In spite of the therapeutic functions, the above nanostructures have two diagnostic functions: positioning tumor tissues and monitoring drug release.

The most amazing theranostic nanostructure is developed using mesoporous silica layer as shells and up-conversion luminescent (UCL) GdOF:Ln (Ln = 10%Yb/1%Er/4%Mn) as cores by Lin et al. Under NIR irradiation, GdOF:Ln could efficiently transfer NIR energy to the conjugated PDT agent (ZnPc) and emit bright red up-conversion emission. The shell decorated with carbon dots also can generate photothermal effect at the same time. Gd/Yb has the strong X-ray attenuation endowing nanostructures for computed tomography (CT) contrast agents, meanwhile Gd-based particles can be harnessed as contrast agents for MRI. This nanostructure with excellent and rational design is appropriate for both various imaging (UCL, CT, MRI, PT) and various therapies (PDT, PTT, chemotherapy), thus achieving multimodal imaging guided combination therapies (Lv et al., 2015).

With the development of nanotheranostics, many researchers believe that the integration of diagnosis and therapy to single modality would really benefit patient over independently managed diagnosis and therapy (Kelkar and Reineke, 2011). However, recent development of theranostics in MSNs was limited to "how can theranostics modalities in nanoparticles be realized" rather than "why can theranostics modalities in nanoparticles benefit the patients." In hospital, patients have no opportunity to occupy the diagnostic tools all the time, so the concept of real-time monitoring translating to clinic may be only few hours monitoring time to examine patients totally. And multimodal imaging provides good alternatives for patients, but we should weigh advantages and disadvantages. It is because that the more imaging modes nanoparticles can be applied in, the more complicated structure nanoparticles possess. In most cases, four or more imaging modes in nanostructures make no benefits to the patient compared to one imaging mode. We suggest that development of theranostic nanostructures should be based on clinical demand and clinical practice, which is the key for translational medicine.

CONCLUSION AND OUTLOOK

In this review, we summarized the recent progress in HCC theranostic applications based on MSNs. We generalized the precision delivery strategies applied for HCC in recent researches, including passive targeting, active targeting and stimuli-responsive release. The multiple therapy and diagnosis

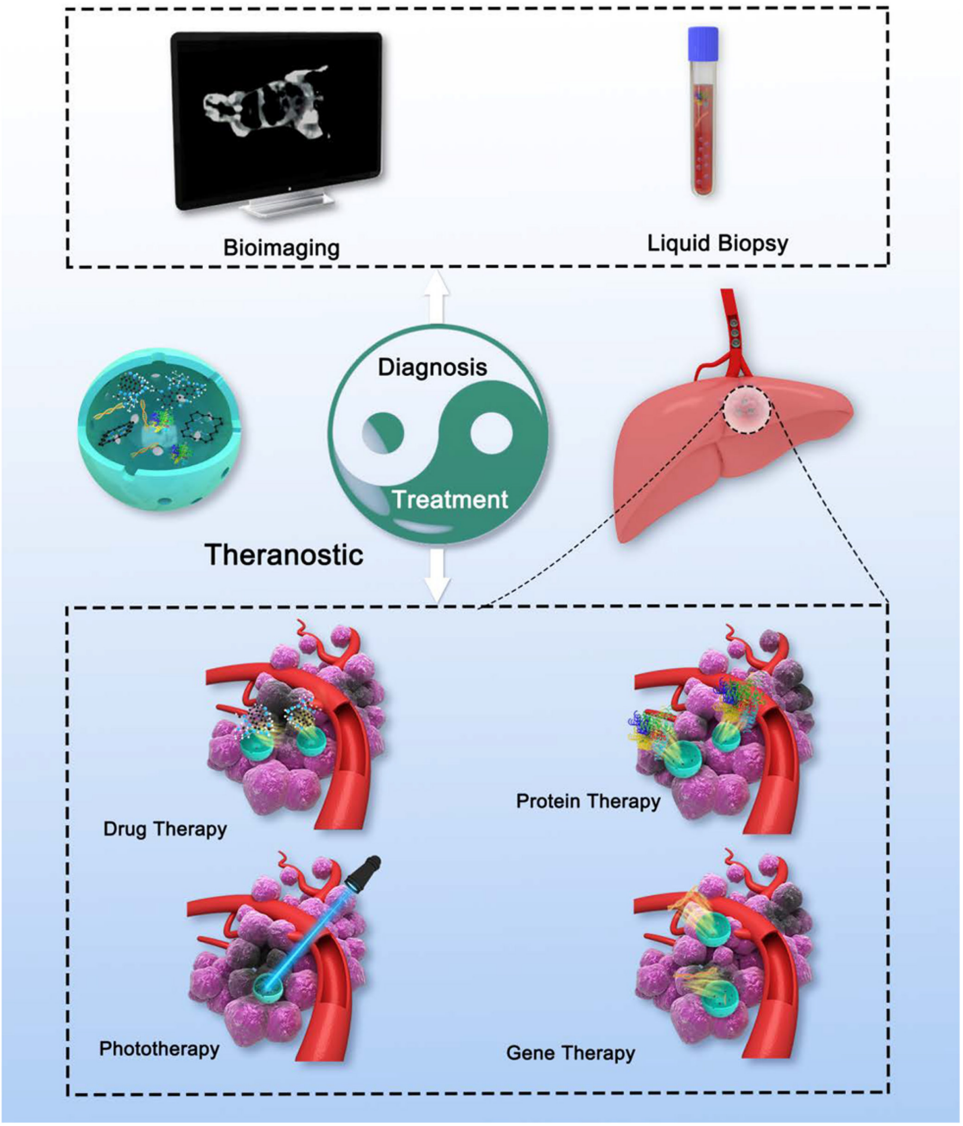

FIGURE 5 | Schematic illustration of theranostic MSNs. MSNs with rational design could integrate various diagnosis and treatment function, which is similar to Tai Chi all-embracing.

approaches had been realized in MSNs. Among a large amount of applications, we highlighted theranostic hybrid nanostructures, in which combination of the modalities of diagnostic imaging and therapy endowed MSNs-based nanostructures the ability to image and monitor the tumor tissue during treatment making possible more timely adjustment of therapy.

Despite the extensive researches, some emerging therapy and diagnosis approaches have not been used in MSNs for HCC. Most recently, cancer immune therapy is growing obviously, including cancer vaccinations, chimeric antigen receptor (CAR) T-cell therapy and immune checkpoint blockade therapy (Zhang and Chen, 2018). Actually, many MSNs-based immune therapies have been reported in other cancers (Ding et al., 2018; Li et al., 2018a; Xie et al., 2019). In addition, a lot of clinical trials about immune checkpoint blockade therapy such as PD-1 therapy for HCC are underway. Therefore, immune therapy is a potential development point for MSNs-based HCC therapy. Positron Emission Tomography (PET) is important for metastasis and prognostic assessment in patients with HCC (Filippi et al., 2019). Some Radiolabeling MSNs also have been reported for PET (Ni et al., 2018), thus it is hopeful to accomplish for more accurate diagnosis of HCC due to its smart recognition to tumor cells.

Although the preclinical trials of MSNs are successfully completed, currently, there are no MSNs that have been approved applied in clinic. There remain several critical challenges that need to be overcame for MSNs. First, the current small animal

models are not suitable to evaluate the delivery efficiency and long-term toxicity of nanoparticles in humans. Second, the laboratory scale production of MSNs cannot easily repeat in the industrial scale of production for clinical application, especially for the complicated modified MSNs. Third, there is no thorough evaluation criterion, which may confuse the researchers to improve the existing MSNs. Nevertheless, there are some clinical trials in silica nanoparticles, the prospect of clinic translation for MSNs was less than good. We should focus our efforts in the following aspects: (1) Try to use big animals to assess safety and efficacy of the MSNs; (2) Improve and simplify production process of MSNs; (3) Establish a homogenized evaluation system; (4) modulate the theranostic functions of MSNs closer to the clinic. The long-wind road for clinical translation and commercialization of MSNs still needs researchers going on.

AUTHOR CONTRIBUTIONS

XX brought forward the subject and guided the writing. YT gathered the research data and wrote the manuscript. JW supervised the writing and revising. All authors critically revised the manuscript and approved it for publication.

FUNDING

This work was supported by the National Major Science and Technology Projects of China (No. 2017ZX10203205), National Natural Science Foundation of China (Nos. 81570589 and 81801824), and China National Funds for Distinguished Young Scientists (No. 81625003).

REFERENCES

An, J., Zhang, X., Guo, Q., Zhao, Y., Wu, Z., and Li, C. (2015). Glycopolymer modified magnetic mesoporous silica nanoparticles for MR imaging and targeted drug delivery. *Colloids Surf. Physicochem. Eng. Aspects* 482, 98–108. doi: 10.1016/j.colsurfa.2015.04.035

Ao, M., Xiao, X., and Ao, Y. (2018). Low density lipoprotein modified silica nanoparticles loaded with docetaxel and thalidomide for effective chemotherapy of liver cancer. *Braz. J. Med. Biol. Res.* 51, 1–10. doi: 10.1590/1414-431X20176650

Ashley, C. E., Carnes, E. C., Phillips, G. K., Padilla, D., Durfee, P. N., Brown, P. A., et al. (2011). The targeted delivery of multicomponent cargos to cancer cells by nanoporous particle-supported lipid bilayers. *Nat. Mater.* 10, 389–397. doi: 10.1038/nmat2992

Babaei, M., Abnous, K., Taghdisi, S. M., Amel Farzad, S., Peivandi, M. T., Ramezani, M., et al. (2017). Synthesis of theranostic epithelial cell adhesion molecule targeted mesoporous silica nanoparticle with gold gatekeeper for hepatocellular carcinoma. *Nanomedicine* 12, 1261–1279. doi: 10.2217/nnm-2017-0028

Bae, K. H., Chung, H. J., and Park, T. G. (2011). Nanomaterials for cancer therapy and imaging. *Mol. Cells* 31, 295–302. doi: 10.1007/s10059-011-0051-5

Bellin, M. F., Vasile, M., and Morel-Precetti, S. (2003). Currently used non-specific extracellular MR contrast media. *Eur. Radiol.* 13, 2688–2698. doi: 10.1007/s00330-003-1912-x

Benezra, M., Penate-Medina, O., Zanzonico, P. B., Schaer, D., Ow, H., Burns, A., et al. (2011). Multimodal silica nanoparticles are effective cancer-targeted probes in a model of human melanoma. *J. Clin. Invest.* 121, 2768–2780. doi: 10.1172/JCI45600

Bray, F., Ferlay, J., Soerjomataram, I., Siegel, R. L., Torre, L. A., and Jemal, A. (2018). Global cancer statistics 2018: GLOBOCAN estimates of incidence and mortality worldwide for 36 cancers in 185 countries. *CA Cancer J. Clin.* 68, 394–424. doi: 10.3322/caac.21492

Bruix, J., Takayama, T., Mazzaferro, V., Chau, G.-Y., Yang, J., Kudo, M., et al. (2015). Adjuvant sorafenib for hepatocellular carcinoma after resection or ablation (STORM): a phase 3, randomised, double-blind, placebo-controlled trial. *Lancet Oncol.* 16, 1344–1354. doi: 10.1016/s1470-2045(15)00198-9

Castillo, R. R., and Vallet-Regi, M. (2019). Functional mesoporous silica nanocomposites: biomedical applications and biosafety. *Int. J. Mol. Sci.* 20:E929. doi: 10.3390/ijms20040929

Chen, C., Yao, W., Sun, W., Guo, T., Lv, H., Wang, X., et al. (2019). A self-targeting and controllable drug delivery system constituting mesoporous silica nanoparticles fabricated with a multi-stimuli responsive chitosan-based thin film layer. *Int. J. Biol. Macromol.* 122, 1090–1099. doi: 10.1016/j.ijbiomac.2018.09.058

Chen, D., Jiang, M., Li, N., Gu, H., Xu, Q., Ge, J., et al. (2010). Modification of magnetic silica/iron oxide nanocomposites with fluorescent polymethacrylic acid for cancer targeting and drug delivery. *J. Mater. Chem.* 20:6422. doi: 10.1039/c0jm00320d

Chen, H., Zhang, W., Zhu, G., Xie, J., and Chen, X. (2017). Rethinking cancer nanotheranostics. *Nat. Rev. Mater.* 2:17024. doi: 10.1038/natrevmats.2017.24

Chen, M., Chen, Z., Wang, W., Zhu, L., Tang, H., and Pang, D. (2014). Preparation of RuBpy-doped silica fluorescent nanoprobes and their applications to the recognition of liver cancer cells. *Chinese J. Anal. Chem.* 42, 326–331. doi: 10.1016/s1872-2040(13)60715-x

Chen, Q. Y., Tao, G. P., Liu, Y. Q., and Yang, X. (2012). Synthesis, characterization, cell imaging and anti-tumor activity of multifunctional nanoparticles. *Spectrochim. Acta A Mol. Biomol. Spectrosc.* 96, 284–288. doi: 10.1016/j.saa.2012.05.033

Chen, X., Sun, H., Hu, J., Han, X., Liu, H., and Hu, Y. (2017). Transferrin gated mesoporous silica nanoparticles for redox-responsive and targeted drug delivery. *Colloids Surf. B. Biointerfaces* 152, 77–84. doi: 10.1016/j.colsurfb.2017.01.010

Chen, Y., Chiu, W., Chang, C., Wu, P., Tu, T., Lin, H., et al. (2018). Chemo-photothermal effects of doxorubicin/silica–carbon hollow spheres on liver cancer. *RSC Adv.* 8, 36775–36784. doi: 10.1039/c8ra08538b

Cheng, S. B., Liu, H. T., Chen, S. Y., Lin, P. T., Lai, C. Y., and Huang, Y. C. (2017). Changes of oxidative stress, glutathione, and its dependent antioxidant enzyme activities in patients with hepatocellular carcinoma before and after tumor resection. *PLoS One* 12:e0170016. doi: 10.1371/journal.pone.0170016

Cheng, W., Nie, J., Xu, L., Liang, C., Peng, Y., Liu, G., et al. (2017). pH-sensitive delivery vehicle based on folic acid-conjugated polydopamine-modified mesoporous silica nanoparticles for targeted cancer therapy. *ACS Appl. Mater. Interfaces* 9, 18462–18473. doi: 10.1021/acsami.7b02457

Choi, Y., Lee, J. E., Lee, J. H., Jeong, J. H., and Kim, J. (2015). A biodegradation study of SBA-15 microparticles in simulated body fluid and *in vivo*. *Langmuir* 31, 6457–6462. doi: 10.1021/acs.langmuir.5b01316

Dai, L., Li, J., Zhang, B., Liu, J., Luo, Z., and Cai, K. (2014). Redox-responsive nanocarrier based on heparin end-capped mesoporous silica nanoparticles for targeted tumor therapy in vitro and in vivo. *Langmuir* 30, 7867–7877. doi: 10.1021/la501924p

Das, S. K., Menezes, M. E., Bhatia, S., Wang, X. Y., Emdad, L., Sarkar, D., et al. (2015). Gene therapies for cancer: strategies, challenges and successes. *J. Cell. Physiol.* 230, 259–271. doi: 10.1002/jcp.24791

Deodhar, G. V., Adams, M. L., and Trewyn, B. G. (2017). Controlled release and intracellular protein delivery from mesoporous silica nanoparticles. *Biotechnol. J* 12:1600408. doi: 10.1002/biot.201600408

Ding, B., Shao, S., Yu, C., Teng, B., Wang, M., Cheng, Z., et al. (2018). Large-pore mesoporous-silica-coated upconversion nanoparticles as multifunctional immunoadjuvants with ultrahigh photosensitizer and antigen loading efficiency for improved cancer photodynamic immunotherapy. *Adv. Mater.* 30:e1802479. doi: 10.1002/adma.201802479

El-Boubbou, K. (2018). Magnetic iron oxide nanoparticles as drug carriers: clinical relevance. *Nanomedicine* 13, 953–971. doi: 10.2217/nnm-2017-0336

Epler, K., Padilla, D., Phillips, G., Crowder, P., Castillo, R., Wilkinson, D., et al. (2012). Delivery of ricin toxin a-chain by peptide-targeted mesoporous silica

nanoparticle-supported lipid bilayers. *Adv. Healthc. Mater.* 1, 348–353. doi: 10.1002/adhm.201200022

Escoto, J. L. V. (2013). Nanovehicles for intracellular protein delivery. *J. Biotechnol. Biomater.* 03:e117. doi: 10.4172/2155-952X.1000e117

Fan, Y., Yu, D., Li, D., and Wang, X. (2019). Prevention of local tumor recurrence after surgery by thermosensitive gel-based chemophotothermal therapy in mice. *Lasers Surg. Med.* doi: 10.1002/lsm.23206[Epub ahead of print].

Fei, W., Zhang, Y., Han, S., Tao, J., Zheng, H., Wei, Y., et al. (2017). RGD conjugated liposome-hollow silica hybrid nanovehicles for targeted and controlled delivery of arsenic trioxide against hepatic carcinoma. *Int. J. Pharm.* 519, 250–262. doi: 10.1016/j.ijpharm.2017.01.031

Filippi, L., Schillaci, O., and Bagni, O. (2019). Recent advances in PET probes for hepatocellular carcinoma characterization. *Expert Rev. Med. Devices* 16, 1–10. doi: 10.1080/17434440.2019.1608817

Fu, C., Liu, T., Li, L., Liu, H., Chen, D., and Tang, F. (2013). The absorption, distribution, excretion and toxicity of mesoporous silica nanoparticles in mice following different exposure routes. *Biomaterials* 34, 2565–2575. doi: 10.1016/j.biomaterials.2012.12.043

Gao, B., Shen, L., He, K. W., and Xiao, W. H. (2015). GNRs@SiO(2)-FA in combination with radiotherapy induces the apoptosis of HepG2 cells by modulating the expression of apoptosis-related proteins. *Int. J. Mol. Med.* 36, 1282–1290. doi: 10.3892/ijmm.2015.2358

Gao, J., Shi, Z., Xia, J., Inagaki, Y., and Tang, W. (2015). Sorafenib-based combined molecule targeting in treatment of hepatocellular carcinoma. *World J. Gastroenterol.* 21, 12059–12070. doi: 10.3748/wjg.v21.i42.12059

GBD (2013). Mortality and Causes of Death Collaborators (2015). Global, regional, and national age–sex specific all-cause and cause-specific mortality for 240 causes of death, 1990–2013: a systematic analysis for the Global Burden of Disease Study 2013. *Lancet* 385, 117–171. doi: 10.1016/s0140-6736(14)61682-2

Hakeem, A., Zahid, F., Duan, R., Asif, M., Zhang, T., Zhang, Z., et al. (2016). Cellulose conjugated FITC-labelled mesoporous silica nanoparticles: intracellular accumulation and stimuli responsive doxorubicin release. *Nanoscale* 8, 5089–5097. doi: 10.1039/c5nr08753h

Hao, W., Shen, Y., Liu, D., Shang, Y., Zhang, J., Xu, S., et al. (2017). Dual-pH-sensitivity and tumour targeting core–shell particles for intracellular drug delivery. *RSC Adv.* 7, 851–860. doi: 10.1039/c6ra25224a

He, Q., Cui, X., Cui, F., Guo, L., and Shi, J. (2009). Size-controlled synthesis of monodispersed mesoporous silica nano-spheres under a neutral condition. *Microporous Mesoporous Mater.* 117, 609–616. doi: 10.1016/j.micromeso.2008.08.004

He, Q., and Shi, J. (2014). MSN anti-cancer nanomedicines: chemotherapy enhancement, overcoming of drug resistance, and metastasis inhibition. *Adv. Mater.* 26, 391–411. doi: 10.1002/adma.201303123

He, Q., Shi, J., Chen, F., Zhu, M., and Zhang, L. (2010a). An anticancer drug delivery system based on surfactant-templated mesoporous silica nanoparticles. *Biomaterials* 31, 3335–3346. doi: 10.1016/j.biomaterials.2010.01.015

He, Q., Zhang, J., Shi, J., Zhu, Z., Zhang, L., Bu, W., et al. (2010b). The effect of PEGylation of mesoporous silica nanoparticles on nonspecific binding of serum proteins and cellular responses. *Biomaterials* 31, 1085–1092. doi: 10.1016/j.biomaterials.2009.10.046

He, Y., Liang, S., Long, M., and Xu, H. (2017). Mesoporous silica nanoparticles as potential carriers for enhanced drug solubility of paclitaxel. *Mater. Sci. Eng. C Mater. Biol. Appl.* 78, 12–17. doi: 10.1016/j.msec.2017.04.049

Hu, L., Zhou, H., Li, Y., Sun, S., Guo, L., Ye, M., et al. (2009). Profiling of endogenous serum phosphorylated peptides by titanium (IV) immobilized mesoporous silica particles enrichment and MALDI-TOFMS detection. *Anal. Chem.* 81, 94–104. doi: 10.1021/ac801974f

Hu, Y., Wang, J., Zhi, Z., Jiang, T., and Wang, S. (2011). Facile synthesis of 3D cubic mesoporous silica microspheres with a controllable pore size and their application for improved delivery of a water-insoluble drug. *J. Colloid Interface Sci.* 363, 410–417. doi: 10.1016/j.jcis.2011.07.022

Hu, Z., Tan, J., Lai, Z., Zheng, R., Zhong, J., Wang, Y., et al. (2017). Aptamer combined with fluorescent silica nanoparticles for detection of hepatoma cells. *Nanoscale Res. Lett.* 12:96. doi: 10.1186/s11671-017-1890-6

Huh, S., Wiench, J. W., Yoo, J.-C., Pruski, M., and Lin, V. S. Y. (2003). Organic functionalization and morphology control of mesoporous silicas via a co-condensation synthesis method. *Chem. Mater.* 15, 4247–4256. doi: 10.1021/cm0210041

Jiang, Y., Cheng, J., Yang, C., Hu, Y., Li, J., Han, Y., et al. (2017). An ultrasensitive fluorogenic probe for revealing the role of glutathione in chemotherapy resistance. *Chem. Sci.* 8, 8012–8018. doi: 10.1039/c7sc03338a

Jin, C., Wang, J., Wang, Y., Tang, H., and Lu, T. (2014). Fabrication of hierarchically porous silica nanospheres through sol–gel process and pseudomorphic transformation. *J. Solgel Sci. Technol.* 70, 53–61. doi: 10.1007/s10971-014-3273-0

Karimian, A., Azizian, K., Parsian, H., Rafieian, S., Shafiei-Irannejad, V., Kheyrollah, M., et al. (2019). CRISPR/Cas9 technology as a potent molecular tool for gene therapy. *J. Cell. Physiol.* 234, 12267–12277. doi: 10.1002/jcp.27972

Keasberry, N. A., Yapp, C. W., and Idris, A. (2017). Mesoporous silica nanoparticles as a carrier platform for intracellular delivery of nucleic acids. *Biochemistry* 82, 655–662. doi: 10.1134/S0006297917060025

Kelkar, S. S., and Reineke, T. M. (2011). Theranostics: combining imaging and therapy. *Bioconjug. Chem.* 22, 1879–1903. doi: 10.1021/bc200151q

Kesse, S., Boakye-Yiadom, O. K., Ochete, O. B., Opoku-Damoah, Y., Akhtar, F., Filli, S. M., et al. (2019). Mesoporous silica nanomaterials: versatile nanocarriers for cancer theranostics and drug and gene delivery. *Pharmaceutics* 11:77. doi: 10.3390/pharmaceutics11020077

Kim, J., Park, S., Jung, Y., Chang, S., Park, J., Zhang, Y., et al. (2016). Programmable real-time clinical photoacoustic and ultrasound imaging system. *Sci. Rep.* 6:35137. doi: 10.1038/srep35137

Kim, S. M., Im, G. H., Lee, D. G., Lee, J. H., Lee, W. J., and Lee, I. S. (2013). Mn^{2+}-doped silica nanoparticles for hepatocyte-targeted detection of liver cancer in T1-weighted MRI. *Biomaterials* 34, 8941–8948. doi: 10.1016/j.biomaterials.2013.08.009

Kim, S. Y., An, J., Lim, Y.-S., Han, S., Lee, J.-Y., Byun, J. H., et al. (2017). MRI with liver-specific contrast for surveillance of patients with cirrhosis at high risk of hepatocellular carcinoma. *JAMA Oncol.* 3, 456–463. doi: 10.1001/jamaoncol.2016.3147

Kobler, J., and Bein, T. (2008). Porous thin films of functionalized mesoporous silica nanoparticles. *ACS Nano* 2, 2324–2330. doi: 10.1021/nn800505g

Kumar, K., Kumar Doddi, S., Arunasree, M. K., and Paik, P. (2015). CPMV-induced synthesis of hollow mesoporous SiO2 nanocapsules with excellent performance in drug delivery. *Dalton Trans.* 44, 4308–4317. doi: 10.1039/c4dt02549k

Lan, S., Lin, Z., Zhang, D., Zeng, Y., and Liu, X. (2019). Photocatalysis enhancement for programmable killing of hepatocellular carcinoma through self-compensation mechanisms based on black phosphorus quantum-dot-hybridized nanocatalysts. *ACS Appl. Mater. Interfaces* 11, 9804–9813. doi: 10.1021/acsami.8b21820

Lee, D., Beack, S., Yoo, J., Kim, S.-K., Lee, C., Kwon, W., et al. (2018). *In vivo* photoacoustic imaging of livers using biodegradable hyaluronic acid-conjugated silica nanoparticles. *Adv. Funct. Mater.* 28:1800941. doi: 10.1002/adfm.201800941

Lee, J., Kim, J., and Kim, W. J. (2016). Photothermally controllable cytosolic drug delivery based on core–shell MoS2-porous silica nanoplates. *Chem. Mater.* 28, 6417–6424. doi: 10.1021/acs.chemmater.6b02944

Lee, S., Ferrari, M., and Decuzzi, P. (2009). Shaping nano-/micro-particles for enhanced vascular interaction in laminar flows. *Nanotechnology* 20:495101. doi: 10.1088/0957-4484/20/49/495101

Li, A. W., Sobral, M. C., Badrinath, S., Choi, Y., Graveline, A., Stafford, A. G., et al. (2018a). A facile approach to enhance antigen response for personalized cancer vaccination. *Nat. Mater.* 17, 528–534. doi: 10.1038/s41563-018-0028-2

Li, L., Liu, T., Fu, C., Meng, X., and Liu, H. (2016). Size effect of mesoporous and hollow silica nanoparticles on solid tumor targeting and penetration. *J. Nanosci. Nanotechnol.* 16, 6766–6772. doi: 10.1166/jnn.2016.11372

Li, L., Tang, F., Liu, H., Liu, T., Hao, N., Chen, D., et al. (2010). *In vivo* delivery of silica nanorattle encapsulated docetaxel for liver cancer therapy with low toxicity and high efficacy. *ACS Nano* 4, 6874–6882. doi: 10.1021/nn100918a

Li, Z., Han, J., Yu, L., Qian, X., Xing, H., Lin, H., et al. (2018b). Synergistic sonodynamic/chemotherapeutic suppression of hepatocellular carcinoma by targeted biodegradable mesoporous nanosonosensitizers. *Adv. Funct. Mater.* 28:1800145. doi: 10.1002/adfm.201800145

Li, Z., Zhang, H., Han, J., Chen, Y., Lin, H., and Yang, T. (2018c). Surface nanopore engineering of 2D MXenes for targeted and synergistic multitherapies of hepatocellular carcinoma. *Adv. Mater.* 30:e1706981. doi: 10.1002/adma.201706981

Liao, Y. T., Liu, C. H., Yu, J., and Wu, K. C. (2014). Liver cancer cells: targeting and prolonged-release drug carriers consisting of mesoporous silica nanoparticles and alginate microspheres. *Int. J. Nanomedicine* 9, 2767–2778. doi: 10.2147/IJN.S60171

Lin, X., Wu, M., Li, M., Cai, Z., Sun, H., Tan, X., et al. (2018). Photo-responsive hollow silica nanoparticles for light-triggered genetic and photodynamic synergistic therapy. *Acta Biomater.* 76, 178–192. doi: 10.1016/j.actbio.2018.07.007

Liu, H., Chen, D., Li, L., Liu, T., Tan, L., Wu, X., et al. (2011). Multifunctional gold nanoshells on silica nanorattles: a platform for the combination of photothermal therapy and chemotherapy with low systemic toxicity. *Angew. Chem. Int. Ed. Engl.* 50, 891–895. doi: 10.1002/anie.201002820

Liu, J., Liu, W., Zhang, K., Shi, J., and Zhang, Z. (2019). A magnetic drug delivery system with "OFF–ON" state via specific molecular recognition and conformational changes for precise tumor therapy. *Adv. Healthc. Mater.* 9:1901316. doi: 10.1002/adhm.201901316

Liu, J., Luo, Z., Zhang, J., Luo, T., Zhou, J., Zhao, X., et al. (2016). Hollow mesoporous silica nanoparticles facilitated drug delivery via cascade pH stimuli in tumor microenvironment for tumor therapy. *Biomaterials* 83, 51–65. doi: 10.1016/j.biomaterials.2016.01.008

Liu, T., Li, L., Teng, X., Huang, X., Liu, H., Chen, D., et al. (2011). Single and repeated dose toxicity of mesoporous hollow silica nanoparticles in intravenously exposed mice. *Biomaterials* 32, 1657–1668. doi: 10.1016/j.biomaterials.2010.10.035

Liu, X., Li, Y., He, J., Zhao, T., Chen, C., Gu, H., et al. (2017). Paclitaxel-loaded pluronic F127/P123 silica nanocapsules with surface conjugated rhTRAIL for targeted cancer therapy. *RSC Adv.* 7, 30250–30261. doi: 10.1039/c7ra04503d

Liu, Y., Bhattarai, P., Dai, Z., and Chen, X. (2019). Photothermal therapy and photoacoustic imaging via nanotheranostics in fighting cancer. *Chem. Soc. Rev.* 48, 2053–2108. doi: 10.1039/C8CS00618K

Liu, Z., Xiong, L., Liu, Z., Miao, X., Lin, L., and Wen, Y. (2014). *In vivo* and *in vitro* evaluation of the cytotoxic effects of Photosan-loaded hollow silica nanoparticles on liver cancer. *Nanoscale Res. Lett.* 9:319. doi: 10.1186/1556-276X-9-319

Llovet, J. M., Zucman-Rossi, J., Pikarsky, E., Sangro, B., Schwartz, M., Sherman, M., et al. (2016). Hepatocellular carcinoma. *Nat. Rev. Dis. Primers* 2:16018. doi: 10.1038/nrdp.2016.18

Lu, F., Wu, S. H., Hung, Y., and Mou, C. Y. (2009). Size effect on cell uptake in well-suspended, uniform mesoporous silica nanoparticles. *Small* 5, 1408–1413. doi: 10.1002/smll.200900005

Lu, J., Wang, J., and Ling, D. (2018). Surface engineering of nanoparticles for targeted delivery to hepatocellular carcinoma. *Small* 14:1702037. doi: 10.1002/smll.201702037

Lv, R., Yang, P., He, F., Gai, S., Li, C., Dai, Y., et al. (2015). A yolk-like multifunctional platform for multimodal imaging and synergistic therapy triggered by a single near-infrared light. *ACS Nano* 9, 1630–1647. doi: 10.1021/nn5063613

Lv, Y., Li, J., Chen, H., Bai, Y., and Zhang, L. (2017). Glycyrrhetinic acid-functionalized mesoporous silica nanoparticles as hepatocellular carcinoma-targeted drug carrier. *Int. J. Nanomedicine* 12, 4361–4370. doi: 10.2147/IJN.S135626

Maeda, H., Nakamura, H., and Fang, J. (2013). The EPR effect for macromolecular drug delivery to solid tumors: improvement of tumor uptake, lowering of systemic toxicity, and distinct tumor imaging *in vivo*. *Adv. Drug Deliv. Rev.* 65, 71–79. doi: 10.1016/j.addr.2012.10.002

Maeda, H., Wu, J., Sawa, T., Matsumura, Y., and Hori, K. (2000). Tumor vascular permeability and the EPR effect in macromolecular therapeutics: a review. *J. Control. Release* 65, 271–284. doi: 10.1016/S0168-3659(99)00248-5

Menard, M., Meyer, F., Affolter-Zbaraszczuk, C., Rabineau, M., Adam, A., Ramirez, P. D., et al. (2019). Design of hybrid protein-coated magnetic core-mesoporous silica shell nanocomposites for MRI and drug release assessed in a 3D tumor cell model. *Nanotechnology* 30:174001. doi: 10.1088/1361-6528/aafe1c

Meng, H., Xue, M., Xia, T., Ji, Z., Tarn, D. Y., Zink, J. I., et al. (2011a). Use of size and a copolymer design feature to improve the biodistribution and the enhanced permeability and retention effect of doxorubicin-loaded mesoporous silica nanoparticles in a murine xenograft tumor model. *ACS Nano* 5, 4131–4144. doi: 10.1021/nn200809t

Meng, H., Yang, S., Li, Z., Xia, T., Chen, J., Ji, Z., et al. (2011b). Aspect ratio determines the quantity of mesoporous silica nanoparticle uptake by a small GTPase-dependent macropinocytosis mechanism. *ACS Nano* 5, 4434–4447. doi: 10.1021/nn103344k

Miller, M. A., Chandra, R., Cuccarese, M. F., Pfirschke, C., Engblom, C., Stapleton, S., et al. (2017). Radiation therapy primes tumors for nanotherapeutic delivery via macrophage-mediated vascular bursts. *Sci. Transl. Med.* 9:eaal0225. doi: 10.1126/scitranslmed.aal0225

Natfji, A. A., Ravishankar, D., Osborn, H. M. I., and Greco, F. (2017). Parameters affecting the enhanced permeability and retention effect: the need for patient selection. *J. Pharm. Sci.* 106, 3179–3187. doi: 10.1016/j.xphs.2017.06.019

Ni, D., Jiang, D., Ehlerding, E. B., Huang, P., and Cai, W. (2018). Radiolabeling silica-based nanoparticles via coordination chemistry: basic principles, strategies, and applications. *Acc. Chem. Res.* 51, 778–788. doi: 10.1021/acs.accounts.7b00635

Pei, Y., Li, M., Hou, Y., Hu, Y., Chu, G., Dai, L., et al. (2018). An autonomous tumor-targeted nanoprodrug for reactive oxygen species-activatable dual-cytochrome c/doxorubicin antitumor therapy. *Nanoscale* 10, 11418–11429. doi: 10.1039/c8nr02358a

Qian, X., Zheng, Y., and Chen, Y. (2016). Micro/nanoparticle-augmented sonodynamic therapy (SDT): breaking the depth shallow of photoactivation. *Adv. Mater.* 28, 8097–8129. doi: 10.1002/adma.201602012

Quan, G., Pan, X., Wang, Z., Wu, Q., Li, G., Dian, L., et al. (2015). Lactosaminated mesoporous silica nanoparticles for asialoglycoprotein receptor targeted anticancer drug delivery. *J. Nanobiotechnol.* 13:7. doi: 10.1186/s12951-015-0068-6

Roberto, M., Umberto, A., and Renato, T. (2016). Hepatocellular carcinoma: Where are we? *World J. Exp. Med.* 6, 21–36. doi: 10.5493/wjem.v6.i1.21

Rudzka, K., Viota, J. L., Munoz-Gamez, J. A., Carazo, A., Ruiz-Extremera, A., and Delgado, A. V. (2013). Nanoengineering of doxorubicin delivery systems with functionalized maghemite nanoparticles. *Colloids Surf. B. Biointerfaces* 111, 88–96. doi: 10.1016/j.colsurfb.2013.05.010

Shao, D., Li, J., Zheng, X., Pan, Y., Wang, Z., Zhang, M., et al. (2016). Janus "nano-bullets" for magnetic targeting liver cancer chemotherapy. *Biomaterials* 100, 118–133. doi: 10.1016/j.biomaterials.2016.05.030

Shao, T., Wen, J., Zhang, Q., Zhou, Y., Liu, L., Yuwen, L., et al. (2016). NIR photoresponsive drug delivery and synergistic chemo-photothermal therapy by monodispersed-MoS2-nanosheets wrapped periodic mesoporous organosilicas. *J. Mater. Chem. B* 4, 7708–7717. doi: 10.1039/c6tb02724e

Shim, G., Kim, D., Le, Q. V., Park, G. T., Kwon, T., and Oh, Y. K. (2018). Nonviral delivery systems for cancer gene therapy: strategies and challenges. *Curr. Gene Ther.* 18, 3–20. doi: 10.2174/1566523218666180119121949

Sun, W., Thiramanas, R., Slep, L. D., Zeng, X., Mailander, V., and Wu, S. (2017). Photoactivation of anticancer Ru complexes in deep tissue: How deep can we go? *Chem. Eur. J.* 23, 10832–10837. doi: 10.1002/chem.201701224

Tang, F., Li, L., and Chen, D. (2012). Mesoporous silica nanoparticles: synthesis, biocompatibility and drug delivery. *Adv. Mater.* 24, 1504–1534. doi: 10.1002/adma.201104763

Tang, Z., Gao, Y., Li, D., and Zhou, S. (2017). Controllably switched drug release from successively dual-targeted nanoreservoirs. *Adv. Healthc. Mater.* 6, 1600919. doi: 10.1002/adhm.201600919

Tao, L., Song, C., Huo, C., Sun, Y., Zhang, C., Li, X., et al. (2016). Anti-CD155 and anti-CD112 monoclonal antibodies conjugated to a fluorescent mesoporous silica nanosensor encapsulating rhodamine 6G and fluorescein for sensitive detection of liver cancer cells. *Analyst* 141, 4933–4940. doi: 10.1039/c5an01908g

Thorat, N. D., Tofail, S. A. M., von Rechenberg, B., Townley, H., Brennan, G., Silien, C., et al. (2019a). Physically stimulated nanotheranostics for next generation cancer therapy: focus on magnetic and light stimulations. *Appl. Phys. Rev.* 6:041306. doi: 10.1063/1.5049467

Thorat, N. D., Townely, H., Brennan, G., Parchur, A. K., Silien, C., Bauer, J., et al. (2019b). Progress in remotely triggered hybrid nanostructures for next-generation brain cancer theranostics. *ACS Biomater. Sci. Eng.* 5, 2669–2687. doi: 10.1021/acsbiomaterials.8b01173

Verslype, C., Rosmorduc, O., and Rougier, P. (2012). Hepatocellular carcinoma: ESMO-ESDO clinical practice guidelines for diagnosis, treatment and follow-up. *Ann. Oncol.* 23(Suppl. 7), vii41–vii48. doi: 10.1093/annonc/mds225

Wang, J., Wang, H., Li, J., Liu, Z., Xie, H., Wei, X., et al. (2016). iRGD-decorated polymeric nanoparticles for the efficient delivery of vandetanib to hepatocellular carcinoma: preparation and *in vitro* and *in vivo* evaluation. *ACS Appl. Mater. Interfaces* 8, 19228–19237. doi: 10.1021/acsami.6b03166

Wang, J. K., Zhou, Y. Y., Guo, S. J., Wang, Y. Y., Nie, C. J., Wang, H. L., et al. (2017). Cetuximab conjugated and doxorubicin loaded silica nanoparticles for tumor-targeting and tumor microenvironment responsive binary drug delivery of liver cancer therapy. *Mater. Sci. Eng. C Mater. Biol. Appl.* 76, 944–950. doi: 10.1016/j.msec.2017.03.131

Wang, Y., Zhao, R., Wang, S., Liu, Z., and Tang, R. (2016). *In vivo* dual-targeted chemotherapy of drug resistant cancer by rationally designed nanocarrier. *Biomaterials* 75, 71–81. doi: 10.1016/j.biomaterials.2015.09.030

Wang, Z., Chang, Z., Lu, M., Shao, D., Yue, J., Yang, D., et al. (2017a). Janus silver/silica nanoplatforms for light-activated liver cancer chemo/photothermal therapy. *ACS Appl. Mater. Interfaces* 9, 30306–30317. doi: 10.1021/acsami.7b06446

Wang, Z., Chang, Z., Lu, M., Shao, D., Yue, J., Yang, D., et al. (2018). Shape-controlled magnetic mesoporous silica nanoparticles for magnetically-mediated suicide gene therapy of hepatocellular carcinoma. *Biomaterials* 154, 147–157. doi: 10.1016/j.biomaterials.2017.10.047

Wang, Z., Chang, Z., Shao, D., Zhang, F., Chen, F., Li, L., et al. (2019). Janus gold triangle-mesoporous silica nanoplatforms for hypoxia-activated radio-chemo-photothermal therapy of liver cancer. *ACS Appl. Mater. Interfaces* 11, 34755–34765. doi: 10.1021/acsami.9b12879

Wang, Z., Shao, D., Chang, Z., Lu, M., Wang, Y., Yue, J., et al. (2017b). Janus gold nanoplatform for synergetic chemoradiotherapy and computed tomography imaging of hepatocellular carcinoma. *ACS Nano* 11, 12732–12741. doi: 10.1021/acsnano.7b07486

Wang, Z., Wang, Y., Lu, M., Li, L., Zhang, Y., Zheng, X., et al. (2016). Janus Au–mesoporous silica nanocarriers for chemo-photothermal treatment of liver cancer cells. *RSC Adv.* 6, 44498–44505. doi: 10.1039/c6ra04183c

Wang, Z., Wu, P., He, Z., He, H., Rong, W., Li, J., et al. (2017d). Mesoporous silica nanoparticles with lactose-mediated targeting effect to deliver platinum(iv) prodrug for liver cancer therapy. *J. Mater. Chem. B* 5, 7591–7597. doi: 10.1039/c7tb01704a

World Health Organization [WHO] (2018). *Global Health Observatory [Online]*. Geneva: World Health Organization.

Wu, L., Wu, M., Zeng, Y., Zhang, D., Zheng, A., Liu, X., et al. (2015). Multifunctional PEG modified DOX loaded mesoporous silica nanoparticle@CuS nanohybrids as photo-thermal agent and thermal-triggered drug release vehicle for hepatocellular carcinoma treatment. *Nanotechnology* 26:025102. doi: 10.1088/0957-4484/26/2/025102

Wu, Y., Zhou, H., Wei, W., Hua, X., Wang, L., Zhou, Z., et al. (2012). Signal amplification cytosensor for evaluation of drug-induced cancer cell apoptosis. *Anal. Chem.* 84, 1894–1899. doi: 10.1021/ac202672x

Xia, Q., Li, L., and Zhao, L. (2017). Silica nanoparticle-based dual-responsive nanoprodrug system for liver cancer therapy. *Exp. Ther. Med.* 14, 2071–2077. doi: 10.3892/etm.2017.4768

Xiao, X., He, Q., and Huang, K. (2010). Novel amino-modified silica nanoparticles as efficient vector for hepatocellular carcinoma gene therapy. *Med. Oncol.* 27, 1200–1207. doi: 10.1007/s12032-009-9359-9

Xie, J., Lee, S., and Chen, X. (2010). Nanoparticle-based theranostic agents. *Adv. Drug Deliv. Rev.* 62, 1064–1079. doi: 10.1016/j.addr.2010.07.009

Xie, M., Xu, Y., Shen, H., Shen, S., Ge, Y., and Xie, J. (2014). Negative-charge-functionalized mesoporous silica nanoparticles as drug vehicles targeting hepatocellular carcinoma. *Int. J. Pharm.* 474, 223–231. doi: 10.1016/j.ijpharm.2014.08.027

Xie, W., Deng, W. W., Zan, M., Rao, L., Yu, G. T., Zhu, D. M., et al. (2019). Cancer cell membrane camouflaged nanoparticles to realize starvation therapy together with checkpoint blockades for enhancing cancer therapy. *ACS Nano* 13, 2849–2857. doi: 10.1021/acsnano.8b03788

Xing, H., Wang, Z., Shao, D., Chang, Z., Ge, M., Li, L., et al. (2018). Janus nanocarriers for magnetically targeted and hyperthermia-enhanced curcumin therapy of liver cancer. *RSC Adv.* 8, 30448–30454. doi: 10.1039/c8ra05694c

Xu, L., Xu, S., Wang, H., Zhang, J., Chen, Z., Pan, L., et al. (2018). Enhancing the efficacy and safety of doxorubicin against hepatocellular carcinoma through a modular assembly approach: the combination of polymeric prodrug design, nanoparticle encapsulation, and cancer cell-specific drug targeting. *ACS Appl. Mater. Interfaces* 10, 3229–3240. doi: 10.1021/acsami.7b14496

Xu, X., Wu, C., Bai, A., Liu, X., Lv, H., and Liu, Y. (2017). Folate-functionalized mesoporous silica nanoparticles as a liver tumor-targeted drug delivery system to improve the antitumor effect of paclitaxel. *J. Nanomater.* 2017, 1–13. doi: 10.1155/2017/2069685

Xu, Z. Y., Wang, K., Li, X. Q., Chen, S., Deng, J. M., Cheng, Y., et al. (2013). The ABCG2 transporter is a key molecular determinant of the efficacy of sonodynamic therapy with Photofrin in glioma stem-like cells. *Ultrasonics* 53, 232–238. doi: 10.1016/j.ultras.2012.06.005

Xue, H., Yu, Z., Liu, Y., Yuan, W., Yang, T., You, J., et al. (2017). Delivery of miR-375 and doxorubicin hydrochloride by lipid-coated hollow mesoporous silica nanoparticles to overcome multiple drug resistance in hepatocellular carcinoma. *Int. J. Nanomedicine* 12, 5271–5287. doi: 10.2147/IJN.S135306

Yang, X., He, D., He, X., Wang, K., Zou, Z., Li, X., et al. (2015). Glutathione-mediated degradation of surface-capped $Mno_2$for drug release from mesoporous silica nanoparticles to cancer cells. *Part. Part. Syst. Charact.* 32, 205–212. doi: 10.1002/ppsc.201400092

Ye, Q., Ling, S., Zheng, S., and Xu, X. (2019). Liquid biopsy in hepatocellular carcinoma: circulating tumor cells and circulating tumor DNA. *Mol. Cancer* 18:114. doi: 10.1186/s12943-019-1043-x

Yegin, E. G., Oymaci, E., Karatay, E., and Coker, A. (2016). Progress in surgical and nonsurgical approaches for hepatocellular carcinoma treatment. *Hepatobiliary Pancreat. Dis. Int.* 15, 234–256. doi: 10.1016/S1499-3872(16)60097-8

Yu, C., Qian, L., Uttamchandani, M., Li, L., and Yao, S. Q. (2015). Single-vehicular delivery of antagomir and small molecules to inhibit miR-122 Function in hepatocellular carcinoma cells by using "smart" mesoporous silica nanoparticles. *Angew. Chem. Int. Ed. Engl.* 54, 10574–10578. doi: 10.1002/anie.201504913

Yue, J., Luo, S. Z., Lu, M. M., Shao, D., Wang, Z., and Dong, W. F. (2018a). A comparison of mesoporous silica nanoparticles and mesoporous organosilica nanoparticles as drug vehicles for cancer therapy. *Chem. Biol. Drug Des.* 92, 1435–1444. doi: 10.1111/cbdd.13309

Yue, J., Wang, Z., Shao, D., Chang, Z., Hu, R., Li, L., et al. (2018b). Cancer cell membrane-modified biodegradable mesoporous silica nanocarriers for berberine therapy of liver cancer. *RSC Adv.* 8, 40288–40297. doi: 10.1039/c8ra07574c

Zeng, C., Shang, W., Wang, K., Chi, C., Jia, X., Fang, C., et al. (2016). Intraoperative identification of liver cancer microfoci using a targeted near-infrared fluorescent probe for imaging-guided surgery. *Sci. Rep.* 6:21959. doi: 10.1038/srep21959

Zhang, B., Luo, Z., Liu, J., Ding, X., Li, J., and Cai, K. (2014). Cytochrome c end-capped mesoporous silica nanoparticles as redox-responsive drug delivery vehicles for liver tumor-targeted triplex therapy in vitro and in vivo. *J. Control. Release* 192, 192–201. doi: 10.1016/j.jconrel.2014.06.037

Zhang, H., and Chen, J. (2018). Current status and future directions of cancer immunotherapy. *J. Cancer* 9, 1773–1781. doi: 10.7150/jca.24577

Zhang, L., Wang, T., Yang, L., Liu, C., Wang, C., Liu, H., et al. (2012). General route to multifunctional uniform yolk/mesoporous silica shell nanocapsules: a platform for simultaneous cancer-targeted imaging and magnetically guided drug delivery. *Chem. Eur. J.* 18, 12512–12521. doi: 10.1002/chem.201200030

Zhao, R., Li, T., Zheng, G., Jiang, K., Fan, L., and Shao, J. (2017). Simultaneous inhibition of growth and metastasis of hepatocellular carcinoma by co-delivery of ursolic acid and sorafenib using lactobionic acid modified and pH-sensitive chitosan-conjugated mesoporous silica nanocomplex. *Biomaterials* 143, 1–16. doi: 10.1016/j.biomaterials.2017.07.030

Zhao, Z., Han, Y., Lin, C., Hu, D., Wang, F., Chen, X., et al. (2012). Multifunctional core-shell upconverting nanoparticles for imaging and photodynamic therapy of liver cancer cells. *Chem. Asian J.* 7, 830–837. doi: 10.1002/asia.201100879

Zheng, G., Zhao, R., Xu, A., Shen, Z., Chen, X., and Shao, J. (2018). Co-delivery of sorafenib and siVEGF based on mesoporous silica nanoparticles for ASGPR mediated targeted HCC therapy. *Eur. J. Pharm. Sci.* 111, 492–502. doi: 10.1016/j.ejps.2017.10.036

Zhou, J., Huang, A., and Yang, X. (2016). Liquid biopsy and its potential for management of hepatocellular carcinoma. *J. Gastrointest. Cancer* 47, 157–167. doi: 10.1007/s12029-016-9801-0

Zhu, A. X., Duda, D. G., Sahani, D. V., and Jain, R. K. (2011). HCC and angiogenesis: possible targets and future directions. *Nat. Rev. Clin. Oncol.* 8, 292–301. doi: 10.1038/nrclinonc.2011.30

Zhu, Y., Shi, J., Li, Y., Chen, H., Shen, W., and Dong, X. (2005a). Storage and release of ibuprofen drug molecules in hollow mesoporous silica spheres with modified pore surface. *Microporous Mesoporous Mater.* 85, 75–81. doi: 10.1016/j.micromeso.2005.06.015

Zhu, Y., Shi, J., Shen, W., Chen, H., Dong, X., and Ruan, M. (2005b). Preparation of novel hollow mesoporous silica spheres and their sustained-release property. *Nanotechnology* 16, 2633–2638. doi: 10.1088/0957-4484/16/11/027

Conflict of Interest: The authors declare that the research was conducted in the absence of any commercial or financial relationships that could be construed as a potential conflict of interest.

frontiers in Bioengineering and Biotechnology

REVIEW
published: 05 May 2020
doi: 10.3389/fbioe.2020.00381

PLGA-Based Drug Delivery Systems for Remotely Triggered Cancer Therapeutic and Diagnostic Applications

Xue Shen[1], Tingting Li[2,3], Xiaoxue Xie[2], Yi Feng[2], Zhongyuan Chen[2], Hong Yang[2,3], Chunhui Wu[2,3], Shengqi Deng[1] and Yiyao Liu[2,4]**

[1] Sichuan Industrial Institute of Antibiotics, Chengdu University, Chengdu, China, [2] School of Life Sciences and Technology, University of Electronic Science and Technology of China, Chengdu, China, [3] Center for Information in Biology, University of Electronic Science and Technology of China, Chengdu, China, [4] Hospital of Chengdu University of Traditional Chinese Medicine, Chengdu, China

Intelligent drug delivery systems based on nanotechnology have been widely developed and investigated in the field of nanomedicine since they were able to maximize the therapeutic efficacy and minimize the undesirable adverse effects. Among a variety of organic or inorganic nanomaterials available to fabricate drug delivery systems (DDSs) for cancer therapy and diagnosis, poly(D,L-lactic-co-glycolic acid) (PLGA) has been extensively employed due to its biocompatibility and biodegradability. In this paper, we review the recent status of research on the application of PLGA-based drug delivery systems (DDSs) in remotely triggered cancer therapy and the strategies for tumor imaging provided by PLGA-based DDSs. We firstly discuss the employment of PLGA-based DDSs for remotely triggered cancer therapy, including photo-triggered, ultrasound-triggered, magnetic field-triggered, and radiofrequency-triggered cancer therapy. Photo-triggered cancer therapy involves photodynamic therapy (PDT), photothermal therapy (PTT), and photo-triggered chemotherapeutics release. Ultrasound-triggered cancer therapy involves high intensity focused ultrasound (HIFU) treatment, ultrasound-triggered chemotherapeutics release, and ultrasound-enhanced efficiency of gene transfection. The strategies which endows PLGA-based DDSs with imaging properties and the PLGA-based cancer theranostics are further discussed. Additionally, we also discuss the targeting strategies which provide PLGA-based DDSs with passive, active or magnetic tumor-targeting abilities. Numerous studies cited in our review demonstrate the great potential of PLGA-based DDSs as effective theranostic agent for cancer therapy and diagnosis.

Keywords: PLGA-based DDSs, targeting, remotely triggered cancer therapy, imaging, theranostics

OPEN ACCESS

Edited by:
Andrea Ragusa,
University of Salento, Italy

Reviewed by:
Alessandra Quarta,
Institute of Nanotechnology (CRN), Italy
Shiyong Song,
Henan University, China

****Correspondence:***
Shengqi Deng
dq1155@sina.com
Yiyao Liu
liuyiyao@uestc.edu.cn

Specialty section:
This article was submitted to Nanobiotechnology, a section of the journal Frontiers in Bioengineering and Biotechnology

Received: *05 February 2020*
Accepted: *06 April 2020*
Published: *05 May 2020*

Citation:
Shen X, Li T, Xie X, Feng Y, Chen Z, Yang H, Wu C, Deng S and Liu Y (2020) PLGA-Based Drug Delivery Systems for Remotely Triggered Cancer Therapeutic and Diagnostic Applications. Front. Bioeng. Biotechnol. 8:381. doi: 10.3389/fbioe.2020.00381

INTRODUCTION

The utilization of nanotechnology in drug delivery has been extensively supposed to alter the pattern of the pharmaceutical industries for the predictable future (Farokhzad and Langer, 2009; Lim et al., 2013; Farooq et al., 2019). Intravenous chemotherapy is one of the common cancer treatments. However, the normal tissues and organs will be damaged owing to the undesirable side effects caused by non-specific distribution of chemotherapeutic drugs and lack of specificity

for tumor cell recognition (Jia et al., 2012; Shen et al., 2017). Besides, the repeated treatment with one single drug can cause multidrug resistance in tumor cells, compromising the anticancer effects of chemotherapeutic drugs (Yang et al., 2018). Currently, the rise of nanotechnology have provided an versatile drug delivery systems (DDSs) for the efficient treatment of cancer, which offers a solution to the problem of body tissue damage caused by non-specific distribution of traditional chemotherapeutic drugs (Shi et al., 2010). The developed DDSs with a diameter between 10 and 200 nm exhibits favorable pharmacokinetic property, prolonged systemic circulation time, sustained drug release profile, and enhanced intratumoral accumulation when compared to the free drugs (Hu and Zhang, 2012). With the continuous improvement of the performance of intelligent DDSs, it is possible to achieve (1) improved stability of hydrophobic drugs and the possibility of hydrophobic drugs for systemic administration; (2) targeted drug delivery; (3) combined delivery of two or more drugs or other therapeutic agents for combination therapy; (4) combined delivery of the therapeutic agents and imaging agents for the visualization of drug delivery; (5) favorable biodistribution and pharmacokinetic property of drugs and finally realizing the enhanced therapeutic effects and reduced side effects (Farokhzad and Langer, 2009).

Since liposomes were proposed as protein and drug delivery vehicles for the treatment of diseases in the 1960s, nanotechnology has had a huge impact on the development of novel DDSs for controlled drug delivery and combination therapy (Shi et al., 2010). A variety of inorganic or organic materials have been utilized to prepare novel DDSs including inorganic nanoparticles (Li et al., 2016), liposomes (Zhao et al., 2015), polymer micelles (Shi et al., 2014), and polymer nanoparticles (Yang et al., 2016; Shen et al., 2019) for the effective cancer treatment. Among all these nanocarriers, one kind of polymer nanoparticles based on poly(D,L-lactic-co-glycolic acid) (PLGA) have attracted considerable attention due to their unique physical and chemical properties, such as tunable particle size, regular morphology, large surface area, favorable pharmacokinetic property, excellent biocompatibility, and biodegradability (Deng et al., 2014; Yang et al., 2015, 2018; Shen et al., 2017, 2019). Polymer nanoparticles are colloidal particles ranging in size from 10 to 1,000 nm, which can be fabricated by using synthetic polymers, such as poly(butylcyanoacrylates) (PBCA), poly(lactic acid) (PLA), poly(D,L-lactic-co-glycolic acid) (PLGA), or natural polymers, such as chitosan, gelatin, and albumin (Bamrungsap et al., 2012; Mc Carthy et al., 2015). A majority of polymer nanoparticles are biodegradable and biocompatible and their reactive functional groups allows easy conjugation with other ligands or polymers. PBCA nanoparticles are commonly used to deliver some conventional drugs such as chemotherapeutic drugs or nucleic acids such as plasmids (Alyautdin et al., 1995; Schneider et al., 2008). However, polycyanoacrylic acid and alcohol as the hydrolysis products of PBCA are cytotoxic, which limits the application of PBCA as a nanocarrier in the field of biomedicine (Mc Carthy et al., 2015). Contrarily, PLGA and PLA have been preferentially used for the preparation of nanocarriers since they can be degraded into lactic acid and glycolic acid, which are natural and non-toxic and able to be eventually degraded into water and carbon dioxide (Graf et al., 2012). Moreover, PLGA has been approved for the medical applications by the United States Food and Drug Administration (FDA) (Hamori et al., 2015). The various targeting moieties can be introduced to the surface of PLGA-based DDSs, providing them with tumor-targeting capability. And the appropriate outer surface engineering (such as PEGylation) of PLGA-based DDSs may prolong the blood circulation time of the DDSs (Graf et al., 2012). Chemotherapeutic drugs, photosensitizers, photothermal agents, therapeutic gene/siRNA, small-molecule inhibitors, and other therapeutic agents can be easily loaded in the PLGA-based DDSs for tumor treatment (Lee et al., 2012; Zhao et al., 2015; Shen et al., 2017, 2019). Furthermore, the imaging agents can also be integrated into PLGA-based DDSs to acquire the imaging property for tumor diagnosis (Chen et al., 2016). Co-loading the therapeutic agents and imaging agents into PLGA-based DDSs can make them the potential candidates for cancer therapeutics and diagnostics (known as cancer "theranostics") (Jia et al., 2012).

Several previous literatures have summarized the application of DDSs based on PLGA in cancer therapy and imaging from the aspects of preparation methods of PLGA-based nano- and microparticles, uptake of PLGA particles into cancer cells, controlled drug release property, and combination treatments (Rezvantalab et al., 2018; Swider et al., 2018; Kim et al., 2019). In this review, we introduce the recent status of research on the application of PLGA-based DDSs in remotely triggered cancer therapy and the strategies for tumor imaging provided by PLGA-based DDSs. We firstly emphasize the external stimuli-triggered cancer therapy approach and then discuss the strategies for tumor imaging provided by PLGA-based DDSs, the cancer theranostics in biomedical applications as well as the targeting strategies which endow the PLGA-based DDSs with passive, active or magnetic tumor-targeting abilities are further discussed. We introduced various types of PLGA-based DDSs in this review, some of them are nano-scaled, while the others are micro-scaled. Hao et al. (2015) have synthesized the tumor-targeted and gold nanoshell-surrounded PLGA-based nanoparticles (denoted as ANG/GS/PLGA/DTX NPs) for cancer chemotherapy and PTT, which were spherical with a size of about 200 nm. The nano-sized particles can more easily accumulate in tumor regions owing to the leaky vasculature and poor lymphatic drainage and their smaller size than the cell gaps of vascular endothelial cells of tumors (Torchilin, 2011; Bamrungsap et al., 2012; Shen et al., 2019). Nanoparticles are appropriate for various administration routes including intravenous administration. ANG/GS/PLGA/DTX NPs with exposure to an 808 nm laser irradiation displayed considerable tumor inhibition efficiency after the intravenous administration. Their pharmacokinetic parameters were further analyzed. The AUC of ANG/GS/PLGA/DTX NPs was higher than that of DTX solution with a 1.42-fold increase, and the clearance of ANG/GS/PLGA/DTX NPs was much lower than that of DTX solution. These results indicated that the nano-sized ANG/GS/PLGA/DTX NPs exhibited the prolonged blood circulation time and could improve the bioavailability of free DTX. Fang et al. (2015) have designed and synthesized the

magnetic responsive PLGA microspheres contained DOX (DOX-MMS) for combined chemotherapy and hyperthermia, of which the average size was measured to be 2.4 μm. Benefiting from their hollow structure and large size, the quantities of loaded DOX in DOX-MMS were 6.2%, and the encapsulation efficiency of DOX was up to 85%. The micro-sized DOX-MMS were intratumorally administrated, and showed an effective tumor inhibition effect in 4T1 tumor-bearing nude mice with exposure to alternating current magnetic field (ACMF). Niu et al. (2013) have designed and constructed the gas-filled multifunctional polymer microbubbles (MPMBs) to co-encapsulate iron oxide nanoparticles and DOX for tumor lymph node detection and therapy. Although these gas-filled microbubbles are not suitable for intravenous injection, the gas-filled microbubbles can be used as the drug/gene delivery systems and they have been proven to be capable of enhancing the ultrasound signals when used as the ultrasound agent (Hernot and Klibanov, 2008; Eisenbrey et al., 2010).

PLGA-BASED DDSs FOR REMOTELY TRIGGERED CANCER THERAPY

Cancer is one of the most fatal diseases and has long been a threat to human health. Their heterogeneity and complexity make tumors grow aggressively, leading to a significant increase in patient mortality (Das et al., 2009; Mohanty et al., 2011; Parhi et al., 2012). The nanocarriers based on PLGA has been demonstrated to be the most promising DDSs due to their unique physical and chemical properties, such as tunable particle size, favorable stability, excellent biocompatibility, and biodegradability (Deng et al., 2014; Yang et al., 2015, 2018; Shen et al., 2017, 2019). PLGA-based DDSs can load hydrophobic and hydrophilic chemotherapeutic drugs, photosensitizers, photothermal agents, therapeutic gene/siRNA, and other therapeutic agents and display the prolonged blood circulation time and tumor-targeting capability after the appropriate surface modification, resulting in the improved antitumor efficacy (Lee et al., 2012; Schleich et al., 2013; Topete et al., 2014; Zhao et al., 2015; Luo et al., 2018). Remotely triggered cancer therapy can allow for selective and precise eradication of the tumors and the controlled release of chemotherapeutics by putting the external stimuli (photo, ultrasound, magnetic field, and radiofrequency) on targeted regions (Rai et al., 2010; Shenoi et al., 2013). Moreover, remotely triggered cancer therapy can determine when the treatment starts and how long it lasts, allowing for precise treatment and reduced systemic toxicity. The external stimuli-triggered cancer therapy approach [photodynamic therapy (PDT), photothermal therapy (PTT), photo-triggered chemotherapeutics release, high intensity focused ultrasound (HIFU) treatment, ultrasound-triggered chemotherapeutics release, ultrasound-enhanced efficiency of gene transfection, magnetic field-triggered cancer therapy, and radiofrequency-triggered cancer therapy] provided by PLGA-based DDSs will be briefly summarized as follows. Representative applications of PLGA-based DDSs for remotely triggered cancer therapy are listed in **Table 1**.

Photo-Triggered Cancer Therapy

PLGA-based DDSs have been developed for the photo-triggered therapeutic application including the PDT, PTT, and photo-triggered chemotherapeutics release by employing an external light as a trigger. It has been demonstrated that photo-triggered cancer therapy could selectively and precisely eradicate the solid tumors by putting the laser probe on targeted regions, realizing the satisfactory antitumor efficacy (Su et al., 2015; Yan et al., 2016b).

Photodynamic therapy (PDT) can be used as a crucial approach for the treatment of various types of cancer by irradiating the photosensitizer-enriched tumor sites with light, the generating reactive oxygen species (ROS) can directly kill the cancer cells (Jang et al., 2011; Master et al., 2013; Chen et al., 2014). The photosensitizer-loaded PLGA-based DDSs have been widely concerned because of their good targeting capability and biocompatibility (Ricci-Junior and Marchetti, 2006). Importantly, the hydrophobic photosensitizers can be integrated into the PLGA-based DDSs, making it possible for the hydrophobic anticancer drugs to achieve the tumor-targeted delivery (Lee et al., 2012). Rojnik et al. (2012) designed the PEGylated PLGA nanoparticles for delivery of temoporfin, a effective second generation photosensitizer. In this study, the temoporfin delivered by PEGylated PLGA nanoparticles exhibited less dark cytotoxicity than the free temoporfin, while the phototoxicity of temoporfin-loaded PEGylated PLGA nanoparticles was not reduced when compared to the free temoporfin. The zinc(II) phthalocyanine (ZnPc)-loaded PLGA nanoparticles synthesized by Ricci-Junior and Marchetti (2006) showed the spherical morphology with a narrow size distribution and exhibited excellent biocompatibility due to their low dark toxicity assessed by the MTT assay. The significant photocytotoxicity of ZnPc-loaded PLGA nanoparticles showed them the great potential as the photosensitizer-loaded nanocarriers for PDT. Lee et al. (2012) have fabricated the PEGylated PLGA nanoparticles to co-load chlorin e6 (Ce6, a photosensitizer that can generate ROS upon the laser irradiation) and iron oxide (T_2 contrast agent) for tumor diagnosis and PDT. Firstly, Ce6 and mPEG were respectively coupled to the terminal hydroxyl group of PLGA, and then the obtained PLGA-mPEG and PLGA-Ce6 were used to synthesize the multifunctional PLGA nanoparticles through the double emulsion method, and the feeding ratio of PLGA-Ce6 and PLGA-mPEG was 75%: 25% (w/w) (**Figure 1A**). The whole body fluorescence imaging of KB tumor-bearing nude mice after intravenous administration of Ce6/iron oxide co-loaded PLGA nanoparticles (NP1) showed a remarkable fluorescence signal of Ce6 in the tumor region, while the mice after intravenous administration of free Ce6 exhibited a weak fluorescence signal of Ce6 in the tumor region, demonstrating the efficient tumor targeting capability of Ce6/iron oxide co-loaded PLGA nanoparticles (NP1) (**Figure 1B**). The subcutaneous tumor volume of NP1 (equivalent 0.1 mg Ce6/kg body) treated KB tumor-bearing nude mice was about 1.5 or 3 times smaller than those of free Ce6 (2.5 mg/kg) or PBS treated nude mice (**Figure 1C**). The low-dose administration of NP1 (equivalent 0.1 mg Ce6/kg body) displayed better tumor inhibition effect than high-dose administration

TABLE 1 | Summary of recent applications of PLGA-based DDSs for remotely triggered cancer therapy.

Remote trigger	Therapy	Formulation	Therapeutic agent	Administration route	Applications	References
Photo	PDT	Ce6/iron oxide co-loaded PLGA	Ce6	Intravenous administration	Human oral epidermoid cancer treatment (KB cells)	Lee et al., 2012
	PTT, Chemotherapy	DOXO-loaded BGNSH-HSA-ICG-FA	DOX, ICG, gold nanoshells	Intravenous administration	Cervical and breast cancer treatment (Hela cells, MDA-MB-231)	Topete et al., 2014
	Photo-triggered chemotherapeutics release, PTT	ANG/GS/PLGA/DTX	DTX, gold nanoshell	Intravenous administration	Glioblastoma treatment (U87MG cells)	Hao et al., 2015
Ultrasound	HIFU treatment	Fe_3O_4/PLGA	–	Percutaneous injection	Breast cancer treatment (VX2 squamous carcinoma cell line)	Sun et al., 2012
	Ultrasound-triggered chemotherapeutics release	MPMBs	DOX	Percutaneous injection	Tumor lymph node treatment (VX2 squamous carcinoma cell line)	Niu et al., 2013
	Ultrasound-enhanced efficiency of gene transfection	PLGA/PEI/DNA	pDNA	Intravenous administration	Human prostate cancer treatment (DU145 cells)	Chumakova et al., 2008
Magnetic field	Magnetic hyperthermia, chemotherapy	DOX-MMS	DOX, γ-Fe_2O_3 nanoparticles (IOs)	Intratumoral administration	Breast cancer treatment (4T1 cells)	Fang et al., 2015
Radiofrequency	RF ablation	DLM@PLGA	DL-menthol (DLM)	Intratumoral administration	Human cervical carcinoma treatment (Hela cells)	Zhang K. et al., 2016

of free Ce6 (2.5 mg/kg), suggesting that the Ce6-loaded PLGA nanoparticles showed enhanced PDT for tumor.

Photothermal therapy (PTT) has been proposed to be an attractive method for solid tumor elimination, which utilizes the light-absorbing agents to convert light energy into heat energy, thus the generated local hyperthermia can destroy the cancer cells irreversibly without causing damage to the healthy tissues (Dong et al., 2016; Yan et al., 2016a; Wang et al., 2017). Compared to the radiotherapy, chemotherapy and surgery, PTT has been supposed to be a less invasive, controllable and efficient cancer treatment approach (Shen et al., 2015). A large number of nanomaterials have been reported to act as the light-absorbing agents for PTT, such as gold nanomaterials (Wu et al., 2017), carbon nanotubes (Robinson et al., 2010), and graphene (Markovic et al., 2011), which have strong absorption in the near-infrared region. Indocyanine green (ICG), as an organic molecule, is another kind of near-infrared light-absorbing agent (Li et al., 2017). Notably, the near-infrared light with a wavelength range of 650–950 nm has low phototoxicity to skin and tissues due to the minimal light absorption of skin and tissues in near-infrared region (Yu et al., 2016). Topete et al. (2014) have designed and synthesized a multifunctional nanoplatform for tumor diagnosis and therapy. As shown in **Figure 1D**, the primarily synthesized DOXO-loaded PLGA nanoparticles were subsequently modified with the chitosan biopolymer, then the Au seeds were deposited onto the surface of chitosan-modified DOXO-loaded PLGA nanoparticles, next the DOXO-loaded branched gold nanoshells (BGNSHs) were obtained in the presence of $HAuCl_4/K_2CO_3$ and ascorbic acid through a seeded-growth surfactant-less method, and finally the human serum albumin (HSA)-ICG-FA conjugated and DOXO-loaded branched gold nanoshells (DOXO-loaded BGNSH-HSA-ICG-FA) were obtained by adsorbing the prefabricated HSA-ICG-FA complex to the DOXO-loaded BGNSHs. The photothermal efficiency of the nanoplatforms were further evaluated. As shown in **Figure 1E**, the temperature of BGNSH-HSA-ICG-FA was rapidly increased and the ΔT of BGNSH-HSA-ICG-FA was ∼19°C after 5 min of irradiation (808 nm, 2 W/cm^2), as compared to those of BGNSHs (ΔT = 15°C), free ICG(ΔT = 6°C), and buffer solutions (ΔT = 1°C). The enhanced photothermal efficiency of BGNSH-HSA-ICG-FA was mainly due to the strong absorption of gold nanoshells and ICG molecules in the NIR region, implying the great potential of BGNSH-HSA-ICG-FA for PTT of cancer. The cell viability of HeLa cells treated with BGNSH-HSA-ICG-FA in the presence of NIR laser irradiation was much lower than that of HeLa cells treated with BGNSH-HSA-ICG-FA in the absence of NIR laser irradiation, indicating the remarkable photocytotoxicity of BGNSH-HSA-ICG-FA as a consequence of the hyperthermia generated from gold nanoshells and ICG molecules. And the cell viability of HeLa cells treated with DOXO-loaded BGNSH-HSA-ICG-FA in the presence of NIR laser irradiation was the lowest among all groups, suggesting the significant phototoxicity of DOXO-BGNSH-HSA-ICG-FA and their latent capability for combined chemotherapy and PTT of cancer (**Figure 1F**).

The light as an external stimuli has also been used for on-demand drug release from the PLGA-based DDSs at the suitable position (e.g., tumor region). The DOX and ICG co-loaded PLGA-based nanoparticles (DINPs) fabricated by Zheng et al. (2013) exhibited the faster DOX release property and enhanced cellular uptake of DOX and ICG in MCF-7 and MCF-7/ADR cells under NIR laser irradiation. Hao et al. (2015) synthesized

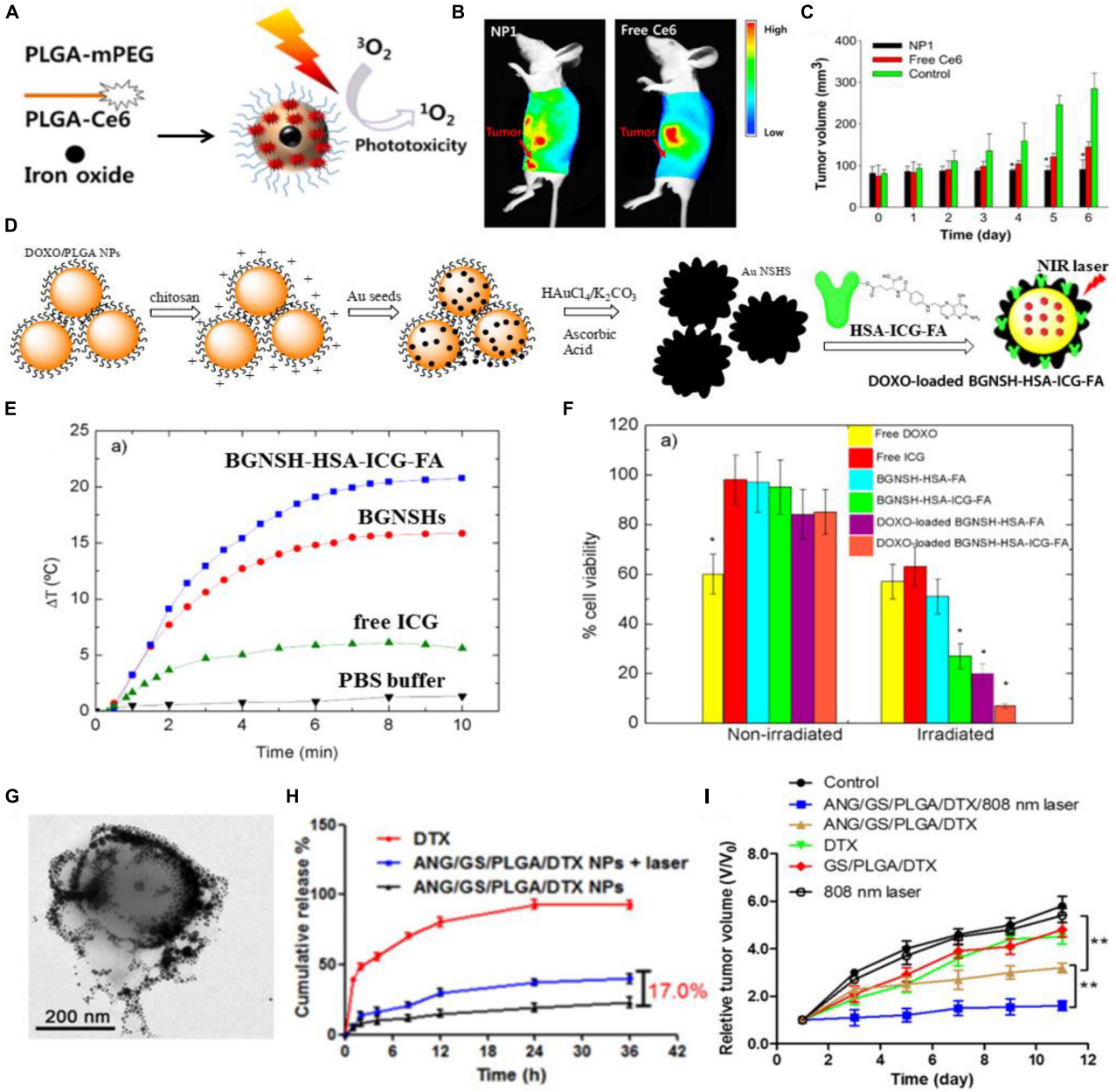

FIGURE 1 | The photo-triggered cancer therapy based on PLGA-based DDSs. **(A)** Schematic illustration of Ce6/iron oxide co-delivered PEGylated PLGA nanoparticles (NP1). **(B)** The whole body fluorescence imaging of KB tumor-bearing nude mice after intravenous administration of Ce6/iron oxide co-loaded PEGylated PLGA nanoparticles (NP1) or free Ce6. **(C)** Tumor volume changes in KB tumor-bearing nude mice after intravenous administration of NP1 (equivalent Ce6 0.1 mg/kg body), free Ce6 (2.5 mg/kg) or PBS (control). Adapted with permission from Lee et al. (2012). Copyright 2012, Elsevier. **(D)** Schematic illustration of the synthetic process of DOXO-loaded BGNSH-HSA-ICG-FA. **(E)** The temperature profiles of BGNSH-HSA-ICG-FA, BGNSHs, free ICG and PBS buffer under continuous NIR laser irradiation (808 nm, 2 W/cm^2). **(F)** Cell viability of the various nanoplatforms treated HeLa cells after 24 h of incubation in the presence and absence of NIR laser irradiation (808 nm, 2 W/cm^2). Adapted with permission from Topete et al. (2014). Copyright 2014, American Chemical Society. **(G)** Transmission electron microscopy (TEM) image of ANG/GS/PLGA/DTX NPs after 808 nm laser irradiation for 5 min. **(H)** The *in vitro* drug release profiles of DTX and ANG/GS/PLGA/DTX NPs with or without laser irradiation treatment. **(I)** Relative tumor volume of various treatment groups. Adapted with permission from Hao et al. (2015). Copyright 2015, Elsevier.

the docetaxel (DTX)-loaded PLGA@Au nanoparticles, and then the angiopep-2, one kind of brain tumor-targeted peptide, was conjugated onto the gold nanoshell of DTX-loaded PLGA@Au nanoparticles via Au-S bond to form the tumor-targeted and gold nanoshell-surrounded PLGA-based nanoparticles (denoted as ANG/GS/PLGA/DTX NPs) for cancer chemotherapy and PTT. ANG/GS/PLGA/DTX NPs showed the excellent photothermal response and their structure observed by TEM was collapsed, the

core-shell structure of the nanoparticles was also destroyed due to the local hyperthermia (**Figure 1G**). The *in vitro* drug release profile demonstrated the photo-triggered chemotherapeutics release property of ANG/GS/PLGA/DTX NPs. As shown in **Figure 1H**, the drug release of ANG/GS/PLGA/DTX NPs treated with 808 nm laser irradiation was fast and their final cumulative chemotherapeutics release percentage has increased by ∼17.0% compared to that of ANG/GS/PLGA/DTX NPs without 808 nm laser irradiation. The *in vivo* anti-glioma efficiency of drug-loaded NPs was further assessed, as shown in **Figure 1I**, ANG/GS/PLGA/DTX NPs with exposure to an 808 nm laser irradiation displayed considerable tumor inhibition efficiency, when compared to the GS/PLGA/DTX NPs and ANG/GS/PLGA/DTX NPs without laser irradiation, implying the promising application of ANG/GS/PLGA/DTX NPs in glioma-targeted chemotherapy and PTT.

Ultrasound-Triggered Cancer Therapy

Ultrasound has been widely used in medicine for multifarious diagnostic and therapeutic purposes due to their advantages of feasibility and non-invasiveness (Ferrara, 2008; Zhang X. et al., 2014). This section will focus on ultrasound-triggered cancer therapy based on PLGA nano-/micro-particles which involved HIFU treatment, ultrasound-triggered chemotherapeutics release, and ultrasound-enhanced efficiency of gene transfection.

High intensity focused ultrasound (HIFU) is an advanced technology that was proposed for the first time in the 1940s (Manthe et al., 2010; Zhang K. et al., 2014). HIFU ablation has been demonstrated to be a feasible, non-invasive, and effective procedure for solid tumor treatment (Wu et al., 2004; Kennedy, 2005; Orsi et al., 2010). Sun et al. (2012) in their 2012 Biomaterials article, used PLGA to load the hydrophobic Fe_3O_4 nanoparticles for improving the therapeutic efficiency of HIFU ablation of breast cancer and realizing the ultrasound/magnetic resonance dual-modality imaging of tumors (**Figure 2A**). The obtained Fe_3O_4/PLGA microcapsules were characterized by uniform spherical morphology and an average diameter of 885.6 nm. The therapeutic effect of HIFU ablation for the breast cancer-bearing rabbits was further assessed. The tumor was treated with HIFU (150 W of acoustic power for 5 s) after percutaneous injection of Fe_3O_4/PLGA (saline and pure PLGA microcapsules was used as the control). After the treatment, the coagulative necrosis volume of the excised tumor tissues from the rabbits was calculated and the results showed a larger coagulative necrosis volume and lower positive index of proliferating cell nuclear antigen (PCNA) in tumor tissues of Fe_3O_4/PLGA microcapsules treated group when compared to the other groups treated with saline and the pure PLGA microcapsules (**Figures 2B,C**). These results were mainly attributed to the most obvious acoustic signal enhancement in the breast tumor region induced by the administration of Fe_3O_4/PLGA microcapsules and exposure to HIFU.

Ultrasound (US) can be used as another promising external trigger for on-demand drug release from the PLGA-based DDSs at the tumor region. Multifunctional polymer microbubbles (MPMBs) were designed by Niu et al. (2013) to co-encapsulate iron oxide nanoparticles and DOX for tumor lymph node detection and therapy. **Figure 2D** shows the process of MPMBs delivery into tumor lymph node and the controllable release of DOX from MPMBs triggered by low frequency US sonication. The workers recorded the *in vitro* DOX release profiles of MPMBs with or without low intensity sonication. As illustrated in **Figure 2E**, the cumulative drug release of MPMBs with low frequency US sonication showed an ∼90% of the released DOX from MPMBs, compared to that of MPMBs without low frequency US sonication showed <75% of the released DOX after 48 h. This result proved that the DOX-loaded MPMBs can be remotely triggered by US and then promote the DOX release from the microbubbles, showing the great potential for controllable drug release and accumulation of drugs into the targeted sites under US imaging guidance. The therapeutic efficacy of the MPMBs against tumor lymph nodes was further assessed. And the cell proliferation of the various treatment groups was evaluated in tumor lymph nodes model by using immunohistochemical staining methods. The results showed that the expression of PCNA could be observed in all groups and the proliferative index (PI) of tumor lymph nodes in the group treated with MPMBs and low frequency US sonication is substantially lower than those of any other groups (**Figure 2F**). However, no obvious difference for the PI was observed between the saline treated group and the pure MB (PLGA microbubble without loading iron oxide nanoparticles and DOX) combined with low frequency US sonication treated group. These results revealed that the developed MBMPs could remarkably improve the therapeutic efficacy against tumor lymph nodes when exposed to low frequency US sonication, which might be attributed to the controllable drug release behavior upon US irradiation and the cavitation effect.

Ultrasound has been utilized for gene delivery in recent years (Huber and Pfisterer, 2000; Pitt et al., 2004; Zarnitsyn and Prausnitz, 2004; Larina et al., 2005b). Larina et al. (2005a) has confirmed that combining the gene delivery systems based on nanoparticles with ultrasound may enhance the gene and drug delivery in targeted areas. Chumakova et al. (2008) fabricated the PLGA/PEI/DNA nanoparticles and combined them with ultrasound to improve the gene transfection efficiency in a nude mouse model. They firstly used PEI to absorb the β-galactosidase plasmids, and then the obtained PEI/DNA nanoparticles were loaded on the PLGA nanoparticles to form the PLGA/PEI/DNA nanoparticles. Polyethylenimine (PEI) as one type of cationic polymers has been used for gene delivery for the first time in the 1990s (Boussif et al., 1995). In recent years, PEI molecules with high molecular weight have been considered as one of the most efficient non-viral gene vectors for gene delivery (Gary et al., 2007). The PLGA/PEI/DNA nanoparticles were intravenously injected into the nude mice with DU145 human prostate tumors and then transfection efficiency was assessed by western blot analysis. As shown in **Figures 2G,H**, the expression of β-galactosidase showed an ∼8-fold enhancement in ultrasound irradiated tumors when compared to the control tumors. The enhanced transfection efficiency might be attributed to the changed structure of tumor cell membrane and tumor vasculature induced by ultrasound. These results indicated that the combination of PLGA/PEI/DNA nanoparticles with ultrasound was an efficient approach for *in vivo* gene transfection.

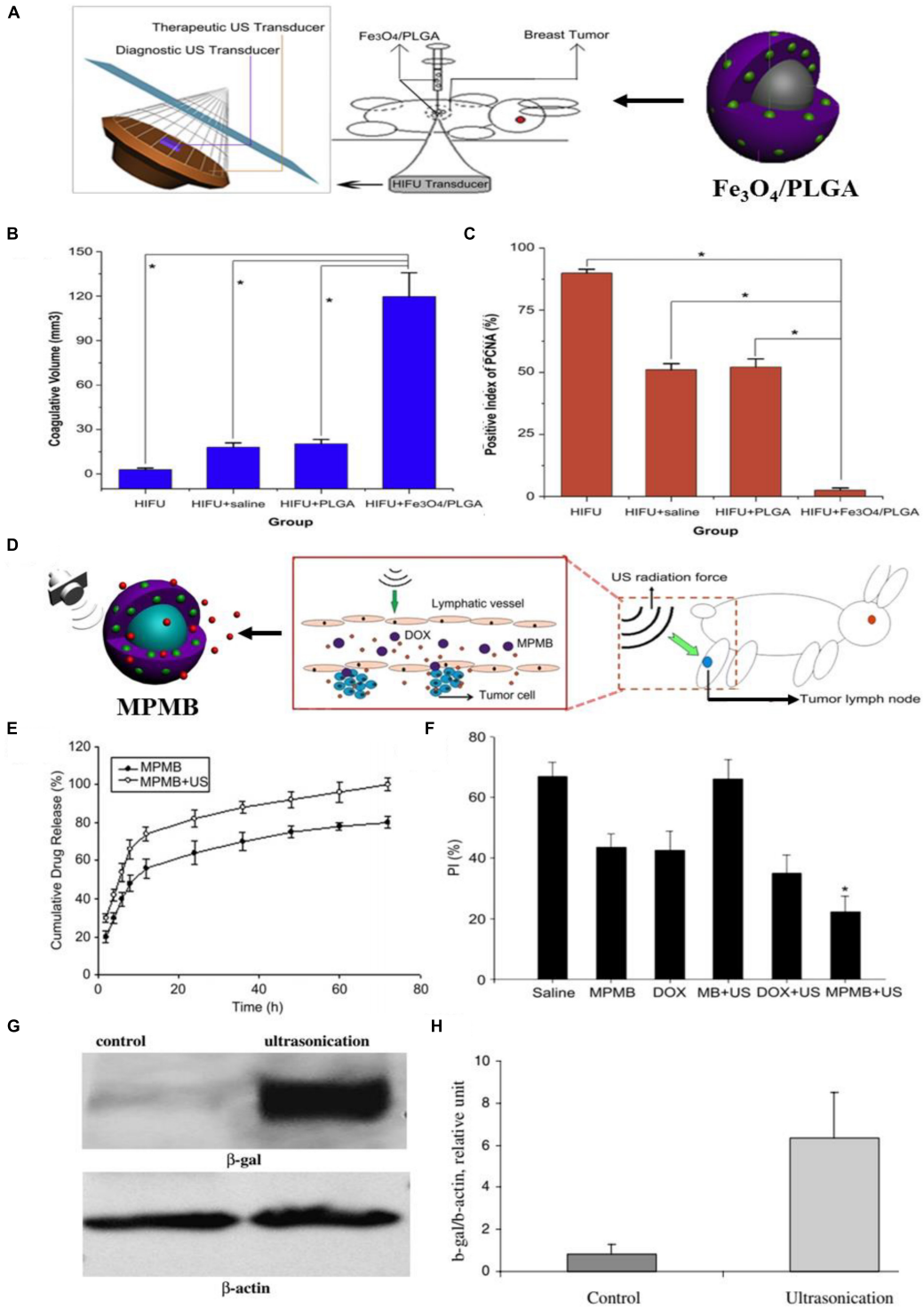

FIGURE 2 | The ultrasound-triggered cancer therapy based on PLGA-based DDSs. **(A)** Schematic illustration of the developed Fe_3O_4/PLGA microcapsules used for HIFU ablation of breast cancer in rabbits. **(B)** The volume of coagulative necrosis in excised tumor tissues from different groups exposed to HIFU (*$P < 0.05$). **(C)** Positive index (PI) of PCNA in tumor tissues from different groups after HIFU ablation (*$P < 0.05$). Adapted with permission from Sun et al. (2012). Copyright 2012, Elsevier. **(D)** Schematic illustration of the process of MPMBs delivery into tumor lymph node and the controllable release of DOX from MPMBs triggered by low frequency US sonication. **(E)** The *in vitro* DOX release profiles of MPMBs with or without low intensity sonication. **(F)** The proliferative index (PI) of tumor lymph nodes in various groups. *$P < 0.05$ vs. the other groups. Adapted with permission from Niu et al. (2013). Copyright 2013, Elsevier. **(G)** The expression of β-galactosidase (β-gal) in control and ultrasound irradiated tumors assessed by western blot analysis. **(H)** Densitometry analysis of the β-gal expression from **Figure 3G**. Adapted with permission from Chumakova et al. (2008). Copyright 2008, Elsevier.

Magnetic Field-Triggered Cancer Therapy

Magnetic hyperthermia induced by ACMF has been demonstrated to be a promising antitumor approach due to their relative non-invasive property (Jaber and Mohsen, 2013; Ramimoghadam et al., 2015). It has been proved that the magnetic nanoparticles (MNPs) could be used to produce magnetic hyperthermia via dipole relaxation under an external ACMF placed in the tumor regions, which can be employed to induce apoptosis of the tumor cells and make the tumor cells more sensitive to chemotherapy (Johannsen et al., 2007; Issels, 2008; Torres-Lugo and Rinaldi, 2013; Shen et al., 2015).

Fang et al. (2015) have designed and synthesized the magnetic responsive microspheres based on PLGA for combined chemotherapy and hyperthermia. **Figure 3A** shows the preparation procedure of magnetic PLGA microspheres contained DOX (DOX-MMS). Firstly, the workers in this study used the modified double emulsion solvent evaporation method to develop the DOX-loaded PLGA microspheres (DOX-MS). And then the positively charged polyethylenimine (PEI) was decorated on the surface of DOX-MS by electrostatic deposition to form an interlayer. Ultimately, the DOX-MMS were obtained by adsorbing the γ-Fe_2O_3 nanoparticles (IOs) on the surface of DOX-MS through the electrostatic incorporation. SEM images of the DOX-MMS after ACMF treated for 30 min showed that the DOX-MMS were broken and the pores could be observed on the surface of DOX-MMS (**Figure 3C**), while the SEM images of DOX-MMS without exposure to ACMF showed no obvious changes in morphology and almost all the microspheres could be observed to maintain the integrated structure (**Figure 3B**). The destroyed structure of DOX-MMS after exposure to ACMF was induced by the heat effect generating from the IOs on the PLGA shell triggered by ACMF, which can lead to an accelerated DOX release behavior of DOX-MMS. **Figure 3D** shows the cell viability of 4T1 cells treated with DOX-MMS at different DOX concentrations with or without exposure to ACMF for 30 min. There was an apparent DOX dose-dependent decrease of cell viability in the ACMF treated group. However, the cell viability of 4T1 cells without exposure to ACMF exhibited a slight decline with the increase of DOX concentration. The *in vivo* tumor inhibition assay revealed that the DOX-MMS treated with ACMF showed an effective tumor inhibition effect in 4T1 tumor-bearing nude mice models. The severe necrotic tumor tissues with dark gray color can be observed and the relative tumor volume in DOX-MMS treated mice with exposure to ACMF was the lowest among all experimental groups (**Figures 3E,F**). And there was no significant body weight loss observed in all groups (**Figure 3G**). The hematoxylin and eosin (H&E) staining, TUNEL staining, and immunohistochemical anti-CD31 staining of the tumor tissues from mice in all groups were further performed. As shown in **Figure 3H**, the visible necrotic areas, necrotic or apoptotic cells stained brown, and the low microvessel density of tumor tissues can be observed from the DOX-MMS treated mice with exposure to ACMF. These results indicated that the local hyperthermia triggered by the ACMF and the accelerated drug release behavior could enhance the antitumor effect of DOX-MMS.

Radiofrequency-Triggered Cancer Therapy

Besides the ultrasound- and ACMF-triggered cancer therapy approach, the anti-cancer strategy triggered by radiofrequency (RF) has been extensively applied in various types of tumors (Miao et al., 2000; Dromain et al., 2002; Heynick et al., 2003). Although radiofrequency is a minimally invasive tool to inhibit tumor growth, the necessary high output power and long irradiation time of RF is needed, which can inevitably cause the damages to normal organs and tissues (Ryan et al., 2000). Magnetic metal nanoparticle have been validated to improve the ablated volume of tumors and in consequence promote the RF ablation of tumors, however, the high output power of RF is still needed to get high oscillating magnetic field (Kruse et al., 2011; Xu et al., 2012; Yun et al., 2014). Recently, the bubbles-induced cavitation has been proposed to be a promising strategy to enhance RF ablation of tumors.

Zhang K. et al. (2016) introduced the biocompatible DL-menthol (DLM) (melting point: 32–36°C) to a PLGA nanocapsule to construct a DLM encapsulated PLGA-based nanocapsule (abbreviated as DLM@PLGA). The solid DLM possesses the property of continuous solid-liquid-gas (SLG) triphase transformation, which is perfectly suitable for RF ablation (Zhang K. et al., 2014). The continuous cavitation triggered by radiofrequency solidoid vaporization (RSV) can result in the continuous enhancement of RF ablation in a reduced RF power output and shorten irradiation time manner. And the external RF-mediated local heat in the RSV process can trigger the vaporization of encapsulated solid DLM and resulting in DLM bubbles continuously generating from DLM@PLGA (**Figure 4A**). SEM image of as-prepared DLM@PLGA exhibited the uniform spherical morphology with an average particle size of 450 nm (**Figure 4B**). A plenty of DLM bubbles with different particle sizes can be observed in the confocal laser scanning microscope (CLSM) image of DLM@PLGA suspension after exposure to RF heating (60°C) (**Figure 4C**). The efficiency of RF ablation based on continuous cavitation was further evaluated in HeLa tumor-bearing nude mice models after intratumoral injection of PBS, PLGA, free DLM, and DLM@PLGA with exposure to RF (1 W of the output power and 30 s of the irradiation time). The obtained excised tumors from each group were used to calculate the ablated volume. As shown in **Figures 4D,E**, the DLM@PLGA treated HeLa tumors showed the largest ablated volume. And the three isolated ablation regions observed in the free DLM treated HeLa tumors were mainly resulting from the non-uniform distribution and agglomeration of free DLM induced by their hydrophobic property. Furthermore, tunnel staining and PCNA assay were further carried out to evaluate the molecular mechanism of the enhanced RF ablation. As shown in **Figure 4F**, the most apoptotic cells (brown color areas) but the least proliferating cells (brown color areas) were both observed in the DLM@PLGA treated

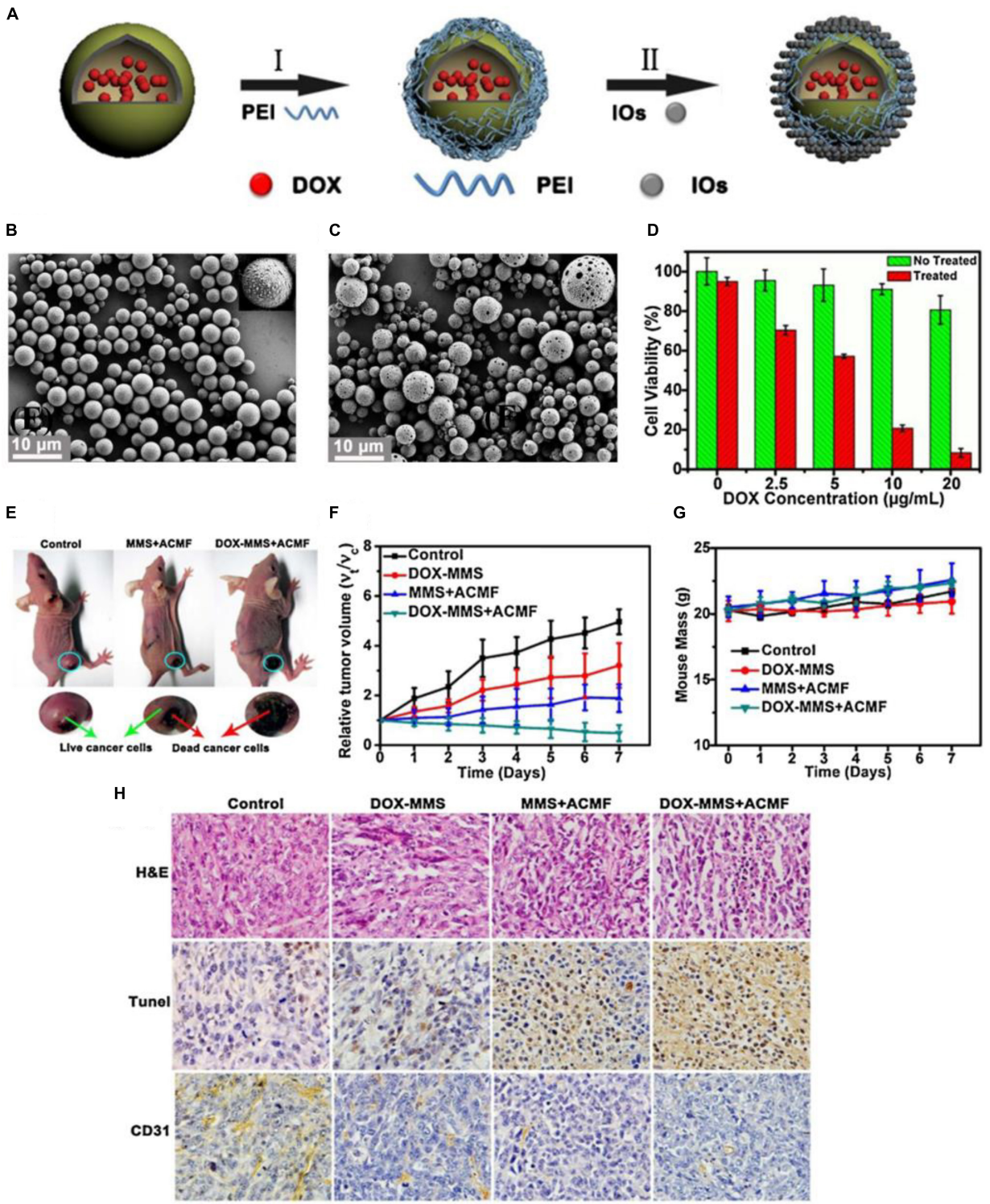

FIGURE 3 | The magnetic field-triggered cancer therapy based on PLGA-based DDSs. **(A)** The preparation procedure of magnetic PLGA microspheres contained DOX (DOX-MMS). **(B)** SEM images of the DOX-MMS without exposure to ACMF. **(C)** SEM images of the DOX-MMS with exposure to ACMF. **(D)** Cell viability of the 4T1 cells treated with DOX-MMS at different DOX concentrations with or without exposure to ACMF. **(E)** The 4T1 tumor-bearing nude mice treated with PBS (control), MMS (containing no DOX) with ACMF, and DOX-MMS with ACMF after 7 days. **(F)** Relative tumor volume of various treatment groups. **(G)** Body weight changes in mice from the various treatment groups. **(H)** The hematoxylin and eosin (H&E) staining, TUNEL staining, and immunohistochemical anti-CD31 staining of the tumor tissues from mice in each group. Adapted with permission from Fang et al. (2015). Copyright 2015, Elsevier.

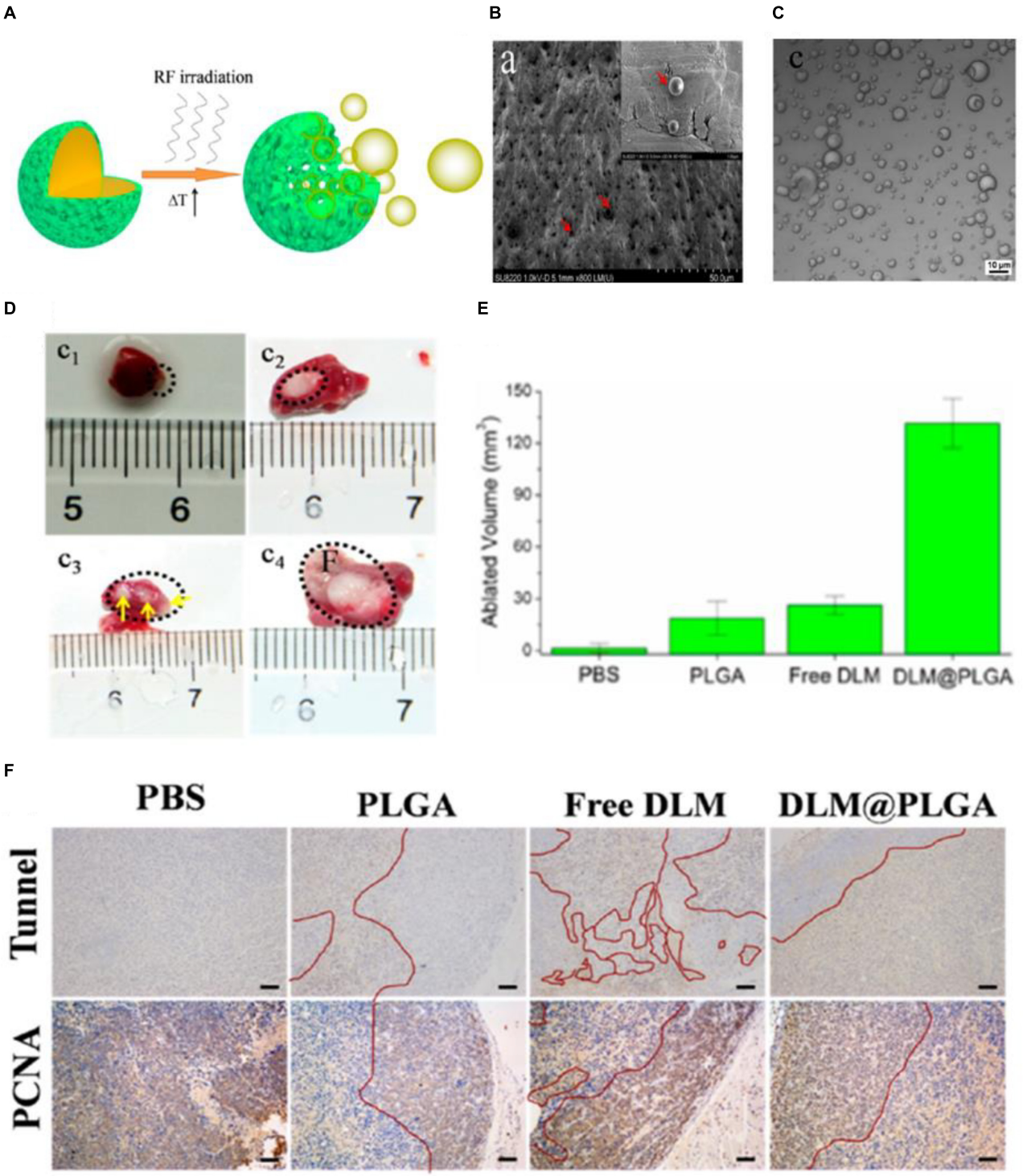

FIGURE 4 | The radiofrequency-triggered cancer therapy based on PLGA-based DDSs. **(A)** Schematic illustration of an external RF-triggered RSV process mediated by DLM@PLGA. **(B)** SEM image of as-prepared DLM@PLGA (indicated by red arrows). **(C)** Confocal laser scanning microscope (CLSM) image of DLM@PLGA suspension after exposure to RF heating. **(D)** Optical images of the HeLa tumors treated with PBS (c_1), PLGA (c_2), free DLM (c_3), and DLM@PLGA (c_4) upon exposure to RF (1 W of the output power and 30 s of the irradiation time). **(E)** The corresponding ablated volumes of HeLa tumors calculated from **Figure 5D**. **(F)** Tunnel staining and PCNA immunochemistry analysis of tumor tissues, wherein the ablated and un-ablated regions were separated by the red curves (scale bar is 100 μm). Adapted with permission from Zhang K. et al. (2016). Copyright 2016, American Chemical Society.

HeLa tumors. These results demonstrated that the solid DLM encapsulated into the PLGA nanocapsules could strengthen RF ablation through the continuous cavitation which mediated by the RSV process triggered by RF field.

DESIGN OF PLGA-BASED DDSs WITH IMAGING PROPERTY

In recent years, contrast agents have opened up a new development direction for tumor imaging, gradually become a new hotspot for cancer diagnosis and treatment (Chen et al., 2014). Applying the contrast agents into tumor diagnosis can realize imaging of tumors with a high spatial resolution and sensitivity (Shen et al., 2017; Yang et al., 2017). At present, the commonly used diagnostic methods in clinic mainly includes ultrasound imaging, X-ray computed tomography imaging (CT), magnetic resonance imaging (MRI), which can provide certain information for the preoperative staging and prognosis of tumors (James and Gambhir, 2012). However, because of some drawbacks of contrast agents including poor stability, rapid elimination from the body, and lack of targeting, the location of the lesions cannot be accurately located during diagnosis, which may lead to the compromised therapeutic effect of tumors (Kirchherr et al., 2009; Niu et al., 2013). It has been demonstrated that loading imaging agents into PLGA-based DDSs could improve the targeting ability and biocompatibility of imaging agents (Shen et al., 2017, 2019). The imaging agents can be encapsulated into PLGA-based DDSs or conjugated on to the outer surface of PLGA-based DDSs through the covalently linking with functional groups (such as carboxylic acid and hydroxyl groups) of PLGA (Martins et al., 2018). For example, the imaging agents which possess the amine groups can be covalently linked to the terminal carboxylic acid groups of PLGA by forming an amide linkage (Malinovskaya et al., 2017). Additionally, the imaging agents can also be introduced into PLGA by an appropriate linker such bifunctional PEG linker (El-Gogary et al., 2014; Park et al., 2014). T_2-contrast agents based on superparamagnetic Fe_3O_4 nanoparticles can be encapsulated into the PLGA-based DDSs aiming for magnetic resonance (MR) imaging of tumors, which is a powerful and non-invasive imaging technique with relatively high temporal and spatial resolution (Li et al., 2013; Shen et al., 2017). A series of fluorescent dyes, near-infrared fluorescent imaging agents, and quantum dots, etc. can also be introduced into the PLGA-based DDSs aiming for fluorescence imaging of tumors, which plays an important role in the research of tumorigenesis and development due to its high sensitivity and low cost property (Edgington et al., 2009; Rotman et al., 2011). ICG, as a near-infrared (NIR) fluorescent imaging agent with low toxicity, has been used for cardiac function monitoring, liver output, and retinal angiography (Owens, 1996). Moreover, ICG can be utilized as a photoacoustic imaging contrast agent to produce the enhanced photoacoustic signal due to its strong NIR light absorbance, realizing the photoacoustic (PA) imaging of tumors in a non-invasive manner (Chen et al., 2016). It is noted that the gold nanomaterials could be encapsulated into the PLGA-based DDSs or coated onto the surface of the PLGA-based DDSs for PA imaging or X-ray CT (Hao et al., 2015; Song et al., 2015). The high-resolution tissue structure image of tumors will be obtained when employing the gold nanomaterials as the contrast agents for X-ray CT, which possesses the advantages of fast acquisition time, simple operation, and high availability (Li et al., 2010; Chen et al., 2014).

PLGA-BASED CANCER THERANOSTICS

Nowadays, clinical diagnosis and treatment of tumors are two separate processes, patients usually need to be diagnosed before treatment, and the two separate medical procedures are likely to delay the best time to treat diseases (Wang et al., 2012). With the rapid development of molecular imaging technology, various imaging modes have been studied to improve diagnostic imaging. Therefore, the development of a multifunctional nanoplatform with diagnostic and therapeutic functions has been the future development trend of nanomedicine (Song et al., 2017). By applying the nanoplatform which integrated diagnostic and therapeutic agents to tumor treatment, the entire process of chemotherapy can be monitored in real time, and whether the chemotherapeutic drugs are effectively delivered to the tumor sites can be monitored. The position, size change, and metastasis of the tumors can also be monitored to determine whether the chemotherapeutic drugs are effective in killing tumors. Many researchers have developed various types of PLGA-based DDSs that can be used for MRI, CT, fluorescence imaging, ultrasound imaging, and photoacoustic (PA) imaging of tumors to achieve the accurate tumor detection, meanwhile these PLGA-based DDSs can also be used to load the therapeutic drugs such as chemotherapeutic drugs, small molecule inhibitors, photosensitizers, photothermal agents and siRNA (**Figure 5**; Menon et al., 2013). Yang et al. (2018) have developed the charge-reversal PLGA-based ultrasound nanobubbles to co-load Dox and P-gp shRNA for reversal of drug resistance and enhancing the antitumor effect of chemotherapeutics. The *in vitro* and *in vivo* data substantiated that the drug and gene co-delivered PLGA-based nanobubbles could be used as an available theranostic agent for ultrasound imaging-guided chemotherapy and gene therapy of multiple drug resistance (MDR) tumors. Another novel PLGA nanoparticles coated with cancer cell membrane for dual-modal imaging-guided photothermal cancer therapy was prepared by Chen et al. (2016). The near-infrared light absorbing agent, ICG, was firstly encapsulated into the PLGA nanoparticles to obtain the ICG loaded PLGA nanoparticles which were employed as the core, then cancer cell membrane shell was coated onto the surface of ICG loaded PLGA cores by co-extruding the membrane vesicles and ICG loaded PLGA cores through a 220 nm polycarbonate membrane. The ultimately obtained cancer cell membrane-coated PLGA nanoparticles (ICNPs) with ICG loaded PLGA cores and cancer cell membrane shell were validated to have a favorable photothermal response and homologous targeting effect both at the cellular level and animal level. The results demonstrated that ICNPs could substantially

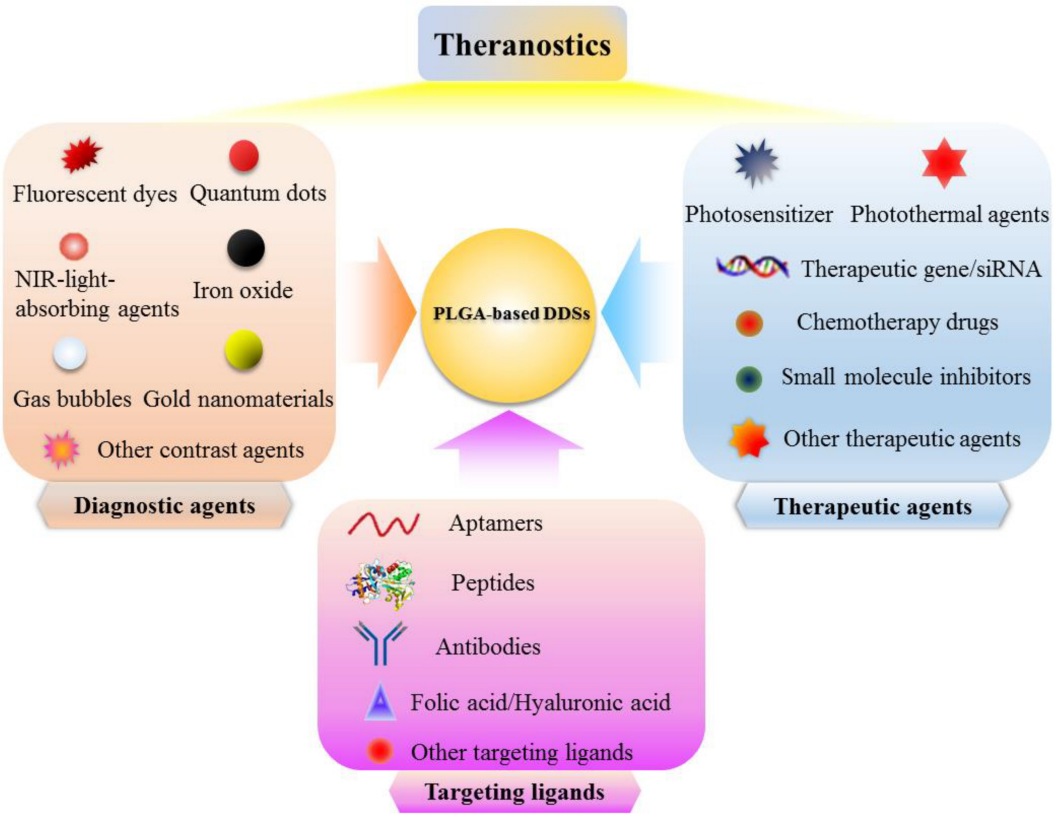

FIGURE 5 | Schematic illustration of PLGA-based DDSs which integrated diagnostic agents, therapeutic agents, and targeting ligands for effective diagnosis and treatment of cancer.

accumulate into subcutaneous breast cancer tissues in MCF-7 tumor-bearing nude mice through homologous targeting and EPR effect, and can be used as the fluorescence imaging and photoacoustic (PA) imaging agents to clearly identify tumor locations and boundaries. The *in vivo* results also corroborated that ICNPs could eradicate the tumors upon exposure to NIR laser and prevent the recurrence of tumors, showing the great potential of the developed cancer cell membrane-coated PLGA nanoparticles as the versatile nanoplatform for homologous-targeting and fluorescence/photoacoustic imaging-guided PTT. Gu et al. (2016) have reported a facile approach to construct a multifunctional nanocapsule based on PLGA to co-load BSA capped gold nanoclusters (AuNCs) and ICG. Because of the carboxyl groups existed on the surface of AuNCs and ICG co-loaded mPEG-PLGA (AuIP) nanocapsules, the amino groups of RGD peptides can be coupled to AuIP nanocapsules by forming the amide linkage. The obtained AuIP-RGD nanocapsules were demonstrated to be able to specifically target the U87-MG cancer cells that overexpress integrin $\alpha_v\beta_3$ by CLSM analysis. The results further validated the satisfactory performance of AuIP-RGD in both one-photon and two-photon fluorescence imaging of tumors as well as the PTT of tumors, showing the great potential of AuIP-RGD nanocapsules as the theranostic nanoplatform for tumor diagnosis and treatment applications.

TARGETING STRATEGIES

The PLGA-based DDSs should be developed to achieve the effective drug delivery. In brief, the drugs loaded in the PLGA-based DDSs should be able to reach the targeted tumor site after administration, and the loss of drug activity and dose in the blood circulation before reaching the targeted site should be minimal. More importantly, the drug should only kill tumor cells without harmful effects on normal tissues and organs. Various modifications can be performed to fabricate the PLGA-based DDSs, such as changing their size, shape, structure, chemical and physical properties, etc. to make them accumulate into the tumor regions through passive targeting or active targeting approach (Torchilin, 2000; Farokhzad and Langer, 2009).

DDSs are inclined to passively extravasate through the leaky vasculature, which is the unique pathophysiological characteristics of solid tumors, and preferentially accumulate into tumor tissues through the passive targeting (Shen et al., 2019). Generally, the abundant tumor vasculature are leaky, and the pore size of the leaky vascular endothelial cell gap ranges from 100 to 800 nm (Torchilin, 2011). Meanwhile, the tumor tissues lack effective lymphatic drainage (Bamrungsap et al., 2012), which can lead to the decreasing diffusion process, ultimately resulting in the prolonged retention time of DDSs.

Therefore, the DDSs with a particle size smaller than the pore diameter can easily penetrate the interstitium and finally become accumulated in tumor sites. The phenomenon of passive accumulation of DDSs into tumor tissues is referred to the enhanced permeability and retention (EPR) effect (Danhier et al., 2010; Greish, 2010).

PLGA-based DDSs has been demonstrated to be the multifunctional DDSs that can target tumor sites owing to their characteristics such as small and tunable particle size, high stability, excellent biocompatibility, and simple surface modification (Deng et al., 2014; Yang et al., 2015, 2018; Shen et al., 2017, 2019). Appropriate surface modification (such as PEGylation, poloxamers and Tween 80 conjugation) of the PLGA-based DDSs can evade the phagocytic uptake by the reticuloendothelial system (RES) (Cai et al., 2016), leading to the prolonged circulation time in blood, which provide more opportunities for these surface-modified PLGA-based DDSs to accumulate into the tumor regions through passive targeting approach (**Figure 6A**). In our previously published literature, we have designed the PLGA-based nanoparticles modified with bovine serum albumin (BSA) to co-load near-infrared dye, indocyanine green (ICG) and chemotherapeutic drug, doxorubicin (DOX) for passive tumor-targeted combination cancer therapy (Shen et al., 2019). BSA modification can not only act as a surface stabilizer but also a biocompatible shell of the PLGA-based nanoparticles to evade the non-specific adsorption of plasma protein and the recognition of macrophage. The enhanced fluorescence signals of PLGA-based theranostic nanoplatform (denoted as IDPNs) were detected in tumor region after 24 h intravenous injection when compared to free ICG molecules, suggesting that the IDPNs possess the capability of passive accumulation into tumor sites via the EPR effect (**Figure 6C**).

To improve the targeting efficiency of PLGA-based DDSs to the targeted sites, affinity ligands such as antibodies (Venugopal et al., 2018), peptides (Graf et al., 2012), aptamers (Wu et al., 2010), or small molecules (Shen et al., 2012) can be introduced onto the surface of PLGA-based DDSs, which can be recognized by the specific receptors overexpresses on tumor cells and then bind tumor cells through ligand-receptor interactions, achieving the active targeting and accumulation of PLGA-based DDSs into tumor sites via the receptor-mediated cell uptake, as illustrated in **Figure 6B**. Folic acid (FA) is a kind of small molecule nutrient, as an non-immunogenic targeting ligand, it possesses high binding affinity to the folate receptor, which overexpresses on the surface of various types of human cancer cell membranes (Shen et al., 2012). Folate receptor (FR) has been extensively utilized for active tumor-targeting of nanocarriers via the receptor-mediated endocytosis (El-Gogary et al., 2014). Besides the passive and active targeting, magnetic targeting is another targeting strategy, which can be achieved by loading the magnetic nanoparticles into PLGA-based DDSs before exposing to an external magnetic field (Yu et al., 2016; Shen et al., 2017). Our group has developed the folic acid-conjugated PEGylated PLGA nanoparticles co-encapsulated with CdSe/ZnS quantum dots, doxorubicin and Fe_3O_4 nanoparticles followed by the adsorption of vascular endothelial growth factor (VEGF)-targeted small hairpin RNA (abbreviated as LDM-PLGA/PPF/VEGF shRNA) for tumor targeted drug delivery and cancer imaging (Shen et al., 2017). The folic acid modified on the surface of nanocomposites and the Fe_3O_4 nanoparticles encapsulated into the nanocomposites endow LDM-PLGA/PPF/VEGF shRNA with folate and magnetic dual targeting functions by folate receptor-mediated endocytosis and magnetic guidance. HeLa cells treated with LDM-PLGA/PPF nanocomposites exhibited the increase of intracellular DOX fluorescence signal along with the decreasing distance from the magnet, while an increased fluorescence signal of DOX in HeLa cells without free folate pretreatment was observed compared to the cells with free folate pretreatment, demonstrating the enhanced cellular uptake of LDM-PLGA/PPF by HeLa cells via magnetic guidance and folate receptor-mediated endocytosis (**Figure 6D**).

Currently, applying the intrinsic homologous adhesion property of the cancer cells to tumor targeting is another promising active tumor-targeting approach. Surface adhesion molecules such as galectin-3 or N-cadherin expressed on cancer cells have been proven to be the leading cause of multicellular aggregation formation. Therefore, the cancer cell membrane can be utilized for the surface functionalization of DDSs in order to obtain the homologous targeting capability. Chen et al. (2016) reported a cancer cell membrane-coated PLGA nanoparticles with encapsulation of indocyanine green (ICG) molecules for specific homologous tumor-targeted and photoacoustic/fluorescence imaging-guided photothermal cancer therapy. The results of the *in vivo* biodistribution and photoacoustic/fluorescence imaging showed a remarkably enhanced tumor accumulation of MCF-7 cell membrane-coated PLGA nanoparticles at 24 h post-injection when compared to the non-cancer cell membrane-coated PLGA nanoparticles in human breast cancer cells (MCF-7) bearing nude mice models. The illustrated examples validate that the PLGA-based DDSs with appropriate surface functionalization can provide a promising approach for passive tumor-targeting via the EPR effect or active tumor-targeting through ligand-receptor interactions, resulting in the enhanced delivery and accumulation of PLGA-based DDSs into tumors.

CONCLUSION AND PERSPECTIVES

In this review article, we summarize the recent status of research on the application of PLGA-based DDSs in remotely triggered cancer therapy and the strategies for tumor imaging provided by PLGA-based DDSs, specifically focusing on employment of PLGA-based drug DDSs for external stimuli-triggered cancer therapy including photo-triggered, ultrasound-triggered, magnetic field-triggered, and radiofrequency-triggered cancer therapy. These drug delivery systems based on PLGA were shown to possess excellent biocompatibility and biodegradability, uniform particle size,

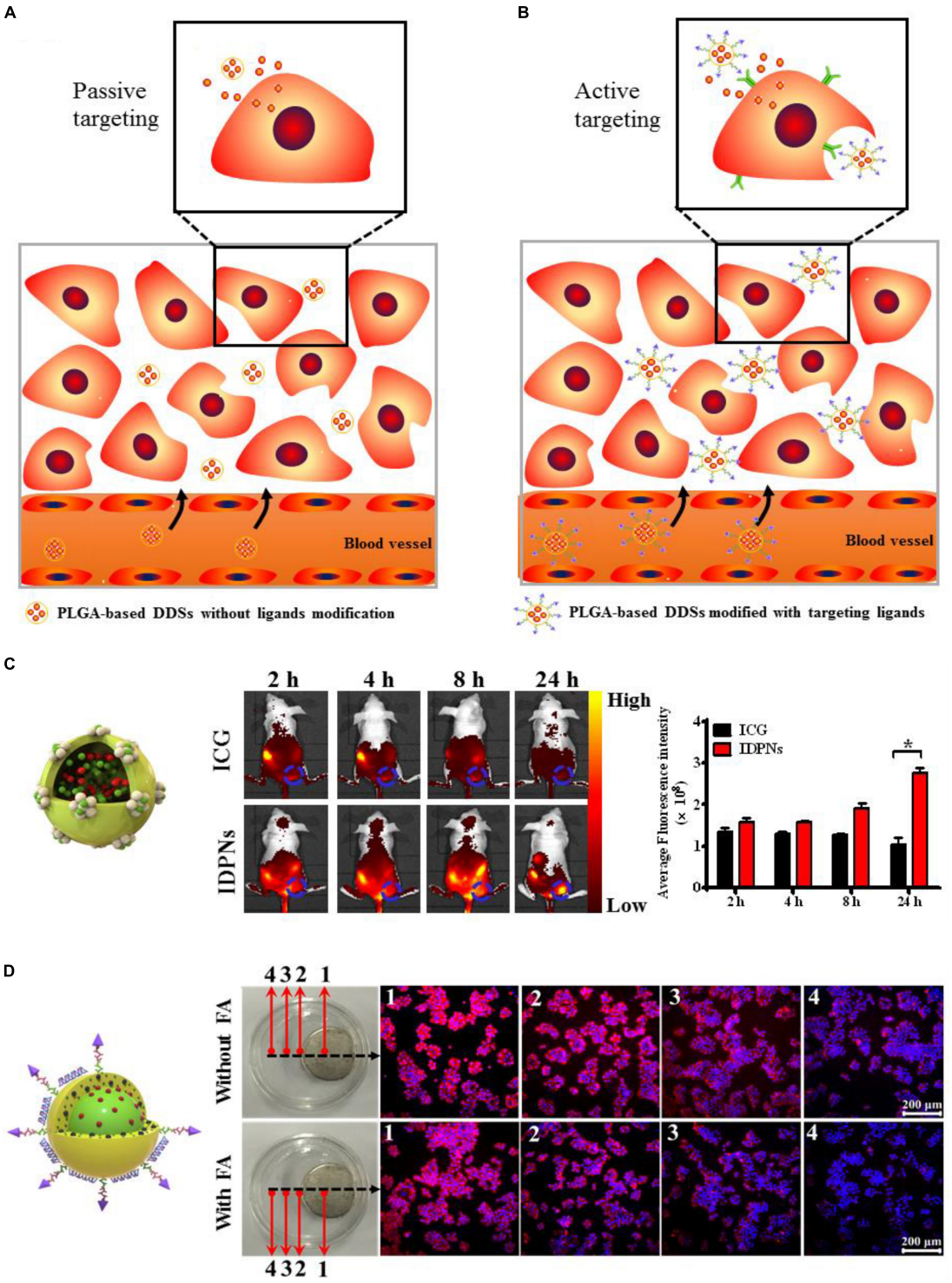

FIGURE 6 | (A) Schematic illustration of the passive tumor-targeting approach of the non-ligand-modified PLGA-based drug delivery systems (DDSs). **(B)** Schematic illustration of the active tumor-targeting approach of the targeting ligand-modified PLGA-based DDSs. **(C)** The whole body fluorescence imaging of EMT-6 tumor-bearing nude mice after intravenous administration of free ICG and IDPNs and the fluorescent quantitative analysis of the tumor sites. Adapted with permission from Shen et al. (2019). Copyright 2019, American Chemical Society. **(D)** Fluorescence images of HeLa cells treated with LDM-PLGA/PPF nanocomposites for 8 h under exposure to an external magnet with or without free folic acid (FA) pretreatment. Adapted with permission from Shen et al. (2017). Copyright 2017, Dove Medical Press.

on-demand drug release behavior and external stimuli-triggered cancer therapy approach, with the overall goal to enhance the antitumor efficacy by the enhancement of drug accumulation in tumor region and reduced side-effects of PLGA-based DDSs.

Although a variety of inorganic or organic materials have been utilized to fabricate the smart DDSs including inorganic nanoparticles, liposomes, polymer micelles, and polymer nanoparticles which can be used to co-deliver therapeutic agents and imaging agents for cancer theranostic applications, several problems are still needed to be solved, such as the complicated synthesis process, non-biodegradability, and uncontrollable drug release behavior of some DDSs. For instance, the inorganic nanomaterials such as gold and silica which have poor biodegradability are most likely to cause the long-term toxicity and raise the safety concerns. And other metal nanomaterials such as copper and silver also exhibit some cytotoxicity. Moreover, the uncontrollable drug release behavior of some DDSs is highly likely to cause the compromised anticancer effect. However, polymer nanoparticles based on poly(D,L-lactic-co-glycolic acid) (PLGA) have attracted considerable attention due to their unique physical and chemical properties, such as tunable particle size, uniform and regular morphology, large surface area, favorable pharmacokinetic property, excellent biocompatibility and biodegradability. More importantly, PLGA has been approved for the medical applications by the United States FDA, making them a favorable material to construct the nano- or micro-platforms for medical applications. Unlike the polymer nanoparticles based on poly(butylcyanoacrylates) (PBCA) of which the hydrolysis products are cytotoxic polycyanoacrylic acid and alcohol, the PLGA-based polymer nanoparticles can be degraded into the non-toxic lactic acid and glycolic acid, which can be eventually degraded into water and carbon dioxide. The biocompatible and biodegradable nature of PLGA makes them preferentially used to prepare the nano- or micro-platform. And the appropriate outer surface engineering (such as PEGylation, BSA modification and conjugation of targeting ligands) of PLGA-based DDSs can endow them with a prolonged blood circulation and enhanced accumulation in tumor sites.

Besides the hydrophilic therapeutic drugs and imaging agents, the hydrophobic therapeutic drugs and imaging agents can be encapsulated into the PLGA nanoparticles by using the water-in-oil-in-water (W/O/W) double emulsion method, which can improve the targeting and bioavailability of hydrophobic drugs and imaging agents, and eventually achieving the goal of cancer theranostics. However, it is not appropriate to design the extremely complicated nano- or micro-platform based on PLGA, since their unstability or potential uncertainty in physiological environment may lead to the unfavorable tumor inhibition effect. How to design and build a versatile but simple drug delivery systems with the effective antitumor activity remains a challenge for the new research. Employing external stimuli to trigger the cancer therapy is a promising antitumor approach, which can selectively and precisely eradicate the solid tumors and remotely control the drug release. However, the applications of remotely triggered cancer therapy remains limited. For example, the PDT efficacy will be weakened with the oxygen consumption during PDT (Wang et al., 2017). Developing a strategy that can afford sufficient oxygen for photosensitizers to consume and continuously generate ROS, has been proved to be a promising approach for enhancing PDT efficacy (Tang et al., 2018). In addition, the tissue penetration depth of the irradiation light is an essential issue for the photo-triggered therapeutic application. Employing the light in the NIR region may address this issue due to their advantages of real-time dosage adjustment, high spatiotemporal precision, and deep tissue penetration (Lin et al., 2016; Zhang P. et al., 2016; Shen et al., 2019).

Although the PLGA-based DDSs have been extensively studied, which can provide a safe and reliable approach for the tumor diagnosis and therapy in a minimally invasive manner, most of them are just preclinical studies, and still face many challenges. The property of low drug loading, high production costs, and inability to mass-produce of PLGA-based DDSs may limit their clinical applications. In order to apply the PLGA-based DDSs load with diagnostic and therapeutic agents to the clinic, the researchers should firstly overcome the obstacles of large-scale production of the nanoparticles. And it will provide a solid foundation for the application of PLGA-based DDSs in tumor therapy if more methods are provided to improve the drug loading capacity of PLGA-based DDSs. In addition, the cytotoxicity and immune response of all components of the PLGA-based DDSs in the body should be evaluated. The clinical transformation of PLGA-based DDSs can be further promoted with the continuous development of materials science and nanotechnology. And the great efforts have been made to improve their biocompatibility, stability, safety, drug loading capacity, and targeted delivery, which will endow PLGA-based DDSs with great potential in cancer diagnosis and treatment.

AUTHOR CONTRIBUTIONS

All authors listed have made a substantial, direct and intellectual contribution to the work, and approved it for publication.

FUNDING

This work was supported, in part or in whole, by the National Natural Science Foundation of China (81671821, U19A2006, 11772088, 31700811, 11802056, 31800780, 11972111, and 31900940), the China Postdoctoral Science Foundation (2018M640904, 2019T120831), the Sichuan Science and Technology Program (2019YJ0183 and 2019YJ0184), and the Fundamental Research Funds for the Central Universities (ZYGX2019J117).

REFERENCES

Alyautdin, R., Gothier, D., Petrov, V., Kharkevich, D., and Kreuter, J. (1995). Analgesic activity of the hexapeptide dalargin adsorbed on the surface of polysorbate 80-coated poly(butyl cyanoacrylate) nanoparticles. *Eur. J. Pharm. Biopharm.* 41, 44–48.

Bamrungsap, S., Zhao, Z., Chen, T., Wang, L., Li, C., Fu, T., et al. (2012). Nanotechnology in therapeutics: a focus on nanoparticles as a drug delivery system. *Nanomedicine* 7, 1253–1271. doi: 10.2217/nnm.12.87

Boussif, O., Lezoualc'h, F., Zanta, M. A., Mergny, M. D., Scherman, D., Demeneix, B., et al. (1995). A versatile vector for gene and oligonucleotide transfer into cells in culture and in vivo: polyethylenimine. *Proc. Natl. Acad. Sci. U.S.A.* 92, 7297–7301. doi: 10.1073/pnas.92.16.7297

Cai, Q., Wang, L., Deng, G., Liu, J., Chen, Q., and Chen, Z. (2016). Systemic delivery to central nervous system by engineered PLGA nanoparticles. *Am. J. Transl. Res.* 8, 749–764.

Chen, Q., Wang, C., Cheng, L., He, W., Cheng, Z., and Liu, Z. (2014). Protein modified upconversion nanoparticles for imaging-guided combined photothermal and photodynamic therapy. *Biomaterials* 35, 2915–2923. doi: 10.1016/j.biomaterials.2013.12.046

Chen, Z. Y., Wang, Y. X., Lin, Y., Zhang, J. S., Yang, F., Zhou, Q. L., et al. (2014). Advance of molecular imaging technology and targeted imaging agent in imaging and therapy. *Biomed. Res. Int.* 2014:819324. doi: 10.1155/2014/819324

Chen, Z., Zhao, P., Luo, Z., Zheng, M., Tian, H., Gong, P., et al. (2016). Cancer cell membrane-biomimetic nanoparticles for homologous-targeting dual-modal imaging and photothermal therapy. *ACS Nano* 10, 10049–10057. doi: 10.1021/acsnano.6b04695

Chumakova, O. V., Liopo, A. V., Andreev, V. G., Cicenaite, I., Evers, B. M., Chakrabarty, S., et al. (2008). Composition of PLGA and PEI/DNA nanoparticles improves ultrasound-mediated gene delivery in solid tumors in vivo. *Cancer Lett.* 261, 215–225. doi: 10.1016/j.canlet.2007.11.023

Danhier, F., Feron, O., and Preat, V. (2010). To exploit the tumor microenvironment: passive and active tumor targeting of nanocarriers for anti-cancer drug delivery. *J. Control. Release* 148, 135–146. doi: 10.1016/j.jconrel.2010.08.027

Das, M., Mohanty, C., and Sahoo, S. K. (2009). Ligand-based targeted therapy for cancer tissue. *Expert. Opin. Drug Deliv.* 6, 285–304. doi: 10.1517/17425240902780166

Deng, L., Li, L., Yang, H., Li, L., Zhao, F., Wu, C., et al. (2014). Development and optimization of doxorubicin loaded poly(lactic-co-glycolic acid) nanobubbles for drug delivery into HeLa cells. *J. Nanosci. Nanotechnol.* 14, 2947–2954. doi: 10.1166/jnn.2014.8633

Dong, Z. L., Gong, H., Gao, M., Zhu, W. W., Sun, X. Q., Feng, L. Z., et al. (2016). Polydopamine nanoparticles as a versatile molecular loading platform to enable imaging-guided cancer combination therapy. *Theranostics* 6, 1031–1042. doi: 10.7150/thno.14431

Dromain, C., de Baere, T., Elias, D., Kuoch, V., Ducreux, M., Boige, V., et al. (2002). Hepatic tumors treated with percutaneous radio-frequency ablation: CT and MR imaging follow-up. *Radiology* 223, 255–262. doi: 10.1148/radiol.2231010780

Edgington, L. E., Berger, A. B., Blum, G., Albrow, V. E., Paulick, M. G., Lineberry, N., et al. (2009). Noninvasive optical imaging of apoptosis by caspase-targeted activity-based probes. *Nat. Med.* 15, 967–973. doi: 10.1038/nm.1938

Eisenbrey, J. R., Burstein, O. M., Kambhampati, R., Forsberg, F., Liu, J. B., and Wheatley, M. A. (2010). Development and optimization of a doxorubicin loaded poly(lactic acid) contrast agent for ultrasound directed drug delivery. *J. Control. Release* 143, 38–44. doi: 10.1016/j.jconrel.2009.12.021

El-Gogary, R. I., Rubio, N., Wang, J. T., Al-Jamal, W. T., Bourgognon, M., Kafa, H., et al. (2014). Polyethylene glycol conjugated polymeric nanocapsules for targeted delivery of quercetin to folate-expressing cancer cells in vitro and in vivo. *ACS Nano* 8, 1384–1401. doi: 10.1021/nn405155b

Fang, K., Song, L., Gu, Z., Yang, F., Zhang, Y., and Gu, N. (2015). Magnetic field activated drug release system based on magnetic PLGA microspheres for chemo-thermal therapy. *Colloids Surf. B Biointerfaces* 136, 712–720. doi: 10.1016/j.colsurfb.2015.10.014

Farokhzad, O. C., and Langer, R. (2009). Impact of nanotechnology on drug delivery. *ACS Nano* 3, 16–20. doi: 10.1021/nn900002m

Farooq, M. A., Aquib, M., Farooq, A., Haleem Khan, D., Joelle Maviah, M. B., Sied Filli, M., et al. (2019). Recent progress in nanotechnology-based novel drug delivery systems in designing of cisplatin for cancer therapy: an overview. *Artif. Cells Nanomed. Biotechnol.* 47, 1674–1692. doi: 10.1080/21691401.2019.1604535

Ferrara, K. W. (2008). Driving delivery vehicles with ultrasound. *Adv. Drug Deliv. Rev.* 60, 1097–1102. doi: 10.1016/j.addr.2008.03.002

Gary, D. J., Puri, N., and Won, Y. Y. (2007). Polymer-based siRNA delivery: perspectives on the fundamental and phenomenological distinctions from polymer-based DNA delivery. *J. Control. Release* 121, 64–73. doi: 10.1016/j.jconrel.2007.05.021

Graf, N., Bielenberg, D. R., Kolishetti, N., Muus, C., Banyard, J., Farokhzad, O. C., et al. (2012). αVβ3 integrin-targeted PLGA-PEG nanoparticles for enhanced anti-tumor efficacy of a Pt(IV) prodrug. *ACS Nano* 6, 4530–4539. doi: 10.1021/nn301148e

Greish, K. (2010). Enhanced permeability and retention (EPR) effect for anticancer nanomedicine drug targeting. *Methods Mol. Biol.* 624, 25–37. doi: 10.1007/978-1-60761-609-2_3

Gu, W., Zhang, Q., Zhang, T., Li, Y., Xiang, J., Peng, R., et al. (2016). Hybrid polymeric nano-capsules loaded with gold nanoclusters and indocyanine green for dual-modal imaging and photothermal therapy. *J. Mater. Chem. B* 4, 910–919. doi: 10.1039/c5tb01619c

Hamori, M., Shimizu, Y., Yoshida, K., Fukushima, K., Sugioka, N., Nishimura, A., et al. (2015). Preparation of methacrylic acid copolymer S nano-fibers using a solvent-based electrospinning method and their application in pharmaceutical formulations. *Chem. Pharm. Bull.* 63, 81–87. doi: 10.1248/cpb.c14-00563

Hao, Y., Zhang, B., Zheng, C., Ji, R., Ren, X., Guo, F., et al. (2015). The tumor-targeting core-shell structured DTX-loaded PLGA@Au nanoparticles for chemo-photothermal therapy and X-ray imaging. *J. Control. Release* 220(Pt A), 545–555. doi: 10.1016/j.jconrel.2015.11.016

Hernot, S., and Klibanov, A. L. (2008). Microbubbles in ultrasound-triggered drug and gene delivery. *Adv. Drug Deliv. Rev.* 60, 1153–1166. doi: 10.1016/j.addr.2008.03.005

Heynick, L. N., Johnston, S. A., and Mason, P. A. (2003). Radio frequency electromagnetic fields: cancer, mutagenesis, and genotoxicity. *Bioelectromagnet. Suppl.* 6, S74–S100. doi: 10.1002/bem.10162

Hu, C. M. J., and Zhang, L. F. (2012). Nanoparticle-based combination therapy toward overcoming drug resistance in cancer. *Biochem. Pharmacol.* 83, 1104–1111. doi: 10.1016/j.bcp.2012.01.008

Huber, P. E., and Pfisterer, P. (2000). In vitro and in vivo transfection of plasmid DNA in the Dunning prostate tumor R3327-AT1 is enhanced by focused ultrasound. *Gene Ther.* 7, 1516–1525. doi: 10.1038/sj.gt.3301242

Issels, R. D. (2008). Hyperthermia adds to chemotherapy. *Eur. J. Cancer* 44, 2546–2554. doi: 10.1016/j.ejca.2008.07.038

Jaber, J., and Mohsen, E. (2013). Synthesis of Fe3O4@silica/poly(N-isopropylacrylamide) as a novel thermo-responsive system for controlled release of H3PMo12O40 nano drug in AC magnetic field. *Colloids Surf. B Biointerfaces* 102, 265–272. doi: 10.1016/j.colsurfb.2012.08.024

James, M. L., and Gambhir, S. S. (2012). A molecular imaging primer: modalities, imaging agents, and applications. *Physiol. Rev.* 92, 897–965. doi: 10.1152/physrev.00049.2010

Jang, B., Park, J. Y., Tung, C. H., Kim, I. H., and Choi, Y. (2011). Gold nanorod-photosensitizer complex for near-infrared fluorescence imaging and photodynamic/photothermal therapy in vivo. *ACS Nano* 5, 1086–1094. doi: 10.1021/nn102722z

Jia, Y., Yuan, M., Yuan, H., Huang, X., Sui, X., Cui, X., et al. (2012). Co-encapsulation of magnetic Fe3O4 nanoparticles and doxorubicin into biodegradable PLGA nanocarriers for intratumoral drug delivery. *Int. J. Nanomed.* 7, 1697–1708. doi: 10.2147/IJN.S28629

Johannsen, M., Gneveckow, U., Thiesen, B., Taymoorian, K., Cho, C. H., Waldofner, N., et al. (2007). Thermotherapy of prostate cancer using magnetic nanoparticles: feasibility, imaging, and three-dimensional temperature distribution. *Eur. Urol.* 52, 1653–1661. doi: 10.1016/j.eururo.2006.11.023

Kennedy, J. E. (2005). High-intensity focused ultrasound in the treatment of solid tumours. *Nat. Rev. Cancer* 5, 321–327. doi: 10.1038/nrc1591

Kim, K. T., Lee, J. Y., Kim, D. D., Yoon, I. S., and Cho, H. J. (2019). Recent Progress in the Development of Poly(lactic-co-glycolic acid)-based

nanostructures for cancer imaging and therapy. *Pharmaceutics* 11:E280, doi: 10.3390/pharmaceutics11060280

Kirchherr, A. K., Briel, A., and Mader, K. (2009). Stabilization of indocyanine green by encapsulation within micellar systems. *Mol. Pharm.* 6, 480–491. doi: 10.1021/mp8001649

Kruse, D. E., Stephens, D. N., Lindfors, H. A., Ingham, E. S., Paoli, E. E., and Ferrara, K. W. (2011). A radio-frequency coupling network for heating of citrate-coated gold nanoparticles for cancer therapy: design and analysis. *IEEE Trans. Biomed. Eng.* 58, 2002–2012. doi: 10.1109/TBME.2011.2124460

Larina, I. V., Evers, B. M., Ashitkov, T. V., Bartels, C., Larin, K. V., and Esenaliev, R. O. (2005a). Enhancement of drug delivery in tumors by using interaction of nanoparticles with ultrasound radiation. *Technol. Cancer Res. Treat.* 4, 217–226. doi: 10.1177/153303460500400211

Larina, I. V., Evers, B. M., and Esenaliev, R. O. (2005b). Optimal drug and gene delivery in cancer cells by ultrasound-induced cavitation. *Anticancer Res.* 25, 149–156.

Lee, D. J., Park, G. Y., Oh, K. T., Oh, N. M., Kwag, D. S., Youn, Y. S., et al. (2012). Multifunctional poly (lactide-co-glycolide) nanoparticles for luminescence/magnetic resonance imaging and photodynamic therapy. *Int. J. Pharm.* 434, 257–263. doi: 10.1016/j.ijpharm.2012.05.068

Li, F. Y., Yang, H., Bie, N. N., Xu, Q. B., Yong, T. Y., Wang, Q., et al. (2017). Zwitterionic Temperature/Redox-Sensitive Nanogels for Near-Infrared Light-Triggered SYNERGISTIC THERMO-CHEMOTHERAPY. *ACS Appl. Mater. Interfaces* 9, 23564–23573. doi: 10.1021/acsami.7b08047

Li, J., Chaudhary, A., Chmura, S. J., Pelizzari, C., Rajh, T., Wietholt, C., et al. (2010). A novel functional CT contrast agent for molecular imaging of cancer. *Phys. Med. Biol.* 55, 4389–4397. doi: 10.1088/0031-9155/55/15/013

Li, J., Zheng, L., Cai, H., Sun, W., Shen, M., Zhang, G., et al. (2013). Polyethyleneimine-mediated synthesis of folic acid-targeted iron oxide nanoparticles for in vivo tumor MR imaging. *Biomaterials* 34, 8382–8392. doi: 10.1016/j.biomaterials.2013.07.070

Li, T., Shen, X., Geng, Y., Chen, Z., Li, L., Li, S., et al. (2016). Folate-functionalized magnetic-mesoporous silica nanoparticles for drug/gene codelivery to potentiate the antitumor efficacy. *ACS Appl. Mater. Interfaces* 8, 13748–13758. doi: 10.1021/acsami.6b02963

Lim, E. K., Jang, E., Lee, K., Haam, S., and Huh, Y. M. (2013). Delivery of cancer therapeutics using nanotechnology. *Pharmaceutics* 5, 294–317. doi: 10.3390/pharmaceutics5020294

Lin, J., Chen, X., and Huang, P. (2016). Graphene-based nanomaterials for bioimaging. *Adv. Drug Deliv. Rev.* 105(Pt B), 242–254. doi: 10.1016/j.addr.2016.05.013

Luo, L., Zhu, C., Yin, H., Jiang, M., Zhang, J., Qin, B., et al. (2018). Laser immunotherapy in combination with Perdurable PD-1 blocking for the treatment of metastatic tumors. *ACS Nano* 12, 7647–7662. doi: 10.1021/acsnano.8b00204

Malinovskaya, Y., Melnikov, P., Baklaushev, V., Gabashvili, A., Osipova, N., Mantrov, S., et al. (2017). Delivery of doxorubicin-loaded PLGA nanoparticles into U87 human glioblastoma cells. *Int. J. Pharm.* 524, 77–90. doi: 10.1016/j.ijpharm.2017.03.049

Manthe, R. L., Foy, S. P., Krishnamurthy, N., Sharma, B., and Labhasetwar, V. (2010). Tumor ablation and nanotechnology. *Mol. Pharm.* 7, 1880–1898. doi: 10.1021/mp1001944

Markovic, Z. M., Harhaji-Trajkovic, L. M., Todorovic-Markovic, B. M., Kepic, D. P., Arsikin, K. M., Jovanovic, S. P., et al. (2011). In vitro comparison of the photothermal anticancer activity of graphene nanoparticles and carbon nanotubes. *Biomaterials* 32, 1121–1129. doi: 10.1016/j.biomaterials.2010.10.030

Martins, C., Sousa, F., Araujo, F., and Sarmento, B. (2018). Functionalizing PLGA and PLGA derivatives for drug delivery and tissue regeneration applications. *Adv. Healthc. Mater.* 7:1701035. doi: 10.1002/adhm.201701035

Master, A., Livingston, M., and Sen Gupta, A. (2013). Photodynamic nanomedicine in the treatment of solid tumors: perspectives and challenges. *J. Control. Release* 168, 88–102. doi: 10.1016/j.jconrel.2013.02.020

Mc Carthy, D. J., Malhotra, M., O'Mahony, A. M., Cryan, J. F., and O'Driscoll, C. M. (2015). Nanoparticles and the blood-brain barrier: advancing from in-vitro models towards therapeutic significance. *Pharm. Res.* 32, 1161–1185. doi: 10.1007/s11095-014-1545-6

Menon, J. U., Jadeja, P., Tambe, P., Vu, K., Yuan, B., and Nguyen, K. T. (2013). Nanomaterials for photo-based diagnostic and therapeutic applications. *Theranostics* 3, 152–166. doi: 10.7150/thno.5327

Miao, Y., Ni, Y., Mulier, S., Yu, J., De Wever, I., Penninckx, F., et al. (2000). Treatment of VX2 liver tumor in rabbits with "wet" electrode mediated radiofrequency ablation. *Eur. Radiol.* 10, 188–194. doi: 10.1007/s003300050031

Mohanty, C., Das, M., Kanwar, J. R., and Sahoo, S. K. (2011). Receptor mediated tumor targeting: an emerging approach for cancer therapy. *Curr. Drug Deliv.* 8, 45–58. doi: 10.2174/156720111793663606

Niu, C., Wang, Z., Lu, G., Krupka, T. M., Sun, Y., You, Y., et al. (2013). Doxorubicin loaded superparamagnetic PLGA-iron oxide multifunctional microbubbles for dual-mode US/MR imaging and therapy of metastasis in lymph nodes. *Biomaterials* 34, 2307–2317. doi: 10.1016/j.biomaterials.2012.12.003

Orsi, F., Arnone, P., Chen, W., and Zhang, L. (2010). High intensity focused ultrasound ablation: a new therapeutic option for solid tumors. *J. Cancer Res. Ther.* 6, 414–420. doi: 10.4103/0973-1482.77064

Owens, S. L. (1996). Indocyanine green angiography. *Br. J. Ophthalmol.* 80, 263–266. doi: 10.1136/bjo.80.3.263

Parhi, P., Mohanty, C., and Sahoo, S. K. (2012). Nanotechnology-based combinational drug delivery: an emerging approach for cancer therapy. *Drug Discov. Today* 17, 1044–1052. doi: 10.1016/j.drudis.2012.05.010

Park, J. H., Lee, J. Y., Termsarasab, U., Yoon, I. S., Ko, S. H., Shim, J. S., et al. (2014). Development of poly(lactic-co-glycolic) acid nanoparticles-embedded hyaluronic acid-ceramide-based nanostructure for tumor-targeted drug delivery. *Int. J. Pharm.* 473, 426–433. doi: 10.1016/j.ijpharm.2014.07.038

Pitt, W. G., Husseini, G. A., and Staples, B. J. (2004). Ultrasonic drug delivery–a general review. *Expert Opin. Drug Deliv.* 1, 37–56. doi: 10.1517/17425247.1.1.37

Rai, P., Mallidi, S., Zheng, X., Rahmanzadeh, R., Mir, Y., Elrington, S., et al. (2010). Development and applications of photo-triggered theranostic agents. *Adv. Drug Deliv. Rev.* 62, 1094–1124. doi: 10.1016/j.addr.2010.09.002

Ramimoghadam, D., Bagheri, S., and Abd Hamid, S. B. (2015). Stable monodisperse nanomagnetic colloidal suspensions: an overview. *Colloids Surf. B Biointerfaces* 133, 388–411. doi: 10.1016/j.colsurfb.2015.02.003

Rezvantalab, S., Drude, N. I., Moraveji, M. K., Guvener, N., Koons, E. K., Shi, Y., et al. (2018). PLGA-Based nanoparticles in cancer treatment. *Front. Pharmacol.* 9:1260. doi: 10.3389/fphar.2018.01260

Ricci-Junior, E., and Marchetti, J. M. (2006). Zinc(II) phthalocyanine loaded PLGA nanoparticles for photodynamic therapy use. *Int. J. Pharm.* 310, 187–195. doi: 10.1016/j.ijpharm.2005.10.048

Robinson, J. T., Welsher, K., Tabakman, S. M., Sherlock, S. P., Wang, H., Luong, R., et al. (2010). High performance in vivo near-IR ((1 mum) imaging and photothermal cancer therapy with carbon nanotubes. *Nano Res.* 3, 779–793. doi: 10.1007/s12274-010-0045-1

Rojnik, M., Kocbek, P., Moret, F., Compagnin, C., Celotti, L., Bovis, M. J., et al. (2012). In vitro and in vivo characterization of temoporfin-loaded PEGylated PLGA nanoparticles for use in photodynamic therapy. *Nanomedicine* 7, 663–677. doi: 10.2217/nnm.11.130

Rotman, M., Snoeks, T. J., and van der Weerd, L. (2011). Pre-clinical optical imaging and MRI for drug development in Alzheimer's disease. *Drug Discov. Today Technol.* 8, e117–e125. doi: 10.1016/j.ddtec.2011.11.005

Ryan, K. L., D'Andrea, J. A., Jauchem, J. R., and Mason, P. A. (2000). Radio frequency radiation of millimeter wave length: potential occupational safety issues relating to surface heating. *Health Phys.* 78, 170–181. doi: 10.1097/00004032-200002000-00006

Schleich, N., Sibret, P., Danhier, P., Ucakar, B., Laurent, S., Muller, R. N., et al. (2013). Dual anticancer drug/superparamagnetic iron oxide-loaded PLGA-based nanoparticles for cancer therapy and magnetic resonance imaging. *Int. J. Pharm.* 447, 94–101. doi: 10.1016/j.ijpharm.2013.02.042

Schneider, T., Becker, A., Ringe, K., Reinhold, A., Firsching, R., and Sabel, B. A. (2008). Brain tumor therapy by combined vaccination and antisense oligonucleotide delivery with nanoparticles. *J. Neuroimmunol.* 195, 21–27. doi: 10.1016/j.jneuroim.2007.12.005

Shen, J. M., Guan, X. M., Liu, X. Y., Lan, J. F., Cheng, T., and Zhang, H. X. (2012). Luminescent/magnetic hybrid nanoparticles with folate-conjugated peptide

composites for tumor-targeted drug delivery. *Bioconjug. Chem.* 23, 1010–1021. doi: 10.1021/bc300008k

Shen, S., Wang, S., Zheng, R., Zhu, X., Jiang, X., Fu, D., et al. (2015). Magnetic nanoparticle clusters for photothermal therapy with near-infrared irradiation. *Biomaterials* 39, 67–74. doi: 10.1016/j.biomaterials.2014.10.064

Shen, X., Li, T., Chen, Z., Geng, Y., Xie, X., Li, S., et al. (2017). Luminescent/magnetic PLGA-based hybrid nanocomposites: a smart nanocarrier system for targeted codelivery and dual-modality imaging in cancer theranostics. *Int. J. Nanomed.* 12, 4299–4322. doi: 10.2147/IJN.S136766

Shen, X., Li, T., Chen, Z., Xie, X., Zhang, H., Feng, Y., et al. (2019). NIR-Light-triggered anticancer strategy for dual-modality imaging-guided combination therapy via a bioinspired hybrid PLGA nanoplatform. *Mol. Pharm.* 16, 1367–1384. doi: 10.1021/acs.molpharmaceut.8b01321

Shenoi, M. M., Iltis, I., Choi, J., Koonce, N. A., Metzger, G. J., Griffin, R. J., et al. (2013). Nanoparticle delivered vascular disrupting agents (VDAs): use of TNF-Alpha conjugated gold nanoparticles for multimodal cancer therapy. *Mol. Pharm.* 10, 1683–1694. doi: 10.1021/mp300505w

Shi, J., Votruba, A. R., Farokhzad, O. C., and Langer, R. (2010). Nanotechnology in drug delivery and tissue engineering: from discovery to applications. *Nano Lett.* 10, 3223–3230. doi: 10.1021/nl102184c

Shi, S., Shi, K., Tan, L. W., Qu, Y., Shen, G. B., Chu, B. Y., et al. (2014). The use of cationic MPEG-PCL-g-PEI micelles for co-delivery of msurvivin T34A gene and doxorubicin. *Biomaterials* 35, 4536–4547. doi: 10.1016/j.biomaterials.2014.02.010

Song, J., Yang, X., Jacobson, O., Lin, L., Huang, P., Niu, G., et al. (2015). Sequential drug release and enhanced photothermal and photoacoustic effect of hybrid reduced graphene oxide-loaded ultrasmall gold Nanorod vesicles for cancer therapy. *ACS Nano* 9, 9199–9209. doi: 10.1021/acsnano.5b03804

Song, L. Z., Zhao, N., and Xu, F. J. (2017). Hydroxyl-rich polycation brushed multifunctional rare-earth-gold core-shell nanorods for versatile therapy platforms. *Adv. Funct. Mater.* 27:1701255. doi: 10.1002/adfm.201701255

Su, S., Tian, Y., Li, Y., Ding, Y., Ji, T., Wu, M., et al. (2015). "Triple-punch" strategy for triple negative breast cancer therapy with minimized drug dosage and improved antitumor efficacy. *ACS Nano* 9, 1367–1378. doi: 10.1021/nn505729m

Sun, Y., Zheng, Y., Ran, H., Zhou, Y., Shen, H., Chen, Y., et al. (2012). Superparamagnetic PLGA-iron oxide microcapsules for dual-modality US/MR imaging and high intensity focused US breast cancer ablation. *Biomaterials* 33, 5854–5864. doi: 10.1016/j.biomaterials.2012.04.062

Swider, E., Koshkina, O., Tel, J., Cruz, L. J., de Vries, I. J. M., and Srinivas, M. (2018). Customizing poly(lactic-co-glycolic acid) particles for biomedical applications. *Acta Biomater.* 73, 38–51. doi: 10.1016/j.actbio.2018.04.006

Tang, W., Yang, Z., Wang, S., Wang, Z., Song, J., Yu, G., et al. (2018). Organic semiconducting photoacoustic nanodroplets for laser-activatable ultrasound imaging and combinational cancer therapy. *ACS Nano* 12, 2610–2622. doi: 10.1021/acsnano.7b08628

Topete, A., Alatorre-Meda, M., Iglesias, P., Villar-Alvarez, E. M., Barbosa, S., Costoya, J. A., et al. (2014). Fluorescent drug-loaded, polymeric-based, branched gold nanoshells for localized multimodal therapy and imaging of tumoral cells. *ACS Nano* 8, 2725–2738. doi: 10.1021/nn406425h

Torchilin, V. (2011). Tumor delivery of macromolecular drugs based on the EPR effect. *Adv. Drug Deliv. Rev.* 63, 131–135. doi: 10.1016/j.addr.2010.03.011

Torchilin, V. P. (2000). Drug targeting. *Eur. J. Pharm. Sci.* 11, S81–S91. doi: 10.1016/S0928-0987(00)00166-4

Torres-Lugo, M., and Rinaldi, C. (2013). Thermal potentiation of chemotherapy by magnetic nanoparticles. *Nanomedicine* 8, 1689–1707. doi: 10.2217/nnm.13.146

Venugopal, V., Krishnan, S., Palanimuthu, V. R., Sankarankutty, S., Kalaimani, J. K., Karupiah, S., et al. (2018). Anti-EGFR anchored paclitaxel loaded PLGA nanoparticles for the treatment of triple negative breast cancer. In-vitro and in-vivo anticancer activities. *PLoS One* 13:e0206109. doi: 10.1371/journal.pone.0206109

Wang, H., Wang, S., Liao, Z., Zhao, P., Su, W., Niu, R., et al. (2012). Folate-targeting magnetic core-shell nanocarriers for selective drug release and imaging. *Int. J. Pharm.* 430, 342–349. doi: 10.1016/j.ijpharm.2012.04.009

Wang, Y., Xie, Y., Li, J., Peng, Z. H., Sheinin, Y., Zhou, J., et al. (2017). Tumor-penetrating nanoparticles for enhanced anticancer activity of combined photodynamic and Hypoxia-activated therapy. *ACS Nano* 11, 2227–2238. doi: 10.1021/acsnano.6b08731

Wang, Z., Li, S., Zhang, M., Ma, Y., Liu, Y., Gao, W., et al. (2017). Laser-Triggered Small Interfering RNA releasing gold Nanoshells against heat shock protein for sensitized Photothermal therapy. *Adv. Sci.* 4:1600327. doi: 10.1002/advs.201600327

Wu, C., Li, D., Wang, L., Guan, X., Tian, Y., Yang, H., et al. (2017). Single wavelength light-mediated, synergistic bimodal cancer photoablation and amplified photothermal performance by graphene/gold nanostar/photosensitizer theranostics. *Acta Biomater.* 53, 631–642. doi: 10.1016/j.actbio.2017.01.078

Wu, F., Wang, Z. B., Chen, W. Z., Wang, W., Gui, Y., Zhang, M., et al. (2004). Extracorporeal high intensity focused ultrasound ablation in the treatment of 1038 patients with solid carcinomas in China: an overview. *Ultrason Sonochem.* 11, 149–154. doi: 10.1016/j.ultsonch.2004.01.011

Wu, Y. R., Sefah, K., Liu, H. P., Wang, R. W., and Tan, W. H. (2010). DNA aptamer-micelle as an efficient detection/delivery vehicle toward cancer cells. *Proc. Natl. Acad. Sci. U.S.A.* 107, 5–10. doi: 10.1073/pnas.0909611107

Xu, Y., Karmakar, A., Heberlein, W. E., Mustafa, T., Biris, A. R., and Biris, A. S. (2012). Multifunctional magnetic nanoparticles for synergistic enhancement of cancer treatment by combinatorial radio frequency thermolysis and drug delivery. *Adv. Healthc. Mater.* 1, 493–501. doi: 10.1002/adhm.201200079

Yan, F., Duan, W., Li, Y., Wu, H., Zhou, Y., Pan, M., et al. (2016a). NIR-Laser-controlled drug release from DOX/IR-780-Loaded temperature-sensitive-Liposomes for Chemo-Photothermal Synergistic tumor therapy. *Theranostics* 6, 2337–2351. doi: 10.7150/thno.14937

Yan, F., Wu, H., Liu, H., Deng, Z., Liu, H., Duan, W., et al. (2016b). Molecular imaging-guided photothermal/photodynamic therapy against tumor by iRGD-modified indocyanine green nanoparticles. *J. Control. Release* 224, 217–228. doi: 10.1016/j.jconrel.2015.12.050

Yang, H., Chen, Y., Chen, Z., Geng, Y., Xie, X., Shen, X., et al. (2017). Chemo-photodynamic combined gene therapy and dual-modal cancer imaging achieved by pH-responsive alginate/chitosan multilayer-modified magnetic mesoporous silica nanocomposites. *Biomater. Sci.* 5, 1001–1013. doi: 10.1039/c7bm00043j

Yang, H., Deng, L. W., Li, T. T., Shen, X., Yan, J., Zuo, L. M., et al. (2015). Multifunctional PLGA Nanobubbles as theranostic agents: combining doxorubicin and P-gp siRNA Co-delivery into human breast cancer cells and ultrasound cellular imaging. *J. Biomed. Nanotechnol.* 11, 2124–2136. doi: 10.1166/jbn.2015.2168

Yang, H., Shen, X., Yan, J., Xie, X. X., Chen, Z. Y., Li, T. T., et al. (2018). Charge-reversal-functionalized PLGA nanobubbles as theranostic agents for ultrasonic-imaging-guided combination therapy. *Biomater. Sci.* 6, 2426–2439. doi: 10.1039/c8bm00419f

Yang, H., Xu, M., Li, S., Shen, X., Li, T. T., Yan, J., et al. (2016). Chitosan hybrid nanoparticles as a theranostic platform for targeted doxorubicin/VEGF shRNA co-delivery and dual-modality fluorescence imaging. *RSC Adv.* 6, 29685–29696. doi: 10.1039/c6ra03843c

Yu, J., Ju, Y., Zhao, L., Chu, X., Yang, W., Tian, Y., et al. (2016). Multistimuli-regulated Photochemothermal cancer therapy remotely Controlled via Fe5C2 Nanoparticles. *ACS Nano* 10, 159–169. doi: 10.1021/acsnano.5b04706

Yun, H., Liu, X., Paik, T., Palanisamy, D., Kim, J., Vogel, W. D., et al. (2014). Size- and composition-dependent radio frequency magnetic permeability of iron oxide nanocrystals. *ACS Nano* 8, 12323–12337. doi: 10.1021/nn504711g

Zarnitsyn, V. G., and Prausnitz, M. R. (2004). Physical parameters influencing optimization of ultrasound-mediated DNA transfection. *Ultrasound Med. Biol.* 30, 527–538. doi: 10.1016/j.ultrasmedbio.2004.01.008

Zhang, K., Chen, H., Li, F., Wang, Q., Zheng, S., Xu, H., et al. (2014). A continuous tri-phase transition effect for HIFU-mediated intravenous drug delivery. *Biomaterials* 35, 5875–5885. doi: 10.1016/j.biomaterials.2014.03.043

Zhang, X., Zheng, Y., Wang, Z., Huang, S., Chen, Y., Jiang, W., et al. (2014). Methotrexate-loaded PLGA nanobubbles for ultrasound imaging and Synergistic Targeted therapy of residual tumor during HIFU ablation. *Biomaterials* 35, 5148–5161. doi: 10.1016/j.biomaterials.2014.02.036

Zhang, K., Li, P., Chen, H., Bo, X., Li, X., and Xu, H. (2016). Continuous cavitation designed for enhancing radiofrequency ablation via a special radiofrequency solidoid vaporization process. *ACS Nano* 10, 2549–2558. doi: 10.1021/acsnano.5b07486

Zhang, P., Hu, C., Ran, W., Meng, J., Yin, Q., and Li, Y. (2016). Recent progress in light-triggered nanotheranostics for cancer treatment. *Theranostics* 6, 948–968. doi: 10.7150/thno.15217

Zhao, X., Li, F., Li, Y. Y., Wang, H., Ren, H., Chen, J., et al. (2015). Co-delivery of HIF1 α siRNA and gemcitabine via biocompatible lipid-polymer hybrid nanoparticles for effective treatment of pancreatic cancer. *Biomaterials* 46, 13–25. doi: 10.1016/j.biomaterials.2014.12.028

Zheng, M., Yue, C., Ma, Y., Gong, P., Zhao, P., Zheng, C., et al. (2013). Single-step assembly of DOX/ICG loaded lipid–polymer nanoparticles for highly effective chemo-photothermal combination therapy. *ACS Nano* 7, 2056–2067. doi: 10.1021/nn400334y

Conflict of Interest: The authors declare that the research was conducted in the absence of any commercial or financial relationships that could be construed as a potential conflict of interest.

frontiers in Bioengineering and Biotechnology

ORIGINAL RESEARCH
published: 14 May 2020
doi: 10.3389/fbioe.2020.00451

Tagged Halloysite Nanotubes as a Carrier for Intercellular Delivery in Brain Microvascular Endothelium

Mahdi Yar Saleh†, Neela Prajapati†, Mark A. DeCoster and Yuri Lvov**

Institute for Micromanufacturing and Biomedical Engineering Program, Louisiana Tech University, Ruston, LA, United States

Neurological disorders that are characterized by unpredictable seizures affect people of all ages. We proposed the use of nanocarriers such as halloysite nanotubes to penetrate the blood–brain barrier and effectively deliver the payload over an extended time period. These 50-nm diameter tubes are a natural biocompatible nanomaterial available in large quantities. We proved a prolonged gradual drug delivery mechanism by the nanotube encapsulating rhodamine isothiocyanate and then ionomycin into brain microvascular endothelial cells (BMVECs). Through delayed diffusion, the nanotubes effectively delivered the drug to the primary BMVECs without killing them, by binding and penetration in time periods of 1 to 24 h.

Keywords: halloysite (HNT), brain delivery, endothelia cell, nanomaterial application, drug–drug interactions

OPEN ACCESS

Edited by:
Stefano Leporatti, Institute of Nanotechnology, Italian National Research Council, Italy

Reviewed by:
Marina Massaro, University of Palermo, Italy
Mel De Villiers, University of Wisconsin–Madison, United States
Xiangyang Shi, Donghua University, China

****Correspondence:***
Mark A. DeCoster
decoster@latech.edu
Yuri Lvov
ylvov@latech.edu

† These authors have contributed equally to this work

Specialty section:
This article was submitted to Nanobiotechnology, a section of the journal Frontiers in Bioengineering and Biotechnology

Received: *13 March 2020*
Accepted: *20 April 2020*
Published: *14 May 2020*

Citation:
Saleh MY, Prajapati N, DeCoster MA and Lvov Y (2020) Tagged Halloysite Nanotubes as a Carrier for Intercellular Delivery in Brain Microvascular Endothelium. Front. Bioeng. Biotechnol. 8:451. doi: 10.3389/fbioe.2020.00451

INTRODUCTION

Brain diseases, such as central nervous system disorders, are of the most poorly treated diseases in today's world. Occurring frequently in people of all ages, impacting their way of life, and increasing the chances of premature death. Epilepsy is a common example of a neurological disorder that is characterized by unpredictable seizures that results in unusual behavior, such as involuntary movements. Around the globe today, an estimated 50 million people are diagnosed with this disorder causing it to be one of the most common brain diseases. Thus, if the disease could be treated properly through various methods, such as nanotechnology, up to 70% of diagnosed patients could be cured (Silva, 2008; Bennewitz and Saltzman, 2009; Pehlivan, 2013; World Health Organization [WHO], 2020). Current anti-seizure medication has a wide range of side effects which include dizziness, tiredness, and trouble speaking. Utilizing nanosized carriers is an effective route to determine targeted and slow release drug delivery techniques to minimize these side effects and provide an overall more effective treatment. Using less than 50 nm capsules promises better penetration into cells, especially if one uses tubule drug carriers which have improved efficiency in passing cell membrane as defined by the smallest cross-section size. Gamma-amino-*n*-butyric acid (GABA), glutamic acid, and dopamine are important brain neurotransmitters for epilepsy research, and their nano-formulation for intracellular sustained delivery is promising for higher efficiency.

Brain microvascular endothelial cells (BMVECs) are the key cells in the blood–brain barrier, which is the multicellular membrane between the brain's blood vessels and a brain tissue. BMVECs constitutes the tight junction proteins which prevent the entry of pathogens and other toxic substances into the brain, but it also prevents most potential drugs against neurological and mental disorders to cross the barrier and readily reach into the brain tissue (Mahringer et al., 2013; Lvov et al., 2016). We exploit halloysite clay nanotubes (HNT) to penetrate the endothelial cells and effectively deliver the payload over an extended time. Our hypothesis is based on the conception of "nano-torpedo" when rod-like tubule hollow clay capsules bind or penetrate through

cell membrane exploiting its very small, 50-nm diameter cross-section and deliver the drug load in the interior.

Halloysite nanotubes are formed by 10–15 revolutions of 0.7 nm thick kaolin aluminosilicate sheets and have diameters ranging between 50 and 60 nm, lumen diameters of 12–15 nm, and lengths within 500–900 nm (**Figure 1**) (Liu et al., 2014; Lvov et al., 2016). It is an environmentally friendly, natural, and cheap tubule nanomaterial available in large quantities. Halloysites outer surface is composed of SiO_2, and the tube's interior is composed of Al_2O_3, which are oppositely (negative/positive) charged in the pH range of 3–9. The structure of halloysite in **Figure 1** shows how the payload can be loaded inside the positively charged lumen of halloysite, which is especially efficient for spontaneous adsorption of negatively charged drug molecules. Based on geometrical sizes of halloysite, one may conclude the maximal volume load inside the tubes of 10–12 vol.%, which may reach for organic drugs ca 15 wt.%. This is a typical drug load given in many publications, as summarized in Santos et al. (2019). Higher drug loading means that drug molecules are adsorbed on the tube external surface, which may change the formulation properties that are observed through zeta-potential and colloidal stability. Zeta potential is an important though indirect indication of the innermost drug loading. Thus, inner adsorption of negative molecules usually increases the electrical potential magnitude from ca. −30 mV in pristine to minus 45–50 mV in loaded nanotubes, simultaneously improving the sample colloidal stability (Liu et al., 2019). Drugs that were used are khellin, oxytetracycline, gentamicin, ciprofloxacin, vancomycin, atorvastatin, metronidazole, dexamethasone, doxorubicin, furosemide, nifedipine, curcumin, resveratrol, povidone iodine, amoxicillin, brilliant green, chlorhexidine, and DNA and viral genes were also successfully loaded in halloysite (Santos et al., 2019).

Halloysite is a biocompatible material with low toxicity assessments (Vergaro et al., 2010; Dzamukova et al., 2015b; Kruchkova et al., 2016; Hu et al., 2017; Kamalieva et al., 2018; Mehdia et al., 2018; Wang et al., 2018; Fakhrullina et al., 2019; Zhao et al., 2019). Many researchers reached a consensus that these clay nanotubes are safe up to a 10 mg/mL formation, which is less toxic than common table salt (Vergaro et al., 2010). This was tested on several *in vitro* and *in vivo* systems: cells lines, microworms, infusoria, fishes, mice, and rats (Santos et al., 2019). The only minor toxic effect was found with high oral halloysite consumption. When acidic clay decomposes, the stomach increased Al^{3+}accumulation (Kamalieva et al., 2018). The mice that were orally fed with low nanoclay doses (5 mg/kg mice weight, which corresponds to 3 g of halloysite daily consumption for adult human for 1 month) have shown no oxidative stress or other toxicity signs, and even demonstrated higher growth rates.

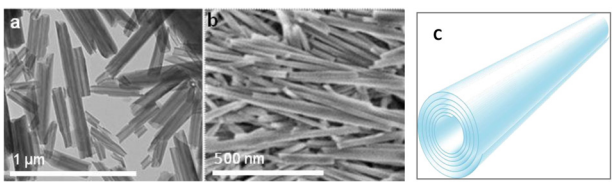

FIGURE 1 | A TEM and SEM image of halloysite nanotubes **(a,b)**. A scheme of rolled clay **(c)**.

Clay nanotube loaded with drugs will penetrate cells more efficiently than spherical particles of the same mass (Dzamukova et al., 2015a; Wang et al., 2018). This approach allowed for an effective halloysite delivery of doxorubicin and other anticancer drugs (Yang et al., 2016; Zhang et al., 2019). HNT/brilliant green formulations with intracellular delivery allowed for preferable elimination of human lung carcinoma cells (À549) as compared with hepatoma cells (Hep3b) due to different -intracellular penetration (Dzamukova et al., 2015a).

In this work, we studied halloysite nanotube penetration into primary rat BMVECs, which are the main cell type that prevent entry of drugs through the blood–brain barrier. We demonstrated with fluorescent rhodamine B isothiocyanate dye that halloysite binds on the cell, penetrates the cell interior, concentrates around the nuclei, and may deliver a drug load. Next, we developed a model for brain cell stimulation using halloysite loaded with ionomycin, a widely used Ca^{2+} ionophore (Morgan and Jacob, 1994; Kaushik et al., 2018; Long et al., 2018; Wu et al., 2018) to monitor calcium transport across membrane and to stimulate a response from brain cells. Ionomycin-HNT formulations resulted in intracellular delivery, which was monitored by Ca^{2+} changes in the cells, showing gradual and prolonged delivery of ionomycin into the brain endothelial cells. An outline in **Scheme 1** displays the progressive change in calcium signals throughout the stimulation, proving halloysite formulations have the potential as an efficient carrier for drugs or selected neurotransmitters (glutamate) targeted for brain disorders treatments.

MATERIALS AND METHODS

Halloysite Loading With Rhodamine Isothiocyanate

Halloysite samples were prepared by loading rhodamine B isothiocyanate (RITC) and ionomycin through stirring, centrifugation, and sonication at various ratios including 10 mg halloysite/1 mL DI water per 0.5, 1, and 2 mg of RITC. The solutions were then sonicated and vortexed for 1 min, then mixed on a stir plate for 24 h at room temperature. The mixture was washed once by centrifugation at 2500 RPM for 2.5 min and then dried at 70°C for 24 h. When loading ionomycin, 20 mg of pristine halloysite clay nanotubes were stirred with 1 mM ionomycin for 24 h. The mixture was then washed with sterile water by centrifugation 2500 RPM for 3 min one time. The solution was then freeze dried for 20 min and placed in a vacuum for 24 h to remove the excess solution. Samples were then characterized by the zeta potential analyzer, which displays the surface charge and thermogravimetric analysis, allowing us to calculate the loading percentage.

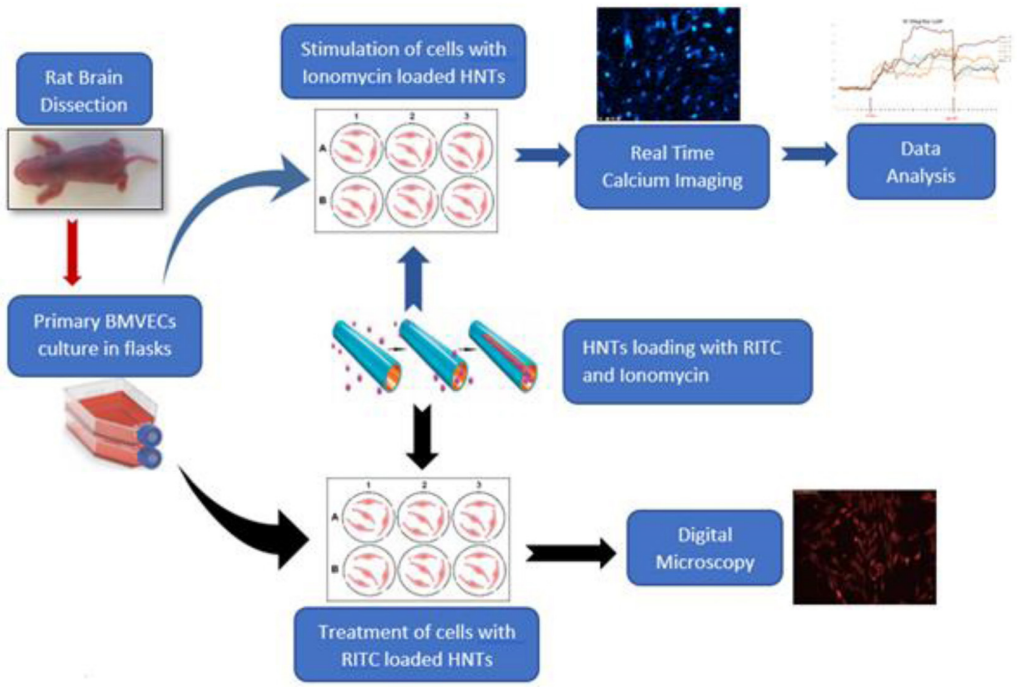

SCHEME 1 | Loading clay nanotubes with fluorescent rhodamine (RITC) and ionomycin and treating the endothelium cells with the loaded nanotubes. Ionomycin-HNT upper route with Ca^{2+} imaging monitoring and RITC – lower route accomplished with visualization.

Neurotransmitter Loading

This procedure is accomplished by taking 50 mg of etched or pristine halloysite with 50 mg of glutamic acid separately in 5 mL of DI water, creating a super saturated solution through sonication for 5 min and stirring for 24 h at room temperature. The last step is for the suspensions to dry in the oven for 24 h at 70°C. After loading the halloysite samples were characterized through zeta potential analyzer and thermogravimetric analysis to determine a surface charge and measure the percentage of material loaded.

Cell Culture

Primary brain microvascular endothelial cells (BMVECs) were obtained directly from the rat brain cortex. Rat pups, 1 or 2 days old were euthanized to obtain the rat brain cortex. Cortex obtained by dissection of the pup's skull is cleared out of meninges under the microscope. The cortical tissue thus obtained were then treated with trypsin and triturated, with the process repeated at least three times in order to break the brain tissue into cells. After each trituration, cells were incubated at room temperature under sterile conditions for about 10 min and supernatant was collected in a 15 mL tube. The collected supernatant was then centrifuged to obtain a pellet of mixed culture of brain cells. BMVECs were isolated from this primary culture by treating them with 5.5 μM of puromycin dihydrochloride to kill all other cell types except the endothelial cells as shown in **Figure 2A**. Endothelial cells are encoded with a puromycin *N*-acetyl transferase gene (PAC gene), which confer resistance to the action of puromycin (Thiel and Audus, 2001; Wang et al., 2012). Thus, isolated BMVECs were then cultured *in vitro* at 5% CO_2 and 37°C in rat endothelial growth medium (Sigma Aldrich). The cells were characterized by staining them against Von Willebrand Factor (VWF), **Figure 2B**, an essential blood clotting protein specific to endothelial cells (Mbagwu and Filgueira, 2020).

Treatment With Rhodamine Isothiocyanate (RITC) Loaded Halloysites

Brain microvascular endothelial cells between primary passages of 3 and 7 were used for the experiments. Cells were plated in 48 well cell culture plates at 10K per well density and treated with RITC loaded halloysite, halloysite alone (negative control) and RITC alone (positive control) at 50–70% confluency. Cells were treated with 10 μg/mL of halloysite alone (negative control) and 10 μg/mL of halloysite loaded with RITC [for all nanoclay samples loaded with different concentration of RITC (1:5 and 1:10)]. The concentration of RITC alone was chosen to correspond to the loaded halloysite formulations.

Brain Microvascular Endothelial Cells (BMVECs) Stimulation Using Ionomycin Loaded Halloysite

Primary BMVECs were plated at the density of 10K per well in 48 well plates. At the confluency of 70 to 80% each well-containing the cells were loaded with 500 μL of Fluo-3 AM loading solution, i.e., Lockes' solution with Fluo-3 AM dye (1:500) and pluronic

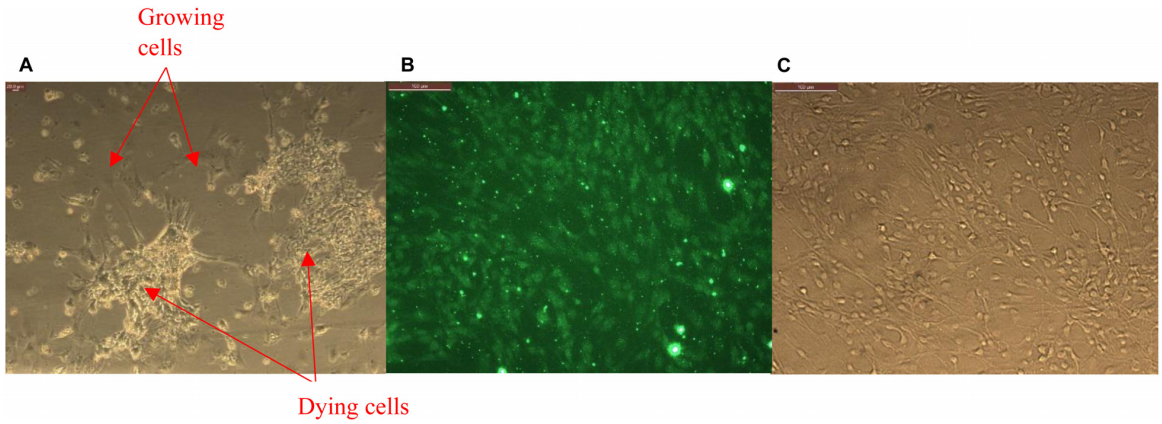

FIGURE 2 | (A) Primary glia treated with puromycin for isolation of brain microvascular endothelial cells (BMVECs) showing killing of all other cell types except the BMVECs. **(B)** Primary BMVECs characterized by staining against VWF using fluorescence microscopy, and **(C)** phase image of stained cells.

acid (1:1000) (Yamamoto et al., 2011). The cells were treated with this solution for 1 h at 37°C, in 5% CO_2 incubator and then – with 500 μL of recovery solution for 1 h. The recovered cells were then stimulated with halloysite loaded with ionomycin (10 and 50 μg/mL), halloysite alone (50 μg/mL), ATP 100 μM, and ionomycin 1 μM at different instances depending on the experiment. Real time intracellular calcium (Ca^{2+}) change due to ionomycin transport across the system was recorded by capturing images every 4 s with InCyt Im1 software on the imaging system. The images were then used for Ca^{2+} signal analysis, which utilizes change in fluorescence intensity as the function of time as a measure for quantifying calcium changes in cells.

RESULTS

Intracellular Rhodamine Isothiocyanate (RITC) Delivery With Clay Nanotubes

An observation of halloysite binding and penetration into the endothelial cells was visualized as red fluorescence concentrated within the cells, **Figure 3**. The addition of only RITC dye did not color the cells interior within 30 min of treatment; while the dye loaded halloysite bound or penetrated the cells and start releasing the dye inside the cells, coloring them red. Within a 4-h time frame RITC and RITC-HNT both showed cells with more fluorescence compared to the same samples in the 30 min exposure time. Furthermore, RITC-HNT formulations displayed greater fluorescence compared to RITC only, proving the dye delivery into the cells.

The timeframe of these images is 30 min after delivery of both samples (RITC and HNT + RITC) to the cells, with a concentration of 10 μg/mL for HNT + RITC and 2 μg/mL of RITC alone. The loading of RITC in HNTs was 20 wt.%, thus making the same amount of RITC added to the samples. The small bright dots found in the bottom images of **Figure 3E** are the aggregated halloysite tubes that contain RITC. HNT-RITC aggregation is displayed mostly along the cellular membrane and inside the endothelial cells as indicated by nuclear exclusion.

Therefore, halloysite nanotubes are highly capable of encapsulating, transporting, and slowly releasing the dye (or drugs as we will show with an example of ionomycin) over a few hours. It is important to note that we did not modify the surface of the halloysite with any type of polymer or silane coating. **Figure 3B** displays RITC alone added at the same concentration showing a much dimmer visualization of the cell's responsiveness to this non-encapsulated dye.

Results for the 24-h treatment were similar with more profound fluorescence in both conditions but RITC loaded halloysite delivered more dye into the cells at every time period as compared to just the dye alone, **Figure 4**. Images at a time point of 24 h displayed the nanotubes distribution more evenly over the cell interior, still contained within the cell body **Figure 4**. One could see that RITC-HNT concentrated in some smaller spots of ca 1 μm dimeter, which may be the nuclear surrounding, as it was found for MCF-7 cells treated with halloysite (Vergaro et al., 2010). Throughout the trials, we detected a nuclear exclusion, extended length of fluorescence, and that the tubes did not stress or kill the cells. The clay nanotubes are displayed as small dots in **Figure 4E** and are brighter than the dye spread inside the cells. The merged image (**Figure 4F**) of phase and fluorescence settings (**Figures 4D,E**) for cells treated with HNT-RITC gives a clear picture of the localized nanotubes with red dye in the cell cytoplasm with distinct nuclear exclusion, which displays greater binding and aggregation of the tubes on the cell surface in 24 h compared to the 30 min treatment. After cell fixation (4 days), we see that cells treated with dye only was washed away with only minimal fluorescence remaining on the cells. While the HNT-RITC treated cells still showed significant fluorescence indicating a prolonged delivery of the dye from the clay nanotubes. **Figures 4G,H** show that the cells treated with halloysite nanotubes alone (negative controls) do not show any fluorescence by themselves.

The fluorescence images (middle) highlights nanotubes or dye localization in the outer region of the cell networks, while

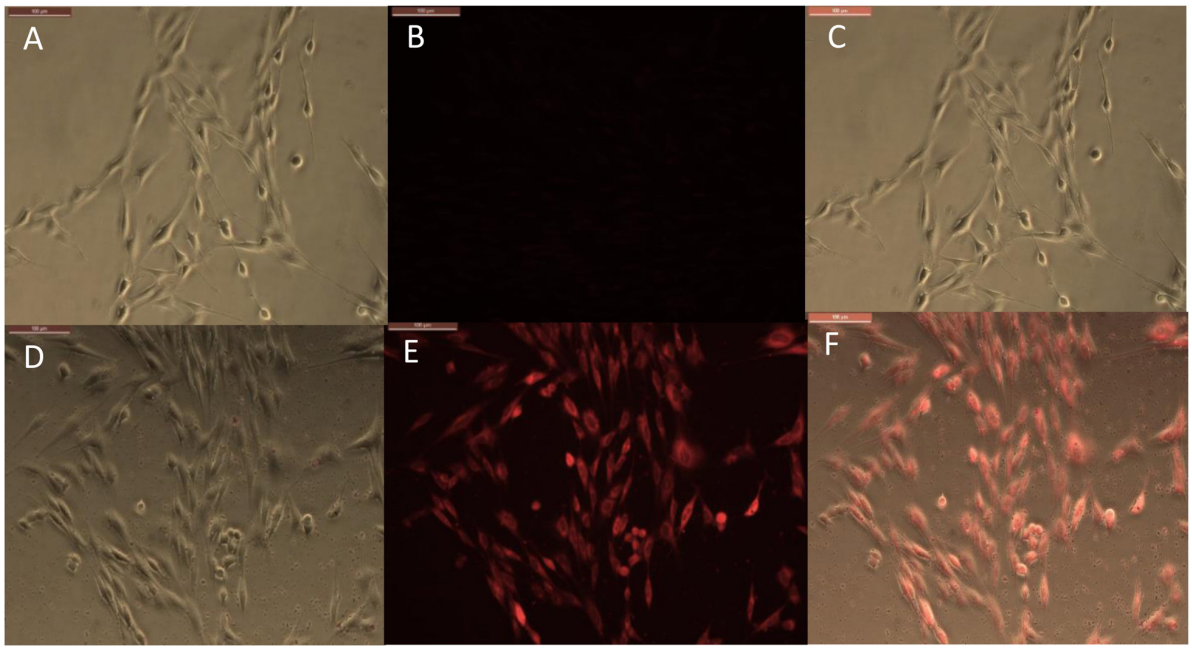

FIGURE 3 | Phase and fluorescence imaging of primary brain endothelial cells treated with RITC only **(A,B)**, and with halloysite clay nanotubes loaded with RITC **(D,E)** after 30 min exposure. Merged images for the phase and fluorescence settings **(C,F)**. Magnification 200X, scale bar = 200 μm.

the merged images (left) illustrate a clear picture of materials (nanotubes and dye) localization inside or on the cell surface.

Halloysite Loading With Glutamic Acid and Ionomycin

Glutamic acid has a negative charge and being loaded into the tube's lumens demonstrated weight percent change of 3.4 ± 0.2 wt l%, corresponding to the halloysite loading. Loading of ionomycin was 16.2 ± 0.2 wt% (**Figure 5**). The percentages of glutamic acid and ionomycin encapsulation were estimated based on the weight change at different temperatures using thermogravimetric analysis. There is a consistency in the drugs loading results, probably, based on the similar loading mechanism enhanced by an attraction of negative drug molecules into the positive lumen of nanotubes. The used pristine halloysite had a zeta-potential value of −30 ± 2 mV and after the drugs loading, it became −45 ± 1 and −48 ± 2 mV correspondingly for ionomycin and glutamic acid. These formulations provided an enhanced colloidal stability that took 3–4 h for settling for pure halloysite and 8–10 h in the loaded samples. The precipitation time for aqueous unloaded and loaded halloysite ranged from minutes to days, in correspondence to the respective zeta-potential that were measured. Therefore, the ability to load these neurotransmitters into clay nanotubes is achievable but further testing on the surface area and inner lumen with the transmitters need to be performed to know their exact location along with *in vitro* testing.

These results demonstrate that one can sufficiently load selected brain drugs into halloysite nanotubes and deliver them into the cells in a manner similar to the procedure of loading RITC. Furthermore, we will concentrate on the analysis of ionomycin delivery because we have a well-elaborated method to characterize the drug release kinetics with Ca^{2+} analysis.

Delivery of Ionomycin – Halloysite Formulations Into Endothelial Cells (Ca^{2+}-Analysis)

In real time calcium imaging, we observed that the cells response to ionomycin had a spiked increase in Ca^{2+} which decayed quickly due to clearance by cells as shown in baseline (**Figure 6A**). When we used halloysite alone, there was only a small response (**Figure 6B**). When ionomycin was encapsulated with halloysite, we achieved a higher response of Ca^{2+} for the same concentration (1 μM) loaded that was also used for the control resulting in a gradual rise in Ca^{2+} which remained higher for a longer time period until it was diluted by the addition of any other stimuli. This increase of Ca^{2+} indicates the gradual and prolonged transport of ionomycin through halloysite across the cell membrane (**Figures 6B,C**). Each experiment was ended with ionomycin stimulation to ensure that the stimulus did not kill the cell under observation. To ensure that the cells were healthy and responding normally to other physiological stimuli, cells were tested with ATP, a well-known stimulator for BMVECs. Ionomycin is a well-known antibiotic and has been also known to induce cancer cell death and proliferation. Results showing sustained delivery of ionomycin might suggest a potential application of these formulations for cancer treatment (Park et al., 2005; MacLean and Yuste, 2009; Han et al., 2013).

All cells were stimulated with ionomycin at the end of experiment (B-E), except (A) which was stimulated by

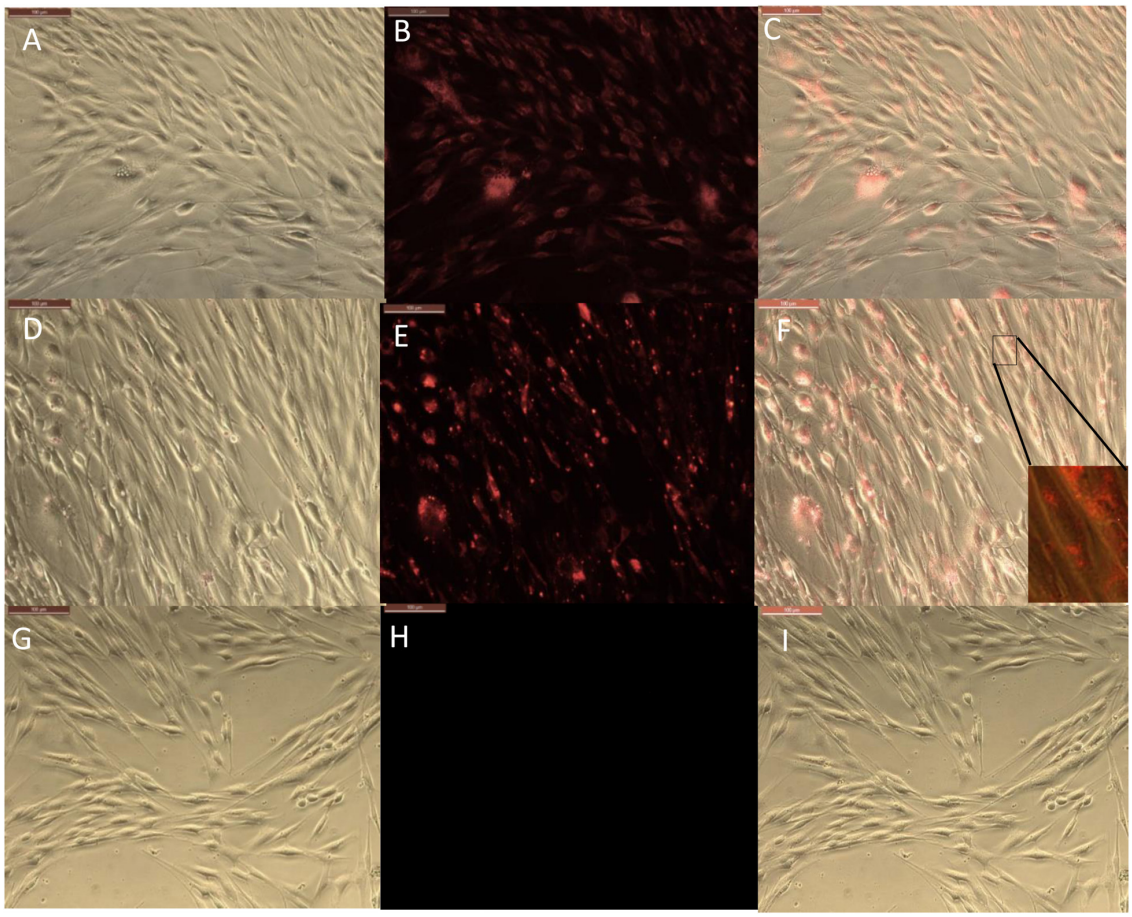

FIGURE 4 | Phase and fluorescence microscopic imaging of primary endothelial cells that were treated with RITC only **(A,B)**, treatment with HNT-RITC formulations **(D,E)**, and treatment with HNT only **(G,H)** in both phase (right) and fluorescent (middle) settings for 24 h exposure. Merged images for the phase and fluorescence settings **(C,F,I)**. Magnification = 200X, scale bar = 100 μM.

HNT-ionomycin of 50 μg/mL. This demonstrated that the cells were still responsive to Ca^{2+} changes, ensuring no cell death, and avoiding occurrence of false signals during the experiments.

Ca^{2+} peak analysis presented in **Figure 7** allows us to come to following conclusions: stimulation by ionomycin (positive control) shows an instant peak of Ca^{2+} that decays quickly compared to HNT-ionomycin nanocapsules (50 and 10 μg/mL) which shows a gradual influx of Ca^{2+} and higher delivery of ionomycin in the cells for both concentration (**Figures 7A,B**). Cells that responded to ATP showed a significant peak that is normally observed for physiological conditions (**Figure 7C**). Stimulus by halloysite alone produces a slight Ca^{2+} response, which was much less compared to HNT-ionomycin formulations with the cells showing no visible toxicity as well as remaining active afterward.

Statistical Analysis of Calcium Response to Different Stimuli

The graphs in **Figure 7** show signals obtained for only 5 cells for each condition for simplification and clear representation of the data. The number of cells captured per frame for a condition being tested in an experiment act as a region of interest, and it ranged from 41 to 140 cells. After obtaining the calcium signals for different stimulations, the Ca^{2+} fluorescence intensity data as a function of time are used to extract the percentage of peak Ca^{2+} response above the baseline (**Figure 8B**) and the cells that responded to the stimuli (**Figure 8C**). The time taken for the stimuli to reach the peak response (**Figure 8D**) was also extracted. The bar graphs are obtained by averaging the values over the region of interest from each condition used for the experiment. At least five conditions were tested here, three times. Overall, the number of cells analyzed was 1,232 for all wells and conditions reported for calcium imaging.

One can see that the calcium peak response above baseline gave us an idea of how high the calcium response to a stimulus is. The results (**Figure 8B**) shows that the increase in peak calcium response above the baseline was 120% for HNT-ionomycin (50 μg/mL), and it was greater than for ionomycin alone (positive control) at 82 ± 2%.

The halloysite (negative controls) showed a slight Ca^{2+} response, which was insignificant at 16% compared to the high

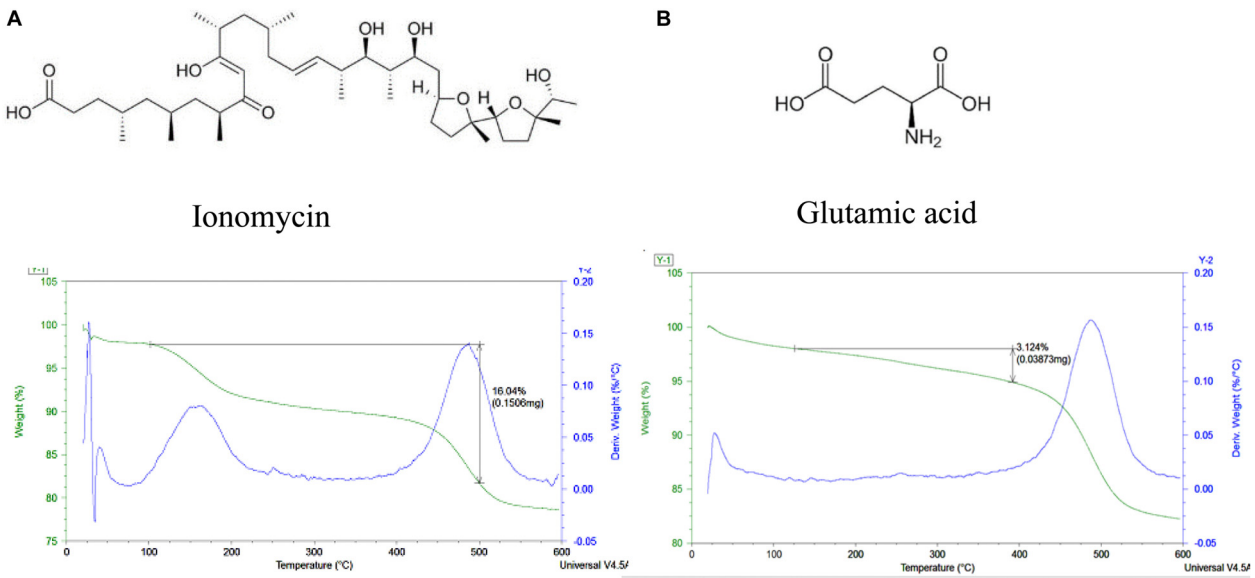

FIGURE 5 | Thermogravimetric data for halloysite loaded with ionomycin and glutamic acid **(A,B)**.

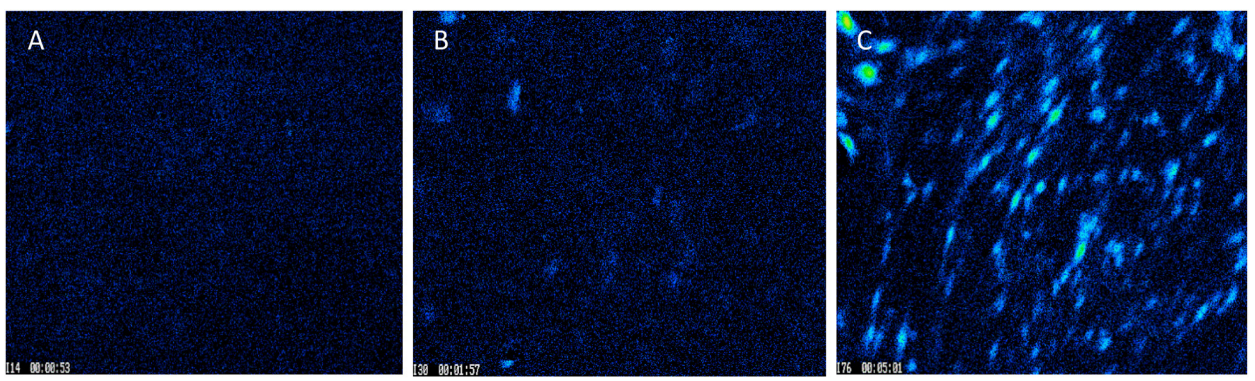

FIGURE 6 | Images captured for BMVECs during Ca^{2+} treatment: **(A)** before stimulation; **(B)** peak stimulation by 50 μg/mL of empty halloysite nanotube, and **(C)** peak stimulation by 50 μg/mL nanotubes loaded with ionomycin. Magnification = 200X.

response of 94% for the same concentration of the HNT-ionomycin samples. The results that the nanotubes alone can also produce much smaller 16% peak Ca^{2+} response suggest us that there is some form of advantageous cellular interaction and communication between the nanoclay and endothelial cell networks which is served by the signaling molecule, calcium. For ATP stimulation the signal was 40%. The peak response to ATP showed that the cells were healthy and at normal physiological condition.

Each experiment had different numbers of cells giving rise to different regions of interest. **Figure 8C** represents the percentage of cells that responded for the given stimulus in an experiment. One can see that a higher number of cells responded to the HNT – ionomycin formulation with 97% for concentration of 10 μg/mL and at 92% for 50 μg/mL, while it was 65% for 50 μg/mL halloysite alone, 72% for 1 μM ionomycin, and 76% for 100 μM ATP. This result indicates that all the parameters discussed here are supported by a high response of cells, but the data specifically displays a higher value in the loaded samples compared to the other conditions tested.

Figure 8D represents the time taken for the cells to produce the peak calcium response. It tells us how delayed or instant the peak response was, indicating the delivery properties of halloysite clay nanotubes. The duration of release until peak calcium response after the stimulation was found to be 80 s for the nanoclay loaded with ionomycin at 10 μg/mL, 54 s for halloysite loaded with ionomycin at 50 μg/mL and 66 s for 50 μg/mL halloysite alone. This result along with results of **Figures 8B,C** explains that using a low concentration 10 μg/mL HNT-ionomycin formulation is enough to get enhanced delivery of ionomycin for a prolonged time as compared to using just ionomycin itself. Using a higher concentration (50 μg/mL) can increase this response further but delay is better achieved with the use of lower concentrations.

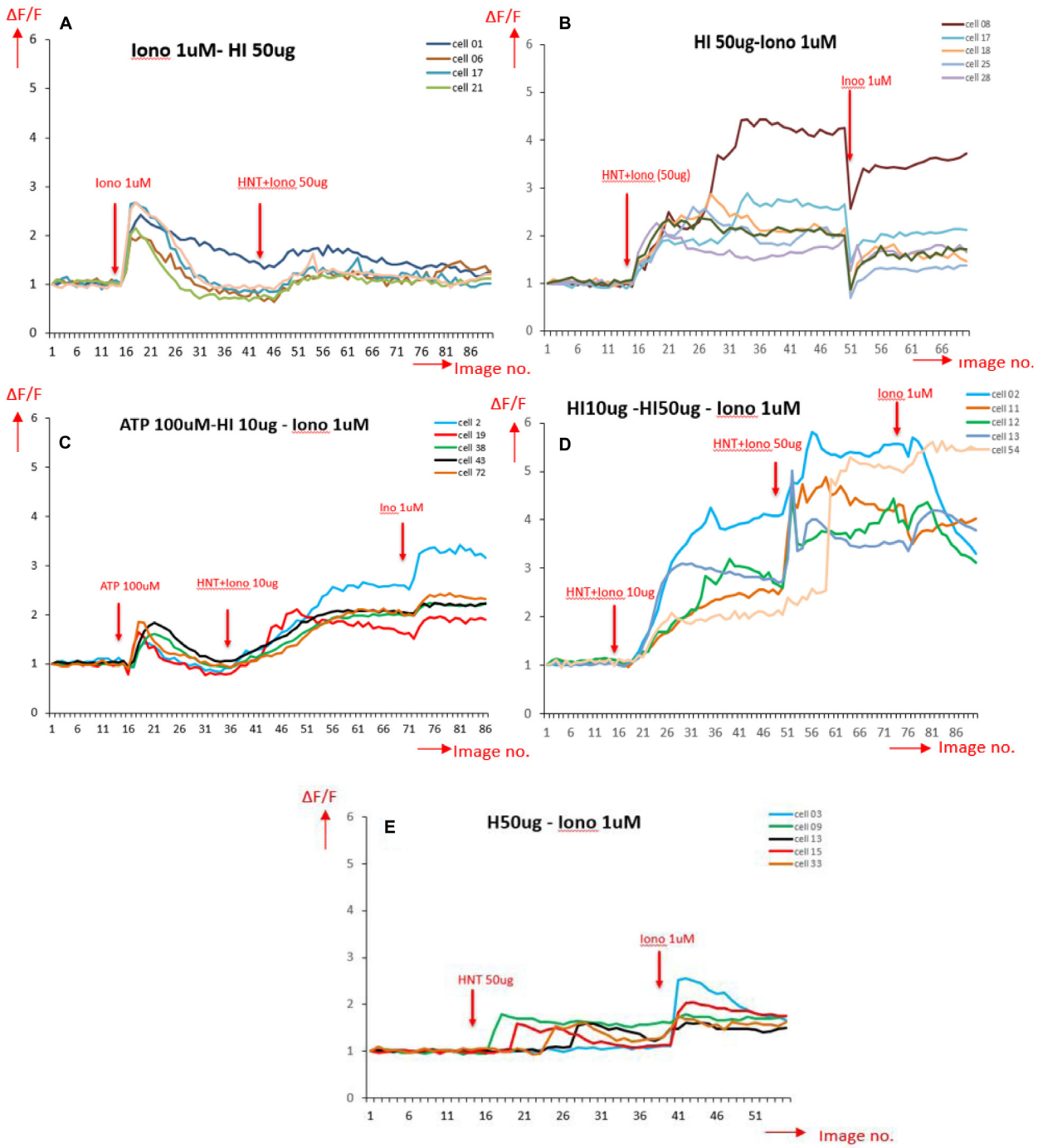

FIGURE 7 | Ca^{2+} peak intensity obtained for different stimulation on BMVECs, in the horizontal axis is the image number indicating time periods with total range of 4 s each (1 image no. = 4 s); and in the vertical axis is the normalized values for fluorescence intensity corresponding to calcium activity **(A)** stimulated by ionomycin (Iono) 1 μM (positive control); **(B)** stimulated by 50 μg/mL HNT- ionomycin (sample tested); **(C)** stimulated by ATP, a well-known Ca^{2+} stimulator (positive control indicating healthy cells), followed by HNT-ionomycin formulation (10 μg/mL) showing the comparison between the Ca^{2+} responses of physiological stimulation (ATP) and HNT-ionomycin formulation for the same cells. **(D)** Cells stimulated by 10 and 50 μg/mL of HNT-ionomycin showing comparative results for the cells when stimulated by lower and higher dose of HNT-ionomycin; **(E)** stimulated by 50 μg/mL of empty HNTs (negative control).

In contrast, the duration was very short for ionomycin 1 μM at 13 s and ATP at 16 s. The duration was found higher for the halloysite loaded and unloaded samples as compared to ionomycin and ATP in their soluble forms. This indicates that there is delayed diffusion from the nanotubes due to the soluble ionomycin and ATP release being much faster.

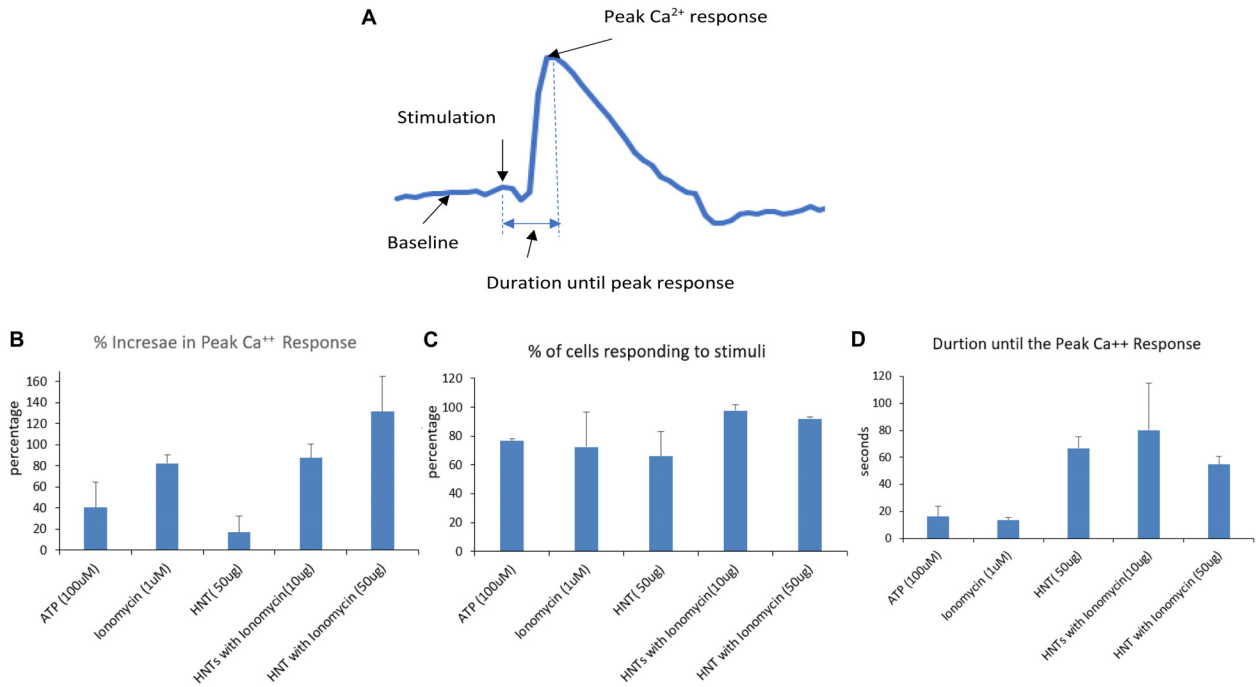

FIGURE 8 | (A) Signal analysis scheme. **(B–D)** Parameters obtained from each calcium signal averaged over the region of interests ranging from 41 to 140 for each condition in a single experiment and then averaged for three experiments. The error bars represent the standard deviations in between the experiments.

All the results discussed in **Figures 7**, **8** indicate that the halloysite loaded with ionomycin showed delayed and gradual release of ionomycin into the cells, that once it reaches the peak response it continues to diffuse for a prolonged time which is expected to be up to 24 h as was observed for the nanotubes loaded with RITC **Figures 3**, **4**. 24 h treatment of BMVECs with ionomycin concentration of 1 μM used throughout the experiment didn't show any cytotoxicity to the cells.

CONCLUSION

Halloysite nanotubes have a great potential in delivering drugs effectively to the brain because they were not toxic to the endothelial cells, they were capable of slowly releasing drugs over various time spans ranging from minutes to hours, and are attracted to the cells that reside in the blood–brain barrier. The ability of halloysite to enhance the calcium response in BMVECs by loading it with ionomycin drastically extended the delivery time of the compound compared to the use of the ionophore alone (non-encapsulated). With this new information, we can extend this approach for treating brain cancer cells through drug delivery based upon the data of inhibitory effects of ionomycin on the cells and its use as a chemosensitizer. We confirmed a delayed and prolonged diffusion of the drug delivery mechanism due to the halloysite nanotubes loading cell probes (ionomycin + RITC). This provides a sustained delivery strategy for drug penetration across the blood–brain barrier.

DATA AVAILABILITY STATEMENT

All datasets generated for this study are included in the article/supplementary material.

ETHICS STATEMENT

The animal study was reviewed and approved for all cell studies carried out in this work, which used primary tissues derived from laboratory animals as approved by Louisiana Tech University IACUC (Louisiana Tech University IACUC, Center for Biomedical Engineering and Rehabilitation Science, Ruston, LA, United States).

AUTHOR CONTRIBUTIONS

MS: nanoformulation experiments under YL supervision. NP: cell culture treatments under MD: supervision. YL and MD writing the manuscript.

FUNDING

We thank Louisiana Board of Regents grant LaSpace-GSRA#19-287 for support of this work. Support by NSF – 1632891 grant was acknowledged. Any opinions, findings, and conclusions, or recommendations expressed in this report are those of authors and do not necessarily reflect the view of National Science Foundation.

REFERENCES

Bennewitz, M., and Saltzman, W. (2009). Nanotechnology for delivery of drugs to the brain for epilepsy. *Neurotherapeutics* 6, 323–336. doi: 10.1016/j.nurt.2009.01.018

Dzamukova, M., Naumenko, E., Badrutdinov, A., Lvov, Y., and Fakhrullin, R. (2015a). Enzyme-activated intracellular drug delivery with tubule clay nanoformulation. *Sci. Rep.* 5:10560. doi: 10.1038/srep10560

Dzamukova, M., Naumenko, E., Rozhina, E., Trifonov, A., and Fakhrullin, R. (2015b). Cell surface engineering with polyelectrolyte-stabilized magnetic nanoparticles: a facile approach for fabrication of artificial multicellular tissue-mimicking clusters. *Nano Res.* 8, 2515–2532.

Fakhrullina, G., Khakimova, E., Akhatova, F., Lazzara, G., Parisi, F., and Fakhrullin, R. (2019). Selective antimicrobial effects of curcumin @ halloysite nanoformulation: a *Caenorhabditis elegans* study. *ACS Appl. Mater. Interf.* 11, 23050–23064. doi: 10.1021/acsami.9b07499

Han, S., Tie, X., Meng, L., Wang, Y., and Wu, A. (2013). PMA and ionomycin induce glioblastoma cell death: activation-induced cell-death-like phenomena occur in glioma cells. *PLoS One* 8:e76717. doi: 10.1371/journal.pone.0076717

Hu, Y., Chen, J., Li, X., Sun, Y., Huang, S., Li, Y., et al. (2017). Multifunctional halloysite nanotubes for targeted delivery and controlled release of doxorubicin in-vitro and in-vivo studies viability tests and microscopy study. *Nanotechnology* 28:375101. doi: 10.1088/1361-6528/aa8393

Kamalieva, R., Ishmukhametov, I., Batasheva, S., Rozhina, E., and Fakhrullin, R. (2018). Uptake of halloysite clay nanotubes by human cells: colourimetric. *Nano Struct. Nano Objects* 15, 54–60.

Kaushik, V., Yakisich, J., Kumar, A., Azad, N., and Iyer, A. (2018). Ionophores: potential use as anticancer drugs and chemosensitizers. *Cancers* 10:360. doi: 10.3390/cancers10100360

Kruchkova, M., Danilushkina, A., Lvov, Y., and Fakhrullin, R. (2016). *In vivo* toxicity study of nanoclays and graphene oxide with *Paramecium caudatum*. *Environ. Sci. Nano* 3, 442–452.

Liu, M., Fakhrullin, R., Novikov, A., Vinokurov, V., Panchal, A., Fu, Y., et al. (2019). Tubule nanoclay-organic heterostructures for biomedical applications. *Macromol. Biosci.* 19:1800419. doi: 10.1002/mabi.201800419

Liu, M., Jia, Z., Jia, D., and Zhou, C. (2014). Recent advances in halloysite research. *Prog. Polym. Sci.* 39, 1498–1514.

Long, Z., Wu, Y.-P., Gau, H.-Y., Li, Y.-F., He, R.-R., and Liu, M. (2018). Functionalization of halloysite nanotubes via grafting of dendrimer for efficient intracellular delivery of siRNA. *Bioconjugate Chem.* 29, 2606. doi: 10.1021/acs.bioconjchem.8b00321

Lvov, Y., Wang, W., Zhang, L., and Fakhrullin, R. (2016). Halloysite clay nanotubes for loading and sustained release of functional compounds. *Adv. Mater.* 28, 1227–1250. doi: 10.1002/adma.201502341

MacLean, J., and Yuste, R. (2009). Imaging action potentials with calcium indicators. *Cold Spring Harb. Protoc.* 2009:pdb.prot5316. doi: 10.1101/pdb.prot5650

Mahringer, A., Ott, M., and Fricker, G. (2013). "The blood–brain barrier: an introduction to its structure and function," in *The Blood Brain Barrier*, Vol. 10, eds G. Fricker, M. Ott, and A. Mahringer (Berlin: Springer), 1–20. doi: 10.1177/0333102418786261

Mbagwu, S., and Filgueira, L. (2020). Differential expression of CD31 and von willebrand factor on endothelial cells in different regions of the human brain: potential implications for cerebral malaria pathogenesis. *Brain Sci.* 10:31. doi: 10.3390/brainsci10010031

Mehdia, Y., Fizira, M., Itatahinea, A., Hea, H., and Dramoua, P. (2018). Preparation of multifunctional PEG-graft-halloysite nanotubes for controlled drug release, Tumor cell targeting, and bio-imaging. *Coll. Surfaces B Biointerf.* 170, 322–329. doi: 10.1016/j.colsurfb.2018.06.042

Morgan, A. J., and Jacob, R. (1994). Ionomycin enhances Ca2+ influx by stimulating store-regulated cation entry and not by a direct action at the plasma membrane. *Biochem. J.* 300, 665–672. doi: 10.1042/bj3000665

Park, C., Hahm, E., Lee, J., Jung, K., Rhee, H., Yang, C., et al. (2005). Ionomycin downregulates β-catenin/Tcf signaling in colon cancer cell line. *Carcinogenesis* 26, 1929–1933. doi: 10.1093/carcin/bgi145

Pehlivan, S. (2013). Nanotechnology-based drug delivery systems for targeting, imaging and diagnosis of neurodegenerative diseases. *Pharm. Res.* 30:2499. doi: 10.1007/s11095-013-1156-7

Santos, A., Pereira, I., Veiga, F., Reis, S., Saleh, M., and Lvov, Y. (2019). Biomedical potential of clay nanotube formulations and their toxicity assessment. *Expert Opin. Drug Deliv.* 16, 1169–1182. doi: 10.1080/17425247.2019.1665020

Silva, G. (2008). Nanotechnology approaches to crossing the blood-brain barrier and drug delivery to the CNS. *BMC Neurosci.* 9:S4. doi: 10.1186/1471-2202-9-S3-S4

Thiel, V., and Audus, K. (2001). Nitric oxide and blood–brain barrier integrity. *Antioxid. Redox Signal.* 3, 273–278.

Vergaro, V., Abdullayev, E., Cingolani, R., Lvov, Y., and Leporatti, S. (2010). Cytocompatibility and uptake for clay nanotubes. *Biomacromolecules* 11, 820–229.

Wang, G., Qian, P., Xu, Z., Zhang, J., Wang, Y., Cheng, S., et al. (2012). Regulatory effects of the JAK3/STAT1 pathway on the release of secreted phospholipase A2-IIA in microvascular endothelial cells of the injured brain. *J. Neuroinflammation* 9:170. doi: 10.1186/1742-2094-9-170

Wang, X., Gong, J., Gui, Z., Hu, T., and Xu, X. (2018). Halloysite nanotubes-induced Al accumulation and oxidative damage in liver of mice after 30-day repeated oral administration. *Environ. Toxicol.* 33, 623–631. doi: 10.1002/tox.22543

World Health Organization [WHO] (2020). *Epilepsy*. Geneva: World Health Organization. Available online at: https://www.who.int/news-room/fact-sheets/detail/epilepsy

Wu, Y.-P., Yang, J., Gao, H.-Y., Shen, Y., Jiang, L., Zhou, C., et al. (2018). Folate-conjugated halloysite nanotubes, an efficient drug carrier, deliver doxorubicin for targeted therapy of breast cancer. *ACS Appl. Nano Mater.* 1, 595–608.

Yamamoto, K., Furuya, K., Nakamura, M., Kobatake, E., Sokabe, M., and Ando, J. (2011). Visualization of flow-induced ATP release and triggering of Ca2+ waves at caveolae in vascular endothelial cells. *J. Cell Sci.* 124, 3477–3483. doi: 10.1242/jcs.087221

Yang, J., Wu, Y., Shen, Y., Zhou, C., Li, Y.-F., He, R.-R., et al. (2016). Enhanced therapeutic efficacy of doxorubicin for breast cancer using chitosan oligosaccharide-modified halloysite nanotubes. *ACS Appl. Mater. Interfaces* 8, 26578–26590. doi: 10.1021/acsami.6b09074

Zhang, Z., Luo, X., Wu, Y.-P., Wu, F., Li, Y.-F., He, R.-R., et al. (2019). Rod in tube: a novel nanoplatform for highly effective chemo-photothermal combination therapy toward breast cancer. *ACS Appl. Mater. Interfaces* 11, 3690–3703. doi: 10.1021/acsami.8b17533

Zhao, X., Wan, Q., Fu, X., Meng, X., Ou, X., Zhong, R., et al. (2019). Toxicity evaluation of one-dimensional nanoparticles using caenorhabditis elegans: a comparative study of halloysite nanotubes and chitin nanocrystals. *ACS Sustain. Chem. Eng.* 7, 18965–18975.

Conflict of Interest: The authors declare that the research was conducted in the absence of any commercial or financial relationships that could be construed as a potential conflict of interest.

frontiers in Bioengineering and Biotechnology

REVIEW
published: 25 May 2020
doi: 10.3389/fbioe.2020.00503

Smart Nanotheranostics Responsive to Pathological Stimuli

Alessandro Parodi[1]*, *Magdalena Rudzinska*[1], *Stefano Leporatti*[2], *Yuri Anissimov*[1,3] and *Andrey A. Zamyatnin Jr.*[1,4]*

[1] Institute of Molecular Medicine, Sechenov First Moscow State Medical University, Moscow, Russia, [2] CNR NANOTEC - Istituto di Nanotecnologia, Polo di Nanotecnologia, Lecce, Italy, [3] School of Environment and Sciences, Griffith University, Gold Coast, QLD, Australia, [4] Belozersky Institute of Physico-Chemical Biology, Lomonosov Moscow State University, Moscow, Russia

The development of nanotheranostics represents one of the most dynamic technological frontiers in the treatment of different pathological conditions. With the goal in mind to generate nanocarriers with both therapeutic and diagnostic properties, current research aims at implementing these technologies with multiple functions, including targeting, multimodal imaging, and synergistic therapies. The working mechanism of some nanotheranostics relies on physical, chemical, and biological triggers allowing for the activation of the therapeutic and/or the diagnostic properties only at the diseased site. In this review, we explored new advances in the development of smart nanotheranostics responsive to pathological stimuli, including altered pH, oxidative stress, enzymatic expression, and reactive biological molecules with a deep focus on the material used in the field to generate the particles in the context of the analyzed disease.

Keywords: nanotheranostics, smart nanoparticles, pH-responsive theranostics, ROS-responsive theranostics, Enzyme-responsive theranostics

OPEN ACCESS

Edited by:
Gabriele Candiani, Politecnico di Milano, Italy

Reviewed by:
Enzo Terreno, University of Turin, Italy
Melani Solomon, University of Maryland, United States
Jing Lin, Shenzhen University, China

***Correspondence:**
Alessandro Parodi
aparodi.sechenovuniversity@gmail.com
Andrey A. Zamyatnin Jr.
zamyat@belozersky.msu.ru

Specialty section:
This article was submitted to Nanobiotechnology, a section of the journal Frontiers in Bioengineering and Biotechnology

Received: *04 March 2020*
Accepted: *29 April 2020*
Published: *25 May 2020*

Citation:
Parodi A, Rudzinska M, Leporatti S, Anissimov Y and Zamyatnin AA Jr (2020) Smart Nanotheranostics Responsive to Pathological Stimuli. Front. Bioeng. Biotechnol. 8:503. doi: 10.3389/fbioe.2020.00503

INTRODUCTION

Nanotheranostic development perhaps represents the highest level of technological advance in the nanomedicine field, and it aspires to combine in the same delivery platform therapeutic and diagnostic properties (Wong et al., 2020). Nanotheranostics are nanoparticles designed to provide real-time information about drug biodistribution, release, and targeted treatment *in vivo*, representing one of the last frontiers in personalized medicine (Jo et al., 2016). Nanotheranostics are usually generated through complex synthetic protocols (Silva et al., 2019) necessary to transfer multiple functions to the same delivery platform. For this reason, in several cases, nanotheranostics' targeting simply relies on particle passive accumulation in the diseased tissue *via* enhanced permeability and retention effect (EPR) usually achieved with biological coating (i.e., albumin, peptides) or polyethylene glycol (PEG) surface modification.

However, beyond exploiting a specific targeting, nanotheranostic selectivity for the pathological area can derive from a specific "responsiveness" of the carriers to an external stimulus (Sneider et al., 2017). This "activation trigger" (e.g., near-infrared light) is usually remotely applied directly in the area of interest (Wang et al., 2017b) and has benefits of non-invasiveness. Typical diagnostic or therapeutic carriers are generally in the "on" state (Zhao et al., 2017), and their detection and payload release occur from the moment of their administration. On the other hand, the designing of carriers with "off-on" theranostic properties (Yu et al., 2018) can favor a personalized assessment of the amount of drug that effectively reaches the pathological site. For this reason, responsive nanotheranostics have the potentialities to open new avenues for optimizing and controlling the

treatment dose and repetition (Fan et al., 2016; Yang et al., 2016b). In this scenario, it seems almost impossible to increase further the level of complexity of these technologies. To date, many theranostics can permit multimodal imaging and therapy for enhancing diagnostic accuracy and treatment efficacy (Dong et al., 2016). However, new trends in nanomedicine aim at imparting the carriers with responsiveness to the biological environment conditions. In other words, the physiological alterations that differentiate diseased from healthy tissue can serve as "triggers" to turn *in vivo* the nanotheranostics "on" (Ma et al., 2016). Also, these concepts showed the potential to improve current experimental protocols. For example, nanotheranostics that can enhance their detection signal in response to precise biological stimuli could mitigate the background noise issues related to the imaging of fluorescently modified carriers (Wu et al., 2014).

The working mechanism of the stimuli-responsive carriers, often referred to as "smart" theranostics, usually depends on functional molecules or chemical linkers used to assemble the nanoparticles (Karimi et al., 2016). However, in some cases, it is the intimate structure of the particles that changes or responds to the environmental conditions, like in the case of polymers (Li et al., 2019a). In this review, we explored recent advances in the development of nanotheranostics that can respond to biological stimuli. These carriers were designed to provide their curative and/or diagnostic properties only in the pathological site, exploiting altered chemical and biological features of the diseased tissue. These concepts, as well as the field of nanomedicine, are traditionally applied to cancer disease because tumor tissue undergoes profound changes in cell metabolism, generating significant variations in local pH and oxidative stress. Sometimes the nanoparticles were designed to respond to more than one biological stimuli as well as in combination with physical stimuli that can be remotely administered. Also, tumor growth very often depends on the differential expression of enzymes that can be exploited as biological triggers as well (Xiao et al., 2018). However, recent evidence demonstrated that the concepts of biologically responsive nanotheranostic could be beneficial also for other pathological conditions, expanding the application of these technologies to a new whole portfolio of clinical conditions.

PH-RESPONSIVE THERANOSTICS

In the area of cancer therapy, pH represents an essential cue of differentiation compared to healthy tissue. Even though not all the regions of the tumor become significantly acidified, changes in cancer metabolism [i.e., the Warburg effect (Tekade and Sun, 2017; Shamsi et al., 2018)], can induce an overall average decrease of 0.2–0.4 points, although values <6 were registered as well (Liu et al., 2014a). In this scenario, the tumor microenvironment pH can eventually represent a targetable characteristic. Also, after cell internalization, the nanoparticles are usually sequestered in the endolysosomal compartment, where the pH drops significantly below 5 (Wang et al., 2017a), making these organelles optimal targets for pH-responsive technologies.

pH-responsive properties can be coupled with the activation of different therapeutic mechanisms, including reactive oxygen species (ROS)-based cytostatic therapeutics, as well as different imaging modalities. In this context, sono-, photo-, and chemodynamic therapies are treatments in which the cytostatic properties rely on the overproduction of ROS. In sono- and photodynamic therapy (PDT), ROS can be generated upon an external stimulus. In contrast, chemodynamic therapy (CDT) depends just on the chemical properties of the carriers or the payload responsible for ROS generation, usually when interacting with the cellular H_2O_2 (Lin et al., 2018).

The pH-responsiveness can derive from pH-sensitive linkers used to stabilize the particles (Kanamala et al., 2016) or its payload in the carrier structure. An extensive overview of this topic can be found in Cao et al. (2019). Acotinyl linkers were intensely investigated in the field to impart pH responsiveness to the carriers. For example, Zhu et al. generated pH-responsive theranostics incorporating gold nanoparticles in poly(amidoamine) dendrimers (Zhu et al., 2018). The gold nanoparticles represented an optimal contrast agent in computed tomography (CT) imaging. The dendrimers were modified on their surface with folic acid *via* EDC chemistry to provide the particles with high tumor targeting. Cis-aconitic anhydride pH-sensitive linkers were used to conjugate Doxorubicin (DOX) to the particles. Drug release was triggered by the acidic conditions (typical of the tumor microenvironment and the endosomal compartment) even though *in vivo* proof of the efficacy of this technology was not reported. Similarly, nanotheranostics were generated with bovine serum albumin (BSA) linked to the porphyrin photosensitizer pheophorbide-a *via* cis-aconityl pH-sensitive linkers. Stable nanoparticles were generated by complexing this structure with graphene oxide *via* π-π stacking and hydrophobic interactions (Battogtokh and Ko, 2016). The carriers were further modified with pegylated folate to impart the system with extended circulation properties and tumor targeting. Porphyrins are known for their therapeutic potential (PDT) and fluorescent properties, but their administration requires encapsulation since they are strongly hydrophobic (Yan et al., 2015). This complex facilitated dual therapy through PDT and photothermal therapy (PTT) due to the porphyrin payload and the graphene oxide, respectively, upon irradiation at 670 nm. *In vivo*, compared with the free administered photosensitizer, the particle highly accumulated in the tumor tissue through EPR effect. Here they could release their payload due to the pH-sensitive linkers both in the acidic tumor microenvironment and well as in the cell cytoplasm after internalization favored by the folate functionalization. The pH-sensitive mechanism was fundamental to activate the theranostic properties of the porphyrin since this molecule is affected by aggregation-caused quenching (ACQ) effect when encapsulated.

On the other hand, different materials can be manipulated in the nanoscale and dissolve (releasing a payload) in acidic pH. Calcium carbonate ($CaCO_3$) nanoparticles represent a well-investigated delivery platform (Idris et al., 2019; Vidallon et al., 2020) in this field. At physiological pH, $CaCO_3$ nanoparticles are stable, but under acid conditions, they degrade into Ca^{2+} and CO_2, releasing whatever payload was previously

loaded. Pegylated $CaCO_3$ nanoparticles were synthesized by gas diffusion-reaction in combination with the photodynamic theranostic agent chlorin e6 (Ce6) (Dong et al., 2016). Like porphyrins, Ce6 is *per se* a theranostic because it can serve as a therapeutic tool for PDT while emitting a detectable fluorescent signal upon near-infrared light (NIR) irradiation (Liu et al., 2014b). The particles were also doped with Mn^{2+}, to favor the photosensitizer precipitation with the $CaCO_3$. Mn^{2+} also allowed for detecting particle degradation and payload release *via* magnetic resonance imaging (MRI), and it provided a mean for CDT increasing ROS levels *via* Fenton-like reaction with tissue H_2O_2. In this chemical reaction a transition metal (i.e., Fe, Al, Mn, Cu, Zn) interacting with H_2O_2 is oxidized while catalyzing the formation of a hydroxyl radical and a hydroxide ion (Das et al., 2015). The system was characterized by a mesoporous structure compatible with the loading of conventional chemotherapeutics like DOX that, in acidic conditions, was released as well. The particles were also modified with PEG allowing for extravasation in the tumor microenvironment *via* EPR. Under the acidic conditions of cancer tissue, they could exert their theranostic properties demonstrating high cytostatic properties both *in vitro* and *in vivo* against a model of breast cancer, The authors demonstrated that chemotherapy (DOX), CDT (Mn^{2+}) and PDT (Ce6) could work synergistically against cancer cell growth (Dong et al., 2016) accomplishing multimodal therapy.

Another example of pH-responsive structure was proposed by Xiao et al. (2019) that developed a theranostic platform named MCDION-Se able to provide at the same time chemodynamic and limotherapy while representing an optimal contrast agent for MRI application. The system was composed of a core of manganese carbonate-deposited iron oxide nanoparticles coated with negatively charged selenium nanoparticles coordinated to the core *via* polyethylenimine (PEI) (**Figure 1**). The manganese carbonate in the system could easily dissolve in slightly acidic conditions releasing Mn^{2+} for CDT and MRI while inhibiting ATP generation. On the other hand, the presence of the selenium enhanced the formation of H_2O_2, fueling the Fenton-like reaction catalyzed by the iron oxide nanoparticles to form ROS that further inhibited ATP synthesis. The combination of these elements was designed to breakdown in the tumor microenvironment and tumor cells after internalization, triggering different cascades of events affecting the energetic metabolism (limotherapy) while accelerating cell apoptosis *via* CDT. *In vivo*, the particles showed a higher circulation time and tumor accumulation than free Mn^{2+}, probably *via* the EPR effect even though specific modifications to favor this phenomenon were not described. Manganese was also exploited by Liu et al. that designed PEG-coated MnO_2 nanoparticles stabilized with BSA. The particles were loaded with the radiosensitizer hafnium and a prodrug form of cisplatin. The core of MnO_2 could catalyze the conversion of tumor H_2O_2 to O_2 to revert hypoxic tumor conditions while the hafnium synergistically increased radiotherapy efficiency. After particle extravasation *via* EPR, the particles dissolved in acidic conditions offering an optimal contrast agent for MRI. Besides, the prodrug could be internalized by tumor cells and converted to cisplatin *via* cellular glutathione. The system provided a dual therapy mechanism (chemo and radiotherapy) effective against a model of breast cancer *in vivo* (Liu et al., 2017).

Finally, it is worth reporting the work of Li et al. (2020a) that exploited the acidic properties of the tumor microenvironment to increase the generation of ROS in hypoxic tissue, where this strategy is usually not achievable due to the lack of oxygen (Chen et al., 2015). The system was composed of biodegradable magnetic mesoporous nanocubes that efficiently induced hyperthermia when exposed to an external high frequency alternating magnetic field. The particles were loaded with Vitamin C to selectively kill cancer cells through the formation of the ascorbate radical and H_2O_2 (Yun et al., 2015; Lv et al., 2018). Its release was induced by the material phase-change that turned from the solid to the liquid state when the surrounding temperature was higher than 38°C. More importantly, in acidic conditions, the metallic nature of these nanoparticles induced the transformation of H_2O_2 into O_2 as well as its further conversion to hydroxyl radical *via* Fenton reaction (Cao et al., 2018) while serving as an optimal T_2 MRI contrast agent. The system showed theranostic properties both *in vitro* and *in vivo,* where the particle biodistribution could be tracked *via* MRI. Upon application of the external magnetic field, the generated hyperthermia induced the release of vitamin C with its consequent tumor-killing properties.

As shown in this section, pH responsiveness can be imparted through different chemical linkers and materials sensitive to pH to trigger the therapeutic and/or the imaging properties. The responsiveness of most of these technologies depends on the sensitivity of their ultrastructure to the pH. More importantly, the pH-responsiveness could be exploited for increasing tumor oxygen levels for improving radiotherapy effectiveness or CDT in hypoxic tumor conditions. Finally, pH-sensitivity can be coupled with other mechanisms of responsiveness that rely on external stimuli to increase the carrier therapeutic and diagnostic properties.

ROS-RESPONSIVE THERANOSTICS

Due to their high metabolism and accelerated growth, cancer cells are characterized by an increased generation of ROS (Trachootham et al., 2009). On the other hand, this enhanced oxidative stress is compensated by a higher average content of glutathione (Desideri et al., 2019) that in the field of nanotheranostics is exploited as a biological trigger as well, and will be discussed in the last section of this review. It is worth mentioning that all ROS-responsive mechanisms eventually depend on a biological trigger because their working mechanism depends on the oxygen content in the tissue, and they are ineffective in hypoxic regions (Chen et al., 2015). In some cases, the ROS generation is catalyzed directly by the nanoparticles, that due to the properties of their synthesis material, can activate other features of the carriers like payload release (Sun et al., 2018).

In the field of PDT, new evidence are indicating that the best treatment efficacy occurs when the photosensitizer is coupled with a chemotherapeutic agent generating a synergistic effect.

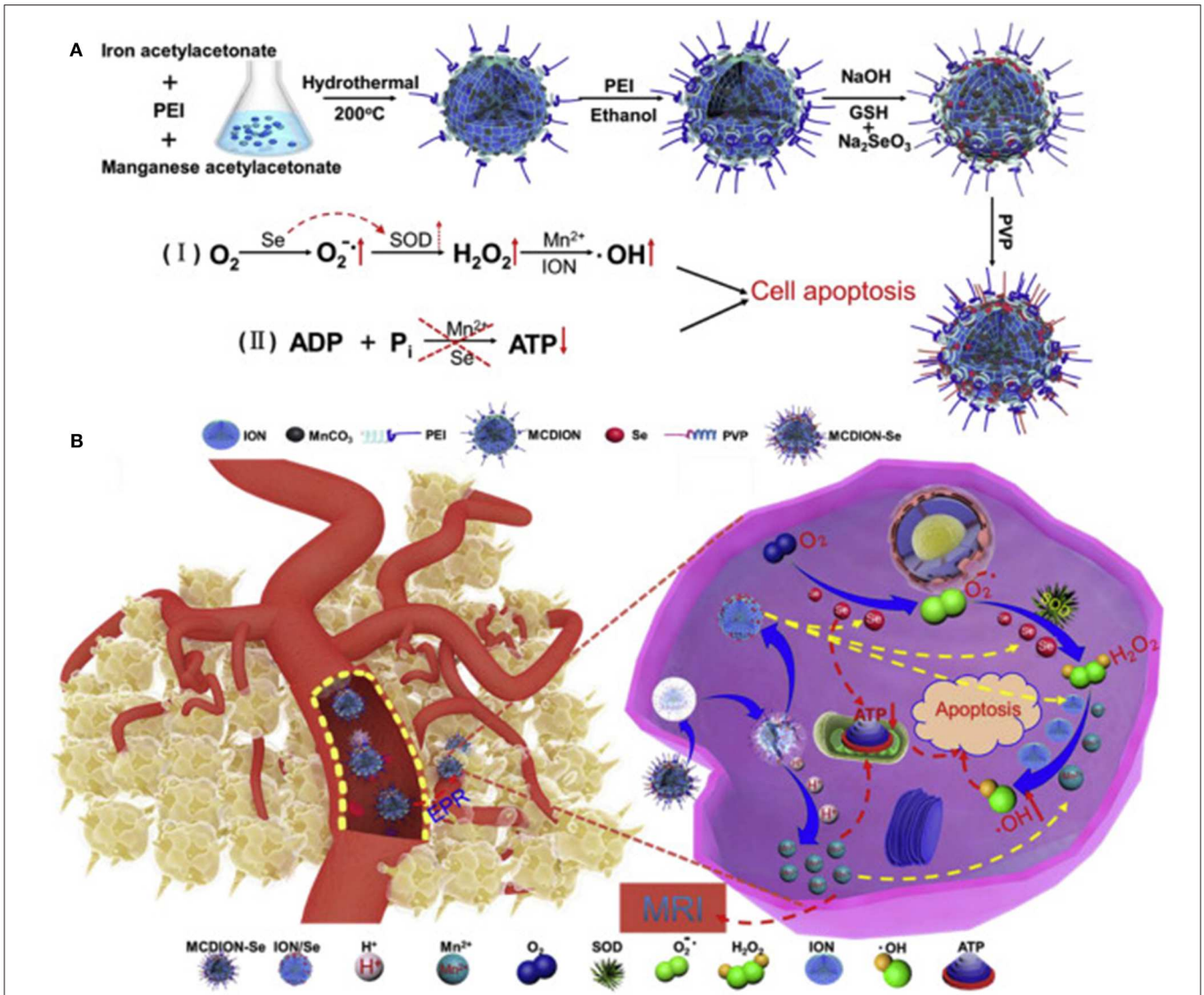

FIGURE 1 | (A) MCDION-Se synthesis. Iron (III) acetylacetonate and manganese acetylacetonate were used as precursors for particle synthesis *via* solvent, thermal decomposition with polyethyleneimine (PEI) as a surfactant. PEI also allowed for further modification with Se nanoparticles *via* electrostatic interactions between the positively charged polymer and the negatively charged Se. Polyvinylpyrrolidone (PVP) was used to stabilize the system. The scheme also illustrates the synergistic action of Mn and Se in inducing the formation of ROS and consequent cell apoptosis. In particular, the selenium nanoparticles induced the formation of superoxide radicals and the activation of the enzyme superoxide dismutase (SOD) to generate H_2O_2. Manganese and iron oxide nanoparticles catalyzed further conversion of H_2O_2 to hydroxyl radical. Mn and Se also negatively impacted on ATP synthesis. **(B)** After IV administration, the particles extravasated in the tumor microenvironment *via* EPR. Here they can be internalized by cancer cells and induce a cascade of reactions that increase cell apoptosis *via* ROS production and inhibition of ATP synthesis. Reproduced with permission from Xiao et al. (2019).

To achieve this goal, it is mandatory designing particles in which the ROS can induce a burst release of the therapeutic (Yang et al., 2016a; Zhou et al., 2017). For this reason, the carriers needed to generate ROS as well as being sensitive to these chemical species. To this goal, Sun et al. (2018) developed nanoparticles of pegylated polyphosphate crosslinked with a thioketal linker *via* (A2 + B3) type polycondensation. The carriers were loaded with the photosensitizer Ce6 and DOX. Under NIR light irradiation, the photosensitizer induced the generation of ROS, while favoring the degradation of the thioketal linker resulting in a burst release of DOX. This strategy was effective in overcoming DOX drug resistance i*n vitro* in a cell line of breast cancer (MCF-7/ADR) overexpressing P-glycoprotein. *In vivo*, the particle demonstrated good tumor accumulation *via* the EPR effect as well as high tumor-killing properties. The system showed bimodal imaging capabilities achieved both *in vitro* and *in vivo,* exploiting Ce6 photoacoustic (PA) properties and gadolinium (loaded in the particles *via* its natural affinity for Ce6) that allowed for efficient MRI. Supported by dual-modal imaging, the tumor sites could be precisely irradiated, sparing healthy organs and reducing kidney and liver toxicity.

Within the cell cytoplasm, mitochondria are the most active organelles in terms of ROS generation (Dunn et al., 2015) and, compared to healthy cells, cancer cells showed a higher mitochondrial membrane potential favoring their targeting *via* internalized cationic molecules (Modica-Napolitano and Aprille, 2001). Inspired by this evidence, Yue et al. developed a nanotheranostic composed of triphenylphosphine, a positively charged molecule with a high affinity for the mitochondria, condensed *via* amphiphilic block polymerization with camptothecin (CPT) and the photosensitizer zinc phthalocyanine (ZnPC) for PDT generation. The drug conjugation occurred through pegylated thioketal linkers sensitive to ROS (Yue et al., 2016). The particles were designed to extravasate in the tumor microenvironment *via* EPR, while tumor cell internalization and mitochondrial targeting were achieved through the membrane penetrating properties of the positively charged triphenylphosphine. The ROS generated by the mitochondria and *via* PDT favored the release of the CPT (topoisomerase-inhibitor) and a dual therapy mode. The system could be detected *via* fluorescence imaging *in vitro* and *in vivo* (when ZnPC was replaced by Ce6) in a subcutaneous model of lung cancer. However, for a more comprehensive description of remotely responsive activated technologies, we suggest the readers look elsewhere (Kim et al., 2013; Zhang et al., 2016) since this review focuses mostly on the nanoplatforms that are activated by tissue- or cell-generated ROS.

In this context, the probe IR790s was recently used to generate a platform named perylene diimide –IR790s–Fe/Pt NPs to detect and trace ROS generation through ratiometric photoacoustic (PA) imaging. Perylene diimide showed a strong NIR light absorption at 680 nm, while IR790 absorbed light at 790 nm. The structure of IR790 could be cleaved by ROS, with a consequent decrease of its adsorption at 790 nm. Ratiometric PA imaging was achieved by irradiating the carriers at 680 and 790 nm. The increase in the Ab_{680}/Ab_{790} value was directly proportional to the ROS concentration. ROS generation was facilited by cisplatin conjugated on the surface of the particles *via* PEG and ferric anions chelated by the perylene diimide. The PEG modification also increased particle biocompatibility and permitted EPR extravasation *in vivo*. After cell internalization, the cell reductive environment (i.e., glutathione) favored the cisplatin release. Besides its cytostatic effect, it activated the nicotinamide adenine dinucleotide phosphate oxidase (NOX) enzyme that transformed the molecular oxygen in $O^{\cdot -}$ furtherly transformed in H_2O_2 *via* superoxide dismutase. The hydrogen peroxide could be further transformed in hydroxyl radical through a reaction catalyzed by the ferric ions inducing effective CDT (Yang et al., 2018b) (**Figure 2**). The synergistic effect of chemotherapy and CDT was confirmed by an improved *in vitro* and *in vivo* tumor cells killing. Qiao et al. (2018) developed a nanotheranostic platform to enhance the temozolomide effect in glioblastoma by reverting the tumor microenvironment immunosuppressive properties through the inhibition of TGF-β expression. The carriers were designed to (1) overcome the blood-brain barrier; (2) target to glioma cells; (3) escape from the endolysosomal compartment; (4) co-deliver temozolomide and the siRNA against TGF-β; (5) be tracked *via* MRI. The system consisted of superparamagnetic iron nanocubes (an excellent MRI contrast agent) encapsulated in poly[(2-acryloyl)ethyl(p-boronic acid benzyl)diethylammonium bromide] polymer loaded with the TGF-β siRNA and coated with zwitterionic lipids coordinating the drug. The particles were additionally modified on their surface with the peptide angiopep-2 targeting low-density lipoprotein receptor-related protein to favor particle translocation through the blood-brain barrier and cancer cell internalization. The system could escape from the endolysosomal compartment through the zwitterionic coating that, in acidic conditions, could acquire a net positive charge destabilizing the membrane of these organelles. Upon interaction with cellular ROS, the benzylboronic acid oxidized reversing the charge of the carriers from positive to negative. This phenomenon induced the release of the therapeutic payloads, and the iron nanoparticles exploited as a contrast agent for MRI.

The application of ROS-responsive theranostics was applied to different conditions. To decrease the generation of H_2O_2 in peripheral artery disease that negatively affects the neoangiogenesis process in this condition, Jung et al. generated a new concept of nanotheranostic to detect the diseased tissue through ultrasound and PA imaging (Jung et al., 2019). The system consisted of boronated maltodextrin that, in the presence of tissue H_2O_2, released 4-hydroxybenzyl alcohol with proven antioxidant and anti-inflammatory properties (Luo et al., 2017; Tan et al., 2018). Also, upon ROS interaction with the boronate, the system generated CO_2 bubbles with echogenic properties for ultrasound imaging. The nanoparticles were loaded with indocyanine green (ICG), allowing for multimodal fluorescent and PA imaging. The theranostic properties of these particles were successfully tested *in vitro* and *in vivo* in a model of hindlimb ischemia *via* intramuscular administration. H_2O_2 is considered a mild but very common ROS in hepatic ischemia/reperfusion injury, which is a potentially fatal condition for many conditions, including liver transplantation, liver surgical resection, and hemorrhagic shock (Ushitora et al., 2010). Kang et al. (2016) designed polymeric nanotheranostic based on poly(vanillin oxalate) that can serve as a scavenger for H_2O_2 while showing anti-inflammatory and antiapoptotic properties. These particles incorporated a prodrug form of vanillin, a compound known for its anti-inflammatory effect, but not extensively investigated in the clinic due to its short half-life. The molecule was loaded in the particles through H_2O_2-sensitive peroxalate ester linkers. More importantly, once activated by H_2O_2, the peroxalate esters decomposed in CO_2 bubbles that could be tracked *via* ultrasound imaging in a model of murine hepatic ischemia/reperfusion injury. In this case, the particles were not targeted to exploit their natural tropism toward the liver.

The development of ROS-responsive molecules showed promising results in preclinical testing. Despite their theranostic properties, they can also serve as *in vivo* nanosensors to measure ROS generation. The responsiveness of some material to ROS can be exploited to generate CO_2 for improving current ultrasound diagnostic methods. Besides, these technologies can be applied to different diseases, since the generation of ROS is a characteristic of various pathological conditions.

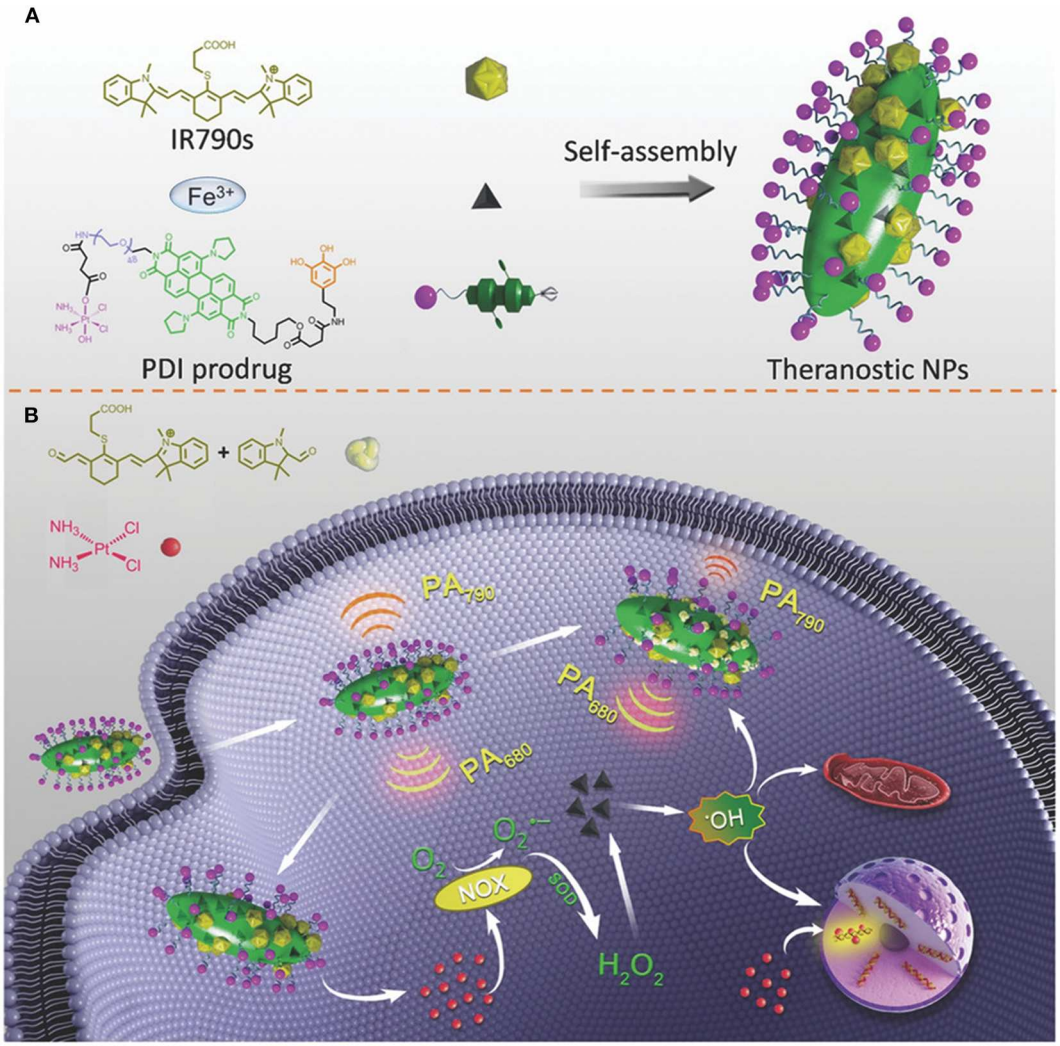

FIGURE 2 | (A) Self-assembly of perylene diimide cisplatin prodrug and the infrared dye IR790 in the presence of ferric ions. One of the amide groups of the PDI was modified with polyphenols coordinating the ferric ions necessary for catalyzing H_2O_2 in hydroxyl radical in acidic conditions. The second amide of the PDI was conjugated with PEG that increased nanoparticle solubility and allowed for further modification with the cisplatin prodrug. **(B)** The working mechanism of the system. After cancer cell internalization, the cisplatin induced the activation of the nicotinamide adenine dinucleotide phosphate oxidase (NOX) transforming molecular oxygen in $O^{\cdot -}$ with consequent generation of H_2O_2 *via* superoxide dismutase. The hydrogen peroxide is further transformed into hydroxyl radicals by the ferric ions inducing cell apoptosis. ROS formation degraded IR790. The measurement of the perylene diimide/IR790 absorption ratio could be used for ratiometric PA imaging of the ROS formation. Reproduced with permission from Yang et al. (2018b).

ENZYME RESPONSIVE THERANOSTICS

Tissue remodeling and the overexpression of the lytic enzymes that govern this process characterize many pathological conditions. These enzymes can be exploited as triggers since they can favor the degradation of the carriers and the consequent release of the theranostic payloads in the diseased area.

In the case of enzyme-responsive theranostics, are not rare examples of nanoparticles with multiple responsive properties. For instance, Chen et al. developed ferritin nanocages sensitive to pH and matrix metalloproteinase (MMP)-13 activity. The particles, named CMFn@HCQ, were conceived to deliver hydroxychloroquine in the cartilage tissue to ameliorate osteoarthritis conditions (Chen et al., 2019b). In osteoarthritis, the joint microenvironment is characterized by an acidic pH (close to 6) (Li et al., 2017) and MMP-13 overexpression. Ferritin was genetically modified to increase its targeting for collagen II through the addition of a specific peptide in its structure. These carriers were further modified with an MMP-13 cleavable peptide conjugated with the near-infrared (NIR) dye cy5.5 and a quencher to provide the system with enzyme-sensitive diagnostic properties. Because of this chemical modification, only after MMP-13 activity separating the dye and the quencher, the diagnostic signal could be registered. The particles were loaded with the anti-inflammatory hydroxychloroquine, and their structure degraded under acidic conditions inducing the

release of the payload. The resulting nanocages had a size of 20 nm, favoring their diffusion in the dense protein matrix of the joint. These carriers demonstrated high therapeutic properties as well as the ability to detect MMP-13 overexpression *in vitro* and *in vivo* when administered *via* intra-articular injections. Ren et al. (2019) engineered a carrier named HA-Ce6 DOX composed of a hyaluronic acid ultrastructure that, despite the ability to offer a natural targeting for the CD44 receptor, overexpressed on cancer cells, also granted the presence of multiple modification sites. The system was conjugated with Ce6 (for PDT and fluorescent detection) and DOX through a pH-sensitive hydrazine bond (**Figure 3**). The release of the photosensitizer and the chemotherapeutic was further accelerated by the enzyme hyaluronidase, overexpressed in the tumor microenvironment. The enzymatic degradation of the particles was fundamental for the activation of the diagnostic properties of the system since, when encapsulated, Ce6 was affected by the aggregation-caused quenching (ACQ) effect (Li et al., 2020b). CPT-loaded mesoporous silica nanoparticles were functionalized with a cyclo-RGD peptide, and another peptide conjugated with a fluorescent dye and a quencher. Both the peptides were sensitive to the proteolytic action of MMP2. Cyclo-RGD had the function of improving cancer cell targeting and stabilizing the drug in the carriers' pores. When the particles were internalized in the cells, both the peptides were digested inducing the quencher and the dye separation with consequent fluorescent signal detection and drug release (Hu et al., 2016). More investigation will be necessary to test the efficacy of this theranostic platform *in vivo*. Gold nanorods were used to generate a dual stimuli theranostic nanocarrier to provide efficient PTT as well as a detectable diagnostic signal in response to tumor pH and MMPs (Zhao et al., 2017). The gold nanorods were modified with an asymmetric cyanine *via* an MMP sensible linker. This dye could emit near-infrared fluorescence in a pH-dependent manner (Zhao et al., 2015), presenting a reversible "off/on" signal emission as a function of this parameter. Despite its sensitivity for the pH, the gold nanorods represented a significant FÖrster resonance energy transfer (FRET) quencher for the asymmetric cyanine that could emit the fluorescent signal only when in free form. Both the gold nanorods and the asymmetric cyanine allowed for PTT upon irradiation at 808 nm. Finally, drug delivery was achieved through an additional functionalization with glycosyl groups that significantly increased particle biocompatibility, EPR effect, and tumor targeting *via* GLUT-1 receptor. Liu et al. (2016b) designed a nanotheranostic system based on fluorescent quantum dots embedded in a nanoporous silica matrix with pH-activatable targeting properties and a protease-sensitive drug delivery mechanism. The system was surface modified with a zwitterionic anti-biofouling layer composed of chemical groups with positive and negative charges [COO^- and $-HN^+(Me)$, respectively]. In physiological pH conditions, the particles showed high circulation time, reduced sequestration in the organ of the mononuclear phagocytic system, and reduced protein corona formation due to their neutral surface charge. To this purpose, this strategy was previously demonstrated to be more effective and stable than PEG surface modification (Holmlin et al., 2001; Gui et al., 2013). When exposed to pH below 6.8, like in the tumor microenvironment, they acquired a positive charge favoring their uptake into the tumor cells. The pores of the silica could be loaded with a drug (DOX) and coated with the polymer polycaprolactone that was exploited to stabilize the drug in the particle structure. This polymer was sensitive to the enzyme esterase that is overexpressed and secreted by cancer cells, making tumor microenvironment and cells favorable sites for drug release. Also, it is important to highlight that the enzymatic degradation was further favored at acidic pH, where the particles acquired a positive charge and were more accessible to the enzyme and prone to cell internalization.

The enzyme-responsive theranostic working mechanism usually depends on hydrolytic enzymes favoring carrier or peptide linkers degradation. This phenomenon can also be exploited through coatings used to stabilized the therapeutics or the diagnostic molecules in the particles. The efficient application of enzyme-responsive theranostics strictly depends on the over-expression of some enzymes that can characterize different pathological conditions. Their synthesis relies on the engineering of biological substrates, usually functionalized with other molecules (including targeting modifications). Some of these modifications aim at providing higher biocompatibility and biological interaction, opening new avenues of research in the field of bioinspired nanomedicine.

THERANOSTICS RESPONSIVE TO OTHER BIOLOGICAL STIMULI

Glutathione (GSH) is a reactive molecule controlling the cellular redox balance. Cancer cells significantly overexpress this molecule, pointing out its potential role as a targetable trigger for the development of smart nanotheranostics (Liu et al., 2016a). To this purpose, theranostic platforms based on GSH reactivity are usually composed of a targeted particle modified with a disulfide bond coordinating a chemotherapeutic and/or a fluorescent probe (Han et al., 2017). A typical example of GSH-responsive theranostic based on a facile synthesis is represented by nanoparticles generated through hydrophilic polymers conjugated with hydrophobic drugs. The amphiphilic monomers can favor nanoparticle self-assembly, leaving room for further modification with a diagnostic probe. Exploiting these principals, Li et al. (2019b) generated multimodal imaging and therapeutic nanotheranostics named DHP. These carriers consisted of a disulfide-bond-linked hydroxyethyl starch conjugated with the chemotherapeutic paclitaxel (PXT). The addition of dioctadecyl-3,3,3,3-tetramethylindotricarbocyanine iodide (DiR) in the synthesis solution resulted in the entrapment of the dye in the hydrophobic core of the particles through one single step of dialysis. DiR allowed for both fluorescent and PA imaging, and when irradiated with at 808 nm, PTT providing synergistic effects with the chemotherapeutic. When packaged within the nanoparticle structure, the dye was affected by ACQ. However, after particle internalization, the cellular GSH induced the release of the theranostic payloads (Li et al., 2019b) (**Figure 4**). These properties were proven *in vitro* and *in vivo*

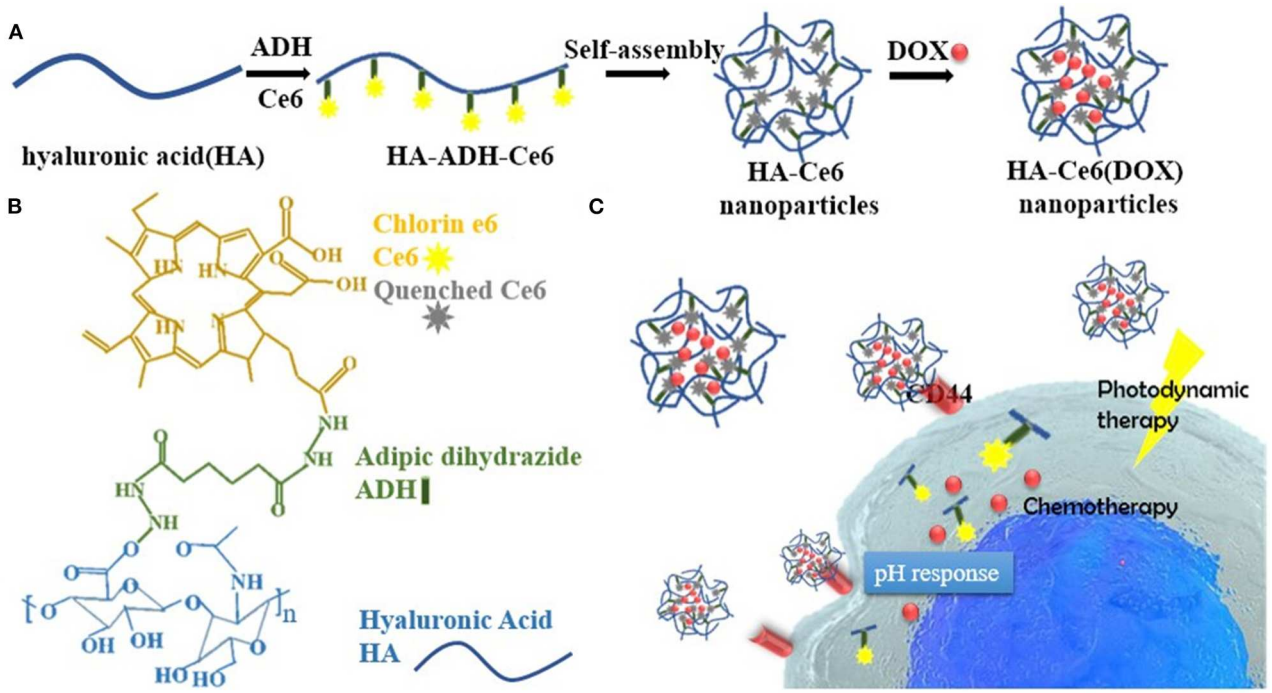

FIGURE 3 | (A) Synthetic process of HA-Ce6 (DOX) nanoparticles. Hyaluronic acid (HA) and adipic dihydrazide (ADH) were dissolved in the presence of Ce6-NHS ester and EDCI catalyzing the reaction of particle self-assembly in acidic conditions. Doxorubicin (DOX) loading was performed post-synthesis. **(B)** Illustration of the different components forming the particles. **(C)** the working mechanism of HA-Ce6 (DOX). After intravenous injection, the particles targeted the tumor *via* EPR and were internalized by the cancer cells through the CD44 HA receptor. In tumor microenvironment and cells, the particle could dissolve releasing DOX and Ce6, whose fluorescence was previously inhibited by the presence of a quencher in particle structure. Particle degradation was favored by the acidic conditions acting on the pH-sensitive hydrazine linkers and by the enzyme hyaluronidase degrading the nanoparticle matrix. Reproduced with permission from Ren et al. (2019).

in a model of breast cancer. These particles could efficiently accumulate in the tumor *via* EPR due to the high circulation properties offered by the hydroxyethyl starch. Similarly, a GSH-sensitive platform was synthesized through low molecular weight heparin polymerization that, in the presence of cystamine, polymerized with Ce6 in biocompatible carriers (Yang et al., 2018a). In addition, heparin was previously shown to possess antimetastatic and anti-angiogenic properties (Yang et al., 2015; Mei et al., 2017). The system offered sensitivity to a reductive environment since the cystamine linker contained a disulfide bond in its structure. GSH induced particle degradation and Ce6 release activating the theranostic properties of the dye that, when encapsulated, was affected by the ACQ effect. Finally, the system was also loaded with PXT in combination with alpha-tocopherol succinate (Yang et al., 2018a) to provide therapeutic synergism between chemotherapy and PDT. When injected intravenously, the particles accumulated *via* EPR in a model of 4T1 breast cancer. After cell internalization, the particles were degraded by the abundant levels of GSH releasing PXT and Ce6 that in free form was easily detectable through NIR imaging and inducible for PDT. Song et al. (2017) engineered iron oxide nanoparticles to be responsive to ATP, which is highly generated in tumor cells when compared to healthy tissue as well as to a decrease in tissue pH. The system was composed of small clusters of superparamagnetic iron nanoparticles and tannic acid that self-assembled in water-soluble aggregates smaller than 100 nm due to hydrophobic interactions. The particles were modified with ICG and DSPE-PEG *via* non-covalent hydrophobic interactions and hydrogen bonds, respectively. The presence of PEG increased particle circulation and tumor accumulation *via* EPR. The core of iron oxide permitted strong MRI properties while its high affinity for ATP induced particle disassembly in the presence of this molecule (Yu et al., 2013). On the other hand, the ICG permitted particle fluorescence detection after degradation (since the dye was affected by the ACQ effect) as well as PTT applications when irradiated at 808 nm. Particle degradation was further boosted in acidic pH, perhaps due to the protonation of the hydroxyl groups of the tannic acid that lowered the affinity of this molecule for the iron oxide nanoparticle structure. The disassembly of the system was pivotal to activate its imaging properties as well as its renal clearance. The system was successfully tested i*n vitro* and *in vivo* in a subcutaneous tumor model for its theranostic and responsiveness properties obtained through facile synthesis and loading protocols.

Biological responsiveness was also used to ameliorate the conditions of diseases different than cancer. In Alzheimer's disease, the aberrant generation of plaques of soluble β-Amyloid proteins in the central nervous system occurs (Benilova et al., 2012). This phenomenon is favored by the accumulation of

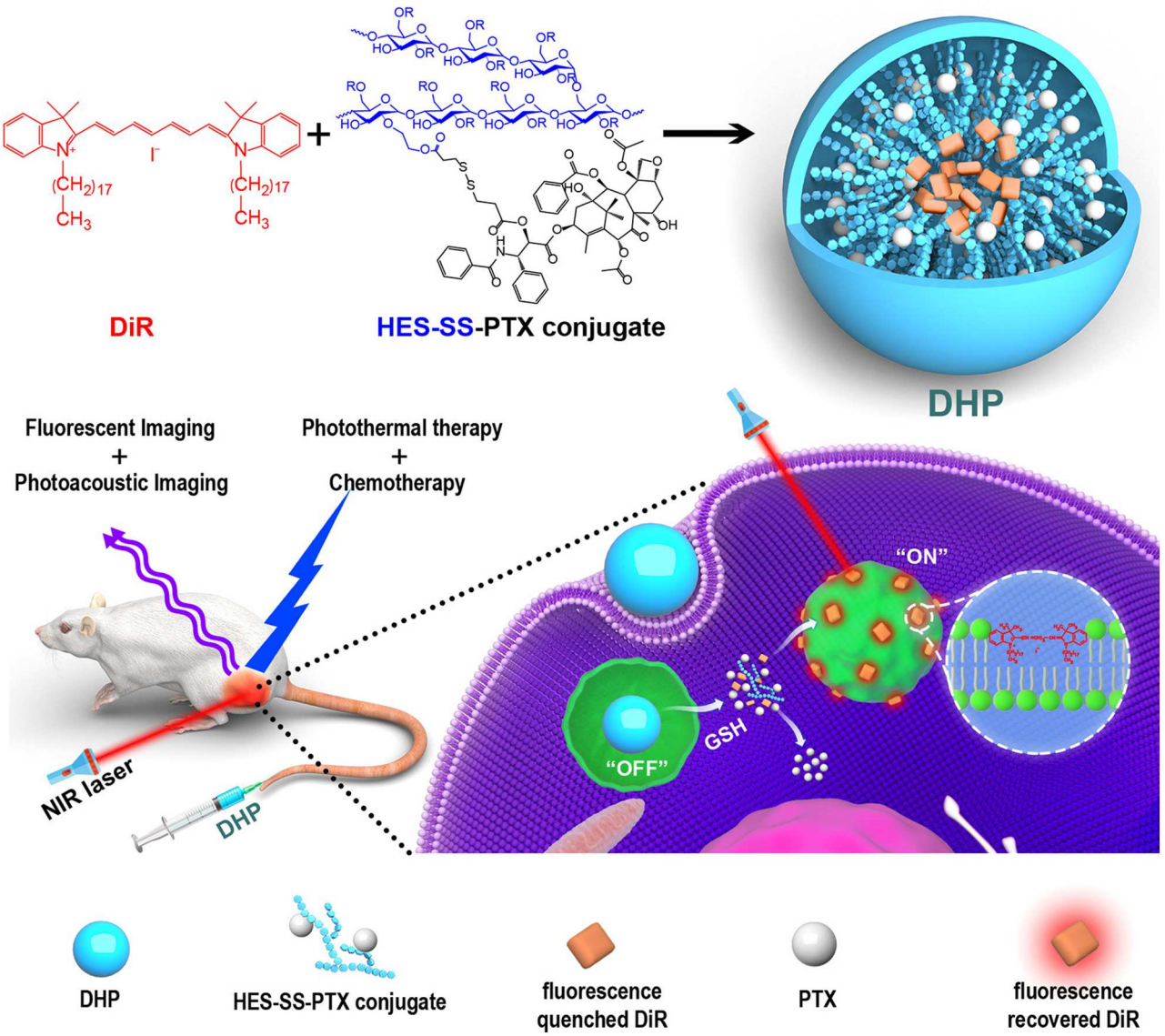

FIGURE 4 | The major components of DHP nanoparticles are the disulfide-bond-linked hydroxyethyl starch paclitaxel conjugate (HES-SS-PTX) and the near-infrared dye cyanine fluorophore DiR. The particles were designed to exert dual imaging (fluorescent and photoacoustic imaging) and dual therapy (photothermal and chemotherapy) properties. The HES shell provided the particles with EPR properties. After intravenous injection, the particles could accumulate in the tumor microenvironment and be internalized inside the cells. In the cell cytoplasm, the disulfide bond degradation occurred due to the cellular GSH that favored the release of PXT (chemotherapy) and DiR. When encapsulated in the particles, DiR was affected by ACQ, but upon its release, it could exert its therapeutic (photothermal therapy) and diagnostic (photoacoustic and fluorescent imaging) properties. Reproduced with permission from Li et al. (2019b).

metal ions in the tissue like copper, which *via* ROS generation can support protein aggregation (Atwood et al., 2018). Cui et al. designed upconversion NaYF4:Yb/Er/Tm nanocrystals conjugated with 8-hydroxyquinoline-2-carboxylic (HQC) and DSPE-PEG to provide the carriers with diagnostic, therapeutic and biocompatibility properties, respectively (Cui et al., 2016). The particles were designed to (1) detect Cu^{2+} *via* luminescence resonance energy transfer from the particle to the copper, (2) targeting and imaging of the β-Amyloid- Cu^{2+} complexes by registering the upconverted light signal emitted further NIR light irradiation (demonstrated *in vitro* and *ex-vivo*) (3) chelate the copper *via* HCQ. The theranostic properties of this system were successfully proven in a zebrafish model and *ex-vivo*.

These examples demonstrated that any reactive molecules could be exploited as a tool to generate responsive nanoparticles. GSH, in particular, was extensively investigated in literature for this purpose since cancer cells are characterized by a very high content of this molecule. On the other hand, they are also characterized by the high generation of ROS. For this reason, further advances in the field need to take into consideration the

TABLE 1 | Summary table of the different technologies and their theranostic properties.

Stimulus	Nanocarrier	Size (nm)	Administration/ targeting	Disease/therapeutic	Imaging	References
pH	poly(amidoamine) dendrimers	2.8	N.A./FA vs. FAr	TU/DOX (Ch.T.)	Au NP (CT)	(Zhu et al., 2018)
	graphene oxide/BSA/PheoA NP	182	IV/FA vs. Far	TU/PheoA (PDT)+GO (PTT)	PheoA (FL)	(Battogtokh and Ko, 2016)
	CaCO3 NP	140	IV/EPR	TU/Ce6(PDT)+ Ch.T. (DOX)+Mn (CDT)	Mn (MRI)+ Ce6 (FL)	(Dong et al., 2016)
	MnCO3/FeO/Se NP	100	IV/ EPR	TU/Mn and Se (CDT+limotherapy)	Mn (MRI)	(Xiao et al., 2019)
	magnetic mesoporous nanocubes (MMM)	142	IV//EPR+ magnetic guidance+FA vs. FAr	TU/Vc (CDT)+MMM (HT)	MMM (MRI)	(Li et al., 2020a)
pH+ enzyme	Ferritin nanocages	20	Intrarticular/ pep vs. collII	Osteoarthritis/ hydroxychloroquine (AI)	Cy5.5 (FL)	(Chen et al., 2019a)
	Hyaluronic acid (HA) NP	90	N.A./HA vs CD44	TU/DOX (Ch.T)+ Ce6 (PDT)	Ce6 (FL)	(Ren et al., 2019)
	Mesoporous silica	200	N.A./EPR	TU/DOX (Ch.T.)	Quantum dots (FL)	(Liu et al., 2016b)
pH+ enzyme+NIR	Gold nanorods	50 × 12	IV/glycosyl groups vs. GLUT-1	TU/gold nanorods and asymmetric cyanine (PTT)	Asymmetric cyanine(FL)	(Zhao et al., 2017)
pH + ATP	Fe/tannic acid NP	79	IV/ EPR	TU/ICG (PTT)	Fe (MRI)+ ICG(FL)	(Song et al., 2017)
pH+GSH	BSA/MNO2 NP	160	IV/EPR	TU/CIS (Ch.T)+hafnium (RT)	Mn (MRI)	(Liu et al., 2017)
ROS	superparamagnetic Fe nanocubes	120	IV/angiopep-2 vs LRP1	TU/TMZ (Ch.T)+TGFβ siRNA	Fe (MRI)	(Qiao et al., 2018)
	boronated maltodextrin NP	350	IM/N.A.	Peripheral artery disease/4HBA (Sc,AI)	CO_2 (US)+ ICG (PA)	(Jung et al., 2019)
	Poly(vanillineoxalate) NP	550	IV/N.A.	Hepatic ischemia/reperfusion injury/ Vanillin (Sc.)	CO_2 (US)	(Kang et al., 2016)
ROS + GSH	perylene diimide NP	120	IV/EPR	TU/CIS (Ch.T)+/Fe (CDT)	PDI/IR790 (ratiometric PA)	(Yang et al., 2018b)
GSH. + NIR	hydroxyethyl starch NP	160	IV/N.A.	TU/PXY (Ch.T)+DiR (PTT)	DiR (FL+ PA)	(Li et al., 2019b)
	Heparin/cystamine NP	211	IV/EPR	TU/Ce6 (PDT)+PXY (Ch.T.)	Ce6 (FL)	(Yang et al., 2018a)
Cu	upconversion NaYF4:Yb/Er/Tm nanocrystals	27	N.A./Cu	Alzheimer's disease/HCQ (Cu chelation)	luminescence resonance energy transfer	(Cui et al., 2016)
MMP-2	Mesoporous silica	150	N.A./cRGD vs integrin	TU/CPT (Ch.T.)	TAMRA (FL)	(Hu et al., 2016)

AI, anti inflammatory; Ch.T., Chemotherapy; CDT, Chemodynamic therapy; CPT, Camptothecin; DOX, Doxorubicin; EPR, Enhanced permeability and retention effect; FA, Folic acid; Far, Folic acid receptor; FL, Fluorescence; GO, Graphen Oxide; GSH, Glutathione; HA, Hyaluronic acid; HT, Hyperthermal therapy; IV, intravenous; LRP1, low-density lipoprotein receptor related protein 1; MMP, Matrix metallo proteinases; MRI, Magnetic resonance Imaging; NIR, Nearinfrared light; NP, Nanoparticles; PA, Photoacoustic imaging; PDT, Photodynamic tehrapy; Pep, peptide; PTT, Photheral therapy; PXT, Paclitaxel; ROS, Reactive oxygen species; RT, Radiotherapy; Sc, scavenger; TU, Tumor; US, Ultrasound imaging.

efficient alteration of this balance, both when generating GSH- as well as ROS-responsive carriers.

CONCLUSIONS

The fine-tuning of the therapeutic regimens and diagnostic methods represents an emerging need in all the fields of experimental medicine. Current efforts of the scientific community are paving the way to achieve this goal through the generation of materials that are sensitive and can respond to chemical, physical, and biological triggers. Therapeutic and diagnostic properties can reside in the same molecule embedded in the nanocarrier structure that can be activated at the injury site, or they can independently derive from different chemicals loaded into and/or conjugated onto the surface of the nanoparticles. Also, the very same structure of the particles can alternatively provide therapeutic or diagnostic properties. In this work, we presented some examples of pathological stimuli-responsive theranostics with multiple therapeutic and diagnostic properties,

sometimes combined with external stimuli-responsive materials (**Table 1**). The goal of this work was to present the current strategies and materials used for imparting the theranostics with biological-responsiveness.

To our knowledge, no nanotheranostic was FDA approved to date (Anselmo and Mitragotri, 2019). However, clinical trials are currently active to evaluate their efficacy and safety. In this effort, most of the theranostic under clinical trials base their working mechanisms on remotely applied stimuli. In particular, iron (Nardecchia et al., 2019) and gold (Pedrosa et al., 2015) nanoparticles are extensively tested in humans for their multimodal imaging modalities, PDT and PTT properties as well as for their relatively easy synthesis and functionalization. External stimuli-responsive carriers activation strongly depends on the penetration and the precision of the external signal, and most importantly, they can be activated only in the areas that current diagnostic tools detect as disease sites. On the other hand, the responsiveness of theranostics to pathological stimuli theoretically depends solely on their ability to target the environmental conditions of the diseased tissue or cell, with no further interventions of external procedures. In this context, they could reveal and be activated in sick areas that were not detected by other imaging tools. Precise targeting, therefore, represents their main limitation. Due to the complex nature of these technologies, targeting is usually imparted through the pegylation of the carriers and depends on their passive accumulation in the diseased tissue through the EPR effect. However, this kind of targeting could jeopardize their responsiveness. For example, in some cases, the carriers need to be internalized in the cells to perform their theranostic functions while PEG functionalization could affect this process (Moros et al., 2012). The complexity of their synthesis protocols, as well as their low biocompatibility and inherent toxicity, represent other significant limitations in the clinical translation of these technologies (Kunjachan et al., 2015). However, more investigations on the development of theranostic molecules like porphyrins, Ce6, or Mn^{2+} could streamline their synthetic routes while combining the advantages of external- and biological-responsive theranostics. Finally, relying on biological stimuli, they could suffer from unspecific activation in other tissues (i.e., the organs of the mononuclear phagocytic system). For this reason, more research to evaluate their adverse effect, metabolization, and excretion is necessary for future developments.

AUTHOR CONTRIBUTIONS

AP and YA: conceptualization. AP and MR writing (original draft preparation). SL review and editing. AZ supervision and funding acquisition.

FUNDING

This research was supported by the Russian Science Foundation (grant # 16-15-10410) and by the Russian Academic Excellence Project 5-100.

REFERENCES

Anselmo, A. C., and Mitragotri, S. (2019). Nanoparticles in the clinic: an update. *Bioeng. Trans. Med.* 4:e10143. doi: 10.1002/btm2.10143

Atwood, C. S., Huang, X., Moir, R. D., Tanzi, R. E., and Bush, A. I. (2018). "Role of free radicals and metal ions in the pathogenesis of alzheimer's disease," in *Metal Ions in Biological Systems* (Routledge: CRC Press, Taylor and Francis publishing group- New york), 309–364. doi: 10.1201/9780203747605-10

Battogtokh, G., and Ko, Y. T. (2016). Graphene oxide-incorporated pH-responsive folate-albumin-photosensitizer nanocomplex as image-guided dual therapeutics. *J. Control. Release* 234, 10–20. doi: 10.1016/j.jconrel.2016.05.007

Benilova, I., Karran, E., and De Strooper, B. (2012). The toxic Aβ oligomer and alzheimer's disease: an emperor in need of clothes. *Nat. Neurosci.* 15, 349–57. doi: 10.1038/nn.3028

Cao, Z., Li, W., Liu, R., Li, X., Li, H., Liu, L., et al. (2019). pH-and enzyme-triggered drug release as an important process in the design of anti-tumor drug delivery systems. *Biomed. Pharmacother.* 118:109340. doi: 10.1016/j.biopha.2019.109340

Cao, Z., Zhang, L., Liang, K., Cheong, S., Boyer, C., Gooding, J. J., et al. (2018). Biodegradable 2D Fe-Al hydroxide for nanocatalytic tumor-dynamic therapy with tumor specificity. *Adv. Sci.* 5:1801155. doi: 10.1002/advs.201801155

Chen, C., Gao, K., Lian, H., Chen, C., and Yan, X. (2019a). Single-particle characterization of theranostic liposomes with stimulus sensing and controlled drug release properties. *Biosens. Bioelectron.* 131, 185–192. doi: 10.1016/j.bios.2019.02.016

Chen, H., Qin, Z., Zhao, J., He, Y., Ren, E., Zhu, Y., et al. (2019b). Cartilage-targeting and dual MMP-13/pH responsive theranostic nanoprobes for osteoarthritis imaging and precision therapy. *Biomaterials* 225:119520. doi: 10.1016/j.biomaterials.2019.119520

Chen, H., Tian, J., He, W., and Guo, Z. (2015). H_2O_2-activatable and O_2-evolving nanoparticles for highly efficient and selective photodynamic therapy against hypoxic tumor cells. *J. Am. Chem. Soc.* 137, 1539–1547. doi: 10.1021/ja511420n

Cui, Z., Bu, W., Fan, W., Zhang, J., Ni, D., Liu, Y., et al. (2016). Sensitive imaging and effective capture of Cu2+: towards highly efficient theranostics of alzheimer's disease. *Biomaterials* 104, 158–167. doi: 10.1016/j.biomaterials.2016.06.056

Das, T. K., Wati, M. R., and Fatima-Shad, K. (2015). Oxidative stress gated by fenton and haber weiss reactions and its association with alzheimer's disease. *Arch. Neurosci.* 2:e60038. doi: 10.5812/archneurosci.20078

Desideri, E., Ciccarone, F., and Ciriolo, M. R. (2019). Targeting glutathione metabolism: partner in crime in anticancer therapy. *Nutrients* 11:1926. doi: 10.3390/nu11081926

Dong, Z., Feng, L., Zhu, W., Sun, X., Gao, M., Zhao, H., et al. (2016). $CaCO_3$ nanoparticles as an ultra-sensitive tumor-pH-responsive nanoplatform enabling real-time drug release monitoring and cancer combination therapy. *Biomaterials* 110, 60–70. doi: 10.1016/j.biomaterials.2016.09.025

Dunn, J. D., Alvarez, L. A., Zhang, X., and Soldati, T. (2015). Reactive oxygen species and mitochondria: a nexus of cellular homeostasis. *Redox Biol.* 6, 472–485. doi: 10.1016/j.redox.2015.09.005

Fan, Z., Sun, L., Huang, Y., Wang, Y., and Zhang, M. (2016). Bioinspired fluorescent dipeptide nanoparticles for targeted cancer cell imaging and real-time monitoring of drug release. *Nat. Nanotechnol.* 11, 388–94. doi: 10.1038/nnano.2015.312

Gui, A. L., Luais, E., Peterson, J. R., and Gooding, J. J. (2013). Zwitterionic phenyl layers: finally, stable, anti-biofouling coatings that do not passivate electrodes. *ACS Appl. Mater. Interfaces* 5, 4827–4835. doi: 10.1021/am400519m

Han, L., Zhang, X.-Y., Wang, Y.-L., Li, X., Yang, X.-H., Huang, M., et al. (2017). Redox-responsive theranostic nanoplatforms based on inorganic nanomaterials. *J. Control. Release* 259, 40–52. doi: 10.1016/j.jconrel.2017.03.018

Holmlin, R. E., Chen, X., Chapman, R. G., Takayama, S., and Whitesides, G. M. (2001). Zwitterionic SAMs that resist nonspecific adsorption of protein from aqueous buffer. *Langmuir* 17, 2841–2850. doi: 10.1021/la0015258

Hu, J.-J., Liu, L.-H., Li, Z.-Y., Zhuo, R.-X., and Zhang, X.-Z. (2016). MMP-responsive theranostic nanoplatform based on mesoporous silica nanoparticles for tumor imaging and targeted drug delivery. *J. Mater. Chem. B* 4, 1932–1940. doi: 10.1039/C5TB02490K

Idris, S., Arifah, A., Jesse, F., Ramanoon, S., Basit, M., Zakaria, Z., et al. (2019). Synthesis, characterization, and *in vitro* release of oxytetracycline loaded in pH-responsive $CaCO_3$ nanoparticles. *J. Appl. Pharm. Sci.* 9, 019–027. doi: 10.7324/JAPS.2019.91103

Jo, S. D., Ku, S. H., Won, Y.-Y., Kim, S. H., and Kwon, I. C. (2016). Targeted nanotheranostics for future personalized medicine: recent progress in cancer therapy. *Theranostics* 6, 1362–1377. doi: 10.7150/thno.15335

Jung, E., Lee, J., Jeong, L., Park, S., Lee, M., Song, C., et al. (2019). Stimulus-activatable echogenic maltodextrin nanoparticles as nanotheranostic agents for peripheral arterial disease. *Biomaterials* 192, 282–291. doi: 10.1016/j.biomaterials.2018.11.022

Kanamala, M., Wilson, W. R., Yang, M., Palmer, B. D., and Wu, Z. (2016). Mechanisms and biomaterials in pH-responsive tumour targeted drug delivery: a review. *Biomaterials* 85, 152–167. doi: 10.1016/j.biomaterials.2016.01.061

Kang, C., Cho, W., Park, M., Kim, J., Park, S., Shin, D., et al. (2016). H_2O_2-triggered bubble generating antioxidant polymeric nanoparticles as ischemia/reperfusion targeted nanotheranostics. *Biomaterials* 85, 195–203. doi: 10.1016/j.biomaterials.2016.01.070

Karimi, M., Ghasemi, A., Zangabad, P. S., Rahighi, R., Basri, S. M. M., Mirshekari, H., et al. (2016). Smart micro/nanoparticles in stimulus-responsive drug/gene delivery systems. *Chem. Soc. Rev.* 45, 1457–1501. doi: 10.1039/C5CS00798D

Kim, T. H., Lee, S., and Chen, X. (2013). Nanotheranostics for personalized medicine. *Expert Rev. Mol. Diagn.* 13, 257–269. doi: 10.1586/erm.13.15

Kunjachan, S., Ehling, J., Storm, G., Kiessling, F., and Lammers, T. (2015). Noninvasive imaging of nanomedicines and nanotheranostics: principles, progress, and prospects. *Chem. Rev.* 115, 10907–10937. doi: 10.1021/cr500314d

Li, C., Li, H., Wang, Q., Zhou, M., Li, M., Gong, T., et al. (2017). pH-sensitive polymeric micelles for targeted delivery to inflamed joints. *J. Control. Release* 246, 133–141. doi: 10.1016/j.jconrel.2016.12.027

Li, F., Liang, Z., and Ling, D. (2019a). Smart organic-inorganic nanogels for activatable theranostics. *Curr. Med. Chem.* 26, 1366–1376. doi: 10.2174/0929867324666170920164614

Li, J., Liu, Y., Li, X., Liang, G., Ruan, C., and Cai, K. (2020a). ROS self-generation and hypoxia self-enhanced biodegradable magnetic nanotheranostics for targeted tumor therapy. *Nanoscale Horizons*. 5, 350–358 doi: 10.1039/C9NH00490D

Li, J., Wang, J., Li, H., Song, N., Wang, D., and Tang, B. Z. (2020b). Supramolecular materials based on AIE luminogens (AIEgens): construction and applications. *Chem. Soc. Rev*. 49, 1144–1172. doi: 10.1039/C9CS00495E

Li, Y., Wu, Y., Chen, J., Wan, J., Xiao, C., Guan, J., et al. (2019b). A simple glutathione-responsive turn-on theranostic nanoparticle for dual-modal imaging and chemo-photothermal combination therapy. *Nano Lett.* 19, 5806–5817. doi: 10.1021/acs.nanolett.9b02769

Lin, H., Chen, Y., and Shi, J. (2018). Nanoparticle-triggered in situ catalytic chemical reactions for tumour-specific therapy. *Chem. Soc. Rev.* 47, 1938–1958. doi: 10.1039/C7CS00471K

Liu, D., Yang, F., Xiong, F., and Gu, N. (2016a). The smart drug delivery system and its clinical potential. *Theranostics* 6, 1306–1323. doi: 10.7150/thno.14858

Liu, J., Chen, Q., Zhu, W., Yi, X., Yang, Y., Dong, Z., et al. (2017). Nanoscale-coordination-polymer-shelled manganese dioxide composite nanoparticles: a multistage Redox/pH/H_2O_2-responsive cancer theranostic nanoplatform. *Adv. Func. Mater.* 27:1605926. doi: 10.1002/adfm.201605926

Liu, J., Huang, Y., Kumar, A., Tan, A., Jin, S., Mozhi, A., et al. (2014a). pH-sensitive nano-systems for drug delivery in cancer therapy. *Biotechnol. Adv.* 32, 693–710. doi: 10.1016/j.biotechadv.2013.11.009

Liu, P., Yue, C., Sheng, Z., Gao, G., Li, M., Yi, H., et al. (2014b). Photosensitizer-conjugated redox-responsive dextran theranostic nanoparticles for near-infrared cancer imaging and photodynamic therapy. *Polym. Chem.* 5, 874–881. doi: 10.1039/C3PY01173A

Liu, Z., Chen, X., Zhang, X., Gooding, J. J., and Zhou, Y. (2016b). Carbon-quantum-dots-loaded mesoporous silica nanocarriers with pH-switchable zwitterionic surface and enzyme-responsive pore-cap for targeted imaging and drug delivery to tumor. *Adv. Healthc. Mater.* 5, 1401–1407. doi: 10.1002/adhm.201600002

Luo, L., Kim, S.-W., Lee, H.-K., Kim, I.-D., Lee, H., and Lee, J.-K. (2017). Anti-oxidative effects of 4-hydroxybenzyl alcohol in astrocytes confer protective effects in autocrine and paracrine manners. *PLoS ONE* 12:e0177322. doi: 10.1371/journal.pone.0177322

Lv, H., Wang, C., Fang, T., Li, T., Lv, G., Han, Q., et al. (2018). Vitamin C preferentially kills cancer stem cells in hepatocellular carcinoma via SVCT-2. *NPJ Precis. Oncol.* 2:1. doi: 10.1038/s41698-017-0044-8

Ma, Y., Huang, J., Song, S., Chen, H., and Zhang, Z. (2016). Cancer-targeted nanotheranostics: recent advances and perspectives. *Small* 12, 4936–4954. doi: 10.1002/smll.201600635

Mei, L., Liu, Y., Xia, C., Zhou, Y., Zhang, Z., and He, Q. (2017). Polymer-drug nanoparticles combine doxorubicin carrier and heparin bioactivity functionalities for primary and metastatic cancer treatment. *Mol. Pharm.* 14, 513–522. doi: 10.1021/acs.molpharmaceut.6b00979

Modica-Napolitano, J. S., and Aprille, J. R. (2001). Delocalized lipophilic cations selectively target the mitochondria of carcinoma cells. *Adv. Drug Deliv. Rev.* 49, 63–70. doi: 10.1016/S0169-409X(01)00125-9

Moros, M., HernáEz, B., Garet, E., Dias, J. T., SáEz, B., Graz,ú, V., et al. (2012). Monosaccharides versus PEG-functionalized NPs: influence in the cellular uptake. *ACS Nano* 6, 1565–1577. doi: 10.1021/nn204543c

Nardecchia, S., Sánchez-Moreno, P., De Vicente, J., Marchal, J. A., and Boulaiz, H. (2019). Clinical trials of thermosensitive nanomaterials: an overview. *Nanomaterials* 9:191. doi: 10.3390/nano9020191

Pedrosa, P., Vinhas, R., Fernandes, A., and Baptista, P. V. (2015). Gold nanotheranostics: proof-of-concept or clinical tool? *Nanomaterials* 5, 1853–1879. doi: 10.3390/nano5041853

Qiao, C., Yang, J., Shen, Q., Liu, R., Li, Y., Shi, Y., et al. (2018). Traceable nanoparticles with dual targeting and ROS response for RNAi-based immunochemotherapy of intracranial glioblastoma treatment. *Adv. Mater.* 30:1705054. doi: 10.1002/adma.201705054

Ren, Q., Liang, Z., Jiang, X., Gong, P., Zhou, L., Sun, Z., et al. (2019). Enzyme and pH dual-responsive hyaluronic acid nanoparticles mediated combination of photodynamic therapy and chemotherapy. *Int. J. Biol. Macromol.* 130, 845–852. doi: 10.1016/j.ijbiomac.2019.03.030

Shamsi, M., Saghafian, M., Dejam, M., and Sanati-Nezhad, A. (2018). Mathematical modeling of the function of warburg effect in tumor microenvironment. *Sci. Rep.* 8:8903. doi: 10.1038/s41598-018-27303-6

Silva, C. O., Pinho, J. O., Lopes, J. M., Almeida, A. J., Gaspar, M. M., and Reis, C. (2019). Current trends in cancer nanotheranostics: metallic, polymeric, and lipid-based systems. *Pharmaceutics* 11:22. doi: 10.3390/pharmaceutics11010022

Sneider, A., Vandyke, D., Paliwal, S., and Rai, P. (2017). Remotely triggered nano-theranostics for cancer applications. *Nanotheranostics* 1, 1–22. doi: 10.7150/ntno.17109

Song, X. R., Li, S. H., Dai, J., Song, L., Huang, G., Lin, R., et al. (2017). Polyphenol-inspired facile construction of smart assemblies for ATP-and pH-responsive tumor MR/optical imaging and photothermal therapy. *Small* 13:1603997. doi: 10.1002/smll.201603997

Sun, C.-Y., Cao, Z., Zhang, X.-J., Sun, R., Yu, C.-S., and Yang, X. (2018). Cascade-amplifying synergistic effects of chemo-photodynamic therapy using ROS-responsive polymeric nanocarriers. *Theranostics* 8, 2939–2953. doi: 10.7150/thno.24015

Tan, J., Deng, Z., Liu, G., Hu, J., and Liu, S. (2018). Anti-inflammatory polymersomes of redox-responsive polyprodrug amphiphiles with inflammation-triggered indomethacin release characteristics. *Biomaterials* 178, 608–619. doi: 10.1016/j.biomaterials.2018.03.035

Tekade, R. K., and Sun, X. (2017). The Warburg effect and glucose-derived cancer theranostics. *Drug Discov. Today* 22, 1637–1653. doi: 10.1016/j.drudis.2017.08.003

Trachootham, D., Alexandre, J., and Huang, P. (2009). Targeting cancer cells by ROS-mediated mechanisms: a radical therapeutic approach? *Nat. Rev. Drug Discov.* 8, 579–591. doi: 10.1038/nrd2803

Ushitora, M., Sakurai, F., Yamaguchi, T., Nakamura, S.-I., Kondoh, M., Yagi, K., et al. (2010). Prevention of hepatic ischemia-reperfusion injury by pre-administration of catalase-expressing adenovirus vectors. *J. Control. Release* 142, 431–437. doi: 10.1016/j.jconrel.2009.11.024

Vidallon, M. L. P., Douek, A. M., Quek, A., Mcliesh, H., Kaslin, J., Tabor, R. F., et al. (2020). Gas-generating, pH-responsive calcium carbonate hybrid particles with biomimetic coating for contrast-enhanced ultrasound imaging. *Part. Part. Syst. Char.* 37:1900471. doi: 10.1002/ppsc.201900471

Wang, J., Macewan, S. R., and Chilkoti, A. (2017a). Quantitative mapping of the spatial distribution of nanoparticles in endo-lysosomes by local pH. *Nano Lett.* 17, 1226–1232. doi: 10.1021/acs.nanolett.6b05041

Wang, J., Tao, W., Chen, X., Farokhzad, O. C., and Liu, G. (2017b). Emerging advances in nanotheranostics with intelligent bioresponsive systems. *Theranostics* 7, 3915–3919. doi: 10.7150/thno.21317

Wong, X. Y., Sena-Torralba, A., Alvarez-Diduk, R., Muthoosamy, K., and Merkoçi, A. (2020). Nanomaterials for nanotheranostics: tuning their properties according to disease needs. *ACS Nano* 14, 2585–2627. doi: 10.1021/acsnano.9b08133

Wu, X., Sun, X., Guo, Z., Tang, J., Shen, Y., James, T. D., et al. (2014). *In vivo* and *in situ* tracking cancer chemotherapy by highly photostable NIR fluorescent theranostic prodrug. *J. Am. Chem. Soc.* 136, 3579–3588. doi: 10.1021/ja412380j

Xiao, J., Zhang, G., Xu, R., Chen, H., Wang, H., Tian, G., et al. (2019). A pH-responsive platform combining chemodynamic therapy with limotherapy for simultaneous bioimaging and synergistic cancer therapy. *Biomaterials* 216:119254. doi: 10.1016/j.biomaterials.2019.119254

Xiao, M., Sun, W., Fan, J., Cao, J., Li, Y., Shao, K., et al. (2018). Aminopeptidase-N-activated theranostic prodrug for NIR tracking of local tumor chemotherapy. *Adv. Func. Mater.* 28:1805128. doi: 10.1002/adfm.201805128

Yan, X., Niu, G., Lin, J., Jin, A. J., Hu, H., Tang, Y., et al. (2015). Enhanced fluorescence imaging guided photodynamic therapy of sinoporphyrin sodium loaded graphene oxide. *Biomaterials* 42, 94–102. doi: 10.1016/j.biomaterials.2014.11.040

Yang, G., Sun, X., Liu, J., Feng, L., and Liu, Z. (2016a). Light-responsive, singlet-oxygen-triggered on-demand drug release from photosensitizer-doped mesoporous silica nanorods for cancer combination therapy. *Adv. Func. Mater.* 26, 4722–4732. doi: 10.1002/adfm.201600722

Yang, K., Feng, L., and Liu, Z. (2016b). Stimuli responsive drug delivery systems based on nano-graphene for cancer therapy. *Adv. Drug Deliv. Rev.* 105, 228–241. doi: 10.1016/j.addr.2016.05.015

Yang, X., Du, H., Liu, J., and Zhai, G. (2015). Advanced nanocarriers based on heparin and its derivatives for cancer management. *Biomacromolecules* 16, 423–436. doi: 10.1021/bm501532e

Yang, X., Shi, X., Ji, J., and Zhai, G. (2018a). Development of redox-responsive theranostic nanoparticles for near-infrared fluorescence imaging-guided photodynamic/chemotherapy of tumor. *Drug Deliv.* 25, 780–796. doi: 10.1080/10717544.2018.1451571

Yang, Z., Dai, Y., Yin, C., Fan, Q., Zhang, W., Song, J., et al. (2018b). Activatable semiconducting theranostics: simultaneous generation and ratiometric photoacoustic imaging of reactive oxygen species *in vivo*. *Adv. Mater.* 30:1707509. doi: 10.1002/adma.201707509

Yu, C.-J., Wu, S.-M., and Tseng, W.-L. (2013). Magnetite nanoparticle-induced fluorescence quenching of adenosine triphosphate-BODIPY conjugates: application to adenosine triphosphate and pyrophosphate sensing. *Anal. Chem.* 85, 8559–8565. doi: 10.1021/ac400919j

Yu, G., Yung, B. C., Zhou, Z., Mao, Z., and Chen, X. (2018). Artificial molecular machines in nanotheranostics. *ACS Nano* 12, 7–12. doi: 10.1021/acsnano.7b07851

Yue, C., Yang, Y., Zhang, C., Alfranca, G., Cheng, S., Ma, L., et al. (2016). ROS-responsive mitochondria-targeting blended nanoparticles: chemo-and photodynamic synergistic therapy for lung cancer with on-demand drug release upon irradiation with a single light source. *Theranostics* 6, 2352–2366. doi: 10.7150/thno.15433

Yun, J., Mullarky, E., Lu, C., Bosch, K. N., Kavalier, A., Rivera, K., et al. (2015). Vitamin C selectively kills KRAS and BRAF mutant colorectal cancer cells by targeting GAPDH. *Science* 350, 1391–1396. doi: 10.1126/science.aaa5004

Zhang, P., Hu, C., Ran, W., Meng, J., Yin, Q., and Li, Y. (2016). Recent progress in light-triggered nanotheranostics for cancer treatment. *Theranostics* 6, 948–968. doi: 10.7150/thno.15217

Zhao, X., Li, Y., Jin, D., Xing, Y., Yan, X., and Chen, L. (2015). A near-infrared multifunctional fluorescent probe with an inherent tumor-targeting property for bioimaging. *Chem. Commun.* 51, 11721–11724. doi: 10.1039/C5CC03878B

Zhao, X., Yang, C.-X., Chen, L.-G., and Yan, X.-P. (2017). Dual-stimuli responsive and reversibly activatable theranostic nanoprobe for precision tumor-targeting and fluorescence-guided photothermal therapy. *Nat. Commun.* 8:14998. doi: 10.1038/ncomms14998

Zhou, F., Feng, B., Wang, T., Wang, D., Cui, Z., Wang, S., et al. (2017). Theranostic prodrug vesicles for reactive oxygen species-triggered ultrafast drug release and local-regional therapy of metastatic triple-negative breast cancer. *Adv. Func. Mater.* 27:1703674. doi: 10.1002/adfm.201703674

Zhu, J., Wang, G., Alves, C. S., TomáS., H., Xiong, Z., et al. (2018). Multifunctional dendrimer-entrapped gold nanoparticles conjugated with doxorubicin for pH-responsive drug delivery and targeted computed tomography imaging. *Langmuir* 34, 12428–12435. doi: 10.1021/acs.langmuir.8b02901

Conflict of Interest: The authors declare that the research was conducted in the absence of any commercial or financial relationships that could be construed as a potential conflict of interest.

frontiers in Bioengineering and Biotechnology

ORIGINAL RESEARCH
published: 26 May 2020
doi: 10.3389/fbioe.2020.00424

Selective Cytotoxic Activity of Prodigiosin@halloysite Nanoformulation

Ivan Guryanov[1], Ekaterina Naumenko[1], Farida Akhatova[1], Giuseppe Lazzara[2,3]*, Giuseppe Cavallaro[2,3], Läysän Nigamatzyanova[1] and Rawil Fakhrullin[1]**

[1] Institute of Fundamental Medicine and Biology, Kazan Federal University, Kazan, Russia, [2] Dipartimento di Fisica e Chimica, Università degli Studi di Palermo, Palermo, Italy, [3] Consorzio Interuniversitario Nazionale per la Scienza e Tecnologia dei Materiali, INSTM, Florence, Italy

Prodigiosin, a bioactive secondary metabolite produced by *Serratia marcescens*, is an effective proapoptotic agent against various cancer cell lines, with little or no toxicity toward normal cells. The hydrophobicity of prodigiosin limits its use for medical and biotechnological applications, these limitations, however, can be overcome by using nanoscale drug carriers, resulting in promising formulations for target delivery systems with great potential for anticancer therapy. Here we report on prodigiosin-loaded halloysite-based nanoformulation and its effects on viability of malignant and non-malignant cells. We have found that prodigiosin-loaded halloysite nanotubes inhibit human epithelial colorectal adenocarcinoma (Caco-2) and human colon carcinoma (HCT116) cells proliferative activity. After treatment of Caco-2 cells with prodigiosin-loaded halloysite nanotubes, we have observed a disorganization of the F-actin structure. Comparison of this effects on malignant (Caco-2, HCT116) and non-malignant (MSC, HSF) cells suggests the selective cytotoxic and genotoxic activity of prodigiosin-HNTs nanoformulation.

Keywords: cancer, anti-cancer drugs, comet assay, drug delivery, genotoxic effect, halloysite nanotubes, malignant cells, prodigiosin

OPEN ACCESS

Edited by:
Salvador Pané Vidal, ETH Zürich, Switzerland

Reviewed by:
Alessandra Quarta, CNR NANOTEC, Italy
Paolo Bigini, Istituto Di Ricerche Farmacologiche Mario Negri, Italy

****Correspondence:***
Ivan Guryanov
ivan.guryanov@gmail.com
Giuseppe Lazzara
giuseppe.lazzara@unipa.it
Rawil Fakhrullin
kazanbio@gmail.com

Specialty section:
This article was submitted to Nanobiotechnology, a section of the journal Frontiers in Bioengineering and Biotechnology

Received: *27 January 2020*
Accepted: *14 April 2020*
Published: *26 May 2020*

Citation:
Guryanov I, Naumenko E, Akhatova F, Lazzara G, Cavallaro G, Nigamatzyanova L and Fakhrullin R (2020) Selective Cytotoxic Activity of Prodigiosin@halloysite Nanoformulation. Front. Bioeng. Biotechnol. 8:424. doi: 10.3389/fbioe.2020.00424

INTRODUCTION

Currently, the number of effective chemotherapeutic agents for the therapy of neoplasms is very limited (Patel et al., 2010). Existing drugs often have toxic side effects on adjacent non-malignant cells and tissues. The problem of safety of the medications used in chemotherapy is of pivotal importance, one of the ways to solve it is the search for non-toxic substances and fabrication of new drug formulations. Natural drugs that can suppress the proliferation of cancer cells and metastasis formation are becoming increasingly popular (Huryn and Wipf, 2014). Prodigiosin, a bioactive secondary metabolite produced by *Serratia marcescens* and certain other bacteria is of particular interest (Williamson et al., 2006). The antitumor properties of prodigiosin have already been confirmed in previous studies (Montaner and Perez-Tomas, 2003; Perez-Tomas et al., 2003; Francisco et al., 2007; Lins et al., 2015). Prodigiosin can induce apoptosis in hematopoietic, colorectal, gastric cancer cells (Montaner and Perez-Tomas, 2003), human breast carcinoma cell lines (Lu et al., 2012), choriocarcinoma (Zhao et al., 2019) and prostate cancer cell lines (PC3) *in vitro* and JEG3 and PC3 tumor-bearing nude mice *in vivo* (Li et al., 2018)

with metastases suppression (Zhang et al., 2005). The cytotoxic activity of prodigiosin against various human cancer cell lines and relatively lower toxicity toward non-malignant cells has been demonstrated previously (Francisco et al., 2007; Stankovic et al., 2014; Zhao et al., 2019). In addition, prodigiosin can be used to replace synthetic colorants in food industry and sunscreen cosmetics (Darshan and Manonmani, 2015).

Hydrophobic nature of prodigiosin is an obvious disadvantage for medical and biotechnology applications. Limited aqueous solubility of prodigiosin result in poor absorption and low bioavailability (Tran et al., 2019), as well as it may disturb regular distribution of prodigiosin in biological fluids. Bioavailability of prodigiosin can be enhanced similarly, as reported previously for anticancer drug doxorubicin (Li et al., 2017) and curcumin (Ni et al., 2019), employing fabrication of nanoscale drug formulations to overcome the limitations caused by the intrinsic hydrophobicity prodigiosin. Recently, a technique of prodigiosin encapsulation was developed and anticancer effect of targeted nanoformulations of prodigiosin was investigated (Zhao et al., 2019).

Targeted delivery and controlled release of antitumor drugs, antibiotics, enzymes, and nucleic acids are currently among of the most significant challenges in biomedicine (Martín del Valle et al., 2009; Tiwari et al., 2012; Yendluri et al., 2017). The pharmacokinetics and pharmacodynamics of a number of drugs require special procedures for their administration. Using nanoscale drug delivery vehicles is one of the most promising approaches for targeted drug delivery systems (Miyazaki and Islam, 2007). Nanocarrier-based drugs allow preventing possible side effects of drugs and to overcome physiological barriers of the body (for example, blood–brain barrier) (De Jong and Borm, 2008). Nanoscale anticancer formulations can be designed using natural substances or derivatives, such as chitosan, dextran, gelatin, alginate, liposomes (De Jong and Borm, 2008), gold (Kohout et al., 2018; Singh et al., 2018) and magnetic iron oxide nanoparticles (Dulińska-Litewka et al., 2019; Rozhina et al., 2019), mesoporous silica nanoparticles (Li et al., 2019), carbon nanotubes (Cirillo et al., 2019) and clay nanotubes (Naumenko and Fakhrullin, 2017, 2019; Yendluri et al., 2017). Natural aluminosilicate halloysite, due to its tubular structure and surface chemistry, is a potent platform to fabricate nanocontainers for drug-delivery systems. Halloysite has a hollow tubular structure, with the length of up to 1 μm, external diameter 70 nm and an inner lumen 15 nm (Shchukin et al., 2005). Halloysite nanotubes are widely used for the fabrication of polymeric nanocomposites to enhance their tensile strength and stability (Naumenko et al., 2016; Suner et al., 2019). The tubular structure of halloysite allows the internal cavity to be loaded with various macromolecules including drugs, proteins, and nucleic acids, followed by the release of the loaded compounds in the delivery region (Joussein et al., 2005). Such features as very low toxicity (Lai et al., 2013; Fakhrullina et al., 2015) and directed modification of the surface and internal cavity (Abdullayev et al., 2012; Tarasova et al., 2019; Rozhina et al., 2020) make halloysite nanotubes promising candidates for the fabrication of nanocontainers for theranostic targeted drug delivery (Hu et al., 2017). Halloysite nanotubes can be efficiently filled with hydrophobic drug via physical entrapping in the internal cavity (Naumenko and Fakhrullin, 2017, 2019; Fakhrullina et al., 2019). As a result, halloysite-based drug formulation demonstrate lower drug side effects, render the protection of drug molecules from possible degradation in aggressive conditions (low/high pH, enzymatic activity), increase the aqueous solubility of hydrophobic insoluble drugs, accumulate in pathological sites in the body, and help controlling drug release rates (De Jong and Borm, 2008; Naumenko and Fakhrullin, 2017, 2019).

In this paper we report for the first time fabrication of prodigiosin-based nanoformulation (p-HNTs) and its effects on viability of malignant and non-malignant cells.

MATERIALS AND METHODS

Prodigiosin-HNTs Fabrication and Characteristics

The red pigment prodigiosin was obtained by cultivation of the producer strain *S. marcescens ATCC 9986* on agarized peptone–glycerol medium. Pigment purification was performed as described previously (Guryanov et al., 2013). Ethanol solution (96% vol. 300 μl of purified prodigiosin (4.4 μg) was mixed with glycerol (70 μL), dry HNTs (30 mg) in centrifuge tube and placed into desiccator for loading by vacuum displacement (**Supplementary Figure S1**). Prodigiosin loading procedure was performed for 24 h. Subsequently, the loading efficiency was evaluated by thermogravimetric analysis (TGA) while Fourier transform infrared spectroscopy (FT-IR) highlighted the interaction mechanism and involved functional groups. Optical absorption spectra of purified prodigiosin in ethanol and extracts of glycerol-HNTs and prodigiosin-HNTs after 30 min and 2 h exposure in PBS were obtained and compared for estimation of pigment release from loaded halloysite nanotubes. Absorption spectra were analyzed using a Lambda 35 spectrometer (PerkinElmer).

Dark-Field Imaging and Hyperspectral Microscopy

Dark-field images and reflected light spectra were obtained using an Olympus BX51 (Olympus) upright microscope equipped with a CytoViva® enhanced dark-field condenser with a halogen light source (150 W) Fibre-Lite DC-950 (Dolan-Jener) and control module ProScan III (JH Technologies). Images were obtained using acquisition software for visualization Exponent 7 (Dage-MTI). Spectra were registered using a Specim V10E spectrometer and CCD camera in the range between 400 and 1000 nm with a spectral resolution –2 nm. Hyperspectral data were collected with ENVI software, version 4.8 (Harris Geospatial Solutions) (Akhatova et al., 2018). The presence of prodigiosin inside the treated cells was visualized using a CytoViva dual fluorescence module. Images were processed using ImageJ freeware (NIH). The cells were fixed on coverslips, nuclei of the cells were stained with DAPI. An X-cite 120Q wide-field fluorescence microscope excitation light source (Excelitas Technologies) and CytoViva® Dual Mode Fluorescence system equipped with the

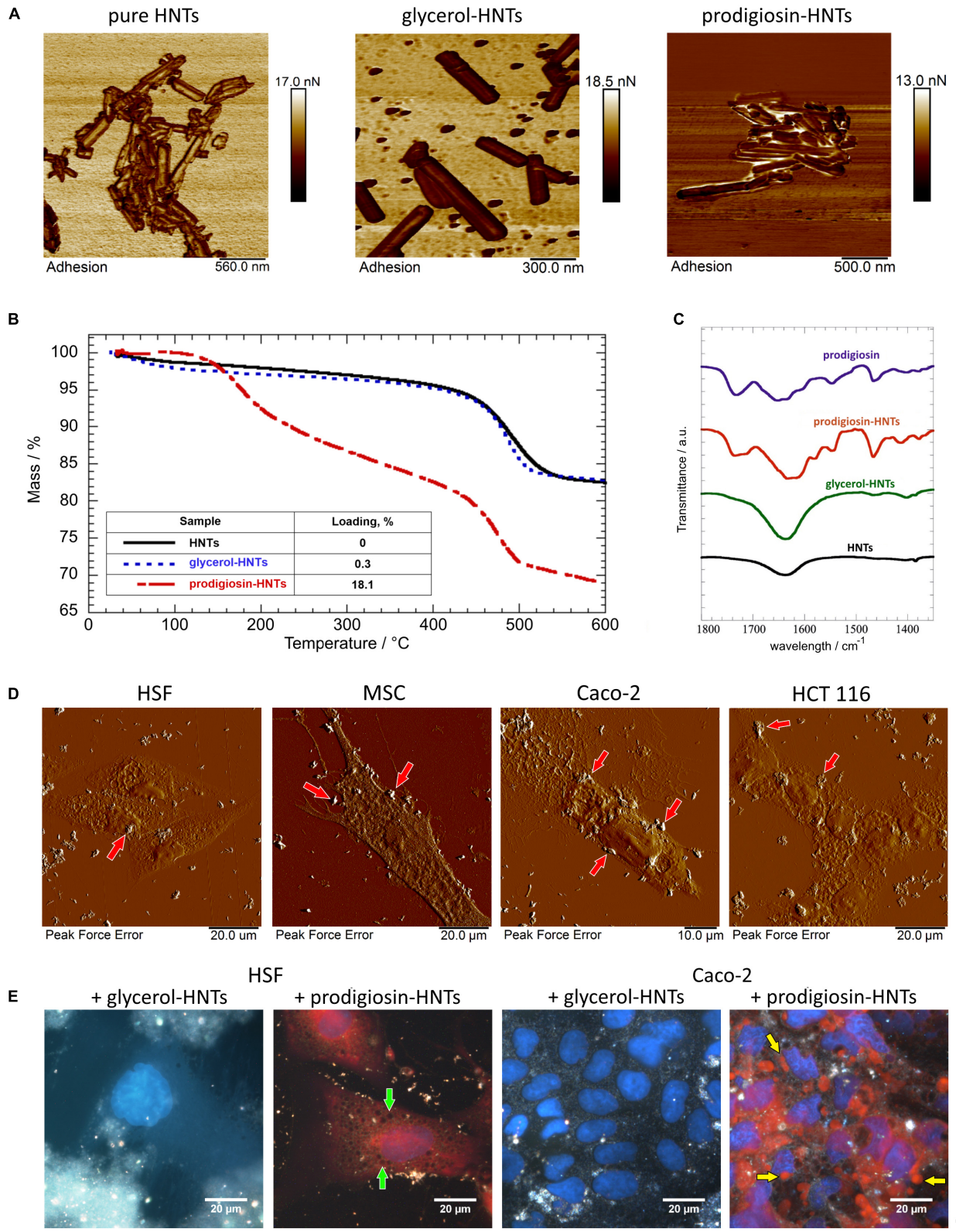

FIGURE 1 | Characterization of prodigiosin-HNTs. Atomic force microscopy images **(A)** of pure HNTs and loaded with glycerol and prodigiosin, demonstrating the change of nanotubes surfaces adhesiveness. TGA analysis **(B)** of prodigiosin-loaded HNTs demonstrated that this complex contains 18% of prodigiosin. FT-IR spectra **(C)** in the wavelength range between 1350 and 1800 cm^{-1}. AFM images of the cells **(D)** indicate that hydrophobic prodigiosin-HNTs strongly attach to the cell membrane, forming large clusters. **(E)** prodigiosin exhibits autofluorescence, therefore its leakage from the nanotubes and the presence in the cytoplasm can be visualized using fluorescence module of hyperspectral microscope CytoViva®. More details see in **Supplementary Figure S4**.

Triple Pass Filter were used to image DAPI nuclear staining with transmitted fluorescence illumination imaging, exposure time was 100 μs. Fluorescence nuclei images were rendered with artificial red color to enhance local contrast using GIMP software, version 2.10.8. The resulting dark-field images were merged with transmission fluorescence images using the freely available image processing GIMP.

Fourier Transform Infrared Spectroscopy

Fourier transform infrared spectra were registered using a Frontier FTIR spectrometer (PerkinElmer). The measurements were conducted on KBr pellets at room temperature in the range between 500 and 4000 cm^{-1} with a spectral resolution of 2 cm^{-1}.

Thermogravimetry

Thermogravimetry (TG) experiments were carried out by means of a Q5000 IR apparatus (TA Instruments) under the nitrogen flows of 25 cm^3 min^{-1} for the sample and 10 cm^3 min^{-1} for the balance. The mass of each sample was ca. 5 mg. TG measurements were conducted between 25 and 600°C using a constant heating rate of 20°C min^{-1}. The temperature calibration was carried out by means of the Curie temperatures of standards (nickel, cobalt, and their alloys) (Blanco et al., 2014). The encapsulation efficiency into HNTs was determined by considering the rule of mixtures for the residual mass at 600°C. Details are provided in literature (Lisuzzo et al., 2019).

Atomic Force Microscopy

Atomic force microscopy (AFM) images of HNTs and cells were made using a Dimension Icon microscope (Bruker) operating in PeakForce Tapping mode. ScanAsyst-air (Bruker) probes were used to obtain images (nominal length 115 μm, tip with a radius of 2 nm, spring stiffness 0.4 N m^{-1}). Images were obtained at 512–1024 scan lines at a scanning speed of 0.8–0.9 Hz. The adhesion of the nanoparticles was analyzed using an atomic force microscope and calculated from 30 × 30 nm sites on the nanoparticles surface. The obtained data were processed using Nanoscope Analysis software version 1.7 (Bruker).

Cell Culture

A frozen stock of HCT116, Caco-2, rat adipose-derived MSCs and human skin fibroblasts (HSF) was grown for 7 days in α-MEM (Sigma-Aldrich) supplemented with 10% of fetal bovine serum (Thermo Fisher Scientific), 100 IU/ml penicillin, 100 μg/ml streptomycin and 2 mM L-glutamine on 25 cm^2 tissue culture flasks in humidified atmosphere with 5% CO_2 at 37°C. After cultivation, cells (2.5×10^5) were seeded on 24 well cell culture plates (BD Biosciences) and cultured for 48 h in CO_2 incubator at 37°C. Glycerol-HNTs or prodigiosin-HNTs in PBS were added to each well to final concentration 100 μg per ml and cells were incubated for 48 h.

Comet Assay (Alkaline Comet Assay)

Live trypsinized cells were mixed with low-melting agarose (1.5%) and added to fully frosted slides precoated with 1% normal melting point agarose. After solidification, the slides were lysed in buffer and alkaline solutions (lysis buffer pH 10, alkaline solution pH 13, Tris-acetate-EDTA buffer 2 h at 4°C. After lysis, the slides were immersed in the neutralizing solution (0.4 M Tris, pH 7.5) for 15 min. Then the slides were placed in the alkaline solution (300 mM NaOH, 1 mM EDTA-Na_2, pH 13) for 20 min to allow DNA unwinding and subsequently electrophoresed for 30 min at 20 V, 300 mA. Upon completion of the electrophoresis the slides were placed in 70% ethyl alcohol for 5 min at room temperature, for DNA fixation. After drying at room temperature for 1 h the slides were stored in a dry and dark place until further analysis. Finally, the slides were stained with ethidium bromide and then visualized using confocal microscopy (Carl Zeiss LSM 780) equipped with diode laser (405nm), argon laser (488 nm) and He-Ne laser (633nm). Hundred randomly captured nuclei were examined from each slide in two independent experiments. The analysis does not include comet DNA of apoptotic cells detected on microscopic preparations as fluorescent comets with a broad diffuse tail and a very small head, so-called hedgehogs. Data was processed using CometScore software (v. 2.0).

TABLE 1 | Thermogravimetric parameters for HNTs, glycerol-HNTs and prodigiosin-HNTs.

Material	ML_{150}/wt%	MR_{600}/wt%
HNTs	1.30	82.3
Glycerol-HNTs	2.26	82.9
Prodigiosin-HNTs	0.707	68.7

Cytoskeleton Visualization

F-actin was stained with Alexa Fluor 488® conjugate of phalloidin according to the protocol, provided by Life Technologies, nuclei were stained with DAPI. Samples were visualized using confocal microscopy. Images were processed using ZEN software.

Live/Dead Staining of Cell Cultures

Viability of cells was tested using Cell Viability Imaging Kit (Blue/Green) (Life Technologies) according to the protocol, provided by producer. Samples were using confocal microscopy. Living cells were visualized as blue, and dead cells as green.

RESULTS AND DISCUSSION

We have isolated prodigiosin by acidic ethanol extraction from *S. marcescens* bacteria and purified as described previously (Guryanov et al., 2013). Prodigiosin purity was confirmed using UV–vis spectroscopy (**Supplementary Figure S1**). Next, prodigiosin was loaded (dissolved in ethanol/glycerol solvent) into the lumens of halloysite nanotubes via vacuum-facilitated loading (Dzamukova et al., 2015), as schematically shown in **Supplementary Figure S2**. To determine the stability of prodigiosin loaded halloysite nanotubes we investigated prodigiosin leakage in phosphate buffered saline (PBS) at 37°C (**Supplementary Figure S1**). Absorption spectra of p-HNTs suspension in PBS confirm the prodigiosin binding to halloysite. Spectrophotometry data demonstrate non-specific prodigiosin

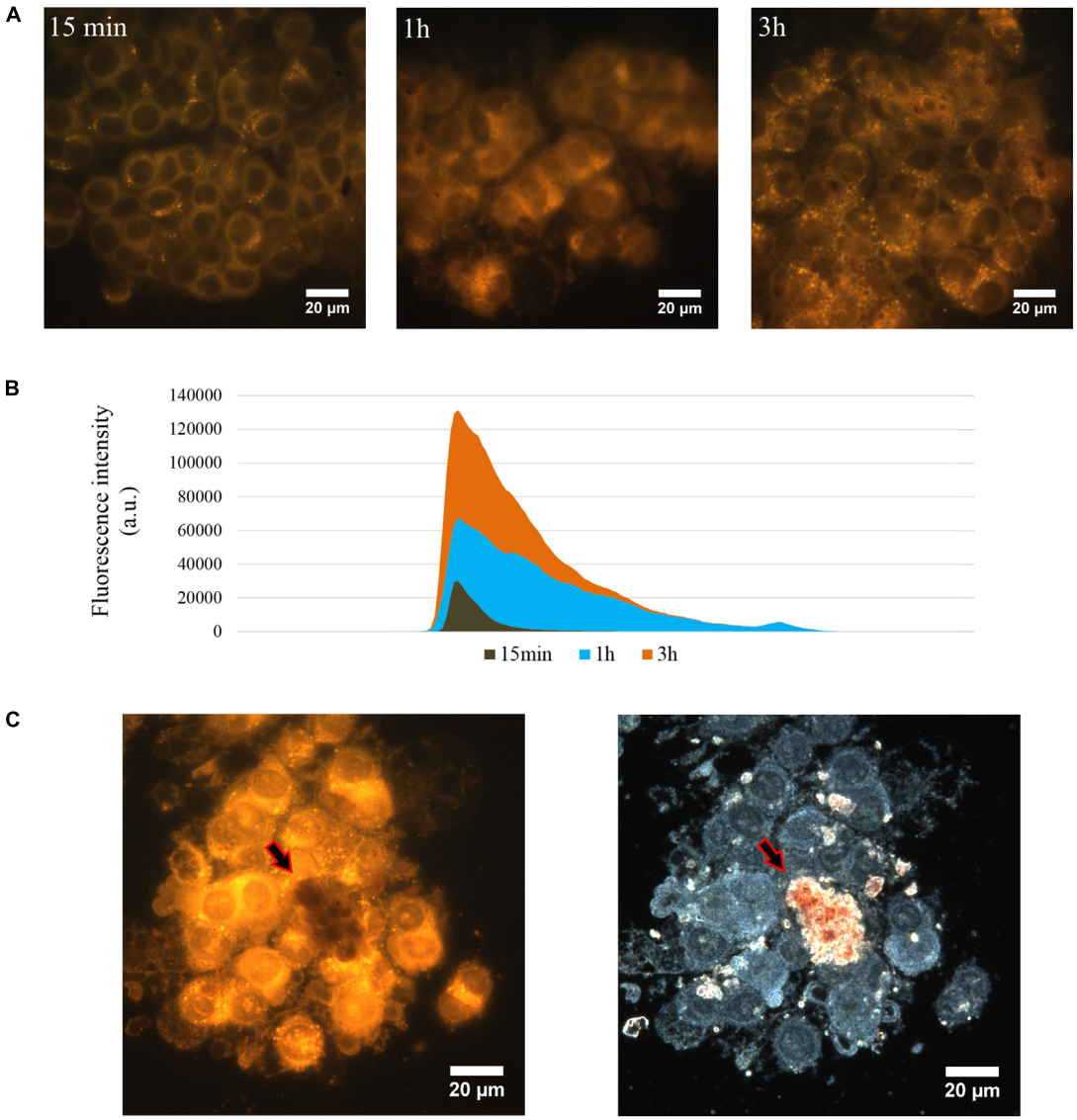

FIGURE 2 | The release of prodigiosin from p-HNTs in cytoplasm of HCT116 cells. Fluorescence images of p-HNTs-treated cells were taken after 15 min, 1 and 3 h of incubation **(A)**. fluorescence intensity histogram **(B)** demonstrated that the fluorescence intensity increased proportionally to the incubation time. Comparative analysis of dark-field and fluorescencee images **(C)** demonstrates the absence of extracellular leakage of prodigiosin. The arrows indicate the red colored p-HNTs aggregate on the cell surface which cannot be visualized on fluorescent image.

absorption, the increase of absorption value over time in this experiment can be explained by the following dissociation of hydrophilic HNTs in PBS solution. Spectral signatures of p-HNTs obtained in reflected light mode demonstrate the effective loading of prodigiosin due to the presence of characteristic peaks of pure HNTs and prodigiosin in complex spectra (**Supplementary Figure S3**).

The detailed characterization of HNTs results are shown in **Figure 1**. Prodigiosin, as a hydrophobic compound (de Araújo et al., 2010), after the loading into halloysite can located within halloysite lumen and on the surface of the tubes (**Figure 1A**). This, in turn, increases the adhesion of prodigiosin-loaded halloysite nanotubes. AFM images of halloysite nanotubes loaded with glycerol and prodigiosin (**Figure 1A**) confirm the increase of non-specific adhesion activity after prodigiosin loading (10.5 ± 0.7 nN) compared with the control pristine halloysite nanotubes (4.5 ± 0.6 nN). We also observe a slight increase in surface adhesion of nanotubes with glycerol (7.3 ± 0.5 nN). We suggest that an increase in the adhesion of the surface of the p-HNTs may contribute to their aggregation.

The thermal behavior of modified HNTs (glycerol-HNTs and prodigiosin-HNTs) was investigated by thermogravimetric method as described previously (Blanco et al., 2014). As evidenced in **Figure 1B** both glycerol-HNTs and p-HNTs exhibit a mass loss in the temperature interval between 450°C and 550°C. These results highlighted that the presence of the interlayer

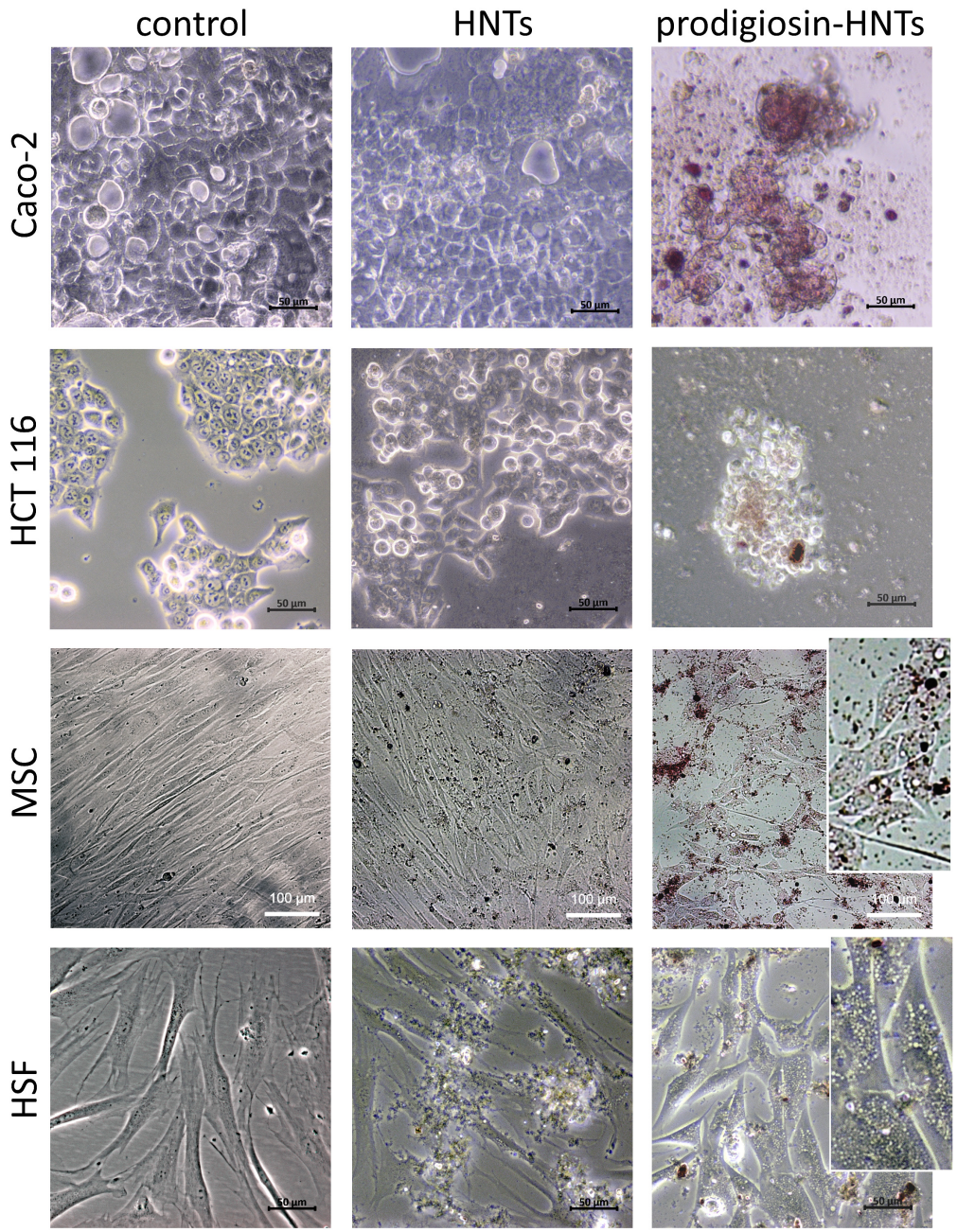

FIGURE 3 | Comparison of the effect of halloysite nanotubes loaded with glycerol (HNTs) and prodigiosin-HNTs on malignant (Caco-2, HCT116) and non-malignant cells (MSC, HSF). All cultures were grown in Minimum Essential Medium Eagle – Alpha Modification (α-MEM) with 5% CO_2 in air and humidity at 37°C. The addition of prodigiosin-HNTs during the cultivation of cancer cells (Caco-2, HCT116) led to aberration of their morphology and subsequent detachment from the surface of the dish (Caco-2/prodigiosin-HNTs, HCT116/prodigiosin-HNTs). Glycerol-loaded HNTs which were used as a control did not affect the morphology and viability of all cell types. The presence of prodigiosin-HNTs in the culture medium of non-malignant cells increased the cytoplasm vacuolization of some cells (MSC/prodigiosin-HNTs and HSF/prodigiosin-HNTs inserts).

water molecules of halloysite is preserved in the functionalized HNTs. Moreover, p-HNTs showed an additional degradation step in the temperature range between 180 and 320°C that can be attributed due to the destabilization of bonds in the prodigiosin molecule (Sumathi et al., 2014). The corresponding mass loss was estimated at 8.73 wt%. According to literature, the mass loss between 25°C and 120°C (ML_{120}) can be ascribed to the moisture content of the investigated material (Cavallaro et al., 2018). **Table 1** evidences that the addition of glycerol generated an enhancement of the water amount physically adsorbed on HNTs, while the opposite effect was detected after the introduction of prodigiosin in the halloysite nanostructure.

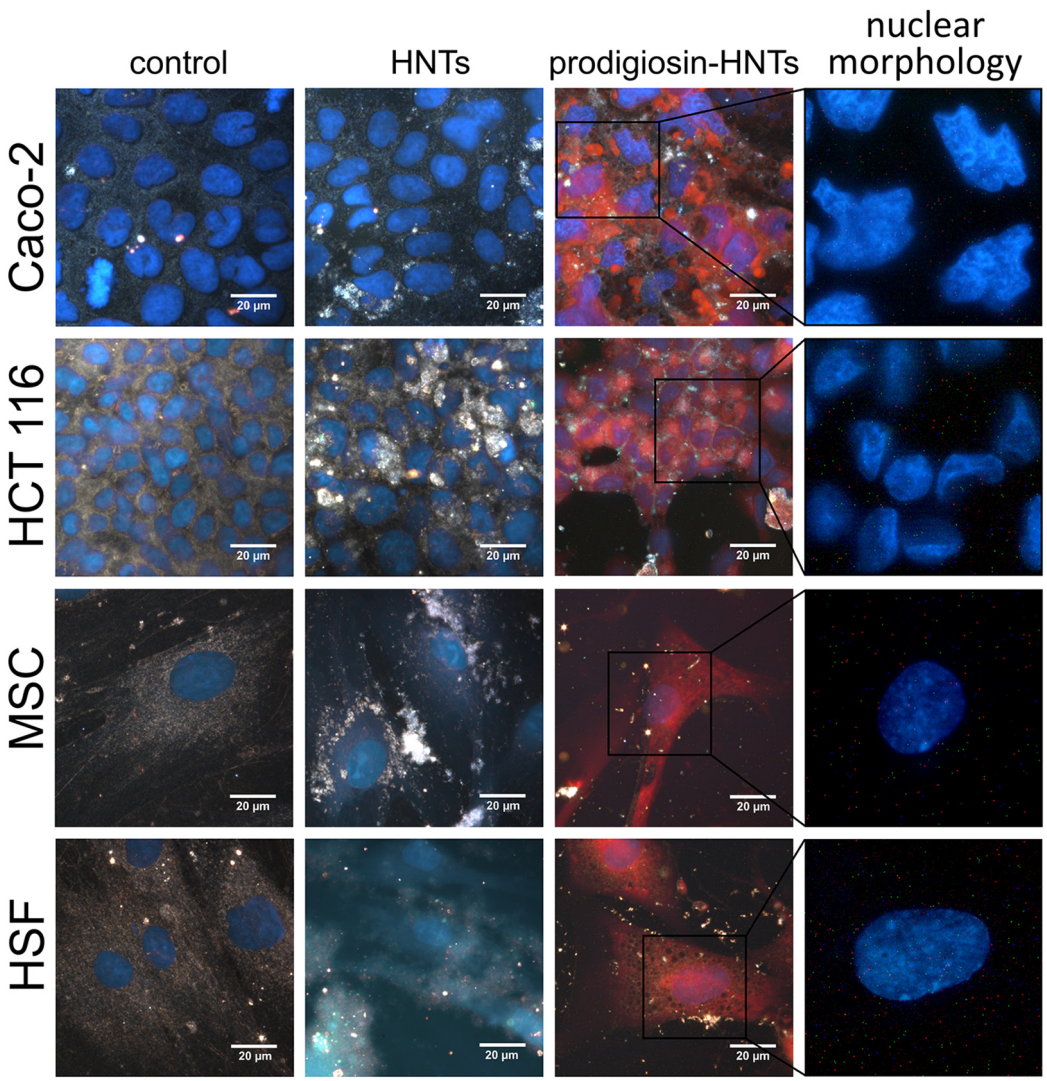

FIGURE 4 | Hyperspectral images for comparison of the effect of halloysite nanotubes loaded with glycerol (HNTs) and prodigiosin-HNTs on malignant (Caco-2, HCT 116) and non-malignant cells (MSC, HSF). All cultures were grown in α-MEM with 5% CO_2 in air and humidity at 37°C. Nuclei (blue) were labeled with DAPI. Purple non-specific staining of the cells cytoplasm (prodigiosin-HNTs column) is the result of autofluorescence of prodigiosin released from prodigiosin-HNTs into the cytoplasm. Changes in nuclear morphology of Caco-2 and HCT 116 cells treated with p-HNTs shown in the far right column.

Further insights on the functionalization of HNTs surfaces were obtained by comparing the residual masses at 600°C (MR_{600}). We estimated similar MR_{600} values for HNTs and glycerol-HNTs. By contrast, the presence of prodigiosin induced a significant MR_{600} reduction indicating the successful modification of halloysite.

Figure 1 compares the FT-IR spectra of modified HNTs (glycerol-HNTs and prodigiosin-HNTs) with those of pristine HNTs and prodigiosin (**Figure 1C**). The wavelength range between 1350 cm^{-1} and 1800 cm^{-1} can be considered as a fingerprint region for prodigiosin, which presents numerous characteristic signals that were not detected neither for pure HNTs nor for glycerol-HNTs. On the other hand, the typical FT-IR peaks of the drug at 1467 cm^{-1} (bending of C–H) and 1548 cm^{-1} (aromatic C=C, NO_2 stretch) (Suryawanshi et al., 2014) were observed in the p-HNTs confirming the successful loading. Interestingly, the band at 1734 cm^{-1} (C=O stretching vibration) (Arivizhivendhan et al., 2015) of prodigiosin was split in two peaks (1734 and 1717 cm^{-1}) in the p-HNTs. According to the literature (Cavallaro et al., 2012), this result could indicate that the delocalization of the negative charge along the carboxylate group of the drug is no longer present in the loaded HNTs. On this basis, the loading of prodigiosin in HNTs might be partly related to electrostatic interactions between the two components.

The changes of nanotubes adhesiveness after loading of prodigiosin affects their distribution over the cell surface (**Figure 1D**, red arrows). One can clearly distinguish relatively large amorphous aggregates of p-HNTs on cells (**Figure 1D**). HNTs *per se* distributed more evenly and less aggregate that was demonstrated in **Supplementary Figure S4**. The overall

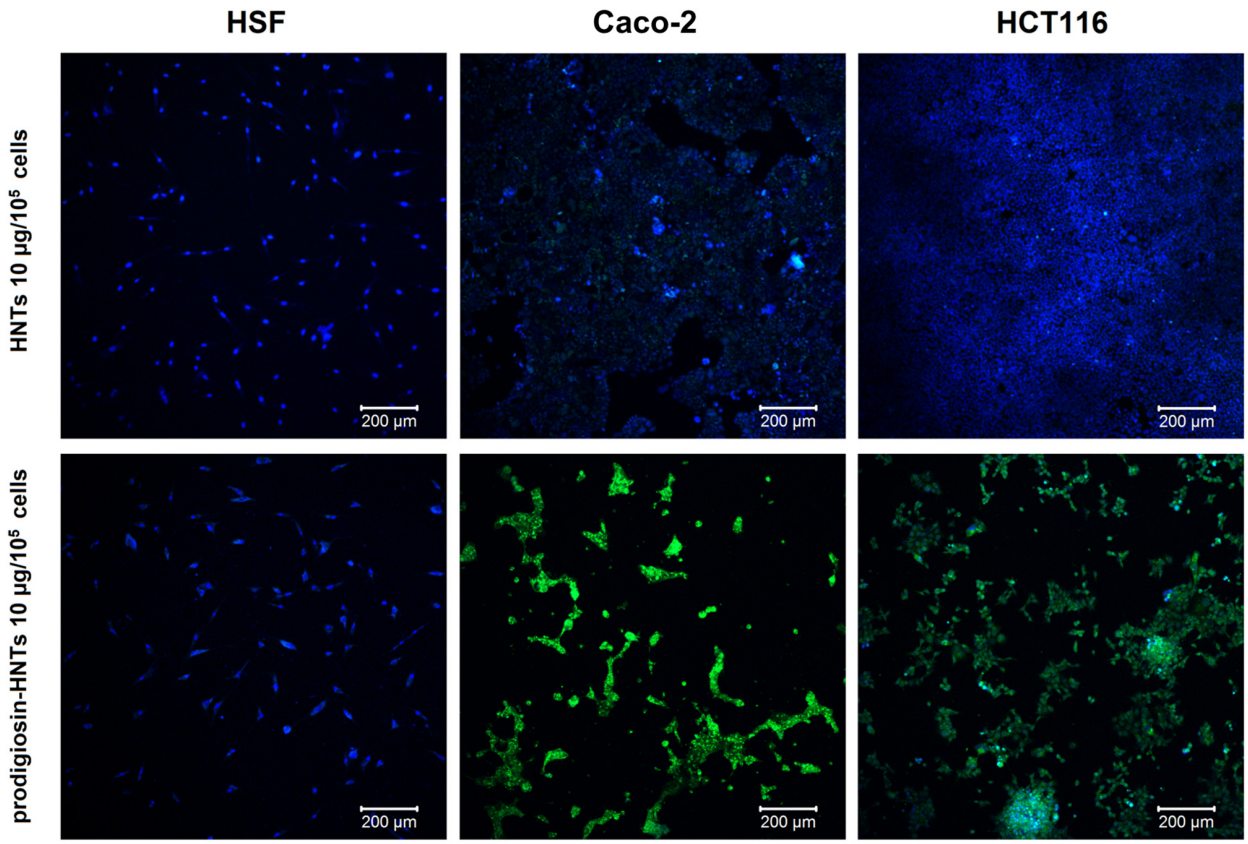

	HSF		Caco-2		HCT 116	
	HNTs	p-HNTs	HNTs	p-HNTs	HNTs	p-HNTs
living cells, %	100	100	75.58±4.68	0	100	17.37±4.29
dead cells, %	0	0	24.42±4.68	100	0	82.63±4.29

FIGURE 5 | Live/Dead staining (green – dead cells, blue – living cells, Live/Dead kit (Life Technologies) of cells treated with HNTs and prodigiosin-HNTs (p-HNTs). Living cells appear blue and dead cells appearing green on the color-coded confocal images.

morphology of both HSF and MSC cells remains unaffected when cells interact with HNTs or p-HNTs, while some morphology changes observed in malignant cells (**Figures 1D**, **3** and **Supplementary Figure S4**). Internalization of p-HNTs and prodigiosin release from nanotubes started immediately after adding of nanotubes and increased in course of incubation time (**Figure 2B**). We observed the accumulation of prodigiosin in the perinuclear space as red fluorescent vesicles (**Figures 2A,B**). Prodigiosin leakage from loaded nanotubes into cytoplasm during cell cultivation may cause disorganization of the nucleus structure and reduce the volume of the cytoplasm in Caco-2 and HCT116 cells (**Figures 1E**, **4**). In Caco-2 cells exposed to p-HNTs extracellular vesicles filled with prodigiosin can be observed (**Figure 1E**, yellow arrows). Noteworthy, we detected small vacuoles in the cytoplasm of p-HNTs treated fibroblasts (**Figure 1E**, green arrows). Vacuolization of HCT116 cells also was demonstrated after incubation of cells with p-HNTs for 3 h (**Figure 2A**). In **Figure 2C** the arrows indicate the absence of extracellular release of prodigiosin that can be seen in simultaneously taken dark-field and fluorescence images (red colored p-HNTs aggregate on the cell surface and cannot be visualized on fluorescence images).

The addition of p-HNTs during the cultivation of cancer cells led to aberration of their morphology and subsequent detachment from the bottom of the dish (**Figure 3**). Glycerol-loaded HNTs used as a control did not affect the morphology and viability of all types of cells. The lack of long-term toxicity were observed for different type of test-organisms including yeast cells, Protista and worms (Konnova et al., 2013; Fakhrullina et al., 2015; Kryuchkova et al., 2016). The presence of p-HNTs in the culture medium of non-malignant cells led to increasing of vacuolization in some

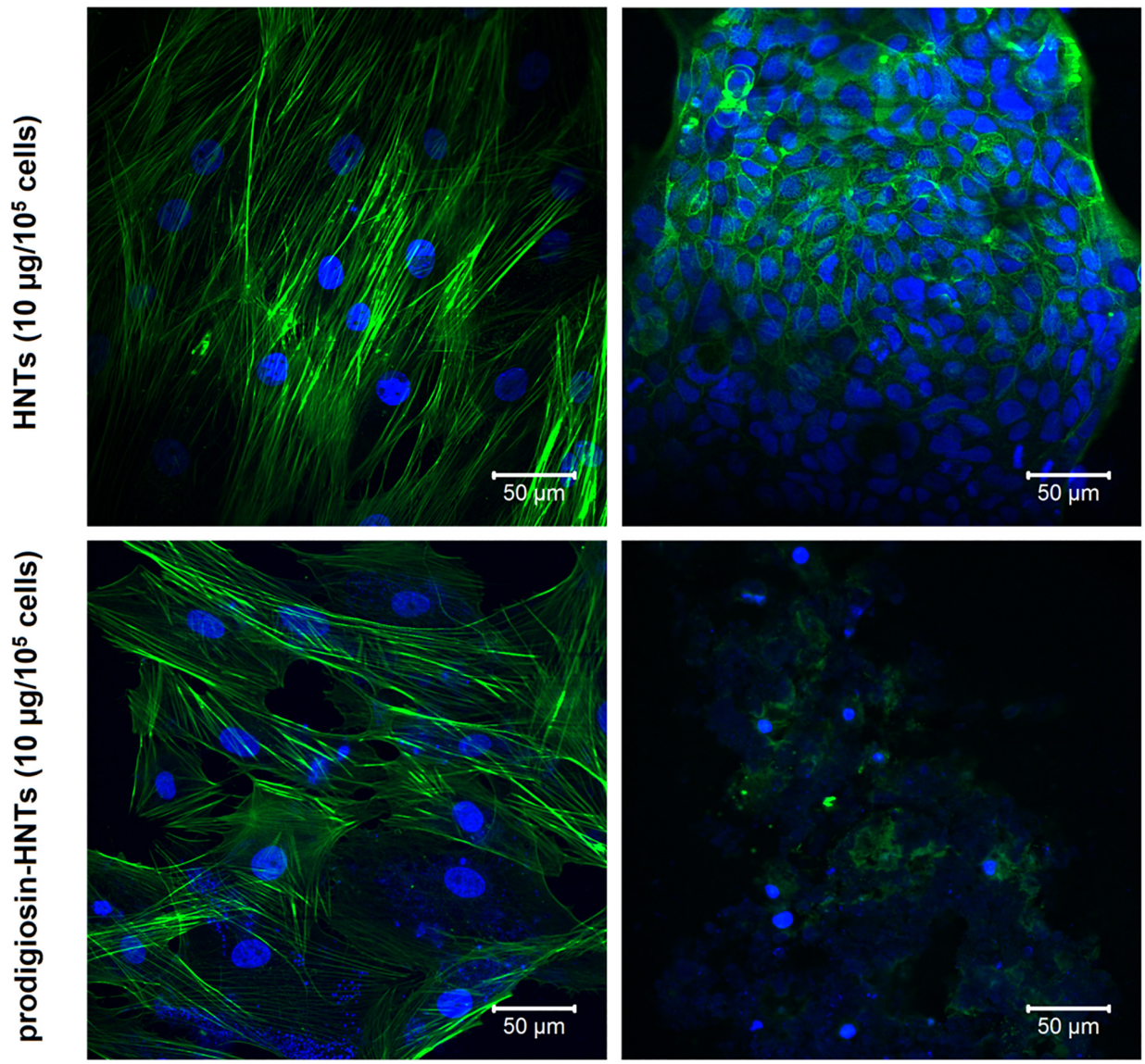

FIGURE 6 | F-actin visualization in non-malignant (MSC) and malignant (Caco-2) cells after incubation with HNTs and prodigiosin-HNTs. Note the disorganization of F-actin after treatment of Caco-2 cells with prodigiosin-HNTs. MSC and Caco-2 cells where stained with DAPI (blue) and Alexa Fluor 488® phalloidin (green). Figure shows a cytoskeleton disruption in cancer cells and the absence of such effect in MSCs (bottom images). Upper images clearly demonstrate that the occurrence of such effect is due to the prodigiosin action.

of them (**Figure 3**, inserts). However, fibroblasts and MSCs maintained normal morphology and viability as demonstrated using Live/Dead staining (**Figure 5**) where blue fluorescence indicates the nuclei of all cells while green stain is located exclusively in the nuclei of dead cells with compromised plasma membranes and cytoskeleton visualization (**Figure 6**). We summarized in **Figure 5** the numerical data demonstrating the sensitivity of cells to HNTs and p-HNTs. Caco-2 cells were less resistant to HNTs in culture medium. The interaction with p-HNTs in concentration of 10μg per 10^5 cells resulted to rapid 100% cell death. In opposite, the viability of non-malignant cells (HSF) did not change in all experimental variants. Considering the fact that prodigiosin can suppress cell proliferation, it is expected that the sensitivity of cancer cells to the inhibitory activity of prodigiosin depends on cell proliferation rates (Liu et al., 2018; Sam and Ghoreishi, 2018; Ji et al., 2019).

Cytoskeleton components are a known target for certain anticancer drugs (Yvon et al., 1999; Lin et al., 2016), which suppress microtubule dynamics, inhibiting, as a result, cell

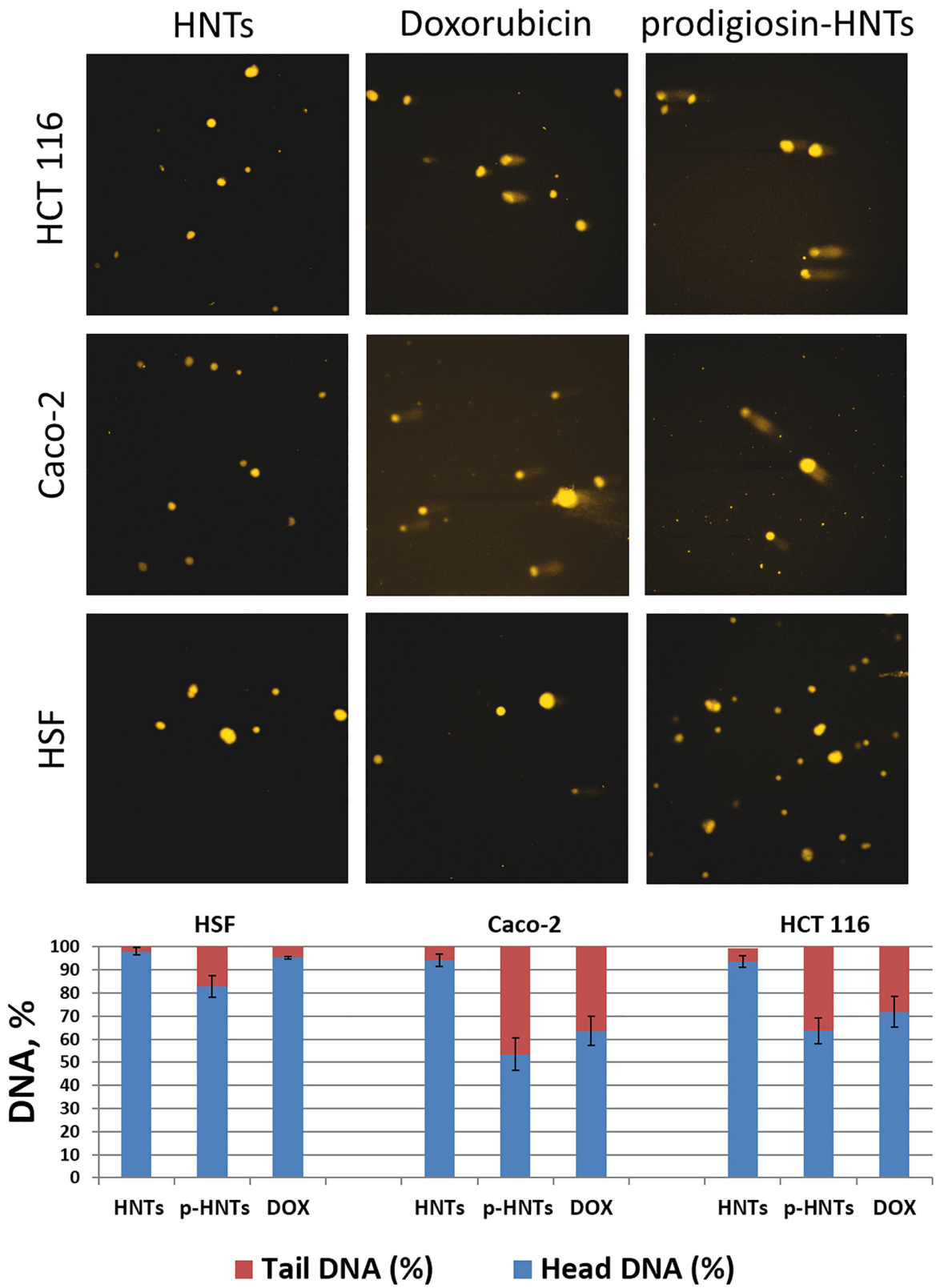

FIGURE 7 | Genotoxic effects of prodigiosin-HNTs (p-HNTs) were evaluated using Comet Assay. Upper image – representative fields of view (fluorescent microscopy) with characteristic undamaged nucleoids and comets in each variant of experiment (specified in figure). The histogram shows the ratio of the DNA percentage in the tail and head of the comets. The semi-automated image analysis system Comet Score was used to evaluate 100 comets per sample.

proliferation rates. Interestingly, treatment with prodigiosin demonstrates the same effects (**Figure 6**), apparently due to binding to cytoskeleton components followed by their structure disruption that in turn disrupts cytoskeleton functions. Thus, in this study we have found for the first time the changes in the morphology and viability of cancer cells and absence of such effect in non-malignant cells after exposure to prodigiosin-loaded halloysite nanotubes.

To assess DNA damage caused by p-HNTs we used the Comet Assay or single-cell gel electrophoresis (Lorenzo et al., 2013) (**Figure 7**), which allows detecting DNA degradation in individual cells. Briefly, cells were embedded in agarose gel and distributed on adhesive microscope slide, then cells were lysed, leaving nucleoids (DNA structures without nuclear membrane), and then electrophoresed in alkali conditions. DNA with strand breaks are relaxed and extend toward the anode during the electrophoresis, forming a comet-like tail viewed by fluorescence microscopy with ethidium bromide staining. DNA damage (strand breaks frequency) is related to the percentage of DNA in the tail. Undamaged DNA remains in the place of initial cell localization and represent the head of comet-like structure. Anticancer drug doxorubicin was used as a positive control. Prodigiosin can bind with DNA by intercalation and acts mainly as inhibitors of topoisomerases I and II (Lins et al., 2015). This effect can cause DNA damage, which is directly correlated with the level of cytotoxicity and genotoxicity of p-HNTs in our study. We found that genotoxic effect of p-HNTs studied by Comet Assay was more pronounced in the case of malignant cells (Caco-2, HCT116). The formation of strand breaks of DNA was observed with much less frequency in human skin fibroblasts treated with p-HNTs. HNTs without prodigiosin caused only background level of DNA damage in all cell types, therefore we assume that the possible reason for p-HNTs selective antitumor action might be the destruction of malignant cells DNA.

CONCLUSION

In summary, prodigiosin was successfully adsorbed by HNTs surfaces and encapsulated within halloysite lumen. Then, we found that prodigiosin could release in the cytoplasm of cells, while no release occurs extracellularly. *In vitro* anticancer effects of p-HNTs were manifested in the suppression of Caco-2 and HCT116 cells proliferation, followed by alteration of cell morphology and F-actin structure disorganization. Comet assay response where fragmented chromatin were observed, indicating a high therapeutic effect of halloysite formulated prodigiosin. Comparison of the effects of p-HNTs on malignant (Caco-2, HCT116) and non-malignant (MSC, HSF) cells allows to conclude that the p-HNTs demonstrate the selective cytotoxic and genotoxic activity. We hypothesize that prodigiosin entrapped into halloysite may have significant advantages for treatment of living tissues *in vivo,* due to higher bioavailability and extended intracellular release.

DATA AVAILABILITY STATEMENT

The datasets generated for this study are available on request to the corresponding author.

AUTHOR CONTRIBUTIONS

IG, EN, and RF designed the research. IG and EN performed the cell culture studies. FA performed the AFM experiments. GL and GC performed the thermoanalysis. LN and EN performed the dark-field microscopy experiments. All the authors read and approved the final version of the manuscript.

FUNDING

The work was performed according to the Russian Government Program of Competitive Growth of Kazan Federal University. This study was funded by the Russian Foundation for Basic Research grant #20-015-00353 À and RFBR #18-29-11031 mk. GL and GC thank the University of Palermo for financial support.

SUPPLEMENTARY MATERIAL

The Supplementary Material for this article can be found online at: https://www.frontiersin.org/articles/10.3389/fbioe.2020.00424/full#supplementary-material

REFERENCES

Abdullayev, E., Joshi, A., Wei, W., Zhao, Y., and Lvov, Y. (2012). Enlargement of halloysite clay nanotube lumen by selective etching of aluminum oxide. *ACS Nano* 6, 7216–7226. doi: 10.1021/nn302328x

Akhatova, F., Danilushkina, A., Kuku, G., Saricam, M., Culha, M., and Fakhrullin, R. (2018). Simultaneous intracellular detection of plasmonic and non-plasmonic nanoparticles using dark-field hyperspectral microscopy. *Bull. Chem. Soc. Jpn.* 91, 1640–1645. doi: 10.1246/bcsj.20180198

Arivizhivendhan, K. V., Boopathy, R., Maharaja, P., Regina Mary, R., and Sekaran, G. (2015). Bioactive prodigiosin-impregnated cellulose matrix for the removal of pathogenic bacteria from aqueous solution. *RSC Adv.* 5, 68621–68631. doi: 10.1039/C5RA09172A

Blanco, I., Abate, L., Bottino, F. A., and Bottino, P. (2014). Thermal behaviour of a series of novel aliphatic bridged polyhedral oligomeric silsesquioxanes (POSSs)/polystyrene (PS) nanocomposites: the influence of the bridge length on the resistance to thermal degradation. *Polym. Degrad. Stab.* 102, 132–137. doi: 10.1016/j.polymdegradstab.2014.01.029

Cavallaro, G., Lazzara, G., and Milioto, S. (2012). Exploiting the colloidal stability and solubilization ability of clay nanotubes/ionic surfactant hybrid nanomaterials. *J. Phys. Chem. C.* 116, 21932–21938. doi: 10.1021/jp307961q

Cavallaro, G., Milioto, S., Parisi, F., and Lazzara, G. (2018). Halloysite nanotubes loaded with calcium hydroxide: alkaline fillers for the deacidification of waterlogged archeological woods. *ACS Appl. Mater. Interfaces* 10, 27355–27364. doi: 10.1021/acsami.8b09416

Cirillo, G., Peitzsch, C., Vittorio, O., Curcio, M., Farfalla, A., Voli, F., et al. (2019). When polymers meet carbon nanostructures: expanding horizons in cancer therapy. *Future Med. Chem.* 11, 2205–2231. doi: 10.4155/fmc-2018-0540

Darshan, N., and Manonmani, H. K. (2015). Prodigiosin and its potential applications. *J. Food Sci. Technol.* 52, 5393–5407. doi: 10.1007/s13197-015-1740-4

de Araújo, H. W., Fukushima, K., and Takaki, G. M. (2010). Prodigiosin production by *Serratia marcescens* UCP 1549 using renewable-resources as a low cost substrate. *Molecules* 15, 6931–6940. doi: 10.3390/molecules15106931

De Jong, W. H., and Borm, P. J. (2008). Drug delivery and nanoparticles: applications and hazards. *Int. J. Nanomedicine* 3, 133–149.

Dulińska-Litewka, J., Łazarczyk, A., Hałubiec, P., Szafrański, O., Karnas, K., and Karewicz, A. (2019). Superparamagnetic iron oxide nanoparticles-current and prospective medical applications. *Materials* 12:E617. doi: 10.3390/ma12040617

Dzamukova, M. R., Naumenko, E. A., Lvov, Y. M., and Fakhrullin, R. F. (2015). Enzyme-activated intracellular drug delivery with tubule clay nanoformulation. *Sci. Rep.* 15:10560. doi: 10.1038/srep10560

Fakhrullina, G., Khakimova, E., Akhatova, F., Lazzara, G., Parisi, F., and Fakhrullin, R. (2019). Selective antimicrobial effects of curcumin@halloysite nanoformulation: a *Caenorhabditis elegans* study. *ACS Appl. Mater. Interfaces* 11, 23050–23064. doi: 10.1021/acsami.9b07499

Fakhrullina, G. I., Akhatova, F. S., Lvov, Y. M., and Fakhrullin, R. F. (2015). Toxicity of halloysite clay nanotubes in vivo: a *Caenorhabditis elegans* study. *Environ. Sci. Nano* 2, 54–59. doi: 10.1039/C4EN00135D

Francisco, R., Perez-Tomas, R., Gimenez-Bonafe, P., Soto-Cerrato, V., Gimenez-Xavier, P., and Ambrosio, S. (2007). Mechanisms of prodigiosin cytotoxicity in human neuroblastoma cell lines. *Eur. J. Pharmacol.* 572, 111–119. doi: 10.1016/j.ejphar.2007.06.054

Guryanov, I. D., Karamova, N. S., Yusupova, D. V., Gnezdilov, O. I., and Koshkarova, L. A. (2013). Bacterial pigment prodigiosin and its genotoxic effect. *Rus. J. Bioorganic Chem.* 39, 106–111.

Hu, Y., Chen, J., Li, X., Sun, Y., Huang, S., Li, Y., et al. (2017). Multifunctional halloysite nanotubes for targeted delivery and controlled release of doxorubicin in-vitro and in-vivo studies. *Nanotechnology* 28:375101. doi: 10.1088/1361-6528/aa8393

Huryn, D. M., and Wipf, P. (2014). "Natural product chemistry and cancer drug discovery," in *Cancer Drug Design and Discovery*, Second Edn, ed. S. Neidle (London: Academic Press), 91–120. doi: 10.1016/b978-0-12-396521-9.00003-6

Ji, S., Sun, R., Xu, K., Man, Z., Ji, J., Pu, Y., et al. (2019). Prodigiosin induces apoptosis and inhibits autophagy via the extracellular signal-regulated kinase pathway in K562 cells. *Toxicol. In Vitro* 60, 107–115. doi: 10.1016/j.tiv.2019.05.003

Joussein, E., Petit, S., Churchman, J., and Theng, B. (2005). Halloysite clay minerals - A review. *Clay Miner.* 40, 383–426. doi: 10.1180/0009855054040180

Kohout, C., Santi, C., and Polito, L. (2018). Anisotropic gold nanoparticles in biomedical applications. *Int. J. Mol. Sci.* 19:E3385. doi: 10.3390/ijms19113385

Konnova, S. A., Sharipova, I. R., Demina, T. A., Osin, Y. N., Yarullina, D. R., Ilinskaya, O. N., et al. (2013). Biomimetic cell-mediated three-dimensional assembly of halloysite nanotubes. *Chem. Commun.* 49, 4208–4210. doi: 10.1039/C2CC38254G

Kryuchkova, M., Danilushkina, A., Lvov, Y., and Fakhrullin, R. (2016). Evaluation of toxicity of nanoclays and graphene oxide in vivo: a *Paramecium caudatum* study. *Environ. Sci. Nano* 3, 442–452. doi: 10.1039/c5en0020

Lai, X., Agarwal, M., Lvov, Y. M., Pachpande, C., Varahramyan, K., and Witzmann, F. A. (2013). Proteomic profiling of halloysite clay nanotube exposure in intestinal cell co-culture. *J. Appl. Toxicol.* 33, 1316–1329. doi: 10.1002/jat.2858

Li, D., Liu, J., Wang, X., Kong, D., Du, W., Li, H., et al. (2018). Biological potential and mechanism of prodigiosin from *Serratia marcescens* subsp. lawsoniana in human choriocarcinoma and prostate cancer cell lines. *Int. J. Mol. Sci.* 19:E3465. doi: 10.3390/ijms19113465

Li, K., Zhang, Y., Chen, M., Hu, Y., Jiang, W., Zhou, L., et al. (2017). Enhanced antitumor efficacy of doxorubicin-encapsulated halloysite nanotubes. *Int. J. Nanomed.* 13, 19–30. doi: 10.2147/IJN.S143928

Li, T., Shi, S., Goel, S., Shen, X., Xie, X., Chen, Z., et al. (2019). Recent advancements in mesoporous silica nanoparticles towards therapeutic applications for cancer. *Acta Biomater.* 89, 1–13. doi: 10.1016/j.actbio.2019.02.031

Lin, Z.-Y., Kuo, C.-H., Wu, D.-C., and Chuang, W.-L. (2016). Anticancer effects of clinically acceptable colchicine concentrations on human gastric cancer cell lines. *Kaohsiung J. Med. Sci.* 32, 68–73. doi: 10.1016/j.kjms.2015.12.006

Lins, J. C. L., De Melo, M. E. B., Do Nascimento, S. C., and Adam, M. L. (2015). Differential genomic damage in different tumor lines induced by prodigiosin. *Anticancer Res.* 35, 3325–3332.

Lisuzzo, L., Cavallaro, G., Pasbakhsh, P., Milioto, S., and Lazzara, G. (2019). Why does vacuum drive to the loading of halloysite nanotubes? The key role of water confinement. *J. Coll. Interf. Sci.* 547, 361–369. doi: 10.1016/j.jcis.2019.04.012

Liu, Y., Zhou, H., Ma, X., Lin, C., Lu, L., Liu, D., et al. (2018). Prodigiosin inhibits proliferation, migration, and invasion of nasopharyngeal cancer cells. *Cell. Physiol. Biochem.* 48, 1556–1562. doi: 10.1159/000492278

Lorenzo, Y., Costa, S., Collins, A. R., and Azqueta, A. (2013). The comet assay, DNA damage, DNA repair and cytotoxicity: hedgehogs are not always dead. *Mutagenesis* 28, 427–432. doi: 10.1093/mutage/get018

Lu, C. H., Lin, S. C., Yang, S. Y., Pan, M. Y., Lin, Y. W., Hsu, C. Y., et al. (2012). Prodigiosin-induced cytotoxicity involves RAD51 down-regulation through the JNK and p38 MAPK pathways in human breast carcinoma cell lines. *Toxicol. Lett.* 212, 83–89. doi: 10.1016/j.toxlet.2012.05.002

Martín del Valle, E. M., Galán, M. A., and Carbonell, R. G. (2009). Drug delivery technologies: the way forward in the new decade Ind. *Eng. Chem. Res.* 48, 2475–2486. doi: 10.1021/ie800886m

Miyazaki, K., and Islam, N. (2007). Nanotechnology systems of innovation - An analysis of industry and academia research activities. *Technovation* 27, 661–675. doi: 10.1016/j.technovation.2007.05.009

Montaner, B., and Perez-Tomas, R. (2003). The prodigiosins: a new family of anticancer drugs. *Curr. Cancer Drug Targets* 3, 57–65. doi: 10.2174/1568009033333772

Naumenko, E., and Fakhrullin, R. (2017). "Toxicological evaluation of clay nanomaterials and polymer–clay nanocomposites," in *Functional Polymer Composites With Nanoclays*, eds Y. Lvov, B. Guo, and R. Fakhrullin (London: The Royal Society of Chemistry Publishing), 399–419. doi: 10.1039/9781782626725-00399

Naumenko, E., and Fakhrullin, R. (2019). Halloysite nanoclay/biopolymers composite materials in tissue engineering. *Biotechnol. J.* 14:1900055. doi: 10.1002/biot.201900055

Naumenko, E. A., Guryanov, I. D., Yendluri, R., Lvov, Y. M., and Fakhrullin, R. F. (2016). Clay nanotube–biopolymer composite scaffolds for tissue engineering. *Nanoscale* 8:7257. doi: 10.1039/C6NR00641H

Ni, W., Li, Z., Liu, Z., Ji, Y., Wu, L., Sun, S., et al. (2019). Dual-targeting nanoparticles: codelivery of curcumin and 5-fluorouracil for synergistic treatment of hepatocarcinoma. *J. Pharm. Sci.* 108, 1284–1295. doi: 10.1016/j.xphs.2018.10.042

Patel, V. B., Misra, S., Patel, B. B., and Majumdar, A. P. (2010). Colorectal cancer: chemopreventive role of curcumin and resveratrol. *Nutr. Cancer* 62, 958–967. doi: 10.1080/01635581.2010.510259

Perez-Tomas, R., Montaner, B., Llagostera, E., and Soto-Cerrato, V. (2003). The prodigiosins, proapoptotic drugs with anticancer properties. *Biochem. Pharmacol.* 66, 1447–1452. doi: 10.1016/s0006-2952(03)00496-9

Rozhina, E., Batasheva, S., Gomzikova, M., Naumenko, E., and Fakhrullin, R. (2019). Multicellular spheroids formation: the synergistic effects of halloysite nanoclay and cationic magnetic nanoparticles. *Coll. Surf. A Physicochem. Eng. Asp.* 565, 16–24. doi: 10.1016/j.colsurfa.2018.12.038

Rozhina, E., Panchal, A., Akhatova, F., Lvov, Y., and Fakhrullin, R. (2020). Cytocompatibility and cellular uptake of alkylsilane-modified hydrophobic halloysite nanotubes. *Appl. Clay Sci.* 185:105371. doi: 10.1016/j.clay.2019.105371

Sam, M. R., and Ghoreishi, S. (2018). Prodigiosin produced by *Serratia marcescens* inhibits expression of MMP-9 and survivin and promotes caspase-3 activation with induction of apoptosis in acute lymphoblastic leukaemia cells. *J. Appl. Microbiol.* 125, 1017–1029. doi: 10.1111/jam.13949

Shchukin, D. G., Sukhorukov, G. B., Price, R. R., and Lvov, Y. M. (2005). Halloysite nanotubes as biomimetic nanoreactors. *Small* 1, 510–513. doi: 10.1002/smll.200400120

Singh, P., Pandit, S., Mokkapati, V. R. S. S., Garg, A., Ravikumar, V., and Mijakovic, I. (2018). Gold nanoparticles in diagnostics and therapeutics for human cancer. *Int. J. Mol. Sci.* 19:E1979. doi: 10.3390/ijms19071979

Stankovic, N., Senerovic, L., Ilic-Tomic, T., Vasiljevic, B., and Nikodinovic-Runic, J. (2014). Properties and applications of undecyl-prodigiosin and other bacterial prodigiosins. *Appl. Microbiol. Biot.* 98, 3841–3858. doi: 10.1007/s00253-014-5590-1

Sumathi, C., MohanaPriya, D., Swarnalatha, S., Dinesh, M. G., and Sekaran, G. (2014). Production of prodigiosin using tannery fleshing and evaluating its pharmacological effects. *Sci. World J.* 2014:290327. doi: 10.1155/2014/290327

Suner, S. S., Demirci, S., Yetiskin, B., Fakhrullin, R., Naumenko, E., Okay, O., et al. (2019). Cryogel composites based on hyaluronic acid and halloysite nanotubes as scaffold for tissue engineering. *Int. J. Biol. Macromol.* 130, 627–635. doi: 10.1016/j.ijbiomac.2019.03.025

Suryawanshi, R. K., Patil, C. D., Borase, H. P., Salunke, B. K., and Patil, S. V. (2014). Studies on production and biological potential of prodigiosin by *Serratia marcescens*. *Appl. Biochem. Biotechnol.* 173, 1209–1221. doi: 10.1007/s12010-014-0921-3

Tarasova, E., Naumenko, E., Rozhina, E., Akhatova, F., and Fakhrullin, R. (2019). Cytocompatibility and uptake of polycations-modified halloysite clay nanotubes. *Appl. Clay Sci.* 169, 21–30. doi: 10.1016/j.clay.2018.12.016

Tiwari, G., Tiwari, R., Sriwastawa, B., Bhati, L., Pandey, S., Pandey, P., et al. (2012). Drug delivery systems: an updated review. *Int. J. Pharm. Investig.* 2, 2–11. doi: 10.4103/2230-973X.96920

Tran, P., Pyo, Y.-C., Kim, D.-H., Lee, S.-E., Kim, J.-K., and Park, J.-S. (2019). Overview of the manufacturing methods of solid dispersion technology for improving the solubility of poorly water-soluble drugs and application to anticancer drugs. *Pharmaceutics* 11:E132. doi: 10.3390/pharmaceutics11030132

Williamson, N. R., Fineran, P. C., Leeper, F. J., and Salmond, G. P. (2006). The biosynthesis and regulation of bacterial prodiginines. *Nat. Rev. Microbiol.* 4, 887–899. doi: 10.1038/nrmicro1531

Yendluri, R., Lvov, Y., de Villiers, M. M., Vinokurov, V., Naumenko, E., Tarasova, E., et al. (2017). Paclitaxel encapsulated in halloysite clay nanotubes for intestinal and intracellular delivery. *J. Pharm. Sci.* 106, 3131–3139. doi: 10.1016/j.xphs.2017.05.034

Yvon, A.-M. C., Wadsworth, P., and Jordan, M. A. (1999). Taxol suppresses dynamics of individual microtubules in living human tumor cells. *Mol. Biol. Cell* 10, 947–959. doi: 10.1091/mbc.10.4.947

Zhang, J., Shen, Y., Liu, J., and Wei, D. (2005). Antimetastatic effect of prodigiosin through inhibition of tumor invasion. *Biochem. Pharmacol.* 69, 407–414. doi: 10.1016/j.bcp.2004.08.037

Zhao, K., Li, D., Cheng, G., Zhang, B., Han, J., Chen, J., et al. (2019). Targeted delivery prodigiosin to choriocarcinoma by peptide-guided dendrigraft poly-l-lysines nanoparticles. *Int. J. Mol. Sci.* 20:5458. doi: 10.3390/ijms20215458

Conflict of Interest: The authors declare that the research was conducted in the absence of any commercial or financial relationships that could be construed as a potential conflict of interest.

frontiers in Bioengineering and Biotechnology

REVIEW
published: 29 May 2020
doi: 10.3389/fbioe.2020.00504

Ultrashort Peptide Self-Assembly: Front-Runners to Transport Drug and Gene Cargos

Seema Gupta[1]*, *Indu Singh*[1,2], *Ashwani K. Sharma*[2]* and *Pradeep Kumar*[2]*

[1] Chemistry Department, Acharya Narendra Dev College, University of Delhi, New Delhi, India, [2] Nucleic Acids Research Laboratory, CSIR-Institute of Genomics and Integrative Biology, New Delhi, India

The translational therapies to promote interaction between cell and signal come with stringent eligibility criteria. The chemically defined, hierarchically organized, and simpler yet blessed with robust intermolecular association, the peptides, are privileged to make the cut-off for sensing the cell-signal for biologics delivery and tissue engineering. The signature service and insoluble network formation of the peptide self-assemblies as hydrogels have drawn a spell of research activity among the scientists all around the globe in the past decades. The therapeutic peptide market players are anticipating promising growth opportunities due to the ample technological advancements in this field. The presence of the other organic moieties, enzyme substrates and well-established protecting groups like Fmoc and Boc etc., bring the best of both worlds. Since the large sequences of peptides severely limit the purification and their isolation, this article reviews the account of last 5 years' efforts on novel approaches for formulation and development of single molecule amino acids, ultra-short peptide self-assemblies (di- and tri- peptides only) and their derivatives as drug/gene carriers and tissue-engineering systems.

Keywords: amphiphilicity, peptide, self-assembly, drug delivery, tissue engineering

OPEN ACCESS

Edited by:
Stefano Leporatti,
Italian National Research Council, Italy

Reviewed by:
Remigiusz Marcin Bachor,
University of Wrocław, Poland
Hakan Ceylan,
Max Planck Institute for Intelligent Systems, Germany

***Correspondence:**
Seema Gupta
seemagupta@andc.du.ac.in
Ashwani K. Sharma
ashwani@igib.in
Pradeep Kumar
pkumar@igib.res.in

Specialty section:
This article was submitted to Nanobiotechnology, a section of the journal Frontiers in Bioengineering and Biotechnology

Received: *29 January 2020*
Accepted: *29 April 2020*
Published: *29 May 2020*

Citation:
Gupta S, Singh I, Sharma AK and Kumar P (2020) Ultrashort Peptide Self-Assembly: Front-Runners to Transport Drug and Gene Cargos. Front. Bioeng. Biotechnol. 8:504. doi: 10.3389/fbioe.2020.00504

INTRODUCTION

The global trend is growing toward precise medicines and diagnoses through multi-centered approaches of drug delivery technology. The poor systemic bioavailability, solubility, absorption, and stability of large sized materials pose major challenges in the area of drug delivery. Novel natural biomaterials which can qualify to be biodegradable, biocompatible, non-toxic, renewable, and readily available to deliver therapeutic agents to precise targeted sites in a controlled manner is one of the most sort after research-field. Presently, nanotechnology (Lombardo et al., 2020) has provided a solution by opening up of newer avenues in terms of developing advanced controlled drug delivery and release systems that have met with huge success (Webber et al., 2016; Webber and Langer, 2017; Patra et al., 2018). The customizable nanoparticles with the manipulation in size, surface characteristics and materials used enhance the efficacy of drug delivery in a paramount manner along with the advantage of safer treatment (Eskandari et al., 2017; Rizvi and Saleh, 2018). A relatively newer area to deliver drugs across biological barriers for improved site-specific absorption is also being explored (Kou et al., 2018) i.e., transporter-targeted nanoparticles. A specific application based self-assembled materials, injectable biomaterials, are also being investigated to improve the advancing practices in healthcare (Sahoo et al., 2018b).

Uncomplicated to design and synthesize, biocompatible, embedded with appropriate opportunities for chemical alterations, demonstrating molecular selectivity and specific interaction with diverse types of biological systems- all these characteristics make peptides ideal and flexible candidates for constructing tuneable nanostructures with normal end functionalization (Sun L. et al., 2016; Yu et al., 2016; Galdiero and Gomes, 2017) (**Figure 1**). It is hypothesized that simple amino acids may be the first catalysts for formation of peptide bonds (Luisi, 2015). The evolutionary model put forward by Carny and Gazit on the mechanism of origin of life links the aptitude of short peptides to the creation of the present living systems (Carny and Gazit, 2005). According to this model, the properties like encapsulation, catalytic potential in chemical reactions and a highly ordered template for the assembly of nucleotides, which might be the early events, could lead to create the biological systems. Self-assembling peptides, a category of peptides, assemble spontaneously into ordered nanostructures. Peptides, even as short as dipeptides, are blessed to hold all the desirable molecular information to form well-ordered structures, when worked for nano-scale. The self-assembly of short peptides turning to β-sheet amyloid conformers brings extraordinary structural stability and multi-functionality like; self-replication, catalytic activities and information transfer, which is impossible for the corresponding non-aggregated peptides. The emergence and evolvement of such mutualistic networks may eventually lead to origin of life (Maury, 2018).

Peptide self-assemblies are the gait of 20 amino acids which can be manipulated in terms of number, type, sequence, and side chain groups. These nanostructures can be customized by incorporating modified amino acids in the peptide design to have superior assembling properties and enzymatic stability. This bottom-up science, inspired by the wonders of nature operating on the nanoscale, generates many biological nanostructures such as proteins and DNA/RNA, enabling functioning of life. Even the top-down method, with an advantage over the bottom-up approach supports to discover new peptide sequences aimed to a specific binding site on bio-macromolecules based on their structural properties. It is compelling the scientists to reach after the chemistry of these macromolecules and synthesize newer molecular self-assemblies. The peptide synthesis is a simple and affordable synthetic chemistry via conventional procedures, solution or solid phase. The cost of making peptide is found to be associated with the motif length, purity, chirality of amino acids as well as the expertise of the fabricator. The ability of natural and synthetic amino acid building blocks, both, to form ordered assemblies through self-association process with defined architectures and prominent physical properties has

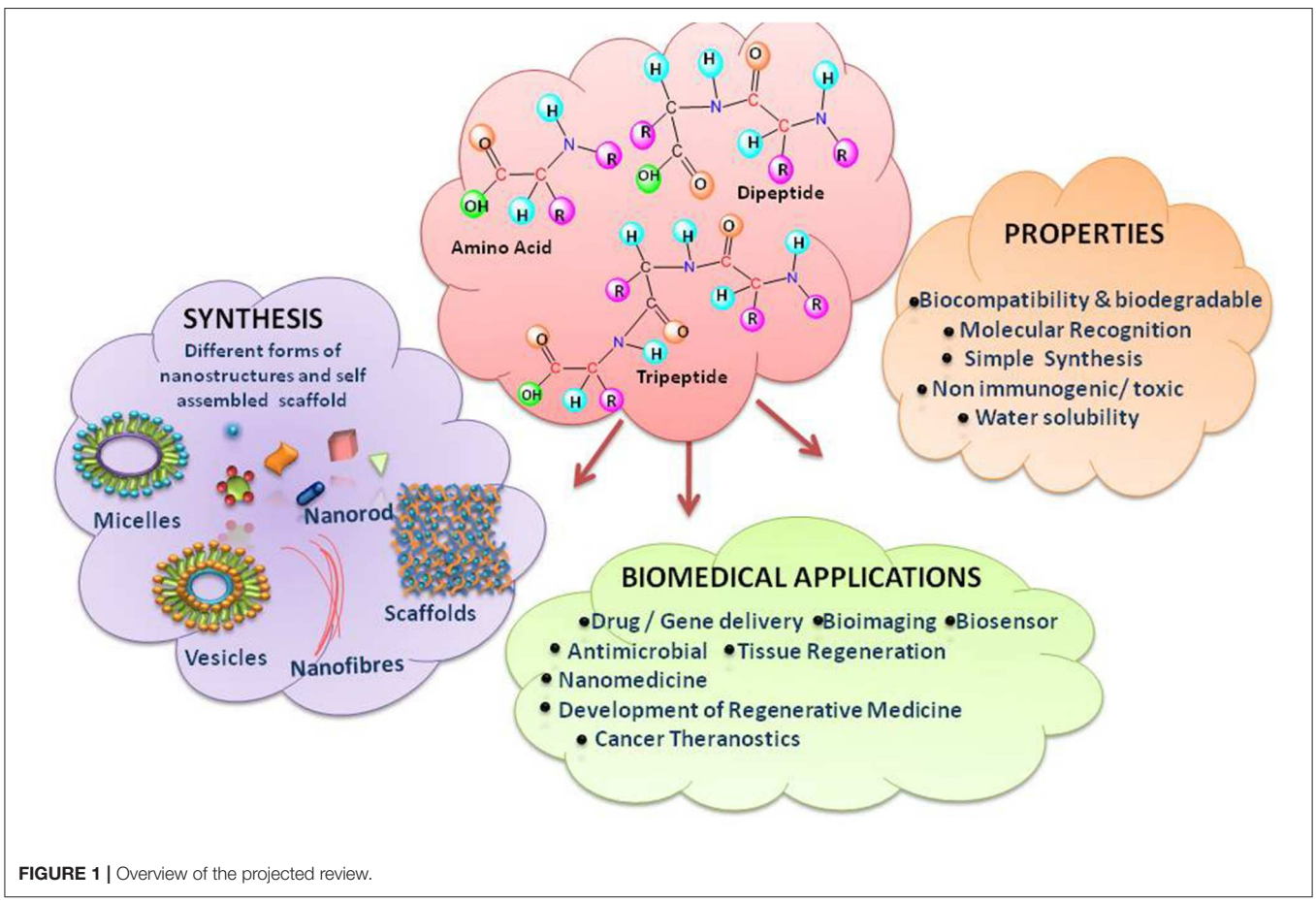

FIGURE 1 | Overview of the projected review.

been reviewed by Chakraborty and Gazit (2018). The review by Lee et al., has summarized the building blocks of peptide self-assemblies categorized by their constituting amino acids, the bound chains/motifs, characteristics and regulatory factors (Lee et al., 2019). The study of ordered nanofibres from protein self-assembly in natural systems has been recognized as reductionist approach, wherein, core peptide building blocks could be derived from the parent protein (Guterman et al., 2016).

Regulators of Self-Assembly

The fundamental mechanisms for the self-assembled nanostructures of different types and structures of peptides are explored regularly (Mandal et al., 2014; Chen et al., 2016; Liao et al., 2016; Fan et al., 2017; Pandit et al., 2018; Mason and Buell, 2019). The constituent amino acid residues govern the supramolecular nanostructures and peptide secondary structures to adopt the conformations led by intra-/intermolecular interactions during peptide self-assembly. The multifunctional materials with highly ordered structures could be achieved by hierarchical architectures with anisotropy and suggested to be facilitated by rational self-control of weak intermolecular interactions regulating the self-assembly process at different steps (Yuan et al., 2019).

Inter/Intramolecular Non-Covalent Interactions

The design and nature of these ordered nanostructures is the outcome of the synergistic effect of various intermolecular non-covalent interactions, comprising H-bonding, π-π bonding, electrostatic forces, hydrophobic, and van der Waals' interactions. Molecular self-assembly, a more stable structure, is formed under thermodynamic equilibrium conditions by arrangements through various non-covalent weak interactions which can generate assemblies of excipient patterns (Mateescu et al., 2015). This alliance of non-covalent interactions strategizes the self-assembly process and determines the thermodynamic stability, though, kinetic parameters also play a critical factor in concluding the dynamic material (Wang et al., 2016a; Liu et al., 2017).

The hydrogen bonds have the competence to assist the growth of biomolecules in one direction with a long-range order to manifest one-dimensional (1D) nanostructures. The hydrogen bond stacking in case of cyclic peptides has been reported to provide the primary structure and comprehensive cylindrical morphology to the self-assembly (Rho et al., 2019). Besides the contribution from individual amino acids, the peptide backbone itself also provides significant stability through hydrogen bonds (Leite et al., 2015).

Electrostatic interactions portray remarkable performance in the self-assembly of peptides and stabilize the nanostructures. Electrostatic attraction between the positively charged peptide fibril and negatively charged small molecule drugs for controlled drug delivery (Mauri et al., 2017).

Amino acids based on amino acid residues can be categorized into hydrophobic and hydrophilic ones. Peptides can form highly ordered self-assembled superstructures due to their hydrophobic property. These hydrophobic interactions are observed to progress from open networks of secondary structures toward closed cylindrical nanostructures (β-sheets or random coils) (Fu et al., 2014).

van der Waals forces, contemplating entire intermolecular forces and relatively weaker to covalent bonds, play an integral role in supramolecular organization in nanotechnology. van der Waals interactions in plane are observed to control not only the molecular self-assembly structure but their phase transition as well (Gao et al., 2015). The dipole-dipole interactions also support in the self-assembly process and are reported to enhance the mechanical properties as dual non-covalent bonding strategy (Cao et al., 2019).

Ionic Interactions

The arrays of ionic interactions are also part of the driving energy of the self-assemblies in water along with the hydrophobic interactions and peptide-backbone hydrogen bonds. Self-assembling, ionic-complementary peptides are also being studied by researchers (Chen, 2005). The synergistic effect of both non-covalent and ionic interactions has been reported to provide better stability to the studied hydrogel (Xie et al., 2016).

Aromatic Interactions

π-π stacking between large π-conjugated surfaces provides an overall stability to supramolecular polymers bound together by non-covalent interactions (Cockroft et al., 2005). Various collagen like peptides mimic the fibril formation and assemble into higher order hierarchical structures through π-π stacking interactions (Chen and Zou, 2019). The hypothesis put forward by Gazit et al. regarding the lead role played by aromatic interactions in the self-assembly of peptide nanotubes/amyloid-like structures has been established time and again (Reches and Gazit, 2005). The aromatic-aromatic interactions have been reported to transform into β-sheet conformation from α-helix on being connected to an aromatic motif at C-terminal (Li J. et al., 2017). Though the importance of aromatic interactions in amyloid formation has been challenged (Lakshmanan et al., 2013) but, are significant in amyloid β-peptide (Genji et al., 2017).

In peptide self-assembly, nonpolar amino acids (aromatic and aliphatic amino acids) aggregate through π-π stacking and hydrophobic interactions, while the polar amino acids, depending on whether they have uncharged or charged residues, stabilize through either electrostatic interactions or hydrogen bonding. The weak bond-based injectable hydrogels based on hydrogen bonding, ionic, hydrophobic and π-π stacking interactions and host-guest chemistry have been reviewed by Ding and Wang (2017). These non-covalent interactions act as driving force in designing the gels (Dou and Feng, 2017). In a characteristic assembly, electrostatic repulsions control the nanofiber length. Addition of a covalent bond forming unit, which could conjugate to the peptide sequence by amide bond condensation altered the balance between hydrogen bond formation and compensated the repulsive electrostatic interactions. Thus formation of covalent bond reinforced hydrogen bonds between peptides enabling the fiber elongation, which otherwise energetically is not possible (Sato et al., 2017). The study on reversible covalent chemistry displayed that the

difference in self-assembly modes at the non-covalent level could also be reflected at the covalent level (Komáromy et al., 2017).

It is difficult to predict the combo of all these molecular forces after the peptide self-assembly. Extra facts about the interaction of these forces are essential to plan much efficient, chemically stable peptide self-assemblies.

Secondary Structural Conformations

Most of the self-assembling peptides are supposed to be readily soluble in water due to the presence of amino acid molecules containing charged residues (alternating hydrophilic and hydrophobic regions), periodically repeated and discrete polar and non-polar surfaces. α-amino acids comprising the peptides have the inclination to adopt various secondary structural conformations like α-helices (Boyle, 2018), β-sheets (Leite et al., 2015), β-hairpins (Nagarkar et al., 2008) and even the folds (Yoo and Lee, 2017; Kulkarni et al., 2019) and this dynamic behavior of the self-assembling peptides at the molecular structural level influences the peptide-based self-assembly processes in water (Gopalan et al., 2015; Bera and Gazit, 2019; Kulkarni et al., 2019). The process continues and these structures assemble further spontaneously to form nanofibers which consequently aggregate into supramolecular scaffolds and can entrap large volumes of water. The hierarchical self-assembly process can potentially stabilize diverse β-sheet hydrogen bonded architectures. Among the secondary structures, hydrogen bonding between carbonyl oxygen and the amino group of every third residue in the helical turn stabilizes an α-helix (each helical turn consisting of 3.6 amino acid residues) while β-sheets originate with hydrogen bonding between two or more β-strands (along which, the backbone of the peptide stretches) (Kulkarni et al., 2019). The self-association phenomenon of aromatic side-chains in β-peptide oligomers supports the helical secondary structure formed by intramolecular backbone-side chain CH-π interactions and yields large vesicles due to the gain in the hydrophobic area (Mándity et al., 2014). In a study, Sarkar et al. (2015) have also demonstrated the effect of solvent interactions on the folding pattern resulting in a change in initial helical conformation and structural diversity of short aromatic γ-peptides. Another architecture, coiled-coil peptide self-assembly, though suffering from the drawback of having longer amino acid sequences compared to other self-assembling peptide systems such as β-sheet fibrillizing peptides or peptide amphiphiles has been reported to offer unique advantages as reviewed by Wu and Collier (2017). All these functional architectures are the result of molecular recognition process and self-assembly led by non-covalent interactions. Zhou et al. enlightened on the adoption of amino acid conformations in the complex interactive process in relation to peptide sequence. The study evidenced that peptides with high sequence similarity could self-assemble into diverse nanostructures though could acquire similar secondary structures while completely different sequences assembled into one type of nanostructures (Zhou et al., 2019).

Various molecular forces make peptides self-assemble in different supramolecular peptides. As per the observations, a peptide with an electrostatically charged/hydrophilic head and a hydrophobic tail would self-assemble in spherical micelles or vesicles which on elongation could lead the way into fibers or tubes, respectively. Peptides with a β-sheet show inclination to assemble into flat structures suchlike tapes or ribbons. Nonetheless, on increasing the concentration of the peptides, these tapes and ribbons could stack on one another and turn into more firmly packed fibers.

A relatively new innovation, the use of co-assembly, to produce nanostructures is also being explored. When an individual component is incompetent to have the basic properties required for the self-assembly, a co-assembly option provides the necessary support. The cooperativity movement is directed by non-covalent interactions, in particular, electrostatic. The combination of experimental justification and computational simulations provides a basic support to identify structural and functional components (Raymond and Nilsson, 2018).

Amphiphilic Peptides

It is an aqueous peptide self-assembly, characteristically spurred by the presence of amphiphilic character in the monomer units, contains hydrophilic and hydrophobic domains, which impulsively arrange to shield hydrophobic groups and minimize contact with bulk water. These molecules contain one or more alkyl chain tails along with a terminal peptidic head group. The fine tuning of balance among the hydrophilic block with polar amino acids and hydrophobic blocks could stabilize various supramolecular structures by hydrophobic, electrostatic, β-sheet hydrogen bonds and π-π stacking interactions (Mikhalevich et al., 2017; Qiu et al., 2018). A naïve investigation by Accardo et al. (2013) wherein use of an intrinsically disordered peptide as a polar head connected to alkyl chain led to some disorder-to-order transition upon their self-assembly in supramolecular aggregates. The group recommended this kind of ordered core and a "disordered" surface as a potential scaffold for future biomaterials. Furthermore, Tesauro et al. (2019) discussed the versatility of arrangements in side chains, option to load charges/functional groups and select physical and chemical patterns to acquire desired biostructures during the design of peptide amphiphile (PA) and suggested the option of using conformational preferences in structured and/or disordered peptides in the review.

The review by Cui et al. has emphasized on controlling the environment of PA self-assembly manufacturing and details of their applications (Cui et al., 2010). Addition of an ionizable/charged amino acid to the PA structure is suggestive to increase the number of charges per aggregate. A self-assembly model of PAs produced by a C_{16} alkyl tail linked to a chain of two lysines ($C_{16}K_2$) or three lysines ($C_{16}K_3$) stand reasonably accurate on the predicted behavior in terms of morphology, size and the state of protonation of the aggregates. The work by Zaldivar et al. revealed that the system followed a charge regulation mechanism and found to decrease electrostatic repulsions between charged lysines (Zaldivar et al., 2019). An atomic level study by Rad-Malekshahi et al. (2015a) analyzed the vesicle surface structure and dynamics of self-assembled nanovesicles along with the intermolecular forces between amphiphilic peptides to improve and tune the biophysical properties of the nanocarrier.

Impact of Chemical Modifications

Different chemical reactions are employed to construct self-assembled nanostructures (Rasale and Das, 2015). A general approach followed by peptide chemists is to incorporate modifications in the form of easy and reversible cleavable appropriate moieties/groups at the carbonyl–nitrogen bond (readily cleavable urethanes containing appropriate alkyl groups such as benzyl and *tert*-butyl liberating the amino groups), incorporating alkyl spacers of various lengths to modulate the chirality (Panda et al., 2019), π-clamping to tune the reactivity (Zhang C. et al., 2016), backbone amide modifications for peptidomimetic hydrogelators with enhanced stability and mechanical properties compared to peptide hydrogelators (Basavalingappa et al., 2019), enforcing a conformational constraint to prevent β-sheet structure (Bowerman and Nilsson, 2010), formulated sequence patterns to optimize charge distribution for conjugating bioactive cargo (Zhang H. et al., 2017), alternating d/l-chirality for 1D- to 2D-self-assembly (Insua and Montenegro, 2019), a racemic mixture of the mirror-image peptides to provide more rigidity to the gel (Nagy-Smith et al., 2017), alternative hydrophobic and hydrophilic residues for catalytic activity (Song et al., 2018), coordination with metal ions to inhibit amyloid-like structure (Ji et al., 2019), fine-tune assembly for hydrogel (Loic, 2017) and so on. N-Acetylation (compound attached to the amino; N-terminus) and C-amidation (compound attached to the carboxyl; C-terminus) is the most usual policy to stabilize nearly all categories of peptides. The peptides, without modification, perhaps may not be toxic, but the impact after the modification, though also unsettled, is being explored (Soleymani-Goloujeh et al., 2018). Amino acids and short peptides bearing moieties like 9-fluorenylmethoxycarbonyl (Fmoc) (Tao et al., 2016), (Chakraborty and Gazit, 2018), aromatic naphthalene-2-methoxycarbonyl (Nmoc) (Rasale et al., 2015), 9-anthracenemethoxycarbonyl (Amoc) (Gavel et al., 2018a), at N-terminal provide extra advantage to the fabrication of self-assemblies due to inherent hydrophobicity and aromaticity and are also, significant in gel formation (Orbach et al., 2012; Fleming et al., 2013; Singh et al., 2015). *tert*-butyloxycarbonyl (Boc) is also used to protect α-amino group in peptide synthesis (Ragnarsson and Grehn, 2013). Introduction of non-natural d-amino acid at the N-terminus, has shown unexpected effects on peptide secondary conformation and even the biological performance and so is another useful strategy to confer self-assembling properties (Melchionna et al., 2016). Small chemical modifications in peptides at the N- or C-terminus, intrinsic to self-assembly into ordered supramolecular architectures and their biomedical applications, have been reviewed by Rad-Malekshahi et al. (2015b). N- and C-terminal of the aromatic components as well as linker segment and peptide sequence have also been demonstrated to control the self-assembly of aromatic peptide amphiphiles (Fleming and Ulijn, 2014).

Recently, guiding principles to customize the kinetics and morphological changes in supramolecular peptide nanostructures have been introduced by Son et al. (2019) upon exposure of matrix metalloproteinase. These guiding principles enumerate systematic customization of enzyme-responsive peptide nanostructures by exchange of just a few amino acids, for general use in performance optimization of enzyme-responsive materials (Son et al., 2019). The advantages of enzyme-instructed self-assembly (EISA) in triggering the molecular self-assembly *in situ*, by overexpression, to prepare supramolecular biofunctional materials and hydrogels has been reviewed by Gao et al. (2019).

The focus has also turned to design self-assemblies of peptide-based conjugates. The multidisciplinary studies involving conjugated short peptides and single amino acids highlighted the role of conjugated material and broadened the horizon of self-assembling materials (Acar et al., 2017; Edwards-Gayle and Hamley, 2017). The reformed attempts to enhance *in vivo* half-life time and widespread applications of peptides are being made by conjugating them with nanoparticles (Jeong et al., 2018; Spicer et al., 2018; Wang et al., 2018; Jiang et al., 2019). A critical comparison of peptide materials with non-peptide materials has been attempted by Santis and Readnov to count on the contribution of peptide self-assemblies in real-life applications i.e., commercial products (De Santis and Ryadnov, 2015). The use of sequence-specific peptides as biological recognition elements has nicely been reviewed by Slocik and Naik (Slocik and Naik, 2017). The insertion of suitable spacers (charged or neutral) between the hydrophobic region and the peptide are reported to uphold flexibility, mobility, and sometimes increase the solubility of the molecule. The linker is supportive for creating functionalized nanofibrils and expand the modules of chemoselective bio-conjugation approaches in site-specific titivation of self-assembling peptides (Biscaglia et al., 2016; Scelsi et al., 2019). Cui and coworkers (Cui and Chen, 2017) worked on a themed issue envisioned to bring leading researchers working on peptides and peptide conjugates to assess the recent progress in utilizing peptide-based constructs and describe the challenges to interface with biology for specific biomedical applications.

The peptide-templated noble metal catalysts also play an important role in chemical biology (Wang W. et al., 2017). Metal coordination to natural and non-natural binding sites of different peptides has been reported to stimulate the peptide self-assembly (Zou et al., 2015). This knowledge of the forces to obtain an ordered organization can assist innovative peptide based materials for more assorted applications.

Applications of Peptide Self-Assemblies

Peptide Self- Assemblies as Drug Carriers

The rich chemistry of various non-covalent interactions has led to swift development of self-assemblies as drug carriers, particularly, in short peptides (Huang et al., 2013; Panda and Chauhan, 2014; Iglesias and Marchesan, 2017; Amit et al., 2018; Raza et al., 2018; Mishra and Jyoti Panda, 2019).

The impact of finite peptide nanostructures for the development of systemic therapeutic delivery vehicles is, in particular, of interest, as the length of the assembly plays important roles during cell uptake and tissue penetration (Mendes et al., 2013) (**Figure 2**). A strategy has been reported,

where the length of charged peptide-amphiphile supramolecular assemblies could be controlled through covalent bond formation (Sato et al., 2017).

The extensive non-covalent interactions provide several advantages in developing self-assembled materials for drug-delivery (Leite et al., 2015). These are mainly at the three working stages, namely, drug loading, self-assembly–drug conjugate transport, and finally the cellular drug delivery (Doane and Burda, 2012; Habibi et al., 2016; Fan et al., 2017). Devadasu et al. have suggested that understanding of the drug and disease is of utmost importance before designing a delivery system (Devadasu et al., 2012). The self-assembled-ordered structures of peptides with extensive π-π and hydrogen bonding, also a precondition for semiconductor properties, has aspired the scientists to assemble such structures for biological semiconductors along-with biocompatible and drug release materials (Tao et al., 2017). A review by Sis and Webber has discussed about the basic designs in peptide self-assemblies and ways to mend the efficacy of drug delivery (Sis and Webber, 2019). Self-assembled photosensitizers resulting from amphiphilic dipeptide- or amino-acid-tuned for photodynamic therapy (PDT) have been reported (Liu et al., 2016). The tuneable size, surface charge and multi-responsiveness toward pH, detergents, and enzymes suggest the simple and efficient self-assembled method to deliver photosensitizers (Li L.L. et al., 2018).

Amphiphilic peptides have brought a paradigm shift toward self-assembled PA in drug delivery. The amphiphilic peptides provide a lot of option in both linear and cyclic peptide sequences, side chains loaded with charges, self–assembled as vesicles, micelles, nanofibers and nanotubes for delivery systems and for other biotechnological applications (Goel et al., 2015). An account on the versatility of cyclic peptides and the safety measures in terms of size control, length and bundle width of nanotubes during the successful delivery of active pharmaceutical ingredients has been presented in a mini-review by Hsieh and Liaw (2019). The impact of amino-acid side-chains or covalently linked hydrophobic chain in PA on their stimuli-responsive drug delivery applications has been reviewed by Song et al. (2017).

Another strategy is to use the self-assembly of amphiphilic drug molecules to do the drug-loading and then deliver the cargo as well on its own. In case of low water-solubility of the drug, hydrophilic segments may be conjugated to bestow amphiphilic behavior. The conjugation pushes the peptide sequences for one-dimensional elongation through β-sheet formation. Their architecture fundamentals administer the self-assembly of PA's into supramolecular systems to be applied in drug delivery (Lock et al., 2013).

Ample attention is also being directed to cell-penetrating peptides (CPPs), as carriers for intracellular transport cargoes such as siRNA, nucleic acids, proteins, various nano-particulate pharmaceutical carriers (e.g., liposomes, micelles), small molecule therapeutic agents as well as quantum dots and MRI contrast agents (Brasseur and Divita, 2010; Bechara and Sagan, 2013; Choi and David, 2014; Copolovici et al., 2014; Wang et al., 2014; Huang et al., 2015; Skotland et al., 2015; Dinca et al., 2016; Guo Z. et al., 2016; Kurrikoff et al., 2016; Lehto et al., 2016; Guidotti et al., 2017; Hoffmann et al., 2018; Panigrahi et al., 2018; Ramaker et al., 2018; Vánová et al., 2019), since these are internalized by cells in an exceedingly effective manner. The study by Ramaker et al. observed a statistically substantial dependence of CPPs' uptake efficiency on both net charge and peptide length; longer CPP possibly due to more ordered α-helical structure with high charge could ferry conjugated cargo across membranes more efficiently (Ramaker et al., 2018). The non-covalent approach for complexing CPPs to nucleic acids or viruses has shown better gene delivery both *in vitro* and *in vivo* (Alhakamy et al., 2013). Gallo et al. have provided a comprehensive list of recognized CPPs along with their reported applications (Gallo et al., 2019). Another review by Borrelli et al. has discussed biological properties of CPP upon conjugation with specific molecules with special emphasis on uses in cancer therapy (Borrelli et al., 2018).

Nanomedicines directly assembled from pharmaceutical ingredients, termed as small molecule nanomedicines (SMNs), have the potential to improve the drug delivery efficiency, biosafety and largely reduce the research and development cost. Xue et al. (2020) highlighted the recent advances in a section on drugs and photosensitizers with peptides and exhibited advantages of SMNs in the review article.

Tailored drug delivery vehicles are continuously gathering attention. Peptide–drug conjugates (PDCs) enable selective delivery of cytotoxic cargoes to target cells (Ma et al., 2017; Wang et al., 2017a; Wang W. et al., 2017; Vrettos et al., 2018). PDCs have exclusive and precise features to build one-component nanomedicines (OCNs) containing only one type of chemical substance. These OCNs do not require additional carriers. In fact, these are equipped with desired physicochemical features to involuntarily aggregate as well as accumulate at target sites (Su et al., 2015). Since peptides can be manufactured effortlessly in large quantities and need simple purification, their range of selection of peptide sequences as per the requisite physicochemical properties like stability, solubility, overall charge and availability of the characteristic groups for the conjugation with the therapeutic payload, these are considered as sought-after prodrugs (He et al., 2019).

Peptide-based hydrogels is another class of drug delivery vehicles programmed via drug encapsulation or conjugated covalently with therapeutics. Small peptide molecules, in general, have the desired state to form specific secondary structures in solution and then self-assemble into fibrillary network under various physical conditions (Fu et al., 2013; Tomasini and Castellucci, 2013; Zhang L. et al., 2015). An analysis of the structural/molecular features of different β-sheet peptide hydrogels and their relation to mechanical properties to design effective hydrogels has been reviewed by Rodriguez et al. (2016). The sticky-ended fibrillation designs, applied in DNA and coiled fibers, have inspired Sarkar et al. (2014) to develop a strategy to form staggered triple helical species assisted by interchain charged pairs. The comparison between the two classes of collagen mimetic peptides having same composition but different domain arrangements showed that the larger nucleation domains resulted in rapid fiber formation and gelation while short nucleation domains left the peptide soluble for longer period (Sarkar et al., 2014). The thixotropic supramolecular hydrogels

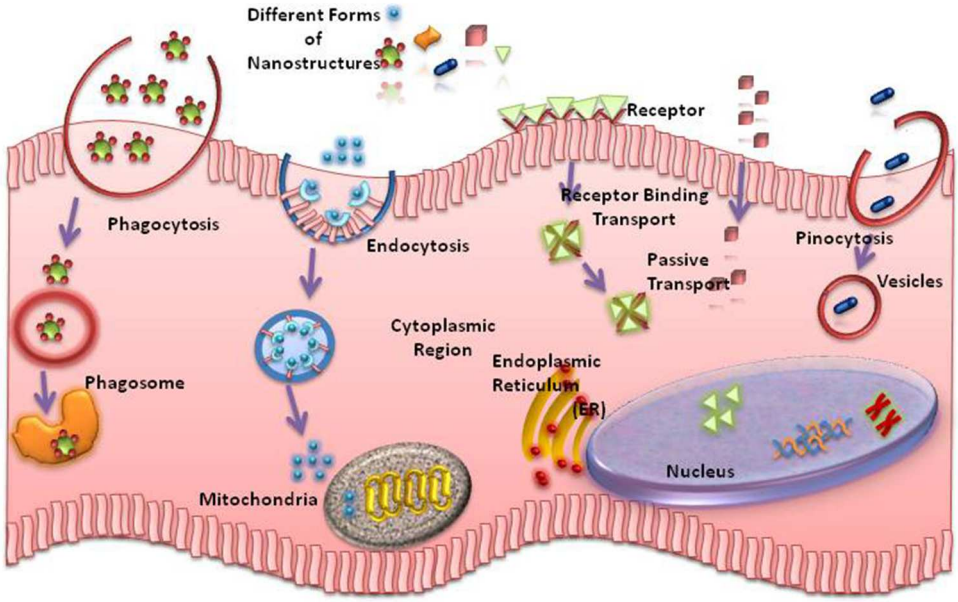

FIGURE 2 | Different routes of entry of nanostructures into the cells.

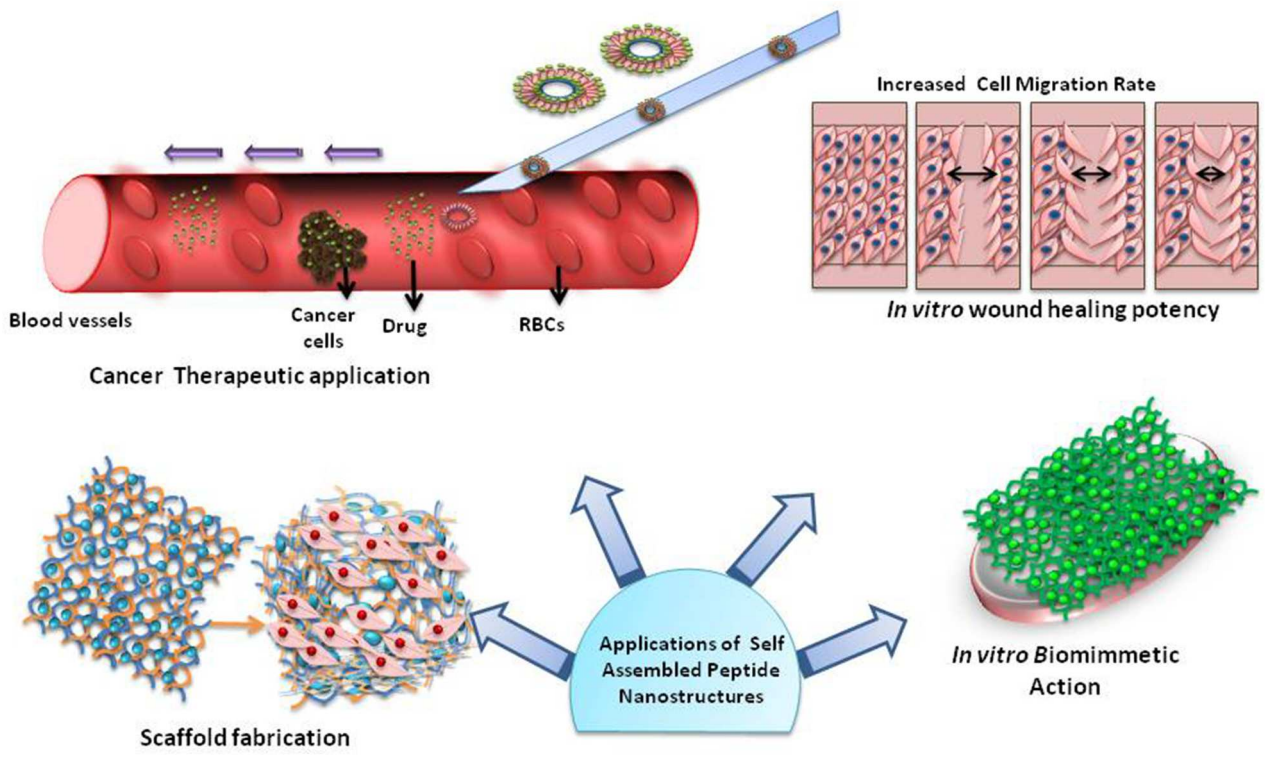

FIGURE 3 | Applications of self-assembled peptide nanostructures.

formed in response to external environmental stimuli have wide ranges of potential biological applications (Levin et al., 2014; Seow and Hauser, 2014; Loic, 2017; Zanna and Tomasini, 2017; Mondal et al., 2020). The stability of peptide-based hydrogels, specially to enzymatic degradation has been reviewed by Yadav et al. (2020). The composition of hydrogel material with tuneable

properties controls the release of sensitive drugs (Du et al., 2015; Raza et al., 2018). Various methods to design and control the self-assembly mechanism in hydrogels for drug-delivery have been elaborated in the literature (Altunbas and Pochan, 2011; Briuglia et al., 2014; Yu et al., 2015; Li et al., 2019b). A review by Zhang et al. has highlighted on tuning the unique features/morphology of the nanostructures functions formed during the gelation process by controlling the morphology-dependent variations (Zhang L. et al., 2015). The loaded drugs not only get physically trapped, but also bring morphological modifications in the peptide hydrogel (Kurbasic et al., 2017; Parisi et al., 2019), thus converting drug–peptide co-assembly into a supramolecular hydrogel. The attempts have also been made to design peptide-based supramolecular hydrogels for protein drug delivery and gene therapy (Li Y. et al., 2016; Youngblood et al., 2018). The incorporation of non-viral vectors within hydrogels to promote tissue regeneration is another challenging area (Rivas et al., 2019). A photo-cross-linking strategy, based on the ruthenium-complex-catalyzed conversion of tyrosine to dityrosine, to enhance the mechanical stability of nanofibers by 104-fold with a storage modulus of ∼100 kPa (perhaps, one of the highest reported so far among the small peptide hydrogels), with potential to be used in tissue engineering and controlled drug release has been reported by Ding et al. (2013). The low molecular mass organic gelators (LMOGs) have gained much interest in recent years with impending applications in drug delivery and tissue engineering (Sagiri et al., 2014; Skilling et al., 2014; Li Z. et al., 2016). The work on nanostructures containing *D*-amino acids, for their role in biologics delivery is also catching attention, but has a long way to go (Wang H. et al., 2016). The covalent conjugation between a drug and a *D*-peptide impacts the gelation properties of a hydrogel including its biostability (Li et al., 2012). Insertion of *D*-amino acids is reported to twist heterochiral self-assembled peptide hydrogels. Its impact on the drug delivery along with other biological performances makes them versatile tools for therapy in future (Fichman and Gazit, 2014; Melchionna et al., 2016). The use of low molecular weight compounds in hydrogels for drug delivery is turning distinctive due to easy injectability, responsiveness to various stimuli and comfort of synthesis (Raeburn et al., 2013; Mayr et al., 2018). Even the presence of a single amino acid can influence the donor–acceptor charge-transfer interaction in a two-component co-assembled nanofibrous hydrogel (Nelli et al., 2017).

β-Hairpin hydrogels, a subgroup of hydrogels, are another exciting candidates as drug delivery vehicle. These are formed through a molecular self-assembly mechanism which occurs only after desired triggering of intramolecular peptide folding. A review by Worthington et al. (Worthington et al., 2017) has discussed the physical properties of this kind of hydrogel network and material properties which can be used for drug delivery.

Another class of self-assembling peptides, multi-domain peptides (MDPs), allows a wide range of modifications in β-sheet motif without disruption so that the materials for delivery can be trapped within the hydrophobic core of the nanofiber depending on the MDP design and cargo. (Kumar et al., 2015; Li I.C. et al., 2016; Moore and Hartgerink, 2017; Lopez-Silva et al., 2018; Chen and Zou, 2019) In a two-component system, in which a porphyrin cap is combined with a cyclic peptide the combination of various binding forces, e.g., hydrogen bonding, metal coordination, and dynamic covalent bonds, allows the delivery of encapsulated ligand (Ozores et al., 2017). These supramolecular injectable biomaterials, that can mimic the natural extracellular matrix nanostructure and show marked cellular infiltration, are ideal scaffolds for tissue engineering strategies. The self-assemble process of MDPs to a nanofibrous hydrogel requires the peptide sequence containing a core of alternating hydrophilic and hydrophobic amino acids and flanked by presence of charged amino acids which further modifies to nanofibers with bilayered β-sheets. These are further modified to a viscoelastic hydrogel processed via nanofiber elongation and cross-linking. The flexible short β-structure and the governing strong forces allow modifications to incorporate functionality, and so are the attractive choices for research (Li and Hartgerink, 2017; Carrejo et al., 2018).

As mentioned earlier, the peptide self-assemblies may have various morphologies and accordingly possess impressive range of applications though sometimes these might be undervalued. To overcome these limitations, assembly of multiple peptidic components can result in a broader range of applications as compared to the self-assemblies of either component. This epitome expands the conformational space of peptide self-assemblies in terms of structural and functional complexities (Makam and Gazit, 2018; Diaferia et al., 2019). For example, mixed dipeptide gelators are assumed to co-assemble to form fibers containing both the gelators randomly. But the pH triggered methodology, determined by the pKa of the gelator, a chemically programmed method, could alter the rate at which self-sorting occurs and forms self-assembled networks (Morris et al., 2013). These sophisticated multicomponent peptide assemblies are being seen as the next-generation bio-inspired materials (Draper and Adams, 2018; Raymond and Nilsson, 2018).

Tissue engineering is a special branch among self-assemblies whose perseverance is the replacement of damaged tissues with newly engineered tissues to restore the normal activity of the target organ, tissue or system. The rudimentary requirement of tissue engineering is a scaffold to sustain the cells and escort the regeneration of the new tissue (**Figure 3**). The self-assembling peptides are able to serve this resolute as scaffolds. The special focus in the review articles of hydrogels and porous scaffolds remains in controlled release of drugs from the tissue engineering platforms (Boekhoven and Stupp, 2014; Loo et al., 2015; Rambhia and Ma, 2015; Koutsopoulos, 2016; Banerjee et al., 2018; Lee, 2018; Inaba and Matsuura, 2019). One of the very important areas in tissue engineering is to explore the ways, to modify the properties of the materials, including mechanical and chemical functionality through changes at the sequence level to influence the cell behavior and modulate the scaffold stability (Zhou et al., 2014). Abbas et al. has reviewed the role of peptide and protein self-assembly in photodynamic and photothermal therapy (Abbas et al., 2017). There is a growing interest in the self-assemblies led by non-covalent hydrogels for three-dimensional cell scaffolding applications. The role of

ultra-short molecules, namely, dipeptides and amino acids, holds special position in this area (Ryan and Nilsson, 2012). The collaboration between the molecular structure of the assembled materials and the mechanism of self-assembly grips the nerve on evolving biochemical and viscoelastic properties in this network (Maude et al., 2013). In one of the literature reports, Sarkar et al. (2018) have included an elaborated discussion on possible approaches to assimilate the functionality of peptide scaffolds that may be implanted *in vivo* at the site of ischemia for application in functional tissue regeneration. A review article by Rubert Pérez et al. (2015) and highlights the self-assembled peptides through solid-phase peptide methodologies, wherein the accurate amino acid sequence can be selected, for constructing bioactive matrices for regenerative medicine. Major advantages, promising applications and current limitations of peptidic materials has been reviewed by Pugliese and Gelain (2017).

Beyond the biological functions, designing peptides, with desired structures and functions by mimicking natural supramolecular systems, are in the air which can provide innovative designing principles to intricate "molecular robots" as next-generation peptide nanomaterials (Inaba and Matsuura, 2019). Handelman et al. (2016b) studied the reconstructive phase transition exhibited by some of the self-assembled ultrashort di- and tripeptide nanostructures to modify optoelectronic properties followed by the appearance of visible photoluminescence. The physics of light propagation (functional properties of linear and non-linear light propagation) in nanostructures of biological origin has been exploited to develop novel integrated nanophotonic devices (Handelman et al., 2016a).

Though the role of self-assembled peptides in drug and gene delivery is blossoming and there is a substantial flow in the research and review articles as mentioned above, but the short peptides (di- and tri-peptides) appear more promising and game changers, due to their simple structure, cost-effectiveness, non-toxic/non-antigenic nature and superior biocompatibility with enhanced bioactivity (Panda and Chauhan, 2014; Goel et al., 2015; Alam et al., 2016; Guo C. et al., 2016; Habibi et al., 2016; Hamley, 2017; Mishra and Jyoti Panda, 2019; Ni and Zhuo, 2019). Furthermore, the low molecular weight of short peptides allows purification via simple HPLC techniques. This review article has been conceptualized to express the potential of nanostructures resulting from single molecule of amino acids, di- and tri-peptides in the field of targeted biologics delivery and tissue engineering.

Single or Modified Single Amino Acids

Preparation of nano-shaped aggregates by self-assembly of simple building blocks is fascinating. It is quite startling that a self-assembly of a single amino acid, H-Phe-OH (Adler-Abramovich et al., 2012), was reported in 2012 much after the self-assembly of a dipeptide, H-Phe-Phe-OH (Reches and Gazit, 2003), in 2003. Single amino acid in nanodomain with a stable structure is rare. The chemical modifications of single amino acids have also been investigated for their potential in self-assembly (Chakraborty and Gazit, 2018). The aromatic α-amino acids; H-Phe-OH, H-His-OH, H-Tyr-OH, and H-Trp-OH, have been found to generate ordered self-assembled architects such as fibrils, ribbons, rods, and twisted nanosheets on varying the solvent systems (Singh et al., 2017).

The nanoparticles formed by a single amino acid derivative, a tryptophan derivative, Fmoc-Trp(Boc)-OH, with the molecular weight of 526.6 Da, showed biocompatibility and ability to release the encapsulated bioactive molecules to various cells by Dube et al. (2017). Protection to N-terminus with the Fmoc group and to the side chain with Boc group impacts the nature of peptide self-assembly and overall morphology. The spherical nanoparticles of Fmoc-Trp(Boc)-OH, with hollow interior at pH 6, showed no significant change in structure/morphology with change in pH and retained stability toward thermal perturbations upto 3 months. This asserted the overall impact of Fmoc and Boc groups. Efficient loading and release capabilities along with enhanced toxicity against cancer cells emphasize the role of self-assembly of a simple amino acid as a drug carrier (Tao et al., 2015; Zanna et al., 2015; Dube et al., 2017).

The study to unravel the stimulatory effect of H-Trp-OH on insulin absorption established that H-Trp-OH also possesses bio-enhancing effect as compared to other hydrophobic amino acids, viz., phenylalanine (Phe), proline (Pro) and isoleucine (Ile). The hypoglycemic reaction and surface plasmon resonance (SPR)-based assay showed enhancement in the oral absorption of insulin but without intermolecular interaction. Further, it showed the ability to enhance intestinal absorption of fluorescently labeled hydrophilic dextrans as well as GLP-1 and Exendin-4 peptide drugs (Kamei et al., 2018). H-Arg-OH, as single amino acid, has also shown the potential as insulin absorption enhancer and can be developed as oral delivery systems for insulin (Kamei et al., 2017). Likewise, the hydrophobic and π-π interactions between Fmoc-Lys-OH and pyrrole groups of Chlorin e6 (Ce6), a hydrophobic photosensitive drug, led to the formation of co-assembly, which showed an improved cellular uptake. The results advocate the promising potential of a non-toxic photosensitizer delivery system (Liu et al., 2016).

The pyrene conjugated H-Phe-OH derivative, Pyrene-Phe-OH, displayed its ability to gelify in aqueous solutions over a wide range of pH. The change in pH brought about significant alterations in its properties, namely, (i) a distinct change in morphology (nanoscale) from a chiral (left-handed helical) nanofibers to achiral (non-helical) tape like nanofibers with increase in pH, and (ii) change in thixotropic (macroscale) property. The thixotropic behavior facilitated the encapsulation of vitamin B_{12} and an anticancer drug, doxorubicin (Dox), within the hydrogel and sustained release paving way to its drug-delivery applicability. The worth mentioning is that Pyrene-Val-OH was unable to form gel owing to absence of π-π interactions for self-association and the gelation process (Nanda et al., 2013).

The hydrophobic interactions hold good position in self-assembly to gel formation. Interestingly, in a research article, it has been shown that phenylketonuria formed due to defective phenylalanine hydroxylase, the H-Phe-OH level in brain increases and the self-assembly forms toxic amyloid fibrils

by hydrophobic interactions. The administration of H-*D*-Phe-OH converts the fibrous formation route of H-Phe-OH to flakes formation and the flakes further restrict H-Phe-OH to form fiber. This slows down the toxic fibril formation (Singh V. et al., 2014), though doxycycline is observed to counteract these toxic effects (De Luigi et al., 2015).

The role of aromatic moieties is quite important in the self-assembly of ultrashort peptides, exclusively Fmoc-peptides, to form hydrogels (Orbach et al., 2012). Small angle neutron scattering (SANS) technique has been used to have a view on gel properties and cross-links of the fiber structures of low molecular weight gels formed by dipeptide gelators (Fleming et al., 2014; Mears et al., 2017). The presence of Fmoc protecting group enhances the hydrophobicity of H-Phe-OH, a hydrophobic amino acid, and lowers the solubility in water. The hydrophobicity of phenyl ring has been reported to contribute toward hydrogel formation ring while its aromaticity brings thermal stability to the supramolecular hydrogel system (Murali and Shanmugam, 2019). The study of the recipe of phenylalanine and Fmoc system for gel formation concluded that the covalent linkage between the two is highly imperative to provide accurate configuration and interactions. The methylene side chain serves in stacking process (in buffer conditions) to facilitate gel formation along with the non-covalent ionic interactions and hydrophobic stacking interactions during close proximity of Phe ring and Fmoc moiety in space. The gel showed enhanced dye diffusion and faster gel erosion at higher temperature suggesting further exploration of the molecule in drug delivery (Singh et al., 2015). The unidirectional hydrogen bonding of the carbamate group within Fmoc-Phe-OH assemblies directed the assembly into 1D fibrils while Fmoc-peptoid analogs displayed 2D/3D morphology due to the alteration in H-bonding (Rajbhandary et al., 2018).

Fmoc-Phe-OH derivatives, modified at the carboxylic acid position with diaminopropane (DAP), (non-fluorinated Fmoc-Phe-DAP, monofluorinated Fmoc-3F-Phe-DAP, Fmoc-F^5-Phe-DAP, and co-assembly of Fmoc-Phe-DAP and Fmoc-F^5-Phe-DAP) twisted to hydrogels on addition of physiologically relevant sodium chloride concentrations. The hydrogels exhibited encapsulation of non-steroidal anti-inflammatory drug, diclofenac, during the self-assembly process and *in vivo* drug release profile showed their usefulness as injectable materials. The release study of diclofenac, which decreased from Fmoc-F^5-Phe-DAP to monofluorinated to the non-fluorinated gelator, demonstrated the role of the molecular structure of the gelators advocating the importance of aromatic benzyl side chain for π-π interactions between the gelator and cargo (**Figure 4**) (Raymond et al., 2019).

An amino acid derivative, *N,N′*-dibenzoyl-L-cystine (DBC), has been turned into a supramolecular hydrogel, as the carrier of salicylic acid (SA), by adjusting the pH of the solution. The DBC molecule with two amide groups and two carboxyl

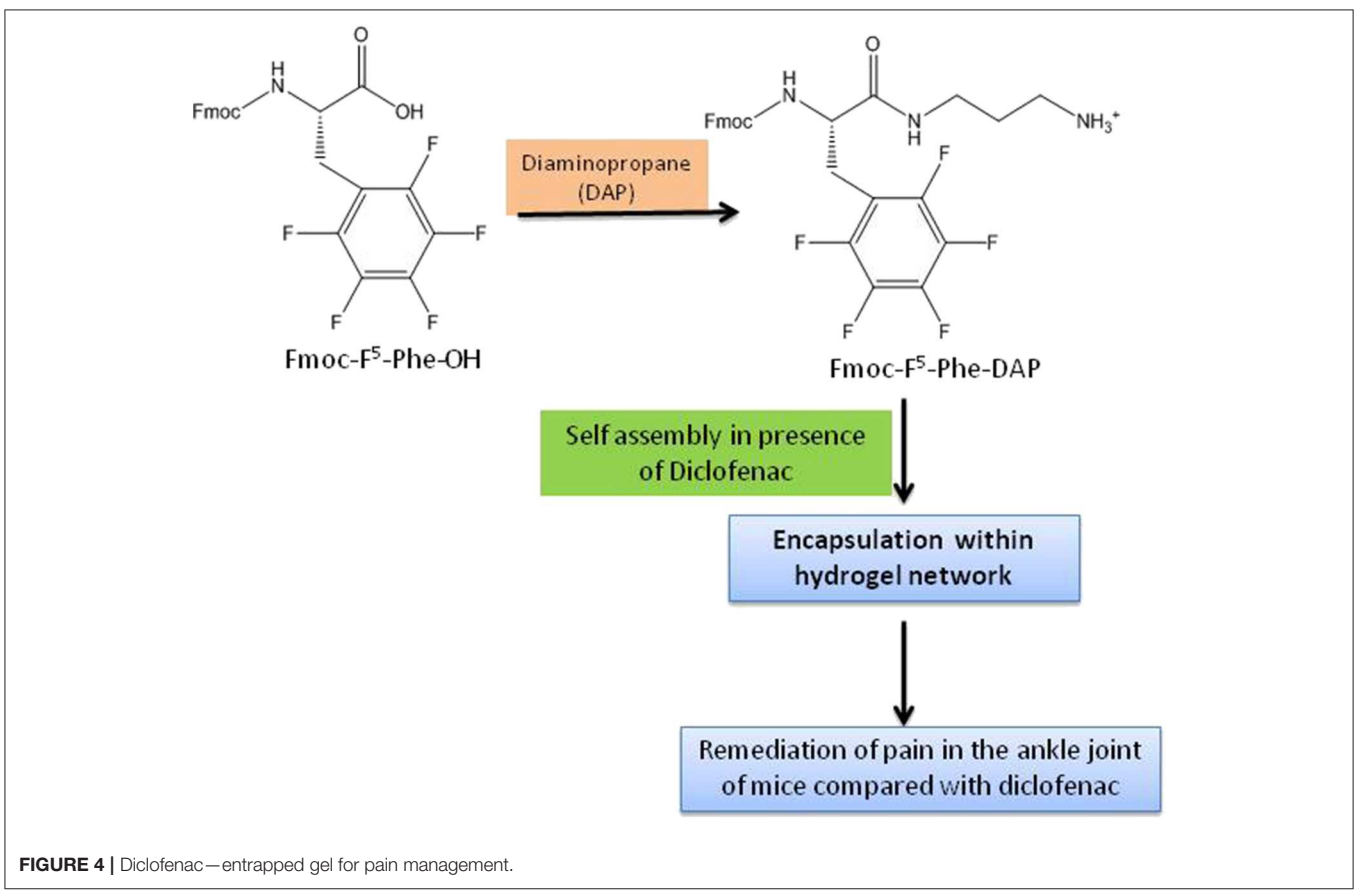

FIGURE 4 | Diclofenac—entrapped gel for pain management.

groups was able to oblige as hydrogen-bond donors and acceptors, respectively. The self-assembly of DBC molecules was facilitated by strong intermolecular hydrogen bonds linking neighboring amides and carboxylic acid as well as π-π stacking interactions amid aromatic rings, and hydrogen bonds among water molecules. The pH-responsive hydrogel along with thermo-reversibility and suitable mechanical properties is another addition to the controlled drug release system (Zhong et al., 2019).

Not much has been reported about fluorescent peptide nanotubes. Babar and Sarkar (Babar and Sarkar, 2017) synthesized stable, homogeneous nanotube type aggregates from individual amino acids, H-Trp-OH and H-Tyr-OH, retaining the characteristic fluorescence, which can be used as drug carriers. A simple approach, sonication followed by deposition onto brass stub, was used in the synthesis which could be extended to various nanotubes from single or mixture of amino acids. An inexpensive derivative of tyrosine, H-Tyr(t-Bu)-OH, is perhaps one of the lightest reported low molecular weight organogelator and only natural amino acid-derived gelator, decked with free -NH_2 and -COOH groups. The analysis outcomes made this molecule more special as the gelation could be carried out in all classes of solvents; be it polar, protic, apolar, etc. The gelation in sunflower oil and diesel makes it an appropriate candidate for drug delivery (Aykent et al., 2019). Further investigations revealed the same capability of other enantiomer, H-*D*-Tyr(tBu)-OH to form the organogel while racemic H-*DL*-Tyr(tBu)-OH was unsuccessful to do so. The new work also exposed the role of tert-butyl moiety as H-Tyr-OH, H-Phe-OH and H-Tyr(Me)-OH could not form gel while H-Tyr(tBu)-OH could do so as mentioned above (Aykent et al., 2019).

Injectable self-assemblies of derivatives of H-Ala-OH, turned into hydrogels, were used to attach Dox, through an imine bond and the resulting Dox-Gel showed regression in tumor. The presence of rotationally-flexible, an aromatic N-protecting group on the H-Ala-OH accentuated the nanofiber creation. The intermolecular hydrogen-bonding in the derivatives, formed with the addition of carboxamide and hydrazide units at the carboxylic end of H-Ala-OH, H-Ala-CAM and H-Ala-HYD, respectively, along with the protonated H-Ala-HYD+, aided in the formation of gel. The imine bond between the hydrogel and drug was reversible which could cleave in the surrounding areas of the tumors and release the drug. The proposed work highlighted the use of self-assembly of molecules with molecular weight <300 Da in anticancer therapy (Singh M. et al., 2014).

A metallo-hydrogel was fabricated using H-Val-OH based ligand, L-3-methyl-2-(pyridine-4-ylmethylamino)-butanoic acid and Zn(II). The results revealed reversible gel-to-sol and xerogel-to-gel phase transitions and demonstrated a release of a polar drug stimulated by change in pH (Saha et al., 2014).

A two-component assembly of Fmoc-Tyr-OH and Fmoc-DOPA-OH (DOPA: 3,4-dihydroxyphenylalanine) resulted in a macroscopic structure with different characteristics from formed by modified amino acids hydrogels individually (Fichman et al., 2015). The amino acid H-Phe-OH in its zwitterionic state, under fibrillization conditions, is reported to be stabilized by hydrogen bonds and aromatic interactions network while organized into an ordered β-sheet-like layered assembly (Mossou et al., 2014). All coded amino acids are suggested to display a layer-like assembly (resembling supramolecular β-sheet structures) which is stabilized by α-amine to α-carboxyl H-bonds regardless of the presence of different side-chains that remarkably differ in their chemical properties though these side-chains govern the higher order organization of the layers. Overall, it recommends that the generic inclination of peptides and the proteins backbones to assemble as layered organizations might be ensued from their basic building block, the amino acid (Bera et al., 2018). Co-assembly, though an efficient strategy to form supramolecular structures, suffers in its tailor made functionality due to the lack of knowledge on structural correlation amid different amino acids. This makes the prediction on the resultant co-assemblies a difficult job. Bera et al. have demonstrated that the co-assembly of naturally occurring amino acids with similar chirality is strongly steered by their interlayer separation distances. a basic rule to predict the supramolecular co-assembly relationship with structure (Bera et al., 2019).

The role of disubstituted 1,2,3-triazoles, with the ability to mimic a trans- or a cis- configuration of the amide bond, prompted the researchers to use it as a co-assembly of isosteric amino acid-based hydrogelators. An amphiphilic N-stearoyl-L-glutamic acid (C18-Glu) and its analog with amide moiety replaced by 1,4-disubstituted 1,2,3-triazole unit (click-Glu) displayed distinctive nanostructures due to different hydrogen-bonding configurations. In C18-Glu, the polar protic environment (with intermolecular hydrogen-bonding between the amide NH-bond and the CO-group of the acid moiety next to the chiral center) favored nano-almond crunch-like structures while the non-polar environment preferred (with equal contribution from both intermolecular and intramolecular hydrogen-bonding) formation of nanofibers. The reverse was true for its analog click-Glu. The co-assembly, triggered by the formation of anticipated nanostructures in specific solvents, was applied for the release of an antibiotic, vancomycin (Bachl et al., 2015).

Dipeptides for Biologics Delivery

Since the beginning of the journey of the self-assembly, H-Phe-Phe-OH, the dipeptide, reported for the first time by Gazit and his group (Reches and Gazit, 2003), has taken the center-stage responding to its various roles. The core-recognition motif of the Alzheimer's disease associated β-amyloid polypeptide, has potential hydrophobic and hydrophilic moieties which are key parameters for molecular assembly. Other than self-assembly by itself, H-Phe-Phe-OH also functions as a co-assembling peptide for adjusting the self-assembly of various functional molecules, providing an easy and efficient method to modulate the morphology and property of these functional molecules. The potential applications of self-assembled dipeptides are catching up in the field of drug delivery and tissue engineering, as these moieties frame into variety of nanostructures, such as, spherical vesicles, nanotubes, and nanowires. The modes of interaction in general are π-π stackings, hydrophobic associations, electrostatic interactions, and hydrogen-bonding. Various morphologies

based on free and protected H-Phe-Phe-OH molecule (Ribeiro et al., 2019) and its analogs/derivatives forming fibrils (Reches and Gazit, 2005), vesicles (Guo et al., 2012), tubes (Reches and Gazit, 2006), wires (Huang et al., 2014; Marchesan et al., 2015b), plates (Tamamis et al., 2009), sheets, flakes (Singh V. et al., 2014), necklaces (Yuran et al., 2012) could be demonstrated by manipulating the stimuli and physical/chemical conditions (Adler-Abramovich and Gazit, 2014; Datta et al., 2018, 2019). Concentration dependent ordered nanoarchitectures such as planar bilayers and other diverse shapes of vesicles, namely, discoid, toroid, ellipsoid, and pot-shaped, have been reported by Guo et al. (2012). Further, by chiral control at different stages, two elementary forms of the peptide self-assembly for the helical twisting of the β sheets were developed. These could turn into wide variety of hierarchical chiral nanostructures, viz., tube-like helical ribbons, twisted ribbons, big twists, nanoscrews and nanosprings (Wang et al., 2015). Even the rarely observed toroid nanostructures could be seen in H-Phe-Phe-OH and H-Phe-Phe-Phe-OH co-assembly (Guo C. et al., 2016) and triaromatic system, Z-Phe-Phe-OH (Z= benzyloxycarbonyl) (Brown et al., 2018).

In one of the studies by Wang et al. (2016b) involving H-Phe-Phe-OH dipeptide molecules, it has also been reported that the non-covalent interactions between trace solvents and peptides performing as solvent-bridged hydrogen bonding lead to directional hydrogen bonding between C-O and N–H in these molecules without inducing π-π stacking. It can promote long-range-ordered arrangement to form nanofibers /nanobelts preferentially along one dimension. The study on H-Gly-Pro-OH dipeptide has supported the ability of $n\rightarrow \pi^*$ interactions between carbonyl groups for the stability of the structure (León et al., 2019). The nanotubes formation in self-assembly of a dipeptide, (S,S)-3-amino-2-(2-fluorophenyl)-3-phenylpropanoic acid and H-Ala-OH, has been observed to be supported by intermolecular N–H···O hydrogen bonds, Cπ-H···O, Cπ-H···F, and van der Waals interactions but no evidence of the presence of stacking interactions between the phenyl moieties has been observed by Bonetti et al. (2015).

The ability of peptides, even the ultrashort peptides as small as dipeptide, to form nano- and microstructures born with unique physical properties is the product of reductionist approach. It proposes the creation of well-ordered, amyloid-like β-sheet-rich assemblies comparable to supramolecular structures made of much larger proteins. This approach is exploited for the design and synthesis of peptide structures of technological utilization while establishing simple *in vitro* model systems to study the parent architecture. This has also resulted in the developing new bio-inspired configurations that could mimic the naturally-occurring architectures while keeping their functional properties intact, or even sometimes new functionalities are born. The similarity in the assembly mechanism between H-Phe-Phe-OH nanostructures and the aromatic amino acid containing amyloid fibrils inspired Brahmachari et al. to use the reductionist approach. Herein, a screening model was set up to identify molecules possibly capable of interfering with the aggregation process and their mode of action on the modulation of both the assembly and disassembly processes of H-Phe-Phe-OH assemblies (Brahmachari et al., 2017). Gazit is pioneer to demonstrate ultrashort peptides forming ordered assemblies by reductionist approach. His review on the reductionist approach educates on future of minimalistic peptide structures and the latitude of bioinspired self-assembly by the final reduction from very short peptides to extremely small metabolites (Gazit, 2018).

The analysis on temperature dependence of the kinetics of H-Phe-Phe-OH assembly, within the skeleton of crystallization theories, exposed that the transition state from solution to crystalline aggregates is enthalpically unfavorable-entropically favorable, qualitatively similar to longer sequences (Mason et al., 2017). Hydrophobic dipeptides, based on crystallization mode, could be categorized as self-assembled crystals composed of (i) elongated helical tubes; narrow hydrophobic channels and (ii) compact helical tubes; wide hydrophilic channels. The molecular mechanism build on density functional theory, advised by González-Díaz et al. recommends the position of the side chain, where it branches, during crystallization, to be the determining factor to drive the dipeptides into either hydrophobic or hydrophilic channels (González-Díaz et al., 2019). The structural transformation of a dipeptide self-assembly just by changing the types/ratios of the metal ion or the dipeptide to inhibit amyloid-like structure has been presented by Ji et al. (2019).

In a pair of dipeptide enantiomers, it is natural for both to exhibit opposite circular dichroism and handedness in self-assembly. In case, one of the amino acids is chiral, this chiral one exploits handedness. The situation is ambiguous, if both the amino acids are chiral. Fu et al. selected four dipeptides derived from *L*- and *D*-alanines and found that the chirality of the alanines at the terminals controls the handedness of their self-assemblies (Fu et al., 2013). The molecular hydrogelators, made of *D*-amino acids, have been shown to improve the selectivity of non-steroidal anti-inflammatory drugs (NSAIDs) (Li et al., 2012). It suggests that the chirality of the C-terminal amino acid commands the chiral orientation of the supramolecular helical nanostructures. In the study of dipeptides, viz., H-Phe-Phe-OH/H-Ala-Ala-OH, with NSAIDs, self-assembled as hydrogels, the peptides made of *D*-amino acids provided assistance to preserve the actions of NSAIDs (Li et al., 2013). Erdogan et al. (2015) observed morphological differences in H-Ala-Val-OH and H-Val-Ala-OH dipeptide molecules in the same solvent medium, though particular solvent property having impact on morphology difference could not be fixed. The two peptides differ in terms of the positional disorder of methyl group side chains in L-Val residues and torsion angles. The symmetrical intra- and intermolecular H-bonds, missing in H-Ala-Val-OH, but, present in H-Val-Ala-OH dipeptides were suggested to be accountable for long-range-ordered structures. The position and as well as number of methyl groups at the α carbons on N-terminus and C-terminus Fmoc-Phe(CH_3)-Phe-OH or Fmoc-Phe-Phe(CH_3)-OH has been observed to impact supramolecular nanostructure and the ability to form hydrogel (Arakawa et al., 2020).

An article dedicated to the role of dipeptides in diverse fields has been published by Panda and Mishra (2016). The bioinspired dipeptides in innovative emerging field of photoelectronics have been highlighted by Chen C. et al. (2015). Marchesan

et al. discussed the preparation, characterization and pointed out the potential of H-Phe-Phe-OH motif in nanomedicine (Marchesan et al., 2015b). Multicomponent metallo-nanodrugs as coordination self-assemblies of Fmoc-His-OH and Z-His-Phe-OH in presence of Zn^{2+} ions, formed by the combined efforts of coordination and multiple non-covalent interactions were studied for cooperative coordination of photosensitizer Ce6. These multifunctional nanodrugs with enhanced tumor-specific delivery showed the potential for clinical translation (Li S. et al., 2018).

A controllable self-assembly of H-Phe-Phe-OH in an evaporative dewetting solution has been reported by Chen J. et al. (2015). The all-atom simulations of the small H-Phe-Phe-OH oligomers could accomplish the role of several driving forces and structural motifs that command initial assembly (Jeon et al., 2013). H-Phe-Phe-OH oligomers are associated by hydrophobic interactions between side chains while the H-Phe-Phe-OH zwitterionic peptides having charged termini form ordered, clustered, and compact shapes (electrostatic interactions steer their backbones into a more ordered state as compared to those of uncharged ones). From here on, the hydrophobic interactions of the side chains further lead to higher order oligomers just like in amphiphilic peptides. Therefore, the projected study concludes that the initial precursors of H-Phe-Phe-OH might first assemble into structures that form portions of the packed hydrophobic regions in the nanotube walls (Jeon et al., 2013; Chronopoulou et al., 2014). The aptness of the peptide prompted to explore the mechanical parameters of the H-Phe-Phe-OH self-assembled tubes. Atomic force microscope studies revealed these to be the stiffest (averaged point stiffness of 160 N/m) and with much higher Young's modulus ($\approx$ 9 GPa) as compared to other biological nanostructures, significantly enough to provide mechanical strength to cytoskeleton (Kol et al., 2005). In peptides nanotubes, since the control over length of nanotubes in solution, posed a challenge, a slower co-assembly process along-with the adjustment in the molecular ratio of the H-Phe-Phe-OH assembly unit and its end-capped analog has been suggested (Adler-Abramovich et al., 2016).

The potential of H-Phe-Phe-OH microtubes as intracellular vehicle to release therapeutic compounds has been explored by Silva et al. (2013). The biological marker, rhodamine B, incorporated at the time of self-assembly, had the possibility to intercalate and showed its presence in the inner core to be accepted as intracellular drug delivery for hydrophilic molecules (Silva et al., 2013). These H-Phe-Phe-OH microtubes were further explored for delivering anti-cancer therapeutics, viz., 5-fluorouracil (5-FU) and anti-inflammatory cargo, flufenamic acid (FFA), by Emtiazi et al. (2017) post-conjugation with folic-acid and magnetic nanoparticles. These were found to show the potential as molecular carriers (Emtiazi et al., 2017).

The hydrophobic forces in these well-ordered tubular structures further facilitated to be soluble in a suitable solvent and self-assemble into well-organized films on various substrates. This technique was tried by Zohrabi et al. (2016) wherein FFA loaded inside the H-Phe-Phe-OH nanotubes were coated onto Au surfaces functionalized with 3-mercaptopropionic acid (MPA). The biocompatibility and *in vitro* release studies confirmed the potential of H-Phe-Phe-OH nanotubes as an alternate system for polymer coating in drugs eluting stents. Further, these H-Phe-Phe-OH nanotubes were also shown to possess anti-biofilm activity (Porter et al., 2018). Among the three H-Phe-Phe-OH variants at terminals, such as H-Phe-Phe-OH (l-enantiomer; carboxylic acid terminus), H-*D*-Phe-*D*-Phe-OH (d-enantiomer; carboxylic acid terminus), and H-Phe-Phe-NH_2, investigated for this purpose, H-Phe-Phe-OH peptide nanotubes were found to be proficient to degrade the biofilm matrix, disrupt cell membranes and hold the potential as efficient drug carrier, though the precise link between these short self-assemblies and biofilm activity needs to be explored.

The peptide-porphyrin macrocycle conjugation has extended its use in biological systems, where the photophysical properties of these molecules and their ability to coordinate metals could be exploited. A review by Biscaglia and Gobbo has presented a survey on biomedical applications of these hybrid compounds, majorly in photodynamic therapy (Biscaglia and Gobbo, 2018). The reversible, biocatalytic and co-assembled nanofibers of Fmoc protected di-peptide (Fmoc-Thr-Leu-NH_2) and its porphyrin derivative [TCPP, tetrakis(4-carboxyphenyl)porphyrin] advocate the role of Fmoc-moiety in biocatalysts (Wijerathne et al., 2019). The biocompatible photothermal nanodots formed by self-assembly of peptide-porphyrin conjugate; TPP-Phe-Phe-OH (TPP= tetraphenylporphyrin) have been found suitable for tumor ablation and stand good potential for biomedical photoactive applications. The peptide moieties could provide aqueous stability (through hydrophilic interactions) as well as a spatial barrier (through the strong π-π-stacking interactions between porphyrin groups) to inhibit the further growth of light-to-heat converted nanodots with totally inhibited fluorescence emission and singlet oxygen production (Zou et al., 2017).

Self-assembled cationic dipeptides (CDP), H-Phe-Phe-OH, nanocarriers have displayed the ability to encapsulate and transport drug molecules *in vitro* at physiological pH condition by the action of enzymes. A covalent bond formed via Schiff base between oligomeric glutaraldehyde and amino groups of CDP followed by aging yielded CDP nanocarriers (CDPNCs). The π-π interactions of aromatic rings have been proposed to be the driving force for the assembled nanocarriers. Remarkably, the auto-fluorescence due to n-π^* transitions of C = N bonds offers visually traceable property in living cells. These highly biocompatible carriers with the ability to encapsulate small guest molecules and enzyme-sensitive nature exhibited a high cytotoxicity against tumor cell proliferation leading to be even used as *in vivo* applications in future (Zhang H. et al., 2015). Though the thermo-induced morphology changes modifying the optical properties in H-Phe-Phe-OH microtubes have been explored by Li et al. (2015), Semin et al. (2015), Nikitin et al. (2016), and Vasilev et al. (2016) the suitability of these H-Phe-Phe-OH based nanocarriers in the intracellular environment of tumor infected tissues was substantiated by Li Q. et al. (2016). Self-assembled hybrid nanospheres, pH- and glutathione (GSH)-responsive, based on H-Phe-Phe-OH and natural alginate dialdehyde as cross linker were used to deliver hydrophobic chemotherapeutic drugs. These nanospheres also contained Au^{3+}, reduced to Au *in situ* by

ADA, and formed H-Phe-Phe-ADA-Au hybrid nanospheres to facilitate ligand exchange reaction of GSH (Li Q. et al., 2016).

The impact of different degrees of hydrogen bonding and nitrogen substitution on mechanical properties of H-Phe-Phe-OH based peptides, indole-diphenylalanine, N-methyl indole-diphenylalanine, benzimidazolone-diphenylalanine and benzimidazole-diphenylalanine, capped at the N-terminus with heterocycles was executed by Martin et al. (2016). In conjugation with NSAIDs, this change altered the gelator properties. H-Phe-Phe-OH covalently conjugated to NSAIDs was found to form hydrogels and exhibit improved selectivity as compared to the native drug displaying its reputation in drug-delivery (Li et al., 2013). Moreover, the inclusion of ferrocene (Fc) moiety in H-Phe-Phe-OH hydrogel, a redox-active site, could change the morphology from nanosphere to nanofiber with the additional feature to reversibly control the self-assembly process of Fc–Phe-Phe-OH by altering the redox state of the Fc group (Wang et al., 2013b).

The study on impact of different N-terminal capping group to vary the aromaticity on hydrogel formation and properties with glyoxylamide mimics as self-assembly hydrogel by Aldilla et al. (2018) showed that the aromatic caps having the bulky indole side chain of tryptophan and another with electronegative substituent on the phenylalanine ring failed to form a hydrogel; might be because of hindrance in the intramolecular stacking. On the other hand, hydrogels with N-naphthalene sulfonyl cap, exhibited a β-sheet secondary structure with viscoelastic properties and topical delivery of ciprofloxacin and recommended as a drug delivery vehicle. Since H-Phe-Phe-OH forms nanofibers with remarkable optical and electrical properties, optical microscopy methods, fluorescence microscopy and super resolution single molecule localization microscopy have been suggested for the study of H-Phe-Phe-OH –based nanostructures (Pujals et al., 2017).

Kuang et al. made an attempt to establish the difference in properties between supramolecular nanofiber assemblies of small molecules and the individual molecules on interaction with the cells. The study of nanofibers formed by the self-assembly of two phenylalanine residues and a naphthyl group, with β-sheet-like-structure revealed the threshold concentration for the formation of nanofibers and suggested hydrophobicity to be responsible for higher cytotoxicity as compared to unassembled monomers (Kuang and Xu, 2013). A photo-responsive hydrogelator, wherein, H-Phe-Phe-OH was protected by 6-nitroveratryloxycarbonyl moiety; Nvoc-Phe-Phe-OH, has been designed and synthesized by Roth-Konforti et al. (2018). The photo-labile trigger, 4,5-dimethoxy-2-nitrobenzyl alcohol, served as a π-π stacking element in place of the aromatic Fmoc group. This stiff 3D-hydrogel displayed responsiveness to UV light irradiation and it completely disassembled subsequently on irradiation at room temperature to release the entrapped drug at the site of administration. The patterning of the photo-responsive peptide based hydrogel along with gradual release of insulin-FITC conferred linear correlation to the stimulus duration. Fmoc-Phe-Phe-OH gel remained unaffected by UV irradiation and showed insignificant FITC-insulin release post-UV application (Roth-Konforti et al., 2018).

The self-supporting gel, Fmoc-Phe-Phe-OH, an ultra-short peptide, is one of the most studied hydrogel. Fmoc-Phe-Phe-OH peptide has been reported by Aviv et al. to deliberate the mechanical rigidity and stability to hyaluronic acid (HA), a major component of the extracellular matrix, without the use of molecules to initiate chemical cross-linking. The Fmoc-Phe-Phe-OH/HA hydrogel, composed of two components, could allow fine-tuning of the hydrogel parameters, adjusted for injection and malleable and facilitating its use in drug-delivery and tissue engineering applications (Aviv et al., 2018). A review by Diaferia et al. describes the immense potential of the hydrogel specially in the field of drug delivery, tissue-engineering and catalytic behavior (Diaferia et al., 2019). Fmoc-Phe-Phe-OH based hydrogel nanoparticles have been explored as nano-carriers to encapsulate and deliver drugs/bioactive molecules. A scalable process for the assembly of Fmoc-Phe-Phe-OH peptide into hydrogel nanoparticles as ensuing drug delivery carriers has been outlined by Ischakov et al. (2013) The results of encapsulated Dox and 5-FU with different structural characteristics endorsed the assumption that the encapsulation ability of nanoparticles could be dependent upon the physicochemical nature of the molecules, thus affecting the release kinetics. Erdogan et al. have used freeze-quenching technique to prepare plasmonic nanoparticle-embedded organogels from Fmoc-Phe-Phe-OH and gold nanorods for efficient drug delivery. The controlled and enhanced release of the Dox was manipulated using laser illumination (Erdogan et al., 2016). The study by Truong et al. (2015) on Fmoc-Phe-Phe-OH self-assembled hydrogels with 5-FU and paclitaxel cautioned that it is the leaching time, not the exposure time which affects the overall cell viability and thus the cytotoxic effects could be observed only after the gel is completely dissolved. Since more stable gels are prone to leach their monomers slower into the neighboring biological environment, the overall concentration of these monomers and any potential adverse effects get reduced. Therefore, the factors controlling the stability of Fmoc-Phe-Phe-OH self-assembled hydrogels are more critical to continue this field (Truong et al., 2015). Argudo et al. have discussed the rules for chemical design through selection of the amino-acid sequence of Fmoc-dipeptides with the self assembling capability for 2D self-assembly at the air/water interface to form supramolecular structures (Argudo et al., 2018). The values of log P and -log S parameters have been proposed based on experimental results which can predict the possibility for a particular Fmoc-dipeptide to self-assemble at fluid interface. A cellular biosensing system, based on 3D culture model using Fmoc-Phe-Phe-OH dipeptide hydrogel employed as both, a 3D cell culture scaffold to provide a confinement in environment and an immobilized enzyme matrix through simple one-pot self-assembly is suggested for the detection of superoxide anion (O●-) by Lian et al. (2017).

A non-centro-symmetric β-sheet structure in Fmoc-Phe-Phe-OH nanofibrils, branded as biomimetic materials with mechanical properties equivalent to the biological gels, also displayed piezoelectric behavior which could enable these assemblies as scaffolds for tissue-engineering (Ryan et al., 2015).

Fmoc-Phe-Phe-OH, hydrogel matrix, has been used by Lian et al. to construct a smart biointerface, followed by enzyme-based electrochemical biosensing and cell monitoring. The encapsulation of horseradish peroxidase (HRP) was achieved during self-assembly, which was subsequently used to detect the release of H_2O_2 from living cells (Lian et al., 2016).

The synergistic effect of the co-assembly of Fmoc-F^5-Phe and Fmoc-Phe-Phe-OH has been reported to result in a ultra-rigid hydrogel with controllable mechanical properties optimum for tissue engineering (**Figure 5**) (Halperin-Sternfeld et al., 2017). The morphological transition from hybrid nanospheres to visible macroscopic films in the co-assembly of the cationic dipeptide (CDP), H-Phe-Phe-NH_2 • HCl and a Keggin-type polyoxometalate (POM), phosphotungstic acid (PTA), upon photothermal treatment was observed which could be suitable for tissue engineering (Xing et al., 2015).

The *in vivo* studies of self-assembled, injectable, fibrous hydrogels obtained by the combination of dipeptide Fmoc-Phe-Phe-OH and poly-L-lysine have been reported to deliver the photosensitive drug Ce6 in a controlled manner at the tumor site and are suggested to work well under the strategy "once injection, multiple-treatments" by Abbas et al. (2018). Taking in and away plan of sheer forces has been observed to work well for the transmission from gel to sol state supporting the self-healing behavior.

Lately, the study by micro-second molecular dynamics simulations on the co-assembly of H-Phe-Phe-OH with different types of non-H-Phe-Phe-OH dipeptides manifested regular-shaped vesicles, single-/multi-cavity assemblies, and planar sheets, which otherwise, are hardly observed in self-assemblies of non-H-Phe-Phe-OH dipeptides. The balancing act between electrostatic repulsion, hydrophobic and aromatic stacking interactions attributes toward the formation of varied structures (Tang et al., 2020). Another novel, multi- component, organic-inorganic peptide-based hydrogel, with two building blocks, viz., Fmoc-Phe-Phe-OH and Fmoc-Arg-OH, and an inorganic material, hydroxyapatite (HAP) as 3D scaffolds was designed for bone tissue regeneration. Fmoc-Phe-Phe-OH served as rigid hydrogel that could mimic the ECM, arginine aided in tissue development and might also be helpful to fine tune the bioactivity of HAP, while HAP itself promoted the mechanical properties of the composite material. An optimum composition of the three resulted in a rigid and biocompatible hybrid suitable for cell adhesion and a bone tissue engineering scaffold (Ghosh et al., 2017).

A multicomponent dipeptide hydrogel from Fmoc-3F-Phe-Arg-NH_2 and Fmoc-3F-Phe-Asp-OH, without covalent connection between Arg and Asp, co-assembled by aromatic, hydrophobic, and coulombic interactions displayed the feasibility in the design of innovative materials for tissue engineering (Liyanage et al., 2015).

It had been established that removal of the N-terminus charge via addition of a Boc group could not stop the formation of H-Phe-Phe-OH like structures (Levin et al., 2014). Boc-Phe-Phe-OH in different solvent conditions was observed to display tuneable structures of two different morphologies: tubular or spherical under different solvent conditions and the presence/absence of superparamagnetic iron oxide (SPIONs) core and studied for dual use (drug delivery and heat generation) (Majid et al., 2017). Also, molecular dynamics simulations had suggested that the N-terminus stabilizes the initial stage aggregates during the self-assembly formation while in the final tube structure, it does not rely on the charged termini regions. So when a mixture of H-Phe-Phe-OH and Boc-Phe-Phe-OH monomers, where the uncharged Boc group was added to the N-terminus of the dipeptide, leaving the aromatic residues free to interact, the fibers with varying morphologies and mechanical properties were grown depending on the ratio of the two monomeric dipeptides. Atomic force microscopy (AFM), fluorescence and FTIR spectroscopy showed a reduced Young's modulus and rigidity as well as reduction in hydrogen bonding along with an alteration in the electronic state

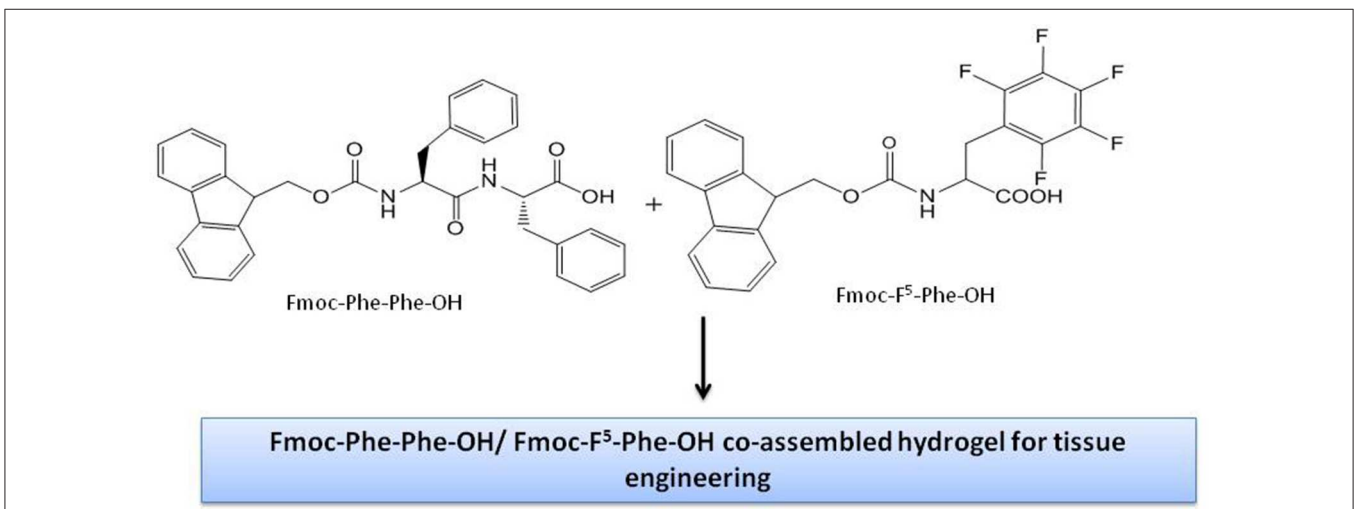

FIGURE 5 | Multicomponent co-assembly to yield ultra-rigid hydrogel.

of the aromatic residues in co-assembled fibers. So it was hypothesized that this reduction in the hydrogen bonding and a modification in π-π stacking between monomers altered the packing co-assembly. So, the study gives clue to develop various materials with different surface groups resulting in different interactions impacting the mechanical properties of scaffolds to be used in tissue-engineering (Creasey et al., 2016).

The co-assembly of H-Phe-Phe-OH and Boc-Phe-Phe-OH formed the fibers in aqueous conditions with reduced stiffness and curvier morphology. Creasey et al. proposed the disruption of the hydrogen bonding among neighboring N-termini and a variation of π-π stacking between monomers altered the packing of co-assembly and thus provided an option of post-assembly chemical functionality and supramolecular sites for drug delivery vehicles (Creasey et al., 2016). Just to briefly mention, a new prototype, an orthogonal strategy, for the cargo release from micro-compartments by modulating the intrinsic self-assembly state and opening the prospects to use the triggered self-assembly to finally control the transport of various molecular species across interfaces has been demonstrated with Boc-Phe-Phe-OH, which could trigger jet-like release within seconds (Levin et al., 2018). Among the short hybrid dipeptides composed of β(O)-δ5 -amino acids synthesized by Reja et al., the injectable hydrogel, Boc-β(O)-δ5-Phe-β(O)-δ5-Phe showed its utility in 2D-cell culture and could encapsulate proflavine solution in the gel matrix and release slowly (Reja et al., 2019).

Rhein (4,5-dihydroxyanthraquinone-2-carboxylic acid), a traditional Chinese anti-inflammatory compound, exhibiting planar aromatic structure, is branded to enhance intramolecular π-π stacking in dipeptide-based materials. The rhein-Phe-Phe-OH peptide gets muddled into uniform spherical nanoassemblies spontaneously, suggesting its competence as carrier for drug delivery. The virtual screening of rhein-Phe-Phe-OH from Traditional Chinese Medicine (TCM) database (based on MD simulations), showed its significant binding energy toward camptothecin (CPT), known for strong antitumor efficacy but limited in use due to poor solubility and stability (perhaps the first compound to be designed cooperatively by both experimental studies and computation simulations). *In vitro* and *in vivo* experimental evaluations validated the computation simulations (Sun et al., 2019).

Amoc-Leu-Phe-OH; an Amoc-capped dipeptide, wherein, Amoc moiety is supposed to provide optimal hydrophobicity, which in turn, could enhance self-assembling propensity demonstrated anti-inflammatory action using the rat air pouch model and antibacterial efficiency against Gram-positive and Gram-negative bacteria. The non-cytotoxic hydrogel has been suggested to be used in targeted drug/cell delivery and for wound healing applications by Gavel et al. (2018b).

Non-proteinogenic α,β-didehydro-α-amino acids, with peculiar conformational properties- planar conformation due to a double bond, between Cα and Cβ carbon atoms and fixed values of t ϕ and ψ torsion angles, have shown their ability to form hydrogels (Vilaça et al., 2015b) and applicable in drug delivery. A procedure for cheaper, less laborious and less time taken than other methods of dehydropeptide synthesis (α,β-didehydro-α-amino acid) through oxidation of the C-terminal residue in N-Boc-protected and N-Fmoc-protected peptides, both in solution and on the solid support for peptide synthesis has been reported by Wołczanski and Lisowski (Wołczanski and Lisowski, 2018). The ability to form secondary and super secondary structures and highly stable nanostructures has made α,β-didehydrophenylalanine a center of attraction for the researchers (Gupta and Chauhan, 2011). Self-assembled nanoparticles of dipeptide, methionine-dehydrophenylalanine (Met-ΔPhe), having an unsaturated analog of naturally occurring phenylalanine to entrap curcumin, an anticancer agent, have been synthesized and used by Alam et al. (2012). In this study, the role of ΔPhe in self-assembly of H-Met-ΔPhe-OH was compared with the self-assembly of H-Met-Phe-OH having natural L-phenylalanine. The comparison signified that the presence of ΔPhe in H-Met-ΔPhe-OH promoted the formation and stability of self-assembled dipeptide NPs remarkably, and enhanced entrapment efficiency of curcumin. Besides, the combination of dipeptide assembly with curcumin offered several additional advantages such as high biocompatibility of the former, inhibition of the tumor growth and increased longevity of melanoma tumor-bearing animals of the later. Self-assembly of the dipeptide not only demonstrated the entrapment of curcumin, which could not be used up to its potential due to its hydrophobic nature, leading to poor aqueous solubility, but also improved its bioavailability. Therefore, such dipeptide-NPs could also be used to improve the delivery of other effective hydrophobic drug molecules. Further work on the self-assembled nanotubes using two dipeptides with non-natural amino acids, one containing a flexible H-βPhe-Phe-OH amino acid (βPhe–Phe) and the other containing both H-βPhe-Phe-OH as well as a backbone constrained α,β-didehydrophenylalanine amino acid, H-βPhe–ΔPhe-OH, (βPhe–ΔPhe), was reported to have different properties than the native H-Phe–Phe-OH nanotubes. The study also addressed the effect of backbone length, introduction of conformational flexibility (caused by β-Phe) and constraint (produced by ΔPhe) on the self-assembly process and morphology. The dipeptide crystal, H-βPhe–Phe-OH, showed two conformations, viz., a gauche conformer forming the channel and a trans conformer trapped inside the channel formed by the gauche conformer, probably the first example presenting such self-entrapment. The nanotubes could efficiently encapsulate small hydrophobic drug molecules. The efficient delivery of anti-cancerous drug, mitoxantrone, entrapped in nanotubes as compared to free mitoxantrone can lead to development of more biocompatible and proteolytically stable drug delivery vehicles (Parween et al., 2014). Similarly, H-Phe–ΔPhe-OH based nanotubular system as sustained release nanocarriers for intravitreal delivery of the angiogenic drug was investigated. The sustained delivery potential, as pre-loaded and post-loaded options during nanotube formation assembly, was compared to the plain drug. It was speculated that in post-loading approach, there was a possibility of hydrophobic and aromatic π- π stacking interactions between

the drug and the dipeptide. Additionally, certain amount of dipeptide might have released from the nanotube surface which could further entrap the drug within the nanotubes. The hydrophobic nature of the drug speculates its participation in the development of ordered nanotubes. Phenylalanine-α,β-didehydrophenylalanine (Phe-ΔPhe) dipeptide nanotubes were also explored by Khatri et al. to deliver cancer-testis antigens (CTAs). H-Phe-ΔPhe-CTA nanocomplex showed an inhibition in tumor growth in animal studies, opening the door for this dipeptide as *in vivo* delivery vehicle for CTAs (Khatri et al., 2019).

An arginine containing dipeptide, arginine-α,β-didehydrophenylalanine (Arg-ΔPhe), showed the capability to condense the plasmid DNA into positively charged nanoparticles of spherical morphology and deliver it inside the cells and distribute in cytosol and endosomes. The methodology offers simple synthesis route and characterization, viz., stability, biocompatibility and significant transfection efficiency, and made H-Arg-ΔPhe-OH a suitable contender for *in vivo* gene delivery applications (Khatri et al., 2017). The introduction of non-protein amino acid, namely N-methylated amino acid, *D*-amino acid and α,β,-didehydroamino acid, in peptides provides enhanced stability with regard to enzymatic degradation. Self-assembled nanoparticles of H-Arg-ΔPhe-OH were synthesized, characterized and derivatized with folic acid which showed high affinity for its cell surface receptors. The results exhibited significant cellular uptake and tumor regression toward different cancer cells compared to free drug, Dox /drug-loaded underivatized NPs both *in vitro* and *in vivo*. Iron oxide nanoparticles (IONP) conjugated H-Arg-ΔPhe-OH also showed heat-induced cytotoxicity on lung cancer cells which resulted in the death of these cells (Baskar et al., 2017). Further, it was demonstrated that the presence of arginine in the cationic dipeptide nanoparticles endorsed pH responsive behavior. FTIR and XRD analysis results for compatibility assessment ensured the retention of Dox activity and efficiency within the developed H-Arg-ΔPhe-Dox NPs. pH dependent release studies showed signs of maximum release at acidic pH and so, an excellent choice for site-specific drug delivery in tumors and tissues harboring acidic microenvironment like that of stomach (Singh et al., 2018). The H-Arg-ΔPhe-OH NPs, when conjugated with lactobionic acid (LA), a ligand for the asialoglycoprotein receptors, overexpressed in hepatocellular carcinoma (HCC) cell lines, achieved targeted delivery. H-Arg-ΔPhe-LA/miR NPs demonstrated the selective delivery of miR-199a-3p and so, the formulation could be used in HCC therapy (Varshney et al., 2018).

Spontaneous self-assembly of a dipeptide, leucine-α,β-didehydrophenylalanine (Leu-ΔPhe), into a stable hydrogel, was observed to enhance the antitumor activity of the drug, mitoxantrone. The amphipathic nature of the hydrogel, due to unprotected N- and C-terminals in H-Leu-ΔPhe-OH, could lend polar character. The side chains, bearing a strong hydrophobic character, offer the recipe for the entrapment of both hydrophilic and hydrophobic drugs in the gel matrix and release in a controlled manner (Thota et al., 2016).

Discrete nanoparticles synthesized by combination of different plasmid DNAs with cationic dipeptides. H-Lys-ΔPhe-OH and H-Arg-ΔPhe-OH, showed the potential of these dipeptides to protect DNA from enzymatic degradation and carried them to cellular cytoplasm and nucleus. The results showed that the DNA was packaged inside peptide NPs with no visible cytotoxic effect and exhibited enhanced cellular uptake. Therefore, these could be influential in non-viral mediated gene delivery applications (Panda et al., 2013).

Vilaça et al. synthesized naproxen N-conjugated dehydrodipeptide hydrogelators, having at least one aromatic amino acid (Vilaça et al., 2015b). Also, the evaluation of tryptophan N-capped naproxen and C-terminal dehydrophenylalanine (ΔPhe), dehydroaminobutyric acid (ΔAbu), and dehydroalanine (ΔAla), as protease resistant hydrogelators, demonstrated that Npx-Trp-*Z*-ΔPhe-OH (with C-terminal ΔPhe) was found to be the most suitable nanocarrier among the lot for the delivery of encapsulated low molecular weight drugs (Vilaça et al., 2015a). These results supported the development of a peptide construct, Npx-Ala-*Z*-ΔPhe-Gly-Arg-Gly-Asp-Gly-OH, which was also demonstrated to have properties of an efficient drug carrier (Vilaça et al., 2017). Further studies with tyrosine and aspartic acid residues, tyrosyldehydrophenylalanine [Npx-Tyr-*Z*-ΔPhe-OH] and aspartyldehydrophenyl-alanine [Npx-Asp-*Z*-ΔPhe-OH], showed that the incorporation of superparamagnetic iron oxide nanoparticles (SPIONs) could keep the magnetic behavior alive in spite of the strong diamagnetic contribution from the involved organic matrix. *In vitro* heat generation on magnetic excitation with AMF could convert the gel to a solution, acting as a remote trigger to release SPIONs and encapsulated drugs displaying an image-guided drug delivery through self-reporting mechanism (Carvalho et al., 2019). Recently, a newer dehydropeptide hydrogelator; Npx-Met-*Z*-ΔPhe-OH (containing naproxen and a thioether), was combined with two different architectures, core/shell manganese ferrite/gold nanoparticle and gold-decorated manganese ferrite nanoparticles (acclaiming the affinity of sulfur toward gold) and tested for the delivery of antitumor drug, curcumin by the group (Veloso et al., 2020). ΔPhe is known to endow proteolytic stability and add conformational restraints in the peptide backbone. The naproxen group is added to boost selectivity toward cyclooxygenase. The drug delivery was higher in both irradiated gels as compared to the non-irradiated gels, suggestive for multimodal cancer therapy by combining both the photothermia and controlled drug delivery.

Different metal ions as well as anions modulating the self-assembly of the peptide amphiphiles have been investigated by Sharma et al. advocating an ion responsive behavior to the hydrogels. The group (Sharma et al., 2019) has reported various metal salts to influence self-assembly of histidine based dipeptide amphiphile accompanying a gel to sol transition. In another

study, Fan et al. have shown the capability of a dipeptide, H-Trp-Phe-OH, nanoparticles conjugated with an aptamer to bind Dox, due to the π-π stacking interaction and Zn(II) chelation. The formulation exhibited the possibility to act as optical probe to monitor the drug uptake and release (Fan et al., 2016). As recommended by Gazit, the study on fluorophores derived from green fluorescent protein and dipeptide conjugates sets the stage for new frontiers in peptide optics and to load various aromatic drug molecules into these nanoparticles via aromatic stacking interactions (Gazit, 2016).

The nanotubes of H-Lys-Lys-OH functionalized with camptothecin (CPT) chromophore at the ε-amino position, Ac-Lys-Lys(CPT)-NH_2 and NH_2-Lys-Lys-(CPT)-NH_2, were observed to protect the drug from lactone hydrolysis by sequestering the CPT segment within the hydrophobic nanotube walls, thereby increasing its stability. Herein, CPT conjugated dipeptide played the dual function, both as drug and precursor to the nanostructured carrier (Kim et al., 2015). Similar to this scheme, the research group Sun et al. worked for the delivery of 5-FU and synthesized di-lysine conjugated with 5-fluorouracil (5-FU), wherein hydrophobic π-π association of both uracil and Fmoc could drive β-sheet self-assembly (Sun Y. et al., 2016).

Fluorescein isothiocyanate (FITC) is known as sensitive fluorescent probe which can be detected easily in living cells. The attachment of fluorescein to N-terminal of H-Leu-Leu-OH dipeptide carried out by Kirkham et al. has found to be more cytocompatible as compared to the molecule itself. The strong π-π stacking interactions between the aromatic units in conjugate molecule, Fl-Leu-Leu-OH, formed could be responsible in the induction of self-assembly process. Fl-Leu-Leu-OH adopted a β-sheet structure as shown by FTIR spectroscopy, cryogenic transmission electron microscopy (cryo-TEM) and small-angle X-ray scattering (SAXS) studies. The conjugation improved the capacity of Fl-Leu-Leu-OH to be uptaken by cells without compromising cell viability as compared to FITC alone (Kirkham et al., 2016).

Use of a dipeptide, H-Asp-Phe-OH, to assist the uptake of a therapeutic polypeptide drug, calcitonin, broadly used to treat bone diseases, has been demonstrated by Cao et al. (2017) as co-assembly of the peptide-drug nanoparticles. The dipeptide (Asp-Phe) simply interacted with the Salmon calcitonin (sCT) through hydrophobic and electrostatic interactions leading to the supramolecular nanoparticles of sCT-Asp-Phe-OH. This self-assembly established long-lasting therapeutic effect and could control *in vivo* release of sCT, thereby, shun the need for multiple injections in patients (Cao et al., 2017).

The formation of NDI-Tyr-Phe-NH_2 by thermodynamically driven enzymatic condensation of naphthalenediimide (NDI)-functionalized tyrosine (NDI-Tyr) and phenylalanine-amide (Phe-NH_2) has been reported by Nalluri et al. (2014). The presence of dihydroxy/alkoxy naphthalene donors could produce proficient charge-transfer complexes. The fully reversible self-assemblies driven on minimized free-energy and fewer defects holds potential to develop self-healing materials.

Microvesicles, formed from a water-soluble, synthetic, amphiphilic dipeptide, containing a glutamic acid residue at the C-terminus and hydrophobic residue (Val/Leu/Nva) at N-terminal have been established to deliver and release the encapsulated anticancer drug and a fluorescent dye in response to a stimulus of the presence of calcium ions. The dye/drug-loaded vesicles have been found to be non-toxic using 2-(4,5-dimethyl-1,3-thiazol-2-yl)-3,5-diphenyl-2,3-dihydro-1H-tetrazol-4-ium bromide (MTT) based cytotoxicity assay. These biocompatible microvesicles were reported to have the capability to carry cyclic adenosine monophosphate (cAMP) at the target site suggesting the potential of these delivery vectors to carry drugs and other bioactive molecules (Naskar et al., 2011).

A dipeptide hydrogel, containing double Fmoc-group, self-assembled at very low concentration, exhibiting two-step self-assembly process, cytotoxic, suitable for 2D/3D cell scaffolding has been reported recently. The self-assembly of Fmoc-Lys(Fmoc)-Asp-H is reported to have gained advantage from (i) additional H-bonding from the carbonyl group, (ii) aromatic and hydrophobic interactions from the fluorenyl ring, and (iii) steric optimization from the methoxycarbonyl moiety. The balance between the hydrophobic and hydrophilic functionalities is essential for the self-assembly. So the hydrophobicity due to the additional Fmoc group is suggested to be balanced by the two hydrophilic carboxylic acid moieties present at the C-terminus as well as the Asp side chain (Chakraborty et al., 2020).

As linkers play an important role in speedy and effective delivery of the cytotoxic drugs, a lysosomal protease-cleavable dipeptide H-Val-Cit-OH, has commonly been used in the designing and synthesis of antibody-drug conjugates (ADCs) for delivering cytotoxic drugs to antigen bearing cells. Besides, H-Val-Ala-OH, another important dipeptide, has also been employed for synthesizing next-generation ADCs useful for drug loading and releasing purposes. The comparison studies of H-Val-Cit-OH and H-Val-Ala-OH based ADCs conjugated to the monomethyl auristatin E(MMAE) payload using xenograft model test showed their ability as patent payload for the anti-tumor activity (Wang et al., 2017b; Wang W. et al., 2017). It has also been reported that adding a hydrophilic group to the N-terminus of the valine residue in the H-Val-Cit-OH linker, viz., glutamic acid, prevents the premature cleavage of the linker in mouse plasma which otherwise is susceptible to extracellular carboxylesterase. This enhancement in the polarity of H-Val-Cit-OH linker offers higher *in vivo* stability to the antibody–drug conjugate in mouse plasma and allows the designing of ADC linkers (Anami et al., 2018).

An amphiphilic dendron, N-octadecanoyl-1,5-bis(L-glutamic acid)-L-glutamic diamide with potential to entrap Vitamin B_1 (VB_1) was found to shrink and turn into supergel triggered by monovalent to tetravalent metal ions. The mechanism of continuous, pH-responsive and thermally reversible shrinkage process has been proposed to involve protonation of carboxylic acid groups in presence of metal ions transforming morphology of the hydrogel from nanotubes to nanobelts followed by crosslinking between protonated carboxylic acid groups and metal ions again transforming morphology to nanofibres. During this transition process, the encapsulated water was released but immobilized due to cross-linked 3D structures and VB_1 was released in water phase. The release rate was found to be tuneable upon the shrinking rate of OGAc/metal hydrogel arrangement

(Qin et al., 2013). Since the best shrinkage capability was exhibited by Mg^{2+} ions, this research group used the proposed phase regulation property with change in pH in a further study. It was also observed that the addition of positively charged species accelerated the shrinkage and negatively charged additives suppressed the shrinkage of the supramolecular hydrogel. These pH change and ionic separation properties were exploited for the step-wise release of two-component drugs, pralidoxime iodide and phenol red, first the anionic drug, phenol red, was released through gel shrinkage and then on increasing pH, released the second cationic drug, pralidoxime iodide, through gel collapse, which suggests that the system still demands more sophisticated work to be carried out on the concept (Qin et al., 2014). Another pH- responsive hydrogel from the class of N-acetylglucosamine derivatives, especially, the heptylurea derivative with a *p*-methoxybenzylideneacetal protective group, showed release of trapped naproxen on addition of acid (Goyal et al., 2014).

Cyclic peptides have advantage to linear peptides in terms of structure rigidness and stability against proteolytic enzymes. This structure rigidity can reduce the freedom of possible structural conformations and so enhance the binding affinity of the ligands toward receptors. The cyclo-*D*-Trp-Tyr peptide nanotubes have been synthesized and assessed as carriers of caspase 3 silence shRNA. This could penetrate the intact cornea and deliver the CAP3 pRFP-C-RS DNA reducing the apoptosis in the wounded cornea triggered by corneal epithelial debridement (Lee et al., 2015). The injectable, *in situ* ambidextrous supergelator, cyclo-Phe-Glu(O-*tert*-But) with cytocompatibility has been reported to hold potential in drug delivery and regenerative medicine (Manchineella et al., 2017). A cationic, cyclic dipeptide, photoresponsive hydrogelator, with a diketopiperazine (DKP) derivative containing an unnatural amino acid bearing an azobenzene photoswitch (PAP–DKP); PAP-DKP-Lys favorably encapsulated oligonucleotides and released upon irradiation, thereby showing the potential for tuning the amino acid residue for the particular cargoes (Pianowski et al., 2016).

Tripeptides as Biologics Carriers

Amino acid chirality, considered a key tool to drive peptide self-assembly, exploited at the molecular and supramolecular levels for *D*- and *L*-amino acids positions in case of gelling tripeptides has been reported by Marchesan et al. (2015a), to establish a higher or lower supramolecular order. So, a suitable design of the chirality in sequence of self-assemblies has been suggested to assign and fine-tune the properties of reported tripeptide gel biomaterials. The amphiphilic tripeptides have been reported to generate diverse nanostructures with variable aspect-ratio and geometry as the amino acid is altered by Matson and Stupp. Hydrogen bonding between amide proton donors and adjacent carbonyl proton acceptors leading to β-sheet-type association in self-assembling oligopeptides has been found to favor the formation of high aspect-ratio nanostructures (Matson and Stupp, 2012). Sahoo et al. carried the gelation of tripeptides, by connecting a hydrophobic phenylalanine residue at the N-terminus, a variable amino acid to Ac-Phe-X-Asp-NH_2 to alter the tendency for intermolecular hydrogen bonding [X= G/A/V/L/I residue], and a charged C-terminal aspartic acid residue. They found that even without a strong peptide-specific secondary structure, the tripeptides with last three of the mentioned amino acids formed hydrogels (Sahoo et al., 2017). Furthermore, the work on selected Ac-Phe-X-Asp-NH_2 sequence with high aspect ratio; Ac-Phe-Ile-Asp-NH_2, suggested the requirement of the non-aromatic and uncharged residue in this tripeptide, which in this case was isoleucine–to be at least hydrophobic as well to facilitated high aspect-ratio nanostructure and aid hydrogel formation (Sahoo et al., 2018a). The study by Yang et al., on structural transition in Fmoc-Phe-Phe-Cys-OH from parallel-aligned worm-like micelles to entangled, coiled micelles persuaded by the cross-linking of the disulfide bonding, elucidated the relationship between micelle chirality and gel properties and suggested a strategy to fabricate materials with controlled chirality by means of synchronized non-covalent and covalent self-assembly (Yang et al., 2019). A series of Fmoc- protected tripeptide containing β-amino acid from H-βAla-His-OH [L-carnosine (Car)] joined by covalent link to different Fmoc-*L*-amino acids with a wide range of side-chains having different hydrophobicities were observed by Das et al. The tripeptides were found to be proteolytically stable under physiological condition and produce helical structures and the gelation capability to depend on the hydrophobicity of the side chain moiety where the additional π-π stacking interaction by the phenyl group supported the process. This study also demonstrated that the Fmoc-Phe-βAla-His-OH containing Fmoc-tripeptide exhibited the highest gelation ability among the examined amino acid residues, may be the phenyl group provided π-π stacking interaction. The tyrosine residue, expected for similar associative interaction, showed less gelation ability due to intermolecular H-bonding through the phenolic –OH group (Das Mahapatra et al., 2017).

Two tripeptides, viz., H-Gly-His-Lys-OH and H-Phe-Phe-Asp-OH, co-assembled through non-covalent assimilation, easily formed complex selectively with copper ions and converted into a hydrogel formed of nanofibers from clear solution of nanotapes in response to complexation (Abul-Haija et al., 2017).

A tripeptide, H-Lys-Phe-Gly-OH, accomplished the morphology change in secondary structure with switching of nanostructures from nanospheres (vesicles) to nanotubes reversibly depending on the concentration. A transition in the secondary structure could change the morphology of nanostructures. At the low concentration, the tripeptide formed spherical structures with diameters of 50±10 nm, while, at the higher concentration, the tubular aggregates with diameters of 190±10 nm were observed by Moitra et al. (2014, 2017). Even a temperature-induced change from tubular to vesicular has been observed. The nanovesicles, formed at physiological pH and disrupted at pH 6, a fit condition for the drug-delivery, were loaded with a chemotherapeutic anticancer drug, Dox, which resulted in the intracellular release of the drug.

The self-assembled nanoparticles of Fmoc-Leu-Leu-Leu-OMe have been reported by Li et al. as carriers of hydrophobic porphyrin derivative, meso-tetra(p-hydroxyphenyl) porphine (m-THPP) (Li J. et al., 2018). The doping of peptide

nanoparticles facilitated the solubility of hydrophobic porphyrin in aqueous media. Additionally, the doping preserved the intrinsic fluorescent property and reduced the risk of side effects due to overdose. The doping could enhance the two-photon fluorescence absorption ability of m-THPP. *In vitro* reactive oxygen species detection and the cytotoxicity test suggested high anticancer efficacy of the peptide nanoparticles by the two-photon irradiation (Li J. et al., 2018; Li et al., 2019a).

Fmoc-halogenated phenylalanine hydrogels have also been prepared and reported by Wang et al. (2013a). Out of various fluorinated analogs, Fmoc-4F-Phe-OH was found to be most suitable since the fluorenyl groups stacked more extensively. However, none of these hydrogels were found suitable to serve as a bioactive scaffold for NIH 3T3 cell culture in 2D environments. Thereafter, H-Arg-Gly-Asp-OH peptide was included in Fmoc-4F-Phe-OH to aid the cells' survival. This compound showed 3T3 cell adhesion and competent cell division. The results were suggestive of using similar bioactive scaffolds for drug delivery, tissue engineering and cell culture etc (Wang et al., 2013a). A self-assembled protected tripeptide, containing hydrophobic core, Boc-Pro-Phe-Gly-OMe, showed the ability to encapsulate hydrophobic drugs—eosin, aspirin and curcumin. The stabilization of the encapsulated nanostructures with Vitamin E-TPGS illustrated the controlled release of drugs endorsing their role as drug carriers (Yadav et al., 2015). Later, replacement of phenylalanine with dehydrophenylalanine, a constrained dehydroamino acid, self-assembled as hydrophobic matrix dehydrotripeptide, Boc-Pro-ΔPhe-Gly-OMe. The enhanced encapsulation competence of hydrophobic molecules showed soundness of constrained dehydroamino acids in drug-delivery applications (**Figure 6**) (Deka et al., 2017).

H-Phe-Phe-OH could promote self-assembly and gelation through π-π and hydrophobic interactions to construct gel materials. Also, an amino acid, 11-aminoundecanoic acid (AUDA), non-proteinaceous with long aliphatic chain, could add thixotropic property to the hydrogel. A combination of AUDA and H-Phe-Phe-OH residues as Boc-AUDA-Phe-Phe-COOH could promote both hydrogelation and thixotropic nature. The resultant hydrogel exhibited encapsulation and sustained release of an antibiotic (vancomycin) and vitamin B_{12} at physiological pH and temperature and endorsed itself for drug-delivery applications (Baral et al., 2014).

High-resolution scanning electron microscopic analysis revealed the architectural differences in the synthesized tripeptides, Boc-Phe-Gly-Glu-OH (L_1) and Boc-Phe-Val-Glu-OH (L_2), differing in hydrophobic groups and their corresponding Cu(II) conjugates (Das et al., 2018). The tripeptide with more hydrophobic glycine generated flower-like decorated branches and the less hydrophobic formed well-ordered spherical assemblies with nano-meric dimensions. The corresponding metallic conjugates self-assembled as nano-belt like structures in the former and nano-flake like in the later,

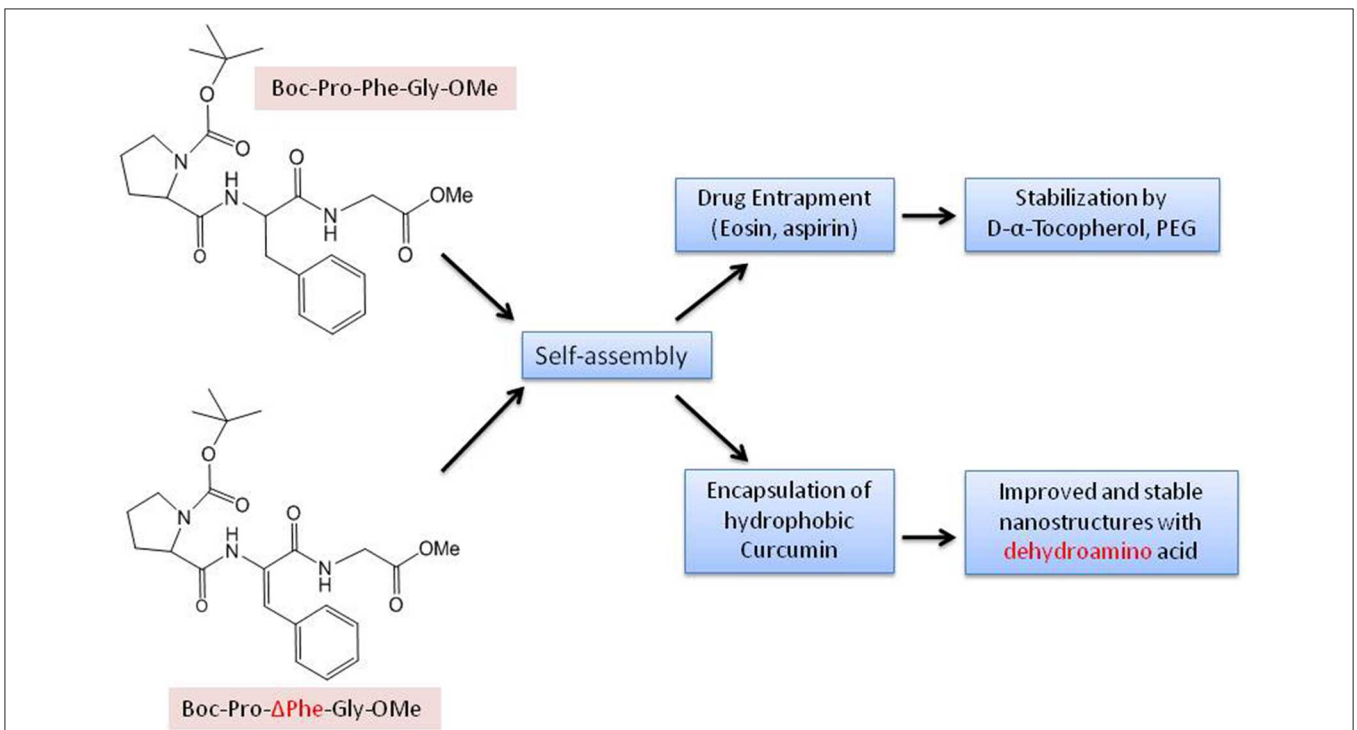

FIGURE 6 | Self-assembly of tripeptides having different aromatic moities.

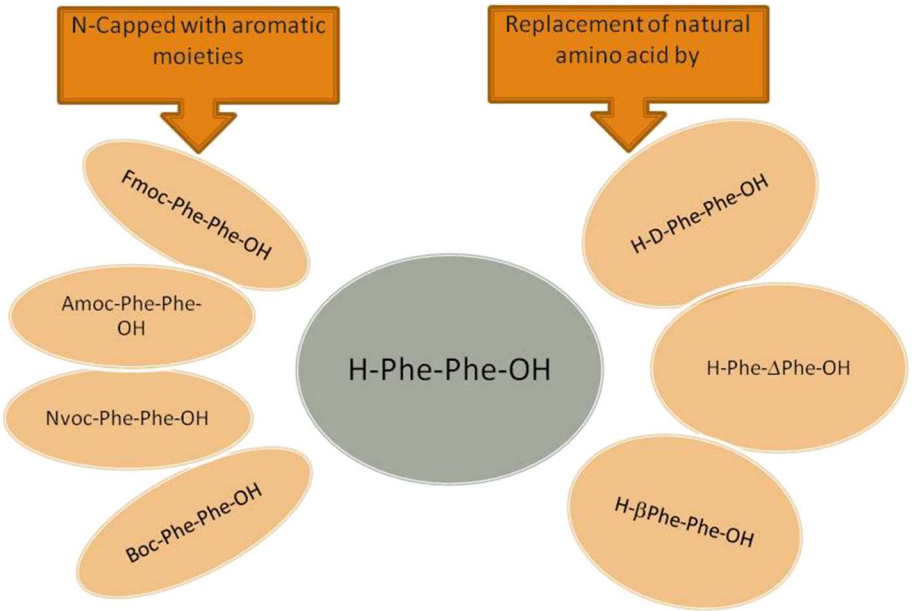

FIGURE 7 | Some of the analogs of H-Phe-Phe-OH.

which could be due to the metal–peptide interactions that controlled the self-assembly process, entailing that the metal–peptide interactions settle on the morphology of the assemblies. The observation on these non-cytotoxic metallo-peptides; Boc-Phe-Gly-Glu-Cu (L_1M) and Boc-Phe-Val-Glu-Cu (L_2M), could establish the role of metal ions- peptides coordination in removal of strong non-covalent interaction and the formation of supramolecular architectures with various morphologies (Das et al., 2018).

Fmoc-tripeptide hydrogels from Fmoc-Phe–Phe–Phe-OH with different chirality were synthesized by Chronopoulou et al. by a lipase-supported reaction in an aqueous phase using genipin as a crosslinker. The proposed crosslinker could modulate the physicochemical features of such hydrogels. Hydrogels displayed release of almost same amount of the entrapped drug, Dexamethasone (DXM), though the release kinetics varied. The *D*-amino acid based hydrogels were observed to be "dense" materials, so could detain the entrapped drugs for longer period than the corresponding *L*-counterparts and could also resist protease degradation. The results could establish the importance of chirality to induce the specific secondary structural features and also modulate physicochemical properties of the hydrogel. These biomaterials hold bright future in drug delivery and scaffolding uses in tissue engineering (Chronopoulou et al., 2014, 2015, 2017).

The prevalent challenges among cell-scaffolding materials are to upkeep with the vital physiognomies of the otherwise complex natural extracellular matrix (ECM) and incorporate the essential characteristics with minimal complexity into a scaffold. A biomimetic, nanofibrous hydrogel, co-assembled from two aromatic PAs, a structural unit, Fmoc-Phe-Phe-OH, and a functional unit, Fmoc-Arg-Gly-Asp-OH showed its supremacy to reconstruct a normal dermal tissue analog with enhanced mechanical strength. Fmoc-Phe-Phe-OH/Fmoc-Arg-Gly-Asp-OH hydrogel with elongated spindle-like morphology resembling myofibroblasts organized the nanofibrous 3D-networks and contracted the gel besides cell secretion of fibronectin and collagen I. As per *in vitro* results, fibronectin deposited ahead of denser collagen I, indicated construction of a normal dermal tissue within the scaffold. This simplified design by Zhou et al. (2014) supplies a pathway to create such versatile cell-scaffolds in skin engineering and similar bioactivities.

The policy to integrate *D*-amino acid residues indicates their potential use in drug delivery. The incorporation of *D*-amino acid residues in three chiral centers of homochiral tripeptide, Boc-Phe-Phe-Phe-COOH, could change the orientation of the corresponding aromatic ring of Phe residue(s) as well as the direction of π-π stacking interaction, which, in turn, could alter the mechanism of drug-delivery. The various combinations tried by Basu et al., hinted that the mechanical strength and proteolytic stability of a particular gelator could be modulated by changing the molecular chirality and placing the D-residue instead of L-residues in the appropriate position (at or toward the C terminus) (Basu et al., 2016).

A heterochiral supramolecular H-*D*-Leu-Phe-Phe-OH tripeptide hydrogel, loaded with an anti-metabolite and pyrimidine analog, hydrophobic antineoplastic drug, 5-fluorouracil (5-FU), formed hydrogel under physiological conditions and demonstrated a fast release. Interacting through π-π stacking between the H-Phe-Phe-OH and 5-FU rings as well as hydrogen bonding between the carboxylic acid group and N-H group of the 5-FU, this work examined the potential of a drug capable to interact non-covalently with a self-assembling tripeptide (Parisi et al., 2019). The outcome of the loading of

the anti-inflammatory drugs, naproxen and ketoprofen, in the tripeptide hydrogel in earlier works could establish that the naphthalene unit engages more efficiently through non-covalent interactions than the benzene rings with the aromatic units of the peptide (Mayr et al., 2018). Though the release of 5-FU was found to be faster than that of naproxen, the role of π-π interaction and hydrogen bonding is concurrent with the hypothesized one. H-Phe-DAla-Phe-OH is an exception to the design rule, where the tripeptides of syndiotactic *L-D-L* stereochemistry adopt an amphipathic conformation, and the side chains in anisotactic configuration enabling the long-range self-organization turn into gel-forming fibers, as the molecule does not possess the required hydrophobicity and steric hindrance and so, it does not turn to hydrogel (Garcia et al., 2018). The attachment of *p*-aminobenzoyl moiety at the N-terminus of the tripeptide, (*p*-aminobenzoyl)- Phe-*D*-Ala- Phe-NH_2, could address both the issues to yield a new gelator (Kieffer et al., 2019) that could be explored further.

The self-assembly of nanodrugs, as self-delivery of drugs, involving a photosensitizer (chlorine e6, Ce6) and Dox as carrier-free nanoparticles which combined photodynamic therapy with chemotherapy to inhibit tumor recurrence, has been tried (Zhang R. et al., 2016). Following the same working model, the supramolecular drug-drug delivery system (SDDDS) comprising of a tripeptide, H-Tyr-Ser-Val-OH (YSV) and Gefitinib (GEF), nanoparticles was studied. The low toxicity of the former and molecular targeting ability of the later led to the co-assembly, that required no chemical modification and performed better in drug efficacy both *in vitro* and *in vivo* as compared to individual drugs (Zhang Z. et al., 2017).

A phosphorylated and succinylated tripeptide, H-Gly-Tyr-Lys-OH, on conjugation with folic acid and Taxol, FA–Gly-Tyr-Lys–Taxol, self-assembled into a molecular hydrogel. The much higher weight percentage of Taxol in this gel compared to other similar gels, proposes it as injectable material to deliver Taxol for long period of time during chemotherapy (Wang and Yang, 2012).

A cytocompatible, photoresponsive hydrogelator with tetrazole-containing moiety, Tet(I)-Gly-Phe-Phe-OH, with fast responses to mild light irradiation, has shown the ability to modulate cellular microenvironment using a bio-orthogonal photoclick reaction. The mechanically strong hydrogel could entrap horse serum (HS) and human mesenchymal stem cells (hMSCs) for longer duration of time and its release could be modulated through photodegradation of the gel matrix (photo-triggered tetrazole-to-pyrazoline transformation). Further investigation holds bright chances to control the biological behavior of the live cells in spatially defined channels (He et al., 2013). Nap-Phe-Phe-Gly-OH, another tripeptide hydrogelator, was found to create surface-induced self-assembly that could inhibit human platelet aggregations. The comparison with Nap-Phe-Phe-OH, which could not inhibit the platelet aggregation, evidenced the status of Gly residue (Zheng et al., 2012). Further exploration on naphthaleneimide (NI) conjugates; NI-Gly-Phe-Phe-OH and NI-Phe-Phe-Gly-OH supramolecular hydrogels, articulated the good biocompatibility of NI-Gly-Phe-Phe-OH with cell lines. The observations could suggest that these supramolecular materials are promising candidates for their use in biomedical applications (Yeh et al., 2016).

Among the hydrogel biomaterials, a tripeptide, Ac-Phe-Phe-Ala-NH_2, developed by Pospišil et al., self-assembled into non-covalent, transparent, stable and biocompatible nanofiber hydrogel scaffolds at physiological pH without use of any organic solvent. The intramolecular hydrogen bonding of cross-β-type structure aggregates and non-covalent interactions between molecules of hydrogelators were proposed to lead the creation of the 3D gel network. The physicochemical and biological properties (*in vitro*) of the hydrogel suggest it as a hopeful scaffold for tissue engineering applications (Pospišil et al., 2016).

Acknowledging the importance of various factors, viz., morphology, rigidity, periodicity and epitope spacing, which impacted the performance of nanostructures and in turn vividly sway cell adhesion and signaling, a peptide-based amphiphile with a rigid amphiphilic structure of the derivative was obtained. A novel compound, N-3β-(4-*tert*-butylbenzoylamine)-(7α,12α-dihydroxy-5β-cholan-24-oyl)-(*S*)-Arg-(*S*)-Gly-(*S*)-Asp (*tert*-but-PhC-RGD), containing the H-Arg-Gly-Asp-OH epitope, a recognition motif involved in cell adhesion processes, was synthesized. This unusual self-assembly, compared to conventional H-Arg-Gly-Asp-OH containing amphiphiles, formed fibers with a circular cross-section and tested positive as scaffolds for tissue regeneration. The circular dichorism results showed weak interactions among H-Arg-Gly-Asp-OH groups as compared to the usual twisted ribbons superstructure which stipulate specific interactions among the chiral groups of the amphiphiles. So, relatively free H-Arg-Gly-Asp-OH groups provided opportunities to interact with the environment and, thereby, were found vital to the applications (Travaglini et al., 2017).

A tri-β-peptide, Ac-βAla-Z-βLys-βAla-OH, self-assembled to form non-toxic, biocompatible and mechanically stable hydrogel, probably the first peptide hydrogel comprising exclusively of β-amino acids, with stiffness similar to brain tissue. This tripeptide contained a β-homo-lysine (K) residue (to enhance solubility of peptide in aqueous buffer) and a C14 acylated alkyl chain (a hydrophobic acyl tail to produce a peptide amphiphile to direct self-assembly into nano-cylinders) and formed stable hydrogels. The peptide monomers, driven by a 3-point hydrogen-bonding motif associated with the 14-helical structure of N-acetyl-β3–peptides, self-assembled into helices in a unique head to-tail fashion. The hydrogel could rapidly recover stiffness since high strain could break just the 3D fibrous network by upsetting the non-covalent interactions and transform to sol, without destroying the fibers, but reorganized to 3D network again on reducing the strain in a relatively short time. This superior self-healing property of the hydrogel with minimal post-operative damage could fasten the recovery (Del Borgo et al., 2013). Following the recipe, Motamed et al. (2016) had developed a new technique to synthesize peptide based self-assembly wherein helical N-acetyl-β3–peptides could spontaneously form fibers, ranging from nano- to macroscale. The β3-tripeptides were observed by Del Borgo et al. to devise distinct self-assembly units segregated by a linker and turn to fibrous assemblies. The linkers within the peptide sequence, whether rigid or flexible, could

be composed of a bioactive α-peptide, could demonstrate fiber formation and create a hybrid α/β peptide scaffold regardless of amino acid sequence, or interruption of the sequence in the presented work (Del Borgo et al., 2018). A structural model developed for self-assembled N-acetyl-β3-peptides as stable three-stranded helical coiled coil could be used to explore the fibril structure for other materials (Christofferson et al., 2018) and be tailored for different applications (Kulkarni et al., 2019). A summary of this content is provided in **Table 1**.

TABLE 1 | Summary of the amino acid/peptide derivatives and their applications (**Figure 7**).

S.No.	Name of the amino acid/peptide	Derivative/co-assembly		Applications	References
Single amino acid					
1	H-Trp-OH	Fmoc-Trp(Boc)-OH	Nanoparticles	Drug delivery; Dox, an anticancer drug	Dube et al., 2017
2	H-Lys-OH	Fmoc-Lys-OH	Nanoparticles	Drug delivery; Chlorin e6 (Ce6), a photosensitive drug	Liu et al., 2016
3	H-Phe-OH	Pyrene-Phe-OH	Hydrogel	Drug delivery; vit B_{12} and Dox	Nanda et al., 2013
4		H-*D*-Phe-OH	Flakes	Therapeutic molecule in phenylketonuria	Singh V. et al., 2014
5		Fmoc-Phe-OH	Hydrogel	Drug delivery; Dye as a model drug	Singh et al., 2015
6		Fmoc-F^5-Phe-DAP	Hydrogel	Drug delivery; NSAID, diclofenac	Raymond et al., 2019
7	H-Cys-OH	N,N′-dibenzoyl-Cys-OH	Hydrogel	Drug delivery; Salicylic acid	Zhong et al., 2019
8	H-Trp-OH, H-Tyr-OH	-	Nanotubes	As drug carriers	Babar and Sarkar, 2017
9	H-Tyr-OH	H-Tyr(*tert*-Bu)-OH, H-*D*-Tyr(*tert*-Bu)-OH	Hydrogel	—-Do—	Aykent et al., 2019
10	H-Ala-OH	H-Ala-CAM, H-Ala-HYD, H-Ala-HYD+	Hydrogel	Drug delivery; Dox	Singh M. et al., 2014
11	H-Val-OH	H-3-methyl-2-(pyridin-4-ylmethylamino)-butanoic acid-OH/Zn^{2+}	Hydrogel	Drug delivery; Caffeine as a model drug	Saha et al., 2014
12	H-Glu-OH	Co-assembly of C18–Glu-OH and analog; Click-Glu-OH (C18=N-stearoyl; Click= amide moiety in C18 replaced by 1,4-disubstituted 1,2,3-triazole unit)	Hydrogel	Drug delivery; antibiotic drug (vancomycin)	Bachl et al., 2015
13	H-His-OH	Fmoc-His-OH/Zn^{2+}	Nanoparticles	Metallo-nanodrugs	Li S. et al., 2018
Dipeptides					
14	H-His-Phe-OH	Z-His-Phe-OH/Zn^{2+} (Z=N-benzyloxycarbonyl)	Nanoparticles	metallo-nanodrugs	Li S. et al., 2018
15	H-Phe-Phe-OH	H-Phe-Phe-OH	Microtubes	Drug delivery; Rhodamine B as model drug	Silva et al., 2013
16		H-Phe-Phe-OH/FA/Fe_3O_4	Nanotubes	Drug delivery; 5-FU, an antimetabolite drug and flufenamic acid, an anti-inflammatory cargo	Emtiazi et al., 2017
17		H-Phe-Phe-OH/FA	Nanotubes	Drug eluting stent	Zohrabi et al., 2016
18		H-Phe-Phe-OH	Nanotubes	Eradication of bacterial biofilms	Porter et al., 2018
19		TPP-Phe-Phe-OH	Nanodots	Photothermal therapy	Zou et al., 2017
20		Cationic H-Phe-Phe-OH/glutaraldehyde	Bola like nanocarriers	Drug delivery; Dox	Zhang H. et al., 2015
21		H-Phe-Phe-NH_2·HCl/phosphotungstic acid	Nanofilms	Tissue engineering; photothermal treatment	Xing et al., 2015

(Continued)

TABLE 1 | Continued

S.No.	Name of the amino acid/peptide	Derivative/co-assembly		Applications	References
22		H-Phe-Phe-ADA-Au	Nanospheres	Drug delivery; camptothecin	Li Q. et al., 2016
23		Nvoc-Phe-Phe-H	Hydrogel	Drug delivery; Insulin	Aldilla et al., 2018
24		H-His-Phe-OH/Hyaluronic acid	Hydrogel	Drug delivery (curcumin) and tissue engineering	Pujals et al., 2017
25		Fmoc-Phe-Phe-OH	Hydrogel	Drug delivery; Dox, 5-FU	Kuang and Xu, 2013
26		Fmoc-Phe-Phe-OH/Au	Organogel	Drug delivery; Dox	Roth-Konforti et al., 2018
27		Fmoc-Phe-Phe-OH	Hydrogel	Drug delivery; 5-FU, paclitaxel	Aviv et al., 2018
28		Fmoc-Phe-Phe-OH	Hydrogel	Biosensor, 3D scaffold	Erdogan et al., 2016
29		Fmoc-F^5-Phe/Fmoc-Phe-Phe-OH	Hydrogel	Tissue engineering	Lian et al., 2017
30		Fmoc-Phe-Phe-OH/poly-L-lysine	Hydrogel	Drug delivery; Ce6	Lian et al., 2016
31		Fmoc-Phe-Phe-OH/Fmoc-Arg-OH/hydroxyapatite (HAP)	Hydrogel	Bone tissue regeneration	Xing et al., 2015
32		Boc-Phe-Phe-OH	Nanoparticles	Cancer therapy	Liyanage et al., 2015
33		H-Phe-Phe-OH Boc-Phe-Phe-OH	Fibers	Drug delivery/Tissue engineering	Creasey et al., 2016
34		Boc-β(O)-δ5-Phe-β(O)-δ5-Phe-OH	Hydrogel	Drug delivery; proflavine	Reja et al., 2019
35		rhein-Phe-Phe-OH	Nanospheres	Drug delivery; camptothecin	Sun et al., 2019
36		H-βPhe-Phe-OH/H-βPhe–ΔPhe-OH	Nanotubes	Drug delivery; anticancer drug, mitoxantrone	Parween et al., 2014
37				Drug delivery; cancer-testis antigens	Khatri et al., 2019
38	H-Arg-Phe-OH	H-Arg-ΔPhe-OH	Nanoparticles	Gene delivery	Khatri et al., 2017
39		H-Arg-ΔPhe-OH/Fe_3O_4	Nanoparticles	As site-specific delivery systems	Baskar et al., 2017
40		H-Arg-ΔPhe-OH	Nanoparticles	Drug delivery; Dox	Singh et al., 2018
41		H-Arg-ΔPhe-La	Nanoparticles	miR-199a-3p delivery	Varshney et al., 2018
42	H-Leu-Phe-OH	Amoc-Leu-Phe-OH	Hydrogel	In drug delivery and tissue engineering	Gavel et al., 2018b
43		H-Leu-ΔPhe-OH	Hydrogel	Drug delivery; mitoxantrone	Thota et al., 2016
44	H-Arg-Phe-OH/H-Lys-Phe-OH	H-Arg-ΔPhe-OH/H-Lys-ΔPhe-OH	Nanoparticles	Gene delivery	Panda et al., 2013
45	H-Trp-Phe-OH	Npx-Trp-*Z*-ΔPhe-OH	Hydrogel	Drug delivery: Npx	Vilaça et al., 2015a
46		H-Trp-Phe-OH/Zn^{2+}	Nanoparticles	Drug delivery; Dox	Fan et al., 2016
47	H-Tyr-Phe-OH and H-Asp-Phe-OH	Npx-Tyr-*Z*-ΔPhe-OH/SPIONS and Npx-Asp-*Z*-ΔPhe-OH/SPIONS	Hydrogel	Drug delivery; Npx	Carvalho et al., 2019
48	H-Met-Phe-OH	Npx-Met-ZΔPhe-OH/manganese ferrite/gold nanoparticle and gold-decorated manganese ferrite nanoparticles	Hydrogel	Drug delivery; curcumin	Veloso et al., 2020
49	H-Lys-Lys-OH	Ac-Lys-Lys(CPT)-NH_2 and NH_2-Lys-Lys-(CPT)-NH_2	Nanotubes 50	Protection of CPT from lactone hydrolysis	Kim et al., 2015
51		H-Lys-Lys-OH/5-FU	Nanotubes/Hydrogel	Drug delivery; 5-FU	Sun Y. et al., 2016
52		Fl-Leu-Leu-OH	β-sheet structure/nanotape	Fluorescent label	Kirkham et al., 2016

(Continued)

TABLE 1 | Continued

S.No.	Name of the amino acid/peptide	Derivative/co-assembly		Applications	References
53	H-Asp-Phe-OH	H-Asp-Phe-OH	Nanoparticles	Drug delivery; calcitonin	Cao et al., 2017
54	H-Tyr-Phe-OH	NDI-Tyr-Phe-NH_2	Nanofibers	Potential self-healer	Nalluri et al., 2014
55	H-glyoxylamide-Phe-OH	H-glyoxylamide-Phe-OH/various aromatic capping	Hydrogel	Drug delivery; ciprofloxacin	Aldilla et al., 2018
56	H-Phe-Arg-OH/H-Phe-Asp-OH	Fmoc-3F-Phe-Arg-NH_2/Fmoc-3F-Phe-Asp-OH	Hydrogel	Tissue engineering	Liyanage et al., 2015
57	H-Glu—Glu-OH	N-octadecanoyl-1,5-bis(L-glutamic acid)-L-glutamic diamide/Mg^{2+}	Nanofibers /Nanotubes /Nanobelts	Vit B_1, anionic and cationic drugs (two-component drugs)	Qin et al., 2014
58	H-Trp-Tyr-OH	cyclo-*D*-Trp-Tyr	Nanotubes	CAP3 pRFP-C-RS DNA	Lee et al., 2015
59	H-Phe-Glu-OH	cyclo-Phe-Glu(O-*tert*-But)	Organogel /Hydrogel	Drug delivery; curcumin	Manchineella et al., 2017
60	Azo-Phe-Lys-OH	PAP-DKP-Lys	Hydrogel	DNA and doxorubicin delivery	Pianowski et al., 2016
Tripeptides					
61	H-Lys-Phe-Gly-OH	H-Lys-Phe-Gly-OH	Nanospheres (vesicles) /nanotubes	Drug delivery; Dox	Moitra et al., 2017
62	H-Leu-Leu-Leu-OH	Fmoc-Leu-Leu-Leu-OMe	Nanoparticles	Porphyrin derivative carriers, anticancer efficacy	Li J. et al., 2018
63	H-Pro-Phe-Gly-OH	Boc-Pro-Phe-Gly-OMe/Vit E-TPGS	Nanoparticles (vesicles)	Drug delivery; eosin, aspirin and curcumin	Yadav et al., 2015
64	H-Pro-Phe-Gly-OH	Boc-Pro-ΔPhe-Gly-OMe/Vitamin E-TPGS	Spherical nanostructures	Drug delivery; curcumin and ornidazole	Deka et al., 2017
65	H-AUDA-Phe-Phe-OH (AUDA=11-aminoundecanoic acid)	Boc-AUDA-Phe-Phe-OH	Hydrogel	Drug delivery; vancomycin and vit B_{12}	Baral et al., 2014
66	H-Phe–Phe–Phe-OH	Fmoc-Phe–Phe–Phe-OH	Hydrogel	Drug delivery; dexamethasone	Chronopoulou et al., 2015
67	H-Phe-Phe-OH/H-Arg-Gly-Asp-OH	Fmoc-Phe-Phe-OH/Fmoc-Arg-Gly-Asp-OH	Hydrogel	Tissue engineering	Zhou et al., 2014
68	H-Phe-Phe-Phe-OH	Boc-Phe-Phe-Phe-OH, Various combinations of *D*-residue instead of *L*-residues	Hydrogel	Drug delivery; Dox	Basu et al., 2016
69	H-Leu-Phe-Phe-OH	H-*D*-Leu-Phe-Phe-OH	Hydrogel	Drug delivery;5-FU	Parisi et al., 2019
70	H-Tyr-Ser-Val-OH	H-Tyr-Ser-Val-OH/Gefitinib	Nanoparticles	Drug delivery; Drug mixture	Zhang Z. et al., 2017
71	H-Gly-Tyr-Lys-OH	FA–Gly-Tyr-Lys–Taxol	Hydrogel	Drug delivery; Taxol	Wang and Yang, 2012
72	H-Gly-Phe-Phe-OH	Tet(I)-Gly-Phe-Phe-OH	Hydrogel	Drug delivery; horse serum (HS) and human mesenchymal stem cells (hMSCs)	He et al., 2013
73	H-Phe-Phe-Gly-OH	Nap-Phe-Phe-Gly-OH	Hydrogel	Inhibition of human platelet aggregations	Zheng et al., 2012
74	H-Gly-Phe-Phe-OH	NI-Gly-Phe-Phe-OH	Hydrogel	For biomedical applications	Yeh et al., 2016
75	H-Phe-Phe-Ala-OH	Ac-Phe-Phe-Ala-NH_2	Hydrogel	Suggested for tissue engineering	Pospišil et al., 2016
76	H-Arg-Gly-Asp-OH	N-3β-(4-t-butylbenzoyl-amine)-(7α,12α-dihydroxy-5β-cholan-24-oyl)-(*S*)-Arg-(*S*)-Gly-(*S*)-Asp (*tert*-but-PhC-RGD)	Hydrogel	Tissue engineering	Travaglini et al., 2017
77	H-Ala-Lys-Ala-OH	Ac-βAla-*Z*-βLys-βAla-OH	Hydrogel	Tissue engineering	Del Borgo et al., 2013

CONCLUSION AND FUTURE PERSPECTIVES

Self-assembly by bioactive molecules is the talent to associate into ordered 3D structures via noncovalent interactions, through a bottom-up approach, without guidance by an external source (Dehsorkhi et al., 2014). In the last 20 years, remarkable expansion has revolutionized, the aptitude has navigated to the potentially useful nanostructure-based materials and has offered newer tools in the field of biological and biomedical sciences. Nanotechnology, the driving force behind this evolution and the revolutionary modifications, has contributed immensely toward the realization of targeted and controlled delivery of available therapeutics. Different materials/systems have been developed with this vision. Except for few, these materials hold their own merits and demerits. Biocompatibility, the nature of the interaction with surrounding tissues, is crucial. Certain materials have claimed to demonstrate biocompatibility, while other developed materials showing toxicity, are proved unsuitable for *in vivo* applications. Cationic lipid-based nanostructures, found to activate immune system, are such an example (Campani et al., 2018). Besides, these are also linked with certain technological issues, such as, reproducibility, stability, low drug-loading, uncontrolled leaching and encapsulation problems. Further polymeric systems have been developed, but the evaluation studies showed these materials also facing similar limitations. The surface functionalization was considered to improve drug or gene-targeting which in general, is complicated (Abd Ellah and Abouelmagd, 2017). Likewise, natural polymers, elicited undesirable immune reactions, illustrated batch to batch inconsistency (Ginjupalli et al., 2017) and so *in vivo* performance of these polymers became debatable.

Peptides and small molecule-based nanostructures can be virtuous alternatives for therapeutic delivery due to characteristics, like, good biocompatibility, easy on design/synthesis and also the functionalization. These distinctive and superior qualities make their self-assembled nanostructures smart tools in biomedical field. The masterstroke lies in the ability of these self-assembled small molecules to exhibit stimuli-responsiveness to the environment (internal/external stimuli), thus enabled to control and sustain the therapeutic release as per the requirement, an exciting prospect for multiple biomedical and bionanotechnology applications in drug delivery (Mart et al., 2006). Thus, virtues like, mild and rapid synthesis setting, non-requirement of specialized equipments, low production expenditure, easy dispersibility in aqueous medium and simple functionalization promote their use as future candidates for diverse applications such as, production of biomaterials, healthcare systems drug/gene delivery, tissue engineering, imaging, sensors, diagnosis, bioelectronics, and so on. Diverse types of structures/architectures can be generated simply by altering the physical or chemical conditions. Thus, this newer area of research is growing at an accelerating pace. Self-assemblies do result in the a variety of type of structures; nanoparticles, nanospheres, nanotubes, nanorods, nanotapes, nanofibers, nanogels, etc., yet there still exist several challenges to be addressed to make these self- assemblies- the materials of choice for research. The limited information on the influence of nanostructures on the organisms, control over size and composition during processing, tenability, behavior in aqueous environment, stability, up-scaling and degree of loading/entrapment of therapeutics are some obstacles which still need sincere attention of the researchers. Besides, follow-on these studies to establish biocompatibility and immunogenicity of these nanostructures are lacking. Nonetheless, it is viable to fine-tune the physicochemical properties by assimilating chemical modifications and so optimize the peptide functionality to minimize the toxicity without threatening their therapeutic activity (Lombardi et al., 2019). Hydrogel based drug delivery systems are of special mention as these are customized for modified release to the target site, reduce toxicity and side effects (Du et al., 2015; Li Y. et al., 2016).

Peptides offer a striking platform as non-viral gene delivery vectors which can minimize the disadvantages associated with viral vectors. Several groups have deliberated on non-viral gene delivery vehicles coupled with targeting peptides (Levine et al., 2013; Sharma et al., 2014; Kang et al., 2019; Wang et al., 2019). Though several functional peptide classes possess essential characteristics to overcome extracellular and intracellular barriers and make gene delivery feasible, still none of these functional peptides have been observed to contain all the essential characteristics required to overcome all of the barriers. Attempts are being made to develop novel multifunctional peptide vectors by combinatorial strategies and high-throughput screening (Jia et al., 2013; Raad et al., 2014; Riley and Vermerris, 2017).

AUTHOR CONTRIBUTIONS

PK and AS conceived the idea to write a review article on peptide self-assembly. SG compiled the article and IS helped in the graphics and compilation. SG, AS, and PK also did editing.

REFERENCES

Abbas, M., Xing, R., Zhang, N., Zou, Q., and Yan, X. (2018). Antitumor photodynamic therapy based on dipeptide fibrous hydrogels with incorporation of photosensitive drugs. *ACS Biomater. Sci. Eng.* 4, 2046–2052. doi: 10.1021/acsbiomaterials.7b00624

Abbas, M., Zou, Q., Li, S., and Yan, X. (2017). Self-assembled peptide-and protein-based nanomaterials for antitumor photodynamic and photothermal therapy. *Adv. Mater.* 29:1605021. doi: 10.1002/adma.201605021

Abd Ellah, N. H., and Abouelmagd, S. A. (2017). Surface functionalization of polymeric nanoparticles for tumor drug delivery: approaches and challenges. *Exp. Opin. Drug Deliv.* 14, 201–214. doi: 10.1080/17425247.2016.1213238

Abul-Haija, Y. M., Scott, G. G., Sahoo, J. K., Tuttle, T., and Ulijn, R. V. (2017). Cooperative, ion-sensitive co-assembly of tripeptide hydrogels. *Chem. Commun.* 53, 9562–9565. doi: 10.1039/C7CC04796G

Acar, H., Srivastava, S., Chung, E. J., Schnorenberg, M. R., Barrett, J. C., LaBelle, J. L., et al. (2017). Self-assembling peptide-based building blocks in medical applications. *Adv. Drug Deliv. Rev.* 110, 65–79. doi: 10.1016/j.addr.2016.08.006

Accardo, A., Leone, M., Tesauro, D., Aufiero, R., Bénarouche, A., Cavalier, J.-F., et al. (2013). Solution conformational features and interfacial properties of an intrinsically disordered peptide coupled to alkyl chains: a new class of peptide amphiphiles. *Mol. BioSyst.* 9, 1401–1410. doi: 10.1039/c3mb25507g

Adler-Abramovich, L., and Gazit, E. (2014). Correction: the physical properties of supramolecular peptide assemblies: from building block association to technological applications. *Chem. Soc. Rev.* 43, 7236–7236. doi: 10.1039/C4CS90080D

Adler-Abramovich, L., Marco, P., Arnon, Z. A., Creasey, R. C., Michaels, T. C., Levin, A., et al. (2016). Controlling the physical dimensions of peptide nanotubes by supramolecular polymer coassembly. *ACS Nano* 10, 7436–7442. doi: 10.1021/acsnano.6b01587

Adler-Abramovich, L., Vaks, L., Carny, O., Trudler, D., Magno, A., Caflisch, A., et al. (2012). Phenylalanine assembly into toxic fibrils suggests amyloid etiology in phenylketonuria. *Nat. Chem. Biol.* 8:701. doi: 10.1038/nchembio.1002

Alam, S., Panda, J. J., and Chauhan, V. S. (2012). Novel dipeptide nanoparticles for effective curcumin delivery. *Int. J. Nanomed.* 7:4207. doi: 10.2147/IJN.S33015

Alam, S., Panda, J. J., Mukherjee, T. K., and Chauhan, V. S. (2016). Short peptide based nanotubes capable of effective curcumin delivery for treating drug resistant malaria. *J. Nanobiotechnol.* 14:26. doi: 10.1186/s12951-016-0179-8

Aldilla, V. R., Martin, A. D., Nizalapur, S., Marjo, C. E., Rich, A. M., Ho, K. K., et al. (2018). Glyoxylamide-based self-assembly hydrogels for sustained ciprofloxacin delivery. *J. Mater. Chem. B,* 6, 6089–6098. doi: 10.1039/C8TB01290C

Alhakamy, N. A., Nigatu, A. S., Berkland, C. J., and Ramsey, J. D. (2013). Noncovalently associated cell-penetrating peptides for gene delivery applications. *Therap. Deliv.* 4, 741–757. doi: 10.4155/tde.13.44

Altunbas, A., and Pochan, D. J. (2011). "Peptide-based and polypeptide-based hydrogels for drug delivery and tissue engineering," in *Peptide-Based Materials*, ed T. Deming (Berlin; Heidelberg: Springer), 135–167. doi: 10.1007/128_2011_206

Amit, M., Yuran, S., Gazit, E., Reches, M., and Ashkenasy, N. (2018). Tailor-made functional peptide self-assembling nanostructures. *Adv. Mater.* 30:1707083. doi: 10.1002/adma.201707083

Anami, Y., Yamazaki, C. M., Xiong, W., Gui, X., Zhang, N., An, Z., et al. (2018). Glutamic acid–valine–citrulline linkers ensure stability and efficacy of antibody–drug conjugates in mice. *Nat. Commun.* 9:2512. doi: 10.1038/s41467-018-04982-3

Arakawa, H., Takeda, K., Higashi, S. L., Shibata, A., Kitamura, Y., and Ikeda, M. (2020). Self-assembly and hydrogel formation ability of Fmoc-dipeptides comprising α-methyl-L-phenylalanine. *Polymer J.* 30, 1–8. doi: 10.1038/s41428-019-0301-5

Argudo, P. G., Contreras-Montoya, R., de Cienfuegos, L. Á., Cuerva, J. M., Cano, M., Alba-Molina, D., et al. (2018). Unravelling the 2D self-assembly of Fmoc-dipeptides at fluid interfaces. *Soft Matter.* 14, 9343–9350. doi: 10.1039/C8SM01508B

Aviv, M., Halperin-Sternfeld, M., Grigoriants, I., Buzhansky, L., Mironi-Harpaz, I., Seliktar, D., et al. (2018). Improving the mechanical rigidity of hyaluronic acid by integration of a supramolecular peptide matrix. *ACS Appl. Mater. Interfaces* 10, 41883–41891. doi: 10.1021/acsami.8b08423

Aykent, G., Zeytun, C., and Marion, A., Özçubukçu, S. (2019). Simple tyrosine derivatives act as low molecular weight organogelators. *Sci. Rep.* 9:4893. doi: 10.1038/s41598-019-41142-z

Babar, D. G., and Sarkar, S. (2017). Self-assembled nanotubes from single fluorescent amino acid. *Appl. Nanosci.* 7, 101–107. doi: 10.1007/s13204-017-0551-5

Bachl, J., Mayr, J., Sayago, F. J., Cativiela, C., and Díaz, D. D. (2015). Amide–triazole isosteric substitution for tuning self-assembly and incorporating new functions into soft supramolecular materials. *Chem. Commun.* 51, 5294–5297. doi: 10.1039/C4CC08593K

Banerjee, J., Radvar, E., and Azevedo, H. (2018). "Self-assembling peptides and their application in tissue engineering and regenerative medicine," in *Peptides and Proteins as Biomaterials for Tissue Regeneration and Repair*, eds M. A. Barbosa and M. C. L. Martins (Duxford: Elsevier), 245–281. doi: 10.1016/B978-0-08-100803-4.00010-3

Baral, A., Roy, S., Dehsorkhi, A., Hamley, I. W., Mohapatra, S., Ghosh, S., et al. (2014). Assembly of an injectable noncytotoxic peptide-based hydrogelator for sustained release of drugs. *Langmuir* 30, 929–936. doi: 10.1021/la4043638

Basavalingappa, V., Guterman, T., Tang, Y., Nir, S., Lei, J., Chakraborty, P., et al. (2019). Expanding the functional scope of the fmoc-diphenylalanine hydrogelator by introducing a rigidifying and chemically active urea backbone modification. *Adv. Sci.* 6:1900218. doi: 10.1002/advs.201900218

Baskar, G., Ravi, M., Panda, J. J., Khatri, A., Dev, B., Santosham, R., et al. (2017). Efficacy of dipeptide-coated magnetic nanoparticles in lung cancer models under pulsed electromagnetic field. *Cancer Investig.* 35, 431–442. doi: 10.1080/07357907.2017.1318894

Basu, K., Baral, A., Basak, S., Dehsorkhi, A., Nanda, J., Bhunia, D., et al. (2016). Peptide based hydrogels for cancer drug release: modulation of stiffness, drug release and proteolytic stability of hydrogels by incorporating D-amino acid residue (s). *Chem. Commun.* 52, 5045–5048. doi: 10.1039/C6CC01744D

Bechara, C., and Sagan, S. (2013). Cell-penetrating peptides: 20 years later, where do we stand? *FEBS Lett.* 587, 1693–1702. doi: 10.1016/j.febslet.2013.04.031

Bera, S., and Gazit, E. (2019). Self-assembly of functional nanostructures by short helical peptide building blocks. *Protein Peptide Lett.* 26, 88–97. doi: 10.2174/0929866525666180917163142

Bera, S., Mondal, S., Rencus-Lazar, S., and Gazit, E. (2018). Organization of amino acids into layered supramolecular secondary structures. *Acc. Chem. Res.* 51, 2187–2197. doi: 10.1021/acs.accounts.8b00131

Bera, S., Mondal, S., Tang, Y., Jacoby, G., Arad, E., Guterman, T., et al. (2019). Deciphering the rules for amino acid co-assembly based on interlayer distances. *ACS Nano* 13, 1703–1712. doi: 10.1021/acsnano.8b07775

Biscaglia, F., Frezza, E., Zurlo, E., and Gobbo, M. (2016). Linker dependent chirality of solvent induced self-assembled structures of porphyrin–α-helical peptide conjugates. *Organ. Biomol. Chem.* 14, 9568–9577. doi: 10.1039/C6OB01633B

Biscaglia, F., and Gobbo, M. (2018). Porphyrin–peptide conjugates in biomedical applications. *Peptide Sci.* 110:e24038. doi: 10.1002/pep2.24038

Boekhoven, J., and Stupp, S. I. (2014). 25th anniversary article: supramolecular materials for regenerative medicine. *Adv. Mater.* 26, 1642–1659. doi: 10.1002/adma.201304606

Bonetti, A., Pellegrino, S., Das, P., Yuran, S., Bucci, R., Ferri, N., et al. (2015). Dipeptide nanotubes containing unnatural fluorine-substituted β2, 3-diarylamino acid and L-alanine as candidates for biomedical applications. *Organ. Lett.* 17, 4468–4471. doi: 10.1021/acs.orglett.5b02132

Borrelli, A., Tornesello, A. L., Tornesello, M. L., and Buonaguro, F. M. (2018). Cell penetrating peptides as molecular carriers for anti-cancer agents. *Molecules* 23:20295. doi: 10.3390/molecules23020295

Bowerman, C. J., and Nilsson, B. L. (2010). A reductive trigger for peptide self-assembly and hydrogelation. *J. Am. Chem. Soc.* 132, 9526–9527. doi: 10.1021/ja1025535

Boyle, A. L. (2018). "Applications of *de novo* designed peptides," in *Peptide Applications in Biomedicine, Biotechnology and Bioengineering* (Elsevier), 51–86. doi: 10.1016/B978-0-08-100736-5.00003-X

Brahmachari, S., Arnon, Z. A., Frydman-Marom, A., Gazit, E., and Adler-Abramovich, L. (2017). Diphenylalanine as a reductionist model for the mechanistic characterization of β-amyloid modulators. *ACS Nano* 11, 5960–5969. doi: 10.1021/acsnano.7b01662

Brasseur, R., and Divita, G. (2010). *Happy Birthday Cell Penetrating Peptides: Already 20 Years*. Amsterdam: Elsevier. doi: 10.1016/j.bbamem.2010.09.001

Briuglia, M.-L., Urquhart, A. J., and Lamprou, D. A. (2014). Sustained and controlled release of lipophilic drugs from a self-assembling amphiphilic peptide hydrogel. *Int. J. Pharm.* 474, 103–111. doi: 10.1016/j.ijpharm.2014.08.025

Brown, N., Lei, J., Zhan, C., Shimon, L. J., Adler-Abramovich, L., Wei, G., et al. (2018). Structural polymorphism in a self-assembled tri-aromatic peptide system. *ACS nano,* 12, 3253–3262. doi: 10.1021/acsnano.7b07723

Campani, V., Giarra, S., and De Rosa, G. (2018). Lipid-based core-shell nanoparticles: evolution and potentialities in drug delivery. *OpenNano* 3, 5–17. doi: 10.1016/j.onano.2017.12.001

Cao, J., Cai, Y., Yu, L., and Zhou, J. (2019). Dual physically crosslinked hydrogels based on the synergistic effects of electrostatic and dipole–dipole interactions. *J. Mater. Chem. B* 7, 676–683. doi: 10.1039/C8TB03032D

Cao, S., Liu, Y., Shang, H., Li, S., Jiang, J., Zhu, X., et al. (2017). Supramolecular nanoparticles of calcitonin and dipeptide for long-term controlled release. *J. Controll. Rel.* 256, 182–192. doi: 10.1016/j.jconrel.2017.04.014

Carny, O., and Gazit, E. (2005). A model for the role of short self-assembled peptides in the very early stages of the origin of life. *FASEB J.* 19, 1051–1055. doi: 10.1096/fj.04-3256hyp

Carrejo, N. C., Moore, A. N., Lopez Silva, T. L., Leach, D. G., Li, I.-C., Walker, D. R., et al. (2018). Multidomain peptide hydrogel accelerates healing of full-thickness wounds in diabetic mice. *ACS Biomate. Sci. Eng.* 4, 1386–1396. doi: 10.1021/acsbiomaterials.8b00031

Carvalho, A., Gallo, J., Pereira, D. M., Valentão, P., Andrade, P. B., Hilliou, L., et al. (2019). Magnetic dehydrodipeptide-based self-assembled hydrogels for theragnostic applications. *Nanomaterials* 9:541. doi: 10.3390/nano9040541

Chakraborty, P., and Gazit, E. (2018). Amino acid based self-assembled nanostructures: complex structures from remarkably simple building blocks. *ChemNanoMat* 4, 730–740. doi: 10.1002/cnma.201800147

Chakraborty, P., Tang, Y., Yamamoto, T., Yao, Y., Guterman, T., Zilberzwige-Tal, S., et al. (2020). Unusual two-step assembly of a minimalistic dipeptide-based functional hypergelator. *Adv. Mater.* 20:1906043. doi: 10.1002/adma.201906043

Chen, C., Liu, K., Li, J., and Yan, X. (2015). Functional architectures based on self-assembly of bio-inspired dipeptides: structure modulation and its photoelectronic applications. *Adv. Colloid Interface Sci.* 225, 177–193. doi: 10.1016/j.cis.2015.09.001

Chen, J., Qin, S., Wu, X., and Chu,; K, P. (2015). Morphology and pattern control of diphenylalanine self-assembly via evaporative dewetting. *ACS Nano* 10, 832–838. doi: 10.1021/acsnano.5b05936

Chen, J., and Zou, X. (2019). Self-assemble peptide biomaterials and their biomedical applications. *Bioactive Mater.* 4, 120–131. doi: 10.1016/j.bioactmat.2019.01.002

Chen, P. (2005). Self-assembly of ionic-complementary peptides: a physicochemical viewpoint. *Colloids Surfaces A* 261, 3–24. doi: 10.1016/j.colsurfa.2004.12.048

Chen, X., He, Y., Kim, Y., and Lee, M. (2016). Reversible, short α-peptide assembly for controlled capture and selective release of enantiomers. *J. Am. Chem. Soc.* 138, 5773–5776. doi: 10.1021/jacs.6b02401

Choi, Y. S., David, A. E. (2014). Cell penetrating peptides and the mechanisms for intracellular entry. *Curr. Pharm. Biotechnol.* 15, 192–199. doi: 10.2174/1389201015666140617093331

Christofferson, A. J., Al-Garawi, Z. S., Todorova, N., Turner, J., Del Borgo, M. P., Serpell, L. C., et al. (2018). Identifying the coiled-coil triple helix structure of β-peptide nanofibers at atomic resolution. *ACS Nano* 12, 9101–9109. doi: 10.1021/acsnano.8b03131

Chronopoulou, L., Margheritelli, S., Toumia, Y., Paradossi, G., Bordi, F., Sennato, S., et al. (2015). Biosynthesis and characterization of cross-linked Fmoc peptide-based hydrogels for drug delivery applications. *Gels* 1, 179–193. doi: 10.3390/gels1020179

Chronopoulou, L., Sennato, S., Bordi, F., Giannella, D., Di Nitto, A., Barbetta, A., et al. (2014). Designing unconventional Fmoc-peptide-based biomaterials: structure and related properties. *Soft Matter.* 10, 1944–1952. doi: 10.1039/c3sm52457d

Chronopoulou, L., Toumia, Y., Cerroni, B., Pandolfi, D., Paradossi, G., and Palocci, C. (2017). Biofabrication of genipin-crosslinked peptide hydrogels and their use in the controlled delivery of naproxen. *New Biotechnol.* 37, 138–143. doi: 10.1016/j.nbt.2016.04.006

Cockroft, S. L., Hunter, C. A., Lawson, K. R., Perkins, J., and Urch, C. J. (2005). Electrostatic control of aromatic stacking interactions. *J. Am. Chem. Soc.* 127, 8594–8595. doi: 10.1021/ja050880n

Copolovici, D. M., Langel, K., Eriste, E., and Langel, U. (2014). Cell-penetrating peptides: design, synthesis, and applications. *ACS Nano* 8, 1972–1994. doi: 10.1021/nn4057269

Creasey, R. C., Louzao, I., Arnon, Z. A., Marco, P., Adler-Abramovich, L., Roberts, C. J., et al. (2016). Disruption of diphenylalanine assembly by a Boc-modified variant. *Soft Matter* 12, 9451–9457. doi: 10.1039/C6SM01770C

Cui, H., and Chen, X. (2017). Peptides and peptide conjugates in medicine. *Adv. Drug Deliv. Rev.* 110, 1–2. doi: 10.1016/j.addr.2017.04.004

Cui, H., Webber, M. J., and Stupp, S. I. (2010). Self-assembly of peptide amphiphiles: from molecules to nanostructures to biomaterials. *Peptide Sci.* 94, 1–18. doi: 10.1002/bip.21328

Das Mahapatra, R., Dey, J., and Weiss, R. G. (2017). L-Carnosine-derived Fmoc-tripeptides forming pH-sensitive and proteolytically stable supramolecular hydrogels. *Langmuir* 33, 12989–12999. doi: 10.1021/acs.langmuir.7b03018

Das, P., Pan, I., Cohen, E., and Reches, M. (2018). Self-assembly of a metallo-peptide into a drug delivery system using a "switch on" displacement strategy. *J. Mater. Chem. B* 6, 8228–8237. doi: 10.1039/C8TB01483C

Datta, D., Harikrishna, A., Nagaraj, R., and Chaudhary, N. (2019). Self-assembly of β-turn motif-connected tandem repeats of Aβ16-22 and its aromatic analogs. *Peptide Sci.* 111:e24099. doi: 10.1002/pep2.24099

Datta, D., Tiwari, O., and Ganesh, K. N. (2018). New archetypes in self-assembled Phe-Phe motif induced nanostructures from nucleoside conjugated-diphenylalanines. *Nanoscale* 10, 3212–3224. doi: 10.1039/C7NR08436F

De Luigi, A., Mariani, A., De Paola, M., Depaolini, A. R., Colombo, L., Russo, L., et al. (2015). Doxycycline hinders phenylalanine fibril assemblies revealing a potential novel therapeutic approach in phenylketonuria. *Sci. Rep.* 5:15902. doi: 10.1038/srep15902

De Santis, E., and Ryadnov, M. G. (2015). Peptide self-assembly for nanomaterials: the old new kid on the block. *Chem. Soc. Rev.* 44, 8288–8300. doi: 10.1039/C5CS00470E

Dehsorkhi, A., Castelletto, V., and Hamley, I. W. (2014). Self-assembling amphiphilic peptides. *J. Peptide Sci.* 20, 453–467. doi: 10.1002/psc.2633

Deka, S. R., Yadav, S., Kumar, D., Garg, S., Mahato, M., and Sharma, A. K. (2017). Self-assembled dehydropeptide nano carriers for delivery of ornidazole and curcumin. *Colloids Surfaces B* 155, 332–340. doi: 10.1016/j.colsurfb.2017.04.036

Del Borgo, M. P., Kulkarni, K., Tonta, M. A., Ratcliffe, J. L., Seoudi, R., Mechler, A. I., et al. (2018). β3-tripeptides act as sticky ends to self-assemble into a bioscaffold. *APL Bioeng.* 2:026104. doi: 10.1063/1.5020105

Del Borgo, M. P., Mechler, A. I., Traore, D., Forsyth, C., Wilce, J. A., Wilce, M. C., et al. (2013). Supramolecular self-assembly of N-acetyl-capped β-peptides leads to nano-to macroscale fiber formation. *Angew. Chem. Int. Edn.* 52, 8266–8270. doi: 10.1002/anie.201303175

Devadasu, V. R., Bhardwaj, V., and Kumar, M. R. (2012). Can controversial nanotechnology promise drug delivery? *Chem. Rev.* 113, 1686–1735. doi: 10.1021/cr300047q

Diaferia, C., Morelli, G., and Accardo, A., (2019). Fmoc-diphenylalanine as suitable building block for the preparation of hybrid materials and their potential applications. *J. Mater. Chem.* 7, 5142–5155. doi: 10.1039/C9TB01043B

Dinca, A., Chien, W.-M., and Chin, M. T. (2016). Intracellular delivery of proteins with cell-penetrating peptides for therapeutic uses in human disease. *Int. J. Mol. Sci.* 17:263. doi: 10.3390/ijms17020263

Ding, X., and Wang, Y. (2017). Weak bond-based injectable and stimuli responsive hydrogels for biomedical applications. *J. Mater. Chem. B* 5, 887–906. doi: 10.1039/C6TB03052A

Ding, Y., Li, Y., Qin, M., Cao, Y., and Wang, W. (2013). Photo-cross-linking approach to engineering small tyrosine-containing peptide hydrogels with enhanced mechanical stability. *Langmuir* 29, 13299–13306. doi: 10.1021/la4029639

Doane, T., and Burda, C. (2012). Nanoparticle mediated non-covalent drug delivery. *Adv. Drug Deliv. Rev.* 65:12. doi: 10.1016/j.addr.2012.05.012

Dou, X. Q., and Feng, C. L. (2017). Amino acids and peptide-based supramolecular hydrogels for three-dimensional cell culture. *Adv. Mater.* 29:1604062. doi: 10.1002/adma.201604062

Draper, E. R., and Adams, D. J. (2018). How should multicomponent supramolecular gels be characterised? *Chem. Soc. Rev.* 47, 3395–3405. doi: 10.1039/C7CS00804J

Du, X., Zhou, J., Shi, J., and Xu, B. (2015). Supramolecular hydrogelators and hydrogels: from soft matter to molecular biomaterials. *Chem. Rev.* 115, 13165–13307. doi: 10.1021/acs.chemrev.5b00299

Dube, T., Mandal, S., and Jyoti Panda, J. (2017). Nanoparticles generated from a tryptophan derivative: physical characterization and anti-cancer drug delivery. *Amino Acids* 49:8. doi: 10.1007/s00726-017-2403-8

Edwards-Gayle, C. J., and Hamley, I. W. (2017). Self-assembly of bioactive peptides, peptide conjugates, and peptide mimetic materials. *Organ. Biomol. Chem.* 15, 5867–5876. doi: 10.1039/C7OB01092C

Emtiazi, G., Zohrabi, T., Lee, L. Y., Habibi, N., and Zarrabi, A. (2017). Covalent diphenylalanine peptide nanotube conjugated to folic acid/magnetic nanoparticles for anti-cancer drug delivery. *J. Drug Deliv. Sci. Technol.* 41, 90–98. doi: 10.1016/j.jddst.2017.06.005

Erdogan, H., Babur, E., Yilmaz, M., Candas, E., Gordesel, M., Dede, Y., et al. (2015). Morphological versatility in the self-assembly of val-ala and ala-val dipeptides. *Langmuir* 31, 7337–7345. doi: 10.1021/acs.langmuir.5b01406

Erdogan, H., Yilmaz, M., Babur, E., Duman, M., Aydin, H. M., and Demirel, G. (2016). Fabrication of plasmonic nanorod-embedded dipeptide microspheres via the freeze-quenching method for near-infrared laser-triggered drug-delivery applications. *Biomacromolecules* 17, 1788–1794. doi: 10.1021/acs.biomac.6b00214

Eskandari, S., Guerin, T., Toth, I., and Stephenson, R. J. (2017). Recent advances in self-assembled peptides: implications for targeted drug delivery and vaccine engineering. *Adv. Drug Deliv. Rev.* 110, 169–187. doi: 10.1016/j.addr.2016.06.013

Fan, T., Yu, X., Shen, B., and Sun, L. (2017). Peptide self-assembled nanostructures for drug delivery applications. *J. Nanomater.* 2017:4562474. doi: 10.1155/2017/4562474

Fan, Z., Sun, L., Huang, Y., Wang, Y., and Zhang, M. (2016). Bioinspired fluorescent dipeptide nanoparticles for targeted cancer cell imaging and real-time monitoring of drug release. *Nat. Nanotechnol.* 11:388. doi: 10.1038/nnano.2015.312

Fichman, G., and Gazit, E. (2014). Self-assembly of short peptides to form hydrogels: design of building blocks, physical properties and technological applications. *Acta Biomaterialia* 10, 1671–1682. doi: 10.1016/j.actbio.2013.08.013

Fichman, G., Guterman, T., Adler-Abramovich, L., and Gazit, E. (2015). Synergetic functional properties of two-component single amino acid-based hydrogels. *CrystEngComm* 17, 8105–8112. doi: 10.1039/C5CE01051A

Fleming, S., Debnath, S., Frederix, P. W., Hunt, N. T., and Ulijn, R. V. (2014). Insights into the coassembly of hydrogelators and surfactants based on aromatic peptide amphiphiles. *Biomacromolecules* 15, 1171–1184. doi: 10.1021/bm401720z

Fleming, S., Debnath, S., Frederix, P. W., Tuttle, T., and Ulijn, R. V. (2013). Aromatic peptide amphiphiles: significance of the Fmoc moiety. *Chem. Commun.* 49, 10587–10589. doi: 10.1039/c3cc45822a

Fleming, S., and Ulijn, R. V. (2014). Design of nanostructures based on aromatic peptide amphiphiles. *Chem. Soc. Rev.* 43, 8150–8177. doi: 10.1039/C4CS00247D

Fu, I. W., Markegard, C. B., Chu, B. K., and Nguyen, H. D. (2014). Role of hydrophobicity on self-assembly by peptide amphiphiles via molecular dynamics simulations. *Langmuir* 30, 7745–7754. doi: 10.1021/la5012988

Fu, Y., Li, B., Huang, Z., Li, Y., and Yang, Y. (2013). Terminal is important for the helicity of the self-assemblies of dipeptides derived from alanine. *Langmuir* 29, 6013–6017. doi: 10.1021/la400910g

Galdiero, S., and Gomes, P. A. (2017). Peptide-based drugs and drug delivery systems. *Molecules* 22:2185. doi: 10.3390/molecules22122185

Gallo, M., Defaus, S., and Andreu, D. (2019). 1988-2018: Thirty years of drug smuggling at the nano scale. Challenges and opportunities of cell-penetrating peptides in biomedical research. *Arch. Biochem. Biophys.* 661, 74–86. doi: 10.1016/j.abb.2018.11.010

Gao, H.-Y., Wagner, H., Held, P. A., Du, S., Gao, H.-J., Studer, A., et al. (2015). In-plane Van der Waals interactions of molecular self-assembly monolayer. *Appl. Phys. Lett.* 106:081606. doi: 10.1063/1.4907777

Gao, J., Zhan, J., and Yang, Z. (2019). Enzyme-Instructed Self-Assembly (EISA) and hydrogelation of peptides. *Adv. Mater.* 32:1805798. doi: 10.1002/adma.201805798

Garcia, A. M., Iglesias, D., Parisi, E., Styan, K. E., Waddington, L. J., Deganutti, C., et al. (2018). Chirality effects on peptide self-assembly unraveled from molecules to materials. *Chemistry* 4, 1862–1876. doi: 10.1016/j.chempr.2018.05.016

Gavel, P. K., Dev, D., Parmar, H. S., Bhasin, S., and Das, A. K. (2018a). Investigations of peptide-based biocompatible injectable shape-memory hydrogels: differential biological effects on bacterial and human blood cells. *ACS Appl. Mater. Interfaces* 10, 10729–10740. doi: 10.1021/acsami.8b00501

Gavel, P. K., Parmar, H. S., Tripathi, V., Kumar, N., Biswas, A., and Das, A. K. (2018b). Investigations of anti-inflammatory activity of a peptide-based hydrogel using rat air pouch model. *ACS Appl. Mater. Interfaces* 11, 2849–2859. doi: 10.1021/acsami.8b19228

Gazit, E. (2016). Peptide nanostructures: aromatic dipeptides light up. *Nat. Nanotechnol.* 11:309. doi: 10.1038/nnano.2015.321

Gazit, E. (2018). Reductionist approach in peptide-based nanotechnology. *Ann. Rev. Biochem.* 87, 533–553. doi: 10.1146/annurev-biochem-062917-012541

Genji, M., Yano, Y., Hoshino, M., and Matsuzaki, K. (2017). Aromaticity of phenylalanine residues is essential for amyloid formation by Alzheimer's amyloid β-peptide. *Chem. Pharm. Bull.* 65, 668–673. doi: 10.1248/cpb.c17-00203

Ghosh, M., Halperin-Sternfeld, M., Grigoriants, I., Lee, J., Nam, K. T., and Adler-Abramovich, L. (2017). Arginine-presenting peptide hydrogels decorated with hydroxyapatite as biomimetic scaffolds for bone regeneration. *Biomacromolecules* 18, 3541–3550. doi: 10.1021/acs.biomac.7b00876

Ginjupalli, K., Shavi, G. V., Averineni, R. K., Bhat, M., Udupa, N., and Upadhya, P. N. (2017). Poly (α-hydroxy acid) based polymers: a review on material and degradation aspects. *Polymer Degradation Stabil.* 144, 520–535. doi: 10.1016/j.polymdegradstab.2017.08.024

Goel, R., Gopal, S., and Gupta, A. (2015). Self-assembly of β-alanine homotetramer: formation of nanovesicles for drug delivery. *J. Mater. Chem. B* 3, 5849–5857. doi: 10.1039/C5TB00652J

González-Díaz, N. E., López-Rendón, and R., Ireta, J. (2019). Insight into the dipeptide self-assembly process using density functional theory. *J. Phys. Chem. C* 123, 2526–2532. doi: 10.1021/acs.jpcc.8b10340

Gopalan, R. D., Del Borgo, M. P., Mechler, A. I., Perlmutter, P., and Aguilar, M.-I. (2015). Geometrically precise building blocks: the self-assembly of β-peptides. *Chem. Biol.* 22, 1417–1423. doi: 10.1016/j.chembiol.2015.10.005

Goyal, N., Mangunuru, H. P., Parikh, B., Shrestha, S., and Wang, G. (2014). Synthesis and characterization of pH responsive D-glucosamine based molecular gelators. *Beilstein J. Organic Chem.* 10, 3111–3121. doi: 10.3762/bjoc.10.328

Guidotti, G., Brambilla, L., and Rossi, D. (2017). Cell-penetrating peptides: from basic research to clinics. *Trends Pharm. Sci.* 38, 406–424. doi: 10.1016/j.tips.2017.01.003

Guo, C., Arnon, Z. A., Qi, R., Zhang, Q., Adler-Abramovich, L., Gazit, E., et al. (2016). Expanding the nanoarchitectural diversity through aromatic di-and tri-peptide coassembly: Nanostructures and molecular mechanisms. *ACS nano* 10, 8316–8324. doi: 10.1021/acsnano.6b02739

Guo, C., Luo, Y., Zhou, R., and Wei, G. (2012). Probing the self-assembly mechanism of diphenylalanine-based peptide nanovesicles and nanotubes. *ACS nano,* 6, 3907–3918. doi: 10.1021/nn300015g

Guo, Z., Peng, H., Kang, J., and Sun, D. (2016). Cell-penetrating peptides: possible transduction mechanisms and therapeutic applications. *Biomed. Rep.* 4, 528–534. doi: 10.3892/br.2016.639

Gupta, M., and Chauhan, V. S. (2011). *De novo* design of α, β-didehydrophenylalanine containing peptides: from models to applications. *Biopolymers* 95, 161–173. doi: 10.1002/bip.21561

Guterman, T., Kornreich, M., Stern, A., Adler-Abramovich, L., Porath, D., Beck, R., et al. (2016). Formation of bacterial pilus-like nanofibres by designed minimalistic self-assembling peptides. *Nat. Commun.* 7, 1–10. doi: 10.1038/ncomms13482

Habibi, N., Kamaly, N., Memic, A., and Shafiee, H. (2016). Self-assembled peptide-based nanostructures: smart nanomaterials toward targeted drug delivery. *Nano Today* 11, 41–60. doi: 10.1016/j.nantod.2016.02.004

Halperin-Sternfeld, M., Ghosh, M., Sevostianov, R., Grigoriants, I., and Adler-Abramovich, L. (2017). Molecular co-assembly as a strategy for synergistic improvement of the mechanical properties of hydrogels. *Chem. Commun.* 53, 9586–9589. doi: 10.1039/C7CC04187J

Hamley, I. W. (2017). Small bioactive peptides for biomaterials design and therapeutics. *Chem. Rev.* 117, 14015–14041. doi: 10.1021/acs.chemrev.7b00522

Handelman, A., Apter, B., Turko, N., and Rosenman, G. (2016a). Linear and nonlinear optical waveguiding in bio-inspired peptide nanotubes. *Acta Biomaterialia* 30, 72–77. doi: 10.1016/j.actbio.2015.11.004

Handelman, A., Kuritz, N., Natan, A., and Rosenman, G. (2016b). Reconstructive phase transition in ultrashort peptide nanostructures and induced visible photoluminescence. *Langmuir* 32, 2847–2862. doi: 10.1021/acs.langmuir.5b02784

He, M., Li, J., Tan, S., Wang, R., and Zhang, Y. (2013). Photodegradable supramolecular hydrogels with fluorescence turn-on reporter for photomodulation of cellular microenvironments. *J. Am. Chem. Soc.* 135, 18718–18721. doi: 10.1021/ja409000b

He, R., Finan, B., Mayer, J. P., and DiMarchi, R. D. (2019). Peptide conjugates with small molecules designed to enhance efficacy and safety. *Molecules* 24:1855. doi: 10.3390/molecules24101855

Hoffmann, K., Milech, N., Juraja, S. M., Cunningham, P. T., Stone, S. R., Francis, R. W., et al. (2018). A platform for discovery of functional cell-penetrating peptides for efficient multi-cargo intracellular delivery. *Sci. Rep.* 8:12538. doi: 10.1038/s41598-018-30790-2

Hsieh, W.-H., and Liaw, J. (2019). Applications of cyclic peptide nanotubes (cPNTs). *J. Food Drug Analysis* 27, 32–47. doi: 10.1016/j.jfda.2018.09.004

Huang, R., Wang, Y., Qi, W., Su, R., and He, Z. (2014). Temperature-induced reversible self-assembly of diphenylalanine peptide and the structural transition from organogel to crystalline nanowires. *Nanoscale Res. Lett.* 9, 1–9. doi: 10.1186/1556-276X-9-653

Huang, Y.-W., Lee, H.-J., Tolliver, L. M., and Aronstam, R. S. (2015). Delivery of nucleic acids and nanomaterials by cell-penetrating peptides: opportunities and challenges. *BioMed Res. Int.* 2015:834079. doi: 10.1155/2015/834079

Huang, Z., Guan, S., Wang, Y., Shi, G., Cao, L., Gao, Y., et al. (2013). Self-assembly of amphiphilic peptides into bio-functionalized nanotubes: a novel hydrolase model. *J. Mater. Chem. B* 1, 2297–2304. doi: 10.1039/c3tb20156b

Iglesias, D., and Marchesan, S. (2017). "Short peptide self-assembled nanostructures for therapeutics innovative delivery," in *Nanostructures for Novel Therapy*, eds D. Ficai and A. M. Grumezescu (Amsterdam: Elsevier), 227–250. doi: 10.1016/B978-0-323-46142-9.00009-8

Inaba, H., and Matsuura, K. (2019). Peptide nanomaterials designed from natural supramolecular systems. *Chem. Record* 19, 843–858. doi: 10.1002/tcr.201800149

Insua, I., and Montenegro, J. (2019). 1D to 2D self assembly of cyclic peptides. *J. Am. Chem. Soc.* 142, 300–307. doi: 10.1021/jacs.9b10582

Ischakov, R., Adler-Abramovich, L., Buzhansky, L., Shekhter, T., and Gazit, E. (2013). Peptide-based hydrogel nanoparticles as effective drug delivery agents. *Bioorgan. Med. Chem.* 21, 3517–3522. doi: 10.1016/j.bmc.2013.03.012

Jeon, J., Mills, C. E., and Shell, M. S. (2013). Molecular insights into diphenylalanine nanotube assembly: all-atom simulations of oligomerization. *J. Phys. Chem. B* 117, 3935–3943. doi: 10.1021/jp308280d

Jeong, W.-J., Bu, J., Kubiatowicz, L. J., Chen, S. S., Kim, Y., and Hong, S. (2018). Peptide–nanoparticle conjugates: a next generation of diagnostic and therapeutic platforms? *Nano Converg.* 5:38. doi: 10.1186/s40580-018-0170-1

Ji, W., Yuan, C., Zilberzwige-Tal, S., Xing, R., Chakraborty, P., Tao, K., et al. (2019). Metal-ion modulated structural transformation of amyloid-like dipeptide supramolecular self-assembly. *ACS Nano* 13, 7300–7309. doi: 10.1021/acsnano.9b03444

Jia, F., Liu, X., Li, L., Mallapragada, S., Narasimhan, B., and Wang, Q. (2013). Multifunctional nanoparticles for targeted delivery of immune activating and cancer therapeutic agents. *J. Controll. Rel.* 172, 1020–1034. doi: 10.1016/j.jconrel.2013.10.012

Jiang, Z., Guan, J., Qian, J., and Zhan, C. (2019). Peptide ligand-mediated targeted drug delivery of nanomedicines. *Biomater. Sci.* 7, 461–471. doi: 10.1039/C8BM01340C

Kamei, N., Khafagy, E.-S., Hirose, J., and Takeda-Morishita, M. (2017). Potential of single cationic amino acid molecule "Arginine" for stimulating oral absorption of insulin. *Int. J. Pharmaceutics* 521, 176–183. doi: 10.1016/j.ijpharm.2017.01.066

Kamei, N., Tamiwa, H., Miyata, M., Haruna, Y., Matsumura, K., Ogino, H., et al. (2018). Hydrophobic amino acid tryptophan shows promise as a potential absorption enhancer for oral delivery of biopharmaceuticals. *Pharmaceutics* 10:182. doi: 10.3390/pharmaceutics10040182

Kang, Z., Meng, Q., and Liu, K. (2019). Peptide-based gene delivery vectors. *J. Mater. Chem. B* 7, 1824–1841. doi: 10.1039/C8TB03124J

Khatri, A., Mishra, A., and Chauhan, V. S. (2017). Characterization of DNA condensation by conformationally restricted dipeptides and gene delivery. *J. Biomed. Nanotechnol.* 13, 35–53. doi: 10.1166/jbn.2017.2325

Khatri, A., Siddiqui, H., Panda, J., and Chauhan, V. (2019). Delivery of cancer-testis antigens using self-assembled dipeptide nanotubes inhibits tumor growth in mice melanoma model. *J. Nanomed. Nanotechnol.* 10:2. doi: 10.35248/2157-7439.19.10.533

Kieffer, M., Garcia, A. M., Haynes, C. J., Kralj, S., Iglesias, D., Nitschke, J. R., et al. (2019). Embedding and positioning of Two FeII4L4 cages in supramolecular tripeptide gels for selective chemical segregation. *Angew. Chem.* 58, 7982–7986. doi: 10.1002/anie.201900429

Kim, S. H., Kaplan, J. A., Sun, Y., Shieh, A., Sun, H. L., Croce, C. M., et al. (2015). The self-assembly of anticancer camptothecin–dipeptide nanotubes: a minimalistic and high drug loading approach to increased efficacy. *Chem. A Eur. J.* 21, 101–105. doi: 10.1002/chem.201404520

Kirkham, S., Hamley, I. W., Smith, A. M., Gouveia, R. M., Connon, C. J., Reza, M., et al. (2016). A self-assembling fluorescent dipeptide conjugate for cell labelling. *Colloids Surfaces B Biointerfaces* 137, 104–108. doi: 10.1016/j.colsurfb.2015.04.062

Kol, N., Adler-Abramovich, L., Barlam, D., Shneck, R. Z., Gazit, E., and Rousso, I. (2005). Self-assembled peptide nanotubes are uniquely rigid bioinspired supramolecular structures. *Nano Lett.* 5, 1343–1346. doi: 10.1021/nl0505896

Komáromy, D., v., Stuart, M. C., Monreal Santiago, G., Tezcan, M., Krasnikov, V. V., et al. (2017). Self-assembly can direct dynamic covalent bond formation toward diversity or specificity. *J. Am. Chem. Soc.* 139, 6234–6241. doi: 10.1021/jacs.7b01814

Kou, L., Bhutia, Y. D., Yao, Q., He, Z., Sun, J., and Ganapathy, V. (2018). Transporter-guided delivery of nanoparticles to improve drug permeation across cellular barriers and drug exposure to selective cell types. *Front. Pharmacol.* 9:27. doi: 10.3389/fphar.2018.00027

Koutsopoulos, S. (2016). Self-assembling peptide nanofiber hydrogels in tissue engineering and regenerative medicine: progress, design guidelines, and applications. *J. Biomed. Mater. Res. Part A* 104, 1002–1016. doi: 10.1002/jbm.a.35638

Kuang, Y., and Xu, B. (2013). Disruption of the dynamics of microtubules and selective inhibition of glioblastoma cells by nanofibers of small hydrophobic molecules. *Angew. Chem. Int. Edn.* 52, 6944–6948. doi: 10.1002/anie.201302658

Kulkarni, K., Habila, N., Del Borgo, M. P., and Aguilar, M.-I. (2019). Novel materials from the supramolecular self-assembly of short helical β3-peptide foldamers. *Front. Chem.* 7:70. doi: 10.3389/fchem.2019.00070

Kumar, V. A., Taylor, N. L., Shi, S., Wickremasinghe, N. C., D'Souza, R. N., and Hartgerink, J. D. (2015). Self-assembling multidomain peptides tailor biological responses through biphasic release. *Biomaterials* 52, 71–78. doi: 10.1016/j.biomaterials.2015.01.079

Kurbasic, M., Romano, C., Garcia, A., Kralj, S., and Marchesan, S. (2017). Assembly of a Tripeptide and anti-inflammatory drugs into supramolecular hydrogels for sustained release. *Gels* 3:29. doi: 10.3390/gels3030029

Kurrikoff, K., Gestin, M., and Langel, Ü. (2016). Recent *in vivo* advances in cell-penetrating peptide-assisted drug delivery. *Exp. Opin. Drug Deliv.* 13, 373–387. doi: 10.1517/17425247.2016.1125879

Lakshmanan, A., Cheong, D. W., Accardo, A., Di Fabrizio, E., Riekel, C., and Hauser, C. A. (2013). Aliphatic peptides show similar self-assembly to amyloid core sequences, challenging the importance of aromatic interactions in amyloidosis. *Proc. Natl. Acad. Sci. U.S.A.* 110, 519–524. doi: 10.1073/pnas.1217742110

Lee, J. H. (2018). Injectable hydrogels delivering therapeutic agents for disease treatment and tissue engineering. *Biomaterials research* 22, 27. doi: 10.1186/s40824-018-0138-6

Lee, S., Trinh, T. H., Yoo, M., Shin, J., Lee, H., Kim, J., et al. (2019). Self-assembling peptides and their application in the treatment of diseases. *Int. J. Mol. Sci.* 20:5850. doi: 10.3390/ijms20235850

Lee, Y.-H., Chang, S.-F., and Liaw, J. (2015). Anti-apoptotic gene delivery with cyclo-(d-Trp-Tyr) peptide nanotube via eye drop following corneal epithelial debridement. *Pharmaceutics* 7, 122–136. doi: 10.3390/pharmaceutics7030122

Lehto, T., Ezzat, K., Wood, M. J. A., and El Andaloussi, S. (2016). Peptides for nucleic acid delivery. *Adv. Drug Deliv. Rev.* 106, 172–182. doi: 10.1016/j.addr.2016.06.008

Leite, D., Barbu, E., Pilkington, G., and Lalatsa, A. (2015). Peptide self-assemblies for drug delivery. *Curr. Top. Med. Chem.* 15:120456. doi: 10.2174/1568026615666150605120456

León, I., Alonso, E. R., Cabezas, C., Mata, S., and Alonso, J. L. (2019). Unveiling the n→ π* interactions in dipeptides. *Commun. Chem.* 2:3. doi: 10.1038/s42004-018-0103-2

Levin, A., Mason, T. O., Adler-Abramovich, L., Buell, A. K., Meisl, G., Galvagnion, C., et al. (2014). Ostwald's rule of stages governs structural transitions and morphology of dipeptide supramolecular polymers. *Nat. Commun.* 5:5219. doi: 10.1038/ncomms6219

Levin, A., Michaels, T. C., Mason, T. O., Müller, T., Adler-Abramovich, L., Mahadevan, L., et al. (2018). Self-assembly-mediated release of peptide nanoparticles through jets across microdroplet interfaces. *ACS Appl. Mater. Interfaces* 10, 27578–27583. doi: 10.1021/acsami.8b09511

Levine, R. M., Scott, C. M., and Kokkoli, E. (2013). Peptide functionalized nanoparticles for nonviral gene delivery. *Soft Matter.* 9, 985–1004. doi: 10.1039/C2SM26633D

Li, I.-C., and Hartgerink, J. D. (2017). Covalent capture of aligned self-assembling nanofibers. *J. Am. Chem. Soc.* 139, 8044–8050. doi: 10.1021/jacs.7b04655

Li, I. C., Moore, A. N., and Hartgerink, J. D. (2016). "Missing tooth" multidomain peptide nanofibers for delivery of small molecule drugs. *Biomacromolecules* 17, 2087–2095. doi: 10.1021/acs.biomac.6b00309

Li, J., Du, X., Hashim, S., Shy, A., and Xu, B. (2017). Aromatic–aromatic interactions enable α-Helix to β-sheet transition of peptides to form supramolecular hydrogels. *J. Am. Chem. Soc.* 139, 71–74. doi: 10.1021/jacs.6b11512

Li, J., Kuang, Y., Gao, Y., Du, X., Shi, J., and Xu, B. (2012). D-amino acids boost the selectivity and confer supramolecular hydrogels of a nonsteroidal anti-inflammatory drug (NSAID). *J. Am. Chem. Soc.* 135, 542–545. doi: 10.1021/ja310019x

Li, J., Kuang, Y., Shi, J., Gao, Y., Zhou, J., and Xu, B. (2013). The conjugation of nonsteroidal anti-inflammatory drugs (NSAID) to small peptides for generating multifunctional supramolecular nanofibers/hydrogels. *Beilstein J. Organ Chem.* 9, 908–917. doi: 10.3762/bjoc.9.104

Li, J., Wang, A., Ren, P., Yan, X., and Bai, S. (2019a). One-step co-assembly method to fabricate photosensitive peptide nanoparticles for two-photon photodynamic therapy. *Chem. Commun.* 55, 3191–3194. doi: 10.1039/C9CC00025A

Li, J., Wang, A., Zhao, L., Dong, Q., Wang, M., Xu, H., et al. (2018). Self-assembly of monomeric hydrophobic photosensitizers with short peptides forming photodynamic nanoparticles with real-time tracking property and without the need of release *in vivo*. *ACS Appl. Mater. Interfaces* 10, 28420–28427. doi: 10.1021/acsami.8b09933

Li, J., Xing, R., Bai, S., and Yan, X. (2019b). Recent advances of self-assembling peptide-based hydrogels for biomedical applications. *Soft Matter.* 15, 1704–1715. doi: 10.1039/C8SM02573H

Li, L. L., Qiao, Z. Y., Wang, L., and Wang, H. (2018). Programmable construction of peptide-based materials in living subjects: from modular design and morphological control to theranostics. *Adv. Mater.*20:1804971. doi: 10.1002/adma.201804971

Li, Q., Chen, M., Chen, D., and Wu, L. (2016). One-pot synthesis of diphenylalanine-based hybrid nanospheres for controllable pH- and GSH-responsive delivery of drugs. *Chem. Mater.* 28, 6584–6590. doi: 10.1021/acs.chemmater.6b02604

Li, Q., Jia, Y., Dai, L., Yang, Y., and Li, J. (2015). Controlled rod nanostructured assembly of diphenylalanine and their optical waveguide properties. *ACS Nano* 9, 2689–2695. doi: 10.1021/acsnano.5b00623

Li, S., Zou, Q., Li, Y., Yuan, C., Xing, R., and Yan, X. (2018). Smart peptide-based supramolecular photodynamic metallo-nanodrugs designed by multicomponent coordination self-assembly. *J. Am. Chem. Soc.* 140, 10794–10802. doi: 10.1021/jacs.8b04912

Li, Y., Wang, F., and Cui, H. (2016). Peptide-based supramolecular hydrogels for delivery of biologics. *Bioeng. Transl. Med.* 1, 306–322. doi: 10.1002/btm2.10041

Li, Z., Cao, J., Li, H., Liu, H., Han, F., Liu, Z., et al. (2016). Self-assembled drug delivery system based on low-molecular-weight bis-amide organogelator: synthesis, properties and in vivo evaluation. *Drug Deliv.* 23, 3168–3178. doi: 10.3109/10717544.2016.1157841

Lian, M., Chen, X., Lu, Y., and Yang, W. (2016). Self-assembled peptide hydrogel as a smart biointerface for enzyme-based electrochemical biosensing and cell monitoring. *ACS Appl. Mater. Interfaces* 8, 25036–25042. doi: 10.1021/acsami.6b05409

Lian, M., Xu, L., Zhu, X., Chen, X., Yang, W., and Wang, T. (2017). Seamless signal transduction from three-dimensional cultured cells to a superoxide anions biosensor via *in situ* self-assembly of dipeptide hydrogel. *Anal. Chem.* 89, 12843–12849. doi: 10.1021/acs.analchem.7b03371

Liao, H.-S., Lin, J., Liu, Y., Huang, P., Jin, A., and Chen, X. (2016). Self-assembly mechanisms of nanofibers from peptide amphiphiles in solution and on substrate surfaces. *Nanoscale* 8, 14814–14820. doi: 10.1039/C6NR04672J

Liu, K., Xing, R., Zou, Q., Ma, G., Möhwald, H., and Yan, X. (2016). Simple peptide-tuned self-assembly of photosensitizers towards anticancer photodynamic therapy. *Angew. Chem. Int. Edn.* 55, 3036–3039. doi: 10.1002/anie.201509810

Liu, Y., Zhang, L., and Wei, W. (2017). Effect of noncovalent interaction on the self-assembly of a designed peptide and its potential use as a carrier for controlled bFGF release. *Int. J. Nanomed.* 12:659. doi: 10.2147/IJN.S124523

Liyanage, W., Vats, K., Rajbhandary, A., Benoit, D. S., and Nilsson, B. L. (2015). Multicomponent dipeptide hydrogels as extracellular matrix-mimetic scaffolds for cell culture applications. *Chem. Commun.* 51, 11260–11263. doi: 10.1039/C5CC03162A

Lock, L. L., LaComb, M., Schwarz, K., Cheetham, A. G., Lin, Y.-A., Zhang, P., et al. (2013). Self-assembly of natural and synthetic drug amphiphiles into discrete supramolecular nanostructures. *Faraday Discuss.* 166, 285–301. doi: 10.1039/c3fd00099k

Loic, S. (2017). *Amino Acids Modification to Improve and Fine-Tune Peptide-Based Hydrogels in Amino Acid-New Insights and Roles in Plant and Animal*. London, UK: IntechOpen. doi: 10.5772/intechopen.68705

Lombardi, L., Falanga, A., Del Genio, V., and Galdiero, S. (2019). A new hope: self-assembling peptides with antimicrobial activity. *Pharmaceutics* 11:166. doi: 10.3390/pharmaceutics11040166

Lombardo, D., Calandra, P., Pasqua, L., and Magazù, S. (2020). Self-assembly of organic nanomaterials and biomaterials: the bottom-up approach for functional nanostructures formation and advanced applications. *Materials* 13:1048. doi: 10.3390/ma13051048

Loo, Y., Goktas, M., Tekinay, A. B., Guler, M. O., Hauser, C. A., and Mitraki, A. (2015). Self-assembled proteins and peptides as scaffolds for tissue regeneration. *Adv. Healthcare Mater.* 4, 2557–2586. doi: 10.1002/adhm.201500402

Lopez-Silva, T. L., Leach, D. G., Li, I.-C., Wang, X., and Hartgerink, J. D. (2018). Self-assembling multidomain peptides: design and characterization of neutral peptide-based materials with ph and ionic strength independent self-assembly. *ACS Biomater. Sci. Eng.* 5, 977–985. doi: 10.1021/acsbiomaterials.8b01348

Luisi, P. L. (2015). Chemistry constraints on the origin of life. *Israel J. Chem.* 55, 906–918. doi: 10.1002/ijch.201400177

Ma, L., Wang, C., He, Z., Cheng, B., Zheng, L., and Huang, K. (2017). Peptide-drug conjugate: a novel drug design approach. *Curr. Med. Chem.* 24, 3373–3396. doi: 10.2174/0929867324666170404142840

Majid, A., Patil-Sen, Y., Ahmed, W., and Sen, T. (2017). Tunable self-assembled peptide structure: a novel approach to design dual-use biological agents. *Mater. Today Proc.* 4, 32–40. doi: 10.1016/j.matpr.2017.01.190

Makam, P., and Gazit, E. (2018). Minimalistic peptide supramolecular co-assembly: expanding the conformational space for nanotechnology. *Chem. Soc. Rev.* 47, 3406–3420. doi: 10.1039/C7CS00827A

Manchineella, S., Murugan, N. A., and Govindaraju, T. (2017). Cyclic dipeptide-based ambidextrous supergelators: minimalistic rational design, structure-gelation studies, and *in situ* hydrogelation. *Biomacromolecules* 18, 3581–3590. doi: 10.1021/acs.biomac.7b00924

Mandal, D., Shirazi, A. N., and Parang, K. (2014). Self-assembly of peptides to nanostructures. *Organ. Biomol. Chem.* 12, 3544–3561. doi: 10.1039/C4OB00447G

Mándity, I. M., Monsignori, A., Fülöp, L., Forr,ó, E., and Fülöp, F. (2014). Exploiting aromatic interactions for β-peptide foldamer helix stabilization: a significant design element. *Chem. Eur. J.* 20, 4591–4597. doi: 10.1002/chem.201304448

Marchesan, S., Styan, K., Easton, C., Waddington, L., and Vargiu, A. V. (2015a). Higher and lower supramolecular orders for the design of self-assembled heterochiral tripeptide hydrogel biomaterials. *J. Mater. Chem. B* 3, 8123–8132. doi: 10.1039/C5TB00858A

Marchesan, S., Vargiu, A. V., and Styan, K. E. (2015b). The Phe-Phe Motif for Peptide Self-assembly in nanomedicine. *Molecules* 20, 19775–19788. doi: 10.3390/molecules201119658

Mart, R. J., Osborne, R. D., Stevens, M. M., and Ulijn, R. V. (2006). Peptide-based stimuli-responsive biomaterials. *Soft Matter.* 2, 822–835. doi: 10.1039/b607706d

Martin, A. D., Wojciechowski, J. P., Warren, H., and Thordarson, P. (2016). Effect of heterocyclic capping groups on the self-assembly of a dipeptide hydrogel. *Soft Matter.* 12, 2700–2707. doi: 10.1039/C6SM00025H

Mason, T. O., and Buell, A. K. (2019). "The kinetics, thermodynamics and mechanisms of short aromatic peptide self-assembly," in *Biological and Bio-Inspired Nanomaterials*, eds S. Perrett, A. K. Buell, and T. Knowles (Singapore: Springer), 61–112. doi: 10.1007/978-981-13-9791-2_3

Mason, T. O., Michaels, T. C., Levin, A., Dobson, C. M., Gazit, E., Knowles, T. P., et al. (2017). Thermodynamics of polypeptide supramolecular assembly in the short-chain limit. *J. Am. Chem. Soc.* 139, 16134–16142. doi: 10.1021/jacs.7b00229

Mateescu, M., Ispas-Szabo, P., and Assaad, E. (2015). "The concept of self-assembling and the interactions involved," in *Controlled Drug Delivery,* eds M. A. Mateescu, P. Ispas-Szabo, and E. Assaad (Cambridge, UK: Elsevier), 1–20.

Matson, J. B., and Stupp, S. I. (2012). Self-assembling peptide scaffolds for regenerative medicine. *Chem. Commun.* 48, 26–33. doi: 10.1039/C1CC15551B

Maude, S., Ingham, E., and Aggeli, A. (2013). Biomimetic self-assembling peptides as scaffolds for soft tissue engineering. *Nanomedicine* 8, 823–847. doi: 10.2217/nnm.13.65

Mauri, E., Chincarini, G. M., Rigamonti, R., Magagnin, L., Sacchetti, A., and Rossi, F. (2017). Modulation of electrostatic interactions to improve controlled drug delivery from nanogels. *Mater. Sci. Eng. C* 72, 308–315. doi: 10.1016/j.msec.2016.11.081

Maury, C. P. J. (2018). Amyloid and the origin of life: self-replicating catalytic amyloids as prebiotic informational and protometabolic entities. *Cell. Mol. Life Sci.* 75, 1499–1507. doi: 10.1007/s00018-018-2797-9

Mayr, J., Saldías, C., and Díaz, D. D. (2018). Release of small bioactive molecules from physical gels. *Chem. Soc. Rev.* 47, 1484–1515. doi: 10.1039/C7CS00515F

Mears, L. L., Draper, E. R., Castilla, A. M., Su, H., Dietrich, B., Nolan, M. C., et al. (2017). Drying affects the fiber network in low molecular weight hydrogels. *Biomacromolecules* 18, 3531–3540. doi: 10.1021/acs.biomac.7b00823

Melchionna, M., E, and Styan, K., Marchesan, S. (2016). The unexpected advantages of using D-amino acids for peptide self-assembly into nanostructured hydrogels for medicine. *Curr. Top. Med. Chem.* 16, 2009–2018. doi: 10.2174/1568026616999160212120302

Mendes, A. C., Baran, E. T., Reis, R. L., and Azevedo, H. S. (2013). Self-assembly in nature: using the principles of nature to create complex nanobiomaterials. *Wiley Interdisc. Rev.* 5, 582–612. doi: 10.1002/wnan.1238

Mikhalevich, V., Craciun, I., Kyropoulou, M., Palivan, C. G., and Meier, W. (2017). Amphiphilic peptide self-assembly: expansion to hybrid materials. *Biomacromolecules* 18, 3471–3480. doi: 10.1021/acs.biomac.7b00764

Mishra, J., and Jyoti Panda, J. (2019). Short peptide-based smart targeted cancer nanotherapeutics: a glimmer of hope. *Therap. Deliv.* 10:5. doi: 10.4155/tde-2019-0005

Moitra, P., Kumar, K., Kondaiah, P., and Bhattacharya, S. (2014). efficacious anticancer drug delivery mediated by a ph-sensitive self-assembly of a conserved tripeptide derived from tyrosine kinase NGF receptor. *Angew. Chem. Int. Edn.* 53, 1113–1117. doi: 10.1002/anie.201307247

Moitra, P., Subramanian, Y., and Bhattacharya, S. (2017). Concentration dependent self-assembly of TrK-NGF receptor derived tripeptide: new insights from experiment and computer simulations. *J. Phys. Chem. B* 121, 815–824. doi: 10.1021/acs.jpcb.6b10511

Mondal, S., Das, S., and Nandi, A. K. (2020). A review on recent advances in polymer and peptide hydrogels. *Soft Matter.* 16, 1404–1454 doi: 10.1039/C9SM02127B

Moore, A. N., and Hartgerink, J. D. (2017). Self-assembling multidomain peptide nanofibers for delivery of bioactive molecules and tissue regeneration. *Accounts Chem. Res.* 50, 714–722. doi: 10.1021/acs.accounts.6b00553

Morris, K. L., Chen, L., Raeburn, J., Sellick, O. R., Cotanda, P., Paul, A., et al. (2013). Chemically programmed self-sorting of gelator networks. *Nat. Commun.* 4:1480. doi: 10.1038/ncomms2499

Mossou, E., Teixeira, S. C., Mitchell, E. P., Mason, S. A., Adler-Abramovich, L., Gazit, E., et al. (2014). The self-assembling zwitterionic form of L-phenylalanine at neutral pH. *Acta Crystallograph. C* 70, 326–331. doi: 10.1107/S2053229614002563

Motamed, S., Del Borgo, M., Kulkarni, K., Habila, N., Zhou, K., Perlmutter, P., et al. (2016). A self-assembling β-peptide hydrogel for neural tissue engineering. *Soft Matter.* 12, 2243–2246. doi: 10.1039/C5SM02902C

Murali, D. M., and Shanmugam, G. (2019). The aromaticity of the phenyl ring imparts thermal stability to a supramolecular hydrogel obtained from low molecular mass compound. *N. J. Chem.* 43, 12396–12409. doi: 10.1039/C9NJ01781J

Nagarkar, R. P., Hule, R. A., Pochan, D. J., and Schneider, J. P. (2008). *De novo* design of strand-swapped β-hairpin hydrogels. *J. Am. Chem. Soc.* 130, 4466–4474. doi: 10.1021/ja710295t

Nagy-Smith, K., Beltramo, P. J., Moore, E., Tycko, R., Furst, E. M., and Schneider, J. P (2017). Molecular, local, and network-level basis for the enhanced stiffness of hydrogel networks formed from coassembled racemic peptides: predictions from Pauling and Corey. *ACS Central Sci.* 3, 586–597. doi: 10.1021/acscentsci.7b00115

Nalluri, S. K. M., Berdugo, C., Javid, N., Frederix, P. W., and Ulijn, R. V. (2014). Biocatalytic self-assembly of supramolecular charge-transfer nanostructures based on n-type semiconductor-appended peptides. *Angew. Chem. Int. Edn.* 53, 5882–5887. doi: 10.1002/anie.201311158

Nanda, J., Biswas, A., and Banerjee, A. (2013). Single amino acid based thixotropic hydrogel formation and pH-dependent morphological change of gel nanofibers. *Soft Matter.* 9, 4198–4208. doi: 10.1039/c3sm27050e

Naskar, J., Roy, S., Joardar, A., Das, S., and Banerjee, A. (2011). Self-assembling dipeptide-based nontoxic vesicles as carriers for drugs and other biologically important molecules. *Organ. Biomol. Chem.* 9, 6610–6615. doi: 10.1039/c1ob05757j

Nelli, S. R., Lin, J.-H., Nguyen, T. N. A., Tseng, D. T.-H., Talloj, S. K., and Lin, H.-C. (2017). Influence of amino acid side chains on the formation of two component self-assembling nanofibrous hydrogels. *New J. Chem.* 41, 1229–1234. doi: 10.1039/C6NJ02820A

Ni, M., and Zhuo, S. (2019). Applications of self-assembling ultrashort peptides in bionanotechnology. *RSC Adv.* 9, 844–852. doi: 10.1039/C8RA07533F

Nikitin, T., Kopyl, S., Shur, V. Y., Kopelevich, Y., and Kholkin, A. (2016). Low-temperature photoluminescence in self-assembled diphenylalanine microtubes. *Phys. Lett. A* 380, 1658–1662. doi: 10.1016/j.physleta.2016.02.043

Orbach, R., Mironi-Harpaz, I., Adler-Abramovich, L., Mossou, E., Mitchell, E. P., Forsyth, V. T., et al. (2012). The rheological and structural properties of Fmoc-peptide-based hydrogels: the effect of aromatic molecular architecture on self-assembly and physical characteristics. *Langmuir* 28, 2015–2022. doi: 10.1021/la204426q

Ozores, H. L., Amorín, M., and Granja, J. R. (2017). Self-assembling molecular capsules based on α, γ-cyclic peptides. *J. Am. Chem. Soc.* 139, 776–784. doi: 10.1021/jacs.6b10456

Panda, J. J., and Chauhan, V. S. (2014). Short peptide based self-assembled nanostructures: implications in drug delivery and tissue engineering. *Polymer Chem.* 5, 4418–4436. doi: 10.1039/C4PY00173G

Panda, J. J., and Mishra, J. (2016). Self-assembled dipeptide-based nanostructures: tiny tots with great applications. *Future Sci.* 15:85. doi: 10.4155/tde.15.85

Panda, J. J., Varshney, A., and Chauhan, V. S. (2013). Self-assembled nanoparticles based on modified cationic dipeptides and DNA: novel systems for gene delivery. *J. Nanobiotechnol.* 11:18. doi: 10.1186/1477-3155-11-18

Panda, S. S., Shmilovich, K., Ferguson, A. L., and Tovar, J. D. (2019). Controlling supramolecular chirality in peptide– π-peptide networks by variation of the Alkyl spacer length. *Langmuir* 35, 14060–14073. doi: 10.1021/acs.langmuir.9b02683

Pandit, G., Roy, K., Agarwal, U., and Chatterjee, S. (2018). Self-assembly mechanism of a peptide-based drug delivery vehicle. *ACS Omega* 3, 3143–3155. doi: 10.1021/acsomega.7b01871

Panigrahi, B., Singh, R. K., Mishra, S., and Mandal, D. (2018). Cyclic peptide-based nanostructures as efficient siRNA carriers. *Artif. Cells Nanomed. Biotechnol.* 46, S763–S773. doi: 10.1080/21691401.2018.1511574

Parisi, E., Garcia, A. M., Marson, D., Posocco, P., and Marchesan, S. (2019). Supramolecular tripeptide hydrogel assembly with 5-fluorouracil. *Gels* 5:5. doi: 10.3390/gels5010005

Parween, S., Misra, A., Ramakumar, S., and Chauhan, V. S. (2014). Self-assembled dipeptide nanotubes constituted by flexible β-phenylalanine and conformationally constrained α, β-dehydrophenylalanine residues as drug delivery system. *J. Mater. Chem. B* 2, 3096–3106. doi: 10.1039/c3tb21856b

Patra, J. K., Das, G., Fraceto, L. F., Campos, E. V. R., del Pilar Rodriguez-Torres, M., Acosta-Torres, L. S., et al. (2018). Nano based drug delivery systems: recent developments and future prospects. *J. Nanobiotechnol.* 16:71. doi: 10.1186/s12951-018-0392-8

Pianowski, Z. L., Karcher, J., and Schneider, K. (2016). Photoresponsive self-healing supramolecular hydrogels for light-induced release of DNA and doxorubicin. *Chem. Commun.* 52, 3143–3146. doi: 10.1039/C5CC09633B

Porter, S. L., Coulter, S. M., Pentlavalli, S., Thompson, T. P., and Laverty, G. (2018). Self-assembling diphenylalanine peptide nanotubes selectively

eradicate bacterial biofilm infection. *Acta Biomaterialia* 77, 96–105. doi: 10.1016/j.actbio.2018.07.033

Pospišil, T., Hamzić, L. F., Ahmed, L. B., Lovrić, M., Gajović, S., and Frkanec, L. (2016). Synthesis, characterization and *in vitro* biocompatibility assessment of a novel tripeptide hydrogelator, as a promising scaffold for tissue engineering applications. *Biomater. Sci.* 4, 1412–1416. doi: 10.1039/C6BM00287K

Pugliese, R., and Gelain, F. (2017). Peptidic biomaterials: from self-assembling to regenerative medicine. *Trends Biotechnol.* 35, 145–158. doi: 10.1016/j.tibtech.2016.09.004

Pujals, S., Tao, K., Terradellas, A., Gazit, E., and Albertazzi, L. (2017). Studying structure and dynamics of self-assembled peptide nanostructures using fluorescence and super resolution microscopy. *Chem. Commun.* 53, 7294–7297. doi: 10.1039/C7CC02176C

Qin, L., Duan, P., Xie, F., Zhang, L., and Liu, M. (2013). A metal ion triggered shrinkable supramolecular hydrogel and controlled release by an amphiphilic peptide dendron. *Chem. Commun.* 49, 10823–10825. doi: 10.1039/c3cc47004k

Qin, L., Xie, F., Duan, P., and Liu, M. (2014). A peptide dendron-based shrinkable metallo-hydrogel for charged species separation and stepwise release of drugs. *Chem. A Eur. J.* 20, 15419–15425. doi: 10.1002/chem.201404035

Qiu, F., Chen, Y., Tang, C., and Zhao, X. (2018). Amphiphilic peptides as novel nanomaterials: design, self-assembly and application. *Int. J. Nanomed.* 13, 5003–5022. doi: 10.2147/IJN.S166403

Raad, M., d., Teunissen, E. A., and Mastrobattista, E. (2014). Peptide vectors for gene delivery: from single peptides to multifunctional peptide nanocarriers. *Nanomedicine* 9, 2217–2232. doi: 10.2217/nnm.14.90

Rad-Malekshahi, M., Lempsink, L., Amidi, M., Hennink, W. E., and Mastrobattista, E. (2015b). Biomedical applications of self-assembling peptides. *Bioconjugate Chem.* 27, 3–18. doi: 10.1021/acs.bioconjchem.5b00487

Rad-Malekshahi, M., Visscher, K. M., Rodrigues, J. P., de Vries, R., Hennink, W. E., Baldus, M., et al. (2015a). The supramolecular organization of a peptide-based nanocarrier at high molecular detail. *J. Am. Chem. Soc.* 137, 7775–7784. doi: 10.1021/jacs.5b02919

Raeburn, J., Cardoso, A. Z., and Adams, D. J. (2013). The importance of the self-assembly process to control mechanical properties of low molecular weight hydrogels. *Chem. Soc. Rev.* 42, 5143–5156. doi: 10.1039/c3cs60030k

Ragnarsson, U., and Grehn, L. (2013). Dual protection of amino functions involving Boc. *RSC Adv.* 3, 18691–18697. doi: 10.1039/c3ra42956c

Rajbhandary, A., Brennessel, W. W., and Nilsson, B. L. (2018). Comparison of the self-assembly behavior of fmoc-phenylalanine and corresponding peptoid derivatives. *Cryst. Growth Des.* 18, 623–632. doi: 10.1021/acs.cgd.7b00709

Ramaker, K., Henkel, M., Krause, T., Röckendorf, N., and Frey, A. (2018). Cell penetrating peptides: a comparative transport analysis for 474 sequence motifs. *Drug Deliv.* 25, 928–937. doi: 10.1080/10717544.2018.1458921

Rambhia, K. J., and Ma, P. X. (2015). Controlled drug release for tissue engineering. *J. Control. Release* 219, 119–128. doi: 10.1016/j.jconrel.2015.08.049

Rasale, D. B., Biswas, S., Konda, M., and Das, A. K. (2015). Exploring thermodynamically downhill nanostructured peptide libraries: from structural to morphological insight. *RSC Adv.* 5, 1529–1537. doi: 10.1039/C4RA09490E

Rasale, D. B., and Das, A. K. (2015). Chemical reactions directed peptide self-assembly. *Int. J. Mol. Sci.* 16, 10797–10820. doi: 10.3390/ijms160510797

Raymond, D., L., Abraham, B., Fujita, T., J., Watrous, M., et al. (2019). Low molecular weight supramolecular hydrogels for sustained and localized *in vivo* drug delivery. *ACS Appl. Bio Mater.* 2:b00125. doi: 10.1021/acsabm.9b00125

Raymond, D. M., and Nilsson, B. L. (2018). Multicomponent peptide assemblies. *Chem. Soc. Rev.* 47, 3659–3720. doi: 10.1039/C8CS00115D

Raza, F., Zafar, H., Zhu, Y., Ren, Y., Ullah, A., Khan, A. U., et al. (2018). A review on recent advances in stabilizing peptides/proteins upon fabrication in hydrogels from biodegradable polymers. *Pharmaceutics* 10:16. doi: 10.3390/pharmaceutics10010016

Reches, M., and Gazit, E. (2003). Casting metal nanowires within discrete self-assembled peptide nanotubes. *Science* 300, 625–627. doi: 10.1126/science.1082387

Reches, M., and Gazit, E. (2005). Self-assembly of peptide nanotubes and amyloid-like structures by charged-termini-capped diphenylalanine peptide analogues. *Israel J. Chem.* 45, 363–371. doi: 10.1560/5MC0-V3DX-KE0B-YF3J

Reches, M., and Gazit, E. (2006). Designed aromatic homo-dipeptides: formation of ordered nanostructures and potential nanotechnological applications. *Phys. Biol.* 3:S10. doi: 10.1088/1478-3975/3/1/S02

Reja, R. M., Patel, R., Kumar, V., Jha, A., and Gopi, H. N. (2019). Divergent supramolecular gelation of backbone modified short hybrid δ-peptides. *Biomacromolecules* 20, 1254–1262. doi: 10.1021/acs.biomac.8b01684

Rho, J. Y., Cox, H., Mansfield, E. D., Ellacott, S. H., Peltier, R., Brendel, J. C., et al. (2019). Dual self-assembly of supramolecular peptide nanotubes to provide stabilisation in water. *Nat. Commun.* 10, 1–9. doi: 10.1038/s41467-019-12586-8

Ribeiro, A. C., Souza, G. A., Pereira, D. H., Cordeiro, D. S., Miranda, R. S., Custóio, R., et al. (2019). Phe–Phe Di-peptide nanostructure self-assembling modulated by luminescent additives. *ACS Omega* 4, 606–619. doi: 10.1021/acsomega.8b02732

Riley, M., and Vermerris, W. (2017). Recent advances in nanomaterials for gene delivery—a review. *Nanomaterials* 7:94. doi: 10.3390/nano7050094

Rivas, M., del Valle, L. J., Alemán, C., and Puiggalí, J. (2019). Peptide self-assembly into hydrogels for biomedical applications related to hydroxyapatite. *Gels* 5:14. doi: 10.3390/gels5010014

Rizvi, S. A., and Saleh, A. M. (2018). Applications of nanoparticle systems in drug delivery technology. *Saudi Pharm. J.* 26, 64–70. doi: 10.1016/j.jsps.2017.10.012

Rodriguez, L. M. D. L., Hemar, Y., Cornish, J., and Brimble, M. A. (2016). Structure–mechanical property correlations of hydrogel forming β-sheet peptides. *Chem. Soc. Rev.* 45, 4797–4824. doi: 10.1039/C5CS00941C

Roth-Konforti, M. E., Comune, M., Halperin-Sternfeld, M., Grigoriants, I., Shabat, D., and Adler-Abramovich, L. (2018). UV light–responsive peptide-based supramolecular hydrogel for controlled drug delivery. *Macromol. Rapid Commun.* 39:1800588. doi: 10.1002/marc.201800588

Rubert Pérez, C. M., Stephanopoulos, N., Sur, S., Lee, S. S., Newcomb, C., and Stupp, S. I. (2015). The powerful functions of peptide-based bioactive matrices for regenerative medicine. *Ann. Biomed. Eng.* 43, 501–514. doi: 10.1007/s10439-014-1166-6

Ryan, D. M., and Nilsson, B. L. (2012). Self-assembled amino acids and dipeptides as noncovalent hydrogels for tissue engineering. *Polymer Chem.* 3, 18–33. doi: 10.1039/C1PY00335F

Ryan, K., Beirne, J., Redmond, G., Kilpatrick, J. I., Guyonnet, J., Buchete, N.-V., et al. (2015). Nanoscale piezoelectric properties of self-assembled fmoc–FF peptide fibrous networks. *ACS Appl. Mater. Interfaces* 7, 12702–12707. doi: 10.1021/acsami.5b01251

Sagiri, S. S., Behera, B., Rafanan, R. R., Bhattacharya, C., Pal, K., Banerjee, I., et al. (2014). Organogels as matrices for controlled drug delivery: a review on the current state. *Soft Mater.* 12, 47–72. doi: 10.1080/1539445X.2012.756016

Saha, S., Bachl, J., Kundu, T., Díaz, D. D., and Banerjee, R. (2014). Dissolvable metallohydrogels for controlled release: evidence of a kinetic supramolecular gel phase intermediate. *Chem. Commun.* 50, 7032–7035. doi: 10.1039/C4CC02771J

Sahoo, J. K., Nazareth, C., VandenBerg, M. A., and Webber, M. J. (2017). Self-assembly of amphiphilic tripeptides with sequence-dependent nanostructure. *Biomater. Sci.* 5, 1526–1530. doi: 10.1039/C7BM00304H

Sahoo, J. K., Nazareth, C., VandenBerg, M. A., and Webber, M. J. (2018a). Aromatic identity, electronic substitution, and sequence in amphiphilic tripeptide self-assembly. *Soft Matter.* 14, 9168–9174. doi: 10.1039/C8SM01994K

Sahoo, J. K., VandenBerg, M. A., and Webber, M. J. (2018b). Injectable network biomaterials via molecular or colloidal self-assembly. *Adv. Drug Deliv. Rev.* 127, 185–207. doi: 10.1016/j.addr.2017.11.005

Sarkar, B., Nguyen, P. K., Gao, W., Dondapati, A., Siddiqui, Z., and Kumar, V. A. (2018). Angiogenic self-assembling peptide scaffolds for functional tissue regeneration. *Biomacromolecules* 19, 3597–3611. doi: 10.1021/acs.biomac.8b01137

Sarkar, B., O'Leary, L. E., and Hartgerink, J. D. (2014). Self-assembly of fiber-forming collagen mimetic peptides controlled by triple-helical nucleation. *J. Am. Chem. Soc.* 136, 14417–14424. doi: 10.1021/ja504377s

Sarkar, R., Debnath, M., Maji, K., and Haldar, D. (2015). Solvent assisted structural diversity: supramolecular sheet and double helix of a short aromatic γ-peptide. *RSC Adv.* 5, 76257–76262. doi: 10.1039/C5RA12831E

Sato, K., Ji, W., Palmer, L. C., Weber, B., Barz, M., and Stupp, S. I. (2017). Programmable assembly of peptide amphiphile via noncovalent-to-covalent bond conversion. *J. Am. Chem. Soc.* 139, 8995–9000. doi: 10.1021/jacs.7b03878

Scelsi, A., Bochicchio, B., and Pepe, A. (2019). Labeling of nanofiber-forming peptides by site-directed bioconjugation: effect of spacer length on self-assembly. *Curr. Organic Synth.* 16, 319–325. doi: 10.2174/1570179416666181127150142

Semin, S., Van Etteger, A., Cattaneo, L., Amdursky, N., Kulyuk, L., Lavrov, S., et al. (2015). Strong thermo-induced single and two-photon green luminescence in self-organized peptide microtubes. *Small* 11, 1156–1160. doi: 10.1002/smll.201401602

Seow, W. Y., and Hauser, C. A. (2014). Short to ultrashort peptide hydrogels for biomedical uses. *Mater. Today* 17, 381–388. doi: 10.1016/j.mattod.2014.04.028

Sharma, A. R., Kundu, S. K., Nam, J.-S., Sharma, G., Doss, P., George, C., et al. (2014). Next generation delivery system for proteins and genes of therapeutic purpose: why and how? *BioMed. Res. Int.* 2014:327950. doi: 10.1155/2014/327950

Sharma, P., Kaur, H., and Roy, S. (2019). Inducing differential self-assembling behavior in ultrashort peptide hydrogelators using simple metal salts. *Biomacromolecules* 20, 2610–2624. doi: 10.1021/acs.biomac.9b00416

Silva, R. F., Ara?jo, D. R., Silva, E. R., Ando, R., and, m,. A., Alves, W. A. (2013). L-diphenylalanine microtubes as a potential drug-delivery system: characterization, release kinetics, and cytotoxicity. *Langmuir* 29, 10205–10212. doi: 10.1021/la4019162

Singh, M., Kundu, S., Sreekanth, V., Motiani, R. K., Sengupta, S., Srivastava, A., et al. (2014). Injectable small molecule hydrogel as a potential nanocarrier for localized and sustained in vivo delivery of doxorubicin. *Nanoscale* 6, 12849–12855. doi: 10.1039/C4NR04064C

Singh, P., Brar, S. K., Bajaj, M., Narang, N., Mithu, V. S., Katare, O. P., et al. (2017). Self-assembly of aromatic α-amino acids into amyloid inspired nano/micro scaled architects. *Mater. Sci. Eng. C* 72, 590–600. doi: 10.1016/j.msec.2016.11.117

Singh, P. K., Chibh, S., Dube, T., Chauhan, V. S., and Panda, J. J. (2018). Arginine-α, β-dehydrophenylalanine dipeptide nanoparticles for pH-responsive drug delivery. *Pharm. Res.* 35:35. doi: 10.1007/s11095-017-2299-8

Singh, V., Rai, R. K., Arora, A., Sinha, N., and Thakur, A. K. (2014). Therapeutic implication of L-phenylalanine aggregation mechanism and its modulation by D-phenylalanine in phenylketonuria. *Sci. Rep.* 4:3875. doi: 10.1038/srep03875

Singh, V., Snigdha, K., Singh, C., Sinha, N., and Thakur, A. K. (2015). Understanding the self-assembly of Fmoc–phenylalanine to hydrogel formation. *Soft Matter.* 11, 5353–5364. doi: 10.1039/C5SM00843C

Sis, M. J., and Webber, M. J. (2019). Drug delivery with designed peptide assemblies. *Trends Pharmacol. Sci.* 40, 747–762. doi: 10.1016/j.tips.2019.08.003

Skilling, K. J., Citossi, F., Bradshaw, T. D., Ashford, M., Kellam, B., and Marlow, M. (2014). Insights into low molecular mass organic gelators: a focus on drug delivery and tissue engineering applications. *Soft Matter.* 10, 237–256. doi: 10.1039/C3SM52244J

Skotland, T., Iversen, T., Torgersen, M., and Sandvig, K. (2015). Cell-penetrating peptides: possibilities and challenges for drug delivery *in vitro* and *in vivo*. *Molecules* 20, 13313–13323. doi: 10.3390/molecules200713313

Slocik, J. M., and Naik, R. R. (2017). Sequenced defined biomolecules for nanomaterial synthesis, functionalization, and assembly. *Curr. Opin. Biotechnol.* 46, 7–13. doi: 10.1016/j.copbio.2016.11.025

Soleymani-Goloujeh, M., Nokhodchi, A., Niazi, M., Najafi-Hajivar, S., Shahbazi-Mojarrad, J., Zarghami, N., et al. (2018). Effects of N-terminal and C-terminal modification on cytotoxicity and cellular uptake of amphiphilic cell penetrating peptides. *Artif. Cells Nanomed. Biotechnol.* 46, 91–103. doi: 10.1080/21691401.2017.1414823

Son, J., Kalafatovic, D., Kumar, M., Yoo, B., Cornejo, M. A., Contel, M., et al. (2019). Customizing morphology, size, and response kinetics of matrix metalloproteinase-responsive nanostructures by systematic peptide design. *ACS Nano* 13, 1555–1562. doi: 10.1021/acsnano.8b07401

Song, R., Wu, X., Xue, B., Yang, Y., Huang, W., Zeng, G., et al. (2018). Principles governing catalytic activity of self-assembled short peptides. *J. Am. Chem. Soc.* 141, 223–231. doi: 10.1021/jacs.8b08893

Song, Z., Chen, X., You, X., Huang, K., Dhinakar, A., Gu, Z., et al. (2017). Self-assembly of peptide amphiphiles for drug delivery: the role of peptide primary and secondary structures. *Biomater. Sci.* 5, 2369–2380. doi: 10.1039/C7BM00730B

Spicer, C. D., Jumeaux, C., Gupta, B., and Stevens, M. M. (2018). Peptide and protein nanoparticle conjugates: versatile platforms for biomedical applications. *Chem. Soc. Rev.* 47, 3574–3620. doi: 10.1039/C7CS00877E

Su, H., Koo, J. M., and Cui, H. (2015). One-component nanomedicine. *J. Controll. Release* 219, 383–395. doi: 10.1016/j.jconrel.2015.09.056

Sun, L., Zheng, C., and Webster, T. J. (2016). Self-assembled peptide nanomaterials for biomedical applications: promises and pitfalls. *Int. J. Nanomed.* 12, 73–86. doi: 10.2147/IJN.S117501

Sun, M., Zhang, X., Gao, Z., Liu, T., Luo, C., Zhao, Y., et al. (2019). Probing a dipeptide-based supramolecular assembly as an efficient camptothecin delivering carrier for cancer therapy: computational simulations and experimental validations. *Nanoscale* 11, 3864–3876. doi: 10.1039/C8NR07014H

Sun, Y., Kaplan, J. A., Shieh, A., Sun, H.-L., Croce, C. M., Grinstaff, M. W., et al. (2016). Self-assembly of a 5-fluorouracil-dipeptide hydrogel. *Chem. Commun.* 52, 5254–5257. doi: 10.1039/C6CC01195K

Tamamis, P., Adler-Abramovich, L., Reches, M., Marshall, K., Sikorski, P., Serpell, L., et al. (2009). Self-assembly of phenylalanine oligopeptides: insights from experiments and simulations. *Biophys. J.* 96, 5020–5029. doi: 10.1016/j.bpj.2009.03.026

Tang, Y., Yao, Y., and Wei, G. (2020). Expanding the structural diversity of peptide assemblies by coassembling dipeptides with diphenylalanine. *Nanoscale* 12, 3038–3049. doi: 10.1039/C9NR09317F

Tao, K., Levin, A., Adler-Abramovich, L., and Gazit, E. (2016). Fmoc-modified amino acids and short peptides: simple bio-inspired building blocks for the fabrication of functional materials. *Chem. Soc. Rev.* 45, 3935–3953. doi: 10.1039/C5CS00889A

Tao, K., Makam, P., Aizen, R., and Gazit, E. (2017). Self-assembling peptide semiconductors. *Science* 358:eaam9756. doi: 10.1126/science.aam9756

Tao, K., Yoskovitz, E., Adler-Abramovich, L., and Gazit, E. (2015). Optical property modulation of Fmoc group by pH-dependent self-assembly. *RSC Adv.* 5, 73914–73918. doi: 10.1039/C5RA16412E

Tesauro, D., Accardo, A., Diaferia, C., Milano, V., Guillon, J., Ronga, L., et al. (2019). Peptide-based drug-delivery systems in biotechnological applications: recent advances and perspectives. *Molecules* 24:351. doi: 10.3390/molecules24020351

Thota, C. K., Yadav, N., and Chauhan, V. S. (2016). A novel highly stable and injectable hydrogel based on a conformationally restricted ultrashort peptide. *Sci. Rep.* 6:31167. doi: 10.1038/srep31167

Tomasini, C., and Castellucci, N. (2013). Peptides and peptidomimetics that behave as low molecular weight gelators. *Chem. Soc. Rev.* 42, 156–172. doi: 10.1039/C2CS35284B

Travaglini, L., Giordano, C., D'Annibale, A., Gubitosi, M., di Gregorio, M. C., Schillén, K., et al. (2017). Twisted nanoribbons from a RGD-bearing cholic acid derivative. *Colloids Surfaces B* 159, 183–190. doi: 10.1016/j.colsurfb.2017.07.084

Truong, W. T., Su, Y., Gloria, D., Braet, F., and Thordarson, P. (2015). Dissolution and degradation of Fmoc-diphenylalanine self-assembled gels results in necrosis at high concentrations *in vitro*. *Biomater. Sci.* 3, 298–307. doi: 10.1039/C4BM00244J

Vánová, J., Hejtmánková, A., Kalbáčová, M. H., and Španielová, H. (2019). The utilization of cell-penetrating peptides in the intracellular delivery of viral nanoparticles. *Materials* 12:2671. doi: 10.3390/ma12172671

Varshney, A., Panda, J. J., Singh, A. K., Yadav, N., Bihari, C., Biswas, S., et al. (2018). Targeted delivery of microRNA-199a-3p using self-assembled dipeptide nanoparticles efficiently reduces hepatocellular carcinoma in mice. *Hepatology* 67, 1392–1407. doi: 10.1002/hep.29643

Vasilev, S., Zelenovskiy, P., Vasileva, D., Nuraeva, A., Shur, V. Y., and Kholkin, A. L. (2016). Piezoelectric properties of diphenylalanine microtubes prepared from the solution. *J. Phys. Chem. Solids* 93, 68–72. doi: 10.1016/j.jpcs.2016.02.002

Veloso, S. R., Martins, J., Hilliou, L., Amorim, C., Amaral, V., Almeida, B., et al. (2020). Dehydropeptide-based plasmonic magnetogels: a supramolecular composite nanosystem for multimodal cancer therapy. *J. Mater. Chem. B* 8, 45–64. doi: 10.1039/C9TB01900F

Vilaça, H., Castro, T., Costa, F. M., Melle-Franco, M., Hilliou, L., Hamley, I. W., et al. (2017). Self-assembled RGD dehydropeptide hydrogels for drug delivery applications. *J. Mater. Chem. B* 5, 8607–8617. doi: 10.1039/C7TB01883E

Vilaça, H., Hortelão, A. C., Castanheira, E. M., Queiroz, M.-J., o,. R., Hilliou, L., et al. (2015a). Dehydrodipeptide hydrogelators containing naproxen N-capped tryptophan: self-assembly, hydrogel characterization, and evaluation as potential drug nanocarriers. *Biomacromolecules* 16, 3562–3573. doi: 10.1021/acs.biomac.5b01006

Vilaça, H., Pereira, G., Castro, T., Hermenegildo, B., Shi, J., Faria, T., et al. (2015b). New self-assembled supramolecular hydrogels based on dehydropeptides. *J. Mater. Chem. B* 3, 6355–6367. doi: 10.1039/C5TB00501A

Vrettos, E. I., Mezo, G., and Tzakos, A. G. (2018). On the design principles of peptide–drug conjugates for targeted drug delivery to the malignant tumor site. *Beilstein J. Organ. Chem.* 14, 930–954. doi: 10.3762/bjoc.14.80

Wang, F., Wang, Y., Zhang, X., Zhang, W., Guo, S., and Jin, F. (2014). Recent progress of cell-penetrating peptides as new carriers for intracellular cargo delivery. *J. Controll. Rel.* 174, 126–136. doi: 10.1016/j.jconrel.2013.11.020

Wang, H., Feng, Z., and Xu, B. (2016). D-Amino acid-containing supramolecular nanofibers for potential cancer therapeutics. *Adv. Drug Del. Rev.* 4, 110–111. doi: 10.1016/j.addr.2016.04.008

Wang, H., Feng, Z., and Xu, B. (2019). Supramolecular assemblies of peptides or nucleopeptides for gene delivery. *Theranostics* 9:3213. doi: 10.7150/thno.31854

Wang, H., and Yang, Z. (2012). Molecular hydrogels of hydrophobic compounds: a novel self-delivery system for anti-cancer drugs. *Soft Matter.* 8, 2344–2347. doi: 10.1039/C2SM06923G

Wang, J., Hu, X., and Xiang, D. (2018). Nanoparticle drug delivery systems: an excellent carrier for tumor peptide vaccines. *Drug Deliv.* 25, 1319–1327. doi: 10.1080/10717544.2018.1477857

Wang, J., Liu, K., Xing, R., and Yan, X. (2016a). Peptide self-assembly: thermodynamics and kinetics. *Chem. Soc. Rev.* 45, 5589–5604. doi: 10.1039/C6CS00176A

Wang, J., Liu, K., Yan, L., Wang, A., Bai, S., and Yan, X. (2016b). Trace solvent as a predominant factor to tune dipeptide self-assembly. *ACS Nano* 10, 2138–2143. doi: 10.1021/acsnano.5b06567

Wang, W., Anderson, C. F., Wang, Z., Wu, W., Cui, H., and Liu, C.-J. (2017). Peptide-templated noble metal catalysts: syntheses and applications. *Chem. Sci.* 8, 3310–3324. doi: 10.1039/C7SC00069C

Wang, Y., Cheetham, A. G., Angacian, G., Su, H., Xie, L., and Cui, H. (2017a). Peptide–drug conjugates as effective prodrug strategies for targeted delivery. *Adv. Drug Deliv. Rev.* 110, 112–126. doi: 10.1016/j.addr.2016.06.015

Wang, Y., Fan, S., Zhong, W., Zhou, X., and Li, S. (2017b). Development and properties of valine-alanine based antibody-drug conjugates with monomethyl auristatin e as the potent payload. *Int. J. Mol. Sci.* 18:1860. doi: 10.3390/ijms18091860

Wang, Y., Huang, R., Qi, W., Wu, Z., Su, R., and He, Z. (2013b). Kinetically controlled self-assembly of redox-active ferrocene–diphenylalanine: from nanospheres to nanofibers. *Nanotechnology* 24:465603. doi: 10.1088/0957-4484/24/46/465603

Wang, Y., Qi, W., Huang, R., Yang, X., Wang, M., Su, R., et al. (2015). Rational design of chiral nanostructures from self-assembly of a ferrocene-modified dipeptide. *J. Am. Chem. Soc.* 137, 7869–7880. doi: 10.1021/jacs.5b03925

Wang, Y., Zhang, Z., Xu, L., Li, X., and Chen, H. (2013a). Hydrogels of halogenated Fmoc-short peptides for potential application in tissue engineering. *Colloids Surfaces B* 104, 163–168. doi: 10.1016/j.colsurfb.2012.11.038

Webber, M. J., Appel, E. A., Meijer, E. W., and Langer, R. (2016). Supramolecular biomaterials. *Nat. Mater.* 15, 13–26. doi: 10.1038/nmat4474

Webber, M. J., and Langer, R. (2017). Drug delivery by supramolecular design. *Chem. Soc. Rev.* 46, 6600–6620. doi: 10.1039/C7CS00391A

Wijerathne, N. K., Kumar, M., and Ulijn, R. V. (2019). Fmoc-dipeptide/porphyrin molar ratio dictates energy transfer efficiency in nanostructures produced by biocatalytic coassembly. *Chem. A Eur. J.* 2019:2819. doi: 10.1002/chem.201902819

Wołczanski, G., and Lisowski, M. (2018). A general method for preparation of N-Boc-protected or N-Fmoc-protected α, β-didehydropeptide building blocks and their use in the solid-phase peptide synthesis. *J. Peptide Sci.* 24:e3091. doi: 10.1002/psc.3091

Worthington, P., Langhans, S., and Pochan, D. (2017). beta-hairpin peptide hydrogels for package delivery. *Adv. Drug Deliv. Rev.* 110–111, 127–136. doi: 10.1016/j.addr.2017.02.002

Wu, Y., and Collier, J. H. (2017). α-Helical coiled-coil peptide materials for biomedical applications. *Wiley Interdisc. Rev.* 9:e1424. doi: 10.1002/wnan.1424

Xie, Y., Zhao, J., Huang, R., Qi, W., Wang, Y., Su, R., et al. (2016). Calcium-ion-triggered co-assembly of peptide and polysaccharide into a hybrid hydrogel for drug delivery. *Nanoscale Res. Lett.* 11:184. doi: 10.1186/s11671-016-1415-8

Xing, R., Jiao, T., Feng, L., Zhang, Q., Zou, Q., Yan, X., et al. (2015). Photothermally-induced molecular self-assembly of macroscopic peptide-inorganic hybrid films. *Sci. Adv. Mater.* 7, 1701–1707. doi: 10.1166/sam.2015.2411

Xue, X., Lindstrom, A., Qu, H., and Li, Y. (2020). Recent advances on small-molecule nanomedicines for cancer treatment. *WIREs Nanomed. Nanobiotechnol.* 2:e1607. doi: 10.1002/wnan.1607

Yadav, N., Chauhan, M. K., and Chauhan, V. S. (2020). Short to ultrashort peptide-based hydrogels as a platform for biomedical applications. *Biomater. Sci.* 8, 84–100. doi: 10.1039/C9BM01304K

Yadav, S., Rai, V., Mahato, M., Singh, M., Rekha Deka, S., and Kumar Sharma, A. (2015). Vitamin E–TPGS stabilized self-assembled tripeptide nanostructures for drug delivery. *Curr. Top. Med. Chem.* 15, 1227–1235. doi: 10.2174/1568026615666150330111348

Yang, X., Wang, Y., Qi, W., Xing, R., Yang, X., Xing, Q., et al. (2019). Disulfide crosslinking and helical coiling of peptide micelles facilitate the formation of a printable hydrogel. *J. Mater. Chem. B* 7, 2981–2988. doi: 10.1039/C8TB03121E

Yeh, M.-Y., Huang, C.-T., Lai, T.-S., Chen, F.-Y., Chu, N.-T., Tseng, D. T.-H., et al. (2016). Effect of peptide sequences on supramolecular interactions of naphthaleneimide/tripeptide conjugates. *Langmuir* 32, 7630–7638. doi: 10.1021/acs.langmuir.6b01809

Yoo, S. H., and Lee, H.-S. (2017). Foldectures: 3D molecular architectures from self-assembly of peptide foldamers. *Accounts Chem. Res.* 50, 832–841. doi: 10.1021/acs.accounts.6b00545

Youngblood, R. L., Truong, N. F., Segura, T., and Shea, L. D. (2018). It's all in the delivery: designing hydrogels for cell and non-viral gene therapies. *Mol. Therap.* 26, 2087–2106. doi: 10.1016/j.ymthe.2018.07.022

Yu, C.-Y., Huang, W., Li, Z.-P., Lei, X.-Y., He, D.-X., and Sun, L. (2016). Progress in self-assembling peptide-based nanomaterials for biomedical applications. *Curr. Top. Med. Chem.* 16, 281–290. doi: 10.2174/1568026615666150701114527

Yu, Z., Xu, Q., Dong, C., Lee, S. S., Gao, L., Li, Y., et al. (2015). Self-assembling peptide nanofibrous hydrogel as a versatile drug delivery platform. *Curr. Pharm. Design* 21, 4342–4354. doi: 10.2174/1381612821666150901104821

Yuan, C., Ji, W., Xing, R., Li, J., Gazit, E., and Yan, X. (2019). Hierarchically oriented organization in supramolecular peptide crystals. *Nat. Rev. Chem.* 3, 567–588. doi: 10.1038/s41570-019-0129-8

Yuran, S., Razvag, Y., and Reches, M. (2012). Coassembly of aromatic dipeptides into biomolecular necklaces. *Acs Nano* 6, 9559–9566. doi: 10.1021/nn302983e

Zaldivar, G., Vemulapalli, S., Udumula, V., Conda-Sheridan, M., and Tagliazucchi, M. (2019). Self-assembled nanostructures of peptide-amphiphiles: charge regulation by size regulation. *J. Phys. Chem. C* 123, 17606–17615. doi: 10.1021/acs.jpcc.9b04280

Zanna, N., Merlettini, A., Tatulli, G., Milli, L., Focarete, M. L., and Tomasini, C. (2015). Hydrogelation induced by Fmoc-protected peptidomimetics. *Langmuir* 31, 12240–12250. doi: 10.1021/acs.langmuir.5b02780

Zanna, N., and Tomasini, C. (2017). Peptide-based physical gels endowed with thixotropic behaviour. *Gels* 3:39. doi: 10.3390/gels3040039

Zhang, C., Welborn, M., Zhu, T., Yang, N. J., Santos, M. S., Van Voorhis, T., et al. (2016). π-Clamp-mediated cysteine conjugation. *Nat. Chem.* 8:120. doi: 10.1038/nchem.2413

Zhang, H., Fei, J., Yan, X., Wang, A., and Li, J. (2015). Enzyme-responsive release of doxorubicin from monodisperse dipeptide-based nanocarriers for highly efficient cancer treatment *in vitro*. *Adv. Funct. Mater.* 25, 1193–1204. doi: 10.1002/adfm.201403119

Zhang, H., Park, J., Jiang, Y., and Woodrow, K. A. (2017). Rational design of charged peptides that self-assemble into robust nanofibers as immune-functional scaffolds. *Acta Biomaterialia* 55, 183–193. doi: 10.1016/j.actbio.2017.03.041

Zhang, L., Wang, X., Wang, T., and Liu, M. (2015). Tuning soft nanostructures in self-assembled supramolecular gels: from morphology control to morphology-dependent functions. *Small* 11, 1025–1038. doi: 10.1002/smll.201402075

Zhang, R., Xing, R., Jiao, T., Ma, K., Chen, C., Ma, G., et al. (2016). Carrier-free, chemophotodynamic dual nanodrugs via self-assembly for synergistic antitumor therapy. *ACS Appl. Mater. Interfaces* 8, 13262–13269. doi: 10.1021/acsami.6b02416

Zhang, Z., Shi, L., Wu, C., Su, Y., Qian, J., Deng, H., et al. (2017). Construction of a supramolecular drug–drug delivery system for non-small-cell lung cancer therapy. *ACS Appl. Mater. Interfaces* 9, 29505–29514. doi: 10.1021/acsami.7b07565

Zheng, W., Gao, J., Song, L., Chen, C., Guan, D., Wang, Z., et al. (2012). Surface-induced hydrogelation inhibits platelet aggregation. *J. Am. Chem. Soc.* 135, 266–271. doi: 10.1021/ja308690y

Zhong, J., Fu, H., Jia, X., Lou, H., Wan, T., Luo, H., et al. (2019). A pH-/thermo-responsive hydrogel formed from N, N′-dibenzoyl-l-cystine: properties, self-assembly structure and release behavior of SA. *RSC Adv.* 9, 11824–11832. doi: 10.1039/C8RA09058K

Zhou, M., Ulijn, R. V., and Gough, J. E. (2014). Extracellular matrix formation in self-assembled minimalistic bioactive hydrogels based on aromatic peptide amphiphiles. *J. Tissue Eng.* 5:2041731414531593. doi: 10.1177/2041731414531593

Zhou, P., Wang, J., Wang, M., Hou, J., Lu, J. R., and Xu, H. (2019). Amino acid conformations control the morphological and chiral features of the self-assembled peptide nanostructures: young investigators perspective. *J. Colloid Interface Sci.* 548, 244–254. doi: 10.1016/j.jcis.2019.04.019

Zohrabi, T., Habibi, N., Zarrabi, A., Fanaei, M., and Lee, L. Y. (2016). Diphenylalanine peptide nanotubes self-assembled on functionalized metal surfaces for potential application in drug-eluting stent. *J. Biomed. Mater. Res. Part A* 104, 2280–2290. doi: 10.1002/jbm.a.35764

Zou, Q., Abbas, M., Zhao, L., Li, S., Shen, G., and Yan, X. (2017). Biological photothermal nanodots based on self-assembly of peptide–porphyrin conjugates for antitumor therapy. *J. Am. Chem. Soc.* 139, 1921–1927. doi: 10.1021/jacs.6b11382

Zou, R., Wang, Q., Wu, J., Wu, J., Schmuck, C., and Tian, H. (2015). Peptide self-assembly triggered by metal ions. *Chem. Soc. Rev.* 44, 5200–5219. doi: 10.1039/C5CS00234F

Conflict of Interest: The authors declare that the research was conducted in the absence of any commercial or financial relationships that could be construed as a potential conflict of interest.

frontiers in Bioengineering and Biotechnology

ORIGINAL RESEARCH
published: 12 June 2020
doi: 10.3389/fbioe.2020.00497

Polylactic Acid-Based Patterned Matrixes for Site-Specific Delivery of Neuropeptides On-Demand: Functional NGF Effects on Human Neuronal Cells

Olga A. Sindeeva[1,2†], Olga Kopach[3†], Maxim A. Kurochkin[4], Andrei Sapelkin[5], David J. Gould[6], Dmitri A. Rusakov[3] and Gleb B. Sukhorukov[1,7,8*]*

[1] Center for Neurobiology and Brain Restoration, Skolkovo Institute of Science and Technology, Moscow, Russia, [2] Remote Controlled Theranostic Systems Lab, Department of Nanotechnology, Educational and Research Institute of Nanostructures and Biosystems, Saratov State University, Saratov, Russia, [3] UCL Queen Square Institute of Neurology, University College London, London, United Kingdom, [4] Center for Photonics and Quantum Materials, Skolkovo Institute of Science and Technology, Moscow, Russia, [5] School of Physics and Astronomy, Queen Mary University of London, London, United Kingdom, [6] Biochemical Pharmacology, William Harvey Research Institute, Queen Mary University of London, London, United Kingdom, [7] School of Engineering and Material Science, Queen Mary University of London, London, United Kingdom, [8] Center of Biomedical Engineering, I.M. Sechenov First Moscow State Medical University, Moscow, Russia

The patterned microchamber arrays based on biocompatible polymers are a versatile cargo delivery system for drug storage and site-/time-specific drug release on demand. However, functional evidence of their action on nerve cells, in particular their potential for enabling patterned neuronal morphogenesis, remains unclear. Recently, we have established that the polylactic acid (PLA)-based microchamber arrays are biocompatible with human cells of neuronal phenotype and provide safe loading for hydrophilic substances of low molecular weight, with successive site-specific cargo release on-demand to trigger local cell responses. Here, we load the nerve growth factor (NGF) inside microchambers and grow N2A cells on the surface of patterned microchamber arrays. We find that the neurite outgrowth in local N2A cells can be preferentially directed towards opened microchambers (upon-specific NGF release). These observations suggest the PLA-microchambers can be an efficient drug delivery system for the site-specific delivery of neuropeptides on-demand, potentially suitable for the migratory or axonal guidance of human nerve cells.

Keywords: polylactic acid (PLA), patterned microchamber array, drug delivery system, NGF, human N2A cells

OPEN ACCESS

Edited by:
Stefano Leporatti, Institute of Nanotechnology (CNR), Italy

Reviewed by:
Hakan Ceylan, Max Planck Institute for Intelligent Systems, Germany
Giulia Suarato, Italian Institute of Technology (IIT), Italy

***Correspondence:**
Dmitri A. Rusakov
d.rusakov@ucl.ac.uk
Gleb B. Sukhorukov
g.sukhorukov@qmul.ac.uk

† These authors have contributed equally to this work

Specialty section:
This article was submitted to Nanobiotechnology, a section of the journal Frontiers in Bioengineering and Biotechnology

Received: *02 February 2020*
Accepted: *28 April 2020*
Published: *12 June 2020*

Citation:
Sindeeva OA, Kopach O, Kurochkin MA, Sapelkin A, Gould DJ, Rusakov DA and Sukhorukov GB (2020) Polylactic Acid-Based Patterned Matrixes for Site-Specific Delivery of Neuropeptides On-Demand: Functional NGF Effects on Human Neuronal Cells. Front. Bioeng. Biotechnol. 8:497. doi: 10.3389/fbioe.2020.00497

INTRODUCTION

Micro- and nanostructured matrices have prompted new lines of study focusing on cell behavior (adhesion, proliferation, morphology, alignment, migration, gene expression, and even differentiation) and tissue engineering (Sousa et al., 2019). Photolithography and electroplating techniques enable creation of templates with the choice of different geometries. Such templates can be used either as independent matrices for growing cells, or as templates for the reusable synthesis of patterned films composed of polymers, proteins, and colloids, with nanoscale fidelity.

The current patterning techniques to control nerve cell morphogenesis and function include the NeuroArray device designed for the patterned growing of nerve cells (Li et al., 2014), graphene oxide-based hybrid patterns for guiding axonal growth (Min et al., 2017), microcontact-printed polymeric substrates for directed neuronal regeneration (Schmalenberg and Uhrich, 2005), micropatterned polymer brushes for cell directionality (Pardo-Figuerez et al., 2018), and others. The ultimate goal of these techniques has been, however, to modify neuronal growth and cell proliferation, with no attempts to stimulating activity of individual cells. A recently developed patterned microchamber array (MCA) (Kiryukhin et al., 2018) is, therefore, of particular importance: it provides a reservoir matrix consisting of microchambers (microcontainers). Such a matrix can be made of various synthetic and biocompatible polymers using the layer-by-layer method (Ermakov et al., 2019). MCA could be composed of a variety of hydrophobic polymers, for instance, polylactic acid (PLA) (Zykova et al., 2019), poly(lactic-co-glycolic acid) (Sindeeva et al., 2018a), etc., with various inclusions inserted into the shell of microchambers, such as gold nanoparticles or the aggregates of carbon dots (Sindeeva et al., 2018b; 2019; Kurochkin et al., 2020). Having biologically active substances inside microchambers allows spatially and temporally modulated control of cell function, not only due to the periodic structure of the material (Norman and Desai, 2006; Bettinger et al., 2009; Ge et al., 2015; Sousa et al., 2019) but also due to the encapsulated cargo release (Kopach et al., 2019). A wide range of biocompatible polymers for the MCA synthesis enables control of the cargo release rate. For example, it was shown that the PLGA-based microchambers provided relatively slow, continuous release of adrenaline hydrochloride from the first day after entering the aqueous environment (Sindeeva et al., 2018a), which has a clear advantage in many clinical applications. The release of a significant quantity of cargo can be induced by ultrasound as a result of the simultaneous opening of many microchambers (Sindeeva et al., 2018a), or otherwise individual chambers can be opened by optical laser targeting (Sindeeva et al., 2018b; Kopach et al., 2019; Kurochkin et al., 2020).

Notwithstanding the advantages of MCA as a system for targeted delivery of drugs and biologically active substances, its applications in human cells remain poorly understood; this precludes perspective clinical use of these systems. This is mainly because the methods of encapsulation, the duration of storage, the release rate of the substance depend not only on the shell material (Lee and Yeo, 2015) and container geometry (Macha et al., 2019), but also on the cargo's chemical and physical properties (Albinali et al., 2019), which vary widely. Earlier, we have demonstrated that PLA-based MCA are fully biocompatible with human cells of neuronal phenotype (Kopach et al., 2019). Furthermore, we showed a site-specific cellular response to the release of compounds of low molecular weight from individual microchambers: doxycycline for enhancing biosynthesis of green fluorescent protein in individual C2C12 cells (Gai et al., 2018) and the excitatory neurotransmitter glutamate for activation of N2A cells (Kopach et al., 2019). These observations have validated MCA as an effective delivery system for modifying cell activity on demand.

The site- and time-specific delivery of neuropeptides is another important step in managing nerve cell growth, including directed neurite outgrowth that has strong potential in neuroregenerative medicine. Here, we demonstrate the feasibility of modulating neuronal cell function through loading and site-specific release of the nerve growth factor (NGF), a neuropeptide which is primarily involved in the regulation of neurotrophic activities, growth, and proliferation of nerve cells (Levi-Montalcini, 1987). Since NGF is a neuropeptide, it is particularly sensitive to the small temperature fluctuations characteristic of laser exposure. The laser-triggered NGF release from MCA to the targeted N2A cells growing on the MCA surface was therefore performed using focused near-infrared (NIR) laser light. The advantage of using NIR laser rests with the minimal light absorption of biological tissues within the 650–975 nm spectral range, which minimizes photothermal effects on cells. The site-specific localization of the laser-triggered photothermal influence on the chamber wall was enabled by the inclusion of gold nanoparticles (GNPs) in the shells of microchambers as highly photo-absorbing agents (Wijaya et al., 2009; Agarwal et al., 2011). GNPs is a safe (Sperling et al., 2008; Boisselier and Astruc, 2009), well-established, and widely used thermosensitive material for polymer carrier opening *in vitro* and *in vivo* (Radt et al., 2004; Skirtach et al., 2005; Boisselier and Astruc, 2009; Singh, 2010; Kunzmann et al., 2011).

MATERIALS AND METHODS

Materials

For MCA synthesis, biopolymer PLA (3 mm granules, molecular weight 60,000), chloroform, and NGF-β (molecular weight 13,5 kDa) were purchased from Sigma-Aldrich (UK). The Poly(dimethylsiloxane) (PDMS) kit (Sylgard 184) was purchased from Dow-Corning (Midland, USA).

For gold nanorods (GNRs) synthesis, cetyltrimethylammonium bromide (CTAB, >98.0%), hydrochloric acid (HCl, 37 wt% in water), L-ascorbic acid (>99.9%), and sodium borohydride ($NaBH_4$, 99%) were purchased from Sigma-Aldrich (UK). Hydrogen tetrachloroaurate trihydrate ($HAuCl_4 \cdot 3H_2O$) and silver nitrate ($AgNO_3$, >99%) were purchased from Alfa Aesar.

Synthesis of GNRs

GNRs were fabricated by the modified seed-mediated method (Nikoobakht and El-Sayed, 2003; Khlebtsov et al., 2011). At the first step, the seed solution was obtained by mixing 250 μL of 10 mM $HAuCl_4$ and 10 mL of 0,1 M CTAB. The ice-cold 10 mM $NaBH_4$ was added to the mixture in the volume of 1 mL. At the second step, 10 mL of the seed solution were mixed with 900 μL of 0.1 M CTAB, 20 mL of 4 mM $AgNO_3$, 50 mL of 10 mM $HAuCl_4$, 10 mL of 1 M HCl, and 10 mL of 0.1 M ascorbic acid for preparing GNRs. Then nanorods were centrifuged at 12,000 g for 60 min. The pellet was re-suspended in deionized water. The final solution was containing about 1012 GNRs per mL; their average width was 11 ± 3 nm and length was 40 ± 6 nm. The axial ratio was ∼3.8, according the longitudinal resonance was ∼790 nm.

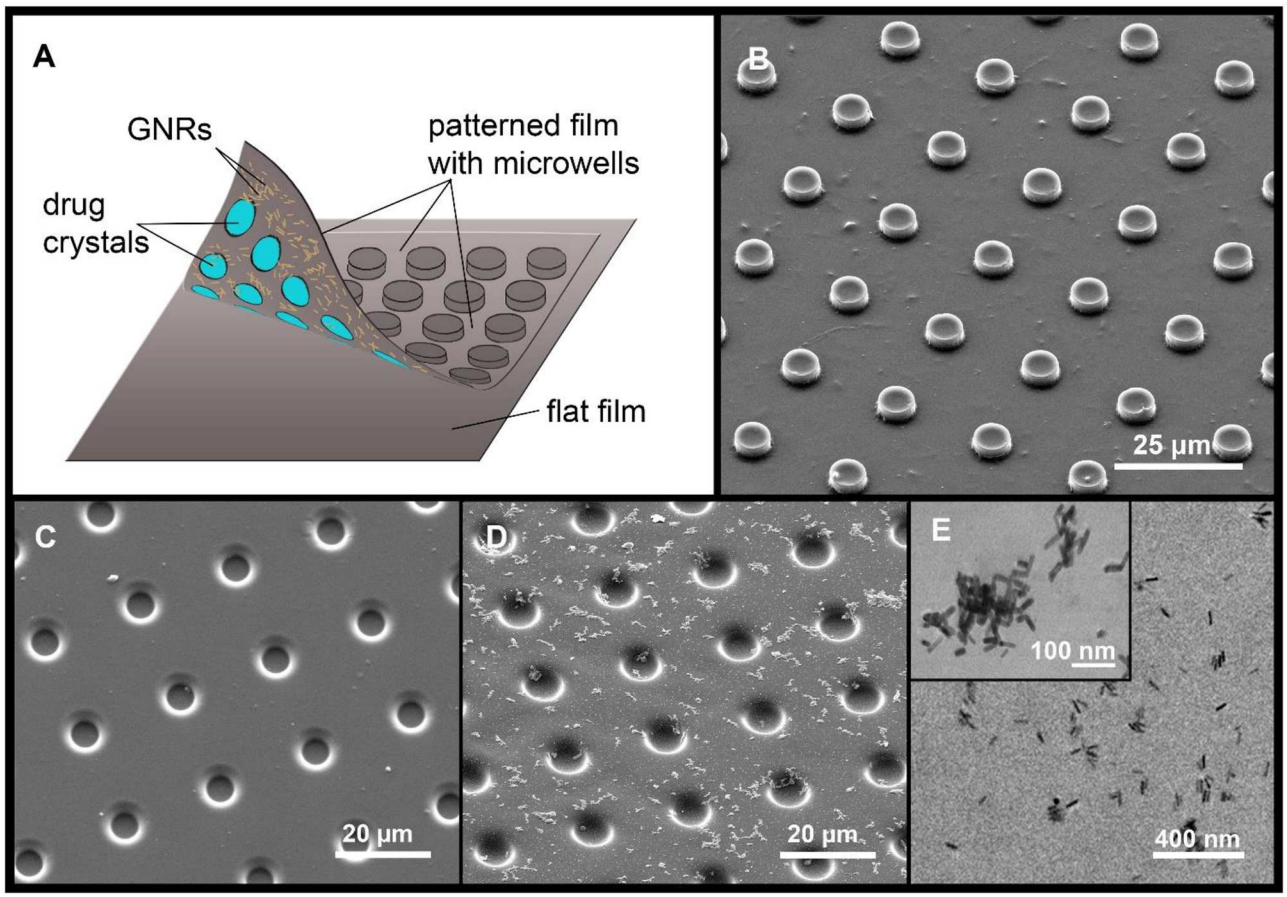

FIGURE 1 | A diagram of the MCA, with a drug cargo and GNRs **(A)**. Typical SEM image of PLA-based MCA with GNRs **(B)**. SEM images of PLA patterned film, without **(C)** and with GNR aggregates **(D)**. The arrangement of GNR aggregates (**E**, TEM image).

Fabrication of PLA-Based MCA

The silicon master was previously made at Shenzhen Semiconductor (Shenzhen, China) using photolithography for MCA synthesis. The pattern on silicon master was represented by a plate with 185,000 cylinders equidistant from each other (diameter 10 μm, height 4 μm, and distance from center to center 20 μm). For the synthesis of patterned films, the PDMS stamp was made as a reverse impression from a silicone master from a mixture of the prepolymer and curing agent (10:1 ratio). The mixture was degassed for 30 min in a vacuum and consolidated (at 70°C for 3 h). After this, the PDMS master was cut out and separated from the silicon master. The shell of the PLA-based MCA was made by sealing (printing) of two films: the patterned and the flat ones (2 kg cm^{-2}, 15 s, at 55°C) (**Figure 1A**). For the synthesis of the patterned film, the PDMS stamp with microwells was dip-coated for 5 s into the 1 wt% PLA chloroform solution; for obtaining the flat PLA microfilm, the same procedure was made with a cover glass. After printing, the PDMS stamp was removed and the MCA was located on cover glass.

The patterned film was covered with GNRs before printing by scattering GNRs on the inner surface of the PLA film by sedimentation (Sindeeva et al., 2018b). For precipitation and sedimentation of GNRs, 200 μL of 0.5 M NaCl solution was added to 200 μL of the nanoparticles solution to enhance aggregation (Madzharova et al., 2018). The resulting solution was centrifuged at 10,000 rpm, and supernatant was removed. Next, GNRs were resuspended in 200 μL of deionized water. After that procedure, aggregates of GNRs started to adsorb on a hydrophobic PLA surface. Aggregates in comparison with non-aggregated particles have a larger size and mass which led to amplification of sedimentation rate (Midelet et al., 2017). As a result, aggregates of gold nanoparticles were visualized with an optical microscope, as well as with scanning electron microscopy (SEM) and transmission electron microscopy (TEM).

NGF Loading Into Microchambers; NGF Leak Test

NGF loading was carried out by applying 10 μL of an aqueous solution (10 μg/mL) on the inner surface of the patterned film after the deposition of GNRs. For homogeneous loading, the solution was evenly distributed over the entire film surface and allowed to completely dry (**Figures 2A–C** and **Supplementary Movie 1**). To confirm homogeneous loading of

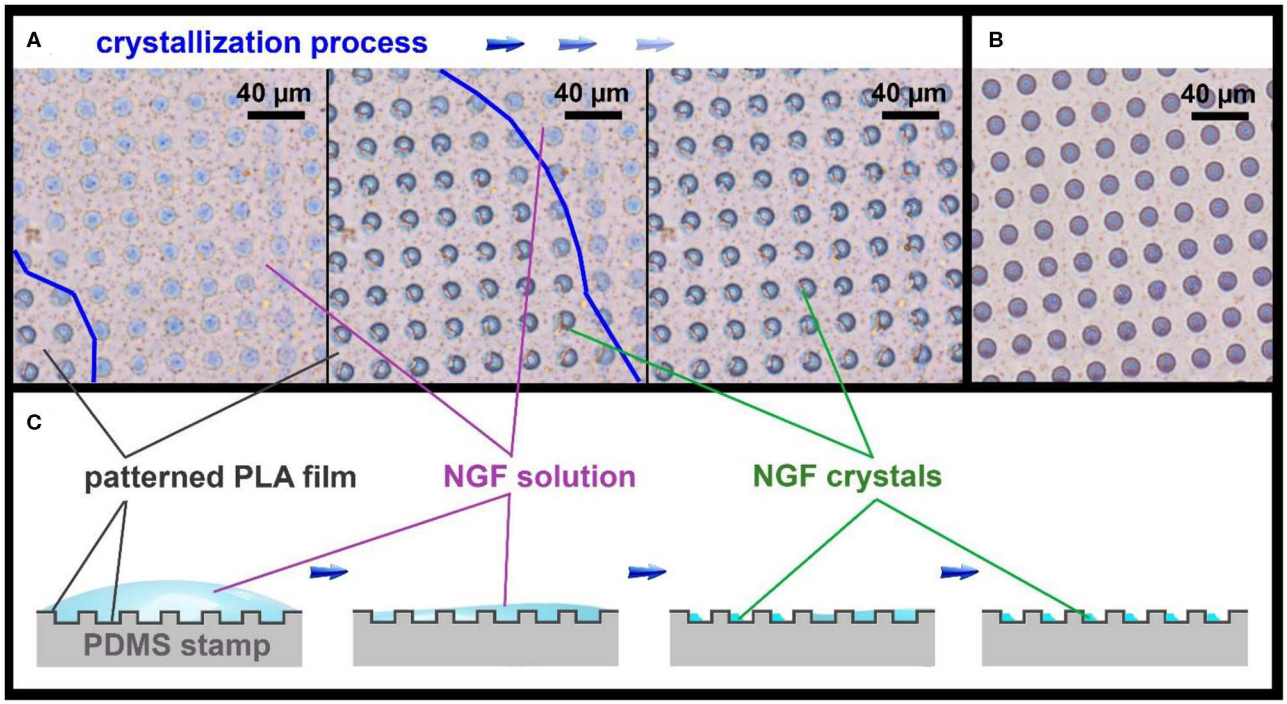

FIGURE 2 | Optical images of the patterned PLA film **(A)**, showing the NGF crystallization process, and an empty patterned film **(B)**, bright-field microscopy in phase contrast mode. The border of NGF solution drop is marked with a blue line. Schematic illustration of the NGF crystallization process on the patterned PLA film **(C)**.

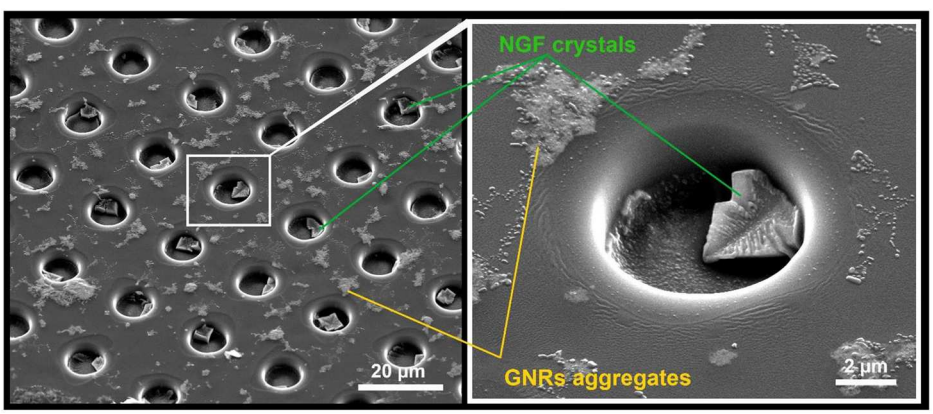

FIGURE 3 | SEM images of NGF crystals inside the microwells on patterned PLA film.

the microwells, NGF crystals were visualized inside the fabricated microchambers with SEM (**Figure 3**).

To test whether spontaneous NGF release from the microchambers could occur after sealing, the fabricated MCA were placed in Dulbecco's phosphate-buffered saline (DPBS) at 37°C (95% O_2 and 5% CO_2) to represent a relatively physiological environment. The amount of NGF was tested in DPBS at different time-points for up to 3 days using the Brilliant Blue G reagent and spectrophotometry.

Laser-Induced Opening of Individual PLA-Based Microchambers

The NIR lasers are widely used for the opening of targeted drug delivery systems as they are associated with good penetration ability in tissue without damaging living cells. Laser-induced opening of individual PLA microchambers with the N2A cells growing on the MCA surface was performed using a home-made system. The in-house-made system was based on an inverted microscope (Olympus ix71, Japan), into the optical path of which

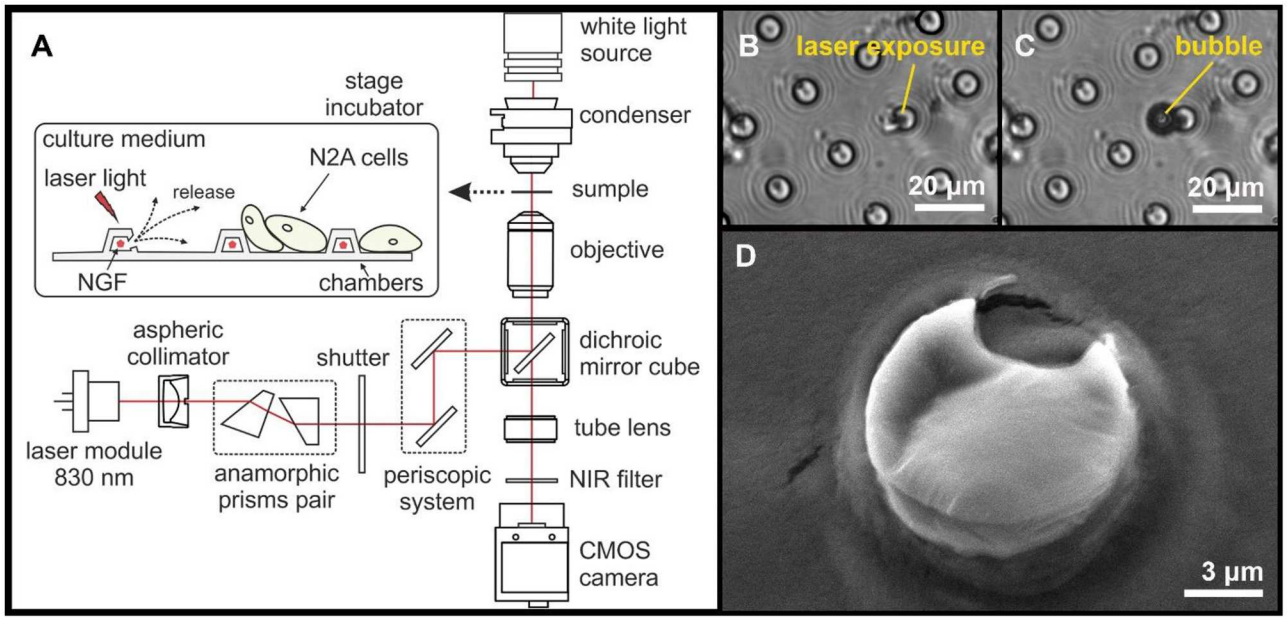

FIGURE 4 | A diagram illustrating the experimental design and the laser-induced opening of MCA with NGF loaded inside **(A)**. Typical images of microchambers before **(B)** and after **(C)** laser exposure (bright-field microscopy). SEM image of an opened microchamber **(D)**.

we integrated a continuous-wave NIR laser module (LD830-MA1W, 830 nm, maximum optical power 1W, Thorlabs Inc., USA) with adjustable output power, to enable photo-thermal activation of selected microchambers (**Figure 4A**). First, NIR laser light was collimated by an aspheric lens and was 3x expanded by an anamorphic prism pair. Next, laser light was directed into the microscope infinity port by a two-mirror periscope. Then, the laser light was directed by an infrared short-pass dichroic mirror (DMSP805, 805 nm cutoff wavelength, Thorlabs Inc., USA) into an exit pupil of an infinity-corrected objective lens LCAch 20x/0.4 PhC (Olympus, Japan) and focused by the objective into a 1 µm spot on the surface of a selected microchamber, at a power of 15 mW over 0.5 s. The laser light irradiation exposure time was controlled by a mechanical shutter. The optical system has been tuned for the confocality between the transmitted light and the NIR channel to control the NIR channel focus by the visible-light focus. Thus, we routinely focused the NIR laser on the microchamber base to minimize damage, if any, to NGF crystals which tend to accumulate toward the top (**Figure 3**). The N2A cell reaction to triggered NGF release was recorded using a monochrome CMOS sensor (DCC3260M, Thorlabs Inc., USA) with an infrared filter.

SEM and TEM Techniques

To visualize MCA morphology at different steps through the fabrication procedure (payload, sealing) and after opening microchamber(s), SEM was used to ensure appropriate samples (FEI Quanta ESEM, electron microscope, FEI, Hillsboro, USA). SEM was carried out using an accelerating voltage of 10 kV, a spot size of 3.5, and a working distance of ∼10 mm.

TEM images of the MCA with GNRs were obtained using a Jeol 2100 microscope (Tokyo, Japan). GNRs diameters and lengths were evaluated from digitized TEM images (Grapher 8, Golden Software, Inc.) of about 500 GNRs.

Human N2A Cell Culture

To test functional effects of laser-triggered release of NGF from PLA-microchambers, we used human N2A cells. The cell line was maintained as we have recently described in detail (Kopach et al., 2019). Briefly, N2A cells were cultured in Dulbecco's modified Eagle medium (DMEM, Invitrogen, Carlsbad, CA, USA), supplemented with 2 mM L-glutamine and 10% fetal bovine serum, 2% penicillin-streptomycin, and 1% non-essential amino acids at 37 °C (5% CO_2). After harvesting, cells were washed out and plated on a surface of PLA-based MCA, pre-treated with UV light for at least 2 h in advance. For cell differentiation to neuronal phenotype, the culturing medium was low serum (2%) DMEM. We used N2A cells at earlier passages only (before cells pass passage 20). Microscopic images of differentiating N2A cells on the fabricated MCA were collected before microchamber opening and afterward at various time-points. For the time-lapse imaging, a MCA with differentiating N2A cells on its surface was placed in a microscope cage incubator (5 cm^2 Petri dish) to maintain experimental conditions favorable for live-cell imaging (37°C, 5% CO_2). Images were acquired every 10 min for up to 60 h total.

In separate experiments, N2A cells were plated on glass coverslips placed into a 8 × 8 wells-plate. Experimental groups consisted of the cells of the same passage grown on glass in culture medium without NGF or NGF supplemented at the

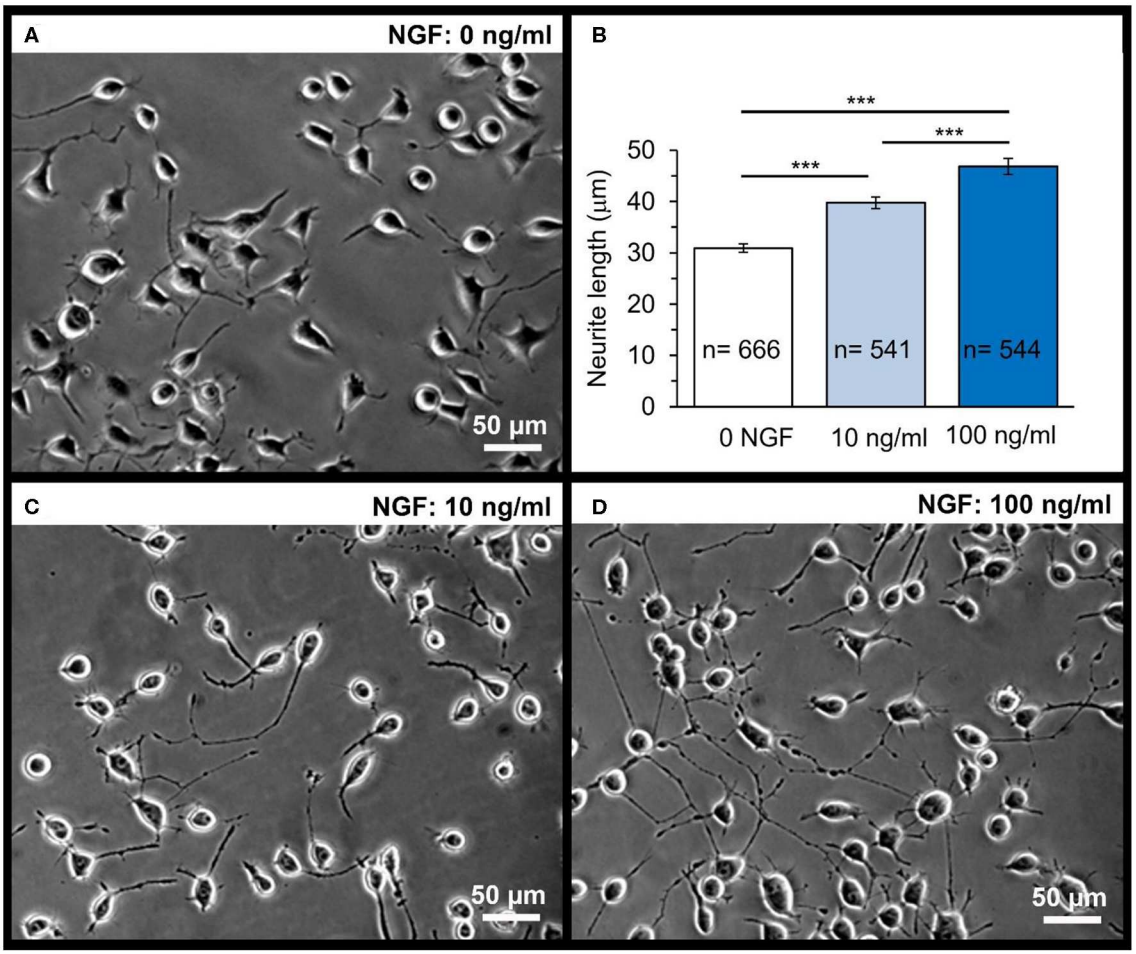

FIGURE 5 | Dose-dependent effect of NGF on the neurite outgrowth in N2A cells on glass coverslips. A snapshot of differentiating N2A cells after 1 day of cell growth on glass **(A)**. Statistical summary of the neurite length in N2A cells grown without or with NGF supplemented to culture medium at the concentration of 10 or 100 ng/mL. Numbers of neurites measured for their length are indicated; at least four independent samples (coverslips) were tested for each group. ***$P < 0.001$ (two-tailed, unpaired *t*-test). **(B)** Representative images of differentiating N2A cells after 1 day of cell growth with NGF at different concentrations: 10 ng/mL **(C)** or 100 ng/mL **(D)**.

concentration of 10 or 100 ng/mL. There were at least four independent samples tested for each experimental group.

Assessment of Neurite Length; Cell Density Analysis

Neurite outgrowth by N2A cells was assessed by measuring the neurite length in different experimental conditions, using a NeuronJ, a plugin of ImageJ software (NIH, Bethesda, USA). Neurites were traced in individual cells manually, using variable digital zooming. Analyses were performed in the cell culture field of view, across multiple areas selected in a pseudo-random manner.

The N2A cell density was analyzed by counting cell bodies on the surface of the fabricated array, within the area of interest (close to the opened microchambers). Cell density was estimated as the number of viable cells per mm^2 over the selected period of time-lapse recording, as indicated.

Statistical Analysis

Data are presented as mean ± standard error of the mean, with n referring to the number of neurites measured for their length, for each experimental group. To determine the statistical difference between experimental groups, two-tailed unpaired Student's *t*-test was used. A $p < 0.05$ was considered as an indicator of the statistically significant difference.

RESULTS AND DISCUSSION

PLA-Based MCA With Gold Nanoparticles: Fabrication and Characterization

We created MCA by printing both flat and patterned films (**Figure 1A**). The thickness of the finished film was 0.8–1.0 µm. GNPs (as a classical method) were included in the MCA composition before printing, to

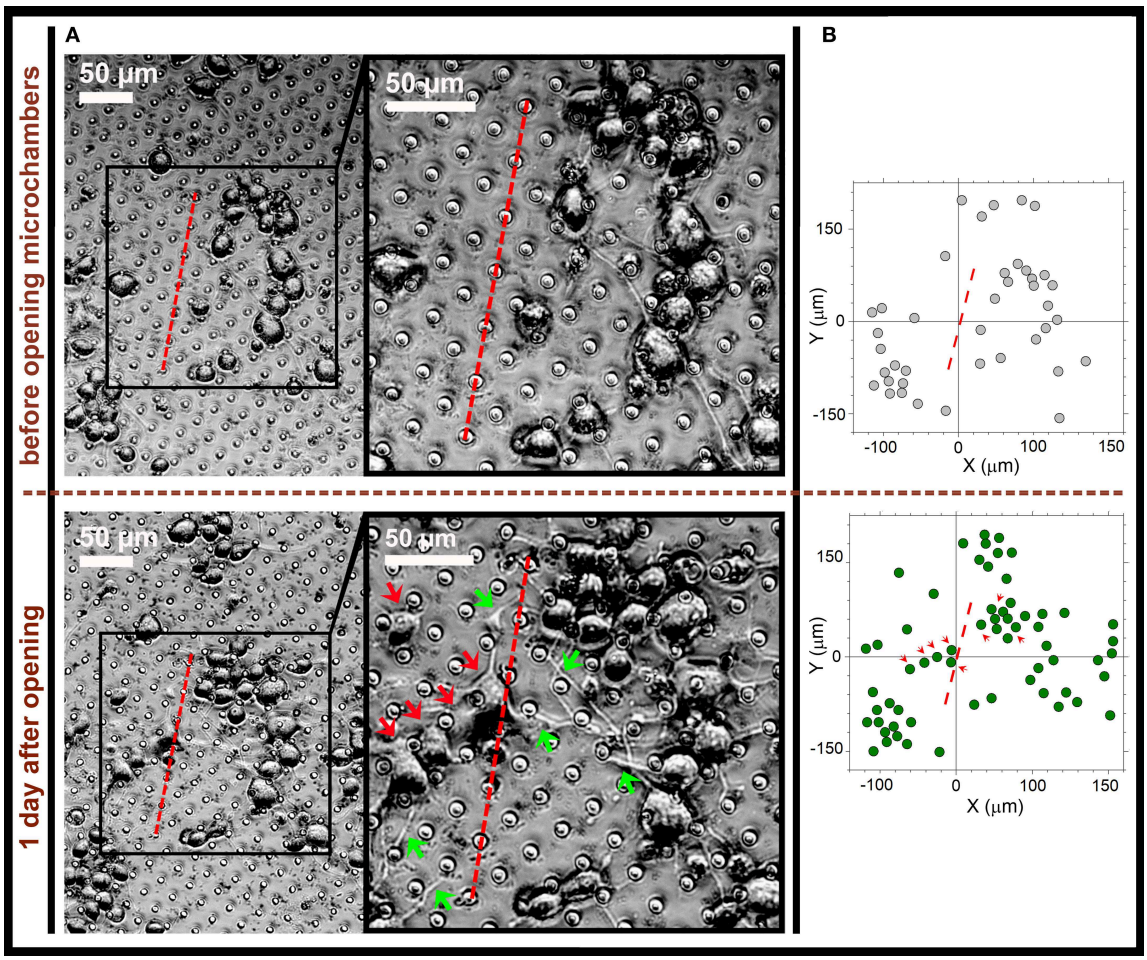

FIGURE 6 | Directed neurite outgrowth by local N2A cells and cell migration toward the laser-opened microchambers with NGF payload inside. **(A)** Representative snapshots of differentiating N2A cells growing on the surface of PLA-based MCA with NGF payload inside microchambers before microchamber opening (upper row) and 1 day after (lower row). Red dotted line, a line segment trajectory for optical targeting microchambers (7 microchambers opened). Red arrows, directed migration of individual cells from their original positions; green arrows, cell neurites directed toward the opened microchambers (NGF release). **(B)** Cell tracking diagrams depicting individual N2A cell positions before laser-triggered microchamber opening (top) and 1 day after (bottom). Note directed migration of local cells (red arrows) from their original positions toward the opened microchambers. Data are representative of images on **(A)**.

enable controlled opening of microchambers with laser light (Singh, 2010; Kunzmann et al., 2011).

For surface modification, an in-advance concentrated water solution with GNRs was prepared (200 mg/mL). Two hundred microliter of this solution were placed on the inner surface of the patterned microfilm with microwells, for 3 h. During this time, the patterned film was horizontally oriented, after which the drop was removed using a micropipette. The entire surface of the patterned film was covered with GNR aggregates, which were clearly visible under an optical microscope. **Figure 1** shows an SEM image (D) and TEM image (E) of the GNR aggregates location. GNRs content in the patterned film was 0.47 pg/μm^2, as estimated from the absorption spectrum change in the solution, before and after deposition of aggregates.

NGF Loading

Microchambers were filled by applying 10 μL of the NGF solution (concentration 10 μg/mL) on the patterned PLA film surface (8.5 × 8.5 mm, 185000 microwells), before printing it on a flat film. Although the PLA film has hydrophobic properties (Alakrach et al., 2018), the NGF solution uniformly wetted the patterned surface due to the low surface tension. The drying of the NGF solution occurred evenly over the entire film surface, with a gradual decrease of the solution drop thickness (**Figure 2A**). When the water layer thickness reached a critical point, the rapid formation of crystals in the wells began over the entire surface (**Figures 2A,C**). The crystallization process could be clearly observed in a light microscope in real time (**Supplementary Movie 1**).

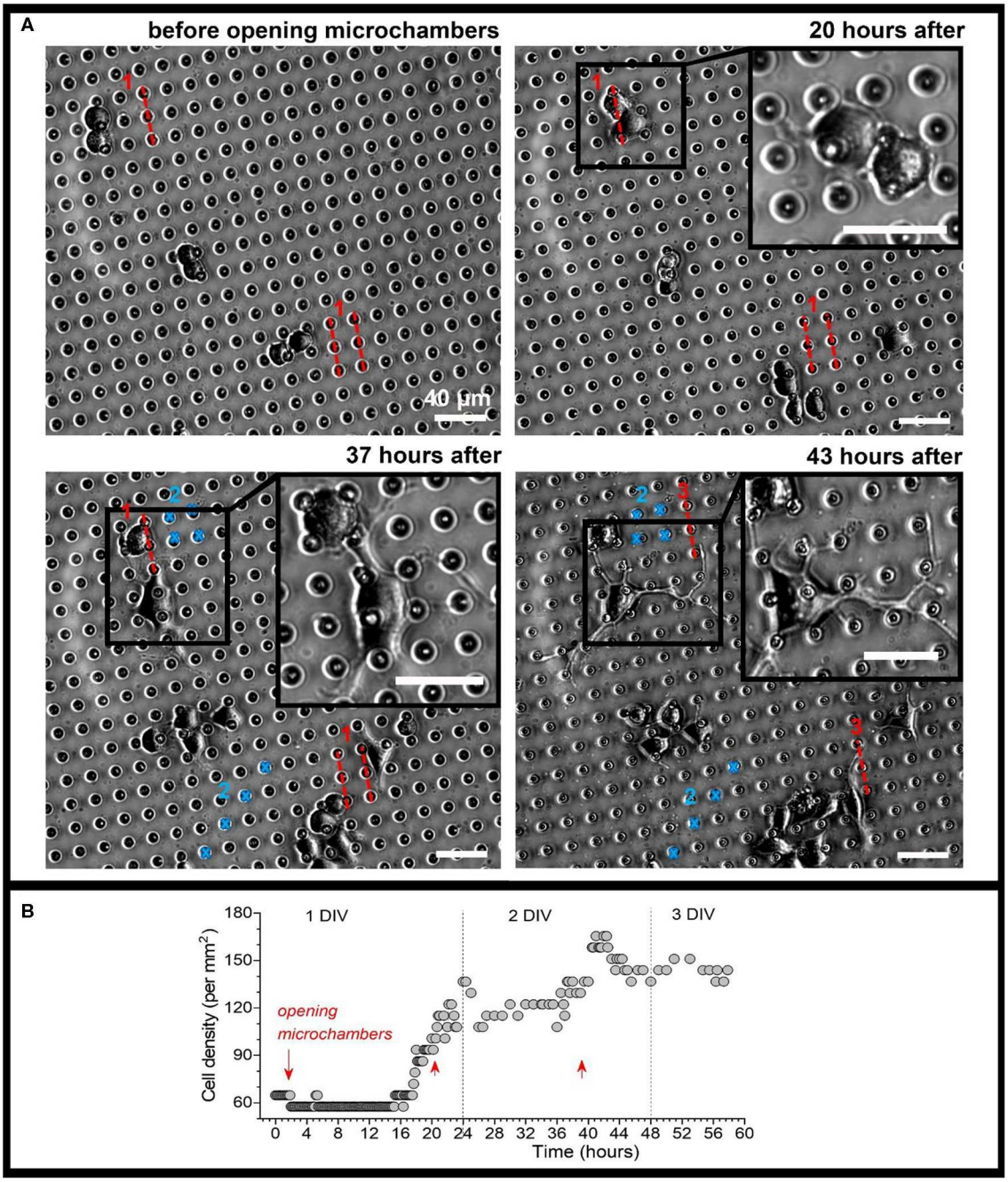

FIGURE 7 | Monitoring morphogenesis of differentiating N2A cells upon triggered, site-specific NGF release from PLA-microchambers. **(A)** Representative snapshots of differentiating N2A cells on the surface of MCA with NGF-loaded microchambers before and following laser-triggered microchamber opening at various time-points. Images taken from the same area of interest; red dotted lines and blue marks, trajectories for optical targeting (the sequence consists of varied trajectory for opening 3 times, ~20 h apart). Scale bars, 40 μm. **(B)** Time-course of cell density changes within the targeted area during the time-lapse imaging (~60 h total) before and following triggered NGF release from PLA-microchambers, shown on **(A)**. Red arrows, time of laser-triggered opening.

The images obtained using SEM confirmed the uniformity of filling the microwells with crystals, and the absence of NGF between them (**Figure 3**).

In general, the amount of NGF was 100 ng per sample (8.5 × 8.5 mm) and 0.54 pg per microchamber. This amount was calculated theoretically, by taking into account the total amount of substance deposited on the patterned film surface, and the number of microwells. This amount of NGF was highest possible to achieve reliable loading into the microwells of pre-designed configuration (diameter of 10 μm, height 4 μm).

Further concentration increases led to the formation of crystals across the entire film surface (outside of the microwells) that prevented tight and reliable sealing of microchambers by the two films.

In order to increase the capability of NGF payload, larger microchambers can be used. At the same time, the use of larger (especially taller) microchambers may cause difficulties for cells to freely move, since the surface topography was found to have substantial effects on the cells behavior in different cell types (Norman and Desai, 2006; Bettinger et al., 2009; Ge et al., 2015; Sousa et al., 2019).

Controllable microchamber permeability is an important issue, which we addressed in some detail in our previous work for the PLA-based MCA loaded with low molecular weight compounds (Kopach et al., 2019). To examine potential leakage of NGF from PLA-microchambers, we next carried out testing of the fabricated MCA loaded with NGF in DPBS (at 37°C, 95% O_2 and 5% CO_2) over time and analyzed the amount of NGF in DPBS at different time-points. The amount of NGF that could leak out did not exceed 10–12% after 3 days of incubation in a mimicked physiological microenvironment (**Supplementary Figure 1**). Notably, that level does not exceed sensitivity of the assay. It should be also noted that we detected no leak of cargo payload in our previous study in which the PLA-microchambers contained the excitatory neurotransmitter glutamate over at least 1 week (Kopach et al., 2019).

Clearly, the release and dissolution kinetics of signaling molecules in aqueous physiological solutions (the point of interest here) could vary widely across molecular species. Furthermore, control over this process could be an important issue in the experimental design. In our case, it has been difficult to detect small amounts of NGF in the medium, so that is why we focused on documenting its neurophysiological effects.

Individual Microchamber Opening Using NIR Laser

The NIR laser light (15 mW for 0.5 s) was focused only onto a ∼1 μm spot over an individual microchamber (i.e., on the microchamber base) to ensure the most local effect on the GNR aggregates in the microchamber wall. The exposure to laser light at 830 nm (**Figure 4B**) was accompanied by the appearance of a small gas bubble (**Figure 4C**) and by structural changes of the microchamber surface (**Figure 4D**). The microscopic bubble formation is associated with the liquid boiling on GNRs surface as a result of energy absorption and fast plasma formation occurring after liquid evaporation and subsequent vapor expansion, which are accompanied by a shock wave (Lauterborn and Ebeling, 1977; Baghdassarian et al., 1999; Link et al., 2000; Link and El-Sayed, 2001).

NIR lasers are used for heating up GNRs in the polymer shell because GNRs efficiently absorb laser energy (Gordel et al., 2014). The heating of light absorber agents such as GNRs by laser irradiation leads to the rapid melting of the carrier walls and subsequent cargo release (Radt et al., 2004; Skirtach et al., 2005, 2007; Singh, 2010). Although we did not measure the dynamics of local temperature during the laser-induced opening, it is known that laser irradiation of metallic plasmonic nanoparticles causes a very local heat increase, especially for isolated GNRs. In such cases, the temperature drops exponentially around plasmonic particles having a negligible impact on the environment (Govorov and Richardson, 2007), which was demonstrated in multilayer capsules with embedded GNR where the elevation of heat is within a one-micron spot (Skirtach et al., 2008). This has been presently confirmed to have no impact on live cells over a micron distance away from the laser exposure zone (Gai et al., 2018; Kopach et al., 2019). Again, we note that light absorption of an aqueous solution peaks at ∼970 nm. At 830 nm used here, it drops ∼20 times: in our case, the bulk of the energy is absorbed by nanoparticles and released as mechanical decomposition rather than heat. Besides, the structural PLA changes were found to take place from above 50°C (Zhou et al., 2015), with the reported PLA glass-melting transition point near 55–60°C (Marek and Veney, 2016). We ensured that no neighboring cells were affected by the NIR laser light during the microchamber opening as evidenced by the images shown.

Directed Neurite Outgrowth by Local N2A Cells Towards the Opened Microchambers With NGF Payload Inside

Next, we sought to test functional effects of NGF following the laser-triggered opening of microchambers. We utilized the human N2A cell line, a cell type providing rapid cell growth and differentiation to neuronal phenotype of human origin, as shown previously (Kopach et al., 2019). As expected, differentiating N2A cells developed typical axon-like processes and numerous neurites 1 d post-plating (**Figure 5A**), which could extend up to 50 μm in length, with morphogenesis progressing during cell growth.

First, we evaluated the NGF-induced effects on differentiating N2A cells grown on glass (control group). Since NGF is a highly potent neuropeptide acting in the ng/mL concentration range, we supplemented NGF to culture medium at the concentration of 10 and 100 ng/mL. There was a clear, dose-dependent effect of NGF on the neurite outgrowth by N2A cells observed after 1 day of cell differentiation with NGF (**Figures 5C,D**). The neurite length was on average ∼31.1 μm in control (0 NGF, $n = 666$ neurites), but ∼40.3 μm in the presence of 10 ng/mL NGF ($n = 541$ neurites; $p < 0.0001$) and ∼46.8 μm with 100 ng/mL NGF ($n = 544$ neurites, $p < 0.0001$; **Figure 5B**) for N2A cells of the same passage.

Next, we placed N2A cells on the surface of the fabricated MCA with NGF payload inside microchambers, and grew the cells on MCA. The cells showed no signs of toxic damage during their growth on the top of the fabricated MCA, thus confirming biocompatibility for this type of carriers. We monitored uninterrupted growth of differentiating N2A cells growing on the top of arrays, and away from the arrays, over at least 3 days, with no detectable location-specific deterioration of any kind. This is consistent with the previously reported biocompatibility of PLA as the constituent material in our recent study involving the same cell type and a variety of microchamber cargo loads (Kopach et al., 2019). We monitored N2A cells before and after laser-triggered opening of microchambers, throughout

the area of interest for several days. We could observe that, after microchamber opening, the cell density increased within the targeted area (**Figures 6A,B**) and that local cells extended their neurites towards the opened microchambers (**Figure 6A**, **Supplementary Figure 2**). These effects were observed across 6 independent experiments (fabricated MCA/cell preparations), at the day 1 or 2 after opening. The effect was observed regardless of the trajectory applied for microchamber opening: a line segment (**Figure 6A**, **Supplementary Figure 2**), or a sequence of line followed by rectangular or square shape (**Figure 7A**, **Supplementary Movies 2, 3**). These physiological effects further demonstrate that the heat-induced PLA melting required to open individual microchambers for site-specific NGF release was highly localized, leaving the integrity of most NGF molecules intact.

Finally, we carried out time-lapse recording of differentiating N2A cells before and after opening microchambers with NGF payload, by collecting images from the area of interest every 10 min, starting soon after plating N2A cells on the PLA arrays, for up to 3 days in total (**Figure 7**, **Supplementary Movie 2**). We detected an increased cell density within the targeted area, with a sharp rise in response to each sequence of microchamber opening (3 times, ∼20 h apart) (**Figure 7B**). On a finer scale, cells growing in close proximity to the opened microchambers directed their neurites towards the sites of NGF release from opened microchambers (**Figure 7**, images on an expanded scale; **Supplementary Movie 3**). These results demonstrate a directed neurite outgrowth triggered by the site-targeted cargo release from PLA-microchambers on demand. Moreover, the physiological effects observed following the light-triggered NGF release after ∼20 h confirm robust preservation of functional NGF inside microchambers over an extended time. This enables prolonged load storage and selective microchamber opening at a required time point, at a selected microscopic location.

The effects of NGF observed here in human N2A cells of neuronal phenotype are similar to those attributed to NGF across the literature when tested in cell lines and primary neuronal cultures (Craig and Banker, 1994; Jareb and Banker, 1997; Brann et al., 1999; Secondo et al., 2015; Selvaraj et al., 2015). This suggests a potential, in using this type of carrier matrixes, for functional modulation of individual cell activity in response to triggered release of neuropeptides.

CONCLUSION

The patterned PLA-based MCA are a versatile drug delivery system for site-specific, geometrically constrained cargo release on demand. Here, we confirm that the PLA-based matrix is fully biocompatible with human-derived cells, which is particularly important for highly sensitive cells of neuronal phenotype. Microchambers appear to provide safe loading for hydrophilic peptides and, because of the presence of light-absorbing gold nanoparticles in the container shell, enable laser-sensitive, site-specific cargo release on demand. Optical targeting of microchambers for drug release has triggered functional cell responses locally. Importantly, N2A cells demonstrate enhanced neurite outgrowth toward individual microchambers releasing NGF. The PLA-based MCA are therefore a potentially suitable platform for site-specific targeting of neuronal cells of human origin.

DATA AVAILABILITY STATEMENT

The raw data supporting the conclusions of this article will be made available by the authors, without undue reservation, to any qualified researcher.

AUTHOR CONTRIBUTIONS

OS, OK, MK, AS, DR, and GS: contributed conception and design of the study. GS, DR, OS, OK, and MK: experiment design and manuscript writing. OS, OK, and MK: conducting experiments. OK: cells state statistical analysis. MK and AS: design and development of optical system for chambers activation. DG: discussions. DR and GS: project supervision. All authors contributed to manuscript writing and revisions, they have approved the submitted version.

FUNDING

This work was supported by the Biological Sciences Research Council grant 315 BB/J001473/1 (DR, AS, and GS); Wellcome Trust Principal Fellowship (212251_Z_18_Z), ERC Advanced Grant (323113), and European Commission NEUROTWIN grant (857562) (DR); Russian Science Foundation - project number 19-75-10043 (OS) (development of NGF encapsulation approach), RFBR project number 19-32-60058 (MK) (optical setup for chambers activation).

ACKNOWLEDGMENTS

We thank Nadezda V. Tarakina for providing help with the gold nanorods TEM visualization.

SUPPLEMENTARY MATERIAL

The Supplementary Material for this article can be found online at: https://www.frontiersin.org/articles/10.3389/fbioe.2020.00497/full#supplementary-material

REFERENCES

Agarwal, A., Mackey, M. A., El-Sayed, M. A., and Bellamkonda, R. V. (2011). Remote triggered release of doxorubicin in tumors by synergistic application of thermosensitive liposomes and gold nanorods. *ACS Nano* 5, 4919–4926. doi: 10.1021/nn201010q

Alakrach, A. M., Noriman, N. Z., Dahham, O. S., Hamzah, R., Alsaadi, M. A., Shayfull, Z., et al. (2018). Chemical and hydrophobic properties

of PLA/HNTs-ZrO 2 bionanocomposites. *J. Phys. Conf. Ser.* 1019:012065. doi: 10.1088/1742-6596/1019/1/012065

Albinali, K., Zagho, M., Deng, Y., and Elzatahry, A. (2019). A perspective on magnetic core–shell carriers for responsive and targeted drug delivery systems. *Int. J. Nanomed.* 14, 1707–1723. doi: 10.2147/IJN.S193981

Baghdassarian, O., Tabbert, B., and Williams, G. A. (1999). Luminescence characteristics of laser-induced bubbles in water. *Phys. Rev. Lett.* 83, 2437–2440. doi: 10.1103/PhysRevLett.83.2437

Bettinger, C. J., Langer, R., and Borenstein, J. T. (2009). Engineering substrate topography at the micro- and nanoscale to control cell function. *Angew. Chemie Int. Ed.* 48, 5406–5415. doi: 10.1002/anie.200805179

Boisselier, E., and Astruc, D. (2009). Gold nanoparticles in nanomedicine: preparations, imaging, diagnostics, therapies and toxicity. *Chem. Soc. Rev.* 38, 1759–1782. doi: 10.1039/b806051g

Brann, A. B., Scott, R., Neuberger, Y., Abulafia, D., Boldin, S., Fainzilber, M., et al. (1999). Ceramide signaling downstream of the p75 neurotrophin receptor mediates the effects of nerve growth factor on outgrowth of cultured hippocampal neurons. *J. Neurosci.* 19, 8199–8206. doi: 10.1523/JNEUROSCI.19-19-08199.1999

Craig, A. M., and Banker, G. (1994). Neuronal polarity. *Ann. Rev. Neurosci.* 17, 267–310. doi: 10.1146/annurev.ne.17.030194.001411

Ermakov, A. V., Prikhozhdenko, E. S., Demina, P. A., Gorbachev, I. A., Vostrikova, A. M., Sapelkin, A. V., et al. (2019). Composite multilayer films based on polyelectrolytes and *in situ*-formed carbon nanostructures with enhanced photoluminescence and conductivity properties. *J. Appl. Polym. Sci.* 136:47718. doi: 10.1002/app.47718

Gai, M., Kurochkin, M. A., Li, D., Khlebtsov, B. N., Dong, L., Tarakina, N., et al. (2018). *In-situ* NIR-laser mediated bioactive substance delivery to single cell for EGFP expression based on biocompatible microchamber-arrays. *J. Control. Release* 276, 84–92. doi: 10.1016/j.jconrel.2018.02.044

Ge, X., Leng, Y., Lu, X., Ren, F., Wang, K., Ding, Y., et al. (2015). Bacterial responses to periodic micropillar array. *J. Biomed. Mater. Res. Part A* 103, 384–396. doi: 10.1002/jbm.a.35182

Gordel, M., Olesiak-Banska, J., Matczyszyn, K., Nogues, C., Buckle, M., and Samoc, M. (2014). Post-synthesis reshaping of gold nanorods using a femtosecond laser. *Phys. Chem. Chem. Phys.* 16, 71–78. doi: 10.1039/C3CP53457J

Govorov, A. O., and Richardson, H. H. (2007). Generating heat with metal nanoparticles. *Nano Today* 2, 30–38. doi: 10.1016/S1748-0132(07)70017-8

Jareb, M., and Banker, G. (1997). Inhibition of axonal growth by brefeldin A in hippocampal neurons in culture. *J. Neurosci.* 17, 8955–8963. doi: 10.1523/JNEUROSCI.17-23-08955.1997

Khlebtsov, B., Khanadeev, V., Pylaev, T., and Khlebtsov, N. (2011). A new T-matrix solvable model for nanorods: TEM-based ensemble simulations supported by experiments. *J. Phys. Chem. C* 115, 6317–6323. doi: 10.1021/jp2000078

Kiryukhin, M. V., Lau, H. H., Goh, S. H., Teh, C., Korzh, V., and Sadovoy, A. (2018). A membrane film sensor with encapsulated fluorescent dyes towards express freshness monitoring of packaged food. *Talanta* 182, 187–192. doi: 10.1016/j.talanta.2018.01.085

Kopach, O., Zheng, K., Sindeeva, O. A., Gai, M., Sukhorukov, G. B., and Rusakov, D. A. (2019). Polymer microchamber arrays for geometry-controlled drug release: a functional study in human cells of neuronal phenotype. *Biomater. Sci.* 7, 2358–2371. doi: 10.1039/C8BM01499J

Kunzmann, A., Andersson, B., Thurnherr, T., Krug, H., Scheynius, A., and Fadeel, B. (2011). Toxicology of engineered nanomaterials: focus on biocompatibility, biodistribution and biodegradation. *Biochim. Biophys. Acta Gen. Subj.* 1810, 361–373. doi: 10.1016/j.bbagen.2010.04.007

Kurochkin, M. A., Sindeeva, O., Brodovskaya, E. P., Gai, M., Frueh, J., Su, L., et al. (2020). Laser-triggered drug release from polymeric 3-D micro-structured films via optical fibers. *Mater. Sci. Eng. C* 110:110664. doi: 10.1016/j.msec.2020.110664

Lauterborn, W., and Ebeling, R. (1977). High-speed holography of laser-induced breakdown in liquids. *Appl. Phys. Lett.* 31, 663–664. doi: 10.1063/1.89495

Lee, J. H., and Yeo, Y. (2015). Controlled drug release from pharmaceutical nanocarriers. *Chem. Eng. Sci.* 125, 75–84. doi: 10.1016/j.ces.2014.08.046

Levi-Montalcini, R. (1987). The nerve growth factor 35 years later. *Science.* 237, 1154–1162. doi: 10.1126/science.3306916

Li, W., Xu, Z., Huang, J., Lin, X., Luo, R., Chen, C. H., et al. (2014). NeuroArray: a universal interface for patterning and interrogating neural circuitry with single cell resolution. *Sci. Rep.* 4:4784. doi: 10.1038/srep04784

Link, S., Burda, C., Nikoobakht, B., and El-Sayed, M. A. (2000). Laser-induced shape changes of colloidal gold nanorods using femtosecond and nanosecond laser pulses. *J. Phys. Chem. B* 104, 6152–6163. doi: 10.1021/jp000679t

Link, S., and El-Sayed, M. A. (2001). Spectroscopic determination of the melting energy of a gold nanorod. *J. Chem. Phys.* 114, 2362–2368. doi: 10.1063/1.1336140

Macha, I. J., Ben-Nissan, B., Vilchevskaya, E. N., Morozova, A. S., Abali, B. E., Müller, W. H., et al. (2019). Drug delivery from polymer-based nanopharmaceuticals—an experimental study complemented by simulations of selected diffusion processes. *Front. Bioeng. Biotechnol.* 7:37. doi: 10.3389/fbioe.2019.00037

Madzharova, F., Heiner, Z., Simke, J., Selve, S., and Kneipp, J. (2018). Gold nanostructures for plasmonic enhancement of hyper-raman scattering. *J. Phys. Chem. C* 122, 2931–2940. doi: 10.1021/acs.jpcc.7b10091

Marek, A. A., and Veney, V. (2016). Photochemical reactivity of PLA at the vicinity of glass transition temperature. the photo-rheology method. *Eur. Polymer. J.* 81, 239–246. doi: 10.1016/j.eurpolymj.2016.06.016

Midelet, J., El-Sagheer, A. H., Brown, T., Kanaras, A. G., and Werts, M. H. V. (2017). The sedimentation of colloidal nanoparticles in solution and its study using quantitative digital photography. *Part. Part. Syst. Char.* 34:1700095. doi: 10.1002/ppsc.201700095

Min, K. J., Kim, T. H., and Choi, J. W. (2017). Magnetic force-driven graphene patterns to direct synaptogenesis of human neuronal cells. *Material* 10:1151. doi: 10.3390/ma10101151

Nikoobakht, B., and El-Sayed, M. A. (2003). Preparation and growth mechanism of gold nanorods (NRs) using seed-mediated growth method. *Chem. Mater.* 15, 1957–1962. doi: 10.1021/cm020732l

Norman, J. J., and Desai, T. A. (2006). Methods for fabrication of nanoscale topography for tissue engineering scaffolds. *Ann. Biomed. Eng.* 34, 89–101. doi: 10.1007/s10439-005-9005-4

Pardo-Figuerez, M., Martin, N. R., Player, D. J., Roach, P., Christie, S. D., Capel, A. J., et al. (2018). Controlled arrangement of neuronal cells on surfaces functionalized with micropatterned polymer brushes. *ACS Omega* 3, 12383–12391. doi: 10.1021/acsomega.8b01698

Radt, B., Smith, T. A., and Caruso, F. (2004). Optically addressable nanostructured capsules. *Adv. Mater.* 16, 2184–2189. doi: 10.1002/adma.200400920

Schmalenberg, K. E., and Uhrich, K. E. (2005). Micropatterned polymer substrates control alignment of proliferating Schwann cells to direct neuronal regeneration. *Biomaterials* 26, 1423–1430. doi: 10.1016/j.biomaterials.2004.04.046

Secondo, A., Esposito, A., Sirabella, R., Boscia, F., Pannaccione, A., Molinaro, P., et al. (2015). Involvement of the Na+/Ca2+ exchanger isoform 1 (NCX1) in neuronal growth factor (NGF)-induced neuronal differentiation through Ca2+-dependent Akt phosphorylation. *J. Biol. Chem.* 290, 1319–1331. doi: 10.1074/jbc.M114.555516

Selvaraj, P., Huang, J. S., Chen, A., Skalka, N., Rosin-Arbesfeld, R., and Loh, Y. P. (2015). Neurotrophic factor-α1 modulates NGF-induced neurite outgrowth through interaction with Wnt-3a and Wnt-5a in PC12 cells and cortical neurons. *Mol. Cell Neurosci.* 68, 222–233. doi: 10.1016/j.mcn.2015.08.005

Sindeeva, O. A., Gusliakova, O. I., Inozemtseva, O. A., Abdurashitov, A. S., Brodovskaya, E. P., Gai, M., et al. (2018a). Effect of a controlled release of epinephrine hydrochloride from PLGA microchamber array: *in vivo* studies. *ACS Appl. Mater. Interfaces* 10, 37855–37864. doi: 10.1021/acsami.8b15109

Sindeeva, O. A., Prikhozhdenko, E. S., Bratashov, D. N., Vostrikova, A. M., Atkin, V. S., Ermakov, A. V., et al. (2018b). Carbon dot aggregates as an alternative to gold nanoparticles for the laser-induced opening of microchamber arrays. *Soft Matter* 14, 9012–9019. doi: 10.1039/C8SM01714J

Singh, S. (2010). Nanomedicine–nanoscale drugs and delivery systems. *J. Nanosci. Nanotechnol.* 10, 7906–7918. doi: 10.1166/jnn.2010.3617

Skirtach, A. G., Dejugnat, C., Braun, D., Susha, A. S., Rogach, A. L., Parak, W. J., et al. (2005). The role of metal nanoparticles in remote release of encapsulated materials. *Nano Lett.* 5, 1371–1377. doi: 10.1021/nl050693n

Skirtach, A. G., Déjugnat, C., Braun, D., Susha, A. S., Rogach, A. L., and Sukhorukov, G. B. (2007). Nanoparticles distribution control by

polymers: aggregates versus nonaggregates. *J. Phys. Chem. C* 111, 555–564. doi: 10.1021/jp065635k

Skirtach, A. G., Karageorgiev, P., De Geest, B. G., Pazos-Perez, N., Braun, D., and Sukhorukov, G. B. (2008). Nanorodsas wavelength-selective absorptioncentersin the visible and near-infraredregions of the electromagnetic spectrum. *Adv. Mater.* 20, 506–510. doi: 10.1002/adma.200701542

Sousa, M. P., Arab-Tehrany, E., Cleymand, F., and Mano, J. F. (2019). Surface micro- and nanoengineering: applications of layer-by-layer technology as a versatile tool to control cellular behavior. *Small* 15:1901228. doi: 10.1002/smll.201901228

Sperling, R. A., Rivera Gil, P., Zhang, F., Zanella, M., and Parak, W. J. (2008). Biological applications of gold nanoparticles. *Chem. Soc. Rev.* 37, 1896–1908. doi: 10.1039/b712170a

Wijaya, A., Schaffer, S. B., Pallares, I. G., and Hamad-Schifferli, K. (2009). Selective release of multiple DNA oligonucleotides from gold nanorods. *ACS Nano* 3, 80–86. doi: 10.1021/nn800702n

Zhou, C., Li, H., Zhang, Y., Xue, F., Huang, S., Wen, H., et al. (2015). Deformation and structure evolution of glassypoly(lactic acid) below the glass transition temperature. *CrystEngComm* 17, 5651–5663. doi: 10.1039/C5CE00669D

Zykova, Y., Kudryavtseva, V., Gai, M., Kozelskaya, A., Frueh, J., Sukhorukov, G., et al. (2019). Free-standing microchamber arrays as a biodegradable drug depot system for implant coatings. *Eur. Polym. J.* 114, 72–80. doi: 10.1016/j.eurpolymj.2019.02.029

Conflict of Interest: The authors declare that the research was conducted in the absence of any commercial or financial relationships that could be construed as a potential conflict of interest.

frontiers in Bioengineering and Biotechnology

ORIGINAL RESEARCH
published: 03 July 2020
doi: 10.3389/fbioe.2020.00690

Lipid-Based Nanovesicles for Simultaneous Intracellular Delivery of Hydrophobic, Hydrophilic, and Amphiphilic Species

Antonella Zacheo[1], Luca Bizzarro[2], Laura Blasi[3], Clara Piccirillo[1], Antonio Cardone[4], Giuseppe Gigli[1,5], Andrea Ragusa[1,6] and Alessandra Quarta[1]**

[1] CNR NANOTEC—Institute of Nanotechnology, c/o Campus Ecotekne, Lecce, Italy, [2] Dipartimento di Scienze Biomolecolari (DISB), University of Urbino Carlo Bo, Urbino, Italy, [3] CNR, Institute for Microelectronics and Microsystems, Lecce, Italy, [4] Institute of Chemistry of OrganoMetallic Compounds—ICCOM, Italian National Council of Research—CNR, Bari, Italy, [5] Department of Mathematics and Physics E. de Giorgi, University of Salento, Campus Ecotekne, Lecce, Italy, [6] Department of Biological and Environmental Sciences and Technologies, University of Salento, Lecce, Italy

OPEN ACCESS

Edited by:
Angela Tino,
National Research Council (CNR), Italy

Reviewed by:
Federica Sodano,
University of Turin, Italy
Alfredo Ambrosone,
University of Salerno, Italy
Monica Terracciano,
University of Naples Federico II, Italy

***Correspondence:**
Andrea Ragusa
andrea.ragusa@unisalento.it
Alessandra Quarta
alessandra.quarta@nanotec.cnr.it

Specialty section:
This article was submitted to Nanobiotechnology, a section of the journal Frontiers in Bioengineering and Biotechnology

Received: 31 March 2020
Accepted: 02 June 2020
Published: 03 July 2020

Citation:
Zacheo A, Bizzarro L, Blasi L, Piccirillo C, Cardone A, Gigli G, Ragusa A and Quarta A (2020) Lipid-Based Nanovesicles for Simultaneous Intracellular Delivery of Hydrophobic, Hydrophilic, and Amphiphilic Species. Front. Bioeng. Biotechnol. 8:690. doi: 10.3389/fbioe.2020.00690

Lipid nanovesicles (NVs) are the first nanoformulation that entered the clinical use in oncology for the treatment of solid tumors. They are indeed versatile systems which can be loaded with either hydrophobic or hydrophilic molecules, for both imaging and drug delivery, and with high biocompatibility, and limited immunogenicity. In the present work, NVs with a lipid composition resembling that of natural vesicles were prepared using the ultrasonication method. The NVs were successfully loaded with fluorophores molecules (DOP-F-DS and a fluorescent protein), inorganic nanoparticles (quantum dots and magnetic nanoparticles), and anti-cancer drugs (SN-38 and doxorubicin). The encapsulation of such different molecules showed the versatility of the developed systems. The size of the vesicles varied from 100 up to 300 nm depending on the type of loaded species, which were accommodated either into the lipid bilayer or into the aqueous core according to their hydrophobic or hydrophilic nature. Viability assays were performed on cellular models of breast cancer (MCF-7 and MDA-MB-231). Results showed that NVs with encapsulated both drugs simultaneously led to a significant reduction of the cellular activity (up to 22%) compared to the free drugs or to the NVs encapsulated with only one drug. Lipidomic analysis suggested that the mechanism of action of the drugs is the same, whether they are free or encapsulated, but administration of the drugs by means of nanovesicles is more efficient in inducing cellular damage, likely because of a quicker internalization and a sustained release. This study confirms the versatility and the potential of lipid NVs for cancer treatment, as well as the validity of the ultrasound preparation method for their preparation.

Keywords: nanovesicle, nanoparticle, doxorubicin, SN-38, breast cancer, lipidomic analysis

INTRODUCTION

Lipid-based vesicles are the most commonly used carriers for drug delivery in nanomedicine thanks to their ease of preparation, excellent biocompatibility, and structural plasticity. They are conventionally defined as spherical vesicles characterized by an outer bilayer of lipids with an internal aqueous cavity. Since the first description of liposomal formulation, almost 60 years ago,

many types of lipid vesicles have been developed for applications in various areas, including drug and gene delivery (Grimaldi et al., 2016). Some of them have been already approved for clinical use in cancer chemotherapy as carriers of pharmaceuticals, such as doxorubicin, irinotecan, cisplatin, and placlitaxel (Bulbake et al., 2017). Other formulations are currently under clinical evaluation for the delivery of drugs in cancer and other diseases.

The considerable research efforts in this area are motivated by the numerous benefits provided by the use of liposomes, including their ability to host both lipophilic and hydrophilic molecules, the presence of an aqueous core that can accommodate large compounds, the high affinity with the cell membrane that facilitates their internalization, the biodegradability and the negligible toxicity of the vesicle components. Indeed, they are generally composed of natural lipids; among them, phospholipids, such as phosphatidylethanolamine and phosphatidylcholine, and sterols, such as cholesterol, have been used as components of the bilayer (Li et al., 2019).

The amount of cholesterol and the length and saturation of the hydrocarbon chains of the phospholipids affect the rigidity and the stability of the bilayer, and in turn the capability of the NVs to host and release drugs/biomolecules (Monteiro et al., 2014). On the other hand, functionalization of the hydrophilic heads of the lipids with polymers or biomolecules, provides additional features to the vesicle surface, thus shaping their interaction with blood components, tissues, and the immune system *in vivo* (Riaz et al., 2018). For instance, surface coating with polyethyleneglycol (PEG) polymer chains has been demonstrated to ameliorate the colloidal stability of the liposomes and hence their capability to elude the immune system and prolong the circulation time (Nkanga et al., 2019).

Depending on the preparation method, it is possible to tune both size and lamellarity of lipid-based vesicles. Conventional synthetic approaches, which include film hydration, reverse-phase evaporation, and detergent dialysis, can produce multilamellar vesicles; however, they suffer from high size polydispersity and low reproducibility (Kraft et al., 2014). On the other hand, methods based on the application of mechanical forces, such as sonication and homogenization, allow for a finer control of the vesicle's size and uniformity. More recently, microfluidic technologies have been applied to the synthesis of uniform lipid vesicles (Carugo et al., 2016).

In a previous work, we also designed a microfluidic system for the preparation of lipid nanovesicles with highly homogeneous size distribution and good reproducibility (Zacheo et al., 2015). However, this method suffers from low particle yield per volume and long preparation times. In the present work, NVs with a similar lipid composition were prepared using the more versatile ultrasonication method (Klingler et al., 2015; Salvi and Pawar, 2019). NVs were synthesized combining two phospholipids [1-lauroyl-2-hydroxy-*sn*-glycero-3-phosphocholine (LPC) and 1,2-dilauroyl-*sn*-glycero-3-phosphocholine (DLPC)] with a ceramide [*N*-lauroyl-D-erythro-sphingosine (CER)] and cholesterol (CHOL). The molar ratio of the lipids was set in order to resemble the lipid composition of vesicles naturally released by cells, that are typically rich in cholesterol, sphingolipids, and phospholipids (Antimisiaris et al., 2018; Skotland et al., 2019). To demonstrate the high versatility of this system, several compounds with different physico-chemical properties (i.e., hydrophilic, hydrophobic, and amphiphilic molecules) and dimensions (with molecular weight ranging from few hundreds Da to hundreds kDa) were encapsulated into the NVs. More specifically, inorganic nanocrystals, such as quantum dots (QDs) and magnetic nanoparticles (MNPs), an organic amphiphilic fluorophore (i.e., DOP-F-DS), the transferrin protein, and two anticancer drugs (i.e., doxorubicin and SN-38) were loaded either into the bilayer or into the core.

Doxorubicin (DOXO) is commonly employed in the chemotherapy of several solid tumors and leukemia, especially in its lipid-based formulation, the first one to be approved for clinical use (Barenholz, 2012). On the other hand, SN-38, namely 7-ethyl-10-hydroxy camptothecin, is a topoisomerase I inhibitor used in cancer therapy against solid tumors such as colon carcinoma, breast, ovarian, and pancreatic cancers (Wallin et al., 2008). It is characterized by low water solubility and poor stability in the blood stream. Therefore, high doses are needed in clinical therapy, also causing serious toxic side-effects in patients. As such, a liposomal formulation of this drug would provide its beneficial protection until reaching the target site and a prolonged circulation time of the active ingredient (Fang et al., 2018).

The prepared NVs were fully characterized and the thermal stability, size, morphology, surface charge, and colloidal stability over time assessed. The efficiency of the drug encapsulation and the effectiveness of the system as anti-cancer carrier were tested on selected human cancer cellular lines—MCF-7 and MDA-MB-231. Furthermore, the effect of the two drugs, either free or loaded into the NVs, on the cancer cells was studied via lipidomic analysis. This type of study is gaining increasing attention as it can provide valuable information about the changes that occur upon a particular stimulus, such as drug administration (Zhao et al., 2015; Perrotti et al., 2016). Lipids are the mayor constituents of the cellular membrane and they are also involved in many biological processes strongly related to carcinogenic pathways, such as transformation, progression, and metastasis, and their composition is altered in many neoplastic diseases (Giudetti et al., 2019). Nuclear magnetic resonance (NMR) analysis of the variation in the lipid composition upon drug treatment can thus provide valuable information about efficacy and progression of the treatment.

MATERIALS AND METHODS

1,2-Dilauroyl-*sn*-glycero-3-phosphocholine (DLPC, 12:0), 1-lauroyl-2-hydroxy-*sn*-glycero-3-phosphocholine (LPC, 12:0), cholesterol (ovine wool >98%, CHOL), and *N*-lauroyl-D-erythro-sphingosine (saturated ceramide, d18: 1/12: 0, CER) were purchased from Avanti Polar Lipids. The molecular formulas of the lipids are reported in **Figure 1**. Doxorubicin and transferrin-TRITC were purchased from Sigma-Aldrich and ThermoFisher, respectively. SN-38 was a kind gift from Ospedale Oncologico Giovanni Paolo II in Bari, Italy. The

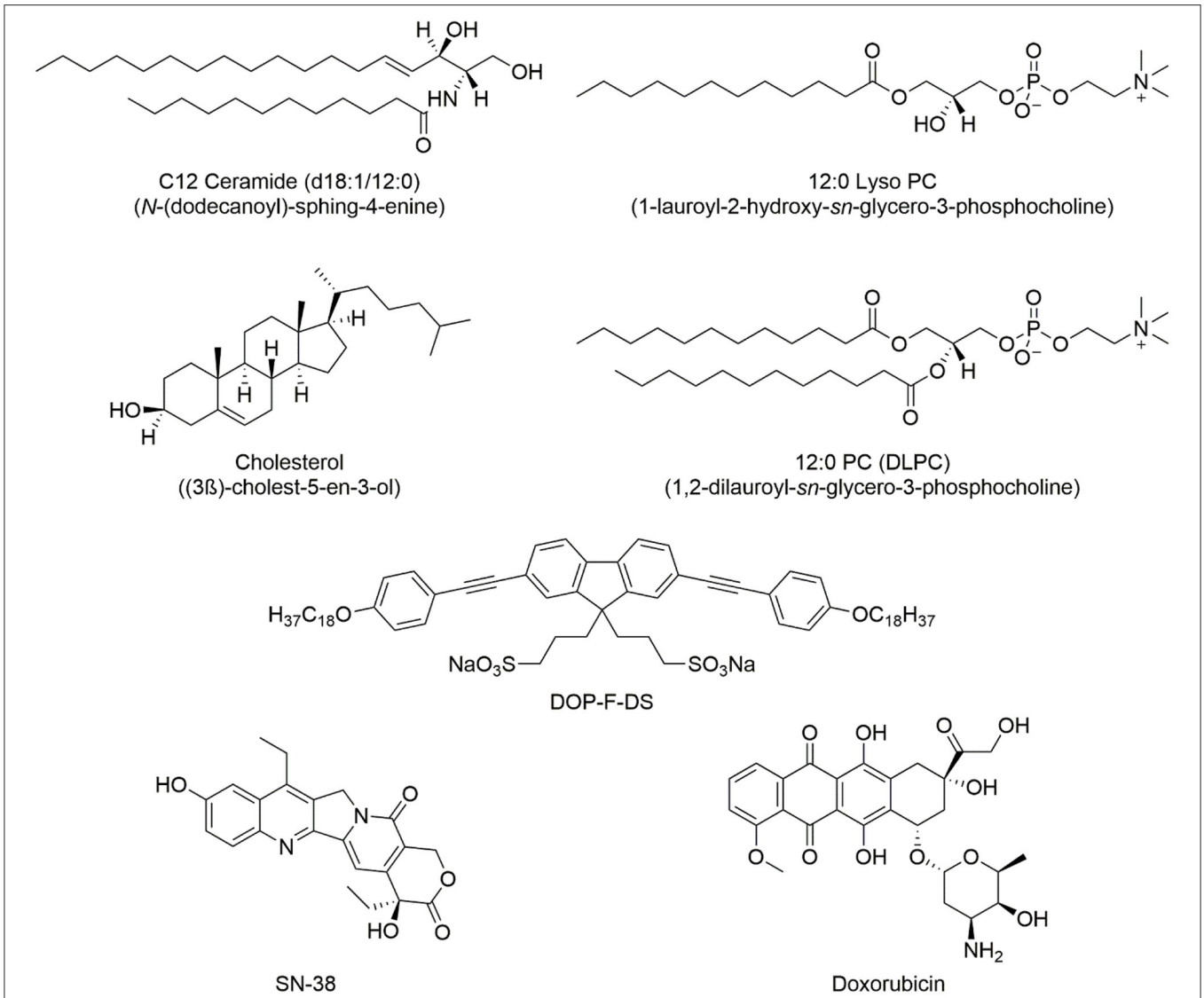

FIGURE 1 | Chemical structure of the lipids used in the synthesis of the NVs and the encapsulated organic molecules, (i.e., the DOP-F-DS fluorophore and the two drugs used in cellular study).

organic fluorophore DOP-F-DS (**Figure 1**) was prepared as previously reported in the literature (Cardone et al., 2012). CdSe/ZnS QDs and iron oxide MNPs were prepared according to the procedures reported in the literature (Dabbousi et al., 1997; Hyeon et al., 2001). The two cell lines, namely MCF-7 and MDA-MB-231, were obtained from ATCC.

Synthesis and Characterization of the Nanovesicles

A mixture of lipids consisting of DLPC, CHOL, LPC, and CER with respective ratios of 4.5:4:1:0.5 was used for the synthesis of the vesicles (final concentration 5 mM in 5 mL of chloroform). The phospholipid solution was stirred for 1 h with the cap closed to prevent any loss of solvent. Subsequently, the cap was removed and the solution left stirring overnight at room temperature to evaporate the solvent. Phosphate saline buffer (PBS) was then added and the solution was sonicated for 4 min at a power of 25 W and at 20 kHz frequency. During the sonication the vial was kept into an ice bath to prevent overheating of the solution.

To prepare the vesicles containing transferrin-TRITC and the blue-emitting DOP-F-DS organic fluorophore, 150 μL of DOP-F-DS (1 mg/mL in DMSO), and 50 μL of transferrin-TRICT (5 mg/mL in PBS) were respectively employed. To load SN-38 into the liposomes, 200 μL of the drug dissolved in DMSO (200 μM) were added to the phospholipids in chloroform and the mixture was left under vigorous stirring for 60 min. Subsequently, the vesicles were prepared following the protocol already described. The hydrophobicity of the SN-38 molecule facilitates its intercalation within the double phospholipidic layer of the liposomes. In the case of doxorubicin, the drug dissolved in PBS (85.8 μM final concentration) was added to the dry phospholipid film. The NVs were then prepared as already

TABLE 1 | Conditions employed for the preparation of the nanovesicles (type of loaded species, volume, concentration, and solvent used) and their application in this study.

Loaded species	Volume	Concentration	Application
DOP-F-DS	15 μL	8.4 mM in DMSO	Uptake analysis
Transferrin-TRITC	25 μL	13 mM in PBS	Uptake analysis
DOP-F-DS	15 μL	8.4 mM in DMSO	Uptake analysis
+ Transferrin-TRITC	25 μL	13 mM in PBS	
Doxorubicin	25 μL	17.2 mM in PBS	Antitumor activity
SN-38	25 μL	2.5 mM in DMSO	Antitumor activity
Doxorubicin	25 μL	17.2 mM in PBS	Antitumor activity
+ SN-38	25 μL	2.5 mM in DMSO	
Surfactant-coated MNPs	25 μL	3 μM in $CHCl_3$	Magnetic responsiveness
Surfactant-coated QDs	15 μL	6 μM in $CHCl_3$	Uptake analysis

described. To load both drugs into the vesicles, solutions at the same concentration as before were used. The NVs were then prepared according to the standard conditions but sonicated for longer time (6 min). To encapsulate the inorganic nanoparticles within the vesicles, few microliters of a chloroform solution of either QDs or MNPs were added to the starting lipid mixture (see **Table 1** for details).

The solution containing the formed vesicles was then transferred into a dialysis tube (50 kDa MWCO), placed into 2 L of PBS, and kept under stirring at 4°C for 48 h. After purification, the nanovesicles were fully characterized.

Size and morphology of the lipid vesicles were monitored through transmission electron microscopy (TEM) and dynamic light scattering (DLS) measures. Low-magnification TEM images of the nanovesicles were recorded on a JEOL Jem1011 microscope operating at an accelerating voltage of 100 kV. DLS and zeta potential measurements were performed in PBS at 25°C using a Zetasizer Nano ZS90 (Malvern Instruments Ldt) equipped with a 4.0 mW He–Ne laser operating at 633 nm and with an avalanche photodiode detector.

Thermal stability was assessed by thermogravimetric analysis (TGA) using SDT Q600 equipment (TA Instruments) with a heat ramp of 5°C/min and an air flow rate of 100 mL/min. After synthesis of the NVs, the solvent was evaporated and the analysis was performed on the residual dry matter. Control analyses were also done on the free lipids, which were mixed in chloroform at the same molar ratio before removing the solvent.

Encapsulation efficiency (*EE*) and release profile of the encapsulated drugs were determined spectrophotometrically with a fluorescence spectrometer (Cary Eclipse) measuring the fluorescence intensity of the drugs. A calibration curve at known concentrations of the molecules was first prepared. The amount of free drug dissolved in the dialysis medium (PBS), after purification, was measured and the *EE*, expressed as percentage of encapsulated molecules over the total, was calculated according to the formula:

$$EE\ (\%) = \frac{(Initial\ drug\ amount - free\ drug\ in\ the\ dyalisis\ medium)}{Initial\ drug\ amount} \times 100$$

To determine the drug release profile, samples were kept at 37°C at two pH (4.5 and 7.4) for different time lengths (6, 24, 48, 96, and 120 h). The vesicles were then pelleted and the amount of drug in the supernatant quantified. The released amount at each time point, expressed as percentage over the total encapsulated, was estimated according to the formula:

$$Released\ amount\ (\%) = \frac{released\ drug\ concentration}{encapsulated\ drug\ concentration} \times 100$$

Cellular Studies

Viability Assays

Two human cell lines of mammary carcinoma, namely MCF-7 and MBA-MB-231, were used. The cells were grown in DMEM medium supplemented with 10% of fetal bovine serum (FBS), 2 mM glutamine, 100 IU/mL of penicillin, and 100 μg/mL of streptomycin, and were cultured in an incubator at 37°C in a humidified atmosphere with 5% CO_2.

Two viability assays were performed, namely MTT and Trypan blue assays. In detail, 5×10^4 cells suspended in 200 μL of culture medium were seeded into each well of 96 multiwell plates. After 24 h incubation at 37°C, the nanovesicles were added to the wells at a defined concentration (each point triplicated) and the cells were kept under incubation for three different times, 24, 48, and 120 h.

In the case of the MTT assay, at the end of the incubation time, the medium was removed, the cells were washed twice with PBS, and 200 μL of fresh serum-free medium containing 1 mg/mL MTT were added to each well. After 3 h of incubation at 37°C, the medium was discarded from the wells and 200 μL of DMSO were added to dissolve the formazan salts. The plate was stirred for a few minutes at ambient temperature and the absorbance of the solution at 570 nm was measured on a microplate reader. To determine the percentage of cell viability, the treated samples were compared to the control samples according to the equation:

$$Cell\ viability\ (\%) = \frac{Absorbance\ of\ the\ NVs - containing\ sample}{Absorbance\ of\ the\ control\ sample} \times 100$$

To check the presence of a synergic effect by the combined delivery of the two drugs, the combination index (CI) was also determined according to the following formula (Chou and Talalay, 1984):

$$CI_{50} = \frac{C_A}{IC_{50A}} + \frac{C_B}{IC_{50B}}$$

where C_A and C_B are the concentrations of drugs A and B co-loaded into the NVs that were used to achieve the IC_{50} effect. IC_{50A} and IC_{50B} are the concentrations of the single drugs used to achieve the same effect on cell viability.

In the case of the Trypan blue assay, at the end of the incubation time, the medium was removed, the cells were washed twice with PBS, and 100 μL of PBS containing Trypan blue diluted 1/10 were added to each well. Soon after, the plates were analyzed under the microscope and the number of viable

and dead cells was counted. The cell viability was determined as follows:

$$Cell\ viability\ (\%) = \frac{Number\ of\ viable\ cells}{Number\ of\ total\ cells} \times 100$$

Lipidomic Analysis

MDA-MB-231 cells (1×10^8 cells/well, three replicates each) were treated with the empty nanovesicles, with the free drugs alone or in combination, and with the nanovesicles loaded with either one or both drugs. After 24 h incubation, cells were quenched and the lipid fraction extracted according to previously published procedures (Sündermann et al., 2016). The extracts were dried under a gentle nitrogen flow, dissolved in 600 μL of deuterated chloroform containing 0.03% of tetramethylsilane (TMS), used as the reference, and transferred into 5 mm NMR tubes.

Spectra were acquired on a Varian INOVA spectrometer (Varian Inc., CA) operating at 499.792 MHz and equipped with a OneNMR Probe-PT (Agilent). Acquisition parameters were set as follows: *s2pul* pulse sequence, 128 scans, 25°C, pulse angle 45°, sw 8012.8 Hz, relaxation delay 1 s, acquisition time 2.045 s, np 32,768, complex points 16,384, observed pulse 4.85, calibration *pw90* 9.70 μs. The resulting spectra were Fourier-transformed, phase corrected, and calibrated to the signal of TMS. The region between 0.5 and 5.5 ppm was binned into 0.02 ppm-wide buckets (equal to 238 variables) and exported to a csv file containing the data for all samples. The obtained matrix was normalized to the total sum and Pareto scaled before multivariate statistical analysis.

Confocal Microscopy Imaging

For cell imaging analysis, 10^5 cells were seeded onto a coverslip placed into each well of a six-well plate. After 24 h, the fluorescent nanovesicles were added to each well and the cells were incubated for the settled time (6, 24, and 48 h). Then, they were washed with PBS and fixed with 4% paraformaldehyde prior to be imaged by means of a Leica confocal microscope (TCS-SP5, Leica, Mannheim, Germany) equipped with an Argon laser source (excitation at 488 nm for green emitting QDs, at 545 nm for Transferrin-TRITC and Phalloidin-TRITC) and a pulsed laser (excitation at 405 nm for DOP-F-DS and DAPI).

For the colocalization study, MDA-MB-231 cells were seeded as already described and then incubated with the NVs loaded with transferrin-TRITC for the settled time (6, 24, and 48 h). Then, cells were washed with PBS and stained with Lysotracker green (Molecular probes) according to the manufacturer protocol. The samples were imaged by means of the confocal laser scanning microscopy (CLSM).

Statistical Analysis

All data represent the average value of at least three independent experiments, unless otherwise specified. Normally distributed data was compared with a two-tailed Student's *t*-test using GraphPad Prism software (version 6.0). The bars in graphs represent mean ± S.D. values. Differences were considered significant when the *p*-value was <0.05. Multivariate statistical analysis in the lipidomic study was performed with SIMCA 14.1 software (MKS Umetrics, Malmö, Sweden) using pairs of classes in each analysis (control vs. free drugs; control vs. encapsulated drugs; free drugs vs. encapsulated drugs; control vs. empty NVs). Orthogonal partial least-squares discriminant analysis (OPLS-DA) was performed using the NMR buckets as variables, the samples as observations, and the formulations (drugs-loaded NVs, empty NVs, free drugs, no drugs) as classes. Cumulative R^2_X and R^2_Y were used as parameters for describing the goodness of the fit.

RESULTS AND DISCUSSION

Synthesis and Characterization of Lipid Nanovesicles

NVs were prepared using the above-mentioned compounds according to the molar ratio DLPC/CHOL/LPC/CER 4.5:4.0:1.0:0.5. The lipid composition of these vesicles was designed to mimic the structure of the extracellular vesicles released physiologically by the cells having important roles in intercellular communication and in the onset and transmission of diseases (Trajkovic et al., 2008; De Toro et al., 2015; Zhang et al., 2015; Sarko and McKinney, 2017; Skotland et al., 2017; Steinbichler et al., 2017). This affinity should in turn facilitate the interaction with the cell membrane and promote cellular uptake.

Simultaneous encapsulation of hydrophobic, hydrophilic, and amphiphilic species inside the NVs was achieved, with the hydrophobic molecules being located into the lipid bilayer while the hydrophilic ones into the aqueous core. An intermediate behavior would be expected in the case of amphiphilic molecules. Several parameters, such as the molar ratios of the three components, sonication time and power together with the volumes of PBS were modulated to obtain particles with an average size around 100 nm and a good size distribution. Particles with the desired characteristics were obtained by sonicating at 25 W for 4 min.

To study the thermal stability of the developed nanovesicles, TGA analysis was performed and the results are reported in **Figure 2**. As a comparison, the test was also performed on the free lipid components. The weight loss percentage (**Figure 2A**) showed a completely different behavior between the nanovesicles and the free lipids; for the lipids, in fact, complete degradation was observed for $200 < T < 600$°C. Such degradation took place in two main steps, the first corresponding to a weight loss of about 70% ($T < 350$°C) while the second of about 25% ($T > 350$°C). The curve of the first derivative (**Figure 2B**) highlighted additional smaller steps at lower temperatures.

On the other hand, the data showed a much higher stability of the nanovesicles, as very small weight loss (about 5%) was observed for $T < 700$°C, while their degradation took place between 700 and 900°C. This behavior was confirmed by the first derivative curve.

Significative differences between the nanovesicles and the free lipids could be also observed in the DTA curves (**Figure 2C**). For the free lipids, in fact, an exothermic peak was observed for $200 < T < 400$°C; this can be due to the combustion of some organic fragments/molecules, in agreement with the

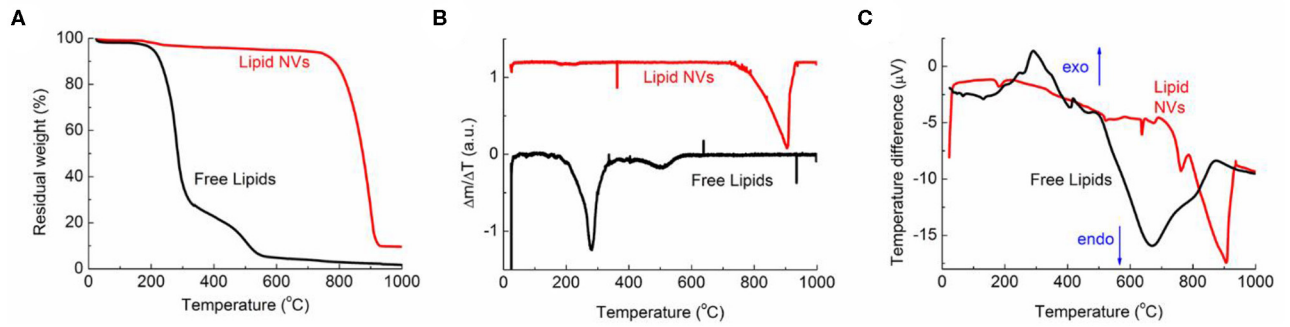

FIGURE 2 | TGA and DSC data for NVs (red curve) and free lipids (black curve). **(A)** Percentage weight, **(B)** first derivative curves, and **(C)** DSC data.

literature (López-González et al., 2015). This peak is not present in the corresponding curve of the nanovesicles, indicating that the formation of the vesicle structure makes the whole system more thermally stable. The endothermic peaks, corresponding to the full chemical degradation of the molecules/nanovesicles, can be observed in both curves, but at different temperatures, (i.e., between $500 < T < 800°C$ and $770 < T < 900°C$ for free lipids and nanovesicles, respectively). Literature data already report of increased thermal stability of the vesicle structure in comparison to the free compounds (Pinilla et al., 2019). This is likely due to the different special arrangements of the molecules; indeed, stronger interactions can take place when lipids are confined in a layer, leading to a more thermally stable system.

Different molecules were loaded into the vesicles, as listed in **Table 1**, either in the lipid bilayer or the aqueous core, according to their physico-chemical characteristics. The same sonication power was used for all experiments, although a longer duration (6 min compared to the four used for all the other cargos) was necessary only when both drugs were encapsulated simultaneously.

The procedure was slightly modified depending on the hydrophobic/hydrophilic/amphiphilic nature of the species to be introduced into the vesicles. In the case of the amphiphilic DOP-F-DS fluorophore or the hydrophobic antineoplastic SN-38 drug, the species were added to the lipid suspension. On the other hand, when hydrophilic molecules, such as the fluorescent transferrin or doxorubicin, had to be encapsulated, they were dissolved in PBS and then added to the lipid dry film before sonication.

The vesicles were analyzed by different techniques to determine their morphology, size, charge and thermal stability. **Figure 3** shows the TEM images of the empty NVs and of the NVs loaded with different species, such as hydrophobic QDs, MNPs, the amphiphilic fluorophore DOP-F-DS, transferrin-TRITC, both DOP-F-DS and transferrin-TRITC, doxorubicin, SN-38, and both drugs.

The empty vesicles displayed an average size of about 65 nm but did not present regular contours. On the other hand, when the vesicles were loaded with inorganic nanoparticles (i.e., QDs and MNPs), their structure became more regular with an evident turgidity and three-dimensionality. This effect could be caused by the evaporation of the solvent during TEM sample preparation, with a different outcome depending on the inner lipid support structure. In fact, while empty vesicles are free to shrink while drying, the presence of inorganic nanoparticles inside the core provides a physical resistance to the contraction. It is likely that both QDs and MNPs accommodate inside the lipid bilayer because of their hydrophobic nature (thanks to the alkyl chains of the surfactants covering the inorganic core). However, the thickness of such layer should be smaller than 4 nm considering that the phospholipids have an alkyl chain of 12 carbon atoms, while the average core diameter of the QDs and of the MNPs is around 4 and 6 nm, respectively, as determined by TEM analysis (**Figure S1**). Moreover, both inorganic NPs are coated by surfactant molecules that would further increase their size of about 1 nm. As a result, the dimension of the inorganic particles should exceed significantly that calculated for the double layer. Despite this, both QDs and MNPs were successfully incorporated in the NVs, probably because of the flexibility of the lipid bilayer. Indeed, other studies already reported the encapsulation of inorganic nanoparticles with size comparable or even larger than that of the bilayer thickness. QDs, for instance, were incorporated into the lipid shell because of such flexibility, leading in some cases to the formation of small protrusions (Al-Jamal et al., 2008; Bothun et al., 2009; Kethineedi et al., 2013).

TEM images of the vesicles encapsulating the nanocrystals showed regular and uniform morphology with an average diameter of about 104 nm in the case of QD-loaded NVs, and of about 125 nm for the magnetic ones (**Table 2**; see also **Figure S4** for the histograms of the size distribution). **Figure 3D** shows the morphology of the lipid vesicles loaded with the organic DOP-F-DS fluorophore, whose average size is about 67 nm, comparable to that of empty liposomes: it is highly plausible that its alkyl chain is situated into the lipid bilayer (Cardone et al., 2012). The image of panel E refers to the vesicles loaded with transferrin-TRICT (a protein with 80 kDa molecular weight): the hydrophilic nature of the protein suggests an accommodation into the aqueous core, leading to an enlargement of the vesicle diameter up to 78 nm. The same sample was imaged after 2 weeks of storage in PBS at 4°C (**Figure S2**): size and the of the vesicles were retained but it can be denoted the presence of debris, material depots on the grid bed that may be due to an initial degradation of the lipid texture. Panel F refers to the vesicles loaded with

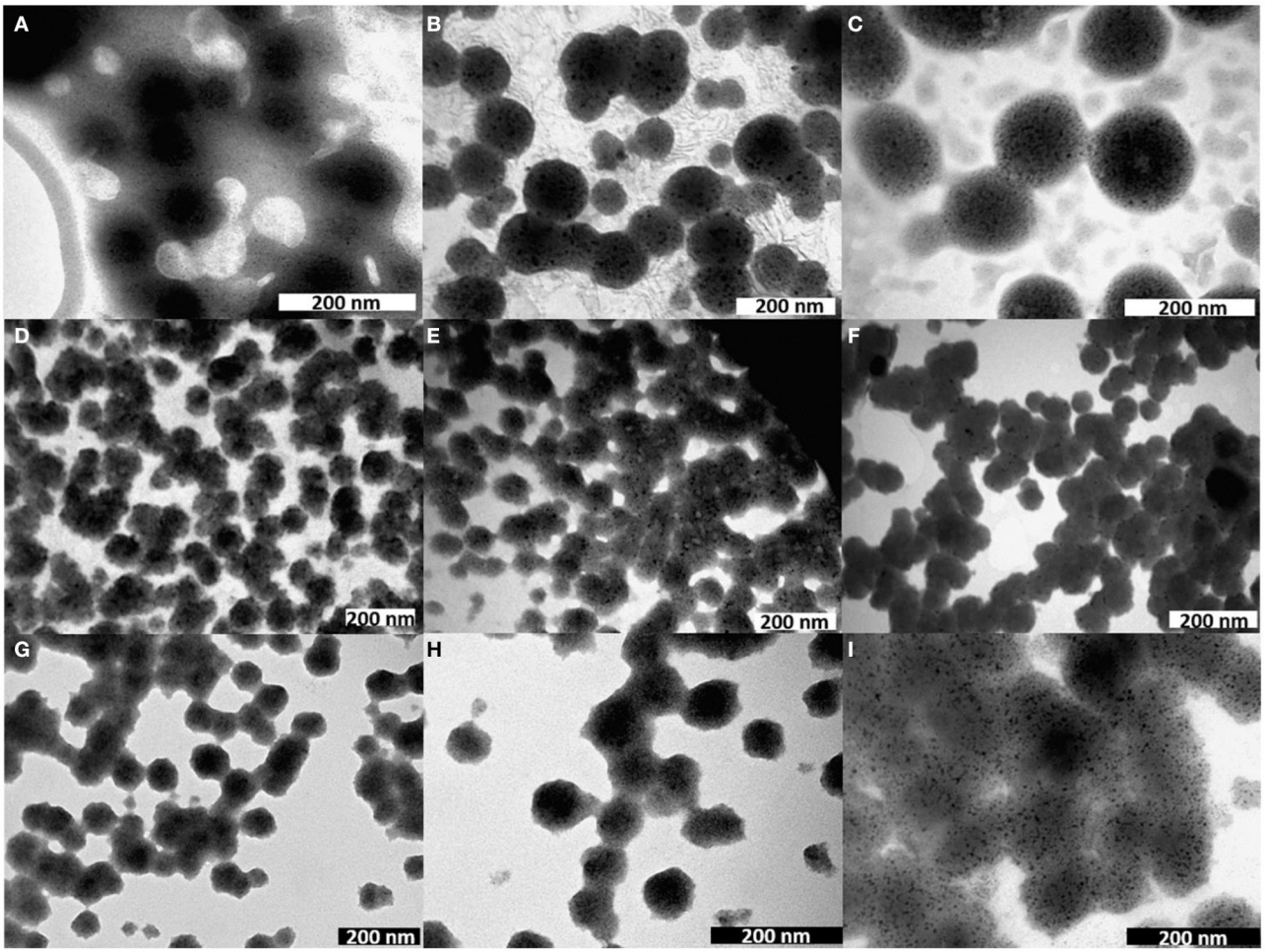

FIGURE 3 | TEM images of nanovesicles either empty **(A)** or loaded with **(B)** QDs, **(C)** MNPs, **(D)** DOP-F-DS, **(E)** transferrin-TRITC, **(F)** DOP-F-DS, and transferrin-TRITC, **(G)** doxorubicin, **(H)** SN-38, and **(I)** both drugs.

TABLE 2 | Average size of the lipid vesicles, either empty or loaded with different molecules, estimated through Image J Software on TEM images of the particles (second column), and by DLS analysis (third column).

Lipid vesicles	Average size from TEM images (nm)	Average size from DLS (nm)	PDI	Surface charge (mV)
Empty	65 ± 8	137 ± 11	0.27	−4.9 ± 0.3
QDs (4 nm size)	104 ± 13	278 ± 21	0.29	−5.7 ± 0.6
MNPs (6 nm size)	125 ± 12	319 ± 24	0.34	−4.8 ± 0.8
DOP-F-DS	67 ± 10	148 ± 8	0.22	−5.2 ± 1.1
Transferrin-TRITC	78 ± 7	207 ± 13	0.28	−8.9 ± 0.7
DOP-F-DS + Transferrin-TRITC	88 ± 9	298 ± 19	0.22	−6.0 ± 1.1
Doxorubicin	71 ± 7	187 ± 21	0.33	−5.3 ± 0.3
SN-38	66 ± 7	163 ± 14	0.20	−5.4 ± 0.1
Doxorubicin and SN-38	103 ± 8	245 ± 9	0.21	−5.8 ± 0.2

The fourth column reports the polydispersity index (PDI), while the last ones shows the values of surface charge for each type of vesicles.

both molecules yielding slightly enlarged NVs compared to those encapsulating either DOP-F-DS or transferrin.

Next, two chemotherapeutic drugs, namely doxorubicin and SN-38, being the former dispersible in water while the latter poorly soluble and instable at physiological pH, were encapsulated into the vesicles. **Figures 3G–I** report the TEM images of the liposomes loaded with doxorubicin, SN-38, and both drugs, respectively. The size of the vesicles loaded with the individual drugs was around 70 nm in both cases, while the particles simultaneously encapsulating the two molecules displayed an average size of around 100 nm (see **Table 2**). As already mentioned, it was necessary to prolong the sonication time to 6 min when preparing vesicles simultaneously loaded with doxorubicin and SN-38. Indeed, after 4 min (that is the time needed for preparing all the other formulations) the vesicles had not formed yet, while closely attached lipid droplets of various sizes could be observed by TEM (**Figure S3**), evidencing the incomplete

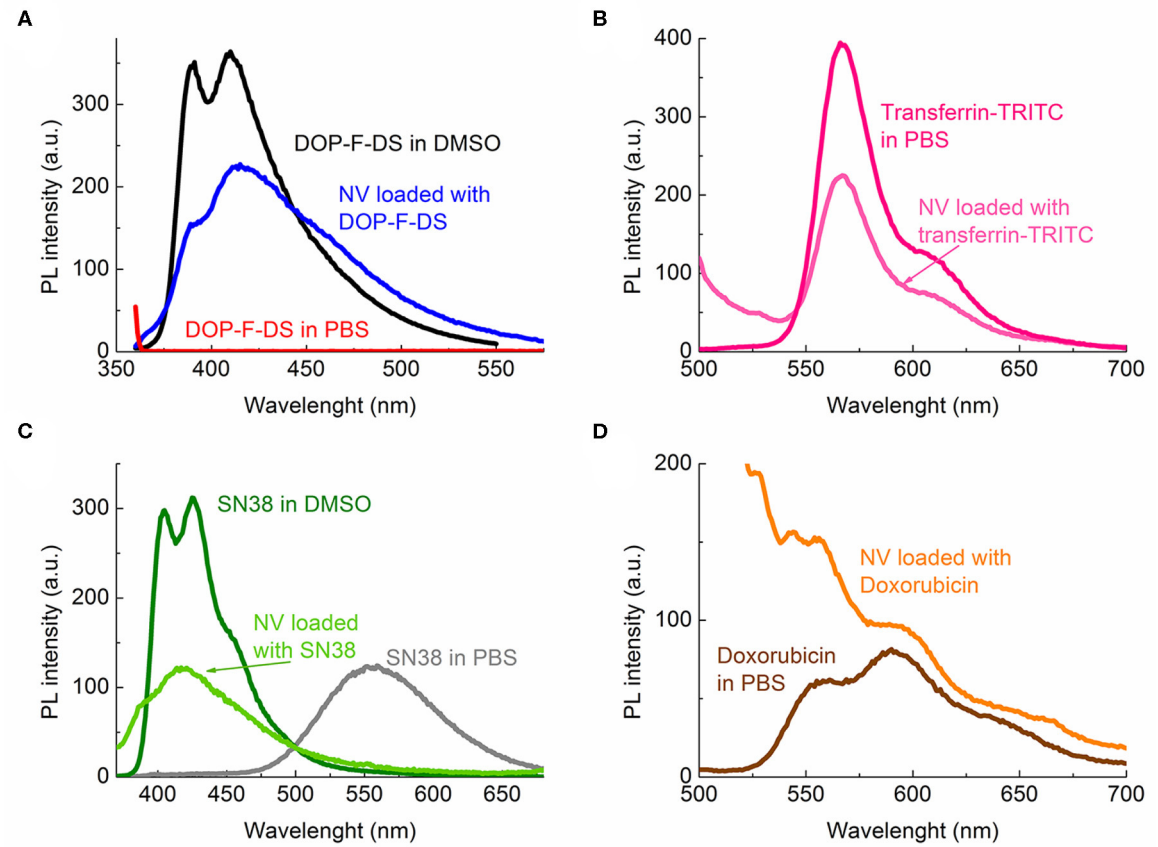

FIGURE 4 | Photoluminescence spectra of the fluorescent species either free or encapsulated: **(A)** DOP-F-DS; **(B)** transferrin-TRITC; **(C)** SN-38; and **(D)** doxorubicin.

formation of the spherical vesicles. The need for prolonged sonication time might be attributed to the interaction between the two drugs that might influence bending and sealing of the bilayer.

The analysis of the hydrodynamic diameter of the vesicles (third column of **Table 2** and **Figure S4**) evidenced a broadening of the size when the particles were hydrated and dispersed in PBS. As expected, the size of the empty vesicles (137 ± 11 nm) was smaller compared to that of the loaded vesicles, as already observed by the TEM analysis. The largest particles were those loaded with both drugs (245 ± 9 nm), QDs (278 ± 21 nm), DOP-F-DS, and transferrin-TRITC (298 ± 19 nm), and the magnetic nanoparticles (319 ± 24 nm). The polydispersity index (PDI) values ranged between 0.2 and 0.3 and the suspensions resulted to be very stable over time, as confirmed by DLS measurements after 7 and 14 days (samples were stored at 4°C but they were kept for 1 h at room temperature before measurement). As shown in **Table S1**, the size of the empty vesicles and of those loaded either with the single drugs or with both doxorubicin and SN-38 remained constant and the suspension did not look altered even after 2 weeks.

The average surface charge of the vesicles was slightly negative (about −6 mV) for all the different formulations prepared, independently of the loading or the dimension of the NVs (**Table 2**).

Incorporation of the MNPs into the NVs conferred a magnetic behavior to the loaded NVs. As a proof of concept, a magnetic field (0.3 T) was applied through a magnet close to the wall of a vial containing a solution with the NVs. As expected, the nanovesicles adhered to the wall adjacent to the magnet within 2 h (**Figure S5**). The process was shown to be reversible and repeatable.

To confirm whether the different species were encapsulated in the bilayer or within the core, the fluorescence spectra of the loaded vesicles were collected. **Figure 4A**) shows the emission spectra of the organic DOP-F-DS fluorophore dissolved in DMSO (black curve), in PBS (red curve), and in the vesicles suspended in PBS (dark blue curve). The fluorescence curve of the encapsulated dye is quite similar to that of the free dye in DMSO, showing the same two peaks (at 390 and 410 nm) although slightly broadened when encapsulated. On the other hand, the DOP-F-DS fluorescence quenches completely in PBS, indicating that the dye most likely settles into the double layer when encapsulated. As shown in **Figure 4B**, the fluorescence spectrum of transferrin-TRITC loaded into the vesicles is comparable to that of the free protein dissolved in PBS.

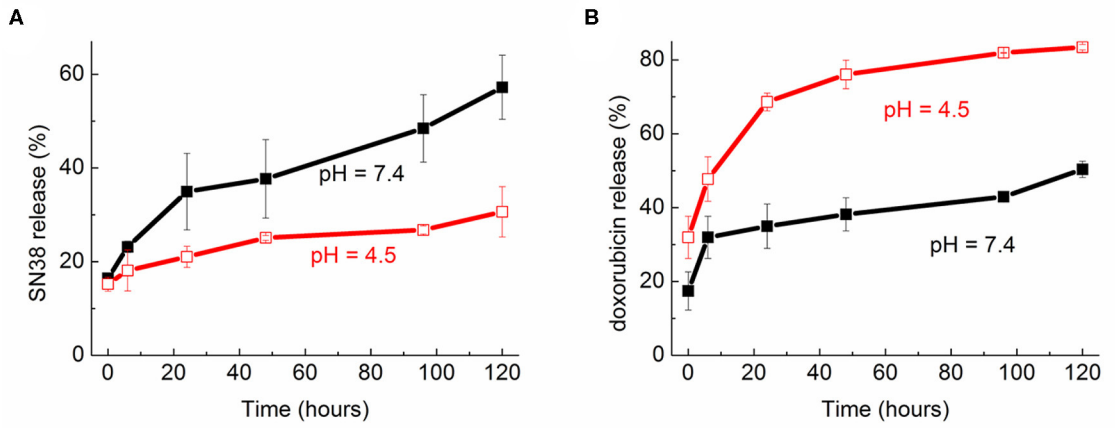

FIGURE 5 | Release profile over time (up to 120 h) of **(A)** SN-38 and **(B)** doxorubicin from the nanovesicles at two pH (7.4 and 4.5).

SN-38 is poorly soluble in aqueous media; indeed, the fluorescence curve of the molecule dissolved in PBS was considerably different from that in DMSO (**Figure 4C**). In this solvent (dark green curve), the spectrum displayed two peaks at 405 and 425 nm, respectively; while in PBS (gray curve) the fluorescence shifted to 555 nm, likely due to spatial arrangement and π-π interactions among the molecules. On the other hand, the fluorescence curve (light green) was slightly shifted toward higher energies when it was encapsulated into the vesicle, with the two peaks detected at 387 and 417 nm, respectively. Therefore, it is reasonable to suppose that, similarly to the DOP-F-DS dye, SN-38 is also hosted into the lipid bilayer of the vesicles.

The main emission peak at 595 nm of free doxorubicin in PBS (dark red curve) was retained when encapsulated into the vesicles (orange curve), as shown in **Figure 4D**. The fluorescence spectrum in PBS of the nanovesicles loaded with the green-emitting QDs was also detected (**Figure S6**) and the obtained curve was similar to that of the free surfactant-coated nanocrystals. However, a slight broadening of the maximum peak was noted, again suggesting encapsulation of the QDs into the lipid bilayer, as also expected since they are not soluble in aqueous medium and their fluorescence would be quenched in this solvent.

Drug Loading and Release From the Lipid Nanovesicles

The optical spectra of doxorubicin and SN-38 were used to monitor the amount of drug incorporated into the NVs and to calculate the encapsulation efficiency (*EE*). As expected, *EE* for doxorubicin was dependent on the concentration of the feeding solution, reaching a maximum of about 6% when using an 85.8 μM initial solution. *EE* dropped to 3.5 and 2.7% when using lower initial concentrations (42.9 and 21.5 μM, respectively). On the other hand, higher *EE* values were generally obtained with SN-38, although a decreased efficiency was observed (40, 30, 20, and 15%) by increasing the concentration of the feeding solution (0.5, 1, 2, and 3 μM, respectively).

Two parameters must be considered to explain the different behavior of the two drugs, i.e. the different solubility and the preparation conditions of the vesicles. SN-38 has a poor solubility in PBS and tends to intercalate spontaneously within the double layer given the greater affinity for the lipophilic environment. On the other hand, doxorubicin is perfectly soluble in PBS and the encapsulated amount mainly depends on the maximum capacity of the vesicle core.

The *in vitro* release kinetics of the two drugs based on the NVs with the highest *EE* were also studied. As reported in **Figure 5**, the release was monitored up to 5 days keeping the samples at 37°C and at two pH values, 7.4 and 4.5, the latter being resembling the condition in the intracellular endolysosomes. As expected, the different solubility of the two drugs also led to completely different patterns. In the case of SN-38 the highest release was observed at physiological pH, reaching 35% after 24 h and 57% after 120 h. The release resulted considerably reduced at lower pH, reaching a maximum of about 30% after 5 days.

On the other hand, there was a quicker and more significant release of doxorubicin at acidic conditions as compared to physiological ones. Indeed, after 24 h incubation at 37°C the release was around 35% at pH 7.4 and almost doubled (68%) at pH 4.5. The highest release was detected after 5 days in acidic solution, reaching 83% of the total encapsulated amount.

Cellular Studies

Viability Assays

Cellular viability studies were performed to assess the effectiveness of the NVs loaded with the chemotherapeutic agents and to evaluate the effects of the empty ones. Two human cell lines derived from breast cancer, MDA-MB-231, and MCF-7, were used.

Two viability assays, namely the metabolic MTT and the Trypan blue exclusion assay, were performed administering the cells with the vesicles encapsulating the drugs, either alone or simultaneously. Additionally, the viability of the cells incubated with the free drugs was also evaluated. Based on our previous studies, the drug amount administered to the cells was fixed

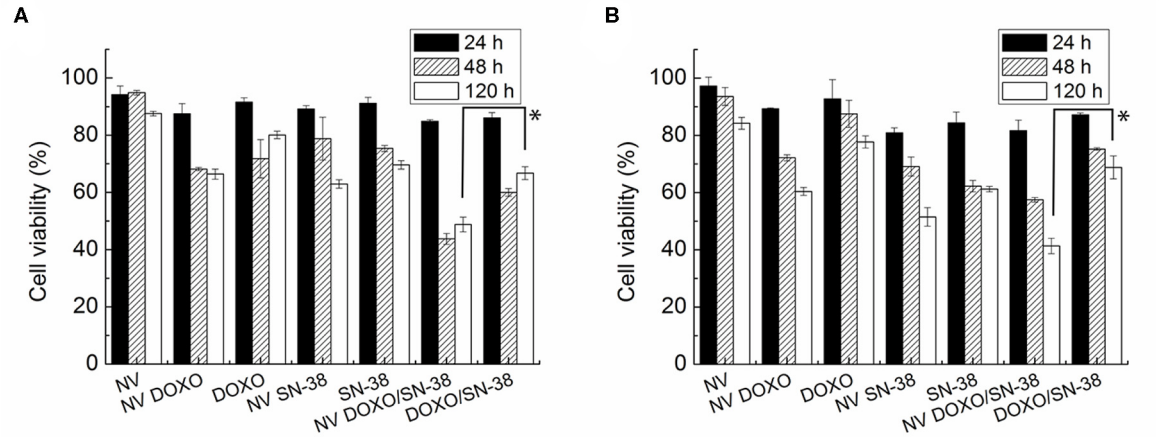

FIGURE 6 | MTT viability assay of **(A)** MDA-MB-231 and **(B)** MCF-7 cells administered for 24, 48, and 120 h with empty nanovesicles, nanovesicles loaded with DOXO, free DOXO, nanovesicles loaded with SN-38, free SN-38, nanovesicles loaded with both drugs, and both free drugs, respectively. The viability of the cells incubated with the loaded nanovesicles was compared with that of the cells incubated with free drugs, at 120 h in both cell lines. Statistical analysis was performed via *t*-test considering it significant for $^*p < 0.05$.

to 0.5 μM for doxorubicin and 0.1 μM for SN-38 (Deka et al., 2011; Elbialy and Mady, 2015; Fang et al., 2018). These values are consistent with average IC_{50} values from the literature for MDA-MB-231 and MCF-7 cells, being between 1.7 and 0.2 μM that for doxorubicin and between 0.3 and 0.02 μM that for SN-38 (https://www.cancerrxgene.org/; Jandu et al., 2016; Lin et al., 2019).

As evidenced in **Figure 6**, the empty NVs displayed negligible toxicity according to the MTT assay, reaching a viability close to 80% after 5 days. At the administered drug concentration, the nanovesicles loaded with doxorubicin led to a reduction of viability up to 60% in both cell lines after 120 h, while the toxic activity of the free drug resulted to be very limited even after 5 days, with viability values close to 70%. In the case of SN-38, after 24 h the viability of both cell lines dropped to 70% when encapsulated, while it settled at 80% when administered as free molecule.

Encapsulation of the drugs into the vesicles increased significantly their effectiveness, likely thanks to a facilitated uptake from the cells. This effect was enhanced when both drugs were encapsulated within the vesicles, and it became more pronounced with increasing incubation times. Indeed, the combined toxic effect led to a reduction in cell viability to values below 50% after 48 h in both cell lines, and down to 26 and 22% after 5 days in MDA-MB-231 and MCF-7, respectively. On the other hand, when doxorubicin and SN-38 were administered simultaneously to the cells as free formulation (at the same concentrations loaded into the NVs), viability reached values close to 75 and 45% after 24 and 120 h, respectively. The increased toxicity of the vesicles loaded with both drugs became statistically significant ($p < 0.005$) in both cell lines only after long incubation time (5 days). These findings suggest that when the encapsulated drugs are internalized by the cells, they are not immediately available to exert their activity but they are released gradually, as confirmed by the drug release kinetic showed in **Figure 5**. The limited activity shown by the combination of the free drugs probably depend on the partial degradation of the molecules, that is prevented when they are encapsulated, as well as on the existence of several drug resistance mechanisms in breast cancer cells, as already reported (Jandu et al., 2016). These effects, (i.e., the protective role of the NVs, the facilitated internalization, and the sustained release, show the advantage of using the vesicles for delivering the drugs). However, from **Figure 6** it is evident that the pharmacological activity of the drug loaded NVs is poor in the first 48 h post administration. Several factors, such as surface chemistry of the NVs, physico-chemical properties of encapsulated drugs, and cells used, can contribute to this effect thus affecting internalization of the carrier, drug release kinetic, and activation of drug efflux pumps. To determine whether the NVs loaded with both drugs induced a synergic cytotoxic effect, the CI was calculated according to the Chou and Talalay's formula (Chou and Talalay, 1984). A value of 0.97 was obtained, suggesting a slight synergic effect.

The data obtained by the vital Trypan blue assay (**Figure S7**) are in agreement with those obtained by the MTT assay, confirming a progressive reduction of the number of viable cells upon incubation with the nanovesicles loaded with the drugs, reaching the highest mortality when both drugs were hosted into the lipid vesicles. Indeed, the toxicity of the NVs loaded with both drugs is statistically significant ($p < 0.005$) in both cell lines after 120 h. This assay also confirmed the biocompatibility of the empty vesicles, that did not impact the number of vital cells; their number, in fact, remained close to that of the control samples after 24 and 48 h, and it still maintained values above 80% after 5 days in both cell lines.

It is worth reminding that the cellular target of doxorubicin and SN-38 is the nucleus. Although their mechanism of action is not fully understood yet, they both inhibit DNA replication and translation, doxorubicin by intercalating into DNA, and inhibiting topoisomerase II, while SN-38, the active form of

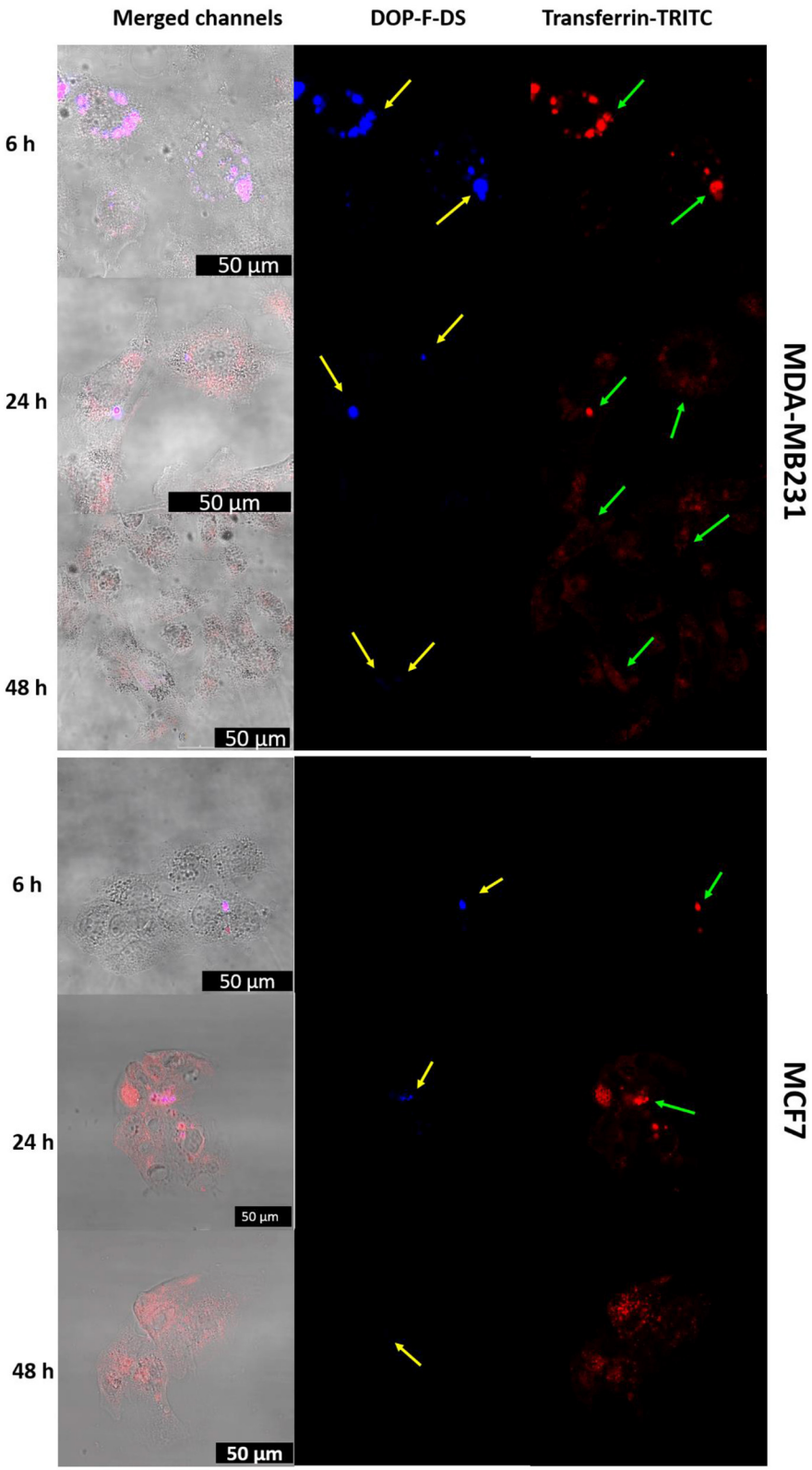

FIGURE 7 | CLSM images of MDA-MB-231 and MCF-7 cells incubated with liposomes loaded with transferrin-TRITC and DOP-F-DS for 6, 24, and 48 h. The left column refers to the fluorescence channels merged with the bright field, while the central and right columns refer to the blue and red fluorescence channels, respectively. The scale bars correspond to 50 µm.

irinotecan, binds to the topoisomerase I-DNA complex (Kawato et al., 1991; Yang et al., 2014). The results obtained by the cellular assays presented in this section show that the drug-loaded NVs affect cell viability of the two cell lines, but they do not shed light on the cellular pathways and the molecular mechanisms involved in this process. Deeper investigation of these effects deserves further studies that, however, are beyond the aims of this work.

Cellular Internalization

To elucidate the internalization process of the nanovesicles and their intracellular localization, cells doped with NVs loaded with fluorescent molecules were analyzed by optical imaging.

In detail, MDA-MB-231 cells were incubated with NVs hosting the DOP-F-DS fluorophore, contained in the lipid bilayer, and the transferrin-TRITC protein, hosted into the vesicle core. After 6, 24, and 48 h the cells were fixed and imaged by CLSM (**Figure 7**, upper panels). The vesicles were already internalized and located into the perinuclear endosomes after 6 h. Complete overlap between the DOP-F-DS signal (blue channel) and the transferrin-TRITC signal (red channel) could be observed, indicating that the vesicles did not yet undergo enzymatic degradation. However, a significant weakening of the fluorescence in the blue channel was observed after 24 h, likely due to initial partial degradation of the bilayer structure, with consequent release of DOP-F-DS and quenching of its fluorescence in aqueous medium. This effect was enhanced after 48 h, when the blue fluorescence almost disappeared. On the other hand, the TRITC-derived fluorescence, which was initially confined into the endosomal vesicles with the typical point-like fluorescence (after 6 and 24 h), seemed to diffuse into the cell cytoplasm after 48 h.

The release of molecules and drugs from the endosomes because of a temporary permeability of the organelle membrane is an already described phenomenon (Singh et al., 2004; Muripiti et al., 2018; Quarta et al., 2019). It can depend on many factors, such as size, molecular weight, charge, and solubility of the molecules that diffuse out and it is triggered by environmental parameters, such as pH and the presence of charged species.

The same CLSM experiment was also performed on MCF-7 cells, confirming the same internalization pathway (**Figure 7**, lower panels). However, despite the similar behavior, internalization seemed to be improved with the MBA-MB-231 cells. After few hours, the two fluorescence signals colocalized into vesicular structures, while the red signal of transferrin started to spread into the cytosol and the blue fluorescence tended to disappear after 24 h.

To confirm the intracellular compartmentalization of the NVs, a colocalization study of the NVs loaded with Transferrin-TRITC was performed with LysoTracker Green in MDA-MB-231 cells (**Figure S8**). Noteworthy, the distribution of the red fluorescence signal of transferrin changed over time: after 6 h some orange spots (due to the overlap of the two fluorescent signals) were visible in the perinuclear region of neighboring cells. After 24 h incubation, the endolysosomes that entrapped the NVs seemed enlarged. Then, after 48 h, the red fluorescence of transferrin started to spread into the cytoplasm (a red background was visible inside some cells) due to its release from the endolysosomal compartment.

On the other hand, when the cells were incubated with the QD-loaded nanovesicles, the fluorescence spot was localized into the endosomes at all the analyzed time points. As shown in **Figure S9**, the nucleus of the cells was labeled with DAPI while the cytoskeleton with phalloidin-TRITC, and the fluorescence signal of the QDs could be detected into perinuclear endosomes even after 48 h. The detection of fluorescence spots after 2 days might be due to continuous uptake of new nanovesicles inside the cells. In fact, once internalized into the endolysosome compartments, the NVs are probably slowly digested leading to fluorescence quenching. Indeed, the QDs, coated only by the lipophilic surfactant layer, are neither soluble nor stable in aqueous environment and their fluorescence is detectable until the vesicles remain intact, while it is quenched when the lipid bilayer is degraded. Moreover, it should be observed that the fluorescence intensity of the QDs signal did not increase over time inside the cells, as instead observed in the case of transferrin-TRITC (due to the progressive internalization of the NVs).

Lipidomic Analysis

To better understand the behavior of the drugs and the influence of the vesicular formulation, a metabolomic study was performed through ^{1}H NMR on the lipid extracts obtained from the MDA-MB-231 cells. Analysis were performed on the cells treated for 24 h with doxorubicin and SN-38 either free or administered through the nanovesicles. MDA-MB-231 extracts of the untreated cells were taken as control reference. The study was performed after 24 h of incubation, as confocal microscopy imaging and MTT assay already showed noteworthy internalization and physiological effect of the drugs after this time; while MDA-MB-231 cells were considered, as NVs internalization was shown to be greater with this cell line compared to the MCF-7 (see **Figure 7**). Multivariate statistical analysis (MVA) was then performed on the registered NMR spectra to check if any differences could be observed between the two types of drug administration. This approach has already proved to be a valuable tool for understanding the mechanism of action of drugs and how they influence normal physiological patterns, as well as for discriminating healthy cells from cancerous ones, both *in vitro* and *ex vivo/in vivo*, thus paving the way toward personalized medicine (Armitage and Southam, 2016; Del Coco et al., 2019; Giudetti et al., 2019).

The OPLS-DA model was able to discriminate between control and cells treated with either free or encapsulated drugs with a R^2_X of 0.766 and 0.813, respectively (**Figures 8A,B**). Moreover, some differences were also observed between the two types of administration (**Figure 8C**). Treatment of the MDA-MB-231 cells with the two types of drug administration induced similar metabolic changes in the control cells, as observed in the profiles of the corresponding *S*-line plots (**Figures 9A,B**). The drugs caused a significant reduction of the total fatty acids (peaks at about 0.8 and 1.2 ppm) and a concomitant increase of the unsaturated fatty acids (peak at about 1.6 ppm). The peak at about 2.8 ppm, corresponding to the *bis*-allylic protons

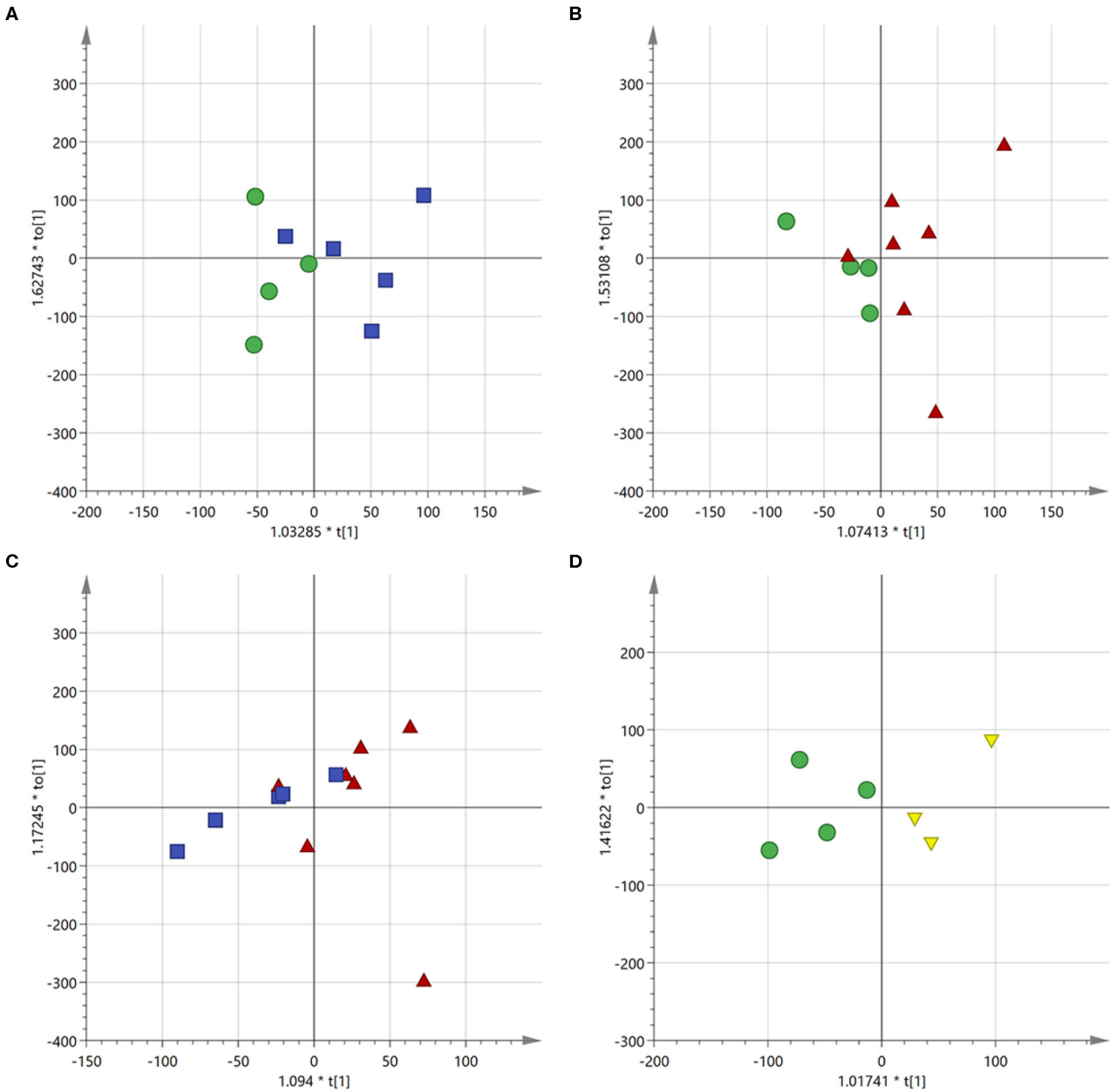

FIGURE 8 | Score scatter plot for the first component of the OPLS-DA models. **(A)** Control cells (green circles) vs. free drugs (blue squares); **(B)** control cells (green circles) vs. drugs encapsulated into the NVs (red triangles); **(C)** cells treated with free drugs (blue squares) vs. those treated with the encapsulated drugs (red triangles); **(D)** control cells (green circles) vs. empty NVs (yellow triangles).

of polyunsaturated fatty acyl chains, and that one at 4.1 ppm, relative to vinylic protons in β to the carboxylic acid of fatty acids, also showed increased intensity in treated cells, although to a minor extent compared to the previous signals. A similar behavior was already observed in cells treated with antitumoral drugs and it has been related to an increased mobility of the cellular membrane, as a consequence of the reduced tight packing of the fatty acids. Eventually, this destabilization increases with time and finally ends up with the membrane disruption, resulting in cellular death and formation of lipid droplets (Hakumäki et al., 1999; Griffin et al., 2003).

The profile of the two curves (**Figures 9A,B**) looks very similar, indicating that the mechanism of action of the drugs does not change significantly depending on the mode of administration. It has to be observed, however, that phosphatidylcholine derivatives (peak at about 3.4 ppm) increased more significantly in cells treated with the free drug, but not in those treated with the loaded NVs. This

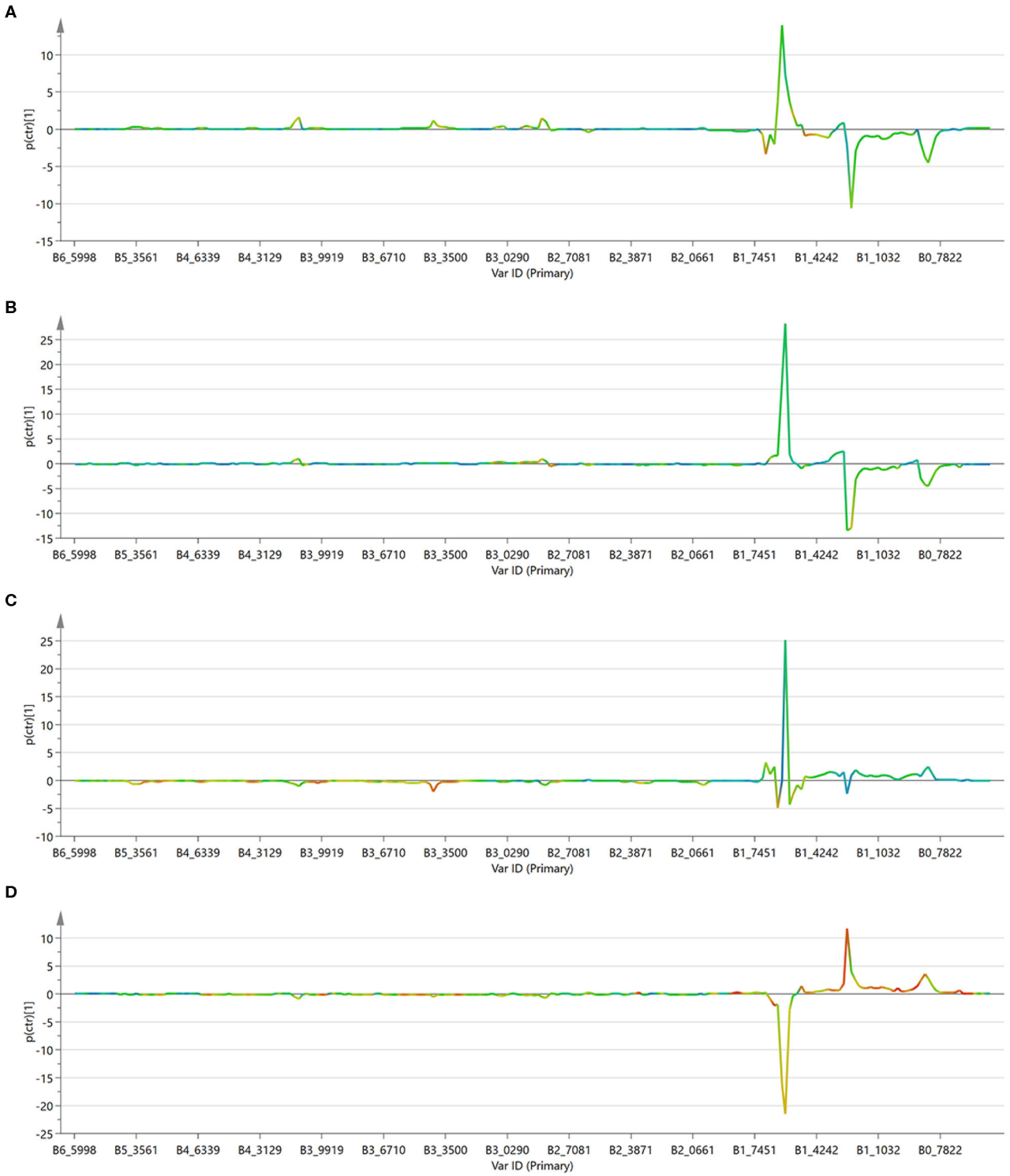

FIGURE 9 | S-line plot for the first component of the OPLS-DA models. **(A)** Control cells vs. free drugs; **(B)** control cells vs. drugs encapsulated into the NVs; **(C)** cells treated with free drugs vs. those treated with the encapsulated drugs; **(D)** control cells vs. empty NVs.

effect might be due to a selective release operated by the nanocarrier in particular regions of the cells and it deserves further investigation.

To better appreciate any differences between the two administration methods, the MVA was also performed directly on these two classes (i.e., free drugs and NVs, **Figure 9C**). This

analysis confirmed what already observed by the independent comparison vs. the untreated cells, (i.e., that they induce similar effects, but it also evidenced how the amount of unsaturated fatty acids is much more abundant in the cells treated with the drug-loaded nanovesicles). This is probably due to the higher concentration of drugs able to enter the cells when administered through the nanovesicles (as already confirmed by the confocal microscopy study showing that liposomes were already internalized into vesicles after just 6 h), thus reaching more efficiently the site of action.

As a further control, untreated cells were compared to cells administered with empty NVs, thus allowing to confirm the observed cytotoxic effect is due exclusively to the drugs (**Figures 8D**, **9D**). Being just composed of cholesterol, ceramide, and phospholipids it is not expected that this type of vectors would induce any cytotoxicity, at least at the administered concentration. In fact, cells doped with the empty NVs showed to have higher amounts of cholesterol and total fatty acids (peaks at 0.8 and 1.2 ppm), but lower quantities of unsaturated ones (peak at 1.6 ppm), as observed in the corresponding *S*-line plot (**Figure 9D**) which is quite specular to those obtained in cells after drug administration (**Figures 9B,C**).

The use of NVs thus leads to a higher efficacy of the treatment, and the efficiency of the system is even more remarkable if we consider the protection of the drugs against degradation and the cumulative therapeutic effect of the sustained release over 5 days.

CONCLUSIONS

As witnessed by the number and relevance of publications in the field, lipid-based nanostructures still gain great attention thanks to their biocompatible and degradable nature, and to their similarity with the vesicles released by the cells in physiological and pathological conditions. Despite the high production cost and the evidence of interactions with the immune system upon *in vivo* injection, several liposomal formulations, such as Onyvide and Doxil, were approved for therapeutic use in cancer.

In this study, lipid nanovesicles composed of phospholipids, cholesterol, and ceramide with an average size of 100 nm were prepared via ultrasonication method. Several species with completely different characteristics were encapsulated into the vesicles, including a small amphiphilic organic fluorophore (DOP-F-DS), a 60 kDa protein, lipophilic (SN-38), and hydrophilic (DOXO) drugs, and also fluorescent, and magnetic inorganic nanoparticles. The morpho-structural features and the thermal properties were studied, showing that this system presents high flexibility and good stability. Viability studies and lipidomic analysis demonstrated that the two drugs induced similar metabolic changes independently of the administration method (either free or encapsulated) but they were significantly more cytotoxic into the nanoformulation, probably because of facilitated entrance, protection against degradation, and sustained release. Imaging of the nanovesicles loaded with two fluorescent organic probes showed that, once engulfed by the cells and internalized into endosomes, the vesicles undergo gradual degradation over time with consequent release of the cargo in the cytosol, first of the lipophilic compounds (loaded into the bilayer) and then of the hydrophilic ones (loaded into the core). The data collected so far proved the excellent versatility of this system as imaging and delivery nanoformulation with potential theranostic applications. Nevertheless, further investigation is needed to optimize drug encapsulation capability (i.e., by using longer fatty acid chains as well as different lipid ratios, and to study their efficacy *in vivo*).

DATA AVAILABILITY STATEMENT

The raw data supporting the conclusions of this article will be made available by the authors, without undue reservation.

AUTHOR CONTRIBUTIONS

AZ and AQ designed and carried out the experiments. LBi, AC, and LBl methodology and investigation. CP and AR: data analysis, writing, and editing. All authors contributed to discussion of the results.

FUNDING

This study was supported by the following grants: Progetto Tecnopolo per la Medicina di precisione, Deliberazione della Giunta Regionale n. 2117 del 21/11/2018, Progetto regionale Lab on a Swab (cod. OTHZY54), and project HApECOrk, funded by Fondazione Con il Sud (project 2015-0243).

SUPPLEMENTARY MATERIAL

The Supplementary Material for this article can be found online at: https://www.frontiersin.org/articles/10.3389/fbioe.2020.00690/full#supplementary-material

REFERENCES

Al-Jamal, W. T., Al-Jamal, K. T., Tian, B., Lacerda, L., Bomans, P. H., Frederik, P. M., et al. (2008). Lipid–quantum dot bilayer vesicles enhance tumor cell uptake and retention *in vitro* and *in vivo*. *ACS Nano* 2, 408–418. doi: 10.1021/nn700176a

Antimisiaris, S. G., Mourtas, S., and Marazioti, A. (2018). Exosomes and exosome-inspired vesicles for targeted drug delivery. *Pharmaceutics* 10:218. doi: 10.3390/pharmaceutics10040218

Armitage, E. G., and Southam, A. D. (2016). Monitoring cancer prognosis, diagnosis and treatment efficacy using metabolomics and lipidomics. *Metabolomics* 12:146. doi: 10.1007/s11306-016-1093-7

Barenholz, Y. (2012). Doxil(R)–the first FDA-approved nano-drug: lessons learned. *J. Control. Release* 160, 117–134. doi: 10.1016/j.jconrel.2012.03.020

Bothun, G. D., Rabideau, A. E., and Stoner, M. A. (2009). Hepatoma cell uptake of cationic multifluorescent quantum dot liposomes. *J. Phys. Chem. B* 113, 7725–7728. doi: 10.1021/jp9017458

Bulbake, U., Doppalapudi, S., Kommineni, N., and Khan, W. (2017). Liposomal formulations in clinical use: an updated review. *Pharmaceutics* 9:12. doi: 10.3390/pharmaceutics9020012

Cardone, A., Lopez, F., Affortunato, F., Busco, G., Hofer, A. M., Mallamaci, R., et al. (2012). An aryleneethynylene fluorophore for cell membrane staining. *Biochim. Biophys. Acta* 1818, 2808–2817. doi: 10.1016/j.bbamem.2012.06.011

Carugo, D., Bottaro, E., Owen, J., Stride, E., and Nastruzzi, C. (2016). Liposome production by microfluidics: potential and limiting factors. *Sci. Rep.* 6:25876. doi: 10.1038/srep25876

Chou, T. C., and Talalay, P. (1984). Quantitative analysis of dose-effect relationships: the combined effects of multiple drugs or enzyme inhibitors. *Adv. Enzyme Regul.* 22, 27–55. doi: 10.1016/0065-2571(84)90007-4

Dabbousi, B. O., Rodriguez-Viejo, J., Mikulec, F. V., Heine, J. R., Mattoussi, H., Ober, R., et al. (1997). (CdSe)ZnS core–shell quantum dots: synthesis and characterization of a size series of highly luminescent nanocrystallites. *J. Phys. Chem. B* 101, 9463–9475. doi: 10.1021/jp971091y

De Toro, J., Herschlik, L., Waldner, C., and Mongini, C. (2015). Emerging roles of exosomes in normal and pathological conditions: new insights for diagnosis and therapeutic applications. *Front. Immunol.* 6:203. doi: 10.3389/fimmu.2015.00203

Deka, S. R., Quarta, A., Di Corato, R., Riedinger, A., Cingolani, R., and Pellegrino, T. (2011). Magnetic nanobeads decorated by thermo-responsive PNIPAM shell as medical platforms for the efficient delivery of doxorubicin to tumour cells. *Nanoscale* 3, 619–629. doi: 10.1039/C0NR00570C

Del Coco, L., Vergara, D., De Matteis, S., Mensa, E., Sabbatinelli, J., Prattichizzo, F., et al. (2019). NMR-based metabolomic approach tracks potential serum biomarkers of disease progression in patients with type 2 diabetes mellitus. *J. Clin. Med.* 8:720. doi: 10.3390/jcm8050720

Elbialy, N. S., and Mady, M. M. (2015). Ehrlich tumor inhibition using doxorubicin containing liposomes. *Saudi Pharm. J.* 23, 182–187. doi: 10.1016/j.jsps.2014.07.003

Fang, Y. -P., Chuang, C. -H., Wu, Y. -J., Lin, H. -C., and Lu, Y. -C. (2018). SN38-loaded <100 nm targeted liposomes for improving poor solubility and minimizing burst release and toxicity: *in vitro* and *in vivo* study. *Int. J. Nanomed.* 13, 2789–2802. doi: 10.2147/IJN.S158426

Giudetti, A. M., De Domenico, S., Ragusa, A., Lunetti, P., Gaballo, A., Franck, J., et al. (2019). A specific lipid metabolic profile is associated with the epithelial mesenchymal transition program. *Biochim. Biophys. Acta Mol. Cell Biol. Lipids* 1864, 344–357. doi: 10.1016/j.bbalip.2018.12.011

Griffin, J. L., Lehtimaki, K. K., Valonen, P. K., Grohn, O. H., Kettunen, M. I., Yla-Herttuala, S., et al. (2003). Assignment of 1H nuclear magnetic resonance visible polyunsaturated fatty acids in BT4C gliomas undergoing ganciclovir-thymidine kinase gene therapy-induced programmed cell death. *Cancer Res.* 63, 3195–3201.

Grimaldi, N., Andrade, F., Segovia, N., Ferrer-Tasies, L., Sala, S., Veciana, J., et al. (2016). Lipid-based nanovesicles for nanomedicine. *Chem. Soc. Rev.* 45, 6520–6545. doi: 10.1039/C6CS00409A

Hakumäki, J. M., Poptani, H., Sandmair, A.-M., Ylä-Herttuala, S., and Kauppinen, R. A. (1999). 1H MRS detects polyunsaturated fatty acid accumulation during gene therapy of glioma: implications for the *in vivo* detection of apoptosis. *Nat. Med.* 5, 1323–1327. doi: 10.1038/15279

Hyeon, T., Lee, S. S., Park, J., Chung, Y., and Na, H. B. (2001). Synthesis of highly crystalline and monodisperse maghemite nanocrystallites without a size-selection process. *J. Am. Chem. Soc.* 123, 12798–12801. doi: 10.1021/ja0 16812s

Jandu, H., Aluzaite, K., Fogh, L., Thrane, S. W., Noer, J. B., Proszek, J., et al. (2016). Molecular characterization of irinotecan (SN-38) resistant human breast cancer cell lines. *BMC cancer* 16:34. doi: 10.1186/s12885-016-2071-1

Kawato, Y., Aonuma, M., Hirota, Y., Kuga, H., and Sato, K. (1991). Intracellular roles of SN-38, a metabolite of the camptothecin derivative CPT-11, in the antitumor effect of CPT-11. *Cancer Res.* 51, 4187–4191.

Kethineedi, V. R., Crivat, G., Tarr, M. A., and Rosenzweig, Z. (2013). Quantum dot-NBD-liposome luminescent probes for monitoring phospholipase A2 activity. *Anal. Bioanal. Chem.* 405, 9729–9737. doi: 10.1007/s00216-013-7422-z

Klingler, J., Vargas, C., Fiedler, S., and Keller, S. (2015). Preparation of ready-to-use small unilamellar phospholipid vesicles by ultrasonication with a beaker resonator. *Anal. Biochem.* 477, 10–12. doi: 10.1016/j.ab.2015.02.015

Kraft, J. C., Freeling, J. P., Wang, Z., and Ho, R. J. Y. (2014). Emerging research and clinical development trends of liposome and lipid nanoparticle drug delivery systems. *J. Pharm. Sci.* 103, 29–52. doi: 10.1002/jps.23773

Li, M., Du, C., Guo, N., Teng, Y., Meng, X., Sun, H., et al. (2019). Composition design and medical application of liposomes. *Eur. J. Med. Chem.* 164, 640–653. doi: 10.1016/j.ejmech.2019.01.007

Lin, H. C., Chuang, C. H., Cheng, M. H., Lin, Y. C., and Fang, Y. P. (2019). High potency of SN-38-loaded bovine serum albumin nanoparticles against triple-negative breast cancer. *Pharmaceutics* 11:569. doi: 10.3390/pharmaceutics11110569

López-González, D., Puig-Gamero, M., Acién, F. G., García-Cuadra, F., Valverde, J. L., and Sanchez-Silva, L. (2015). Energetic, economic and environmental assessment of the pyrolysis and combustion of microalgae and their oils. *Renew. Sustain. Energy Rev.* 51, 1752–1770. doi: 10.1016/j.rser.2015.07.022

Monteiro, N., Martins, A., Reis, R. L., and Neves, N. M. (2014). Liposomes in tissue engineering and regenerative medicine. *J. R. Soc. Interface* 11:20140459. doi: 10.1098/rsif.2014.0459

Muripiti, V., Lohchania, B., Marepally, S. K., and Patri, S. V. (2018). Hepatocellular targeted α-tocopherol based pH sensitive galactosylated lipids: design, synthesis and transfection studies. *MedChemComm* 9, 264–274. doi: 10.1039/C7MD00503B

Nkanga, C. I., Bapolisi, A. M., Okafor, N. I., and Krause, R. W. M. (2019). "General perception of liposomes: formation, manufacturing and applications" in *Liposomes - Advances and Perspectives*, ed A. Catala (IntechOpen). doi: 10.5772/intechopen.84255

Perrotti, F., Rosa, C., Cicalini, I., Sacchetta, P., Del Boccio, P., Genovesi, D., et al. (2016). Advances in lipidomics for cancer biomarkers discovery. *Int. J. Mol. Sci.* 17:1992. doi: 10.3390/ijms17121992

Pinilla, C. M. B., Thys, R. C. S., and Brandelli, A. (2019). Antifungal properties of phosphatidylcholine-oleic acid liposomes encapsulating garlic against environmental fungal in wheat bread. *Int. J. Food Microbiol.* 293, 72–78. doi: 10.1016/j.ijfoodmicro.2019.01.006

Quarta, A., Amorín, M., Aldegunde, M. J., Blasi, L., Ragusa, A., Nitti, S., et al. (2019). Novel synthesis of platinum complexes and their intracellular delivery to tumor cells by means of magnetic nanoparticles. *Nanoscale* 11, 23482–23497. doi: 10.1039/C9NR07015J

Riaz, M. K., Riaz, M. A., Zhang, X., Lin, C., Wong, K. H., Chen, X., et al. (2018). Surface functionalization and targeting strategies of liposomes in solid tumor therapy: a review. *Int. J. Mol. Sci.* 19:195. doi: 10.3390/ijms190 10195

Salvi, V. R., and Pawar, P. (2019). Nanostructured lipid carriers (NLC) system: a novel drug targeting carrier. *J. Drug Deliv. Sci. Technol.* 51, 255–267. doi: 10.1016/j.jddst.2019.02.017

Sarko, D. K., and McKinney, C. E. (2017). Exosomes: origins and therapeutic potential for neurodegenerative disease. *Front. Neurosci.* 11:82. doi: 10.3389/fnins.2017.00082

Singh, R. S., Goncalves, C., Sandrin, P., Pichon, C., Midoux, P., and Chaudhuri, A. (2004). On the gene delivery efficacies of pH-sensitive cationic lipids via endosomal protonation: a chemical biology investigation. *Chem. Biol.* 11, 713–723. doi: 10.1016/j.chembiol.2004.03.026

Skotland, T., Hessvik, N. P., Sandvig, K., and Llorente, A. (2019). Exosomal lipid composition and the role of ether lipids and phosphoinositides in exosome biology. *J. Lipid Res.* 60, 9–18. doi: 10.1194/jlr.R084343

Skotland, T., Sandvig, K., and Llorente, A. (2017). Lipids in exosomes: current knowledge and the way forward. *Prog. Lipid Res.* 66, 30–41. doi: 10.1016/j.plipres.2017.03.001

Steinbichler, T. B., Dudás, J., Riechelmann, H., and Skvortsova, I.-I. (2017). The role of exosomes in cancer metastasis. *Semin. Cancer Biol.* 44, 170–181. doi: 10.1016/j.semcancer.2017.02.006

Sündermann, A., Eggers, L. F., and Schwudke, D. (2016). "Liquid extraction: bligh and dyer," in *Encyclopedia of Lipidomics,* ed. M. R. Wenk (Dordrecht: Springer Netherlands), 1–4. doi: 10.1007/978-94-007-7864-1_88-1

Trajkovic, K., Hsu, C., Chiantia, S., Rajendran, L., Wenzel, D., Wieland, F., et al. (2008). Ceramide triggers budding of exosome vesicles into multivesicular endosomes. *Science* 319, 1244–1247. doi: 10.1126/science.11 53124

Wallin, A., Svanvik, J., Holmlund, B., Ferreud, L., and Sun, X. F. (2008). Anticancer effect of SN-38 on colon cancer cell lines with different metastatic potential. *Oncol. Rep.* 19, 1493–1498.

Yang, F., Teves, S. S., Kemp, C. J., and Henikoff, S. (2014). Doxorubicin, DNA torsion, and chromatin dynamics. *Biochim. Biophys. Acta* 1845, 84–89. doi: 10.1016/j.bbcan.2013.12.002

Zacheo, A., Quarta, A., Zizzari, A., Monteduro, A. G., Maruccio, G., Arima, V., et al. (2015). One step preparation of quantum dot-embedded lipid nanovesicles by a microfluidic device. *RSC Adv.* 5, 98576–98582. doi: 10.1039/C5RA18862H

Zhang, X., Yuan, X., Shi, H., Wu, L., Qian, H., and Xu, W. (2015). Exosomes in cancer: small particle, big player. *J. Hematol. Oncol.* 8:83. doi: 10.1186/s13045-015-0181-x

Zhao, Y. Y., Miao, H., Cheng, X. L., and Wei, F. (2015). Lipidomics: novel insight into the biochemical mechanism of lipid metabolism and dysregulation-associated disease. *Chem. Biol. Interact.* 240, 220–238. doi: 10.1016/j.cbi.2015.09.005

Conflict of Interest: The authors declare that the research was conducted in the absence of any commercial or financial relationships that could be construed as a potential conflict of interest.

frontiers in Bioengineering and Biotechnology

ORIGINAL RESEARCH
published: 11 August 2020
doi: 10.3389/fbioe.2020.00943

Melanoma Peptide MHC Specific TCR Expressing T-Cell Membrane Camouflaged PLGA Nanoparticles for Treatment of Melanoma Skin Cancer

Serkan Yaman[1†], Harish Ramachandramoorthy[1,2†], Gizem Oter[1], Daria Zhukova[1], Tam Nguyen[1], Manoj K. Sabnani[3], Jon A. Weidanz[3] and Kytai T. Nguyen[1,2]**

[1] Department of Bioengineering, The University of Texas at Arlington, Arlington, TX, United States, [2] Joint Bioengineering Program, The University of Texas Southwestern Medical Center, Dallas, TX, United States, [3] Department of Biology, University of Texas at Arlington, Arlington, TX, United States

OPEN ACCESS

Edited by:
Stefano Leporatti,
Institute of Nanotechnology (CNR), Italy

Reviewed by:
Paolo Bigini,
Mario Negri Institute for Pharmacological Research (IRCCS), Italy
Pradipta Ranjan Rauta,
The University of Texas MD Anderson Cancer Center, United States

***Correspondence:**
Jon A. Weidanz
weidanz@uta.edu
Kytai T. Nguyen
knguyen@uta.edu

[†] These authors have contributed equally to this work

Specialty section:
This article was submitted to Nanobiotechnology, a section of the journal Frontiers in Bioengineering and Biotechnology

Received: 07 May 2020
Accepted: 21 July 2020
Published: 11 August 2020

Citation:
Yaman S, Ramachandramoorthy H, Oter G, Zhukova D, Nguyen T, Sabnani MK, Weidanz JA and Nguyen KT (2020) Melanoma Peptide MHC Specific TCR Expressing T-Cell Membrane Camouflaged PLGA Nanoparticles for Treatment of Melanoma Skin Cancer. Front. Bioeng. Biotechnol. 8:943. doi: 10.3389/fbioe.2020.00943

Melanoma is one of the most aggressive skin cancers, and the American Cancer Society reports that every hour, one person dies from melanoma. While there are a number of treatments currently available for melanoma (e.g., surgery, chemotherapy, immunotherapy, and radiation therapy), they face several problems including inadequate response rates, high toxicity, severe side effects due to non-specific targeting of anti-cancer drugs, and the development of multidrug resistance during prolonged treatment. To improve chemo-drug therapeutic efficiency and overcome these mentioned limitations, a multifunctional nanoparticle has been developed to effectively target and treat melanoma. Specifically, poly (lactic-co-glycolic acid) (PLGA) nanoparticles (NPs) were coated with a cellular membrane derived from the T cell hybridoma, 19LF6 endowed with a melanoma-specific anti-gp100/HLA-A2 T-cell receptor (TCR) and loaded with an FDA-approved melanoma chemotherapeutic drug Trametinib. T-cell membrane camouflaged Trametinib loaded PLGA NPs displayed high stability, hemo- and cyto-compatibility. They also demonstrated membrane coating dependent drug release profiles with the most sustained release from the NPs proportional with the highest amount of membrane used. 19LF6 membrane-coated NPs produced a threefold increase in cellular uptake toward the melanoma cell line *in vitro* compared to that of the bare nanoparticle. Moreover, the binding kinetics and cellular uptake of these particles were shown to be membrane/TCR concentration-dependent. The *in vitro* cancer killing efficiencies of these NPs were significantly higher compared to other NP groups and aligned with binding and uptake characteristics. Particles with the higher membrane content (greater anti-gp100 TCR content) were shown to be more effective when compared to the free drug and negative controls. *In vivo* biodistribution studies displayed the theragnostic capabilities of these NPs with more than a twofold increase

in the tumor retention compared to the uncoated and non-specific membrane coated groups. Based on these studies, these T-cell membrane coated NPs emerge as a potential theragnostic carrier for imaging and therapy applications associated with melanoma.

Keywords: membrane-based drug delivery, T-cell membrane-coated nanoparticles, theragnostic nanoparticles, melanoma, cancer therapy

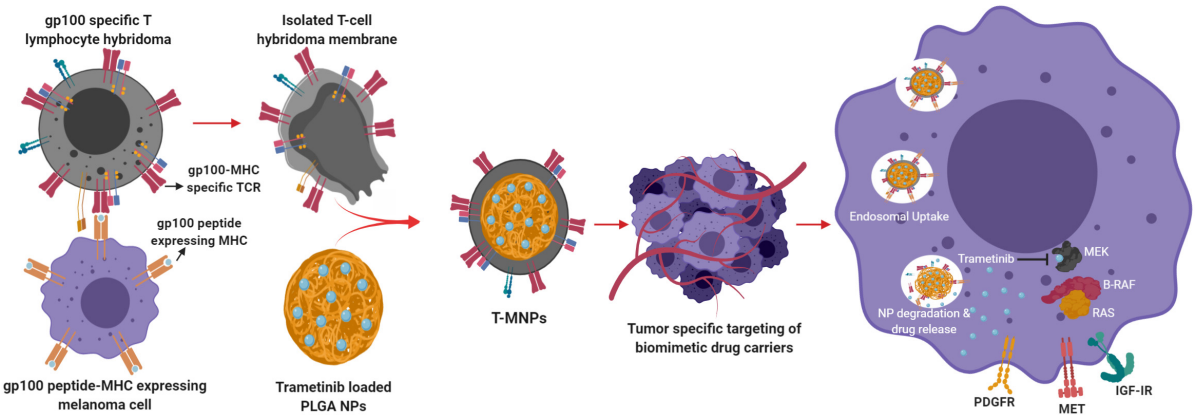

GRAPHICAL ABSTRACT |

INTRODUCTION

Melanoma is one of the most common cancer types in the United States. It is the most aggressive type of skin cancer and influences people of all ages. Heavy exposure to ultraviolet (UV) radiation, from sunlight or the use of indoor tanning devices (classified as carcinogenic by the International Agency for Research on Cancer) are some of the major causes of melanoma. Risk is also increased for people who are sun-sensitive and those with a weakened immune system (Hayes et al., 2016; Wheatley et al., 2016; Street, 2019). Although many advances have been made for the treatment of aggressive melanoma stages, including improved chemotherapy, targeted therapy, immunotherapy, radiotherapy, and the combinations of the two (Hauschild et al., 2003), most advanced melanoma cases are incurable. Chemotherapy and targeted therapy involve the administration of drugs that often stop DNA transcription or block intracellular signaling pathways in the hope of inhibiting cell growth and replication. In chemotherapy, drugs such as dacarbazine, cisplatin, vinblastine, and temozolomide are widely used. A novel mitogen-activated extracellular signal-regulated kinase (MEK) inhibitor, Trametinib, was approved by the United States Food and Drug Administration (FDA) in May 2013 as a single agent for the treatment of BRAF V600E/K mutant metastatic melanoma (Lugowska et al., 2015). While there are a wide number of therapies and drug combinations available for the treatment of melanoma, a key limitation in the efficacy of chemotherapy is the severe side effects and the development of multidrug resistance during prolonged treatment. Chemotherapy and the listed traditional treatments, however, are often accompanied with insufficient response rates and numerous severe side effects owing to the low efficacy and non-specific targeting mechanisms of drug delivery (Lugowska et al., 2015).

One particular focus of interest in immunotherapy encompasses technologies such as cell therapy. Immune cells are isolated from immunosuppressed cancer patients and reprogrammed *in vitro* against cancer antigens (specific to the cancer present in the patient). Current research has mostly focused on the modification of dendritic cells and T-cells, with T-cell based cancer immunotherapy having been used effectively in cancer treatment (Tran et al., 2014). T-cells are collected from patient's own body and engineered to generate specific receptors on their surface. These receptors are referred to as chimeric antigen receptors (CARs), which are a specific type of protein located on tumor cells and provide the T-cells with a way to recognize and kill cancer cells (Zhao and Cao, 2019). Although these methods have been proven to be effective, they are accompanied by several limitations. Along the high costs and complexities of isolation, the long-term presence of re-programmed cells in the body poses some major concerns. The possible risks of long-term survival of re-programmed cells have included the development of autoimmune disease and can subsequently lead to death (Sharpe and Mount, 2015; Charrot and Hallam, 2019; Stoiber et al., 2019).

Nanoparticle-based drug delivery systems have recently gained extensive attention for cancer detection and therapy. Nanoparticles possess several advantages, including increased stability, enhanced carrier capacity, varied feasible methods of administration and the ability to incorporate both hydrophilic and hydrophobic types of drugs (Pinto-Alphandary et al., 2000). Nano-vehicles often serve to protect the drug and can be customized to release the drug in a sustained fashion. Sustained

kinetics could lead to enhanced drug bioavailability at the cancer site and reduced toxicity to healthy tissues. Several currently studied, nano-based drug delivery platforms for melanoma include polymeric carriers, liposomes, polymersomes, carbon-based nanoparticles, and protein-based nanoparticles (Cai et al., 2014). Polymer based nanocarriers are widely studied due to their long-term stability and ability to provide a sustained drug release over prolonged periods of time. Current FDA approved examples of polymers include PLGA (polylactic-co-glycolic acid) and PLA (polylactic acid). Even though such polymers are biocompatible, they are still far from complete immune evasion (Danhier et al., 2012). To overcome the limitations of current drug delivery and immunotherapy methods, numerous novel modifications have been studied over the last few decades in the hopes of giving polymeric nano-carriers the ability to escape the immune surveillance. Several of these modifications include PEGylation, plasma-surface modification and lipid-based or cell membrane masking. In addition, with the emergence of nanotechnology, the use of bio/nano-carriers is widely expected to alter the landscape of cancer treatment. For example, cell membrane-based drug delivery applications have raised an interest due to the ability of providing better "stealth" properties for foreign biomaterial-based vehicles to remain unnoticed in the face of immune cells. Several of the stealth functionalities of synthetic and biopolymers are used to enable prolonged pharmacokinetics and improve bio-distribution of the particles.

In this study, we have hypothesized that membrane-coated nanoparticles present a comprehensive evasion strategy against the multi-faceted nature of immune clearance and a cancer cell specificity approach. Cell membrane coated biomimetic nanoparticles have made an impressive contribution to the improvement of cancer therapy (Fang et al., 2014) due to the cell membrane structure and retained cellular antigens. Biomimetic NPs carry special advantages, such as long blood circulation, ligand recognition, immune escape, homotypic targeting, and the ability for a sustained drug delivery (Tan et al., 2015). Recently, cell membrane coated nano-systems with unique features and functions have been tested and proved to have higher circulation time and immune evasion (Parodi et al., 2013; Hu et al., 2015). In this study, we have used a hybridoma T-cell with specific targeting against the melanoma cancer. The hybridoma 19LF6 expressed gp100 antigen-MHC molecule recognizing moiety. This cell membrane would be extracted and coated on PLGA nanoparticles encapsulating dyes (coumarin-6 for *in vitro* studies/lipophilic DiD for *in vivo* studies)/Drug (Trametinib) wherein serving as a highly melanoma specific carrier for diagnosis/treatment, respectively. The presence of anti-gp100 TCR on T-MNPs would specifically target gp100 presenting melanoma cells and enhance cellular uptake of T-MNPs. The chemo-drug, Trametinib, was selected due to its effectiveness against cell lines carrying a V600E BRAF oncogenic mutation acquired by DM-6 and 1520 cancer cell lines. Trametinib is an FDA approved MEK (MEK 1 and 2) that can also be used in combination with other approved anti-melanoma drugs. PLGA polymer was chosen for its excellent properties, including biocompatibility, biodegradability, FDA and European Medicine Agency approval, adaptability to both hydrophobic and hydrophilic drugs, and sustained drug release kinetics. Properties of T-MNPs, including binding affinity with skin cancer cells, cellular uptake, therapeutic efficacy, particle retention, and biodistribution, were evaluated using cell cultures and animal models. Their results were also compared to non-specific membrane coated (A-MNPs and D-MNPs) and naked PLGA NPs (NNPs).

MATERIALS AND METHODS

Materials

Poly (D, L lactide-co-glycolide) (PLGA) (inherent viscosity 50:50 with carboxyl end groups) was purchased from Akina (PolySciTech; West Lafayette, IN, United States). Poly (vinyl alcohol) (PVA, MW 30,000–70,000) and DCM (Dichloromethane) were obtained from Sigma Aldrich (St. Louis, MO, United States). Trametinib, coumarin-6, Tris-HCL, D-glucose, *B*-Mercaptoethanol, Phenylmethylsulfonyl fluoride (PMSF), Protease inhibitor cocktail, Triton® X-100, Dimethyl sulfoxide (DMSO) and RPMI-1640 were also received from Sigma-Aldrich. The Avanti Polar Lipids Mini Extruder Kit was ordered from Avanti Polar Lipids (Alabaster, AL, United States). RIPA buffer was purchased from Alfa Aesar (Haverhill, MA, United States). SDS-PAGE gel, and Mini PVDF transfer pack were obtained from Bio-Rad. TCR β chain (Armenia Hamster IgG) – antibody and its isotype antibody were bought from BD Biosciences. Nuetravidin biotin binding protein, Superblock solution, BCA assay kit and DNAse were obtained from Thermofisher Scientific. Formvar coated copper TEM grids were purchased from Electron Microscopy Sciences. Fetal bovine serum (FBS), 1X trypsin EDTA, Dulbecco's Modified Eagle's Medium (DMEM) and penicillin-streptomycin were ordered from Invitrogen. Biotinylated gp100-HLA-A2/B2M (gp100 refold) and biotinylated GIGL peptide-HLA-A*201/B2M complexes were synthesized from Dr. Weidanz's laboratory. gp100 refold heavy chain and Beta-2-Microglobulin chain were expressed in and harvested from *Escherichia coli* in the form of inclusion bodies. The complex was biotinylated using Avidin Biotinylation kit [Bulk BirA: BirA biotin-protein ligase bulk reaction kit]. gp100-2M (209–217) peptide was received from Genscript. bGIGL complex was synthesized in a similar fashion. DM-6, and 1520 cell lines were obtained from Dr. Weidanz's lab. T-cell hybridomas 19LF6 and DO11.10 were kind gifts from Dr. Devin Lowes (Texas Tech University Health Sciences Center) and Dr. Philippa Marrack (National Jewish Health, Denver, CO, United States), respectively.

Synthesis of PLGA Nanoparticles

Poly (lactic-co-glycolic acid) nanoparticles (naked NPs; NNPs) were synthesized via a modified single emulsion (O/W) technique as described previously by Menon et al. (2014). Briefly, 90 mg of PLGA 50:50 and 4.5 mg of Trametinib were dissolved in 3 mL of DCM and sonicated at 30 W for 2 min to allow dispersion

of PLGA and Trametinib in the solvent. The resulting solution was added in dropwise to 15 ml of filtered 5% (w/v) PVA solution under stirring conditions. The suspension was then sonicated at 30 W for 10 min and then allowed to stir overnight to evaporate the organic solvent. The obtained nanoparticle suspension was centrifuged at 15,000 rpm for 30 min. The supernatant was saved for the drug loading evaluation, and the PLGA NP pellet was re-suspended in 3 ml of DI water followed by freeze-drying for 24 h. Nanoparticles for imaging/diagnostic techniques were synthesized by a similar procedure with coumarin-6 instead of the Trametinib.

Cell Lines and Culture Conditions

The cell lines used for the experiments, DM-6, 1520, A549 and 19LF6, were maintained in RPMI-1640, supplemented with 10% (v/v) fetal bovine serum (FBS) and 1% (v/v) penicillin streptomycin. DO11.10 and HDF cell lines were maintained in high glucose DMEM, supplemented with 10% (v/v) fetal bovine serum (FBS) and 1% (v/v) penicillin streptomycin. All cells were incubated at 37°C, 5% CO_2.

Synthesis of Cell Membrane-Coated NPs (MNPs)

To harvest the cell membrane, cells were grown to confluency in T-225 cell culture flasks. Cells were isolated by trypsinization and centrifuged at 1,000 rpm for 5 min. To remove any remaining media contents, the cells were washed with cold 1X PBS and centrifuged at 1,000 g for 10 min. The resulting pellet was re-suspended in hypotonic lysis buffer (10 mm Tris-HCL, pH = 7.5) and supplemented with the ready-to-use 1× protease inhibitor cocktail. The solution was kept on ice for 20 min and then centrifuged at 1,000 *g* for 10 min. The pellet was re-suspended in cold 0.25 × PBS and kept on ice for 20 min followed by centrifugation at 800 *g* for 5 min. The final pellet was collected in cold 1× PBS. The cell membrane mix was analyzed for the DNA and protein content using Nano-Drop 1000 Spectrophotometer (Thermo Fisher Scientific)/PicoGreen DNA assays and BCA assay kits, respectively. To eliminate any remaining DNA contents, DNAse reaction was performed on the cell extract by incubation with DNAase (the amount of DNAse added varied with the DNA content in the cell extract sample) for least 1 h at 37°C.

Poly (lactic-co-glycolic acid) (PLGA) nanoparticles (naked NPs; NNPs) were coated with different cell membranes (MNPs) including 19LF6, DO11.10 and A549 by adapting a previously used technique by Hu et al. (2011). These particles were loaded with an FDA-approved chemotherapeutic drug, Trametinib, suitable for treatment of melanoma cell lines containing V600E BRAF mutation. Briefly, NNPs were re-suspended in a cell membrane solution at different NNP weight to membrane protein weight ratios (w/w): 1:0.5, 1:1, 1:2 and 1:3. The mixture was then extruded 15 times using a pre-heated Avanti Polar Lipids Mini Extruder (37°C). The extrusion was performed using a 200-nm polycarbonate membrane. The resulting membrane coated NPs (MNPs) were dialyzed with a 100 kDa MWCO dialysis membrane for 2 h. Prior to freeze-drying, dialyzed MNP solution was supplemented with D-glucose at a final concentration of 1 mg/ml. Three types of membrane-coated NPs were created namely: (1) 19LF6 cell line (T-cells specific to melanoma) coated NPs (T-MNPs) – our treatment, (2) DO11.10 cell line (non-specific T-cells) coated NPs (D-MNPs) – control for T-cells, and (3) A549 cell line (lung cancer) coated NPs (A-MNPs) – control for other cell types.

Physiochemical Characterizations

Nanoparticle size, polydispersity index, and zeta potential were investigated using Dynamic Light Scattering (DLS) technique. To measure the size of the nanoparticles, NP suspension (10 μl of 500 μg/ml) was added to 3 ml of deionized water and inserted into the DLS in a compatible cuvette. To generate TEM images of MNPs, 10 μl of 250 μg/ml MNP suspension was added to plasma treated Formvar Square Mesh Copper Grids and airdried. An H-7500 TEM (Hitachi) transmission electron microscope was used to visualize the particle morphologies. Confirmation of T-cell receptor membrane protein (TCR) on the 19LF6 cell membranes coated nanoparticles was performed via flow cytometry. The particles were also stained with TCR- β chain to evaluate the presence of any TCR or TCR components on synthesized T-MNPs. Briefly, 1mg/ml of T-MNP solution was prepared in a staining buffer (0.5% BSA, 1mm EDTA in 1× PBS). 200 μl of the solutions was added with antibodies Armenian Hamster anti-TCR β and Armenian Hamster IgG antibodies at 1:100 dilution, for test group and isotype control, respectively. The solutions were then incubated for 30 min and then washed 3× times with the staining solution. The cells were collected by centrifuging at 14,000 rpm for 20 min and resuspending in 200 μl of staining buffer. Each of the groups was then analyzed using a BD Biosciences LSR II Flow cytometer without an FSC threshold to be able to detect nanoparticles.

Stability of T-MNPs with varying NP weight to membrane protein weight ratios (w/w) was evaluated by monitoring the particle size at pre-determined time-points using DLS. To observe the stability of T-MNPs, particles of different membrane ratios were incubated in 0.9% saline over 48 h. T-MNP suspensions were prepared as described above, and the size of particles was measured at different time points (0, 0.5, 1, 3, 6, 12, 24, and 48 h).

Binding Kinetics Assay

The binding characteristics of T-MNPs were studied using ResoSens label-free optical detection system. Biotinylated pMHC complexes HLA-A*02:01–IMDQVPFSV ($gp100_{209-217}$) and HLA-A*02:01–GILGFVFTL (Influenza-M, negative control) were synthesized by our group previously. In this study, T-MNPs with the highest and lowest NP weight to membrane weight ratios were tested at varying concentrations. D-MNPs were tested at the highest NP to membrane protein ratio (w/w) (1:2), and at a concentration 2× higher than the highest concentration used for T-MNPs. All samples were tested against a specific gp100-b monomer and non-specific b monomer GILG.

Drug Loading and Drug Release Kinetics of T-MNPs

The drug/dye loading efficiency was calculated by an indirect method where the drug/dye present in the supernatant collected from the nanoparticle synthesis process was measured, and the following formula was used for loading efficiency calculation:

$$\% \text{ loading efficiency} = \frac{\text{Amount of drug used} - \text{Amount of drug in supernatant}}{\text{Amount of drug used}} \times 100$$

The drug (Trametinib) release study was carried out for a period of 28 days. Briefly, 1 mg of NNPs and T-MNPs [NP: membrane protein weight (w/w) ratios of 1:0.5, 1:1 and 1:2] were taken at a concentration of 1 mg/ml and were incubated at 37°C. At each pre-determined time-point, the samples were centrifuged at 14,000 rpm for 30 min, and supernatants were collected and stored at −20°C for later analysis. The pellets were re-suspended in fresh 1× PBS and incubated for further time points. Each of the drug release aliquots was analyzed using a UV-vis Spectrophotometer at 330 nm. The amount of drug released was determined against a standard curve for Trametinib.

In vitro Studies of T-MNPs

Assessment of Glycoprotein Expression (gp100) in Tumor Cells by Western Blot and RT PCR Analysis

The expression of glycoprotein (gp100) expression in melanoma cell lines, DM6 and 1520, and lung carcinoma cells A549 were evaluated by western blotting and RT (reverse transcriptase)-PCR. Cellular proteins were extracted from cancer cells using RIPA lysis buffer containing protease cocktail, and protein concentration was measured using the Pierce BCA protein assay kit (#23227, Thermo Fisher, United States). Cellular proteins (12 and 6 μg from each cell line) were separated by 10% SDS-PAGE and electrophoretically transferred onto PVDF membranes. The membranes were blocked with 5% BSA in TBST for 1 h at room temperature, followed by incubation with primary antibodies overnight at 4°C. The membranes were washed with TBST 3× for 5 min and then incubated with HRP conjugated secondary antibodies for 1 h at room temperature. Protein bands were developed using an ECL detection system and imaged using the Chemidoc TM Imaging system.

Total RNA was extracted from DM6, 1520, and A549 cells by using RNeasy plus Mini kits (Qiagen) according to the manufacturer's instructions. Approximately 3 μg of total RNA was reverse transcribed into cDNA (High-Capacity cDNA RT Kit) and subjected to PCR in Bio-Rad Thermocycler (T100TM) with the following conditions, pre-denaturation at 95°C for 1 min and 30 cycles of denaturation at 95°C for 15 s, primer annealing at 57°C for 30 s, and extension at 72°C for 60 s. The gp100 gene was amplified using the following primers: 5′ GCTTGGTGTCTCAAGGCAACT 3′ (gp100 for) and 5′ CTCCAGGTAAGTATGAGTGAC 3′ (gp100 rev). β-actin gene was amplified using 5′ GGCACCACACCTTCTACAAT 3′ and 5′ GCCTGGATAGCAACGTACAT 3′. The relative amount of each gene was normalized to the amount of β-actin and the RT-PCR result for each gene was expressed as fold change over the basal level.

Cellular Uptake and Therapeutic *in vitro* Studies

To determine the cell specific targeting function of the nanoparticle *in vitro*, cellular uptake studies were conducted. Briefly, 1520 (gp100 positive), DM-6 (gp100 positive) and A549 (gp100 negative) cell lines were seeded in a 96 well plate at a density of 20,000 cells/well. Coumarin-6 (C-6; fluorescent dye) loaded T-MNPs (gp100 refold specific) and D-MNPs (non-specific to gp100 refold) at varying NP to membrane weight ratios: 1:0.5, 1:1 and 1:2, were tested. Serially diluted MNP concentrations (100, 250, 500, and 1000 μg/ml) at different NP to membrane ratios were prepared. The cells were exposed to different NP groups for approximately 2 h, subsequently washed with 1× PBS and lysed with 250 μl/well of 1% Triton® X-100. Cell lysis extracts were then analyzed for the protein content using the Pierce BCA protein assay kit (Thermo Scientific, Rockford, IL, United States) and C-6 fluorescent intensity using a UV-vis Spectrophotometer (458/540 ex/em). Total protein concentration in each lysate was determined using a BSA standard curve. The uptake of the nanoparticles was calculated by normalizing the particle concentration (determined from fluorescence intensity in a lysate) in each sample with total cell protein, which correlated to the number of cells in the sample. Untreated cells were used as a negative control.

For the therapeutic efficiency of Trametinib loaded T-MNPs, melanoma cell lines, DM-6 and 1520, were used. Firstly, the effective concentration (IC50) of the Trametinib on the cell lines were determined by exposing cells seeded in a 96 well plate at density of 5,000 cells/well to a free drug of known concentrations (1.2, 2.5, 5, 10, 15, 20, 25, 50, 75, and 100 μg/mL) for a period of 72 h. After 72 h of incubation, the cell death was analyzed using MTS assays (CellTiter 96® AQueous Non-Radioactive Cell Proliferation Assay, Promega) according to manufacturer instructions. Therapeutic efficiency of different nanoparticle groups including 1:2 NP weight to membrane weight ratio T-MNPs (melanoma-specific), A-MNPs (non-specific), and D-MNPs (non-specific) as well as free drug and NNPs (bare/naked NPs) was determined. Three different NP concentrations (0.83, 1.66, and 2.5 μg/ml for DM-6; 15, 29, and 44 μg/ml for 1520) were used based on the calculation of the IC50 studies. Cells seeded in a 96 well plate at a density of 20,000 cells/well were exposed to the described groups for 72 h, and the cell viability was determined using MTS assays.

Cyto-Compatibility and Hemo-Compatibility

A cyto-compatibility study was performed on human dermal fibroblast cells (HDFs). T-MNPs and NNPs were re-suspended in media and added to cells at various concentrations (50, 100, 250, 500, and 1,000 μg/ml) followed by 24 h of incubation at 37°C. After incubation, cell viability was evaluated using MTS assays. Cells without treatment and cells treated with 1% Triton® X-100 served as positive and negative controls, respectively.

Blood clotting and hemolysis property of T-MNPs were performed on fresh human blood. Briefly, for hemolysis, 200 μl of blood was added with 10 μl of the T-MNPs prepared in 0.9% saline at varying concentrations (50, 100, 250, 500, and 1,000 μg/ml). 10 μl of 0.9% saline and 10 μl of DI water was used as positive and negative controls. The tubes were incubated at 37°C for 2 h under gentle agitation and then were centrifuged at 1,000 *g* for 10 min. The absorbance of sample supernatants was monitored at 545 nm using a UV-vis Spectrophotometer. For hemo-compatibility, 10 μl of T-MNPs at the various concentrations (50, 100, 250, 500, and 1,000 μg/ml) in 0.9% saline was mixed in 50 μl activated blood (0.1 M $CaCI_2$ added blood). At pre-determined time-points (10, 20, 30, and 60 min), 1.5 ml of DI water was added to all samples to inactivate blood clotting, and the samples were incubated for 5 min at room temperature. Supernatants were collected and monitored at 540 nm using a UV-vis Spectrophotometer. 0.9% saline and DI water were used as positive and negative controls.

In vivo Biodistribution Studies of T-MNPs via Near-Infrared Fluorescence Imaging

The tumor specific targeting and accumulation of T-MNPs were assessed using a subcutaneous xenograft model of melanoma. It was established by injecting 0.5×10^6 DM-6 cells in 150 μl of Matrigel (Corning, United States) subcutaneously in athymic nude mice. Tumor volumes were checked at regular intervals and treatment started when the volume reached ∼150 mm^3. For imaging of NP biodistribution *in vivo*, lipophilic DiD (Thermo, United States) dye was incubated with 19LF6 T-MNPs to stain membranes for 30 min and unbound dye was washed away. All nanoparticle groups were injected intravenously through the tail vein. Following, anesthetized mice were scanned at different time points using a Kodak™ *in vivo* imaging system. After 24 h time point, the mice were euthanized under anesthesia. Tumors and organs were excised and prepared for *ex vivo* imaging and fluorescent analysis. Excised organs and tumors then were analyzed by their weights and fluorescent responses.

Statistical Analysis

All results were expressed as mean ± SD performed with $n = 3$ for most of the experiments if not specified. Results were analyzed using either one-way or two-way ANOVA depending on experiments with $p < 0.05$, and the student's *t*-test was used to identify differences between groups. $P < 0.05$ was considered to be statistically significant.

RESULTS

Particle Size, Zeta Potential, and Morphology

The DLS results showed that the T-MNPs with 1:2 NP to membrane ratio had a particle size of about 193 ± 56 nm with a polydispersity of 0.265. The particle size of naked NPs (NNPs) was around 171.7 ± 76 nm with a polydispersity of 0.109. The particle sizes were confirmed with Transmission Electron Microscopy (**Figure 1A**). Furthermore, TEM images of T-MNPs showed that the particles were smooth and spherical with a clear core-shell structure. The T-MNPs also had a stable ZETA potential value of −36 mV compared to a −20 mV ZETA potential of the NNPs. The stability studies also showed that the T-MNPs were stable for the whole incubation period, which was denoted by no significant change in the size of the T-MNPs during the course of experiment and, therefore, there was no sign of significant aggregation (**Figures 1B,C**).

Drug loading efficiency of T-MNPs was found to be 61%. To analyze how different membrane coating ratios would affect Trametinib release from T-MNPs, the drug release kinetics of T-MNPs with different NP to membrane weight ratios (1:0.5, 1:1, and 1:2) and naked NPs were evaluated over 28 days. The rate of release kinetics differed across the three ratios of NP to membrane protein (w/w) T-MNPs. The Trametinib release rate was significantly slower and sustained for all ratios of T-MNPs when compared to MNPs, with the lowest rate of release for 1:2 T-MNPs and the highest one for 1:0.5 (**Figure 1D**). The presence of TCR β chain on 19LF6 cells and T-MNPs were confirmed by flow cytometry analysis as seen by a shift in the absorbance curve (**Figures 2A,B**).

Binding Kinetics of T-MNPs

As shown in **Figure 2C**, T-MNPs bound onto immobilized gp100b in a dose-dependent manner with a higher binding strength observed in samples with higher concentration and higher ratio. In addition, T-MNPs at concentrations 500 and 250 μg/ml were significantly higher when compared to the binding kinetics of 1:2 D-MNPs at 1,000 μg/ml concentration.

Western Blot and Reverse Transcription PCR

DM6 and 1520 cell lines exhibited significant expression of glycoprotein gp100. The expression level in the 1520 cell line was found to be approximately 2× higher than DM-6, whereas the lung cancer cells A549 showed no apparent gp100 protein expression (**Figure 3A**). RT-PCR identified gp100 gene amplicon (751 bp) in all 3 cell lines (**Figure 3B**). The melanoma cancer cell 1520 has demonstrated its higher expression of gp100/HLA-A2 complex protein compared to that of the DM-6 cell line previously (Weidanz et al., 2006).

In vitro Properties of T-MNPs

The cellular uptake of NPs was evaluated on DM-6 (gp100-containing melanoma), 1520 (gp100-containing melanoma), A549 (lung cancer, no gp100 antigen) cell lines. For uptake studies, fluorescent dye (Coumarin 6) loaded NPs were used. To analyze how different NP to membrane weight ratios would affect NP cellular uptake, NPs with 1:0.5, 1:1, and 1:2 ratios were utilized. Such ratios were prepared for D-MNPs and T-MNPs. The results demonstrated that T-MNPs displayed significantly higher uptake compared to the negative control, D-MNPs (**Figures 3C–E**) in gp100-presenting melanoma cell lines. As expected, A549 did not show any selectivity/cellular uptake toward T-MNPs or D-MNPs. Such result was expected

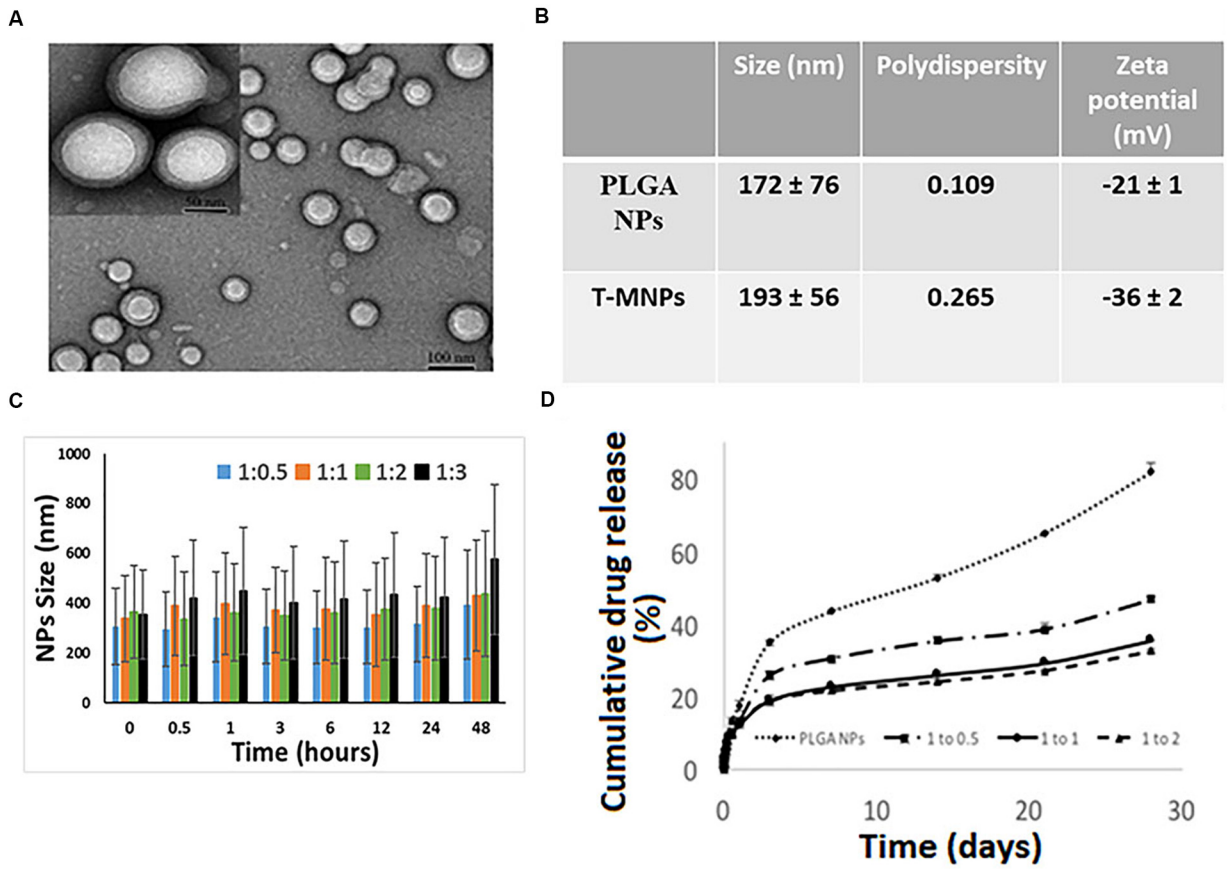

FIGURE 1 | Characterization of T-MNPs. **(A)** TEM images of T-MNPs at 1:2 NP to membrane protein weight ratio. **(B)** Size, polydispersity and zeta potential of PLGA NPs and T-MNPs analyzed using Dynamic Light Scattering (DLS). **(C)** Stability of T-MNPs in 0.9% saline (at varying NP to membrane protein weight ratios: 1:0.5, 1:1, 1:2, and 1:3) evaluated by change in NPs size over a 2-day period using DLS. **(D)** Cumulative% drug release from T-MNPs (varying NP to membrane protein ratios of 1:0.5, 1:1, 1:2 versus PLGA NPs) performed in phosphate buffered saline over 28 days. Samples were analyzed using UV-vis spectrophotometer.

due to the absence of the gp100 antigen on the surface. The IC50 values of Trametinib were calculated to be approximately 29.3 and 1.66 μg/ml for 1520 and DM-6 cell lines, respectively. The therapeutic potential of the Trametinib-loaded T-MNPs was evaluated on both 1520 and DM-6 cell lines. It was shown that T-MNPs had a significantly higher therapeutic efficiency on both melanoma cell lines when compared to the negative controls, specifically at IC50 and IC75 drug concentrations (**Figures 4A,B**).

Cyto- and Hemo-Compatibility Studies

The viability of HDF cells was evaluated after interaction with the T-MNPs and PLGA NPs (naked NPs, NNPs) at various concentrations for 24 h. Since PLGA is an FDA approved and biocompatible polymer, the cytocompatibility of both NNPs and T-MNPs were also observed in our studies. The result illustrated that T-MNPs did not show any toxicity to the cell line up to a concentration of 1,000 μg/ml, similar to PLGA NPs (**Figure 5A**). Blood clotting assay was also performed to elucidate potential blood clotting interferences by T-MNPs. The coagulation time of blood in the presence of T-MNPs was examined at different time-points: 10, 20, 30, and 60 min. Blood coagulation initiates an activation of a cascade of coagulation factors and surface mediated reactions (Smith et al., 2015). At all the tested time points, T-MNPs did not display a significantly different blood clotting pattern when compared to that of the saline control (**Figure 5B**). Furthermore, hemolysis study was performed to test T-MNPs against potential negative effects on red blood cells. T-MNPs showed hemolysis properties lower than 5% up to 1,000 μg/ml concentration.

In vivo Tumor Targeting and Imaging

The *in vivo* tumor targeting and imaging abilities of the T-MNPs were examined to demonstrate whether injected T-MNPs accumulated at the tumor site during the treatment period. *In vivo* imaging results showed that the T-MNPs (melanoma-specific) had better tumor accumulation than those of the control D-MNPs (non-specific) and NNPs or bare PLGA NPs (**Figure 6A**). The T-MNPs mainly accumulated in the tumor within 6 h. Furthermore, the tumor signal from the T-MNPs remained relatively constant throughout 24 h, while the overall signal of the NNP and D-MNP groups was decreased with time. In addition, *ex vivo* organ images revealed that

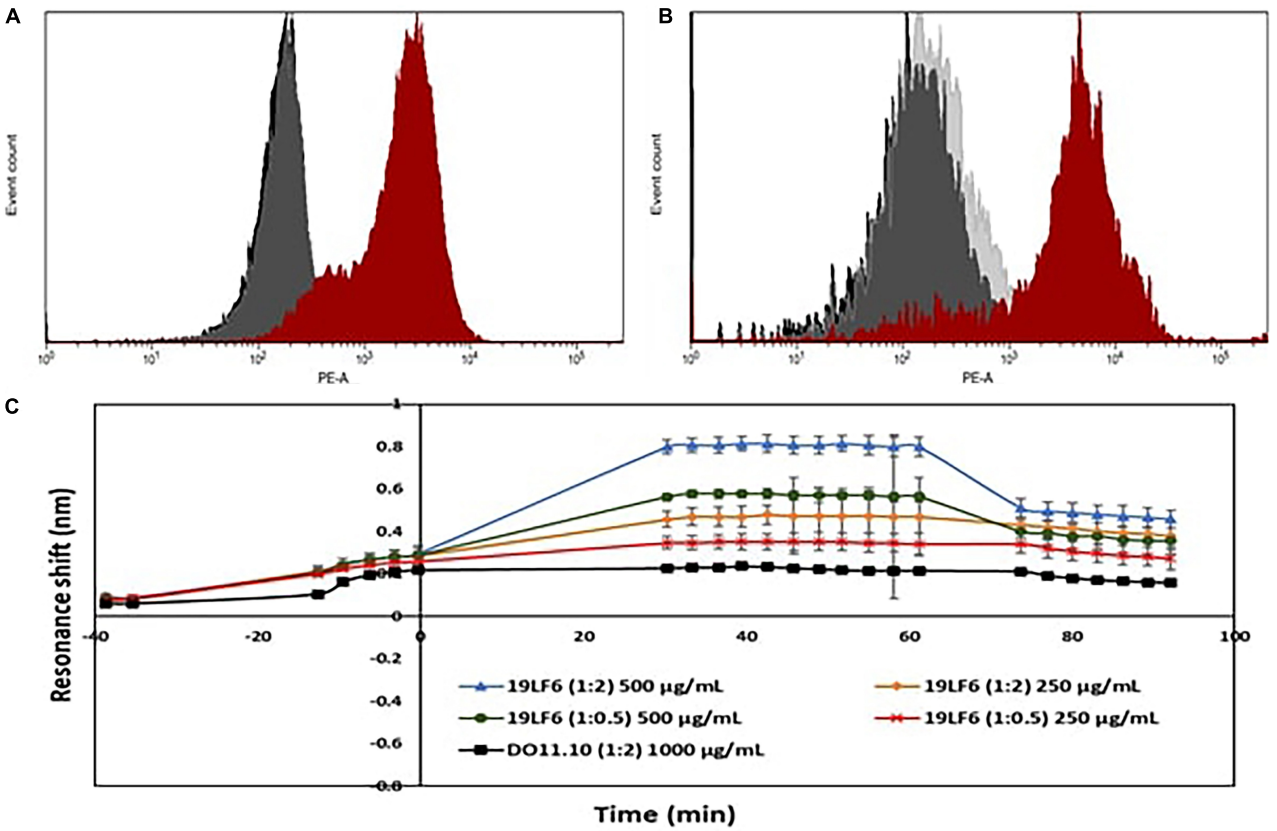

FIGURE 2 | Validation of TCR on T-MNPs. **(A)** Histogram curves demonstrate 19LF6 cells expressing the TCR β chain. 19LF6 cells were stained with either mouse IgG (isotype) or anti-TCR antibody. Unstained, isotype, and stained groups are represented as black, gray, and red curves, respectively. **(B)** T-MNPs also expressed the TCR β chain [19LF6 MNP's were stained with either mouse IgG (isotype) or anti-TCR antibody]. Unstained, isotype, and stained groups are represented as black, gray, and red curves, respectively. Histograms were analyzed using BD LSR II with no threshold on the forward scatter to detect the nanoparticles. **(C)** Binding kinetics of D-MNPs (non-specific control), T-MNPs (our treatment group) and NNPs (negative control) at varying concentrations and NP to membrane protein (w/w) ratios; kinetics were measured in terms of resonance shift over a period of time using ResoSens label-free optical detection.

T-MNPs could efficiently accumulate at tumor tissues and avoid liver accumulation compared to those of D-MNPs and NNPs in a xenograft mouse model as shown in **Figure 6B**. The accumulation of T-MNPs was more than twice the amount of nanoparticle accumulation of D-MNPs or NNPs. This result is also confirmed with fluorescent intensity measurements from homogenized tumor tissues (**Figure 6C**). Therefore, *in vivo* biodistribution results showed that the T-MNP's targeting ability was confirmed via more efficient accumulation than the NNPs and D-MNPs at the tumor sites.

DISCUSSION

We have thus developed a theragnostic system for effective diagnosis and treatment of melanoma. The developed nanoparticle system offers great advantages compared to the conventional drug delivery systems including enhanced retention in the cancer cells and tumor sites compared to non-targeted systems. These NPs also provide controlled/sustained drug release for up to 28 days and the least/null cytotoxic behavior. The NP drug delivery system helps to reduce the cytotoxic effects of chemotherapy drugs and is predicted to minimize immune reactions as the nanoparticles are coated in endogenous T-cell membranes. The dye loaded nanoparticles will serve as an effective tool to accurately visualize the tumor site, whereas the drug loaded nanoparticles will provide the therapeutic effectiveness to treat melanoma. Thus, our results indicate the potential of our designed T-MNPs for theragnostic application to detect and treat melanoma.

In the last decade, it has been proven that cells can be used as effective drug carriers via either themselves or their membranes that can facilitate payload delivery to desired regions (Stephan et al., 2010; Tan et al., 2015). Previous works have also shown that healthy immune cells (i.e., leukocytes) are able to circulate around the body, migrate into tissues, transport through inflamed tissues and adhere to inflamed vessel walls (Muller, 2013). In this manner, cell membrane surface proteins such as ICAM's, CCLs, CXCLs, TCR's, and/or specific CD macromolecules become important to provide an effective drug delivery platform for biomimetic delivery (Thanuja et al., 2018). Recently, studies have shown that cytotoxic T lymphocyte membranes can deliver

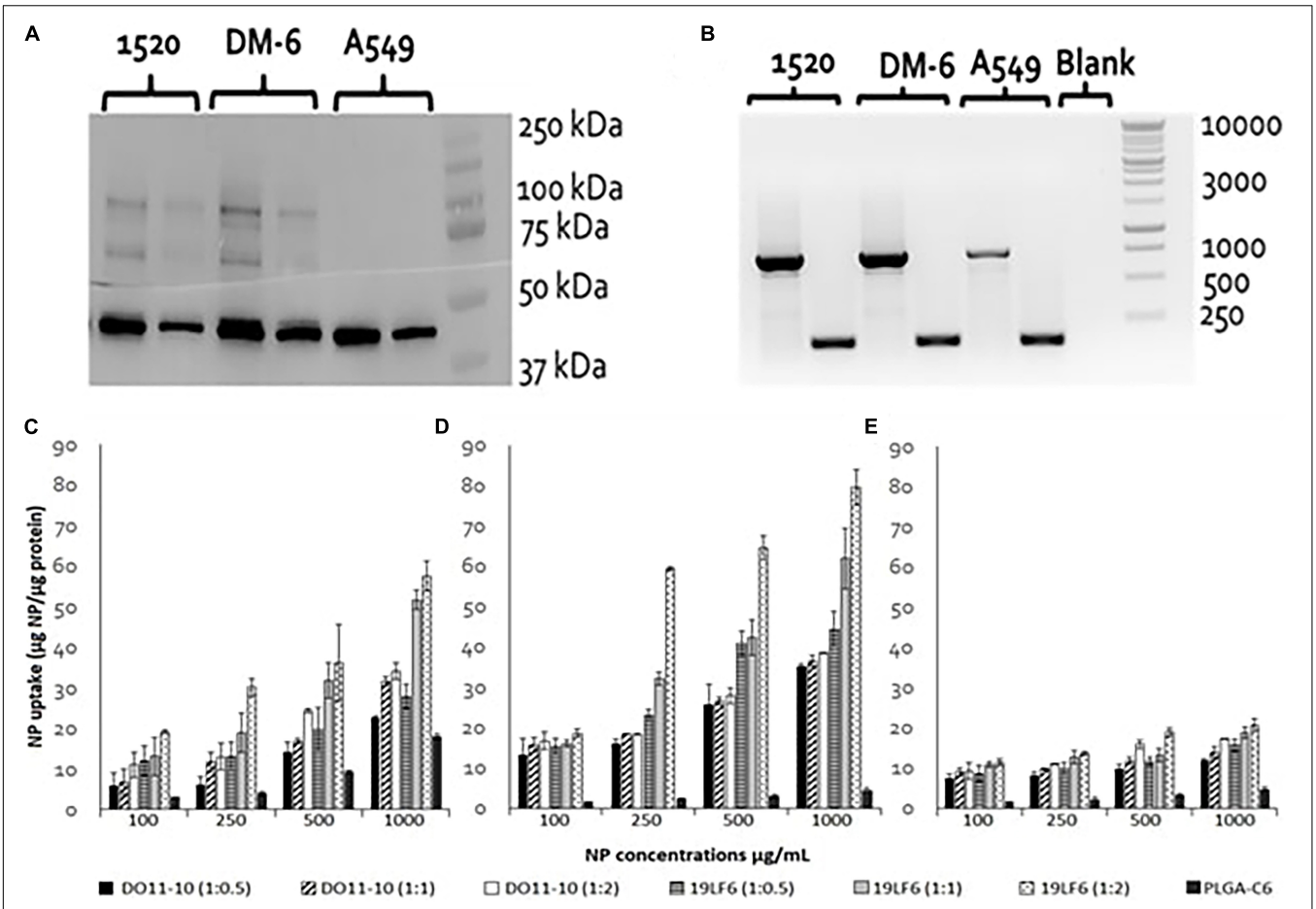

FIGURE 3 | gp100 expression and Cellular uptake of T-MNPs in different cell lines. **(A)** Western blot for assessing of gp100 protein content in 3 cancer cell lines: DM-6, 1520, and A549. β-actin was served as a control (42 kDa). Proteins are represented at two concentrations: 6 µg (right) and 12 µg (left) for each cell line. **(B)** RT-PCR: gp100 (751 bp) expression presented in 1520, DM-6, and A549 cell lines, β-actin served as a control (157 bp). **(C)** DM-6, **(D)** 1520, and **(E)** A549 cell lines were treated with MNPs for 2 h. Cell lysates were analyzed for MNP content using a UV-vis Spectrophotometer and cellular uptake was normalized with total cellular protein. Uptake of D-MNPs, T-MNPs and PLGA NPs (PLGA-C6) are presented at varying NP to membrane protein weight ratios. MNPs were loaded with a fluorescent dye, Coumarin 6 (n = 3).

their payloads to tumor regions; for example, it has been shown that payload delivery can be facilitated through the natural lymphocyte surface proteins such as LFA-1 (Zhang et al., 2017; Huang et al., 2018). Therefore, this study explored the role of target specific cytotoxic T lymphocyte membranes as a drug delivery platform.

The observed shortcomings of several drug/dye-loaded polymeric nanoparticles are their poor stability/increased aggregation, low control over the payload release rate, and rapid clearance from the body. Our results of T-MNPs showed that coating the nanoparticle with cell membranes could overcome these limitations. Physiochemical characterization of synthesized T-MNPs showed excellent colloidal stability in physiological conditions. The increase in stability due to the membrane coating onto the nanoparticles was evident by the stable Zeta potential of the T-MNPs compared to an unstable potential of the NNPs as described by the −30 mV Zeta rule (Kumar and Dixit, 2017). The negative surface charge (−36 mV) of the T-MNPs repel negative charged albumin molecules in the serum, preventing potential aggregations. The stability of T-MNPs in 0.90% saline solution was found to be similar across different NP weight to membrane protein weight (w/w) ratios for up to 2 days (**Figure 1C**). Fang et al. (2014) reported a similar observation where they showed a higher stability of the coated nanoparticle for up to 15 days across a wide range of NP to membrane ratios (1:0.5 to 1:4). The loading efficiency of T-MNPs was observed to be approximately 61%, and the drug release kinetics displayed an initial burst release followed by a sustained release up to 28 days. When comparing T-MNPs and NNPs, it can be clearly seen that cloaking of drug loaded PLGA nanoparticles with T-cell membranes reduced the drug release rates, especially those coated with higher amounts of the cell membrane. This reduction has also been observed in nanoparticles cloaked with membranes from erythrocytes (Hu et al., 2011) where erythrocyte membrane-coated nanoparticles showed slow drug release compared to uncoated nanoparticles. Hu et al. (2011) attributed this effect to the membrane's ability to

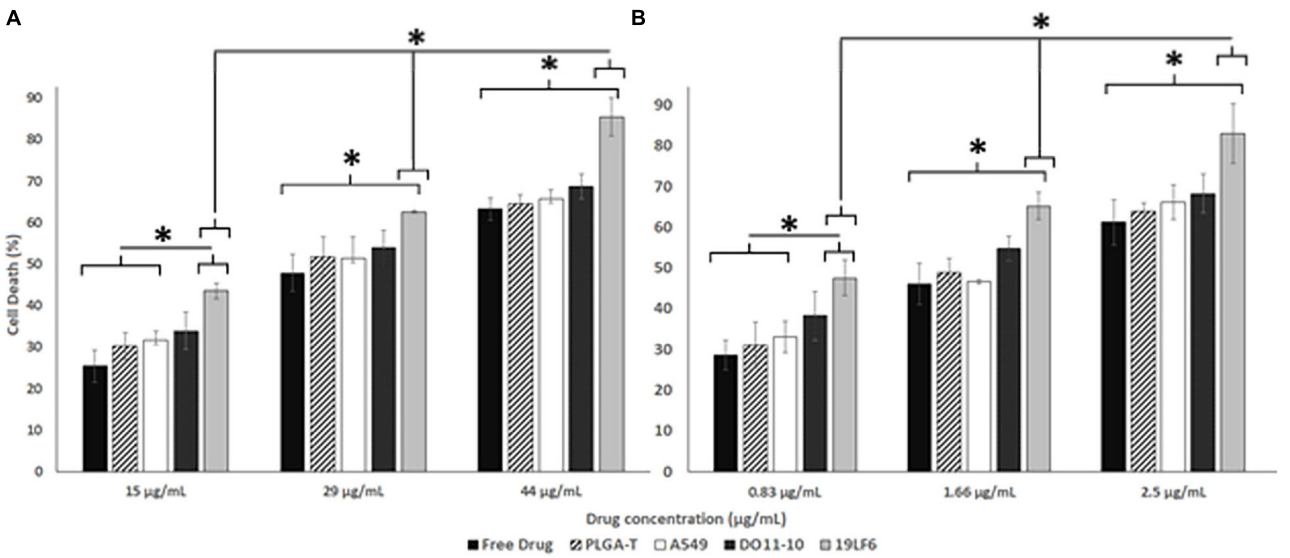

FIGURE 4 | Therapeutic efficiency of T-MNPs. Therapeutic capabilities of T-MNPs, D-MNPs, A-MNPs, NNPs and free Trametinib on **(A)** 1520 melanoma cell line and **(B)** DM-6 melanoma cell lines. Cell were exposed to the nanoparticle suspensions for 72 h (ranging concentrations from IC25 to IC75), and cell viability was evaluated using MTS assays. *Statistically significant with $P < 0.05$.

act as a diffusion barrier to provide better sustained drug release, as compared with PEG-based nanoparticles, thereby enhancing the therapeutic efficacy of the drug in acute myeloid leukemia cells. Furthermore, T-MNPs hold the unique characteristics of natural 19LF6 cell membranes thus avoiding clearance and enhancing circulation. Zhong et al. (2013) previously defined the 19LF6 cell line to contain a metastatic melanoma antigen, gp100 (209–217) – specific T-cell receptor. Our flow cytometric analysis and the binding kinetic results not only confirmed the higher presence of the specific TCR on the nanoparticle coating, but also its ability to bind to its specific target.

As part of the toxicological analysis, the T-MNPs, cyto- and hemo-compatibility were analyzed. The T-MNPs were found to be cyto-compatible up to 1,000 µg/ml concentration, which was shown to be at least as cyto-compatible as NNPs or bare PLGA NPs. This was similar to the results observed by Guo et al. (2015), who demonstrated that erythrocyte-membrane coated PLGA nanoparticles possessed a similar cyto-compatibility compared to bare PLGA nanoparticles. This attributes to the cell mimicking characteristic and the slow drug release characteristics of T-MNPs. Blood clotting characteristics of T-MNPs were compared to the saline control and found to have no significant effect on the blood clotting cascade up to 1,000 µg/ml. According to the criterion in the ASTM E2524-08 standard, percent hemolysis >5% is considered toxic to red blood cells (ASTM E2524-08, 2013). T-MNPs-induced blood hemolysis was observed to be <5% up to 500 µg/ml. Although T-MNPs were found to be toxic to red blood cells at a concentration of 1,000 µg/ml, such high concentrations of the particles might not be used for later studies.

We also continued to investigate the *in vitro* characteristics of these membrane coated nanoparticles and their ability as a highly specific vehicle for cancer targeted delivery. In light of past studies that showed bare PLGA NPs have limitations owing to non-specific targeting and result in uncontrolled tissue distribution of the drug (Danhier et al., 2012) and that cell membrane coating improves immune evasion, target specificity and drug efficacy (Hu et al., 2011), we have devised the proposed design of T-MNPs. Fang et al. (2014), devised surface-engineered PLGA NPs with platelet-membrane-derived vesicles since platelet cells have a natural ability to adhere to injured blood vessels as well as circulating pathogens. Such membrane coating provided the particles with natural platelet-like targeting functions. However, there is no data found in the literature for natural specific targeting (i.e., via TCR receptors) abilities of membrane coated drug carriers so far. The data obtained from our *in vitro* cell studies sheds light to the undiscovered potential of cytotoxic T-cell membrane coated nanoparticles as a biomimicking drug delivery vehicle. In our study, anti-gp100 TCR influence on T-MNP cellular uptake was observed in DM-6 and 1520 melanoma cell lines. Since A549 lung cell lines did not show any apparent gp100 presentation, A549 was used as a negative control cell line. Data collected from binding and cellular uptake studies showed that T-MNPs illustrated superior binding and uptake kinetics attributed to their anti-gp100 TCR. The uptake of T-MNPs at all ratios was significantly higher than that of D-MNPs, the negative control nanoparticles (**Figure 3**). These particles showed selective and effective binding to gp100 carrying melanoma cells when compared to that of D-MNPs made from the negative T-cell control. The uptake of T-MNPs increased with increasing concentrations and was enhanced in the 1520 cell line even more than that of DM-6 cell line. The enhanced 1520 uptake of the T-MNPs might have been due to its ability to better present gp100/HLA-A2

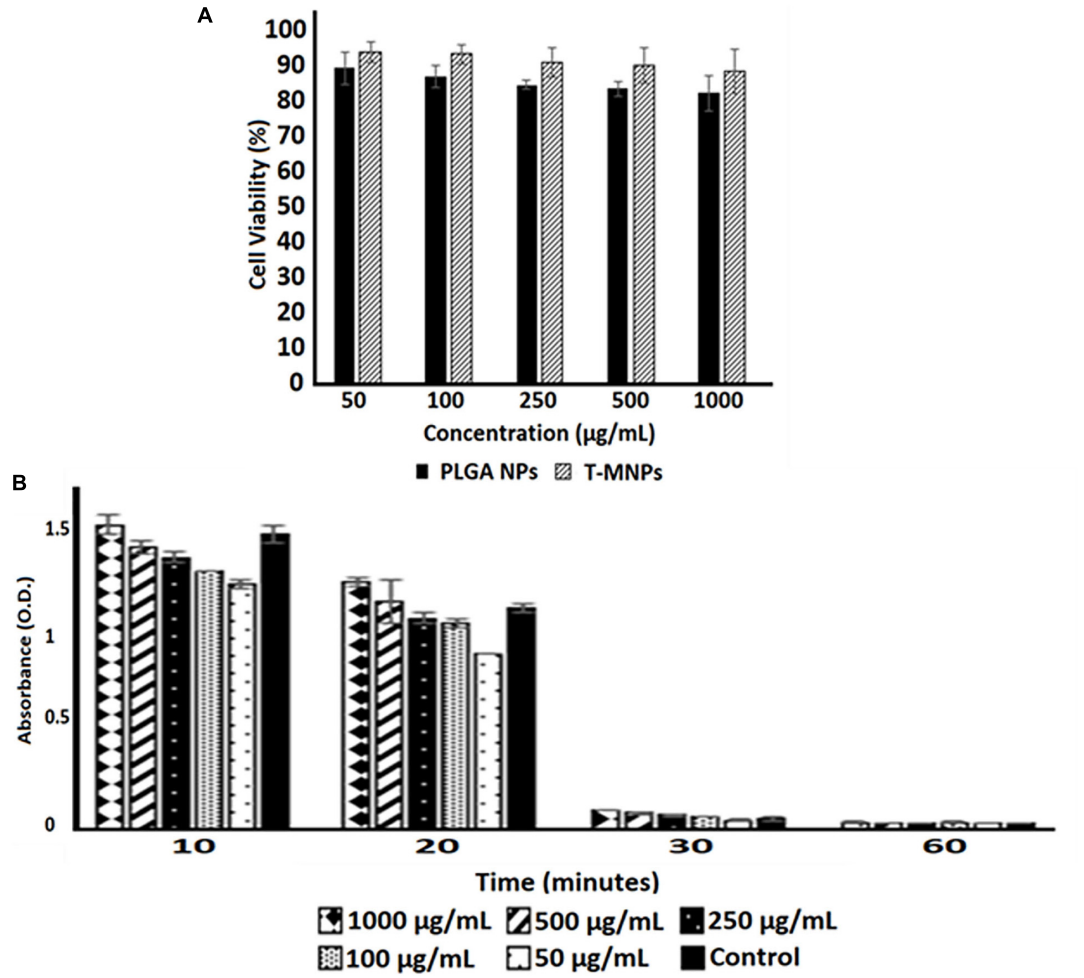

FIGURE 5 | Cyto-/Hemo-compatibility of T-MNPs. **(A)** Cyto-compatibility of T-MNPs was analyzed on human dermal fibroblasts (HDFs) at varying NPs concentrations (50—1,000 μg/ml) for 24 h, and cell viability was quantified using MTS assays (n = 3). **(B)** Blood clotting kinetics of T-MNPs. Clotting efficiency was measured in absorbance units (OD) of the supernatants collected from T-MNPs treated blood samples at pre-determined time-points: 10, 20, 30, and 60 min. The absorbances were quantified using a UV-vis Spectrophotometer (n = 9).

complex protein compared to that of the DM-6 cell line (Weidanz et al., 2006).

Furthermore, therapeutic efficiency of T-MNPs was evaluated. The IC50 values of Trametinib for DM-6 and 1520 were found to be approximately 29 and 1.6 μg/ml, respectively, which were very much similar to the values observed in a previous study by Roller et al. (2016). However, the IC values often depend on numerous human and in-house factors, therefore, they must be performed for each study. T-MNPs were found to be significantly more efficient in killing melanoma cancer cells than any of other groups compared, even much more than free Trametinib at the same concentration, which would attribute to the binding and uptake characteristics of T-MNPs. Particles with a higher membrane content (greater anti-gp100 TCR content) showed to be more effective when compared to that of the lower NP to membrane ratio. These results indicate that proposed membrane coated natural targeting nanoparticles could potentially be used to improve chemotherapeutic efficacy to effectively treat melanoma.

Following the *in vitro* characterizations, the preliminary *in vivo* investigation by the biodistribution study examined whether intravenously injected T-MNPs targeted and recruited/retained at the subcutaneous tumors in the tumor implanted mice. In biodistribution studies, comparing between T-MNPs and other study groups, expected tumor accumulation difference was observed. NPs from almost all groups accumulated mainly at the liver and spleen in 2 h. The T-MNP group showed distinctive accumulation in the tumor region at almost a threefold higher accumulation on the tumor site than D-MNPs and about a twofold increase in accumulation than NNPs. D-MNPs and NNPs, on the other hand, were captured more in the liver. Similarly, Zhang et al. (2017) used non-specific hCTL membranes to target gastric cancer combined with low dose irradiation and observed very similar results in *in vivo* targeting capabilities of hCTL membrane coated nanoparticles. In their study, membrane coated nanoparticles showed a gradual increase in the tumor sites after low dose irradiation exposure.

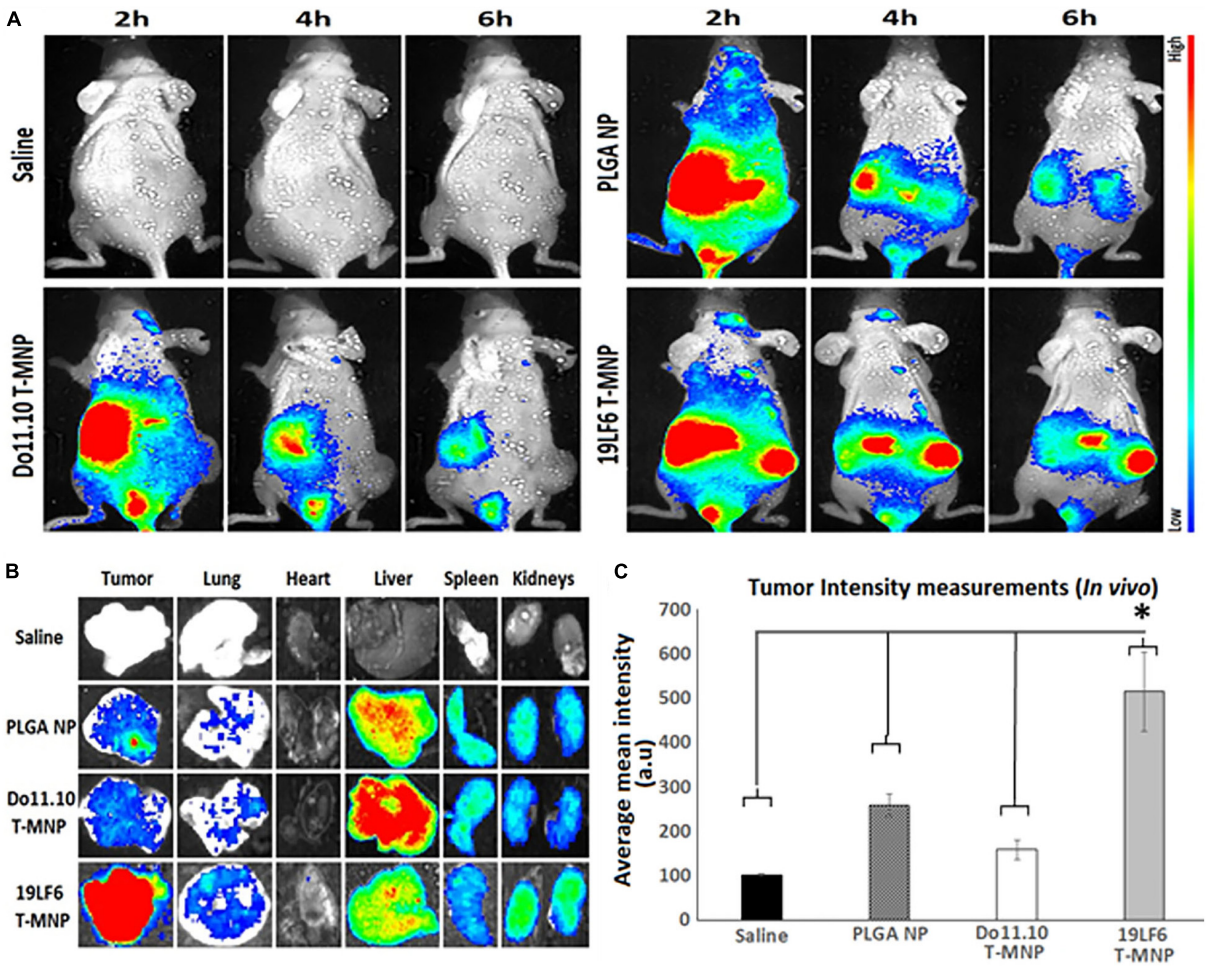

FIGURE 6 | *In vivo* and *ex vivo* analysis of T-MNP biodistribution. **(A)** Real-time tumor targeting characteristics of IV injected NPs on melanoma tumor models. **(B)** *Ex vivo* organ images of biodistribution in different study groups. **(C)** Measured fluorescent intensity of *in vivo* biodistribution study groups in tissue homogenates (n = 6 per group). PLGA, poly-lactic-*co*-glycolic acid; NP, nanoparticle; T-MNPs, T-cell membrane-coated PLGA NPs. D-MNP's, DO10.11 membrane coated PLGA NPs; C-6, coumarin-6; A-MNP's, A549 membrane coated PLGA NPs; NNP, naked nanoparticle; OD, optical density; IC, inhibitory concentration; RT-PCR, reverse transcriptase polymerase chain reaction; UV-Vis, ultraviolet visible; MTS, 3-(4,5-dimethylthiazol-2-yl)-5-(3-carboxymethoxyphenyl)-2-(4-sulfophenyl)-2H-tetrazolium. *Statistically significant with $P < 0.05$.

However, they reported that low dose irradiation was helped for these NPs to accumulate on target tissues at later time points of the study. Surprisingly, they were still able to confirm that non-specific hCTL membrane coated nanoparticles accumulated on tumor tissues without LDI and targeting molecule (Zhang et al., 2017). This effect might be due to the natural adhesion molecules like LFA-1 or integrin of the T-cell membrane surface. In our *in vivo* biodistribution study, anti-gp100 TCR decorated T-cell membranes were able to accumulate on target tissues. What is more to the above-mentioned literature results is tumor tissue accumulation of TCR decorated T-MNPs was superior compared to all control groups from the very early time points. All in all, our proposed T-cell membrane coated drug carrier system showed superior *in vitro* and *in vivo* targeting and uptake capabilities. Therefore, such natural biomaterials as engineered cells, bacteria membranes, biocompatible proteins, viral capsids and others in our drug carrier design can take the theragnostic field further than its current capabilities without compromising the effective drug delivery requirements.

Although cell membrane coated nanocarriers have great potential to deliver drugs to the desired location and could be a promising carrier to improve the theragnostic outcomes in treating melanoma, there are a few associated limitations and challenges. For instance, the cell membrane is comprised of a lot of different protein or peptide types, some of them are required for targeting, evading immune response while the other abundant proteins have unknown interactions in the host environment (Klammt and Lillemeier, 2012). Thus, further in-depth immune response and toxicity profiles must be performed for individual membrane proteins. Cell membrane isolation procedures are not robust and are limited to particular laboratory settings which can be a challenge in clinical translation such as isolation and

culture of abundant T-cells in a short duration. Therefore, quality control such as maintaining the functional and structural aspects of cell membranes for longer periods needs to be investigated. Future work should include the required studies to address the above-mentioned limitations of the proposed research. Yet a new approach, utilization of T-MNPs that have been formulated using donor cells and investigating their drug delivery potential as a translational medicine application might be beneficial toward personalized cancer therapies in the future.

CONCLUSION

Overall, we successfully developed T-cell coated nanoparticle carriers that displayed superior targeting capabilities toward skin cancer cells and that could serve as a potential tool as a theragnostic system to image and treat melanoma. T-MNPs maintained excellent *in vitro* targeting ability and had a biomimicking shell that minimizes toxicity and systemic clearance concerns in the conventional drug carrier designs. The natural targeting molecule TCR receptor on the surface of the T-MNPs was preserved after membrane isolation and synthesis of T-MNPs. *In vitro* assessments of T-MNPs also showed their therapeutic ability as a drug carrier platform. Finally, biodistribution studies showed the *in vivo* targeting abilities of T-MNPs. The cyto-compatibility and natural targeting T-MNPs recruited to the tumor regions and displayed a distinctive accumulation signal. We showed the therapeutic capabilities of T-MNPs including intrinsic targeting, prolonged drug release and therapeutic potential making T-MNPs an excellent biomimicking theragnostic carrier platform for future cancer therapy.

DATA AVAILABILITY STATEMENT

The raw data supporting the conclusions of this article will be made available by the authors, without undue reservation, to any qualified researcher.

ETHICS STATEMENT

The animal study was reviewed and approved by Julia Kissling, IACUC/IBC Specialist, Office of Regulatory Services, The University of Texas at Arlington, Texas-76010.

AUTHOR CONTRIBUTIONS

SY conceived the original idea whereas JW and KN guided in developing the final nanoparticle design and the planned experiments. GO and DZ carried out the synthesis and characterization of designed nanoparticles and performed some *in vitro* experiments. HR cultured and isolated the cell membranes required for coating of nanoparticles used for some *in vitro* experiments and animal studies. SY, HR, TN, and MS designed and performed the *in vivo* (animal) experiments. SY and HR wrote the manuscript. All authors discussed the results and contributed to the final manuscript. JW and KN supervised the work and helped with the editing of the manuscript.

ACKNOWLEDGMENTS

The graphical abstract was created with Biorender.com.

REFERENCES

Cai, Y., Xu, M., Yuan, M., Liu, Z., and Yuan, W. (2014). Developments in human growth hormone preparations: sustained-release, prolonged half-life, novel injection devices, and alternative delivery routes. *Intern. J. Nanomed.* 9:3527. doi: 10.2147/ijn.s63507

Charrot, S., and Hallam, S. (2019). Car-T cells: future perspectives. *Hemasphere* 3:e188. doi: 10.1097/hs9.0000000000000188

ASTM E2524-08 (2013). *Standard Test Method for Analysis of Hemolytic Properties of Nanoparticles*. West Conshohocken, PA: ASTM International. Available online at: https://www.astm.org/

Danhier, F., Ansorena, E., Silva, J. M., Coco, R., Le Breton, A., and Préat, V. (2012). Plga-based nanoparticles: an overview of biomedical applications. *J. Control. Release* 161, 505–522. doi: 10.1016/j.jconrel.2012.01.043

Fang, R. H., Hu, C.-M. J., Luk, B. T., Gao, W., Copp, J. A., Tai, Y., et al. (2014). Cancer cell membrane-coated nanoparticles for anticancer vaccination and drug delivery. *Nano Lett.* 14, 2181–2188. doi: 10.1021/nl500618u

Guo, Y., Wang, D., Song, Q., Wu, T., Zhuang, X., Bao, Y., et al. (2015). Erythrocyte membrane-enveloped polymeric nanoparticles as nanovaccine for induction of antitumor immunity against melanoma. *ACS Nano* 9, 6918–6933. doi: 10.1021/acsnano.5b01042

Hauschild, A., Rosien, F., and Lischner, S. (2003). Surgical standards in the primary care of melanoma patients. *Oncol. Res. Treat.* 26, 218–222. doi: 10.1159/000071616

Hayes, A. J., Maynard, L., Coombes, G., Newton-Bishop, J., Timmons, M., Cook, M., et al. (2016). Wide versus narrow excision margins for high-risk, primary cutaneous melanomas: long-term follow-up of survival in a randomised trial. *Lancet Oncol.* 17, 184–192. doi: 10.1016/s1470-2045(15)00482-9

Hu, C.-M. J., Zhang, L., Aryal, S., Cheung, C., Fang, R. H., and Zhang, L. (2011). Erythrocyte membrane-camouflaged polymeric nanoparticles as a biomimetic delivery platform. *Proc. Natl. Acad. Sci.* 108:10980. doi: 10.1073/pnas.1106634108

Hu, Q., Sun, W., Qian, C., Wang, C., Bomba, H. N., and Gu, Z. (2015). Anticancer platelet-mimicking nanovehicles. *Adv. Mater.* 27, 7043–7050. doi: 10.1002/adma.201503323

Huang, Y., Gao, X., and Chen, J. (2018). Leukocyte-derived biomimetic nanoparticulate drug delivery systems for cancer therapy. *Acta Pharm. Sin. B* 8, 4–13. doi: 10.1016/j.apsb.2017.12.001

Klammt, C., and Lillemeier, B. F. (2012). How membrane structures control T cell signaling. *Front. Immunol.* 3:291. doi: 10.3389/fimmu.2012.00291

Kumar, A., and Dixit, C. K. (2017). Methods for characterization of nanoparticles. *Adv. Nanomed. Deliv. Therap. Nucleic Acids* 2017, 43–58.

Lugowska, I., Koseła-Paterczyk, H., Kozak, K., and Rutkowski, P. (2015). Trametinib: a Mek inhibitor for management of metastatic melanoma. *Oncotargets Ther.* 8:2251. doi: 10.2147/ott.s72951

Menon, J. U., Ravikumar, P., Pise, A., Gyawali, D., Hsia, C. C. W., and Nguyen, K. T. (2014). Polymeric nanoparticles for pulmonary protein and Dna delivery. *Acta Biomater.* 10, 2643–2652. doi: 10.1016/j.actbio.2014.01.033

Muller, W. A. (2013). Getting leukocytes to the site of inflammation. *Vet. Pathol.* 50, 7–22. doi: 10.1177/0300985812469883

Parodi, A., Quattrocchi, N., Van De Ven, A. L., Chiappini, C., Evangelopoulos, M., Martinez, J. O., et al. (2013). Synthetic nanoparticles functionalized with

biomimetic leukocyte membranes possess cell-like functions. *Nat. Nanotechnol.* 8:61. doi: 10.1038/nnano.2012.212

Pinto-Alphandary, H., Andremont, A., and Couvreur, P. (2000). Targeted delivery of antibiotics using liposomes and nanoparticles: research and applications. *Intern. J. Antimicrob. Agents* 13, 155–168. doi: 10.1016/s0924-8579(99)00121-1

Roller, D. G., Capaldo, B., Bekiranov, S., Mackey, A. J., Conaway, M. R., Petricoin, E. F., et al. (2016). Combinatorial drug screening and molecular profiling reveal diverse mechanisms of intrinsic and adaptive resistance to Braf inhibition in V600E Braf mutant melanomas. *Oncotarget* 7:2734. doi: 10.18632/oncotarget.6548

Sharpe, M., and Mount, N. (2015). Genetically modified T cells in cancer therapy: opportunities and challenges. *Dis. Mod. Mech.* 8, 337–350. doi: 10.1242/dmm.018036

Smith, S. A., Travers, R. J., and Morrissey, J. H. (2015). How it all starts: initiation of the clotting cascade. *Crit. Rev. Biochem. Mol. Biol.* 50, 326–336. doi: 10.3109/10409238.2015.1050550

Stephan, M. T., Moon, J. J., Um, S. H., Bershteyn, A., and Irvine, D. J. (2010). Therapeutic cell engineering with surface-conjugated synthetic nanoparticles. *Nat. Med.* 16, 1035–1041. doi: 10.1038/nm.2198

Stoiber, S., Cadilha, B. L., Benmebarek, M.-R., Lesch, S., Endres, S., and Kobold, S. (2019). limitations in the design of chimeric antigen receptors for cancer therapy. *Cells* 8:472. doi: 10.3390/cells8050472

Street, W. (2019). *Cancer Facts & Figures 2019*. Atlanta, GA: American Cancer Society.

Tan, S., Wu, T., Zhang, D., and Zhang, Z. (2015). Cell or cell membrane-based drug delivery systems. *Theranostics* 5:863. doi: 10.7150/thno.11852

Thanuja, M. Y., Anupama, C., and Ranganath, S. H. (2018). Bioengineered cellular and cell membrane-derived vehicles for actively targeted drug delivery: So near and yet so far. *Adv. Drug Deliv. Rev.* 132, 57–80. doi: 10.1016/j.addr.2018.06.012

Tran, E., Turcotte, S., Gros, A., Robbins, P. F., Lu, Y.-C., Dudley, M. E., et al. (2014). Cancer immunotherapy based on mutation-specific Cd4+ T cells in a patient with epithelial cancer. *Science* 344, 641–645. doi: 10.1126/science.1251102

Weidanz, J. A., Nguyen, T., Woodburn, T., Neethling, F. A., Chiriva-Internati, M., Hildebrand, W. H., et al. (2006). Levels of specific peptide-Hla class I complex predicts tumor cell susceptibility to Ctl killing. *J. Immunol.* 177, 5088–5097. doi: 10.4049/jimmunol.177.8.5088

Wheatley, K., Wilson, J. S., Gaunt, P., and Marsden, J. R. (2016). Surgical excision margins in primary cutaneous melanoma: a meta-analysis and Bayesian probability evaluation. *Cancer Treat. Rev.* 42, 73–81. doi: 10.1016/j.ctrv.2015.10.013

Zhang, L., Li, R., Chen, H., Wei, J., Qian, H., Su, S., et al. (2017). Human cytotoxic T-lymphocyte membrane-camouflaged nanoparticles combined with low-dose irradiation: a new approach to enhance drug targeting in gastric cancer. *Intern. J. Nanomed.* 12, 2129–2142. doi: 10.2147/ijn.s126016

Zhao, L., and Cao, Y. J. (2019). Engineered T cell therapy for cancer in the clinic. *Front. Immunol.* 10:2250. doi: 10.3389/fimmu.2019.02250

Zhong, S., Malecek, K., Johnson, L. A., Yu, Z., De Miera, E. V.-S., Darvishian, F., et al. (2013). T-cell receptor affinity and avidity defines antitumor response and autoimmunity in T-cell immunotherapy. *Proc. Natl. Acad. Sci. U.S.A.* 110, 6973–6978. doi: 10.1073/pnas.1221609110

Conflict of Interest: The authors declare that the research was conducted in the absence of any commercial or financial relationships that could be construed as a potential conflict of interest.

The reviewer PR declared a shared affiliation, with no collaboration, with the authors to the handling Editor at the time of review.

frontiers in Bioengineering and Biotechnology

REVIEW
published: 26 October 2020
doi: 10.3389/fbioe.2020.566767

The New Frontiers in Neurodegenerative Diseases Treatment: Liposomal-Based Strategies

Mariafrancesca Cascione[1]*, *Valeria De Matteis*[1], *Stefano Leporatti*[2]* and *Rosaria Rinaldi*[1]

[1] Department of Mathematics and Physics "Ennio De Giorgi," University of Salento, Lecce, Italy, [2] National Research Council Nanotec Institute of Nanotechnology, Lecce, Italy

In the last decade, the onset of neurodegenerative (ND) diseases is strongly widespread due to the age increase of the world population. Despite the intensive investigations boosted by the scientific community, an efficacious therapy has not been outlined yet. The drugs commonly used are only able to relieve symptom severity; following their oral or intravenous administration routes, their effectiveness is strictly limited due to their low ability to reach the Central Nervous System (CNS) overcoming the Blood Brain Barrier (BBB). Starting from these assumptions, the engineered-nanocarriers, such as lipid-nanocarriers, are suitable agents to enhance the delivery of drugs into the CNS due to their high solubility, bioavailability, and stability. Liposomal delivery systems are considered to be the ideal carriers, not only for conventional drugs but also for neuroprotective small molecules and green-extracted compounds. In the current work, the LP-based drug delivery improvements in *in vivo* applications against ND disorders were carefully assessed.

Keywords: neurodegenarative diseases, Blood Brain Barrier (BBB), liposome, solid lipid nanoparticles, nanostrured lipid particles, ethosomes, drug delivery

OPEN ACCESS

Edited by:
Christian Celia,
University of Studies G. d'Annunzio Chieti and Pescara, Italy

Reviewed by:
Giovanni Tosi,
University of Modena and Reggio Emilia, Italy
Maria Chiara Cristiano,
Magna Græcia University of Catanzaro, Italy
Gert Fricker,
Heidelberg University, Germany

***Correspondence:**
Mariafrancesca Cascione
mariafrancesca.cascione@unisalento.it
Stefano Leporatti
stefano.leporatti@nanotec.cnr.it

Specialty section:
This article was submitted to Nanobiotechnology, a section of the journal Frontiers in Bioengineering and Biotechnology

Received: *28 May 2020*
Accepted: *14 September 2020*
Published: *26 October 2020*

Citation:
Cascione M, De Matteis V, Leporatti S and Rinaldi R (2020) The New Frontiers in Neurodegenerative Diseases Treatment: Liposomal-Based Strategies. Front. Bioeng. Biotechnol. 8:566767. doi: 10.3389/fbioe.2020.566767

INTRODUCTION

Pharmacological research is oriented to develop new effective therapeutic strategies in order to treat diseases and, at same time, to improve the life quality of patients. Many studies aim to discover new drugs, taking in consideration that their effectiveness is strictly dependent on the administration route and also on their intrinsic ability to access the organs and tissues in suitable amounts and times. The uptake of drugs is particularly difficult in specific districts of body, such as the Central Nervous System (CNS), in which the presence of a Blood Brain Barrier (BBB) constitutes the major obstacle. The BBB often inhibits neuroreparative and neuroprotective therapies that should carry out their pharmacological action directly on target site. According to the latest available data, it is estimated that 10 % of the world population will be affected by neurological disorders, without geographical and socioeconomic distinctions (Organization, 2006). For this reason, the World Health Organization recommends great efforts to overcome the difficulties in the brain drugs administration. Despite the neuropharmaceutical field constituting the largest sector of drug industry, its development is limited by the complication regarding the BBB crossing. It has been estimated that ca. 98% of the drugs available today for the treatment of neurological diseases, including recombinant proteins, monoclonal antibodies, and genes are not able to effectively overcome the BBB. This is true

due to their deficiency to exploit specific transport mechanisms and their high molecular weight together with polarity (Pardridge and Boado, 2012). In light of this, the regulatory mechanisms of the BBB are fundamental for the development of new therapies dedicated to large groups of brain injuries such as neurodegenerative diseases.

NEURODEGENERATIVE DISEASES

The age-dependent disorders are becoming increasingly prevalent, in part because the elderly population has increased in recent years (Heemels, 2016).

Examples of neurodegenerative diseases are amyotrophic lateral sclerosis, Parkinson's disease, Alzheimer's disease, Huntington's disease, frontotemporal dementia, and the spinocerebellar ataxias. All these pathologies are different in pathophysiologic properties but, at the same time, are associated with memory loss, cognitive impairments, and other adverse effects including a person's inability to move, breathe, and speak (Abeliovich and Gitler, 2016; Wyss-Coray, 2016; Gitler et al., 2017). These pathologies show selective neuronal vulnerability combined with the degeneration of specific brain regions; in addition, an abnormal protein deposit (extracellular or intracellular) occurs in neurons or other types of brain cells (Ross and Poirier, 2004).

Alzheimer's disease (AD) is characterized by neuron degeneration; in particular, in the basal forebrain and hippocampus. In addition, the alteration of synaptic and neuronal connections is involved in the pathogenesis (Selkoe, 2002). The accumulation of amyloid-β (Aβ) peptides and tau protein boosts the development of the pathology progression (Combs et al., 2016). In detail, the Amyloid beta, a 39–43-amino acid residue peptide, is a physiological presence in human brain and is derived from the proteolysis process of the amyloid precursor protein (APP). The extracellular accumulation of amyloid-β (Aβ) peptides induces the formation of amyloid plaques, also called senile plaques, which form the synaptic dysfunction and neuronal loss (Citron, 2002). The tau proteins (T proteins) play a key role in microtubule stabilization and they are abundant in hippocampal areas, cortical areas, and the entorhinal cortex. In AD disease, this protein undergoes a hyperphosphorylation phenomenon that induces tau protein clumping with the consequence of developing intracellular neurofibrillary tangles (NFT): these formations lead to axon degeneration and microtubule disaggregation (Goedert, 2004). The onset of AD may be due to rare genetic mutations, which were found in the APP and in some transmembrane proteins (presenilins) that cleave the APP. Mutations of tau28 protein have been found in non-Parkinson frontotemporal dementia.

Parkinson's disease (PD) is provoked by degeneration of dopaminergic neurons in the substantia nigra of the midbrain and other monoaminergic neurons in the brain stem (Vernier et al., 2004). Despite several progresses, the main cause of PD remains unknown. It is probably born by complicate connections between environmental and genetic factors that are strong effects on cells that trigger mitochondrial dysfunction, oxidative stress, impairment of the ubiquitin proteosome process, as well as defective autophagy process (Dawson et al., 2010; Angeles et al., 2014). However, the exact mechanisms leading to neuronal death are unknown. As a consequence, the loss of several neurotransmitters and neuromodulators in the extranigral neurons, such as noradrenaline (NA), acetylcholine (ACh), glutamate, and serotonin (5-hydroxytryptaminc [5-HT]) occur. These phenomena induce the slowing of movement, muscular rigidity, and tremor (Alexander, 2004).

Numerous gene mutations could induce the early onset of PD, in particular, point mutations or increased gene dosage of the α-synuclein gene. These boost an autosomal dominant PD. Instead, the mutations of genes encoding for DJ-1 or PINK132 and parkin could trigger a recessive early-onset PD. In general, the adult PD onset regards an inclusion body near the nucleus of neurons, immersed in cytoplasm, called Lewy body, in the form of fibrillar aggregates. Several investigations demonstrated the presence of Lewy bodies in the substantial nigra in monoaminergic, cerebral, cortical, and other neurons principally constituted of α-synuclein protein (Stefanis, 2012).

THE BLOOD BRAIN BARRIER (BBB)

The human brain contains about 100 billion of capillaries with a total length of 600 km. This dense vascular network covers an area of about 20 m^2 and represents an effective interface between the blood and the brain, supplying brain cells with oxygen and essential metabolites that support brain functions (Risau and Wolburg, 1990). In addition, the brain consumes 20% of the body's total glucose, increasing the blood flow and oxygen in order to quickly reach the different body's districts (Begley and Brightman, 2003). Capillaries are the major site of blood barrier brain (BBB) that constitutes a real barrier between the bloodstream and the central nervous system acting as selective filter, allowing or preventing substances (ions, glucose, proteins etc.) to move from the blood to the brain parenchyma and to cerebrospinal fluid (CSF). Thanks to this selectivity, the BBB protects the sickly chemical–physical homeostasis of the cerebral fluid environment carrying out a protective role toward CSF and the nervous tissue (Abbott and Romero, 1996).

This can be satisfied by keeping the ionic environment stable and preserving the low amino-acid gradient of the excitatory neurotransmitters (glutamic acids, aspartic acid, and glycine) that is characteristic of the brain extracellular fluid. This phenomenon is critical for reliable synaptic transmission and efficient neuroregulatory activity. BBB prevents the toxic compound uptake in cells, such as metabolites and neurotoxins both endogenous and xenobiotic, which are potentially fatal. In addition, the BBB promotes the longevity of the CNS and prevents premature cell death and neurodegeneration.

The BBB is formed by the endothelium of the brain capillaries, the processes perivascular of the astrocytes surrounding the endothelial cells and from the pericytes which are contractile connective cells that partially surround them. The anatomical structure of the BBB is responsible for its functional peculiarities, such as limited permeability to most substances and limited

paracellular and transcellular transport (Zlokovic, 2008; Kisler et al., 2017). The brain capillaries are anatomically different from peripheral systemic ones since the cells that compose them form a continuous non-fenestrated endothelium, with a reduced number of pinocytic cells (Engelhardt and Liebner, 2014). Brain endothelial cells are connected by tight and adherent junctions. The first prevents the free diffusion of solutes from the blood sector (peripheral or systemic) to the CSF and brain (intrathecal), both at the level of the cerebral capillaries and the chorioid epithelium. The tight junctions involve occluding, claudin I, claudin 3, claudin 5, claudin 12, and the membrane-associated guanylate kinases, proteins ZO1, ZO2, and ZO3. The adherent junctions include cadherins, platelet endothelial cell adhesion molecules (PECAM1), and the junctional adhesions molecules (JAMs) JAMA, JAMB, and JAMC. The gas exchange (oxygen and carbon dioxide) occurs across the endothelium, whereas the pinocytosis deficit is responsible for the limitation of solutes passage (Abbott et al., 2010; Zhao et al., 2015).

Then, in order to target a specific drug to the brain, it is necessary to consider the structural and functional characteristics of the BBB and, at the same time, evaluate the chemical-physical properties of the drug (pKa, molecular weight, lipophilicity, etc.). In addition, it is important to consider the intrinsic ability of BBB to form bonds with the plasma proteins that prevent the CNS crossing, the degree of ionization (pH), and the lipid/water partition coefficient of the drug (Warren, 2018). In particular, it has been demonstrated that small lipid-soluble molecules (high partition coefficient) with a molecular weight <400 Da or containing <8 hydrogen bonds can cross BBB by simple transmembrane diffusion. Contrary, the drugs with low passive diffusion coefficient can be internalized in the brain only by active transports systems (Pardridge, 2015).

TRANSPORT THROUGH THE BBB

Oxygen, carbon dioxide, glucose, nucleosides, vitamins, and some of fat-soluble drugs can cross the BBB by passive diffusion mechanisms or by specific transport mechanisms. The transport systems (**Figure 1**) can be located on the luminal or abluminal side of the BBB and can be classified into three categories (Abbott and Romero, 1996; Begley, 2004): (i) CMT (Carrier Mediated Transport) consists of a transport mediated by specific transport carrier proteins; they are able to move carbohydrates, fatty acids, amino acids, nucleotides, hormones, vitamins, organic cations and anions through BBB; (ii) AET (Active Efflux Transport) consists of an active transport mechanism capable of expelling a large variety of molecules from the brain compartment to the bloodstream; and (iii) RMT (Receptor Mediated Transport) which consists of receptors mediated transport system, able to drive large compounds (peptides and proteins) through an intracellular process in both directions: insulin and transferrin from blood to brain, as well as apolipoproteins (Demeule et al., 2008; Sagare et al., 2012). The transport of native plasma proteins or peptides is limited, but the cationization phenomenon can increase their uptake by adsorptive-mediated transport (AMT).

The CMT and AET systems are responsible for small molecule transport between the blood and the brain, while RMT allows large molecule delivery through the BBB. Among these, the transmembrane transporters called ABC transporters, expressed at the luminal side of BBB, play an important role due to the presence of two cytoplasmic domains useful to bind the ATP boosting transport against the unidirectional gradient (from cytoplasm to extracellular space) (Abbott et al., 2010; Mokgokong et al., 2014).

Therefore, ABC prevents the brain accumulation of xenobiotic agents, and drugs exert an important role in the body detoxification. The first ABC transporter identified is the P-glycoprotein (P-gp or ABCB1) coded by the MDR1 gene. This gene is known for its several polymorphisms (ca. 50) at the level of a single nucleotide, and for this reason, it is responsible for a strong individual variability in absorption and tolerance to drugs (Yan-Hong et al., 2006; Bartels, 2011). In addition to the ABC, OATP (Organic Anion Transporting-Polypeptide) and the OAT (Organic Anion Transporter) members are expressed in the endothelial cells of the BBB. The main function of OATP 1A2 and 2B1 carriers is to uptake several endogenous and xenobiotic compounds (10.1021/acs.molpharmaceut.0c00159), but, unlike the members of the ABC family, the OATP does not hydrolyze ATP, and consequently, they fail to uptake drugs against the concentration gradient (de Boer et al., 2003). Their presence allows the ions exchange according to the ionic gradient. In addition to the possibilities of exploiting or inhibiting these and other physiologically present transport mechanisms on the BBB (Pardridge and Boado, 2012), other approaches that can guarantee are being studied for a more effective delivery of drugs to the CNS. A spread class of carriers, abundant in mammalian neurocytes and brain capillary epithelium membrane, is also represented by glucose transporter proteins (GLUTs), GLUT1, and GLUT3 (McEwen and Reagan, 2004).

The approaches to achieve effective CNS drug concentrations can be invasive (temporary break of tight junctions, intracerebral injection, or use of intracerebral implants such as catheters, microchips, or erodible polymeric systems). It still comes cost-effective and potentially dangerous for patients, since the direct delivery of the drug exposes patients to the risk of developing serious brain infections with a consequent decrease in their compliance. Starting from these assumptions, the non-invasive (chemical, biological, or technological) approach is the hope to treat the brain pathologies (Scherrmann, 2002; Tosi et al., 2011).

In the last years, the use of nanoparticles (NPs) represents a powerful approach to improve the BBB penetration of bioactive molecules; NPs have small size ($3 \div 200$ nm) and good stability, and they can be easy functionalized by surface modifications (attaching active ligands or changing the superficial charge), offering good advantages over the free drug. The NPs can reduce the side effects on healthy cells, improving the pharmacokinetic and pharmacodynamics drug profile and increase drug concentration at the specific sites allowing their application in the neurodegenerative disease treatment.

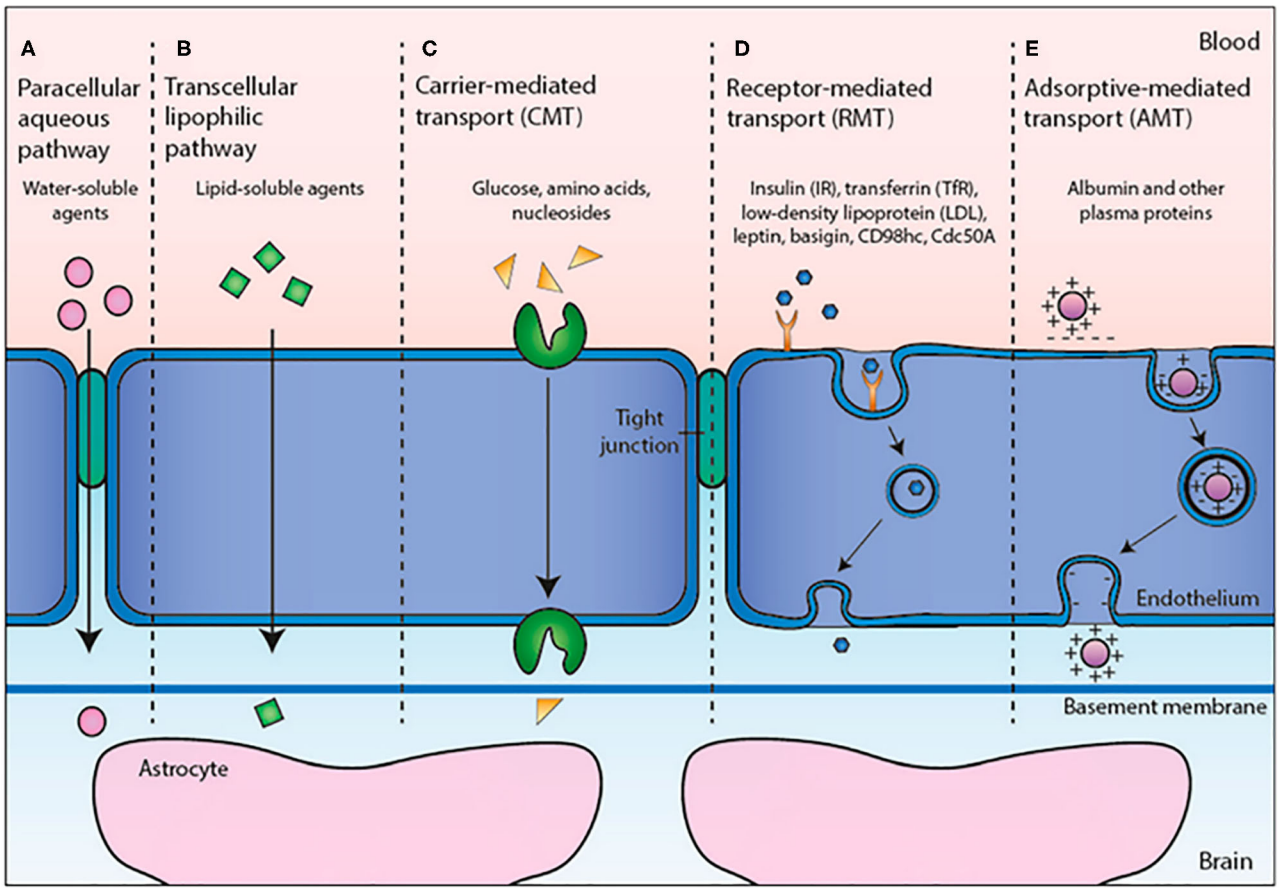

FIGURE 1 | Transport mechanisms through BBB. Reproduced with permission from Cavaco et al. (2020).

LIPID NANOCARRIERS FOR DRUG DELIVERY ACROSS THE BBB

The effectiveness of drugs acting on the CNS has strong limits, due to their inability to overcome the BBB in adequate amounts (de Boer and Gaillard, 2007). The issue of the limited drugs crossing through the BBB is of great interest to the scientific and medical community, which is focused on the execution and optimization of innovative therapeutic strategies against neurodegenerative diseases. In this perspective, the carriers with dimensions at nanoscale level represent a promising drug delivery platform solution for enhancing the drug crossing through the BBB (Chen and Liu, 2012; Pardridge, 2012; Upadhyay, 2014). Theoretically, the tuneable physicochemical properties of nanocarriers permit optimizing the delivery of different kinds of drugs at the specific therapeutic target; nevertheless, a careful design of drug nanocarriers needs to consider many factors, such as biocompatibility, reduction of drug toxic effects, enhancement in drug stability, and optimization of the specific target functionalization. Furthermore, the engineering of such nanocarriers become harder when the therapeutic target is the CNS, as listed by Lockman and colleagues (Lockman et al., 2002).

The growing interest in the suitable drug delivery systems research has encouraged the production of a wide range of nano-scaled carriers (Mishra et al., 2010). Among these, lipid-based carriers are recognized as promising strategies for drug delivery, due to their ability to mimic natural lipid environment constituting the biomembranes, including BBB (Pujara, 2012). In addition, lipid vectors protect the drug from degradation during transport to the target sites, reduce the toxicity, and increase the drug biocompatibility with respect to free administration (Chen et al., 2010; Nunes et al., 2017).

Among different lipid carriers, liposomes (LPs) have been extensively studied for nanomedicine applications (Fenske and Cullis, 2008; Fenske et al., 2008). The mechanism transport across the BBB is still unclear (Agrawal et al., 2017). Initially, it was thought that the liposomes spontaneously crossed several biological membranes including BBB by electrostatic interactions. However, this theory was replaced by the possible mechanism through active transport carriers by transcytosis or a specific receptor (Spuch and Navarro, 2011). The latter hypothesis is more consolidated due to the binding of specific molecules, such as glucose and glutathione, on liposome surfaces that are able to overcome the BBB promoting the liposome translocation (Noble et al., 2014).

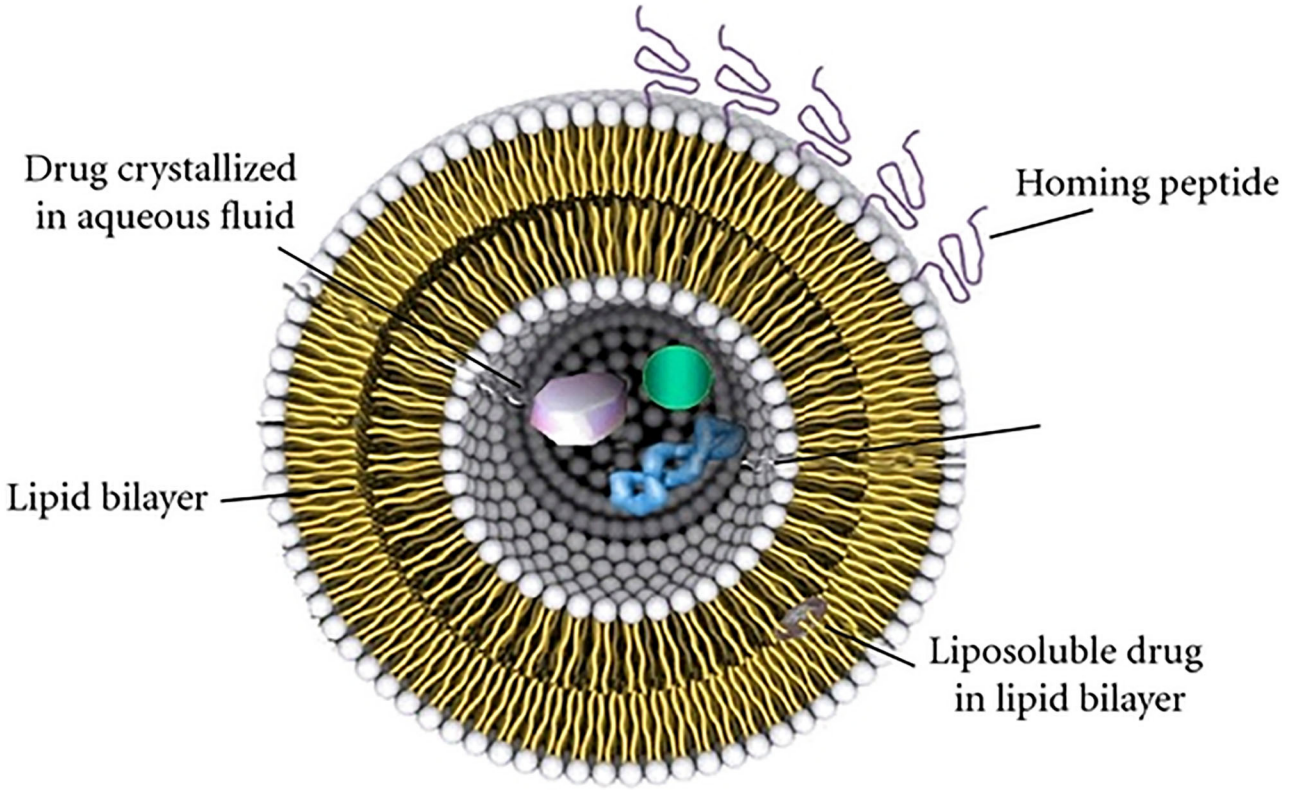

FIGURE 2 | Representation of fundamental architecture of LPs. Reproduced with permission from Bitounis et al. (2012).

Their biochemical architecture (**Figure 2**) is similar to the human cellular membrane; in fact, it is formed by phospholipid double layers that enclose an aqueous core. In these artificial vesicles, with spherical shape, lipophilic and hydrophilic drugs can be encapsulated: instead of lipophilic molecules only confined into phospholipidic bilayers, hydrophilic molecules can be loaded both inside the aqueous cores of LPs and in the external water phase. The encapsulation efficiency is almost equal to the loading rate in the case of lipophilic molecules, whereas it depends on composition and the LP synthetic approach method in the case of hydrophilic drug (Johnsson and Edwards, 2003). However, in any case it was found that drug toxicity is strongly reduced following internalization in the LP.

Conventionally, a first classification of LPs is based on the number of bilayers (lamellarity) and on the size of the structure (Woodle and Papahadjopoulos, 1989) because these two parameters deeply influence both the circulation half-life and the drug encapsulation efficiency. Small unilamellar vesicles (SUVs) and large unilamellar vesicles (LUVs) indicate LPs formed from a single layer with a dimension of (25 ÷ 50) nm or (200 ÷ 800) nm, respectively, while multilamellar vesicles (MLV) are referred to LPs formed by concentric multiple lipid layers, separated from each other by an aqueous solution. Most specific classifications regard the chemical composition, lipid organization, surface charge, or preparation methods (Euliss et al., 2006; Bozzuto and Molinari, 2015).

For the drug delivery aim, the LPs appear a promising system, not only for their ability to protect their cargo to enzymes degradation phenomenon, but also for their unique properties, including low toxicity, flexibility, biocompatibility, biodegradability, and non-immunogenicity. Unfortunately, LPs suffer of some limitations for specific therapeutic applications, namely shelf life and the drug-loading efficiency. In the last decades, several efforts have been made toward the ingegnerization of optimal LPs, and new categories of liposomal carriers were obtained.

Solid lipid nanoparticles (SLN) have established themselves as an alternative system to conventional LPs, due to significant advantages: controlled and targeted drug release, high stability, and effective encapsulation efficiency of drugs. The SLNs structures consist of a solid lipid matrix (tri-, di-, and mono-glycerides, fatty acids, steroids, or waxes) that outlines an aqueous volume in which lipophilic and hydrophilic molecules can be internalized (Uner and Yener, 2007). However, some of the drugs could flow out during the transport following the natural recrystallization process of the SLN shell, formed by a single lipid. For that reason, the delivery efficacy results are jeopardized by the SLN architecture (Blasi et al., 2007).

With the aim to overcome these drawbacks, the nanostructured lipid carriers (NLC) were conceived. The matrix of the NLC structure is composed by a combination of solid and liquid lipids. This latter induces the nanostructuring

process into the inner lipid shell. These results allow the increase of the volume available for drug loading and the boost of a more stable lipid configuration (Iqbal et al., 2012; Beloqui et al., 2016).

Several synthetic routes have been proposed to obtain SLN and NLCs; among these, high-pressure homogenization (HPH) and microemulsion are the most efficient. The microemulsion technique requires the use of hazardous toxic organic solvents; for this reason, the lipidic systems obtained through this procedure are unsuitable for medical purposes. In this perspective, the use of HPH procedure is preferred; however, this technique permits the internalization only of thermostable drugs (Das and Chaudhury, 2011).

The SLN/NLCs systems have been largely employed *in vivo* for the delivery of several kinds of drugs, by intranasal, intragastric, oral, and intravenous administrations. In order to optimize the carriers for dermal delivery, a new class of LPs has been proposed by Touitou and co-workers (Touitou et al., 2000). They modified LPs, adding ethanol, in order to obtain high efficiency in the delivery of different drugs through the skin.

These modified LPs (**Figure 3**), called ethosomes, are lipid vesicular systems composed primarily of phospholipids, water, and ethanol. This latter, added in high concentration (20 ÷ 45 %), interacts with the polar heads of the phospholipids; finally, it is inserted in the lipid stratum corneum, lowering the melting-point of lipidic bilayer. This last phenomenon makes them to be more fluid and permeable for the cell membrane. In addition, in comparison with LPs, ethosomes have small dimensions due to the negative superficial charge induced by ethanol inclusion.

The improved transport mechanism of bioactive molecules through the skin can be applied to the drug delivery to the CNS; in fact, the characteristics of the ethosomes could be useful to promote the BBB penetration.

Therefore, the improvement of the liposomal delivery systems has required the optimization of the physiochemical properties of the liposomal surface in relation to the chemical nature of entrapped drug molecules.

CONVENTIONAL THERAPEUTIC APPROACH IN LIPOSOMAL FORMULATION AGAINST ND PROGRESSION

Currently, the treatment of ND pathologies is still not available; however, many molecules and compounds can mitigate the symptoms and slow down the ND progression (Duraes et al., 2018). The first therapeutic approaches were based on the administration of small hydrophilic molecules (levodopa, rivastigmine, tacrine, donepezil), which can penetrate the BBB through the lipid-mediated diffusion process, exerting neuroprotective effects in several ND models. In recent years, the attention of medical and scientific communities has been focused on natural compounds, to overcome the side effects induced by chemical drug treatments against ND disorders. Due to anticholinesterase and the antioxidative and anti-inflammatory outcomes of different phytochemicals, these

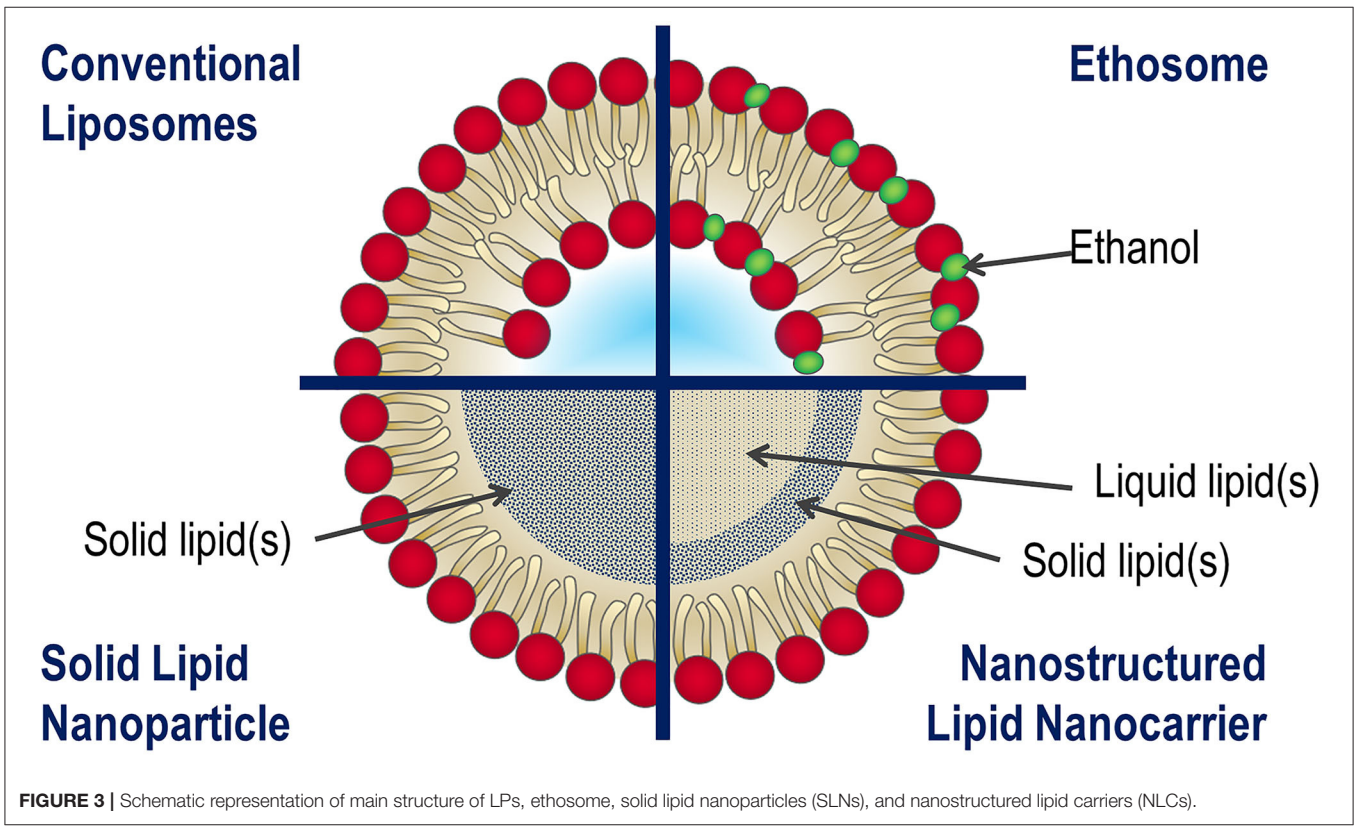

FIGURE 3 | Schematic representation of main structure of LPs, ethosome, solid lipid nanoparticles (SLNs), and nanostructured lipid carriers (NLCs).

could be promising therapeutic agents against ND progression. In detail, the neuroprotective and anti-protein aggregation effects induced by curcumin, quercetin, and resveratrol were extensively investigated.

Despite numerous therapeutic agents showing promising results for ND treatments, the experimental evidences obtained *in vivo* fell short of expectations; in fact, the efficacy of all these molecules is strongly limited due to the low bioavailability and low penetration capability in BBB. In addition, the phytochemicals compounds are poorly water and blood soluble and highlighted a short biological half-life as well as low uptake in the brain (Darvesh et al., 2012; Yang et al., 2014; Kulkarni and Canto, 2015; Tellone et al., 2015; Ay et al., 2017).

The advances in the nanotechnological field have enabled the development of engineered nanocarriers to deliver drugs and to release them in a controlled manner in specific body compartments. In particular, the LPs have become the best theranostic system for anti-ND molecules, since they allow them to overcome their inherent limitations (**Table 1**).

In this section, we describe how LP-based formulations improve the delivery to the brain of conventional therapeutic drugs.

SOLUBILITY, BIOAVAILABILITY, AND STABILITY

The bioavailability of given administered drug depends by several factors, such as the aqueous or blood solubility, BBB permeability and metabolic stability (Helen Chan and Stewart, 1996). Rivastigmine and Donepezil are small hydrophobic molecules largely used in Alzheimer's treatment, because they act as acetylcholinesterase inhibitor, preventing the acetylcholine degradation and increasing its availability at the synapses (Di Stefano et al., 2011).

In order to improve the bioavailability of these drugs: Nageeb El-Helaly et al. (2017) fabricated electrosteric stealth (ESS) LPs in which rivastigmine was encapsulated; meanwhile, Al Asmari et al. (2016) prepared a new liposomal formulation using 1,2-distearyl-sn-glycero-3-phosphocholine, cholesterol, and polyethylene glycol to entrap Donepezil. In details, Nageeb El-Helaly and co-workers (Nageeb El-Helaly et al., 2017) obtained an augmented stability by steric hindrance due to addition of didecyldimethyl ammonium bromide and 1,2-distearoyl-sn-glycero-3-phosphoethanolamine-N-(methoxy (polyethyleneglycol)-2000) to l-α-lecithin from soybean; consequently, the *in vivo* studies performed on 36 rabbits showed that the bioavailability of rivastigmine strongly increased in plasma and brain compartments after intranasal injection. Analogously, the Donepezil bioavailability resulted two times higher in the brain, after intranasal administration, compared to free drug in plasma (Al Asmari et al., 2016).

Among phytochemical compounds, curcumin induces neuroprotective and anti-protein aggregation effects. The low water solubility and bioavailability can be enhanced by internalization into liposomal carriers: Cheng et al. (2017) optimized a pH-driven method to prepare curcumin-loaded LPs (**Figure 4**), testing their bioavailability by the reproduction of gastrointestinal tissue. They found an increased bioavailability (more than twofold) with respect to curcumin solution.

Bulboaca et al. (2018) investigated the therapeutic potential of curcumin in addition to the traditional sumatriptan treatment for migraine disease using an *in vivo* rat model, demonstrating that, after intravenous administration, the shelf life of curcumin largely increased when it was encapsulated in liposomal vectors.

The polyphenolic compound resveratrol (3,4,5-trihydroxystilbene) gained increased attention as a therapeutic agent against ND diseases, due to their ability to promote the non-amyloidogenic cleavage of the amyloid precursor proteins, to improve β amyloid-peptide clearance and to limit neuronal injury (Li et al., 2012). As well as other natural compounds, the encapsulation in liposomal systems augments the drug effectiveness.

The enhancement in resveratrol bioavailability was demonstrated by Neves and collaborators by *in vitro* (Neves et al., 2013) and *in vivo* experiments (Jose et al., 2014), loading it in SLNs and NLCs. The *in vivo* biodistribution study using Wistar rats demonstrated that SLN could significantly increase the brain concentration of resveratrol ($17.28 \pm 0.6344\,\mu g/g$) as compared to non-liposomal formulation ($3.45 \pm 0.3961\,\mu g/g$). In pharmacokinetic studies conducted in male Wistar rats, Pandita et al. (2014) showed that the oral bioavailability of resveratrol was increased 8.035-fold when loaded in stearic acid-based SLNs stabilized by mixture of surfactants PHOSPHOLIPON® 90G/poloxamer 188.

In light of these experimental evidences, it is undeniable that encapsulation in liposomal carriers may offer interesting opportunities to enhance the delivery of anti-ND drugs.

THERAPEUTIC EFFICACY AND DRUG TOXICITY REDUCTION

The encapsulation of anti-NDs drugs in liposomal-based carriers permits to minimize their adverse effects and simultaneously to enhance their therapeutic action.

Among small hydrophobic molecules, Levodopa (L-dopa, L-3, 4-dihydroxyphenylalanine) is the most used molecules in ND treatment; in particular, in the last 4 decades Levodopa (L-DOPA)-based therapy become the golden standard therapy against Parkinson disease (Poewe et al., 2010). After oral administration, <10% of L-DOPA dose reaches the CNS, while the remaining 90% tends to accumulate into the liver and muscles, inducing dyskinesia (Dodel et al., 2001). These adverse effects can be reduced loading L-DOPA in chitosan-coated nano-LPs. Chitosan is a natural hydrogel cationic polysaccharide of co-polymers glucosamine and N-acetyl glucosamine obtained by alkaline deacetylation of chitin that is constitutive of crustacean shells. In addition, it shows a positive charge that can be exploited to form polyelectrolyte vesicular complexes able to act as delivery systems (Elieh-Ali-Komi and Hamblin, 2016). Cao and colleagues performed *in vivo* studies on rats, demonstrating that the abnormal involuntary movement rate significantly decreased

TABLE 1 | The table summarizes the main molecules currently used against neurodegenerative diseases.

Drug	Bioactivities	Limits	Liposomal-based carriers	*In vivo* model	Administration route	Improvements	References
Rivastigmine	Acetylcholinesterase inhibitor	- Low penetration capability across BBB - Low bioavailability	Conventional multilamellar LPs	Wistar rats	Intranasal	LPs increase drug accumulation rate in brain	(Arumugam et al., 2008)
			Electrosteric stealth (EES) LPs	Rabbits	Intranasal	Bioavailability of drugs increases in plasma and brain compartments	(Nageeb El-Helaly et al., 2017)
			LPs and Cell penetrating peptides (CPP) LPs	Murine	Intranasal	LPs and CPP-LPs enhance the permeability across BBB	(Yang et al., 2013)
Donepezil	Acetylcholinesterase inhibitor	- Low bioavailability - Low BBB permeation	LPs	Wistar rats	Intranasal	LP formulation increases the brain bioavailability	(Al Asmari et al., 2016)
Curcumin	Inhibitor of amyloid protein aggregation	- Low water solubility - Low bioavailability	LPs	Wistar-Bratislava albino rats	Intravenous	Increased bioavailability and efficacy of this compound	(Bulboaca et al., 2018)
						Augmented shelf life	
			LPs	Rats	Intranasal	Considerable suppression of cytokine levels	(Sokolik et al., 2017)
						Improved efficacy in terms of cognitive responses	
			Nanosized LPs and nanosized LPs functionalized with anti-Tf antibody	*Ex vivo* human brain tissues	—	Highest therapeutic efficacy	(Mourtas et al., 2014)
						Increased permeation capability, particularly in the case of Anti-Trf LPs	
			SLN and NLC	Rats	Intravenous	Increased drug accumulation in brain tissue, especially in the NLC case	(Sadegh Malvajerd et al., 2019)
						Reduced inflammatory state respect free drug administration	
			Liposomes with WGA (curcumin combined with NGF and/or CL)	Wistar rat	Intraperitoneal	Improved permeation rate across BBB	(Kuo et al., 2017)
						Inhibition of amyloid plaques formation	
						Cholinergic activity stimulation in hippocampus area	
Quercetin	Antioxidative ability Ameliorate cognitive and memory dysfunction	Low solubility in blood poor absorption and difficulty to pass BBB	Mannosylated LPs	Sprague Dawley rat	Carotid injection	Promoted antioxidant enzyme activities	(Sarkar and Das, 2006)

(Continued)

TABLE 1 | Continued

Drug	Bioactivities	Limits	Liposomal-based carriers	*In vivo* model	Administration route	Improvements	References
			LPs	Swiss albino rat	oral	Promoted antioxidant enzyme activities	(Ghosh et al., 2009)
			LPs	Wistar rat	intranasal	Neuroprotective action in hippocampus area	(Phachonpai et al., 2010)
						Amelioration of cognitive performances	(Terdthai et al., 2010)
			ApoE-PA-LPs	Sprague Dawley	Intravenous	Increased permeation capacity	(Kuo et al., 2018)
Resveratrol	promote the non-amyloidogenic cleavage of the amyloid precursor proteins, improves β amyloid-peptides clearance and to limit neuronal injury	Low aqueous solubility and low bioavailability	SLNs and poloxamer 188 coated SLNs	Wistar rats	oral	SLN formulations augment 8-fold the bioavailability of drug suspension	(Pandita et al., 2014)
			SLNs and NLCs	Wistar rats	intraperitoneal	Increased concentration in the brain	(Neves et al., 2013; Jose et al., 2014)
			LPs	Sprague-Dawley rats	Intravenous	Greater reduction of epileptic seizure respect to free resveratrol administration	(Wang et al., 2011)
			LPs	Sprague–Dawley rats	Intravenous	Higher reduction of ROS level and epileptic events in liposomal formulation case	(Ethemoglu et al., 2017)
Levodopa (SHM)	precursor of dopamine	- Cytotoxicity (ROS productions) - Dyskinesia - Low penetration capability across BBB	Chitosan coated LPs	Sprague-Dawley rats	oral	Increased drug accumulation rate in brain	(Cao et al., 2016)
			Superficial charged LPs	Sprague-Dawley rats	Carotid arteries injection	Reduced dyskinesia outcome charged LPs more actively interact with BBB charged LPs better penetrated BBB respect neutral liposomes cationic LPs accumulation rate in brain is highest respect to anionic LPs	(Joshi et al., 2014b)

The limits of the treatments are reported as well as the advantages of their administration in liposomal formulation.

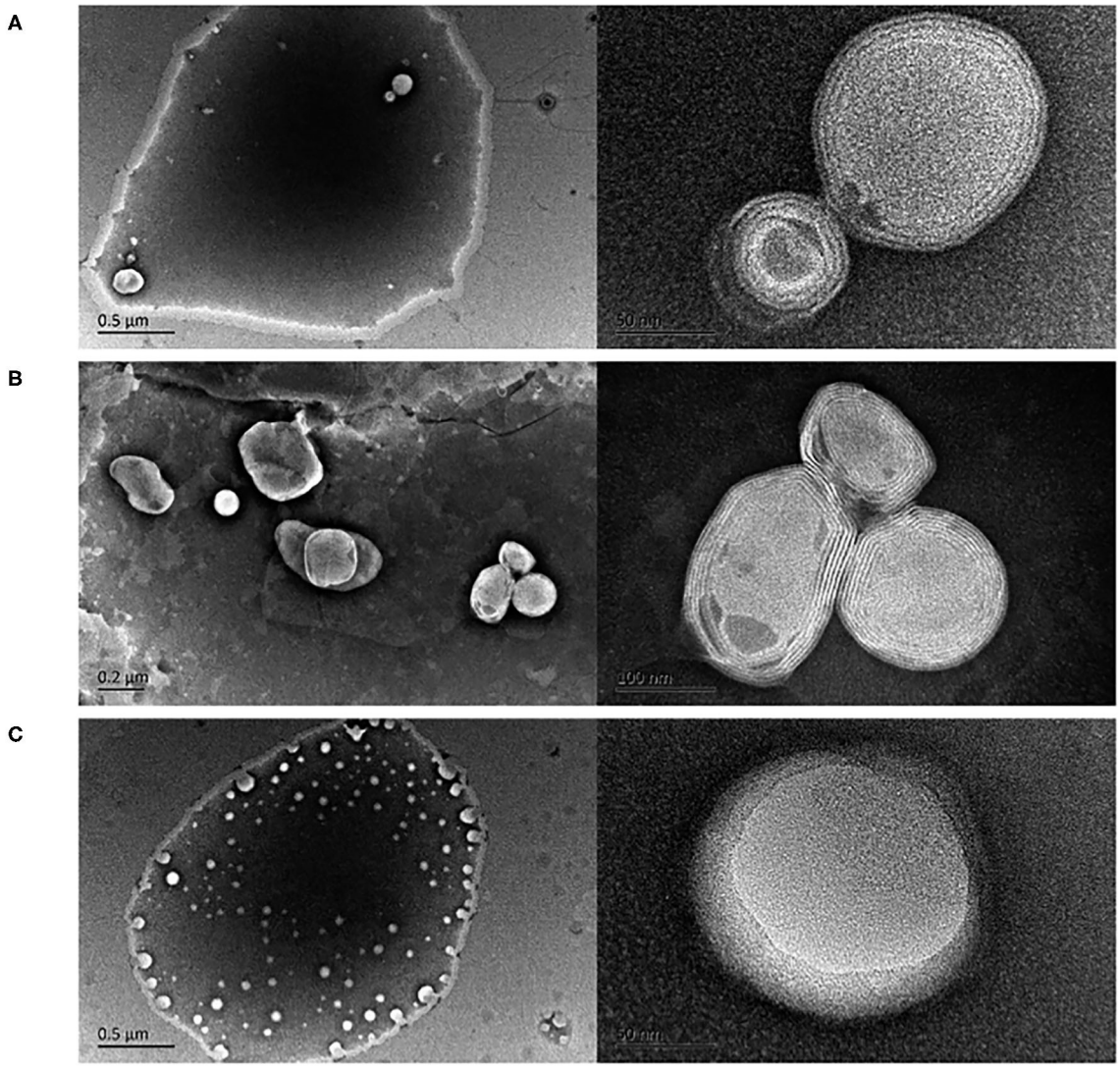

FIGURE 4 | Transmission electron microscopy images of curcumin LPs produced by the **(A)** pH-driven method, **(B)** thin film method, and **(C)** ethanol injection method. Reproduced from Cheng et al. (2017) with permission of The Royal Society of Chemistry.

in rats treated with chitosan-coated L-DOPA NLs than those who received free L-DOPA (Cao et al., 2016).

In the case of phytochemical compounds, the ND synthoms became more attenuated after the administration of curcumin and quercetin encapsulated in liposomal carriers with respect to free formulations. In details, *in vivo* experiments conducted on a rat model by Sadegh Malvajerd et al. (2019) showed a reduction in inflammatory state due to increased anti-oxidant activity after intravenous administrations of encapsulated curcumin into SLN and NLC carriers with respect to free drug; in addition, the pharmacokinetic studies demonstrated that the NLC option ensures higher accumulation into rat brain. Another interesting approach was suggested by Kuo et al. (2017) proposing the combined use of curcumin (CRM) and nerve growth factor (NGF) conjugated with cardiolipin (CL) to treat Alzheimer disorders. In details, the human neuroblastoma (SK-N-MC) cell line insulted with β-amyloid peptide (Aβ) shows how treatment with curcumin CRM-CL LPs prevented the neurodegeneration process through the inhibition of the p38, JNK, and tau protein phosphorylation. Meanwhile, the exposure to NGF-CL/LIP up-regulated the expression of the p-TrkA and p-ERK5, responsible to ensure neuronal viability. The effects of the combined use of these LPs were assessed in Wistar rat models, after intraperitoneal injections. To improve the permeation rate across the BBB, CRM-CL and CRM-CL LPs were implemented with germ agglutinin (WGA). The combined action of WGA-grafted CRM-CL and CRM-CL strongly affected the Aβ plaque formation, increasing the percentage of healthy neurons and promoting the cholinergic activity in the rat hippocampus.

Sokolik et al. compared the efficacy of intranasal administrated curcumin against Alzheimer's disorder in soluble form with liposomal formulations. After neuroinflammatory quantification analysis, they performed cognitive tests on rats to evaluate the impact of curcumin exposure on mnestic functions. They evaluated the impact on the angiotensin converting enzyme activity and cytokine productions in the damaged rat brain. Treatment with CLs reduced cytokines (interleukin-1β, interleukin-6, interleukin-10, tumor necrosis factor α) and angiotensin expression in cerebral cortex and hippocampus area. Finally, the cognitive tests show a reduction in the latent period of conditioned reflex reactions (Sokolik and Shulga, 2016; Sokolik et al., 2016, 2017).

Sarkar and Das have reported that, conversely to free formulation, quercetin loaded in mannosylated LPs and administrated via carotid injection in male Sprague-Dawley rats, in which the ischemia event was induced, meaningfully sustained antioxidant enzyme activity, preventing edema formation (Sarkar and Das, 2006). In addition, Das et al. demonstrated the oral administration of LP-encapsulated quercetin enhanced the antioxidative enzyme activity in adult female Swiss albino rat brains neurodamaged after arsenic exposure (Ghosh et al., 2009). Phachonpai and colleagues (Phachonpai et al., 2010) treated male Wistar rats, used as Alzheimer's disease model, with quercetin in LPs via intranasal administration. After treatment (0.5 mg/daily for 2 weeks), the neuroprotective quercetin action was recorded: the activities of superoxide dismutase, catalase, and glutathione peroxidase increased while the malondialdehyde levels were decreased. The reduction of oxidative stress confirmed the effectiveness of quercetin against Alzheimer's disease. The extension of the time treatment until 4 weeks increased the cholinergic neuron viability in hippocampus and ameliorated cognitive performances (Terdthai et al., 2010).

In the last years, the combination of resveratrol in LPs was explored as potential strategy for ND treatment. Ethemoglu et al. (2017) demonstrated how the resveratrol administration influenced the incidence of epileptic events in rats, in which brain ND disorder was induced by penicillin administration. The treatment with resveratrol reduced the epileptic activity, probably due to the reduction of oxidative stress at the cellular level. This rate further decreased when resveratrol was encapsulated in liposomal carriers.

Wang et al. (2013) assessed the impact of resveratrol derived from *Polygonum cuspidatum* on rats in which Parkinson's outcome was induced. After 14 days of oral treatment, the apoptosis rate of nigral tissue cells and ROS level was decreased while the antioxidant capability increased. These effects were strongly augmented when resveratrol was administered in liposomal vectors, probably due to the enhanced bioavailability.

PERMEABILITY

The main limitation of anti-ND drug efficacy is their poor BBB penetration capability, in fact <98% of the small molecules and nearly 100% of large molecules are able to reach the brain. The encapsulation in liposomal-based carriers can enhance the bioavailability in brain of therapeutic agents; for example Aramugam et al. (2008) treated Wistar rat with rivastigmine encapsulated in conventional multilamellar LPs: after intranasal injection, the rivastigmine level reveled in brain tissue resulted in higher respect to free drug. However, in order to improve the uptake of anti-ND drugs, active targeting strategies have been developed. The chemical modification of LP surfaces essentially consists in attaching ligands which interact with proteins expressed by BBB.

Yang et al. (2013) produced CCP LPs using cell-penetrating peptide (CPP), with the aim to enhance the brain distribution of rivastigmine. In detail, they proceeded by an intranasal administration in order to minimize the collateral effects (including hepatic first pass metabolism and gastrointestinal adverse outcomes), enhancing the permeability of the CPP-LP complex across both the nasal olfactory pathway and the murine BBB. Relative to the extended release and absorption, an intense inhibition of acetylcholinesterase and butyrylcholinesterase activities was detected.

Among receptor-mediated transcytosis, the transferrin (Tf) receptors are the one of the most explored as targets of the drug delivery system (Sharma et al., 2016). In particular, several *in vitro* and *in vivo* studies were performed in order to improve the targeting efficacy of therapeutic molecules across BBB (Pulgar, 2018).

Mourtas et al. (2014) produced a curcumin derivative in nanosized LPs functionalized with the anti-Tf antibody to direction them against Aβ protein in amyloid plaques. The potential efficacy of curcumin-derivative LPs and curcumin-derivative anti-Tf LPs was assessed in *ex vivo* experiments performed on post-mortem extracted brain samples from patients affected by Alzheimer disease. Both LP types exhibited high binding affinity with Aβ proteins; indeed, the thioflavin assay confirmed their ability to slow down the Aβ1-42 peptide aggregation. Although the efficacy of examined carriers was comparable, the anti-Tf receptor-decorated LPs strongly enhanced the brain permeation.

With the aim to improve the efficacy of the neuroprotectant ZL006 against ischemic stroke, Wang and colleagues (Wang et al., 2015) encapsulated it in modified LPs with HAIYPRH (T7) peptide, which directly interacts with TfR. The *in vivo* experiments performed on rat models (Sprague-Dawley and ICR mice) revealed that the T7 functionalization considerably improved the penetration across the BBB. This implied a reduced infarct volume and enhanced neurological deficit with respect to the untargeted LPs or SKfree ZL006.

The Tf functionalization is currently used to improve BBB targeting and transcytosis. In order to enhance the neuronal transfection in gene therapy, Dos Santos Rodrigues et al. (Dos Santos Rodrigues et al., 2018) conceived LPs with double functionalization: Tf and penetratin (Pen); the latter enabled overcoming receptor saturation and increasing the number of internalized LPs. Hydrophilic plasmid for β-galactosidase (pβgal), used as a gene model, were loaded in Pen-Tf LPs in order to explore the efficacy in gene therapy applications. After injection in C57BL/6J mice, the plasmid biodistribution was quantified in different tissues: the liposomal formulation involved

a significant increase in βgal amount in brain, liver, and kidneys with respect to the endogenous levels. In addition, the Pen-Tf functionalization improved the transfection capability only in the brain.

α-Mangostin is a polyphenolic xanthone, largely used in medicine; recently, it was demonstrated its capability to slow down AD progression (Wang et al., 2012); nevertheless, its efficacy is limited by the low penetration capability across the BBB. Moving from these evidences, Chen and colleagues (Chen et al., 2016) modified LPs with Tf in order to enhance the penetration rate of α-Mangostin in brain. α-M was intravenously administrated (5 mg/kg) into the Sprague Dawley rats in different formulations: α-M solution, α-M LP, and Tf(α-M) LP. The pharmacokinetic experiments revealed that encapsulation in Tf LPs augmented the α-M bioavailability in plasma and drug accumulation rate in brain tissue. The authors proposed Tf-LPs as a promising drug delivery system, demonstrating their ability to improve the brain permeation of α-M; however, α-M distribution quantification in different body compartments showed that Tf(α-M) LPs tended to accumulate also in liver tissue; this is due to the expression of TfR on hepatocytes.

The fact that Tf receptors were expressed on several cellular types, including hepatocytes, monocytes, erythrocytes, intestinal cells, epithelial cell of choroid plexus, and neuron besides BBB, represents an important issue in targeting of delivery systems. In addition, the efficiency of the Tf targeting could be dramatically compromised by the physiological presence of high levels of endogenous Tf in the plasma, which saturated the TfR endothelial cells (Sharma et al., 2016).

Like TfR, low-density lipoprotein (LDL) receptors, involved in the specific BBB transport mechanisms, could be exploited in the increase of the drug rate permeation in brain. In particular, human apolipoprotein E (apoE) plays a key role in lipid transport in the CNS (Fan et al., 2001; Hatters et al., 2006). In addition, biological membranes contain a great variety of phospholipids; one among them is phosphatidic acid (PA), which has a special attraction for Aβ and may help rescue neurons from Aβ-induced toxicity. Drug carriers associated with PA and ApoE may improve the affinity to binding to Aβ *in vitro* (Re et al., 2011; Salvati et al., 2013).

Starting from these evidences, Bana et al. (2014) used a Balb/c mice model to test the uptake in brain of modified LPs mApoE-PA-LPs, obtained by functionalizing PA and a synthetic peptide (mApoE; CWGLRKLRKRLLR) that includes the apolipoprotein-E receptor-binding domain. The biodistribution experiments, performed after intravenous administration, demonstrated that mApoE-PA-LPs were more capable of penetrating the BBB respect to PA-LPs.

The apolipoprotein E (ApoE) conjugated with PA was also used by Kuo and co-worker (Kuo et al., 2018) to functionalize LPs (ApoE-PA-LP) able to deliver quercetin and rosmarinic acid to brain, in order to inhibit β-amyloid (1–42) (Aβ1-42) aggregation. The permeation capacity strongly increased in functionalization case respect to free drugs and drugs encapsulated in undecorated LPs. The administration of quercetin and rosmarinic acid in ApoE-PA-LP formulation induced in Aβ-insulted SD rats the diminishment of the acetylcholinesterase activity and the reduction in Aβ plaque formation.

Recently, other potential targeting molecules have been explored to improve the drug internalization exploiting the receptor-mediated transcytosis process. In detail, the nutrient transporters can be used for brain delivery. Among these, glutathione (GSH) is an endogenous tripeptide able to penetrate the BBB as sodium-dependent transporter; this latter is preferentially expressed in CNS and BBB of all mammalian species (Smeyne and Smeyne, 2013; Kuo et al., 2018).

Rip and co-workers fabricated PEGylated LPs with GSH, and they investigated the potential improvement in brain uptake of drug encapsulated in this carrier; for this purpose the authors loaded a fluorescent tracer (carboxifluorescein) in the PEG-GSH modified LPs (Rip et al., 2014). Quantification of carboxifluorescein in brain was obtained by microdialysis experiment on Wistar rats, in which this fluorescent molecule was intravenously administrated in three different forms: free, non-targeted PEG LPs, and GSH-PEG LPs. The results showed that the carboxifluorescein level in brain increased in liposomal formulation; in particular, the GSH-PEG LP option made this level fourfold higher with respect to undecorated PEG LPs. The efficiency of GSH-PEG LP delivery in the brain was also tested for ribavirin drug (Rip et al., 2010; Maussang et al., 2016). The concentration of drug in brain tissue increased in modified LP formulation in Wistar rats after administration by intravenous route; the permeation rate beyond the BBB became proportional to the amount of GSH coating (ranging from 0 to 2%).

In addition, in literature several works reported how the GSH-PEG LP formulation improves in brain delivery of the opioid peptide DAMGO (H-Tyr-d-Ala-Gly-MePhe-Gly-ol) (Lindqvist et al., 2013), the anti-amyloid single-domain antibody fragment (Rotman et al., 2015), flucytosine (Salem et al., 2015), methylprednisolone hemisuccinate (Kanhai et al., 2018), etc.

Another promising strategy to improve penetration capability of anti-ND drug is based on the use of cationic polyelectrolyte in LP preparation. Cationic LPs (CLs) can penetrate the BBB through adsorptive-mediated endocytosis process (Herve et al., 2008). This occurs because the surface of CLs exhibits a positive charge at physiological pH; thus, it electrostatically interacts with the polyanions present in the BBB (Miller et al., 1998).

This event was examined *in vivo* on Sprague–Dawley rats, in which cationic, anionic, and charge-neutral LPs were directly injected into carotid arteries. Joshi et al. reported that superficial charged LPs more actively interact with BBB endothelial cell respect to neutral LPs; in particular, the authors recorded the highest cationic concentration with respect to the anionic LPs into the brain tissue (Joshi et al., 2014a,b; Joshi et al., 2015).

Migliore et al. (2010) stated that the use of CLs as a delivery system enhanced the brain uptake of drug administered by intranasal route in Sprague–Dawley rats.

Recently, another work (Dhaliwal et al., 2020) reported how it is possible to take advantage of cationic LPs to improve the mRNA delivery. After optimization of the liposomal formulation, mRNA was administered by intranasal route to CD-1 mice. Through the GFP and luciferase reporter systems, the authors

have quantified the mRNA biodistribution *in vivo*. The findings demonstrated the cationic LPs improved the penetration rate of mRNA and its accumulation into specific cerebral areas (cortex, striatum, and midbrain).

Although it was demonstrated that the CL formulation enhanced the anti-ND drug penetration rate in the brain, it must be admitted that this rate is limited by non-specific uptake phenomena in peripheral tissues. In addition, the superficial charge of LPs could be reduced by interaction with serum protein before reaching the BBB (Tagalakis et al., 2014).

These issues could be overcome by increasing the amounts of use of CLs, but keeping in consideration their cytotoxic potential.

ADMINISTRATION ROUTES

The main challenge in the treatment of CNS diseases is represented by the presence of the BBB, which makes complicated the delivery of therapeutic agents into the brain. At first, invasive approaches have performed in order to overcome the BBB, including the neurosurgery-based cerebral infusions or implants and the physical or chemical disruption of the BBB to permit the penetration of drug via osmotic shift (Chen et al., 2004). However, these techniques are highly dangerous carry risks of infection and brain tissue damage, and are able to induce chronic neuropathological effects in treated patients (Chen et al., 2004). In recent decades, several non-invasive strategies, based on physiological brain transport mechanisms, have been developed.

As already described in this review, the drug loading in LPs increases its own uptake in the brain; later on, once the importance of LP usage was proven, various studies have tried several routes of administration for finding out if they are more or less adequate.

The intravenous routes are certainly the most common, preferred to the oral route, because in this latter case there is a loss in terms of drug percentage in the gastrointestinal ambient: drug is degraded by the stomach fluids and poorly absorbed by the intestine, while increasing the hepatic and renal load; although in different reported works, it has been proven that the drug loading in LPs prevent the drug degradation. Although the intravenous injection is the most applied, the interest in alternative parenteral routes increased, for finding new direct administrations to the BBB. Among these, the intranasal way gained a noticeable increase by the scientific community, due to its ability to let the drug reach the brain via different pathways: direct ones, through olfactive epithelium, thanks to the presence of olfactory nerves; or indirect ones, through the respiratory epithelium first and the circulatory system after (Hong et al., 2019).

In the last decade, there is a growing interest of administering them via intradermal routes. In this perspective, ethosomes represent the better choice among liposomal systems, due to their ability to increase the drug permeation across the derma. For instance, Ropinirole hydrochloride is commonly used in Parkinson disease. With the aim to evaluate the possibility to administrate Ropinirole hydrochloride via transdermal route, Mishra et al. (2013) synthetized different ethosomal carriers, varying ethanol and lecithin concentrations. The experimental *in vivo* study showed that RHC encapsulated in ethosomes (30 and 4% w/v of ethanol and lecithin, respectively) increased their blood circulation time, becoming comparable to the oral administration case.

Flurbiprofen is largely used in ND treatments for its anti-inflammatory effect. The permeation of ethosomal–flurbiprofen (EF) formulations was assessed in the albino rat model (Paliwal et al., 2019). The reported results showed a high encapsulation drug efficiency (95 %); in addition, the permeation efficacy was equal to (82.56 ± 2.11) g/cm^2 in 24 h, and transdermal flux was found as 226.1 μg/cm^2/h.

Ligustrazine phosphate (LP) is an antioxidant used for the Alzheimer disorder. Shi and co-workers (Shi et al., 2012) optimized the ethosome-based carrier for LP transdermal delivery; in addition, they evaluated the therapeutic impact on rats, in which amnesia disease was induced by scopolamine. Experimental evidence indicated that the penetration ability of the LP ethosomal system was strongly higher than the LP in aqueous solution. Moreover, the LP ethosomal treatment normalized the levels both of antioxidant enzymes and the lipid peroxidation in a healthy rat model.

These *in vivo* evidences suggested the goodness of ethosome-based strategy; nevertheless, for ND disease, only a few studies explored the potential of dermal administration ethosome-mediated.

CONCLUSIONS AND PERSPECTIVE

In the last decades, many efforts have been made to develop an optimal therapeutic strategy against neurodegenerative disorders due to their dramatic incidence worldwide. In this perspective, several new molecules including phytochemical extracts were investigated along with the conventional drugs. Unfortunately, their therapeutic potential was strongly compromised owing to the presence of high selective barrier (BBB) that protects the brain from treatment (CNS).

The effectiveness of drugs against ND diseases increases when they are encapsulated into liposomal-based vectors.

Generally, LPs represent a promising platform for theranostic medicine purposes, thanks to their size, biocompatibility, high biological affinity, immunogenicity, biodegradability, and low toxicity. In addition, LPs have a good ability to deliver both hydrophobic and hydrophilic molecules through BBB.

In this review article, the recent state of the art about the use of liposomal-based carriers for anti-neurodegenerative drug delivery and the *in vivo* applications are extensively examined. In the reported researches, the enhanced efficacy of drug following liposomal encapsulation has been demonstrated, in terms of improved bioavailability, stability, and permeation capability across BBB.

Albeit a great deal of progress has been made in liposomal formulations and their efficiency was demonstrated in several *in vivo* studies, some issues are still present.

The scientific community is called to perform further clinical trials in order to evaluate the LP accumulation

effects induced by long-term exposure and, simultaneously, to optimize the ingegnerization of these carriers in the human body.

AUTHOR CONTRIBUTIONS

MC and VDM: conceptualization and writing (original draft preparation). MC, VDM, SL, and RR: review and editing manuscript. SL and RR: funding acquisition.

ACKNOWLEDGMENTS

MC and VDM kindly acknowledge Programma Operativo Nazionale (PON) Ricerca e Innovazione 2014-2020 Asse I Capitale Umano, Azione I.2, Avviso 'A.I.M: Attraction and International Mobility [F88D18000070001] [CUP F88D1800060001]. SL has been partially supported by Progetto Fondo Integrativo Speciale per la Ricerca (FISR-CNR) Tecnopolo di Nanotecnologia e Fotonica per la Medicina di Precisione [CUP B83B17000010001].

REFERENCES

Abbott, N. J., Patabendige, A. A., Dolman, D. E., Yusof, S. R., and Begley, D. J. (2010). Structure and function of the blood-brain barrier. *Neurobiol. Dis.* 37, 13–25. doi: 10.1016/j.nbd.2009.07.030

Abbott, N. J., and Romero, I. A. (1996). Transporting therapeutics across the blood-brain barrier. *Mol. Med. Today* 2, 106–113. doi: 10.1016/1357-4310(96)88720-X

Abeliovich, A., and Gitler, A. D. (2016). Defects in trafficking bridge parkinson's disease pathology and genetics. *Nature* 539, 207–216. doi: 10.1038/nature20414

Agrawal, M., Ajazuddin, T., D. K., Saraf, S., Saraf, S., Antimisiaris, S. G., Mourtas, S., et al. (2017). Recent advancements in liposomes targeting strategies to cross blood-brain barrier (bbb) for the treatment of alzheimer's disease. *J. Control. Release* 260, 61–77. doi: 10.1016/j.jconrel.2017.05.019

Al Asmari, A. K., Ullah, Z., Tariq, M., and Fatani, A. (2016). Preparation, characterization, and *in vivo* evaluation of intranasally administered liposomal formulation of donepezil. *Drug Des. Devel. Ther.* 10, 205–215. doi: 10.2147/DDDT.S93937

Alexander, G. E. (2004). Biology of parkinson's disease: Pathogenesis and pathophysiology of a multisystem neurodegenerative disorder. *Dialogues Clin. Neurosci.* 6, 259–280.

Angeles, D. C., Ho, P., Chua, L. L., Wang, C., Yap, Y. W., Ng, C., et al. (2014). Thiol peroxidases ameliorate lrrk2 mutant-induced mitochondrial and dopaminergic neuronal degeneration in drosophila. *Hum. Mol. Genet.* 23, 3157–3165. doi: 10.1093/hmg/ddu026

Arumugam, K., Subramanian, G. S., Mallayasamy, S. R., Averineni, R. K., Reddy, M. S., and Udupa, N. A. (2008). Study of rivastigmine liposomes for delivery into the brain through intranasal route. *Acta Pharm.* 58, 287–297. doi: 10.2478/v10007-008-0014-3

Ay, M., Luo, J., Langley, M., Jin, H., Anantharam, V., Kanthasamy, A., et al. (2017). Molecular mechanisms underlying protective effects of quercetin against mitochondrial dysfunction and progressive dopaminergic neurodegeneration in cell culture and mitopark transgenic mouse models of parkinson's disease. *J. Neurochem.* 141, 766–782. doi: 10.1111/jnc.14033

Bana, L., Minniti, S., Salvati, E., Sesana, S., Zambelli, V., Cagnotto, A., et al. (2014). Liposomes bi-functionalized with phosphatidic acid and an apoe-derived peptide affect abeta aggregation features and cross the blood-brain-barrier: implications for therapy of alzheimer disease. *Nanomedicine* 10, 1583–1590. doi: 10.1016/j.nano.2013.12.001

Bartels, A. L. (2011). Blood-brain barrier p-glycoprotein function in neurodegenerative disease. *Curr. Pharm. Des.* 17, 2771–2777. doi: 10.2174/138161211797440122

Begley, D. J. (2004). Delivery of therapeutic agents to the central nervous system: the problems and the possibilities. *Pharmacol. Ther.* 104, 29–45. doi: 10.1016/j.pharmthera.2004.08.001

Begley, D. J., and Brightman, M. W. (2003). Structural and functional aspects of the blood-brain barrier. Progress in drug research. Fortschritte der Arzneimittelforschung. *Progr. Rec. Pharm.* 61, 39–78. doi: 10.1007/978-3-0348-8049-7_2

Beloqui, A., Solinis, M. A., Rodriguez-Gascon, A., Almeida, A. J., and Preat, V. (2016). Nanostructured lipid carriers: promising drug delivery systems for future clinics. *Nanomedicine* 12, 143–161. doi: 10.1016/j.nano.2015.09.004

Bitounis, D., Fanciullino, R., Iliadis, A., and Ciccolini, J. (2012). Optimizing druggability through liposomal formulations: new approaches to an old concept. *ISRN Pharm.* 2012:738432. doi: 10.5402/2012/738432

Blasi, P., Giovagnoli, S., Schoubben, A., Ricci, M., and Rossi, C. (2007). Solid lipid nanoparticles for targeted brain drug delivery. *Adv. Drug Deliv. Rev.* 59, 454–477. doi: 10.1016/j.addr.2007.04.011

Bozzuto, G., and Molinari, A. (2015). Liposomes as nanomedical devices. *Int. J. Nanomed.* 10, 975–999. doi: 10.2147/IJN.S68861

Bulboaca, A. E., Bolboaca, S. D., Stanescu, I. C., Sfrangeu, C. A., Porfire, A., Tefas, L., et al. (2018). The effect of intravenous administration of liposomal curcumin in addition to sumatriptan treatment in an experimental migraine model in rats. *Int. J. Nanomed.* 13, 3093–3103. doi: 10.2147/IJN.S162087

Cao, X., Hou, D., Wang, L., Li, S., Sun, S., Ping, Q., et al. (2016). Effects and molecular mechanism of chitosan-coated levodopa nanoliposomes on behavior of dyskinesia rats. *Biol. Res.* 49:32. doi: 10.1186/s40659-016-0093-4

Cavaco, M., Gaspar, D., Arb Castanho, M., and Neves, V. (2020). Antibodies for the treatment of brain metastases, a dream or a reality? *Pharmaceutics* 12:62. doi: 10.3390/pharmaceutics12010062

Chen, C., Han, D., Cai, C., and Tang, X. (2010). An overview of liposome lyophilization and its future potential. *J. Control. Release* 142, 299–311. doi: 10.1016/j.jconrel.2009.10.024

Chen, Y., Dalwadi, G., and Benson, H. A. (2004). Drug delivery across the blood-brain barrier. *Curr. Drug Deliv.* 1, 361–376. doi: 10.2174/1567201043334542

Chen, Y., and Liu, L. (2012). Modern methods for delivery of drugs across the blood-brain barrier. *Adv. Drug Deliv. Rev.* 64, 640–665. doi: 10.1016/j.addr.2011.11.010

Chen, Z. L., Huang, M., Wang, X. R., Fu, J., Han, M., Shen, Y. Q., et al. (2016). Transferrin-modified liposome promotes alpha-mangostin to penetrate the blood-brain barrier. *Nanomedicine* 12, 421–430. doi: 10.1016/j.nano.2015.10.021

Cheng, C., Peng, S., Li, Z., Zou, L., Liu, W., and Liu, C. (2017). Improved bioavailability of curcumin in liposomes prepared using a ph-driven, organic solvent-free, easily scalable process. *RSC Adv.* 7, 25978–25986. doi: 10.1039/C7RA02861J

Citron, M. (2002). Alzheimer's disease: treatments in discovery and development. *Nat. Neurosci.* 5, 1055–1057. doi: 10.1038/nn940

Combs, B., Hamel, C., and Kanaan, N. M. (2016). Pathological conformations involving the amino terminus of tau occur early in alzheimer's disease and are differentially detected by monoclonal antibodies. *Neurobiol. Dis.* 94, 18–31. doi: 10.1016/j.nbd.2016.05.016

Darvesh, A. S., Carroll, R. T., Bishayee, A., Novotny, N. A., Geldenhuys, W. J., and Van der Schyf, C. J. (2012). Curcumin and neurodegenerative diseases: a perspective. *Expert Opin. Investig. Drugs* 21, 1123–1140. doi: 10.1517/13543784.2012.693479

Das, S., and Chaudhury, A. (2011). Recent advances in lipid nanoparticle formulations with solid matrix for oral drug delivery. *AAPS PharmSciTech* 12, 62–76. doi: 10.1208/s12249-010-9563-0

Dawson, T. M., Ko, H. S., and Dawson, V. L. (2010). Genetic animal models of parkinson's disease. *Neuron* 66, 646–661. doi: 10.1016/j.neuron.2010.04.034

de Boer, A. G., and Gaillard, P. J. (2007). Drug targeting to the brain. *Annu. Rev. Pharmacol. Toxicol.* 47, 323–355. doi: 10.1146/annurev.pharmtox.47.120505.105237

de Boer, A. G., van der Sandt, I. C., and Gaillard, P. J. (2003). The role of drug transporters at the blood-brain barrier. *Annu. Rev. Pharmacol. Toxicol.* 43, 629–656. doi: 10.1146/annurev.pharmtox.43.100901.140204

Demeule, M., Currie, J. C., Bertrand, Y., Che, C., Nguyen, T., Regina, A., et al. (2008). Involvement of the low-density lipoprotein receptor-related protein in the transcytosis of the brain delivery vector angiopep-2. *J. Neurochem.* 106, 1534–1544. doi: 10.1111/j.1471-4159.2008.05492.x

Dhaliwal, H. K., Fan, Y., Kim, J., and Amiji, M. M. (2020). Intranasal delivery and transfection of mrna therapeutics in the brain using cationic liposomes. *Mol. Pharm.* 17, 1996–2005. doi: 10.1021/acs.molpharmaceut.0c00170

Di Stefano, A., Iannitelli, A., Laserra, S., and Sozio, P. (2011). Drug delivery strategies for alzheimer's disease treatment. *Expert Opin. Drug Deliv.* 8, 581–603. doi: 10.1517/17425247.2011.561311

Dodel, R. C., Berger, K., and Oertel, W. H. (2001). Health-related quality of life and healthcare utilisation in patients with parkinson's disease: impact of motor fluctuations and dyskinesias. *Pharmacoeconomics* 19, 1013–1038. doi: 10.2165/00019053-200119100-00004

Dos Santos Rodrigues, B., Oue, H., Banerjee, A., Kanekiyo, T., and Singh, J. (2018). Dual functionalized liposome-mediated gene delivery across triple co-culture blood brain barrier model and specific *in vivo* neuronal transfection. *J. Control. Release* 286, 264–278. doi: 10.1016/j.jconrel.2018.07.043

Duraes, F., Pinto, M., and Sousa, E. (2018). Old drugs as new treatments for neurodegenerative diseases. *Pharmaceuticals* 11:44. doi: 10.3390/ph11020044

Elieh-Ali-Komi, D., and Hamblin, M. R. (2016). Chitin and chitosan: production and application of versatile biomedical nanomaterials. *Int. J. Adv. Res.* 4, 411–427.

Engelhardt, B., and Liebner, S. (2014). Novel insights into the development and maintenance of the blood-brain barrier. *Cell Tissue Res,* 355, 687–699. doi: 10.1007/s00441-014-1811-2

Ethemoglu, M. S., Seker, F. B., Akkaya, H., Kilic, E., Aslan, I., Erdogan, C. S., et al. (2017). Anticonvulsant activity of resveratrol-loaded liposomes *in vivo*. *Neuroscience* 357, 12–19. doi: 10.1016/j.neuroscience.2017.05.026

Euliss, L. E., DuPont, J. A., Gratton, S., and DeSimone, J. (2006). Imparting size, shape, and composition control of materials for nanomedicine. *Chem. Soc. Rev.* 35, 1095–1104. doi: 10.1039/b600913c

Fan, Q. W., Iosbe, I., Asou, H., Yanagisawa, K., and Michikawa, M. (2001). Expression and regulation of apolipoprotein e receptors in the cells of the central nervous system in culture: a review. *J. Am. Aging Assoc.* 24, 1–10. doi: 10.1007/s11357-001-0001-9

Fenske, D. B., Chonn, A., and Cullis, P. R. (2008). Liposomal nanomedicines: an emerging field. *Toxicol. Pathol.* 36, 21–29. doi: 10.1177/0192623307310960

Fenske, D. B., and Cullis, P. R. (2008). Liposomal nanomedicines. *Expert Opin. Drug Deliv.* 5, 25–44. doi: 10.1517/17425247.5.1.25

Ghosh, A., Mandal, A. K., Sarkar, S., Panda, S., and Das, N. (2009). Nanoencapsulation of quercetin enhances its dietary efficacy in combating arsenic-induced oxidative damage in liver and brain of rats. *Life Sci.* 84, 75–80. doi: 10.1016/j.lfs.2008.11.001

Gitler, A. D., Dhillon, P., and Shorter, J. (2017). Neurodegenerative disease: models, mechanisms, and a new hope. *Dis. Model. Mech.* 10, 499–502. doi: 10.1242/dmm.030205

Goedert, M. (2004). Tau protein and neurodegeneration. *Semin. Cell Dev. Biol.* 15, 45–49. doi: 10.1016/j.semcdb.2003.12.015

Hatters, D. M., Peters-Libeu, C. A., and Weisgraber, K. H. (2006). Apolipoprotein e structure: insights into function. *Trends Biochem. Sci.* 31, 445–454. doi: 10.1016/j.tibs.2006.06.008

Heemels, M. T. (2016). Neurodegenerative diseases. *Nature* 539:179. doi: 10.1038/539179a

Helen Chan, O., and Stewart, B. H. (1996). Physicochemical and drug-delivery considerations for oral drug bioavailability. *Drug Discov. Today* 1, 461–473. doi: 10.1016/1359-6446(96)10039-8

Herve, F., Ghinea, N., and Scherrmann, J. M. (2008). Cns delivery via adsorptive transcytosis. *AAPS J.* 10, 455–472. doi: 10.1208/s12248-008-9055-2

Hong, S. S., Oh, K. T., Choi, H. G., and Lim, S. J. (2019). Liposomal formulations for nose-to-brain delivery: recent advances and future perspectives. *Pharmaceutics* 11:540. doi: 10.3390/pharmaceutics11100540

Iqbal, M. A., Md, S., Sahni, J. K., Baboota, S., Dang, S., and Ali, J. (2012). Nanostructured lipid carriers system: recent advances in drug delivery. *J. Drug Target* 20, 813–830. doi: 10.3109/1061186X.2012.716845

Johnsson, M., and Edwards, K. (2003). Liposomes, disks, and spherical micelles: aggregate structure in mixtures of gel phase phosphatidylcholines and poly(ethylene glycol)-phospholipids. *Biophys. J.* 85, 3839–3847. doi: 10.1016/S0006-3495(03)74798-5

Jose, S., Anju, S. S., Cinu, T. A., Aleykutty, N. A., Thomas, S., and Souto, E. B. (2014). *In vivo* pharmacokinetics and biodistribution of resveratrol-loaded solid lipid nanoparticles for brain delivery. *Int. J. Pharm.* 474, 6–13. doi: 10.1016/j.ijpharm.2014.08.003

Joshi, S., Singh-Moon, R., Wang, M., Chaudhuri, D. B., Ellis, J. A., Bruce, J. N., et al. (2014b). Cationic surface charge enhances early regional deposition of liposomes after intracarotid injection. *J. Neurooncol.* 120, 489–497. doi: 10.1007/s11060-014-1584-1

Joshi, S., Singh-Moon, R. P., Ellis, J. A., Chaudhuri, D. B., Wang, M., Reif, R., et al. (2015). Cerebral hypoperfusion-assisted intra-arterial deposition of liposomes in normal and glioma-bearing rats. *Neurosurgery* 76, 92–100. doi: 10.1227/NEU.0000000000000552

Joshi, S., Singh-Moon, R. P., Wang, M., Chaudhuri, D. B., Holcomb, M., Straubinger, N. L., et al. (2014a). Transient cerebral hypoperfusion assisted intraarterial cationic liposome delivery to brain tissue. *J. Neurooncol.* 118, 73–82. doi: 10.1007/s11060-014-1421-6

Kanhai, K. M. S., Zuiker, R., Stavrakaki, I., Gladdines, W., Gaillard, P. J., Klaassen, E. S., et al. (2018). Glutathione-pegylated liposomal methylprednisolone in comparison to free methylprednisolone: slow release characteristics and prolonged lymphocyte depression in a first-in-human study. *Br. J. Clin. Pharmacol* 84, 1020–1028. doi: 10.1111/bcp.13525

Kisler, K., Nelson, A. R., Montagne, A., and Zlokovic, B. V. (2017). Cerebral blood flow regulation and neurovascular dysfunction in alzheimer disease. *Nat. Rev. Neurosci.* 18, 419–434. doi: 10.1038/nrn.2017.48

Kulkarni, S. S., and Canto, C. (2015). The molecular targets of resveratrol. *Biochim. Biophys. Acta* 1852, 1114–1123. doi: 10.1016/j.bbadis.2014.10.005

Kuo, Y.-C., Chen, I.-Y., and Rajesh, R. (2018). Use of functionalized liposomes loaded with antioxidants to permeate the blood–brain barrier and inhibit β-amyloid-induced neurodegeneration in the brain. *J. Taiwan Inst. Chem. Eng.* 87, 1–14. doi: 10.1016/j.jtice.2018.03.001

Kuo, Y. C., Lin, C. Y., Li, J. S., and Lou, Y. I. (2017). Wheat germ agglutinin-conjugated liposomes incorporated with cardiolipin to improve neuronal survival in alzheimer's disease treatment. *Int. J. Nanomed.* 12, 1757–1774. doi: 10.2147/IJN.S128396

Li, F., Gong, Q., Dong, H., and Shi, J. (2012). Resveratrol, a neuroprotective supplement for alzheimer's disease. *Curr. Pharm. Des.* 18, 27–33. doi: 10.2174/138161212798919075

Lindqvist, A., Rip, J., Gaillard, P. J., Bjorkman, S., and Hammarlund-Udenaes, M. (2013). Enhanced brain delivery of the opioid peptide damgo in glutathione pegylated liposomes: a microdialysis study. *Mol. Pharm.* 10, 1533–1541. doi: 10.1021/mp300272a

Lockman, P. R., Mumper, R. J., Khan, M. A., and Allen, D. D. (2002). Nanoparticle technology for drug delivery across the blood-brain barrier. *Drug Dev. Ind. Pharm.* 28, 1–13. doi: 10.1081/DDC-120001481

Maussang, D., Rip, J., van Kregten, J., van den Heuvel, A., van der Pol, S., van der Boom, B., et al. (2016). Glutathione conjugation dose-dependently increases brain-specific liposomal drug delivery *in vitro* and *in vivo*. *Drug Discov. Today Technol.* 20, 59–69. doi: 10.1016/j.ddtec.2016.09.003

McEwen, B. S., and Reagan, L. P. (2004). Glucose transporter expression in the central nervous system: relationship to synaptic function. *Eur. J. Pharmacol.* 490, 13–24. doi: 10.1016/j.ejphar.2004.02.041

Migliore, M. M., Vyas, T. K., Campbell, R. B., Amiji, M. M., and Waszczak, B. L. (2010). Brain delivery of proteins by the intranasal route of administration: a comparison of cationic liposomes versus aqueous solution formulations. *J. Pharm. Sci.* 99, 1745–1761. doi: 10.1002/jps.21939

Miller, C. R., Bondurant, B., McLean, S. D., McGovern, K. A., and O'Brien, D. F. (1998). Liposome-cell interactions *in vitro*: effect of liposome surface charge on the binding and endocytosis of conventional and sterically stabilized liposomes. *Biochemistry* 37, 12875–12883. doi: 10.1021/bi980096y

Mishra, A. D., Patel, C. N., and Shah, D. R. (2013). Formulation and optimization of ethosomes for transdermal delivery of ropinirole hydrochloride. *Curr. Drug Deliv.* 10, 500–516. doi: 10.2174/15672018113100050002

Mishra, B., Patel, B. B., and Tiwari, S. (2010). Colloidal nanocarriers: a review on formulation technology, types and applications toward targeted drug delivery. *Nanomedicine* 6, 9–24. doi: 10.1016/j.nano.2009.04.008

Mokgokong, R., Wang, S., Taylor, C. J., Barrand, M. A., and Hladky, S. B. (2014). Ion transporters in brain endothelial cells that contribute to formation of brain interstitial fluid. *Pflugers Arch.* 466, 887–901. doi: 10.1007/s00424-013-1342-9

Mourtas, S., Lazar, A. N., Markoutsa, E., Duyckaerts, C., and Antimisiaris, S. G. (2014). Multifunctional nanoliposomes with curcumin-lipid derivative and brain targeting functionality with potential applications for alzheimer disease. *Eur. J. Med. Chem.* 80, 175–183. doi: 10.1016/j.ejmech.2014.04.050

Nageeb El-Helaly, S., Abd Elbary, A., Kassem, M. A., and El-Nabarawi, M. A. (2017). Electrosteric stealth rivastigmine loaded liposomes for brain targeting: preparation, characterization, *ex vivo*, bio-distribution and *in vivo* pharmacokinetic studies. *Drug Deliv.* 24, 692–700. doi: 10.1080/10717544.2017.1309476

Neves, A. R., Lucio, M., Martins, S., Lima, J. L., and Reis, S. (2013). Novel resveratrol nanodelivery systems based on lipid nanoparticles to enhance its oral bioavailability. *Int. J. Nanomed.* 8, 177–187. doi: 10.2147/IJN.S37840

Noble, G. T., Stefanick, J. F., Ashley, J. D., Kiziltepe, T., and Bilgicer, B. (2014). Ligand-targeted liposome design: challenges and fundamental considerations. *Trends Biotechnol.* 32, 32–45. doi: 10.1016/j.tibtech.2013.09.007

Nunes, S., Madureira, A. R., Campos, D., Sarmento, B., Gomes, A. M., Pintado, M., et al. (2017). Solid lipid nanoparticles as oral delivery systems of phenolic compounds: overcoming pharmacokinetic limitations for nutraceutical applications. *Crit. Rev. Food Sci. Nutr.* 57, 1863–1873. doi: 10.1080/10408398.2015.1031337

Organization, W. H. (2006). *Neurological Disorders: Public Health Challenges*. Genève: World Health Organization (WHO/OMS).

Paliwal, S., Tilak, A., Sharma, J., Dave, V., Sharma, S., Yadav, R., et al. (2019). Flurbiprofen loaded ethosomes - transdermal delivery of anti-inflammatory effect in rat model. *Lipids Health Dis.* 18:133. doi: 10.1186/s12944-019-1064-x

Pandita, D., Kumar, S., Poonia, N., and Lather, V. (2014). Solid lipid nanoparticles enhance oral bioavailability of resveratrol, a natural polyphenol. *Food Res. Int.* 62, 1165–1174. doi: 10.1016/j.foodres.2014.05.059

Pardridge, W. M. (2012). Drug transport across the blood-brain barrier. *J. Cereb. Blood Flow Metab.* 32, 1959–1972. doi: 10.1038/jcbfm.2012.126

Pardridge, W. M. (2015). Targeted delivery of protein and gene medicines through the blood-brain barrier. *Clin. Pharmacol. Ther.* 97, 347–361. doi: 10.1002/cpt.18

Pardridge, W. M., and Boado, R. J. (2012). Reengineering biopharmaceuticals for targeted delivery across the blood-brain barrier. *Meth. Enzymol.* 503, 269–292. doi: 10.1016/B978-0-12-396962-0.00011-2

Phachonpai, W., Wattanathorn, J., Muchimapura, S., Tong-Un, T., and Preechagoon, D. (2010). Neuroprotective effect of quercetin encapsulated liposomes: a novel therapeutic strategy against alzheimer's disease. *Am. J. Appl. Sci.* 7, 480–485. doi: 10.3844/ajassp.2010.480.485

Poewe, W., Antonini, A., Zijlmans, J. C., Burkhard, P. R., and Vingerhoets, F. (2010). Levodopa in the treatment of parkinson's disease: an old drug still going strong. *Clin. Interv. Aging* 5, 229–238. doi: 10.2147/CIA.S6456

Pujara, N. D. (2012). Self emulsifying drug delivery system: a novel approach. *Int. J. Curr. Pharm. Res.* 4, 18–23.

Pulgar, V. M. (2018). Transcytosis to cross the blood brain barrier, new advancements and challenges. *Front. Neurosci.* 12:1019. doi: 10.3389/fnins.2018.01019

Re, F., Cambianica, I., Sesana, S., Salvati, E., Cagnotto, A., Salmona, M., et al. (2011). Functionalization with apoe-derived peptides enhances the interaction with brain capillary endothelial cells of nanoliposomes binding amyloid-beta peptide. *J. Biotechnol.* 156, 341–346. doi: 10.1016/j.jbiotec.2011.06.037

Rip, J., Appeldoorn, C., Manca, F., Dorland, R., Van Kregten, J., and Gaillard, P. (2010). *Receptor-Mediated Delivery of Drugs Across the Blood-Brain Barrier*. Brussels: Pharmacology and Toxicology of the Blood-Brain Barrier: State of the Art, Needs for Future Research and Expected Benefits for the EU.

Rip, J., Chen, L., Hartman, R., van den Heuvel, A., Reijerkerk, A., van Kregten, J., et al. (2014). Glutathione pegylated liposomes: pharmacokinetics and delivery of cargo across the blood-brain barrier in rats. *J. Drug Target* 22, 460–467. doi: 10.3109/1061186X.2014.888070

Risau, W., and Wolburg, H. (1990). Development of the blood-brain barrier. *Trends Neurosci.* 13, 174–178. doi: 10.1016/0166-2236(90)90043-A

Ross, C. A., and Poirier, M. A. (2004). Protein aggregation and neurodegenerative disease. *Nat. Med.* 10, S10–17. doi: 10.1038/nm1066

Rotman, M., Welling, M. M., Bunschoten, A., de Backer, M. E., Rip, J., Nabuurs, R. J., et al. (2015). Enhanced glutathione pegylated liposomal brain delivery of an anti-amyloid single domain antibody fragment in a mouse model for alzheimer's disease. *J. Control. Release* 203, 40–50. doi: 10.1016/j.jconrel.2015.02.012

Sadegh Malvajerd, S., Azadi, A., Izadi, Z., Kurd, M., Dara, T., Dibaei, M., et al. (2019). Brain delivery of curcumin using solid lipid nanoparticles and nanostructured lipid carriers: Preparation, optimization, and pharmacokinetic evaluation. *ACS Chem. Neurosci.* 10, 728–739. doi: 10.1021/acschemneuro.8b00510

Sagare, A. P., Deane, R., and Zlokovic, B. V. (2012). Low-density lipoprotein receptor-related protein 1: a physiological abeta homeostatic mechanism with multiple therapeutic opportunities. *Pharmacol. Ther.* 136, 94–105. doi: 10.1016/j.pharmthera.2012.07.008

Salem, H. F., Ahmed, S. M., Hassaballah, A. E., and Omar, M. M. (2015). Targeting brain cells with glutathione-modulated nanoliposomes: *in vitro* and *in vivo* study. *Drug Des. Devel. Ther.* 9, 3705–3727. doi: 10.2147/DDDT.S85302

Salvati, E., Re, F., Sesana, S., Cambianica, I., Sancini, G., Masserini, M., et al. (2013). Liposomes functionalized to overcome the blood-brain barrier and to target amyloid-beta peptide: the chemical design affects the permeability across an *in vitro* model. *Int. J. Nanomed.* 8, 1749–1758. doi: 10.2147/IJN.S42783

Sarkar, S., and Das, N. (2006). Mannosylated liposomal flavonoid in combating age-related ischemia-reperfusion induced oxidative damage in rat brain. *Mech. Ageing Dev.* 127, 391–397. doi: 10.1016/j.mad.2005.12.010

Scherrmann, J.-M. (2002). Drug delivery to brain via the blood–brain barrier. *Vascul. Pharmacol.* 38, 349–354. doi: 10.1016/S1537-1891(02)00202-1

Selkoe, D. J. (2002). Alzheimer's disease is a synaptic failure. *Science* 298, 789–791. doi: 10.1126/science.1074069

Sharma, G., Lakkadwala, S., Modgil, A., and Singh, J. (2016). The role of cell-penetrating peptide and transferrin on enhanced delivery of drug to brain. *Int. J. Mol. Sci.* 17:806. doi: 10.3390/ijms17060806

Shi, J., Wang, Y., and Luo, G. (2012). Ligustrazine phosphate ethosomes for treatment of alzheimer's disease, *in vitro* and in animal model studies. *AAPS PharmSciTech* 13, 485–492. doi: 10.1208/s12249-012-9767-6

Smeyne, M., and Smeyne, R. J. (2013). Glutathione metabolism and parkinson's disease. *Free Radic. Biol. Med.* 62, 13–25. doi: 10.1016/j.freeradbiomed.2013.05.001

Sokolik, V., Berchenko, O., and Shulga, S. (2017). Comparative analysis of nasal therapy with soluble and liposomal forms of curcumin on rats with alzheimer's disease model. *J. Alzheimers. Dis. Parkinsonism* 7:357. doi: 10.4172/2161-0460.1000357

Sokolik, V. V., Koliada, O. K., and Shulga, S. M. (2016). Effect of beta-amyloid peptide 42 on the dynamics of expression and formation of capital a, cyrillicbeta40, il−1beta, tnf alpha, il−6, il−10 by peripheral blood mononuclear cells in vitro and its correction by curcumin. *Ukrain. Biochem. J.* 88, 109–118. doi: 10.15407/ubj88.01.109

Sokolik, V. V., and Shulga, S. M. (2016). Effect of curcumin on accumulation in mononuclear cells and secretion in incubation medium of capital a, cyrillicbeta(40) and cytokines under local excess of capital a, cyrillicbeta(42)-homoaggregates. *Ukrain. Biochem. J.* 88, 83–91. doi: 10.15407/ubj88.03.083

Spuch, C., and Navarro, C. (2011). Liposomes for targeted delivery of active agents against neurodegenerative diseases (alzheimer's disease and parkinson's disease). *J. Drug Deliv.* 2011:469679. doi: 10.1155/2011/469679

Stefanis, L. (2012). Alpha-synuclein in parkinson's disease. *Cold Spring Harb. Perspect. Med.* 2:a009399. doi: 10.1101/cshperspect.a009399

Tagalakis, A. D., Kenny, G. D., Bienemann, A. S., McCarthy, D., Munye, M. M., Taylor, H., et al. (2014). Pegylation improves the receptor-mediated transfection efficiency of peptide-targeted, self-assembling, anionic nanocomplexes. *J. Control. Release* 174, 177–187. doi: 10.1016/j.jconrel.2013.11.014

Tellone, E., Galtieri, A., Russo, A., Giardina, B., and Ficarra, S. (2015). Resveratrol: a focus on several neurodegenerative diseases. *Oxid. Med Cell Longev.* 2015:392169. doi: 10.1155/2015/392169

Terdthai, T.-U., Panakaporn, W., Jintanaporn, W., and Wathita, P. (2010). Cognitive-enhancing and antioxidant activities of quercetin liposomes in animal model of alzheimer's disease. *Online J. Biol. Sci.* 10, 84–91. doi: 10.3844/ojbsci.2010.84.91

Tosi, G., Fano, R. A., Bondioli, L., Badiali, L., Benassi, R., Rivasi, F., et al. (2011). Investigation on mechanisms of glycopeptide nanoparticles for drug delivery across the blood-brain barrier. *Nanomedicine* 6, 423–436. doi: 10.2217/nnm.11.11

Touitou, E., Dayan, N., Bergelson, L., Godin, B., and Eliaz, M. (2000). Ethosomes - novel vesicular carriers for enhanced delivery: characterization and skin penetration properties. *J. Control. Release* 65, 403–418. doi: 10.1016/S0168-3659(99)00222-9

Uner, M., and Yener, G. (2007). Importance of solid lipid nanoparticles (sln) in various administration routes and future perspectives. *Int. J. Nanomed.* 2, 289–300.

Upadhyay, R. K. (2014). Drug delivery systems, cns protection, and the blood brain barrier. *BioMed Res. Int.* 2014:869269. doi: 10.1155/2014/869269

Vernier, P., Moret, F., Callier, S., Snapyan, M., Wersinger, C., and Sidhu, A. (2004). The degeneration of dopamine neurons in parkinson's disease: Insights from embryology and evolution of the mesostriatocortical system. *Ann. N Y Acad. Sci.* 1035, 231–249. doi: 10.1196/annals.1332.015

Wang, D. G., Liu, W. Y., and Chen, G. T. (2013). A simple method for the isolation and purification of resveratrol from polygonum cuspidatum. *J. Pharm. Anal.* 3, 241–247. doi: 10.1016/j.jpha.2012.12.001

Wang, Y., Xia, Z., Xu, J. R., Wang, Y. X., Hou, L. N., Qiu, Y., et al. (2012). Alpha-mangostin, a polyphenolic xanthone derivative from mangosteen, attenuates beta-amyloid oligomers-induced neurotoxicity by inhibiting amyloid aggregation. *Neuropharmacology* 62, 871–881. doi: 10.1016/j.neuropharm.2011.09.016

Wang, Y., Xu, H., Fu, Q., Ma, R., and Xiang, J. (2011). Protective effect of resveratrol derived from polygonum cuspidatum and its liposomal form on nigral cells in parkinsonian rats. *J. Neurol. Sci.* 304, 29–34. doi: 10.1016/j.jns.2011.02.025

Wang, Z., Zhao, Y., Jiang, Y., Lv, W., Wu, L., Wang, B., et al. (2015). Enhanced anti-ischemic stroke of zl006 by t7-conjugated pegylated liposomes drug delivery system. *Sci. Rep* 5:12651. doi: 10.1038/srep12651

Warren, K. E. (2018). Beyond the blood: brain barrier: the importance of central nervous system (cns) pharmacokinetics for the treatment of cns tumors, including diffuse intrinsic pontine glioma. *Front. Oncol.* 8:239. doi: 10.3389/fonc.2018.00239

Woodle, M. C., and Papahadjopoulos, D. (1989). Liposome preparation and size characterization. *Meth. Enzymol.* 171, 193–217. doi: 10.1016/S0076-6879(89)71012-0

Wyss-Coray, T. (2016). Ageing, neurodegeneration and brain rejuvenation. *Nature* 539, 180–186. doi: 10.1038/nature20411

Yang, J., Song, S., Li, J., and Liang, T. (2014). Neuroprotective effect of curcumin on hippocampal injury in 6-ohda-induced parkinson's disease rat. *Pathol. Res. Pract.* 210, 357–362. doi: 10.1016/j.prp.2014.02.005

Yang, Z. Z., Zhang, Y. Q., Wang, Z. Z., Wu, K., Lou, J. N., and Qi, X. R. (2013). Enhanced brain distribution and pharmacodynamics of rivastigmine by liposomes following intranasal administration. *Int. J. Pharm.* 452, 344–354. doi: 10.1016/j.ijpharm.2013.05.009

Yan-Hong, L., Yong-Hua, W., Yan, L., and Ling, Y. (2006). Mdr1 gene polymorphisms and clinical relevance. *Acta Genet. Sinica* 33, 93–104. doi: 10.1016/S0379-4172(06)60027-9

Zhao, Z., Nelson, A. R., Betsholtz, C., and Zlokovic, B. V. (2015). Establishment and dysfunction of the blood-brain barrier. *Cell* 163, 1064–1078. doi: 10.1016/j.cell.2015.10.067

Zlokovic, B. V. (2008). The blood-brain barrier in health and chronic neurodegenerative disorders. *Neuron* 57, 178–201. doi: 10.1016/j.neuron.2008.01.003

Conflict of Interest: The authors declare that the research was conducted in the absence of any commercial or financial relationships that could be construed as a potential conflict of interest.

Advantages of publishing in Frontiers

OPEN ACCESS
Articles are free to read for greatest visibility and readership

FAST PUBLICATION
Around 90 days from submission to decision

HIGH QUALITY PEER-REVIEW
Rigorous, collaborative, and constructive peer-review

TRANSPARENT PEER-REVIEW
Editors and reviewers acknowledged by name on published articles

Frontiers
Avenue du Tribunal-Fédéral 34
1005 Lausanne | Switzerland

Visit us: www.frontiersin.org
Contact us: info@frontiersin.org | +41 21 510 17 00

REPRODUCIBILITY OF RESEARCH
Support open data and methods to enhance research reproducibility

DIGITAL PUBLISHING
Articles designed for optimal readership across devices

FOLLOW US
@frontiersin

IMPACT METRICS
Advanced article metrics track visibility across digital media

EXTENSIVE PROMOTION
Marketing and promotion of impactful research

LOOP RESEARCH NETWORK
Our network increases your article's readership